



University
of Cyprus

**DEPARTMENT OF CIVIL AND ENVIRONMENTAL
ENGINEERING**

**SEISMIC BEHAVIOUR AND ASSESSMENT OF
REINFORCED CONCRETE ELEMENTS WITH
BRITTLE DETAILS & RETROFITTING USING
ENGINEERED CEMENTITIOUS COMPOSITES**

DOCTOR OF PHILOSOPHY DISSERTATION

ANTHOS I. IOANNOU

2022



**University
of Cyprus**

**DEPARTMENT OF CIVIL AND ENVIRONMENTAL
ENGINEERING**

**SEISMIC BEHAVIOUR AND ASSESSMENT OF
REINFORCED CONCRETE ELEMENTS WITH
BRITTLE DETAILS & RETROFITTING USING
ENGINEERED CEMENTITIOUS COMPOSITES**

IOANNOU ANTHOS IOANNI

**A Dissertation Submitted to the University of Cyprus in Partial Fulfillment
of the Requirements for the Degree of Doctor of Philosophy**

July 2022

ANTHOS I. IOANNOU

©Anthos I. Ioannou, 2022

VALIDATION PAGE

Doctoral Candidate: Ioannou Anthos Ioanni

Doctoral Thesis Title: Seismic Behavior and Assessment of Reinforced Concrete Elements with Brittle Details & Retrofitting with Engineered Cementitious Composites

*The present Doctoral Dissertation was submitted in partial fulfillment of the requirements for the Degree of Doctor of Philosophy at the **Department of Civil and Environmental Engineering** and was approved on the 29th of July 2022 by the members of the **Examination Committee**.*

Examination Committee:

Research Supervisor: _____

(Prof. Stavroula J. Pantazopoulou)

Research Co-Supervisor : _____

(Prof. Michael F. Petrou)

Research Co-Supervisor: _____

(Assoc. Prof. Dimos C. Charmpis)

Committee Member: _____

(Asst. Prof. Katerina Genikomsou)

Committee Member: _____

(Asst. Nicholas Kyriakides)

Committee Member: _____

(Lect. Mavros Marios)

DECLARATION OF DOCTORAL CANDIDATE

The present doctoral dissertation was submitted in partial fulfillment of the requirements for the degree of Doctor of Philosophy of the University of Cyprus. It is a product of original work of my own, unless otherwise mentioned through references, notes, or any other statements.

.....

Anthos I. Ioannou

ΠΕΡΙΛΗΨΗ

Το αντικείμενο της σεισμικής αποτίμησης υφιστάμενων κατασκευών και της αντιμετώπισης του σεισμικού κινδύνου που αυτές εκπροσωπούν για τον ευρύτερο πληθυσμό και την οικονομία ετέθη σε προτεραιότητα μετά από τους σεισμούς της δεκαετίας του 1990 που προκάλεσαν σημαντικές καταστροφές σε μεγάλα αστικά κέντρα (Loma Prieta 1989, Northridge 1994, Athens 1999, Izmit 1999). Για την επόμενη εικοσαετία έγινε εντατική προσπάθεια για την ανάπτυξη μεθοδολογιών αξιολόγησης των υφιστάμενων κατασκευών, με έμφαση στην αποτίμηση της φέρουσας ικανότητάς τους σε ενδεχόμενου μελλοντικού σεισμού αλλά και σε μεθόδους σεισμικής αναβάθμισής τους. Στο χώρο αυτό εισήλθαν δυναμικά οι τεχνολογίες νέων υλικών οι οποίες σε πολλές περιπτώσεις προσέφεραν εύχρηστες και αποτελεσματικές λύσεις για την εξάλειψη πολλών από τις συστημικές ανεπάρκειες των υφιστάμενων έργων.

Για την πρόβλεψη σύνθετων μηχανισμών συμπεριφοράς των δομικών στοιχείων από οπλισμένο σκυρόδεμα (ΟΣ) οι μέθοδοι αποτίμησης στηρίχθηκαν κυρίως στην πειραματική έρευνα, και κατόπιν στην συνθετική αξιολόγηση βάσεων πειραματικών δεδομένων από το σύνολο της διαθέσιμης πειραματικής βιβλιογραφίας. Λόγω της διαφοροποίησης στις πειραματικές διατάξεις των επιμέρους ερευνών που τροφοδότησαν τις βάσεις δεδομένων, σήμερα ακόμη υφίσταται μεγάλη αβεβαιότητα ως προς τα κριτήρια αντοχής και παραμορφωσιμότητας που έχουν εξαχθεί από αυτές τις μελέτες και τα οποία στην συνέχεια έχουν αποτελέσει την βάση των κανονιστικών μεθόδων σεισμικής αποτίμησης. Η επίδραση αυτή, και οι γεωμετρικές μη-γραμμικότητες που εισάγονται στην συμπεριφορά των δομικών στοιχείων αποτελεί ένα από τα αντικείμενα μελέτης της παρούσας διατριβής. Η εργασία επικεντρώνεται σε στοιχεία με έντονη απομείωση της αντοχής με προϊούσα παραμόρφωση, με χαρακτηριστικά ψαθυρής αστοχίας. Διερευνάται η απομείωση διατμητικής αντοχής που αποδίδεται στην επίδραση του μεγέθους της επιβαλλόμενης πλαστιμότητας (ως δείκτη βλάβης) και εξετάζεται τι μέρος αυτής της απομείωσης είναι φαινομενικό, είναι δηλαδή συνέπεια της μη γραμμικότητας που εισάγει η διάταξη φόρτισης. Σημειώνεται ότι ενώ οι διαθέσιμες μέθοδοι εκτίμησης της διατμητικής αντοχής διαφέρουν καθώς είναι κατά κανόνα εμπειρικές, αναγνωρίζουν τη συνεισφορά των επιμέρους μηχανισμών αντίστασης, δηλ. του σκυροδέματος, του οπλισμού διάτμησης και του αξονικού φορτίου. Η μη γραμμικότητα που μελετάται και αφορά την διάταξη φόρτισης επηρεάζει την τελευταία εκ των τριών αυτών

συμμετοχών. Κατόπιν διόρθωσης των τιμών, τα πειραματικά αποτελέσματα συσχετίζονται με μια αναθεωρημένη διατύπωση της διατμητικής αντοχής υποστυλωμάτων, με ιδιαίτερο ενδιαφέρον στα στοιχεία με ανεπαρκείς κατασκευαστικές λεπτομέρειες διαμόρφωσης οπλισμών. Στα πλαίσια της συσχέτισης αυτής πραγματοποιείται αναλυτική διερεύνηση των υφιστάμενων μοντέλων που έχουν ήδη προταθεί χρησιμοποιώντας αριθμητική προσομοίωση με μοντέλα πεπερασμένων στοιχείων και αλγορίθμων βελτιστοποίησης.

Παράλληλα, εξετάζονται οι σημαντικές παράμετροι συμπεριφοράς που επηρεάζουν την ικανότητα παραμόρφωσης του δομικού στοιχείου, συχνά αναφερόμενη και ως σχετική στροφή. Η παράμετρος αυτή επηρεάζεται καθοριστικά από το ρυθμό απομείωσης της διατμητικής αντοχής με αύξουσα επιβαλλόμενη πλαστικότητα, καθώς δεν είναι εγγενής αλλά αντίθετα ορίζεται σε σχέση με ένα χαρακτηριστικό σημείο στον φθιττό κλάδο της περιβάλλουσας αντίστασης. Για τον λόγο αυτό οι επιπτώσεις της διάταξης φόρτισης στο ρυθμό απομείωσης της περιβάλλουσας και άρα στον ορισμό της ικανότητας στροφής, αλλά και στα κριτήρια αποτίμησης των στοιχείων ΟΣ φαίνεται να έχουν σημαντική πρακτική συνέπεια. Σημειώνεται εδώ ότι οι μηχανισμοί διατμητικής αντίστασης επηρεάζονται σημαντικά από την απουσία επαρκών κατασκευαστικών λεπτομερειών όπλισης, και αποσυντίθενται γρήγορα παρουσία είτε σημαντικού αξονικού θλιπτικού φορτίου, είτε μεγάλου ποσοστού διαμήκους εφελκόμενου οπλισμού, είτε απουσία επαρκών αγκυρώσεων. Ιδιαίτερα, η ικανότητα στροφής παλαιού τύπου στοιχείων με ψαθυρές λεπτομέρειες οπλισμών απομειώνεται δραματικά υπό την παρουσία υψηλού αξονικού φορτίου, ενώ επηρεάζεται το μήκος της πλαστικής άρθρωσης που επίσης συμβάλει στον ορισμό της ικανότητας παραμόρφωσης του στοιχείου. Οι ιδιότητες αυτές μελετώνται στην παρούσα διατριβή μέσω ανελαστικής προσομοίωσης με πεπερασμένα στοιχεία, ως συνέχεια της μελέτης για την σχέση διατμητικής αντοχής και αξονικού φορτίου που προαναφέρθηκε.

Για την αποκατάσταση της φέρουσας ικανότητας στοιχείων ΟΣ παλαιού τύπου με ανεπάρκειες αντοχής και παραμορφωσιμότητας εξετάζεται η χρήση μιας νέας μεθοδολογίας η οποία θεωρείται τοπική ενίσχυση – υπό την έννοια ότι εισάγει ήπια αύξηση της αντοχής αλλά βελτιώνει σημαντικά την ικανότητα παραμόρφωσης χωρίς να επηρεάζει την γεωμετρία του δομικού στοιχείου (όπως θα συνέβαινε με τις παραδοσιακές τεχνικές μανδύα ΟΣ). Ο στόχος αυτός που με πρόσφατες τεχνολογίες επιτυγχάνεται με την προσθήκη μανδύων από ινοπλισμένα πολυμερή (ΙΟΠ), στην παρούσα έρευνα πραγματοποιείται με την αντικατάσταση της επικάλυψης του στοιχείου με μανδύα από ινοπλισμένο τσιμεντούχο κονίαμα (Engineered

Cementitious Composite, ECC) με χαρακτηριστικά κράτυνσης σε αξονικό εφελκυσμό. Η νέα αυτή κατηγορία υλικών προσφέρει πλεονεκτήματα σε σχέση με τις προηγούμενες μεθόδους καθώς απαλλάσσει από τα ζητήματα περιορισμένης διαπνοής που αποτελούν χαρακτηριστικό μειονέκτημα των ΙΟΠ, έχει μεγάλη ανθεκτικότητα, αντοχή και παραμορφωσιμότητα, και εξασφαλίζει έλεγχο της ρηγμάτωσης. Η σημαντική εφελκυστική πλαστιμότητα των υλικών, και ο έλεγχος του ευρους των ρωγμών κατόπιν υπέρβασης του συμβατικού ορίου ρηγμάτωσης που μακροσκοπικά παρουσιάζει χαρακτηριστικά υλικού με κράτυνση οφείλεται αφενός στην ύπαρξη ενός πυκνού δικτύου ιών στην μάζα του υλικού, και αφετέρου στην πολύ λεπτόκοκη και πυκνή σύνθεση του μητρικού κονιάματος.

Η τεχνολογία των αντισεισμικών επισκευών / ενισχύσεων με ECC βρίσκεται ακόμη σε σχετικά πρώιμο στάδιο, καθώς για πολλά έτη η τεχνολογία επικεντρώθηκε στον χαρακτηρισμό των μηχανικών ιδιοτήτων των υλικών και λιγότερο στην εφαρμογή τους σε ενισχύσεις. Στην προτεινόμενη μεθοδολογία η συνεργασία μεταξύ του ECC και του υποστρώματος από απλό σκυρόδεμα σχετικά χαμηλής αντοχής (για παλαιά κτίρια) κρίνεται σημαντική για την επιτυχία της επισκευής/ενίσχυσης. Με την χρήση ενός πειραματικού προγράμματος που περιλαμβάνει δοκιμές διατμητικής αντοχής κατά μήκος κεκλιμένου επιπέδου, άμεσου εφελκυσμού και θλίψης, η εργασία διερευνά τον μηχανισμό μεταφοράς μέσω της διεπιφάνειας των υλικών, με παραμέτρους μελέτης την κλίση της διεπιφάνειας, την τραχύτητα του υποστρώματος, την θλιπτική αντοχή και την σύνθεση του συμβατικού σκυροδέματος. Οι μορφές αστοχίας ελέγχονται τόσο από την τραχύτητα της διεπιφάνειας που προκαλείται από διαφορετικές συνθέσεις σκυροδέματος όσο και από τη γωνία κλίσης της διεπιφάνειας. Με τον υπολογισμό των διατμητικών και ορθών τάσεων στη διεπιφάνεια, το κριτήριο αστοχίας στο σημείο σύνδεσης των υλικών ECC-PC περιγράφεται με τη χρήση ενός μοντέλλου της περιβάλλουσας αστοχίας τύπου Mohr-Coulomb.

Η αντικατάσταση της επικάλυψης με τη χρήση μανδύων περιορισμένου πάχους από υλικά του σύγχρονου αυτού τύπου (ECC) χρησιμοποιείται στην παρούσα πειραματική έρευνα για την εκ των υστέρων ενίσχυση στοιχείων οπλισμένου σκυροδέματος μετά από ρηγμάτωση και ευρύτερη βλάβη που έχει αναπτυχθεί σ' αυτά από προηγούμενη φόρτιση. Οι αρχικές κατασκευαστικές λεπτομέρειες των δοκιμών αντιπροσωπεύουν εφαρμογή παλαιών τύπων μόρφωσης οπλισμού στις κατασκευές οπλισμένου σκυροδέματος, οδηγώντας σε πρόωρες και ψαθυρές αστοχίες. Οι ανεπάρκειες αφορούν τον διαθέσιμο εγκάρσιο οπλισμό και το μήκος αγκύρωσης/μάτισης των διαμηκών ράβδων στα αρχικά δοκίμια. Μετά την δοκιμή σε

μονοτονική και ανακυκλιζόμενη φόρτιση των επισκευασμένων δοκιμίων διερευνήθηκε η συμβολή του περιορισμένου πάχους μανδύα στην ανάκτηση της αντοχής και της παραμόρφωσης του αρχικού δοκιμίου λαμβάνοντας υπόψη τα χαρακτηριστικά της προϋπάρχουσας βλάβης. Τα πειραματικά αποτελέσματα έδειξαν ότι οι μανδύες αντικατάστασης της επικάλυψης από πλάστιμα τσιμεντούχα υλικά (ECC) αποτελούν αποτελεσματική μέθοδο όχι μόνο για αποκατάσταση της αντοχής, αποτροπή ψαθυρών μορφών αστοχίας στο μήκος του στοιχείου, αλλά και ως προς την αύξηση της ικανότητας παραμόρφωσης των επισκευασμένων στοιχείων. Η περιβάλλουσα της πειραματικής απόκρισης βαθμονομήθηκε με την χρήση μη γραμμικής ανάλυσης πεπερασμένων στοιχείων, με κύριο στόχο την βελτίωση της κατανόησης των περιοχών συγκέντρωσης τάσεων και την βαθμονόμηση της μεθοδολογίας αντικατάστασης της επικάλυψης. Διαπιστώθηκε ότι η περίσφιγξη που ασκείται από το μανδύα μπορεί να συσχετιστεί με την εφελκυστική αντοχή του ινοπλισμένου τσιμεντούχου υλικού (ECC) με αποτέλεσμα να ρυθμίζει την ανάκτηση αντοχής. Ωστόσο με την μέθοδο αυτή, αποτρέποντας τις ψαθυρές μορφές αστοχίας στο μήκος του στοιχείου, καθίσταται κρίσιμος ο οπλισμός αγκύρωσης στη θεμελίωση που καθορίζει στη συνέχεια την ικανότητα στροφής του δομικού στοιχείου.

ABSTRACT

Following the seismic events of the 1990s, which caused significant damage to large urban centers, seismic evaluation of existing structures and the management of the seismic risk they represent for the safety of the public and the economy, were identified as pressing priorities by the earthquake engineering community (Loma Prieta 1989, Northridge 1994, Athens 1999, Izmit 1999). For the next two decades, an intensive effort was made to develop methodologies for evaluating existing structures, with the primary emphasis in determining their available load-carrying capacity in the event of a future earthquake, as well as, the design of seismic retrofitting methods. New materials technologies were introduced in this area dynamically and cost-effective solutions to many of the systemic problems of existing construction were developed.

The assessment methods for estimating the behavior of the complex mechanics of reinforced concrete structural elements (R.C) were primarily based on experimental investigation, followed by collective evaluation of experimental databases from the available experimental literature. There is still a lot of uncertainty today about the strength and deformability criteria that have been derived from tests due to the differences in the experimental test setups of the individual research studies that fed into the databases. Following these investigations, the regulatory methods of seismic assessment were developed. One of the topics covered in this thesis is the effect of test setup on the derived criteria, and the second-order effects that the test setups have introduced into the behavior of structural elements. The research focuses on elements that exhibit pronounced strength degradation with plastic deformation and brittle failure characteristics. The shear strength reduction that has been attributed to the magnitude of the imposed ductility (as damage term) is investigated, and it is determined how much of this degradation is recognizable, i.e., how much is a consequence of the experimental set up nonlinearity. While the available methods of assessing shear strength differ because they are all empirical, they all acknowledge the contribution of individual resistance mechanisms, such as concrete, transverse reinforcement, and axial load. The experimental set up nonlinearity has an impact on the last of these three contributions. The experimental results are correlated with a revised formulation of column shear strength after the values have been corrected, with a special focus on elements with inadequate structural detailing configuration. A detailed investigation of the existing models that have already been proposed is carried out within the

framework of this correlation using numerical simulation with finite element models and optimization algorithms.

The important behavioral factors which affect the structural element's deformation capacity, which are commonly referred to as a relative drift, are also investigated. The degradation rate of shear strength with increasing imposed ductility has a significant impact on this parameter, which is defined in relation to a characteristic point in the decaying branch of the envelope resistance curve (i.e., at 80% residual load). As a result, the effects of the experimental setup on the rate of envelope resistance curve degradation and thus on the definition of drift capacity, as well as the criteria for evaluating R.C. elements, appear to have a significant practical consequence. It should be noted that the lack of adequate structural reinforcement details has a significant impact on shear resistance mechanisms, which are quickly decomposed in the presence of either a significant axial compressive load, a high percentage of longitudinal tensile reinforcement, or the absence of adequate anchorages. In the presence of a high axial load, the ability of old-type elements with insufficient construction details to develop lateral drift is dramatically reduced, whereas the length of the plastic hinge is affected significantly, which also contributes to the definition of the element's deformation capacity. As a continuation of the previous study on the relationship between shear strength and axial load, these properties are investigated in the current thesis using inelastic simulation with finite elements.

To restore the load carrying capacity of old type reinforced concrete elements with inadequacies in strength and deformability, a new methodology is being investigated, which is considered to be a local retrofitting scheme – in the sense it that only induces a moderate increase of strength while significantly improving the deformation capacity without affecting the structural element's geometry (as would be the case with conventional jacketing). This goal, which was previously achieved by adding fiber-reinforced polymer (FRP) jackets, is now achieved in the current study by replacing the element's cover with a fiber reinforced cementitious mortar (this material type is known as Engineered Cementitious Composite - ECC) with tension hardening response. This new class of materials has several advantages over previous methods, including the elimination of the limited transpiration that is considered a negative aspect of FRP, high durability, fire resistance, strength, and deformability and crack control. The significant tensile ductility of the ECC materials, as well as the control of crack width after exceeding the conventional cracking limit that macroscopically is interpreted as

tension hardening is owing to the presence of a dense fiber network in the mass of the material, and to the very fine and dense microstructure of the mortar matrix.

The technology of seismic repairs / retrofitting with ECC is still at an early stage, as research has been focused for many years on the characterization of mechanical properties of materials rather than their application in retrofitting techniques. The proposed methodology considers the ECC's interaction with the relatively low strength plain concrete (PC) substrate (for old buildings) as a critical link to the repair / retrofitting success. The project investigates the transfer mechanism through the interface of the materials, with parameters under investigation including interface inclination, substrate roughness, and plain concrete compressive strength, using an experimental program that includes shear strength tests along an inclined plane, direct tensile and compressive tests. The failure modes are affected by the roughness of the interface, which is caused by various concrete mix designs, as well as the angle of the interface inclination. The failure criterion of the interface of ECC-PC materials is described using a model of the Mohr-Coulomb failure envelope type, by calculating the shear and normal stresses at the interface.

The replacement of the plain concrete cover with a low thickness jacket comprising strain hardening ECC materials is used in this experimental investigation for the retrofitting of reinforced concrete elements after cracking and extensive damage that was imparted in them during previous loading. The initial construction details of the specimens represent the application of old reinforcement configuration practices in RC structures, leading to premature and brittle failures. Inadequacies were representative of sparse transverse reinforcement placement and insufficient anchorage/lap-splice lengths of longitudinal reinforcement in the original test specimens. After monotonic and cyclic loading test of the repaired examined specimens, the contribution of the limited jacket thickness to the recovery of the strength and deformation capacity of the original test specimens was investigated considering the characteristics of the pre-damaged condition. The experimental results showed that the cover replacement by ductile concrete materials (ECC) are an effective method not only to restore strength, to prevent brittle mode of failure along the element, but also to increase the deformation capacity of the repaired elements. The envelope curve of the experimental response was calibrated using nonlinear finite element analysis, with the main aim of improving the understanding of the stress concentration areas and calibrating the jacketing replacement methodology. It was found that the confinement exerted by the jacket can be

associated with the high tensile strength of the fiber-reinforced cementitious material (ECC) thus improving the recovery of strength. It is noted however that by preventing the brittle types of failure in the length of the element through ECC jacketing, the anchorage of reinforcement in the foundation may become more vulnerable. This topic is beyond the scope of the present work, however it ought to be addressed in an overall retrofitting design, as it may eventually control the rotation capacity and strength of the retrofitted structural component.

Acknowledgements

The research presented in this thesis was carried out at the University of Cyprus' Department of Civil and Environmental Engineering, under the primary supervision of Professor S. J. Pantazopoulou, and the members of the supervisory committee Professor M. Petrou and D. Charmpis. I'd like to express my gratitude to Prof. S. Pantazopoulou, the project's supervisor, for her outstanding assistance and persistent support. Professor Pantazopoulou was not only present and supportive at every stage of this Thesis's challenge, but she was also an inspiration. Aside from her assistance in formulation the research direction, the experiences she assured I was provided with by participating in multiple webinars and conferences, and the knowledge by being a co-author to the preparation of journal papers are valuable assets that I will carry with me for the rest of my life. The co-supervisors Prof. M. Petrou and Ass. Prof. D. Charmpis supported me throughout the course of my research and provided significant direction and guidance supporting me throughout the project's progress – for all this support I am deeply indebted. The technical staff of the Department of Civil and Environmental Engineering is thanked for their assistance with the experimental program. Dr Antroula Georgiou, a Research Associate in the Department of Civil and Environmental Engineering of the University of Cyprus, provided significant research support by consenting to use the developed mix-design of Fiber Reinforced Concrete from her PhD investigation, while also providing guidance in its mixing on site and insights into the experimental study, and overall support. She and Dr. Ilambas were very helpful in the initiation of the Finite Element Simulations with ABAQUS, and I am very thankful for this collaboration.

Dr Ioannis Balafas, a Special Teaching Staff member at the University of Cyprus' Department of Civil and Environmental Engineering, Charalambos Erotokritou and Panayiotis Persianis, Special Scientists MSc students, are also thanked for their interest in the work and the assistance they provided with the mixing and casting of the specimens. The University of Cyprus financial help in the form of a six-month scholarship under the program "New Researchers" is gratefully acknowledged. In addition, I'd like to thank Tsircon and Kuraray Europe for supplying a part of the PVA fibers used in the experiment, as well as George Garatziotis, Technical Assistant at BASF Construction Chemicals, for providing materials used in the study. Finally, I'd like to offer my heartfelt gratitude to my family for their unwavering support, patience, and understanding.

to my son, wife, parents and sisters

Table of Contents

| | |
|--|----|
| Chapter 1: Introduction | 1 |
| 1.1 Introduction | 1 |
| 1.2 Motivation, Objectives, and General Assumptions | 5 |
| 1.2.1 Motivation | 5 |
| 1.3 Novel Contributions of the Research | 9 |
| 1.4 Structure of the Thesis | 10 |
| Chapter 2: Literature Review | 12 |
| 2.1 Shear transfer mechanism of reinforced concrete column under seismic loading 12 | |
| 2.1.1 Distribution of Normal and Shear Stresses at the Compression Zone | 16 |
| 2.1.2 Shear Failure | 19 |
| 2.1.3 Shear Strength Degradation of Reinforced Concrete Columns Yielding in Flexure | 20 |
| 2.1.4 The Role of Second Order Effects in Shear Strength Degradation | 22 |
| 2.1.5 Findings from Shake Table Tests conducted on Columns | 24 |
| 2.1.6 Static Tests under Cyclic Displacement Reversals | 28 |
| 2.1.7 Summary of Experimental Results – Correction for P-Delta Effects | 31 |
| 2.2 A Review on Fiber Reinforced Cementitious Composites (ECC) | 38 |
| 2.2.1 Historical Evolution Since 1960 and Tensile Strain-hardening | 38 |
| 2.2.1.2 Replacement of Cement by Fly Ash in Concrete | 42 |
| 2.2.3 Available Research in the Literature Related to PC and ECC Interface Interaction | 45 |
| 2.3 Retrofitting strategies through ECC jacketing of RC Columns | 56 |
| 2.3.1 Advantages and Disadvantages of Concrete Jackets | 57 |
| 2.3.2 Jacketing with ECC | 57 |
| 2.4 Review on Finite Element Methods / Analyses of Reinforced Concrete Elements 65 | |
| 2.4.1 General..... | 65 |
| 2.4.2 Literature on Finite Element Analysis Algorithm | 66 |

| | |
|---|-----|
| Chapter 3: Reinforced Concrete Column Limit States | 69 |
| 3.1 Introduction | 69 |
| 3.2 Significant Behaviour Parameters and Open Issues | 71 |
| 3.3 Selection of Dataset Entries | 78 |
| 3.4 Description of Data Base Configurations (Data, Parameters and Description of the Procedure Followed for Data Base Composition) | 79 |
| 3.5 Parametric Analysis for Strength and Deformation Parameters | 84 |
| 3.5.1 Correction for Second Order Effects According to the PEER (Berry et al., 2004) Data Base Manual | 84 |
| 3.5.2 Additional Correction of Second Order Effects | 86 |
| 3.6 Methodology Followed for Dataset Processing | 89 |
| 3.6.1 Shear Strength Degradation | 89 |
| 3.6.2 Correlation of Experimental Values of Drift at Shear and Axial Failure | 94 |
| 3.7 Finite Element Analysis | 97 |
| 3.7.1 Nonlinear Finite Element Analysis | 97 |
| 3.7.1.1 Concrete Damaged Plasticity Model in ABAQUS | 99 |
| 3.7.1.2 Material Modelling | 101 |
| 3.7.1.3 Parametric Analysis | 105 |
| 3.4. Conclusions | 111 |
| Chapter 4: Interface interaction between ECC and Normal-Strength Concrete | 112 |
| 4.1 Introduction | 112 |
| 4.2. The Aim of the Experiment | 114 |
| 4.2.1 Experimental Procedure | 114 |
| 4.2.2 Materials – PC and ECC Mix Designs | 116 |
| 4.3. Specimen Fabrication | 121 |
| 4.3.1 Plain Concrete Preparation | 121 |
| 4.3.2. Fiber Reinforced Concrete Preparation | 122 |
| 4.3.3 Specimen Production Procedure | 125 |
| 4.4 Experiments - Instrumentation Layout | 137 |
| 4.5 Analysis and Discussion of Results | 139 |

| | |
|--|-----|
| 4.5.1 PC and ECC Cylinders under Uniaxial Compression | 139 |
| 4.5.2 Four Point Bending Tests | 140 |
| 4.5.3 Slanted Shear Tests and Direct Tensile Tests | 144 |
| 4.5.4 Parameters affecting the interface | 153 |
| 4.6. Conclusions | 157 |
| Chapter 5: Members under Monotonic Loading | 159 |
| 5.1 Introductions | 159 |
| 5.2 Experimental Program | 161 |
| 5.2.1. Experimental Setup..... | 161 |
| 5.3. Parameters of the Test Specimens | 162 |
| 5.4. Specimen Design | 164 |
| 5.5. Material Properties | 166 |
| 5.6. Retrofitting Procedure | 169 |
| 5.7 Repair Material | 170 |
| 5.8 Instrumentation | 171 |
| 5.9 Observed Experimental Response | 172 |
| 5.9.1 Damage Profiles and Resistance Curves | 172 |
| 5.9.2 Evaluation of the Flexural Strength of the Specimens | 176 |
| 5.9.3. Envelope Resistance Curves..... | 177 |
| 5.10. Conclusions | 179 |
| Chapter 6: Cyclic Testing of RC Elements Repaired with ECC Cover Replacement .. | 181 |
| 6.1 Introduction | 181 |
| 6.2 Specimen preparation and experimental testing | 182 |
| 6.3 Calculation of Member Resistance Values | 185 |
| 6.4 Instrumentation and Experimental testing procedure | 188 |

| | |
|--|------------|
| 6.5 Experimental Results of the Initial Testing Phase | 189 |
| 6.6 Retrofitting Procedure and Repair Material..... | 192 |
| 6.7 Observed Response of Retrofitted Specimens | 195 |
| 6.8 Numerical Modeling to Determine Cover Replacement Effectiveness | 199 |
| 6.9 Conclusions | 205 |
| Chapter 7: Conclusions and Future Work | 206 |
| 7.1 Conclusions | 206 |
| 7.2 Future Research Plans..... | 208 |
| Appendix A..... | 209 |
| A.1 Inverse Analysis..... | 209 |
| Appendix B..... | 211 |
| B.1 Shear critical columns..... | 212 |
| B.2 Flexure-Shear critical columns..... | 243 |
| Appendix C..... | 288 |
| References..... | 292 |

List of Figures

| | |
|--|----|
| Figure 1. 1 : (a) Regional Tectonic Map in the Around Cyprus (Bowman, 2011); (b) Typical state of old construction | 1 |
| Figure 1. 2 : Tectonic setting and location of Cyprus with reference to the major seismic activity in eastern Mediterranean and the Aegean – map of fault movements in the Samo-Izmir earthquake (red star). [from Sylvain Barbot@quakephysics, https://twitter.com/quakephysics/status/1322242343198621696/photo/1] | 2 |
| Figure 1. 3 : Shear failure of columns in the parking garage of the Digicel building (note the 90-degrees hooks in right photo, Paultre et al., 2013). | 6 |
| Figure 1. 4 : Reinforced concrete failures in flexure and buckling: (a) San Fernando Road Overhead damage due to insufficient flexural ductility in the 1971, San Fernando earthquake (Moehle et al., 2000); (b) Longitudinal reinforcement buckling (Miguel, 2013)..... | 7 |
| Figure 1. 5 : Plastic hinges due to inadequate lap-splice and anchorage length: (a) Loma Prieta earthquake, 1989, brittle bond failure of lap splices at column base (Haroun, 2005); (b) Pull out of reinforcement (Saad et al., 2010) | 8 |
| Figure 2. 1: Shear force and lateral drift in frame members due to horizontal displacement. (a) Sample reference frame subjected to ground excitation; (b) Displaced position, (c) definition of drift ratio | 13 |
| Figure 2. 2 : An advanced state of deformation may be seen in the free body diagram along the diagonal shear-slippage fracture. | 15 |
| Figure 2. 3: (a) Column under cyclic loading; (b) Normal stresses and forces in section <i>e</i> ; (c) Normal stresses and forces in section <i>m</i> ; (d) axial load and moment behavior diagram for section <i>m</i> and <i>e</i> | 18 |
| Figure 2. 4 : Schematic of (a) RC frame column subjected to dynamic loading on a shake table; (b) static cyclic loading using hydraulic piston in individual column specimen. | 24 |
| Figure 2. 5 : Typical layout of dynamic data base; (a) columns connected with common type beams; (b) columns connected with rigid beams. (Source: Li et al., 2013); (c) columns connected with rigid beams (Elwood and Moehle, 2003) | 26 |
| Figure 2. 6 : Experimental envelope curves (a) Shear-flexure columns connected with rigid beams; (b) Shear-flexure columns with low-stiffness beams; (c) shear critical beams (Source: Li et al., 2013)..... | 26 |

| | |
|--|----|
| Figure 2.7 : (a) Experimental lay out; (b) Experimental envelope curve of specimen 3CLH18; (c) Methodology for correction of horizontal forces | 29 |
| Figure 2.8 : (a) Experimental set up of Sokoli and Ghannoum (2016); (b) Horizontal force vs drift response of specimen CS60; (c) Experimental set up of Matchulat and Mantamoros (2008); (d) Horizontal force vs drift response of Specimen 1 | 31 |
| Figure 2.9 : Correction of experimental results considering second order effects with regards to loading conditions (a) Case of fixed column with vertical loading action of piston regardless of rotation; (b) Cantilever case by providing piston load following the elastic line (deformed line) of the specimen (follower loads) (Note here that the rotation at the tip of the cantilever, is 1.5 times the chord drift) | 33 |
| Figure 2.10 : Correction of P-Delta effects..... | 34 |
| Figure 2.11 : Correction of experimental results for columns mentioned from Li, 2009..... | 35 |
| Figure 2.12 : Dependence or relationship of P-Delta effects from experimental setup..... | 36 |
| Figure 2.13 : (a) Experimental layout; (b) Experimental envelope curve Kim et al. (2018). | 37 |
| Figure 2.14 : Typical stress-strain curve or elongation in tension up to complete separation: (a) Standard behavior of FRC composite; (b) Standard behavior of HPCFRCC composite (Naaman, 1987)..... | 38 |
| Figure 2.15 : Critical volume percentage of fibers to carry out strain-hardening behavior in tension..... | 42 |
| Figure 2.16 : Slanted shear test..... | 43 |
| Figure 2.17 : Splitting Test (a) rectangular shaped specimen; (b) circular shaped specimen | 44 |
| Figure 2.18 : (a) Combined specimens with inclined interface planes of 50°, 60°, 70°; (b) Interface roughness conditions of test samples; (c) Test set up..... | 45 |
| Figure 2.19 : Specimen failure modes identification | 46 |
| Figure 2.20: Interface failure by a Mohr-Coulomb type model (proposed by Espeche et al., 2011). | 47 |
| Figure 2.21 : (a) Different surface treatments for PC substrates and (b) test specimens for slanted shear test, splitting tensile test and direct tensile test. | 50 |

| | |
|---|----|
| Figure 2. 22: Average roughness, R_a | 53 |
| Figure 2. 23 : Mean peak-to-valley height, R_z | 54 |
| Figure 2. 24 : Reinforced concrete jacketing of different types of existing reinforced concrete columns (Thermou and Elnashai, 2006) | 56 |
| Figure 2. 25 : Concrete jackets in columns (a) the simplest example; (b) jacket bars bundled near corners, engaged by crossties or octagonal tie; (c) jacket bars bundled at corners, dowels at interface with old column; (d) U-bars welded to corner bars; (e) steel plates welded to corner bars; (f), (g), (h) one- or two-sided jackets; (Thermou and Elnashai, 2006) | 57 |
| Figure 2. 26 : Strengthening types for RC columns using ECC | 58 |
| Figure 2. 27 : Retrofitting detailing of RC short columns (Deng et al., 2018)..... | 59 |
| Figure 2. 28: Dimensions and configurations of columns | 62 |
| Figure 2. 29: Free-body diagrams of: (a) concrete core confined by stirrups; (b) concrete core confined by ECC jacket | 62 |
| | |
| Figure 3. 1: EN model for the contribution of the diagonal strut to shear strength (a) Definition of the strut angle, and (b) definition of the critical crack angle, θ_v | 72 |
| Figure 3. 2: Relationship between ξ , $\rho_{l,tot}$ and normalized axial load ratio, ν , for columns at the onset of yielding..... | 74 |
| Figure 3. 3: Generalized Force - Deformation Relation for Concrete Elements or Components (ASCE/SEI 41, 2017)..... | 75 |
| Figure 3. 4 : Schematic representation of the influence of second order effects in the envelope resistance curve..... | 79 |
| Figure 3. 5: Second order effects incidents according to Berry et.al. 2004..... | 84 |
| Figure 3. 6: Additional corrections for second order effects for cases I, II, III, IV | 88 |
| Figure 3. 7 : Procedure followed for second order effects consideration | 90 |
| Figure 3. 8: Correlation of data base elements experimental corrected maximum shear strength vs. proposed models (a) Proposed model by Pardalopoulos et al. (2013); (b) Proposed model by EN1998-3, 2005; Degradation models of flexure-shear failures after correction of the data. (Green line: Eurocode; Yellow: ASCE/SEI -41) | 91 |

| | |
|---|-----|
| Figure 3. 9: Extra validation data for proposed shear strength model from Pardalopoulos et al. (2013). Correlation of the 3-feature formula. | 93 |
| Figure 3. 10: Extra validation data for proposed shear strength model from EN1998-3 2005: Correlation of the 3-feature formula. | 94 |
| Figure 3. 11: Correlation between analytical vs experimental values: (a) drift at shear failure; (b) drift at axial failure; (c) determination of drift at shear failure according to Elwood and Moehle, (2005)..... | 95 |
| Figure 3. 12 : Flexure-shear critical columns classification according to axial load ratio | 96 |
| Figure 3. 13: Matchulat et al. (2008) Specimen 1 details: (a) Geometrical properties of examined specimen; (b) Finite elements of concrete parts and steel reinforcement rebars..... | 98 |
| Figure 3. 14: Yield surfaces in the deviatoric plane ($K_c = 2/3$ corresponds to the Rankine failure criterion, whereas $K_c = 1$ corresponds to the Drucker–Prager criterion)..... | 100 |
| Figure 3. 15: (a) Plastic potential surface and yield surface in the deviatoric plane, (b) Dilation angle and eccentricity in the meridian plane..... | 101 |
| Figure 3. 16: Uniaxial tensile stress-crack width relationship for concrete..... | 102 |
| Figure 3. 17: Uniaxial compressive stress–strain relationship for concrete. | 103 |
| Figure 3. 18: (a) Tensile damage parameter–strain relationship for concrete; (b) Compressive damage parameter–strain relationship for concrete (simplified in linear form). | 104 |
| Figure 3. 19: Specimen 1 from Matchulat et al. (2008) experimental results: (a) Failure mode; (b) Cyclic loading curve; (c) Experimental envelope resistance curve | 106 |
| Figure 3. 20: Matchulat et al. (2008) experimental envelope curve vs FEA pushover curve considering different levels of axial load ratio. | 107 |
| Figure 3. 21 : Comparison of ratios $((V_{max}-V_{ult}) / V_{max})$ vs $((V_{max}-V_{ult}, P_x\Delta)/V_{max})$ according to theoretical shear force values taken from Figure 3.20 | 108 |
| Figure 3. 22 : FEA models failure modes for different levels of axial load ratios..... | 110 |
| Figure 4. 1: Interface stress states for various test methods: (a) direct tension;(b) pure shear; (c) shear slanted and (d) monolithic compression (Youm et al., 2021)..... | 113 |

| | |
|--|-----|
| Figure 4. 2: Types of experiments: (a) compression test (b) four-point bending test for ECC tensile strength evaluation; (c) splitting test for interface tensile strength evaluation; and (d) combined compression - shear test to define the failure surface model of the interface. | 115 |
| Figure 4. 3 : (a) Limestone sand of 0-4mm size; (b) limestone gravel used of 4-10mm grain size | 116 |
| Figure 4. 4: Grain sizes granulation for aggregates (Mitsrou) (a) Gravel 4-10mm and (b) Sand 0-4mm..... | 117 |
| Figure 4. 5: Grain size distribution for silica sand..... | 118 |
| Figure 4. 6: (a) Dry Aggregates; (b) Mixing after water addition; (c) Concrete slump test . | 121 |
| Figure 4. 7: (a) FRC trial production and mixing procedure in planetary mixer; (b) FRC specimens for tensile and compressive strength tests | 123 |
| Figure 4. 8: (a) Three point bending experimental lay out; (b) Installation of strain gauges on rectangular shaped prisms; (c) Compression test under displacement control | 124 |
| Figure 4. 9; (a) Three-point bending test Force vs. Displacement result (b) Compression test results | 124 |
| Figure 4. 10: (a) Weighed quantities (b) Mixing of powders in dry condition (c) Mixing of powders with half the water volume (d) Mixing of powders with half the SP volume (e) PVA fibers' addition (f) Addition of remaining water and final mixture consistency | 125 |
| Figure 4. 11: (a) Casting of slanted shear specimens in horizontal position; (b), (c) Positioning of SP-N-A specimens for configuration of the free surface (d) Casting of SP-N-SPLIT series | 127 |
| Figure 4. 12: (a) Specimens in laboratory environmental conditions; (b) Sample specimen wire screen for roughness parameter processing; (c) Roughness average and (d) Skewness..... | 129 |
| Figure 4. 13: Concrete Surface Profiles (a) CSP 1; (b) CSP 2; (c) CSP 3; (d) CSP 4; (e) CSP 5; (f) CSP 6; (g) CSP 7; (h) CSP 8; (i) CSP 9 (pictures extracted from Maerz and Myers (2001)) | 130 |
| Figure 4. 14: (a) PC parts placement into the molds; (b) Casting of ECC; (c) and (d) experimental specimens | 131 |

| | |
|--|-----|
| Figure 4. 15: Instrumentation lay out of (a) PC cylinder; (b) ECC cylinder; (c) Rectangular prismatic ECC specimen; (d), (e) Combined (slanted) prismatic specimen (ECC and PC) under compression, and (f) splitting test on combined prism. | 138 |
| Figure 4. 16: Average compression stress and stain envelopes for PC-CYL-N and ECC-CYL-N series of (a) first experimental cycle and (b) second experimental cycle. | 140 |
| Figure 4. 17: Load - Deflection response curves and failure modes of FRC-SPN-BEAM series of (a) first experimental cycle and (b) second experimental cycle. | 141 |
| Figure 4. 18: Third Point Loading of Prism to obtain the resistance curve shown in (b) and from there, through inverse analysis the stress-strain curve shown in (c) and the stress-crack opening displacement in (d). | 143 |
| Figure 4. 19: Slanted shear test method for evaluating the repair/concrete bond strength with applied forces | 144 |
| Figure 4. 20: Types of failure modes (a) Direct interface failure; (b) and (c) PC cracking and failure; (d) Failure penetration in ECC | 153 |
| Figure 4. 21: (a) Normal vs shear stress at the interface plane for first and second experimental batch; (b) Mohr diagram and failure envelopes. | 155 |
| Figure 4. 22: (a) Octahedral stresses according to experimental data; (b) Normalized octahedral stresses | 157 |
| | |
| Figure 5. 1 : (a) Deficient cross-section; (b) Retrofit with reinforced concrete jacket; (c) Retrofit with cover replacement using SHCC. | 160 |
| Figure 5. 2: (a) Test setup; (b) Picture of actual setup; (c) Moment and shear diagrams of the simply supported assembly. | 162 |
| Figure 5. 3: (a) M1.6 Φ 10NL steel reinforcement; (b) M1.6 Φ 10L35 steel reinforcement; (c) Table of lap-splicing and anchorage lengths; (d) M1.6 Φ 10NL section; (e) M3.1 Φ 14NL section; (f) M1.6 Φ 10L35 section; (g) M3.1 Φ 10L35 section; (h) Reaction element section. | 165 |
| Figure 5. 4: Specimens' molds and steel reinforcement configuration: (a) with continuous longitudinal bars; (b) with lap-spliced bars. | 166 |
| Figure 5. 5: (a) Cylinder's compression stress vs. lateral and axial strain curves for normal concrete; (b) Steel reinforcement tensile stress-strain curves. | 167 |

| | |
|--|-----|
| Figure 5. 6: Failure patterns of specimens under monotonic loading: (a) M1.6Φ10NL; (b) M3.1Φ14NL; (c) M1.6Φ10L35; (d) M3.1Φ14L35. | 168 |
| Figure 5. 7: (a) Removal of damaged cover to full revelation of the bars; (b) Bottom extendable form for lower cover cast; (c) Side forms for side and top cover cast; (d) Final result of cover replacement. | 169 |
| Figure 5. 8: Cylinder’s compression stress vs. lateral and axial strain curves for fiber-reinforced concrete..... | 171 |
| Figure 5. 9: Instrumentation layout..... | 172 |
| Figure 5. 10: Failure modes of specimens: (a.1) M1.6Φ10NL vs. (a.2) RM1.6Φ10NL; (b.1) M3.1Φ14NL vs. (b.2) RM3.1Φ14NL; (c.1) M1.6Φ10L35 vs. (c.2) RM1.6Φ10L35; (d.1) M3.1Φ14L35 vs. (d.2) RM3.1Φ14L35..... | 173 |
| Figure 5. 11: Envelope curves of specimens: (a) M1.6Φ10NL vs. RM1.6Φ10NL; (b) M3.1Φ14NL vs. RM3.1Φ14NL; (c) M1.6Φ10L35 vs. RM1.6Φ10L35; (d) M3.1Φ14L35 vs. RM3.1Φ14L35..... | 174 |
| Figure 5. 12: (a) Moment vs. curvature relationships: M1.6Φ10NL vs. RM1.6Φ10NL, and M3.1Φ14NL vs. RM3.1Φ14NL. (b) Estimation of confinement stress, and (c) shear stress contribution provided by the ECC jacket..... | 177 |
| Figure 6. 1: (a) Test setup; (b) Picture of actual setup; (c) Moment and shear diagrams of the simply supported assembly (blue: loading downwards, gray: upwards) (d) Schematic representation of shear span..... | 183 |
| Figure 6. 2: (a) C1.6Φ10NL and C3.1Φ14NL steel reinforcement and specimens’ section; (b) C1.6Φ10L35 and C3.1Φ14L35 steel reinforcement and specimens’ section..... | 185 |
| Figure 6. 3: Outline of the instrumentation equipment..... | 188 |
| Figure 6. 4: Cyclic displacement history of the central stub used in all tests (specimens in original and in repaired condition)..... | 189 |
| Figure 6. 5: Failure modes of specimens before retrofit: (a) C1.6Φ10NL; (b) C1.6Φ10L35; (c) C3.1Φ14NL; (d) M3.1Φ14L35..... | 191 |

| | |
|---|-----|
| Figure 6. 6: A modular form is used to cast the jacket: (a) lower cover cast from the side; (b) Side forms are placed for casting of the sides; (c) Leveling of top cover; (d) After formwork removal; (e) retrofitted specimens ready for testing; (f) Sectional detail of the modular form. | 194 |
| Figure 6. 7: Additional retrofitting of central stub and supporting part of the specimen | 194 |
| Figure 6. 8: Cyclic loading curves of specimens: (a) RC1.6Φ10NL; (b) RC3.1Φ14NL; (c) RC1.6Φ10L35; (d) RC3.1Φ14L35. | 195 |
| Figure 6. 9: Failure modes of specimens after retrofitting: (a) RC1.6Φ10NL; (b) RC1.6Φ10L35; (c) RC3.1Φ14NL; (d) RC3.1Φ14L35 | 196 |
| Figure 6. 10: (a) Comparison between monotonically and cyclically loaded specimen pairs. (b) Ratio of retrofitted to initial specimen strength | 197 |
| Figure 6. 11: Finite element model: (a) Partitioning; (b) Boundary conditions | 200 |
| Figure 6. 12: (a) C1.6Φ10NL crack patterns and Monotonic response envelopes; (b) same for RC3.6Φ14L35..... | 200 |
| Figure 6. 13: Comparison of the response curves obtained from the parametric investigation | 203 |
| Figure 6. 14: Cracking patterns (Ultimate limit state) obtained for the parametric cases studied | 204 |
| Figure B. 1: Specimen SCD2 experimental envelope curve and response 2000 section and member analysis (Lynn et al., 1998)..... | 212 |
| Figure B. 2: Specimen 25.033(East) experimental envelope curve and response 2000 section and member analysis (Wight and Sozen, 1971)..... | 213 |
| Figure B. 3: Specimen 25.033(West) experimental envelope curve and response 2000 section and member analysis (Wight and Sozen, 1971)..... | 214 |
| Figure B. 4: Specimen OA2, experimental envelope curve and response 2000 section and member analysis (Arakawa et al., 1989)..... | 215 |
| Figure B. 5: Specimen OA5, experimental envelope curve and response 2000 section and member analysis (D). | 216 |
| Figure B. 6: Specimen CUW, experimental envelope curve and response 2000 section and member analysis (Umehara and Jirsa, 1982). | 218 |

| | |
|---|-----|
| Figure B. 7: Specimen 2CUS, experimental envelope curve and response 2000 section and member analysis (Umehara and Jirsa, 1982). | 219 |
| Figure B. 8: Specimen 1-1, experimental envelope curve and response 2000 section and member analysis (Bett et al., 1985). | 220 |
| Figure B. 9: Specimen SC3, experimental envelope curve and response 2000 section and member analysis (Aboutaha et al., 1999)..... | 221 |
| Figure B. 10: Specimen SC9, experimental envelope curve and response 2000 section and member analysis (Aboutaha et al., 1999)..... | 222 |
| Figure B. 11: Specimen 104-08, experimental envelope curve and response 2000 section and member analysis (Zhou et al., 1987)..... | 223 |
| Figure B. 12: Specimen 114-08, experimental envelope curve and response 2000 section and member analysis (Zhou et al., 1987)..... | 224 |
| Figure B. 13: Specimen B1, experimental envelope curve and response 2000 section and member analysis (Heankhaus et al., 2013). | 225 |
| Figure B. 14: Specimen B2, experimental envelope curve and response 2000 section and member analysis (Heankhaus et al., 2013). | 226 |
| Figure B. 15: Specimen B3, experimental envelope curve and response 2000 section and member analysis (Heankhaus et al., 2013). | 227 |
| Figure B. 16: Specimen B4, experimental envelope curve and response 2000 section and member analysis (Heankhaus et al., 2013). | 228 |
| Figure B. 17: Specimen B5, experimental envelope curve and response 2000 section and member analysis (Heankhaus et al., 2013). | 229 |
| Figure B. 18: Specimen B6, experimental envelope curve and response 2000 section and member analysis (Heankhaus et al., 2013). | 230 |
| Figure B. 19: Specimen B7, experimental envelope curve and response 2000 section and member analysis (Heankhaus et al., 2013). | 231 |
| Figure B. 20: Specimen B8, experimental envelope curve and response 2000 section and member analysis (Heankhaus et al., 2013). | 232 |
| Figure B. 21: Specimen SBd2, experimental envelope curve and response 2000 section and member analysis (Kim et al., 2018)..... | 233 |
| Figure B. 22: Specimen SBd4, experimental envelope curve and response 2000 section and member analysis (Kim et al., 2018). | 234 |

| | |
|--|-----|
| Figure B. 23: Specimen SCd2, experimental envelope curve and response 2000 section and member analysis (Kim et al., 2018). | 235 |
| Figure B. 24: Specimen SDd2, experimental envelope curve and response 2000 section and member analysis (Kim et al., 2018). | 236 |
| Figure B. 25: Specimen SDd4, experimental envelope curve and response 2000 section and member analysis (Kim et al., 2018). | 237 |
| Figure B. 26: Specimen RFd2, experimental envelope curve and response 2000 section and member analysis (Kim et al., 2018). | 238 |
| Figure B. 27: Specimen HPRC10-63 experimental envelope curve and response 2000 section and member analysis (Nagasaka., 1982). | 239 |
| Figure B. 28: Specimen 3SLH18, experimental envelope curve and response 2000 section and member analysis (Lynn et al., 1998). | 240 |
| Figure B. 29: Specimen 3CMD12, experimental envelope curve and response 2000 section and member analysis (Lynn et al., 1998). | 241 |
| Figure B. 30: Specimen 3CMH18, experimental envelope curve and response 2000 section and member analysis (Lynn et al., 1998). | 242 |
| Figure B. 31: Specimen HPRC19-32, experimental envelope curve and response 2000 section and member analysis (Nagasaka., 1982). | 244 |
| Figure B. 32: Specimen 2D16RS, experimental envelope curve and response 2000 section and member analysis (Ohue et al., 1985). | 245 |
| Figure B. 33: Specimen 4D13RS, experimental envelope curve and response 2000 section and member analysis (Ohue et al., 1985). | 246 |
| Figure B. 34: Specimen No 806, experimental envelope curve and response 2000 section and member analysis (Zhou et al., 1985). | 247 |
| Figure B. 35: Specimen No 1007, experimental envelope curve and response 2000 section and member analysis (Zhou et al., 1985). | 248 |
| Figure B. 36: Specimen No 1, experimental envelope curve and response 2000 section and member analysis (Imai and Yamamoto, 1986). | 249 |
| Figure B. 37: Specimen No 1309, experimental envelope curve and response 2000 section and member analysis (Zhou et al., 1985). | 250 |
| Figure B. 38: Specimen 124-08, experimental envelope curve and response 2000 section and member analysis (Zhou et al., 1987). | 251 |

| | |
|---|-----|
| Figure B. 39: Specimen 204-08, experimental envelope curve and response 2000 section and member analysis (Zhou et al., 1987)..... | 252 |
| Figure B. 40: Specimen 223-09, experimental envelope curve and response 2000 section and member analysis (Zhou et al., 1987)..... | 253 |
| Figure B. 41: Specimen 302-07, experimental envelope curve and response 2000 section and member analysis (Zhou et al., 1987)..... | 254 |
| Figure B. 42: Specimen 312-07, experimental envelope curve and response 2000 section and member analysis (Zhou et al., 1987)..... | 255 |
| Figure B. 43: Specimen 322-07, experimental envelope curve and response 2000 section and member analysis (Zhou et al., 1987)..... | 256 |
| Figure B. 44: Specimen CA025C, experimental envelope curve and response 2000 section and member analysis (Ono et al., 1989). | 257 |
| Figure B. 45: Specimen CA060C, experimental envelope curve and response 2000 section and member analysis (Ono et al., 1989). | 258 |
| Figure B. 46: Specimen CB060C, experimental envelope curve and response 2000 section and member analysis (Amitsu, 1991). | 259 |
| Figure B. 47: Specimen 40.033a(East) , experimental envelope curve and response 2000 section and member analysis (Wight and Sozen, 1971). | 260 |
| Figure B. 48: Specimen 40.033a(West), experimental envelope curve and response 2000 section and member analysis (Wight and Sozen, 1971). | 261 |
| Figure B. 49: Specimen 40.048(East), experimental envelope curve and response 2000 section and member analysis (Wight and Sozen, 1971)..... | 262 |
| Figure B. 50: Specimen 40.048(West), experimental envelope curve and response 2000 section and member analysis (Wight and Sozen, 1971). | 263 |
| Figure B. 51: Specimen 40.033(East), experimental envelope curve and response 2000 section and member analysis (Wight and Sozen, 1971)..... | 264 |
| Figure B. 52: Specimen 40.033(West), experimental envelope curve and response 2000 section and member analysis (Wight and Sozen, 1971). | 265 |
| Figure B. 53: Specimen 40.067(East), experimental envelope curve and response 2000 section and member analysis (Wight and Sozen, 1971)..... | 266 |
| Figure B. 54: Specimen 40.067(West), experimental envelope curve and response 2000 section and member analysis (Wight and Sozen, 1971). | 267 |

| | |
|---|-----|
| Figure B. 55: Specimen 40.147(East), experimental envelope curve and response 2000 section and member analysis (Wight and Sozen, 1971)..... | 268 |
| Figure B. 56: Specimen 40.147(West), experimental envelope curve and response 2000 section and member analysis (Wight and Sozen, 1971)..... | 269 |
| Figure B. 57: Specimen 40.082(East), experimental envelope curve and response 2000 section and member analysis (Wight and Sozen, 1971)..... | 270 |
| Figure B. 58: Specimen 40.082(West), experimental envelope curve and response 2000 section and member analysis (Wight and Sozen, 1971). | 271 |
| Figure B. 59: Specimen 2CLH18, experimental envelope curve and response 2000 section and member analysis (Lynn et al., 1998)..... | 272 |
| Figure B. 60: Specimen 3CLH18 experimental envelope curve and response 2000 section and member analysis (Lynn et al., 1998)..... | 273 |
| Figure B. 61: Specimen 2SLH18 experimental envelope curve and response 2000 section and member analysis (Lynn et al., 1998)..... | 274 |
| Figure B. 62: Specimen 3SMD12 experimental envelope curve and response 2000 section and member analysis (Lynn et al., 1998)..... | 275 |
| Figure B. 63: Specimen 2CMH18 experimental envelope curve and response 2000 section and member analysis (Lynn et al., 1998)..... | 276 |
| Figure B. 64: Specimen HC4-8L16-T6-0.1P experimental envelope curve and response 2000 section and member analysis (Xiao and Martirosyan, 1998). | 277 |
| Figure B. 65: Specimen HC4-8L16-T6-0.2P experimental envelope curve and response 2000 section and member analysis (Xiao and Martirosyan, 1998). | 278 |
| Figure B. 66: Specimen 4 experimental envelope curve and response 2000 section and member analysis (Sezen and Moehle, 2002). | 279 |
| Figure B. 67: Specimen 1 experimental envelope curve and response 2000 section and member analysis (Sezen and Moehle, 2002). | 280 |
| Figure B. 68: Specimen 2 experimental envelope curve and response 2000 section and member analysis (Sezen and Moehle, 2002). | 281 |
| Figure B. 69: Specimen CS-60 experimental envelope curve and response 2000 section and member analysis (Sokoli and Ghannoum, 2016)..... | 282 |
| Figure B. 70: Specimen CS-100 experimental envelope curve and response 2000 section and member analysis (Sokoli and Ghannoum, 2016). | 283 |

| | |
|---|-----|
| Figure B. 71: Specimen 1 experimental envelope curve and response 2000 section and member analysis (Matchulat et al., 2005). | 284 |
| Figure B. 72: Specimen 2 experimental envelope curve and response 2000 section and member analysis (Matchulat et al., 2005). | 285 |
| Figure B. 73: Specimen SAd2 experimental envelope curve and response 2000 section and member analysis (Kim et al., 2018). | 286 |
| Figure B. 74: Specimen RGd2 experimental envelope curve and response 2000 section and member analysis (Kim et al., 2018) | 287 |

List of Tables

| | |
|---|-----|
| Table 2. 1: Degradation factors related to shear strength evaluation..... | 21 |
| Table 2. 2 : Studied parameters used in experiments..... | 49 |
| Table 2. 3 : Cohesion and friction coefficients obtained by the direct tensile and slant shear tests | 52 |
| Table 2. 4 : Bond quality is measured in terms of bond strength | 54 |
| Table 2. 5 : Correlation between substrate roughness parameters and bond strength | 55 |
| Table 2. 6 : Specimen details and strengthening effect..... | 59 |
| Table 2. 7 : Material properties for normal concrete | 63 |
| Table 2. 8 : Material properties for UHPFRC..... | 64 |
| | |
| Table 3. 1: Modeling parameters and Numerical Acceptance Criteria for Nonlinear Procedures-Reinforced Concrete Beams according to ASCE/SEI 41, 2017 | 76 |
| Table 3. 2 : Modeling Parameters and Numerical Criteria for Nonlinear Procedures – Reinforced Concrete Columns other than Circular with Spiral Reinforcement or Seismic Hoops as Defined in ACI 318 according to ASCE/SEI 41, 2017 | 77 |
| Table 3. 3: Analysis of data base parameters..... | 80 |
| Table 3. 4: Data set with specimen details..... | 82 |
| Table 3. 5: Specimen Boundary Conditions | 97 |
| | |
| Table 4. 1: Plain concrete mix design of experimental cycle 1 | 117 |
| Table 4. 2: Fly ash declared performance | 119 |
| Table 4. 3: Engineered Cementitious Composite Mix Design..... | 121 |
| Table 4. 4: Experimental specimens coding and dimensions for flexural and compression strength determination | 122 |
| Table 4. 5: Specimen coding scheme and dimensions for flexural and compression strength determination | 126 |

| | |
|---|-----|
| Table 4. 6: First experimental cycle specimens' reference coding and dimensions | 132 |
| Table 4. 7: Substrate level inclination and roughness parameters of PC - first batch of specimens..... | 134 |
| Table 4. 8: Substrate level inclination and roughness parameters of PC second experimental cycle specimens | 136 |
| Table 4. 9: Inverse analysis results of first and second experimental procedures | 143 |
| Table 4. 10: Minimum requirements for interface bond strength of repair material and substrate plain concrete (ACI 546.3R-1413, 2014; Youm et al., 2021)..... | 145 |
| Table 4. 11: Summary of test results at the ultimate | 146 |
| Table 4. 12: Failure modes identified through DIC | 148 |
| Table 4. 13: Splitting tensile strength results | 151 |
| Table 4. 14: DIC from first and second experimental batches..... | 152 |
| Table 5. 1: Specimen parameters' identification code..... | 163 |
| Table 5. 2: Standard concrete mix design and concrete compressive strengths. | 166 |
| Table 5. 3: Strain-hardening ECC mix design. Compressive strength and corresponding compressive strain at peak: $f_{c,ECC} = 45$ MPa, $\epsilon_{co} = 0.0027$ | 170 |
| Table 5. 4: Inverse analysis results..... | 171 |
| Table 5. 5: Characteristic points of the retrofitted envelope curves and ductility μ | 178 |
| Table 6. 1: Cylinder specimens' compressive strengths | 185 |
| Table 6. 2: Bond and lap-splicing strength parameters..... | 187 |
| Table 6. 3: Specimen parameters' identification code. (Letter R stands for repaired) | 188 |
| Table 6. 4: ECC material mix design..... | 193 |
| Table 6. 5: Characteristic points of cyclic loading tests under vertical displacement of the central stub* | 197 |
| Table 6. 6 Concrete Damage Plasticity Model Parameters | 199 |
| Table 6. 7: Normalization of FEA Characteristic points of finite element analysis models under monotonic loading with the respective points emerged from experimental cyclic loading tests | 201 |

| | |
|--|-----|
| Table A. 1 : Inverse analysis parameters | 210 |
| Table C. 1 : Matchulat et al. (2008) Finite Element Analysis Algorithm Details | 288 |
| Table C. 2 : Matchulat et al. (2008) Finite Element Analysis Element Types for Solid Parts | 288 |
| Table C. 3 : Matchulat et al. (2008) Finite Element Analysis Types for Truss Elements (Longitudinal and Transverse Reinforcement) | 289 |
| Table C. 4 : C1.6 Φ 10NL and RC3.6 Φ 14L35 Finite Element Analysis Algorithm Details . | 290 |
| Table C. 5 : : C1.6 Φ 10NL and RC3.6 Φ 14L35 Finite Element Analysis Element Types for Solid Parts | 290 |
| Table C. 6 : C1.6 Φ 10NL and RC3.6 Φ 14L35 Finite Element Analysis Types for Truss Elements (Longitudinal Reinforcement)..... | 291 |
| Table C. 7: C1.6 Φ 10NL and RC3.6 Φ 14L35 Finite Element Analysis Types for Truss Elements (Transverse Reinforcement)..... | 291 |

Chapter 1: Introduction

1.1 Introduction

A large part of the buildings and infrastructure in the developed world was built during the post-world war era, to meet the needs of the intense urbanization that saw the decades following the war. By 1980 structures that represent more than 70% of the built environment had already been constructed. A significant shift in design practices of reinforced concrete, marked by the introduction of ultimate limit states design occurred in the mid-80's. A rapid sequence of revisions occurred in design codes in the 80's and 90's. The version of design methods used today was consolidated in Europe about twenty years ago. A revised version is currently being developed will take hold soon and will govern structural engineering practice for the next few decades till further advances in the state of the art will dictate future revisions.

In Cyprus much of the available reinforced concrete construction was built in a hurry following the invasion and occupation of the Northern part of the island, to meet the housing needs of the refugees. Today these structures are already 50 years old, but they continue to be an integral part of the real estate market on the island and represent an appreciable investment by stakeholders. When examined with regards to the quality of construction, both material-wise and detailing-wise, many of these structures clearly do not meet the current standards (Figure 1.1 (a)). The island combines an appreciable seismic risk, being located in proximity to some active faults (Figure 1.1 (b) and Figure 1.2).

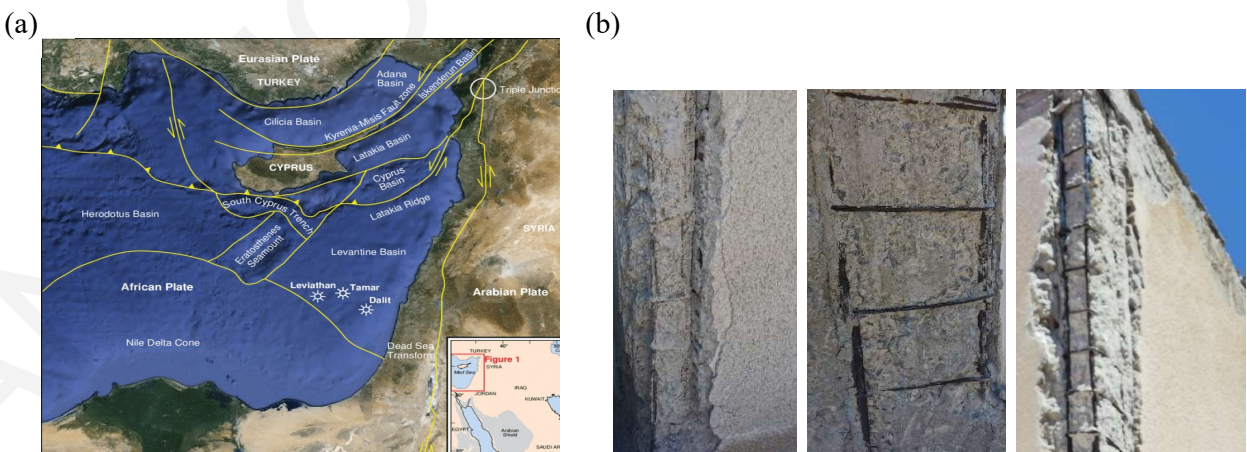


Figure 1.1 : (a) Regional Tectonic Map in the Around Cyprus (Bowman, 2011); (b) Typical state of old construction

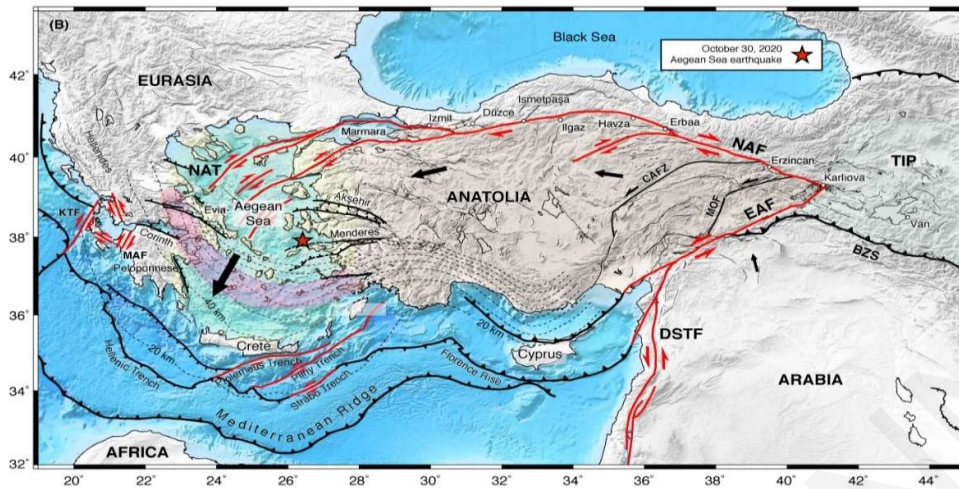


Figure 1. 2 : Tectonic setting and location of Cyprus with reference to the major seismic activity in eastern Mediterranean and the Aegean – map of fault movements in the Samo-Izmir earthquake (red star). [from Sylvain Barbot@quakephysics, <https://twitter.com/quakephysics/status/1322242343198621696/photo/1>]

The question often arises – not only in Cyprus, but in many parts of the world where old construction is exposed to seismic risk: do these structures pose a risk to human life? Time and again, past earthquakes that have hit urban centers indicate that this is a valid concern. At the same time, the same events show that not all older structures have a poor performance – in fact, the vast majority has outlived many earthquakes. Therefore, from the perspective of the duty of care, evaluation of old construction is paramount for the engineering community; coming up with solutions to address the deficiencies is another concern, may be as important as the task of evaluation.

Traditionally, State Authorities have been formulating and enforcing structural design codes and standards, with public safety as the primary objective. As a result, traditional building seismic design codes aim to protect human life by preventing local or global collapse in the case of an earthquake. The requirement for no local collapse usually relates to a rare seismic activity known as "design seismic action" – i.e., an event with a mean return period of 475 years (Fardis, 2009) - in EC8-PART I-2004, the "design seismic action" for ordinary structures has only a 10% chance of being surpassed throughout the period of a 50-year working life, or 0.2% percent in a single year.

The seismic assessment of reinforced concrete structures is based on strength values that can only be accurately evaluated when the failure modes are ductile. When addressing brittle mechanisms of resistance, notably shear transfer and the accompanying deformation capacity, the level of precision is compromised (Chasioti et al., 2014). The major detailing/construction defects associated with RC columns are the poorly anchored and widely spaced transverse reinforcement that promote shear failure and longitudinal compression bar buckling; the presence of smooth longitudinal or transverse reinforcement, the high shear stresses due to short column effects and the inadequate lengths of longitudinal reinforcement lap-splice or anchorage are very common. These characteristics are typical of the development of brittle failures. In significant earthquakes, buildings with columns that have one or more of these vulnerabilities are sensitive to severe damage and may collapse (Opabola et al., 2021, Alvarez, 2017).

Older columns are often slender, and therefore prone to second order effects, a mechanism that consumes part of the available flexural capacity of the member, accelerating the occurrence of failure under lateral excursions such as those caused in sway structures by earthquakes. The geometric second-order effects (also known as $P-\Delta$) have been shown to lead to a considerable increase of the length of the plastic zone, contributing to the destabilizing effects of $P-\Delta$ demands (Burgueño et al., 2016). Second order effects are an integral part of all the experimental studies conducted to study the behaviour of columns; it was shown in the present work that the presence of these effects, although unavoidable in real life, if not recognized explicitly tend to distort the interpretation of the mechanics of shear strength degradation, which is a core component of seismic assessment. For this reason, a large part of the present study is dedicated to the study of degradation of shear strength of columns with brittle details by explicitly recognizing the different mechanisms that are responsible for the decimation of column resistance with increasing lateral swaying displacement.

Concrete is a durable material by nature, but how long it lasts depends on the proportions of the concrete mix, the presence and placement of reinforcement and the detailing, placement, finishing, curing, and maintenance and protection of the structure. Weathering effects and exposure to the elements is known to contribute to deterioration and a possible reduction in its service life. These instances are widespread in existing structures, particularly those built in periods of lax standard enforcement and low construction quality procedures (e.g. site mixing of concrete, empirically). For this reason, the sub-discipline of concrete repair is becoming a

major focus of design and construction as the concrete material technology evolves and the industry develops and grows.

In Cyprus, with the ever increasing number and aged concrete structures, the common practice of neglecting or deferring maintenance, and the increased public awareness of deterioration and maintenance needs as a result of access to information and visual evidence of the performance of structures in earthquakes around the globe, the topic of structural repair is becoming a major focus of design and construction activities. It is noted here that although concrete rehabilitation is thought to combine experience and science, it is rare that engineers and contractors have had any formal training in concrete repair procedures or the performance of repair materials. Personal experience is useful, but it takes time to gain and can be costly in terms of unsuccessful repairs. Even while this is changing, there is currently insufficient data to confidently anticipate repair serviceability and durability. Premature failure of concrete repair will result in financial and serviceability disruptions.

Engineered cementitious composites (ECCs) is a relatively recent advent in cementitious material technology, and their emergence has opened up new opportunities for improving the safety, durability and sustainability of civil infrastructure by minimizing the brittle nature of concrete. ECC has remarkable ductility under tension, a property that was markedly absent in normal concrete. In fact, the strain magnitudes developed by ECC were only seen in ductile metals. This behavior has been made possible by the strategically engineered microstructure of the material and it is manifested by fine closely distributed cracks (Li, 2003; Georgiou, 2017; Shang et al., 2019) that delay the occurrence of crack localization and tensile failure. When considering long-term environmental implications that can be achieved through this substantial crack control, and the savings in reinforcement on account of the intrinsic tensile strength of the material, the advantages of ECC over concrete become much more compelling.

RC structures are prone to cracking due to concrete's poor tensile strength. ECC's high tensile strain capacity can compensate for this limitation, making it an excellent retrofitting material. Several research studies have been conducted investigating the use of ECC in construction details where its ductility would be needed, such as RC beams, columns, and beam-column joints; in some applications, ECC was used for concrete core replacement in damaged plastic hinge zones with remarkable improvements of behavior (Deng et al., 2018; Zhu and Wang 2016; Alsomiri et al., 2021).

In the present study an innovative retrofitting procedure for old RC structural components is developed and studied experimentally and analytically. The procedure effectively replaces the damaged cover of the structural component with an ECC jacket of equal thickness, the advantage of the approach being that the geometric dimensions of the retrofitted component remain unchanged. Previous studies with ECC jacketing for seismic retrofitting of concrete columns have already yielded promising results regarding the functionality of the material as a jacket (Hong et al., 2021); the material used in the present study was designed and made in the laboratory of the University of Cyprus (Georgiou, 2017) after adaptation of past research to the source material availability and their physicochemical properties. Understanding the material properties of these new types of composites, is crucial for considering them in standardized practice. For this reason, apart from the structural retrofitting studies using cover replacement with ECC jackets, the experimental part of the study included thorough characterization tests of the material used against a variety of stress states with particular emphasis on the tensile strain ductility and ECC to Concrete interfacial bond. The study was complemented with detailed finite element simulations of the retrofitted components in order to extend the bounds of the parametric investigation beyond the limits of the experimental program.

1.2 Motivation, Objectives, and General Assumptions

1.2.1 Motivation

Since much of the earthquake design knowledge accumulated gradually over the years, earlier concrete design standards did not include some of the modern essential design criteria to avoid brittle failures during earthquakes. Older construction details (e.g. stirrup layout) were often made with primary motive the simplicity of assembly (e.g. perimeter stirrups, not anchored into the core) and away from regions of reinforcement congestion (e.g. joints); therefore, they do not work well when structural elements are loaded into the inelastic range. Some of the most common earthquake failure mechanisms are:

- [1] Shear failure is a prevalent failure mechanism in older columns, particularly short columns or columns carrying a high axial load. This type of failure is caused by insufficient transverse reinforcement (inadequate spacing, tie-bar diameter and hook anchorage), the large stirrup spacing representing the most serious inadequacy because it may also induce compression reinforcement buckling. Shear failure occurs at low levels of ductility and may occur even before yielding of the longitudinal reinforcement (Figure 1.3). Even if

longitudinal bar yielding precedes, in general, reversed inelastic displacement cycles progressively decrease the column shear capacity, resulting in shear failure following flexural yielding (Moehle et al., 2000). It is noted here that the same result may occur in more modern construction, if the structure is exposure to aggressive environments: because transverse reinforcement has less concrete cover than longitudinal reinforcement, shear load capacity of columns may deteriorate more rapidly than flexural load capacity due to corrosion (Webster, 2000).



Figure 1.3 : Shear failure of columns in the parking garage of the Digicel building (note the 90-degrees hooks in right photo, Paultre et al., 2013).

[2] Column Flexural Strength: For an ideally constructed concrete column subjected to lateral load, the mechanism of failure is flexural. It is noted here that even though most of the inelastic action may be flexural, in the absence of adequate confinement a column with limited ductility may be unable to sustain the imposed flexural deformations (Moehle et al., 2000). Figures 1.4(a) and (b) show instances of columns failing due to insufficient confinement.

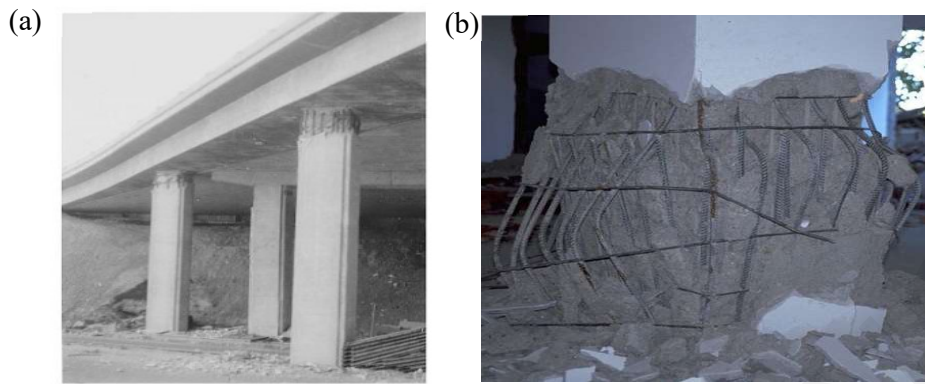


Figure 1.4 : Reinforced concrete failures in flexure and buckling: (a) San Fernando Road Overhead damage due to insufficient flexural ductility in the 1971, San Fernando earthquake (Moehle et al., 2000); (b) Longitudinal reinforcement buckling (Miguel, 2013)

- [3] Inadequate Anchorage and Lap-Splice Length: In RC columns, lap splice failure may be caused by inadequate anchorage length or insufficient confinement over the developed bars (Figure 1.5(a), Haroun 2005). Lap-splices are often located above the footing, where there is a potential plastic hinge zone with high flexural demand. In the absence of adequate confinement, the lap-splices may not be able to develop the column's flexural capacity caused by poor detailing (Pardalopoulos et al., 2011); after a lap failure the member behaves as hinged in the location of the lap splice, which corresponds to a significant reduction of effective stiffness and attainment of nominal strength. In some cases, lap splices were found particularly prone to attracting shear failure before development of yielding because where they occur the effective longitudinal reinforcement ratio is very high; similar effects are seen when large bar sizes, high longitudinal reinforcement yield strengths, short and inadequate concrete cover occur (Priestley et al., 1996). Lap splice failure is caused by a loss of bond; when corrosion affects the bond between steel bars and concrete, this type of failure may be exacerbated. Similarly, inadequate anchoring of the longitudinal reinforcement at the bottom of a column at the foundation interface might cause RC column collapse (Moehle et al., 2000). To provide appropriate post-yield reaction, anchorage is critical, therefore, anchorage failure must be avoided in order to ensure the ductility of the frame. An

example of anchorage failure of a bridge column is depicted in Figure 1.5(b) (Saad et al., 2010).

Motivated by the typical failures outlined in the preceding, which result from common deficiencies in construction details of older structures, and the implications these may have on the value and safety of the existing building stock, the work of this thesis aimed to contribute towards the solutions needed to manage the seismic risk of older construction. This was achieved through analysis of experimental information, intended to understand better brittle failures and contribute towards the evaluation procedures used in seismic assessment; and through testing of new solutions for retrofitting which take advantage of the emerging tension-ductile cement-based materials.

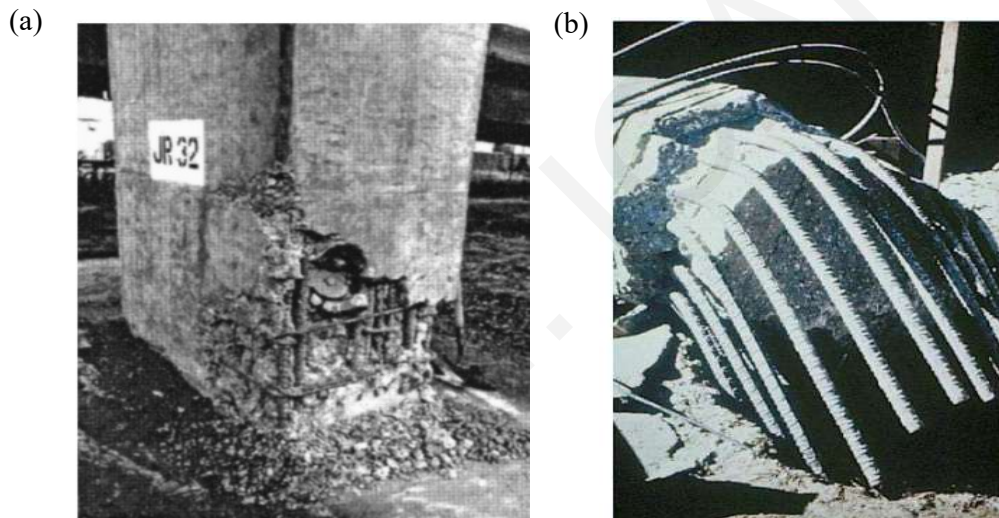


Figure 1.5 : Plastic hinges due to inadequate lap-splice and anchorage length: (a) Loma Prieta earthquake, 1989, brittle bond failure of lap splices at column base (Haroun, 2005); (b) Pull out of reinforcement (Saad et al., 2010)

1.2.2 Objectives of the Work

The available modelling methodologies for estimating the envelope resistance curve of columns – often referred to as backbone curve (ASCE/SEI 41-2017) use closed form, empirical expressions for the strength and deformation terms that define the characteristic points of this envelope. These have been calibrated from experimental databases but are known to be fraught with great scatter and uncertainty. The scatter affects primarily the shear strength estimates and their evolution with deformation demand. In this thesis, a primary objective is to

understand the sources of scatter, and develop improved estimates for this parameter. To achieve that, further experimental calibration of theoretical models was combined with evidence obtained from detailed nonlinear finite element simulation.

A second objective is to contribute to the development through experimental corroboration of retrofitting methods of substandard RC components with the use of advanced cementitious materials with tension-hardening response and to demonstrate they are a viable alternative to function as thin jackets with some improved advantages over FRP wraps. In support of this goal the experimental program included additional characterization tests of the material used for the retrofits. This included documentation of the tension properties and interface test results between conventional concrete and the cementitious jacketing material. Interface roughness was an important variable in this part of the study since retrofitting is applied on rough interfaces. The limits of scope of the experimental research necessarily imposed by the number of variables that could actually be tested in the Lab were extended through a complementary nonlinear finite element parametric investigation, and design expressions for the retrofit methodology were extracted for future practical use.

1.3 Novel Contributions of the Research

The study concentrated in seismic evaluation of reinforced concrete structural components with old type detailing representing former practices and in the development of rehabilitation methods with the help of advanced cementitious composites with large tensile strain capacity beyond the onset of cracking. To reach the objectives of the research, a variety of methods were used involving novel contributions. Evaluation of a database of selected experiments assembled from the literature to represent columns that underwent shear failure under reversed cyclic displacements after yielding was used to corroborate the parametric dependence of the design / assessment methods of shear strength and degradation thereof, and to support the development of new approaches. The rate of degradation of shear strength with increasing displacement demand was re-calibrated after reconsideration of the experimental data to account for the second order effects that tend to accentuate the apparent decay of the postpeak response envelope. The proposed models were developed through AI-based optimization of a physical model for shear strength extracted from first principles; the model was studied parametrically using advanced nonlinear finite element modeling.

The application of novel Engineered Cementitious Composites (ECC) as cover replacement in retrofitting of damaged columns was documented through experimental testing of eight structural components with substandard detailing that modelled old construction practices. These emerging materials have outstanding tensile strain resilience and, upon consideration of their compatibility to concrete structures are considered an ideal alternative to FRP jackets and other forms of retrofit. The study included material characterization tests to secure adequate interfacial strength between the concrete core and the ECC jacket. Design expressions that describe the mechanics of strength and deformation capacity improvements of the encased structural component were derived from first principles and were further corroborated through nonlinear Finite Element Parametric Analysis.

1.4 Structure of the Thesis

The main behavior characteristics and outstanding issues associated to the evaluation – assessment of current reinforced concrete columns in terms of strength and deformability are described in Chapter 2. Next, Chapter 3 presents the methodology for assembling a data base of available reinforced concrete columns that failed in shear before or after flexural yielding was reported, and for consideration of second order effects to account for part of the envelope resistance curve attenuation with increasing displacement ductility. This was followed by a parametric study of shear strength and deformation factors, as well as the proposed model for evaluating reinforced concrete shear strength. A finite element analysis of selected reinforced concrete columns was conducted to verify and confirm the impact of axial load on shear strength magnitude and behavior mechanism while also investigating the impact of plastic hinge length at the column's section above the footing.

The type of experiments carried out for characterization of the mechanical properties of the ECC materials used for retrofitting in the following chapters are described in Chapter 4. The investigation of interface interaction combined specimens from plain concrete (PC) and ECC was also a significant component of the investigation – to this end, Digital Image Correlation (DIC) was used to understand the interface sliding / crushing behavior. Experiments were processed to derive the failure envelope of the interface properties based on the assumptions of plasticity theory.

The experimental evaluation of ECC jackets for the retrofitting of pre-damaged R.C. members under monotonic loading is presented in Chapter 5. Specimen design and preparation, as well

as testing in the first phase to pre-damage the specimens and the retrofitting with cover replacement are presented in detail. The failure modes of retrofitted specimens were also discussed, while design expressions were extracted from mechanistic models that were stated for interpretation of the observed modes of failure.

Chapter 6 extends the description of the experimental program to the cyclically loaded components including again pre-damage and retrofit prior to a final phase of testing. Comparisons are made between monotonically and cyclically loaded samples to gauge the efficacy of the retrofit and the ability of the design equations to quantify the contribution of the jacket. The chapter includes the model description and the results of the parametric finite element investigation conducted to further corroborate the retrofitting methodology. Conclusions of the work are summarized in Chapter 7.

Chapter 2: Literature Review

The objective of the present chapter is to summarize the background work and the state of the art in areas related to the thesis focus. This includes, following the thesis overall layout, three components: (a) A review of assessment methods for shear resistance and drift capacity of RC components; (b) a summary of experimental methodologies used to study the mechanisms of shear transfer in structural RC members; and (c) review of ECC usage as a retrofitting material in jacketing applications.

2.1 Shear transfer mechanism of reinforced concrete column under seismic loading

During seismic excitation with mainly horizontal ground accelerations, structural systems that carry concentrated masses on the floors (such as buildings with stiff diaphragms and bridges) develop horizontal inertial forces due to the acceleration that develops in the center of mass. As a result, the horizontal diaphragm moves from the position of stable equilibrium. The restoring forces that ensure the return to the undeformed configuration after the end of the excitation are the shear forces in the vertical elements as shown in Fig. 2.1. If the deformations developed by the columns during the lateral translation are elastic, then the system returns to its original position. If damage has developed in the columns, then after the completion of the excitation, the system returns to some state of permanent residual displacement from the initial reference point.

The intensity of damage depends on the horizontal maximum relative translation of column ends measured with reference to the undeformed state of the member after elimination of rigid body movements. In order for this translation to be an objective measure of deformation energy or damage intensity, it is given as a fraction of the height of the deformed element and is measured with regards to the tangent at the ends of the element (i.e., as a chord drift or rotation, see Fig. 2.1).

$$\theta = \frac{\delta u}{H} = \theta_i - \theta_j; \quad \delta u = u_i - u_j \quad (2.1)$$

The static relationship between shear and moment is, $V = M/L_s$, where L_s is the distance from the face of the support (critical section) and the point of inflection – referred to in the remainder as shear span. For symmetric moment diagram (same degree of fixity at both ends), where the inflection point is at the mid-height, L_s is equal to $H/2$.

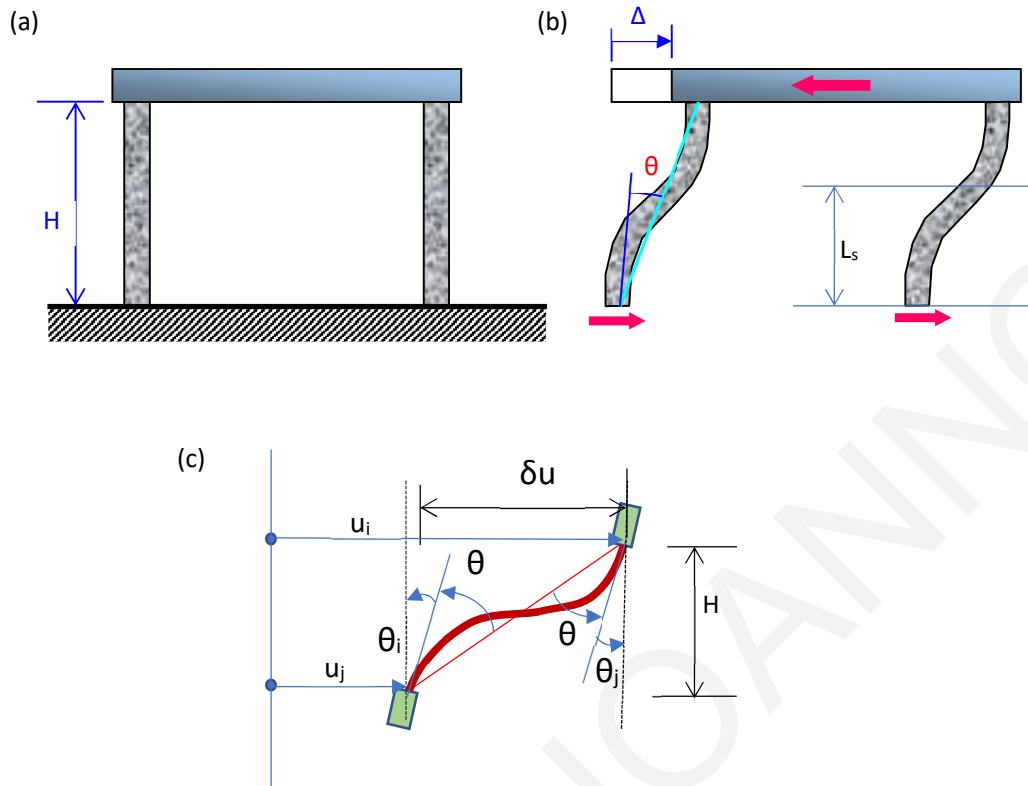


Figure 2. 1: Shear force and lateral drift in frame members due to horizontal displacement. (a) Sample reference frame subjected to ground excitation; (b) Displaced position, (c) definition of drift ratio

Since the earliest literature dating back to the late 19th century, it has been suggested that the shear strength of reinforced concrete members may be estimated as the sum of the contributions of shear reinforcement and concrete: $V_R = V_w + V_c$; [ASCE/SEI 41-2007; EC8-PART III-2005]. Of those terms, V_c was originally treated as a correction to the V_w term which represents the contribution of the stirrups, accounting for the difference between V_w and the experimentally measured resistance of RC members (MacGregor, 1997). Today it is considered to account for the amount of shear force that is transferred, through the compression zone V_{cc} , as well as by the interlocking between aggregates located on opposite sides of the dominant shear crack, V_{ct} , and by dowel action of the reinforcement crossing the shear cracks in the tensile zone V_s (MacGregor, 1997). Over the years an extensive literature has been developed on the subject of shear in reinforced concrete, aiming to formulate predictive expressions and a framework for the estimation of the shear strength of RC elements. The motive for that effort was the

observation that the correlation of design expressions with experimental evidence did not reproduce the parametric sensitivities of the experiments, and in some cases they did not produce conservative approximations of the actual shear strength of elements. This was particularly an issue in cases of seismic action, with a multitude of cases of collapse where shear failures of individual columns or bridge piers caused disproportionately extensive damage to the whole structural system.

It has also been established through thorough review of experimental results, that the carrying capacity of elements is not constant but decreases from the theoretical estimate, as the magnitude of the imposed relative displacement increases. Assessment standards propose relationships for this degradation, where the strength is multiplied with an attenuation coefficient that is inversely proportional to the ductility magnitude of the imposed displacements. This observation, which was first made about 20 years ago, has triggered a major effort in the seismic valuation standards drafting committees in America and Europe with a view to formulate a calibrated reduction factor where the above-mentioned reduction can be estimated with conservatism. Thus, degradation factors have been introduced in the [EC8-PART III-2005](#) and the 2022 draft version, the U.S. standards [ASCE/SEI 41-2007](#), as well as in [KAN.EIIE-2014](#). For example, according to [KAN.EIIE-2014](#), the shear strength, V_R of a reinforced concrete structural element that is subjected to cyclic deformations, decreases depending on the magnitude of the plastic component of the drift ratio, evaluated in the plastic hinge region adjacent to the location of maximum moment.

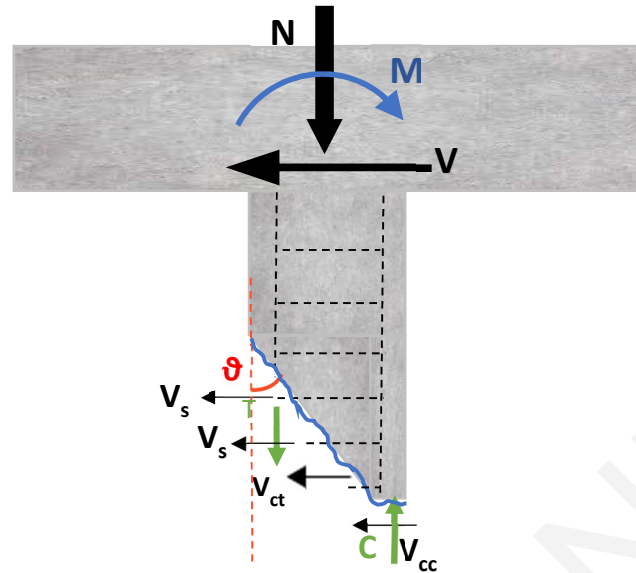


Figure 2. 2 : An advanced state of deformation may be seen in the free body diagram along the diagonal shear-slippage fracture.

According with this approach, the shear strength, as determined at the yielding point of the stirrups, may be considered to decrease with an increasing value of the plastic part of the drift ductility factor, $\mu_{pl,\theta} = \mu_{\theta} - 1$. Similarly, [ASCE/SEI 41-2007](#) uses in the V_R a reduction factor $k(\mu_d)$ which represents the degradation of shear strength as a function of total ductility of displacements. The presence of axial loads on reinforced concrete columns (as opposed to beams) is of paramount importance in the formation of the diagonal cracking mechanism but also in minimizing the effects of reinforcement pullout from supports and lap-splices. This effect is described here both qualitatively and quantitatively. For example, axial compressive stress slows down the formation of diagonal tensile cracks and increases the height of the compression stress zone. At the same time, it increases the value of the shear force that may be carried before the occurrence of diagonal web tensile cracking. Therefore, the resistance against diagonal tensile cracking increases with the value of the axial load ratio ($v = N/(A_c f_{cd})$). An important parameter in the equilibrium of the free body diagram of Fig. 2.2 is the slope of the sliding plane after stirrup yielding (ϑ , measured with respect to the longitudinal axis of the element) because it determines the number of intersected stirrups that are activated in order to maintain equilibrium of the transverse forces. From the first attempts to predict shear strength, the hypothesis that $\vartheta=45^\circ$ was used, which was maintained in the normative relations until recently ([EKΩΣ 2000](#)); recent experimental studies have shown that in the presence of axial

load, the inclination angle with reference to the longitudinal axis of the element decreases close to $25\text{-}30^\circ$ (or vice versa, its complementary, α , the angle of slippage plane with the transverse axis of the element is in the range of 65°); Other parameters that seem to influence the experimental data are the shear ratio of the element and the active surface of the cross-section of the concrete which is used in estimating the term V_c .

2.1.1 Distribution of Normal and Shear Stresses at the Compression Zone

The procedures of the above-mentioned standards ([ASCE/SEI, 41-2007](#); [EC8-PART III, 2005](#); [KAN.EIIE, 2017](#)) are based on the fundamental principles of mechanics where the distribution of shear stresses occurs over the height of the cross section of the bending element. In strength of materials the distribution is parabolic. To simplify the procedure when estimating the contribution of concrete to the shear strength, the parabolic distribution of shear stresses is approximated as an equivalent uniform rectangular distribution extending to the "shear area" of the web, taken equal to $(0.8A_g)$. It is believed that this hypothesis is likely to be problematic, especially during the seismic loading where the open cracks partially obstruct the transfer of the shear to the height of the web. In order to examine this hypothesis, [Syntzirma and Pantazopoulou, 2006](#) had suggested that the axial load should exceed the percentage difference between reinforcement in tension and compression respectively $((\rho_{s1}-\rho_{s2})f_y/f_c)$ as a prerequisite for considering the contribution of the concrete component. This was based on the requirement that shear transfer through the web concrete occurs only when cracks are closed. Indeed, it was recently suggested that only the area of the compression zone of the web $b_w \times c$ should be considered in the calculation of V_c , since this part of the cross-section of the concrete only has the required continuity and consistency for the transfer of stresses ([Frosch et al., 2013](#))

It is also worth noting that the size of the aggregate affects the value of V_c ([Wu et al., 2017](#), [Vechhio et al., 1986](#)), which is thought to be related to the so-called "size effect in shear" discussed in the literature ([Bentz and Collins, 2014](#); [Park et al., 2014](#); [ACI 445 2014](#) and references thereof). Since the term V_{ct} refers to the contribution of concrete to the shear strength, [Bentz et al. \(2006\)](#) correlated it with the size of the force transferred along with the failure level and estimated its value as a function of the longitudinal strain of the element axis (from cross-sectional analysis) and with the amplitude of the dominant shear crack. In addition, committee [ASCE/SEI 41-17, 2017](#) in its recommendation for term V_c noted that it is a function

of the concrete aggregate component, the axial compression force, and the largest ratio of moment to shear times the effective depth for the column under design loadings.

The length and position of the compression zone c varies in the height of the column along with the moment-axial combination that also varies along the height of the laterally swaying column. For example, at the point of inflection where moment is zero, the strains are uniform in the cross section and therefore the entire cross section is in the compression zone. On the other hand, in the ends of the column, where flexural moment is maximum, the compression zone is shrank to a small fraction of the effective depth; this is the region where plastic deformation demands are maximum on account of the combined flexural action in the critical cross section whereas the axial load and the shear force are constant throughout the deformable length of the member. Figure 2.3 depicts the stress conditions occurring at the end cross-section of a swaying column (terms shown under section e) as well as at the mid-height (position of zero curvature, terms identified with section m).

Considering the cross-section in the middle of the column without the bending moment, the compression zone extends to the depth of the entire cross-section. The compressive stress in the cross section is $\nu_o f_c$, where ν_o is the axial load on the column. By contrast, in the end cross section, the normal stress acting in the compression zone c (section e) maintains a compressive force much greater than the axial load due to its parallel action (Fig. 3 (d)). The compressive force F_{ce} is defined by the following equation:

$$F_{ce} + \rho_{s2} b_w d f_{s2,e} - \rho_{s1} b_w d f_{s1,e} - N = 0, \text{ thus } F_{ce} = N + (\rho_{s1} f_{s1,e} - \rho_{s2} f_{s2,e}) b_w d \quad (2.2)$$

where the local compression stress is

$$\sigma_e = \frac{F_{ce}}{b_w c_e} \text{ and } \nu_e = \frac{F_{ce}}{b_w c f_c} \text{ for example, } \nu_e = \frac{\sigma_e}{f_c} \quad (2.3)$$

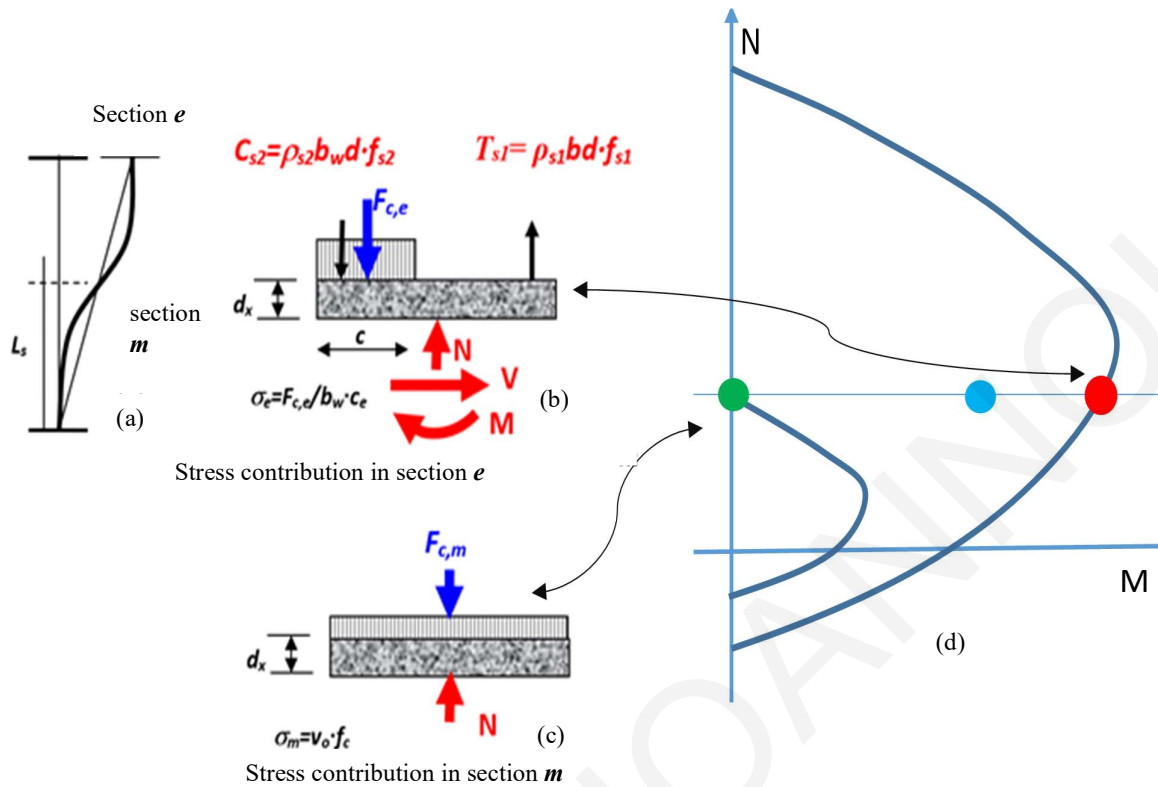


Figure 2. 3: (a) Column under cyclic loading; (b) Normal stresses and forces in section e ; (c) Normal stresses and forces in section m ; (d) axial load and moment behavior diagram for section m and e .

Figure 2.3(d) shows qualitatively the axial load – flexural moment interaction diagram at the failure state of the end cross-section (e) (external envelope curve, red point) and the corresponding diagram for much lower compression stress in the extreme compression fiber and for the corresponding state of stress at the center of column height (m) (green point). The dramatic increase in deformation leading to the external envelope is due to the presence of bending moment in the position (e), (the nominal axial load does not vary, as shown by the horizontal line connecting the red and green marking points; this is an approximation for the sake of illustration; it is valid for the typical column laboratory tests, but in real building conditions, the axial load would fluctuate about the mean value on account of the overturning effect of the earthquake).

2.1.2 Shear Failure

Shear is a predominant stress condition in elements with low aspect ratio a/d , large longitudinal tension reinforcement ratio, ρ_{sl} (or more accurately large difference between tensile and compressive reinforcement ratios), but also in cases with inadequate transverse reinforcement. In these cases, very often the brittle-shear failure may precede the flexural yielding (see blue marking point in Figure 2.3(d)).

To calculate the element shear strength, the local stress at the end cross-sections of the element given in Fig. 2.3 is used as a reference point for calculating the angle of the critical shear crack (i.e. inclination angle ϑ). Here it is assumed that failure develops along the main diagonal crack, while the stirrups that intersect the crack profile are in tension according to the geometry of Moersch truss (Ritter and Moersch, 1909 and MacGregor et al., 1997). Based on the assumption that shear transfer through concrete (term V_c) occurs within the depth of the compression zone, the magnitude of the resulting principal stresses is used to identify two possible failure modes: i.e. (a) by diagonal tension cracking propagating and diminishing the compression zone, (b) by diagonal crushing failure due to compressive strength exceedance. Case (c) is followed by a third form of failure which correlates the strength of the classical Moersch truss model with the yielding transverse reinforcement (Ritter and Moersch, 1909; MacGregor et al., 1997; Ascheeim and Moehle, 1992).

For a linear diagram of the bending moment over the shear span of columns (constant shear force represented by seismic action), the flexural moment at a distance d from the support is: $M_d = (L_s - d) \cdot M_o / L_s$, where M_o is the moment at the support. In addition to bending moment M_d and referring to Equation 2.3, the compressive stress in the compression zone is σ_c while the shear force remains constant. The principal stress direction at the centroid of the compression zone and at a distance d from the support (measured along the longitudinal axis of the member), derived from the basic principles of continuity is:

$$\tan 2\vartheta = \frac{2\tau}{\sigma_x - \sigma_y} \quad (2.4)$$

Setting the principal tensile stress equal to the tensile strength of concrete, the V_c term is estimated from the critical magnitude of shear stress τ_{max} that is obtained from a Mohr-Coulomb type failure criterion after setting $\sigma_x=0$ and $\sigma_y=\sigma_c$ (from Eqn. 2.3):

$$V_c = 0.8\tau_{max} \cdot b_w \cdot c \quad (2.5)$$

The number of stirrups intersecting the critical shear crack is estimated from:

$$n = \frac{d - c}{s} \cdot \tan\vartheta \quad (2.6)$$

and the corresponding contribution of the element web reinforcement to the shear resistance, V_w , is defined by the sum of the forces of the stirrup legs that are parallel to the shear force and intersect the critical shear crack:

$$V_w = A_{s,tr} \cdot f_{y,tr} \cdot \frac{d-c}{s} \cdot \cot\vartheta \quad (2.7)$$

In Equation 2.6, $A_{s,tr}$ is the area of a single stirrup layer crossing the crack plane, $f_{y,tr}$ is the stirrup yield stress, d is the effective height of the cross-section, c is the depth of the compression zone and s is the stirrup spacing.

2.1.3 Shear Strength Degradation of Reinforced Concrete Columns Yielding in Flexure

If the shear strength of the element exceeds its flexural strength (i.e., the shear force required to support flexural yielding), then with the increasing magnitude of seismic displacement, extensive yielding of longitudinal reinforcement spreads in the plastic hinge zone. Beyond this point, the presence of shear generates additional tensile deformations in the transverse and longitudinal reinforcement, thereby widening the diagonal cracks leading to shear failure. The delay (and not the mitigation) of the shear failure after flexural yielding may only be interpreted by the postulate that the shear strength may start off from a high value at small relative drift magnitudes and is gradually reduced with increasing ductility until it is overtaken by the flexural strength of the element which remains almost unaffected by the magnitude of the displacement ductility.

This experimental observation, which was formulated approximately since 1992 (Aschheim and Moehle, 1992) was adopted by many researchers because this kind of postulate can explain the mode of flexure-shear failure often reported in the experimental literature as the occurrence of shear failure after flexural yielding (Lynn and Moehle, 1996; Elwood and Moehle, 2005; Matchulat et al., 2008; Priestley et al., 1996). Thus, many seismic standards

included this information in the process of damage level assessment and failure in real buildings. The approach adopted for shear strength, V_R , is given by the following form:

$$V_R = V_c + V_w = \eta_c \cdot V_{c,o} + \eta_w \cdot V_{w,o} \quad (2.7)$$

where $V_{c,o}$ and $V_{w,o}$ are the reference values for the concrete and transverse reinforcement contribution respectively (Equation 2.7) and $\eta_{c,o}$ and $\eta_{w,o}$ are the degradation factors of the strength conditions with increasing ductility. The literature contains a variety of studies on the determination and correlation of mainly empirical relationships for the evaluation of coefficients $\eta_{c,o}$ and $\eta_{w,o}$ (Kim and Park, 2019; Sezen and Moehle, 2002; Priestley et al., 1994) and even corresponding expressions have been introduced in all known assessment standards (ASCE/SEI 41-17, 2017; EC8-PART, III-2005; KAN.EIPE, 20142). Indicatively, the following table summarizes the most prominent proposals for the shear strength degradation factor values from the literature:

Table 2. 1: Degradation factors related to shear strength evaluation

| Proposed Model | $\eta_{c,o}$ | $\eta_{w,o}$ |
|---------------------------|--|--------------|
| Kim et al. (2019) | $0 \leq (5-\mu)/3 \leq 1$ for seismic detailing $0 \leq (4-\mu)/2 \leq 1$ for limited ductility detailing | 1 |
| Aschheim and Moehle, 1992 | Rectangular shaped columns: $\alpha' = \frac{0.06 \rho_{st} f_{yt}}{\mu_{\Delta}}$ Circular shaped columns: $\alpha' = \frac{0.03 \rho_s f_{yt}}{\mu_{\Delta}}$ | 1 |
| Priestley et al. (1994) | $0.1 \leq k \leq 0.29; \quad \eta = 1-k$ | 1 |

| | | |
|------------------------|--|--|
| Sezen and Moehle, 2002 | $0.7 \leq 1.15 - 0.075\mu_{\Delta} \leq 1$ | $0.7 \leq 1.15 - 0.075\mu_{\Delta} \leq 1$ |
| Biskinis et al. (2004) | $(1 - 0.05 \min(5, \mu_{\Delta}^{pl}))$ | $(1 - 0.05 \min(5, \mu_{\Delta}^{pl}))$ |
| KAN.EHE, 2014 | $(1 - 0.05 \min(5, \mu_{\theta}^{pl}))$ Where, $\mu_{\theta}^{pl} = \mu_{\theta} - 1$ | $(1 - 0.05 \min(5, \mu_{\theta}^{pl}))$ where, $\mu_{\theta}^{pl} = \mu_{\theta} - 1$ |
| ASCE/SEI 41-17, 2017 | $0.7 \leq 1.15 - 0.075\mu_{\Delta} \leq 1$ | $0.7 \leq 1.15 - 0.075\mu_{\Delta} \leq 1$ |

In deriving the above expressions in order to calculate the shear strength, the terms V_{co} and V_{wo} given by Equations 2.8 and 2.9 were used (ASCE/SEI 41-17, 2017).

$$V_{c,o} = \lambda \eta_{c,o} \left(\frac{0.5\sqrt{f_c}}{M/Vd} \sqrt{1 + \frac{P}{0.5\sqrt{f_c}A_g}} \right) 0.8A_g \quad (2.8)$$

$$V_{w,o} = \eta_{w,o} \frac{A_{s,tr} f_{y,tr} d}{s} \quad (2.9)$$

It is noted that Equation 2.9 represents the 45° truss model assumption (i.e., a failure crack oriented at 45° with respect to the longitudinal axis of the element) – a point of significant deviation today between different standards where this parameter has been modified in some cases (e.g., EC-2, 2004b) while maintained in others (e.g., EC8-III, 2004a). The parameter λ which is used in Equation 2.8 is equal to 0.75 for lightweight aggregate concrete and 1 for normal-weight aggregate concrete.

2.1.4 The Role of Second Order Effects in Shear Strength Degradation

It was mentioned earlier that the apparent degradation of shear strength observed in RC structural elements under cyclic horizontal displacement is attributed to mechanisms of decomposition of concrete web that follows after longitudinal reinforcement yielding, such as bi-diagonal cracking and stirrup yielding. However, a recent review of the experiments used to correlate the models used in the relevant standards (e.g. see Table 2.1) indicated that the values of η_c and η_w were extracted from the envelope resistance curves that were obtained from column tests conducted using mostly a cantilever layout under various types of test setups

and boundary conditions. Thus, while the reduction of the envelope resistance curve was partially due to damage accumulation, in many cases a large fraction of the accounted loss appeared to be owing to second-order phenomena caused by the axial load while the column shifted laterally (chord drift). Considering the importance of the degraded shear strength estimate as a function of ductility, $V(\mu)$ in terms of the conclusions it supports in seismic assessment of RC buildings (see EC8-III, 2004(a); KAN.EIIE, 2014), it is necessary to re-examine the experimental research findings. One of the principal objectives of the proposed study is to review the reduction of shear resistance against increasing ductility after correcting the experimental results so that they are compatible with each other (i.e., to represent results with identical boundary conditions and corrected for second-order effects) and then to interpret the mechanical problem with reference to principles of mechanics.

To clarify the influence of the boundary conditions of the pseudo-static cantilever tests, other experimental processes used for column tests are also considered. For example, comparison between the conditions of a dynamic column test conducted on a shake table against the static test where the history of the displacement is driven by a hydraulic actuator at the top of the element (Figure 2.4) highlights the existence of significant differences in the two test categories, mainly for deformations beyond the peak load, owing to the manner of load application. These points are briefly discussed in the next paragraphs.

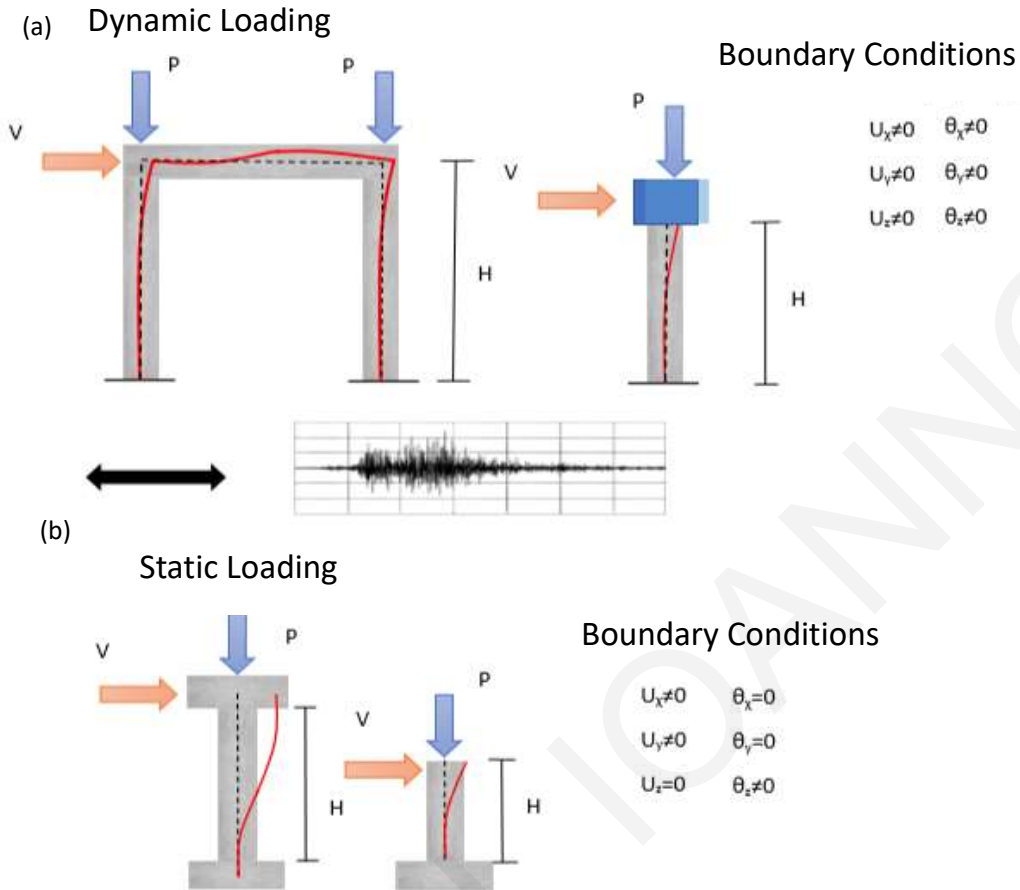


Figure 2.4 : Schematic of (a) RC frame column subjected to dynamic loading on a shake table; (b) static cyclic loading using hydraulic piston in individual column specimen.

2.1.5 Findings from Shake Table Tests conducted on Columns

The number of tests carried out on columns on a shake table to collapse is relatively limited when compared to the hundreds of pseudo-static tests carried out with slow variable static loading and a reversed cyclic displacement history. However, the information that has been extracted is important and relevant to the present study.

Elwood and Moehle (2003) examined shake table tests that were designed to provide information on the degradation of axial load capacity after shear failure of a reinforced concrete column and the subsequent redistribution of shear and axial loads to the remainder of the building system. As shown in Figure 2.5 (c), the test specimens consisted of a three-column frame with a shear-critical central column. The main difference between the two specimens

was the axial load on the middle column. One horizontal component from a scaled ground motion recorded during the 1985 Chile earthquake was applied to both specimens. The specimen with the lower axial load failed in shear but retained the majority of its axial load. For the specimen with a greater axial stress, shear failure of the center column occurred at lower drifts and earlier in the ground motion record, followed by axial failure. Displacement data collected relatively soon after axial failure suggests that the center column shortens via two mechanisms: first, large pulses that cause a sudden increase in vertical displacement after a critical drift is reached; and second, smaller oscillations that appear to "grind down" the shear-failure plane. During the axial failure of the center column, dynamic amplification of axial loads transferred from the center column to the exterior columns was observed.

Li et al. (2013) conducted on several dynamic tests columns on the shake table at U.C.-Berkeley (Elwood, 2003; Ghannoum, 2007; Shin, 2007) and at the National Center for Earthquake Engineering Research (NCEE) in Taiwan (Su, 2007; Kuo, 2008; Wu et al., 2006 and Yavari, 2009). The specimens were subsystems that included columns with reinforcement configuration according to old practices and most were led to failure by applying base excitations of successively increasing intensity. Combined with other similar shake table tests in a Dynamic Database used to correlate the shear strength model (ASCE/SEI 41-17, 2017), the column specimens were categorized into three types depending on the failure mode: flexure, shear-flexure, shear. The grouping criteria were based on the observed column behaviors recorded during the tests.

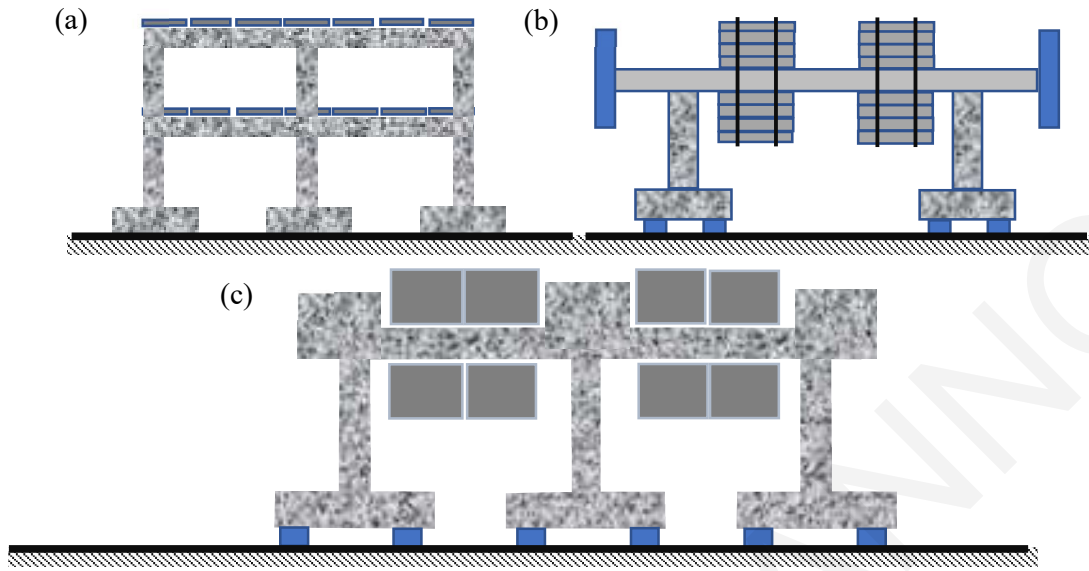


Figure 2. 5 : Typical layout of dynamic data base; (a) columns connected with common type beams; (b) columns connected with rigid beams. (Source: [Li et al., 2013](#)); (c) columns connected with rigid beams ([Elwood and Moehle, 2003](#))

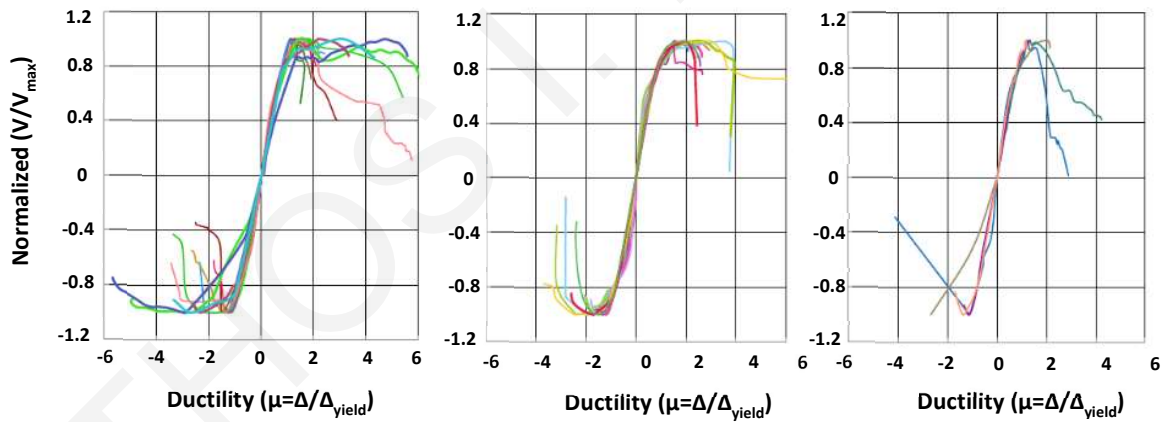


Figure 2. 6 : Experimental envelope curves (a) Shear-flexure columns connected with rigid beams; (b) Shear-flexure columns with low-stiffness beams; (c) shear critical beams (Source: [Li et al., 2013](#)).

Figure 2.6 plots the normalized resistance curve envelopes for the recorded lateral loading in columns where flexure-shear failure mode observed. Here, the activated experimental value of horizontal force has been corrected for the P- Δ phenomena. The x-axis represents ductility,

based on the measured yielding displacement. For uniform definition of terms yield displacement is defined at the point of intersection of the line passing through the point on the envelope that corresponds to 75% of peak and the horizontal line drawn at the peak point of the resistance curve (maximum force measured during the test). Even though all resistance curves showed shear failure (either before or after the flexural yielding), it is noted that all columns had developed ductilities greater than many of the statically tested shear-flexure columns, maintaining their strength without reduction to ductility levels exceeding the value of $\mu = 2$. It is noted that shear failure, i.e. at residual strength equal to 80% of the peak, according with the relationships of Table 2.1, this is achieved at displacement ductility of 4.5 in the Sezen and Moehle model and at 5 in the Eurocode 8/KAN.EPE models. However, the horizontal line at 80% normalized load in Fig. 2.6 (a) intersects the resistance curves at a variety of ductility levels mostly below the value of 4.5 (particularly in the negative response range), indicating that the model may be unconservative for some flexure-shear failure cases obtained from dynamic testing.

Wu et al. (2008) conducted a study on four RC specimens to investigate the envelope resistance curve of short reinforced concrete columns (shear vs. relative drift) until excessive damage or global failure of the element. The specimens carried a relatively low static axial load ($\nu=0.1$) applied using lead loads and were subjected to a simulated seismic excitation of the Chi-Chi earthquake in 1999 [$p_{ga} = 0.221 \text{ m/s}^2$, Wu et al., (2008)]. A comparison with corresponding tests on identical elements under a cyclic static loading showed that the shear strength of the short reinforced concrete elements under dynamic loading was greater than the resulting from the monotonic loading tests. To facilitate the comparison of seismic table experiments with the relevant static loading tests, the experimental values of shear were normalized by the flexural strength V_{flex} , which was calculated from the theoretical yielding moment (after constructing the moment-curvature diagram based on materials experimental properties and for maximum concrete compressive strain equal to 0.003 and monotonic cross-sectional analysis of the member). As shear span of the element, the columns' half height was used which was either 500mm or 375 mm (column sections were 250 mm square, designed to test low and high shear demand, with either ductile or brittle details, as depicted in Figure 2.5). It was found that column shear strength in the dynamic test was slightly higher than in the static cyclic test. The difference was attributed by the higher strain rate in dynamic tests, the energy dissipation within reversed cycles in cyclic testing and the size effect of column specimens in

dynamic test. However, both dynamic and static tests showed strong degradation of lateral resistance – both markedly affected by the presence of P- Δ effects.

2.1.6 Static Tests under Cyclic Displacement Reversals

Contrary to the dynamic tests where the lateral force is owing to the systems' inertia and is therefore generated without external intervention by virtue of the applied base acceleration, the static tests are conducted with the assistance of one or more hydraulic actuators that are supported on a reacting frame/wall. Therefore, the specimen in these setups is only part of a more complex system that comprises all the components linked together and interacting with each other. In this interaction, the stiffness of the specimen as compared with the other components and its connectivity (in parallel or in series with the pistons and the reacting components) may have an important influence on the observed response. In fact, there is the view that the piston – specimen interaction is prominent after the peak (i.e., at the onset of failure). In that stage the piston, acting as a support to the specimen, affects the rate of apparent degradation of strength. Apart from this type of kinematic interaction, which might only be avoided by conducting dynamic tests on a shake table, there is also a variety of other open issues affecting the response of the specimen. One such primary issue is the test's scale: the literature contains hundreds of investigations that have been done on small-scale specimens, but regarding shear strength there is a view that size effects should be considered (Reineck, 2007). In response to this need, in the last 15 years experimental research has been conducted on columns and piers on a 1:1 scale. These tests constitute a point of reference in this study and are therefore collected and reviewed below. The different effects emanating from the experimental test setup are examined and the protocols for the correction of these effects are discussed.

The study of Lynn and Moehle (2001) contains eight full-scale column specimens with light transverse reinforcement (and 90° hook bending), with or without intermediate stirrups (diamond shape stirrups are used to provide lateral support and confinement to the intermediate longitudinal rebars). In this test program, longitudinal reinforcement was considered, with or without lap-splicing. To model old practices, lap-splicing having inadequate length, were placed just above the base. The columns were loaded with a constant axial load and a cyclic horizontal displacement history until the strength loss (loss of vertical load support). During the experiments, all the vertical pistons used to provide the vertical load, contributed to the

maintenance of the stability of horizontal forces due to the inclination of their axis relative to the vertical one (blue arrows in Figure 2.7(c)). These forces were removed from the load which was provided from the horizontal piston to the specimen. However, it should be noted that despite this correction, the second order effects on the specimen itself were not considered, the contribution of which is much greater as shown by the rate of post-peak degradation of the envelope resistance curve after the maximum strength.

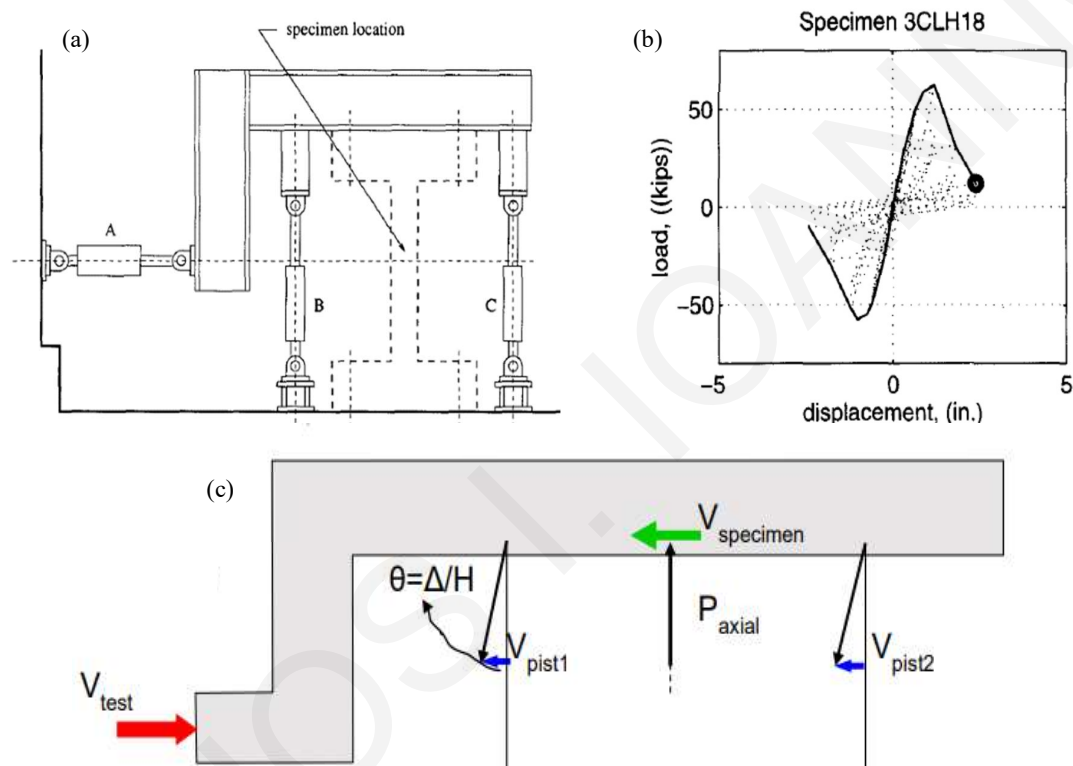


Figure 2.7 : (a) Experimental lay out; (b) Experimental envelope curve of specimen 3CLH18; (c) Methodology for correction of horizontal forces

Free body diagram of experimental layout:

$$P_{test} = P_{pist1} + P_{pist2} \quad P_{axial} = P_{test} \times \cos\theta \approx P_{test}$$

$$\text{Therefore, } V_{pist1} = P_{pist1} \times \sin\theta \approx P_{pist1} \times \theta;$$

$$\text{Similarly, } V_{pist2} = P_{pist2} \times \sin\theta \approx P_{pist2} \times \theta, \text{ και } V_{pist,tot} = P_{test} \times \sin\theta \approx P_{test} \times \theta.$$

Then,

$$V_{\text{specimen}} = V_{\text{test}} - V_{\text{pist1}} - V_{\text{pist2}}$$

Second order effect P-Δ: $2M = V_{\text{specimen}} \times H + P_{\text{test}} \times \Delta$

Thus, the true lateral resistance of the specimen, when referenced to the undeformed configuration is:

$$V_{\text{true}} = (V_{\text{test}} - V_{\text{pist,tot}}) + P_{\text{test}} \cos\theta \times \theta \approx (V_{\text{test}} - V_{\text{pist,tot}}) + P_{\text{test}} \times \theta \approx V_{\text{test}} \quad (2.10)$$

Therefore, this particular test setup has the advantage that is self-corrective – so that the force applied by the horizontal piston is a close approximation to the true shear. Of course, errors exist in this correction, such as for example, that the piston drift is not identical to the specimen drift, since the distance from pivot to pivot is not the same as the deformable length of the specimen. Similarly, the approximations made for the values of the trigonometric functions are becoming increasingly inaccurate with increasing value of the angle.

Due to its self-corrective performance, the type of test setup presented in Fig. 2.7 and 2.8 has been used of recent in many of the larger scale experiments. For example, [Sokoli and Ghannoum \(2016\)](#) among others, have used a similar experimental setup of three reinforced concrete columns with three different types of steel reinforcement detailing. The columns had a similar form of transverse and longitudinal reinforcement and were subjected to high shear stresses resulting from the high percentage of longitudinal reinforcement and at the same time from a relatively high axial load ratio $\nu = 0.27$. The loading procedure of the specimens was applied according to [FEMA 461, 2007](#) where the support of the pistons must be done in such a way so as to apply the target load avoiding any out-of-specimen axis forces and drifts.

[Matchulat and Mantamoros \(2008\)](#) are also worth mentioning. Two full-scale concrete columns were tested as part of a study on the risk of collapse of reinforced concrete building columns built before the mid-1970s. Shear strength reduced the lateral load capability of the columns, which were subjected to high amounts of axial load. The goal of the two tests was to obtain data that would aid in the identification of columns that were experiencing simultaneous shear and axial failure. To model the boundary conditions and reaction of a typical moment-resisting

frame in an actual reinforced concrete building, the columns were loaded in a double curvature configuration as presented in Figure 2.8 (c).

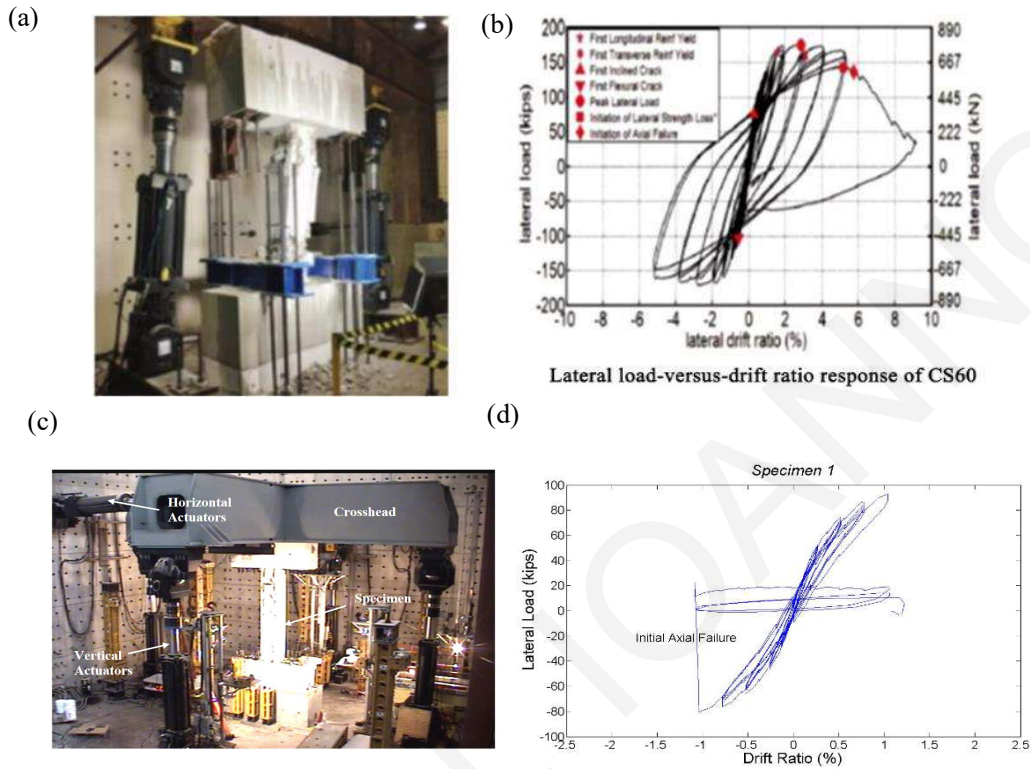


Figure 2.8 : (a) Experimental set up of [Sokoli and Ghannoum \(2016\)](#); (b) Horizontal force vs drift response of specimen CS60; (c) Experimental set up of [Matchulat and Mantamoros \(2008\)](#); (d) Horizontal force vs drift response of Specimen 1

2.1.7 Summary of Experimental Results – Correction for P-Delta Effects

Many test setups that have been used to test columns are not self-corrective. This is particularly the case in half-column specimens that are driven laterally by pistons at the top of the half column. Therefore, in considering specimens from the literature it is essential that the required corrections of shear forces be applied. Usually, the equilibrium of forces is simplified in practice which considering the geometry of the specimen as undeformed. However, as the hydraulic jacks rotate around their pivot, following the drift of the specimen, errors are introduced by the inclination of the pistons. For example, in order for the horizontal force measured from the experimental set up of Fig. 2.9(b) to be considered a good approximation

to the shear force, the piston must act as perpendicular to the longitudinal axis of the element and not run within the 'horizontal' concept. Similarly, if the axial load is provided through a hydraulic piston that follows the chord of the deformed element, then the size of the experimental value cannot be considered as true "axial" load. Therefore, it must be analyzed along the line that connects the centroidal axis of the column at top and bottom (dashed line). In this case, the axial load also contributes to the actual value of the shear force in the loading section, as shown in Fig. 2.9(b). Therefore, each experimental layout presented in the available experimental studies of columns of the literature contains its own, peculiar details that must be considered when analyzing the experimental data. Although the main and final objective is the reliable determination of the degradation percentage of the element shear strength while the displacement ductility is increasing, careful evaluation of the data obtained from the experimental literature is required in order to avoid significant errors in the understanding of mechanical behavior.

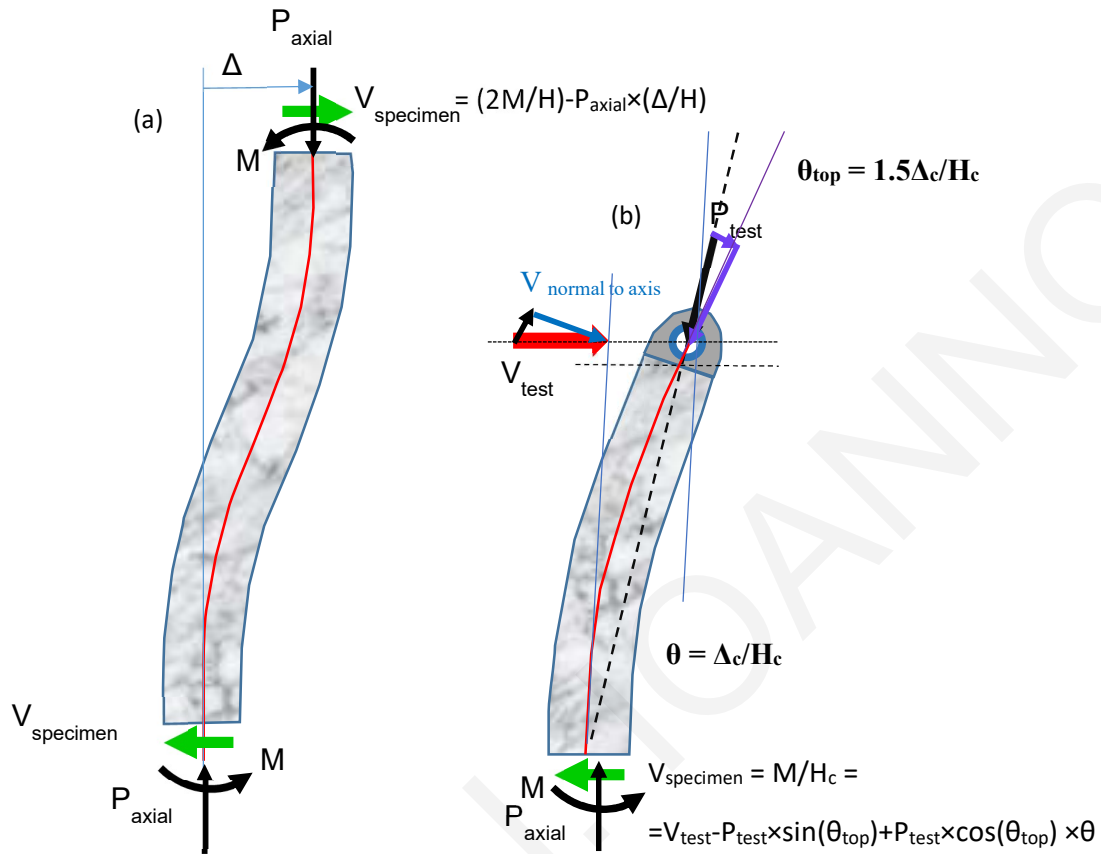


Figure 2. 9 : Correction of experimental results considering second order effects with regards to loading conditions (a) Case of fixed column with vertical loading action of piston regardless of rotation; (b) Cantilever case by providing piston load following the elastic line (deformed line) of the specimen (follower loads) (Note here that the rotation at the tip of the cantilever, is 1.5 times the chord drift).

For the test setup of Fig. 2.10, which is also used frequently in cantilever experiments, the value recorded directly by the lateral force piston or other instruments during testing (Li - database, 2009) need be corrected as follows. With increasing lateral load, the axial load causes secondary moments which consume a part of the available flexural strength of the component. To enable the correction, the following assumptions are made: the nominal flexural strength remains constant as controlled by tension reinforcement yielding; the axial load is constant;

drift is increasing with reference to column base, then the effective lateral force generated by the horizontal piston to maintain equilibrium is linearly reduced according to Eq. 2.10.

$$V_{test} = \frac{M}{L_s} - \frac{P\Delta}{L_s} = \frac{M}{L_s} - P\theta \quad (2.10)$$

Therefore, if the objective is to evaluate any possible strength reduction on account of damage, the following parameter should be examined: $V_{true} = V_{test} + P\theta$. It appears that that when the data was originally assembled in the electronic data bases used to correlate the function $\eta(\mu)$ (see Table 2.1) in the equation: $V(\mu) = \eta(\mu)V_0$, the values of the shear forces used were the values of V_{test} and not V_{true} . This may have led to miscalculation of the degradation of shear strength of the elements in existing buildings, with consequences for the result of the assessment procedure and design.

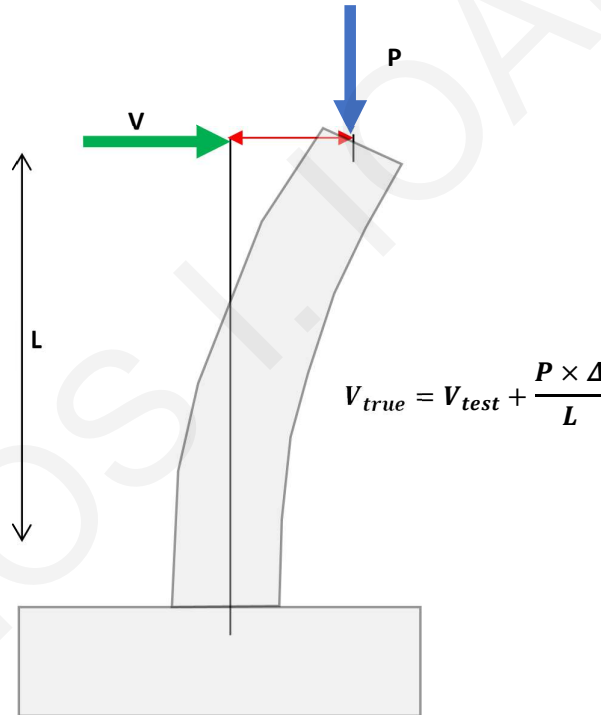


Figure 2.10 : Correction of P-Delta effects

The difference between V_{test} and V_{true} is generally small for low axial load ratios. Especially for brittle-columns, this difference is negligible because the failure occurs at low drift ratios, while the consequences of the correction increase with the magnitude of ductility. An example of this case is the hysteretic response for the 2002-S1-CenC columns tested by [Elwood and Moehle \(2003\)](#) shown in Figure 2.11(a) (with a black line before and with a red line after

correction). As shown in Figure 2.11(b), before correction for the P-Delta phenomena, the ductile column C3 of the P2 test specimen from the NCREE2005 experiments appeared to have undergone severe shear strength degradation after the failure of central column C2, while after second-order effects correction it was found that the column C3 essentially developed a ductile behavior and this may have happened through hardening with increasing deformation as shown by the ascending trend of the last cycles.

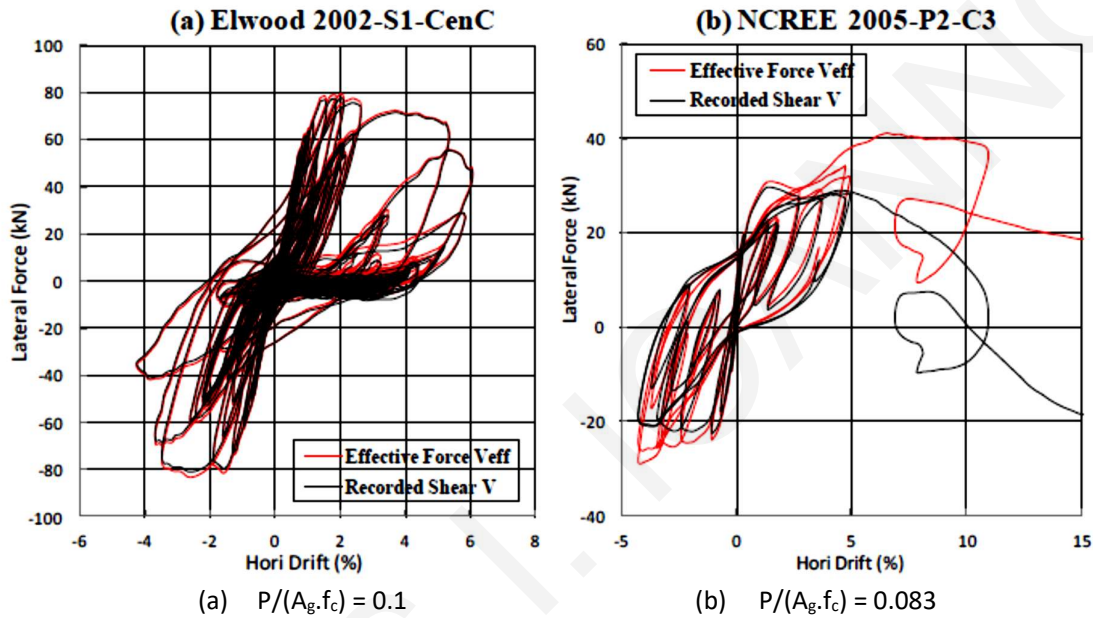


Figure 2. 11 : Correction of experimental results for columns mentioned from Li, 2009

As shown in Fig. 2.9, the P- Δ contribution when the load is provided by rods going through the centroid of the base cross section is smaller – on account of the product $\cos(\theta_{top}) \cdot \theta$; however, the horizontal contribution of the axial load remains a required correction in this case. A realistic depiction of the two different setups conducted on cantilever experiments is shown in Fig. 2.12 (Kim et al., 2018): the idealized setup of Fig. 2.10 is shown in Fig. 2.12(a) and the idealized setup of Fig. 2.9(b) in Fig. 2.12b. As illustrated in Figure 2.13 different manners of load application influence the value of shear strength obtained from the lateral loading piston in different ways; to identify the true degradation of lateral load resistance, therefore, so as to compare with the Code proposals for the ductility – effected strength reduction, the value of V is corrected as follows:

$$\text{Case 1: } V_{true} = V_{test} - P \sin\left(1.5 \frac{\Delta}{L}\right) + P \cos\left(1.5 \frac{\Delta}{L}\right) \cdot \frac{\Delta}{L}$$

$$\text{Case 2: } V_{true} = V_{test} + P \cdot \frac{\Delta}{L}$$

$$\text{Case 3: } V_{true} = V_{test} + P \cdot \sin \frac{\Delta}{L_{top}} + P \cdot \cos \frac{\Delta}{L_{top}} \cdot \frac{\Delta}{L}$$

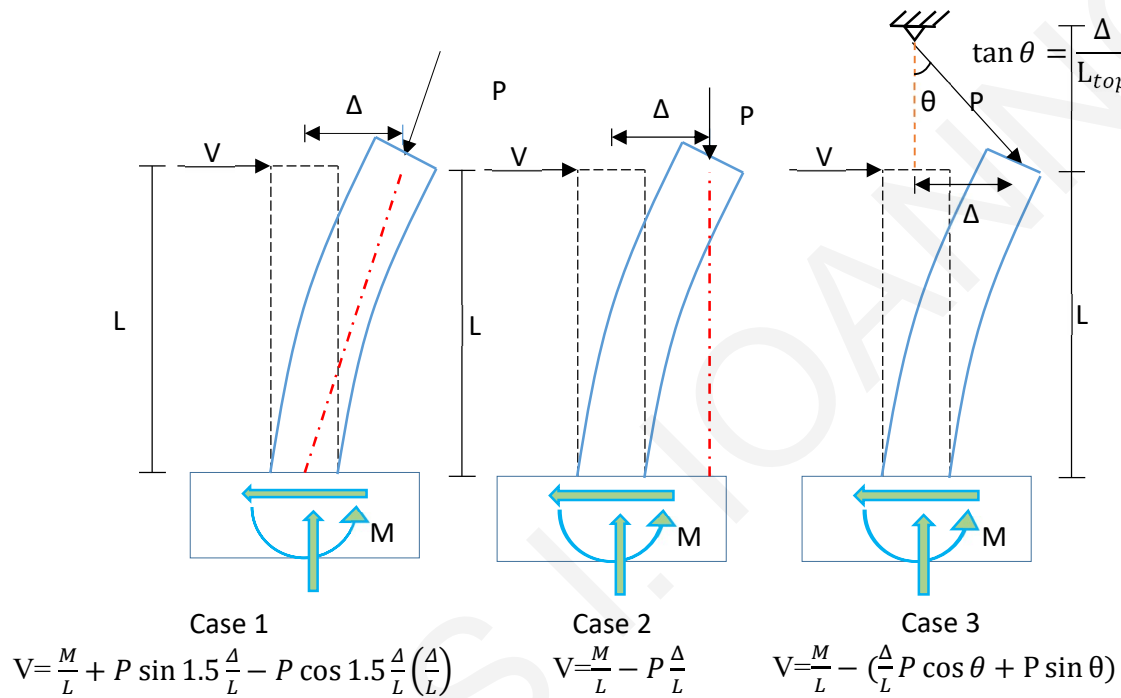


Figure 2. 12 : Dependence or relationship of P-Delta effects from experimental setup

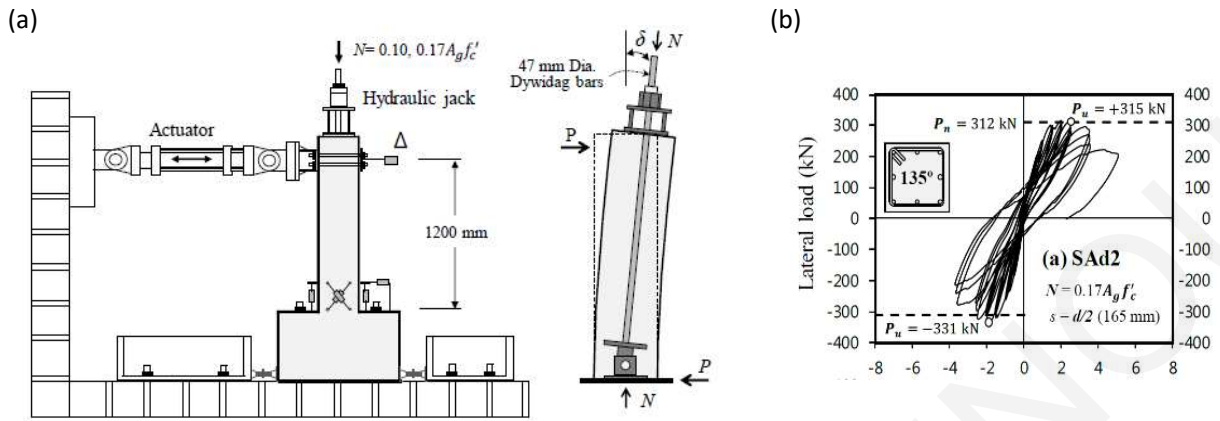


Figure 2. 13 : (a) Experimental layout; (b) Experimental envelope curve [Kim et al. \(2018\)](#)

2.2 A Review on Fiber Reinforced Cementitious Composites (ECC)

2.2.1 Historical Evolution Since 1960 and Tensile Strain-hardening

According to Grosse et al. (2007), fiber cement concrete can be easily classified based on its tensile response, that is, either strain softening or strain hardening. Figure 2.14 shows the characteristic types of the stress and strain response envelope for fiber-reinforced cement composites.

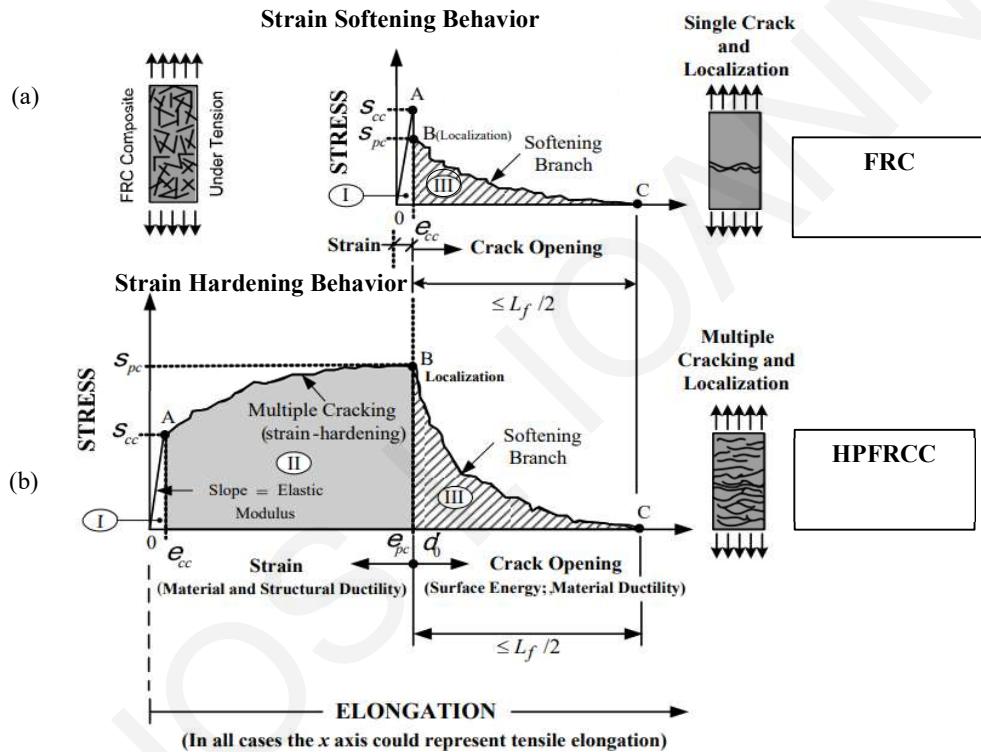


Figure 2. 14 : Typical stress-strain curve or elongation in tension up to complete separation: (a) Standard behavior of FRC composite; (b) Standard behavior of HPFRCC composite (Naaman, 1987).

Points A and B denote, respectively, the two characteristic states, i.e., (1) the peak nominal stress level (point (s_{cc}, e_{cc})) and (2) the critical condition at which macrocracks begin to develop and the damage process transitions into the local failure stage of softening branch (Fig. 2.14(a)). The first category (Fig. 2.14(a)), where softening ensues immediately after cracking are the common FRC materials; the second category depicted in Fig. 2.14(b) have a strain hardening

branch of response after cracking, and are collectively referred to as High Performance Fiber Reinforced Cementitious Composites. Several mixes fall under this classification; materials that attain compressive strengths that exceed 120 MPa or more (CSA S6 – 2019, Annex 8, ACI 239 -218, AFNOR 2013) but exhibit hardening response in tension, are classified as Ultra High Performance Fiber Reinforced Concrete and are usually reinforced by steel fibers. Materials with lesser strength but exhibiting tension hardening are classified as High Performance Fiber Reinforced Concrete and may contain steel, synthetic, or a hybrid combination of fiber. Ductile Cementitious Composites that contain synthetic fiber only, are generally of lower compressive strength but demonstrate substantial capacity for plastic deformation in tension with negligible hardening- these are known as Engineered Cementitious Composites or ECCs (Li and Wu, 1992; Georgiou, 2017). In the present study the focus is on the prospective use of ECC materials as a retrofitting means of old type structural components with brittle details, which are bound to experience significant strength degradation under seismic loads. For this reason, a brief introduction of these materials and their historical background as well as retrofitting applications of reinforced concrete components with the use of ECCs are given below.

2.2.1.1 Historical background

Although Bernard (1874) advocated the use of fibers in concrete, it was not until the early 1960s when Romualdi and Mandel (1964) studied the use of steel fibers in concrete, an idea that led to several contemporary improvements and sparked wide interest in the subject. In the early 1980s, Lankard et al. (1984) proposed a unique type of fiber-reinforced cementitious composite called Slurry Infiltrated Concrete, known as SIFCON. SIFCON was created by completely filling a mold with fiber and then injecting a slurry into the resulting fiber mesh. This production method allowed for a relatively high fiber content, which at the time was between 5% and 12%. The tensile and compressive mechanical properties of SIFCON composites were thoroughly studied by Naman et al. in the 1980, leading to a series of breakthroughs. The tensile stress-elongation curves reported in Naaman and Homrich (1989) described tensile stresses up to 30 MPa and tensile strains at peak stress of up to 1%. Extensive multiple cracking was also observed. SIFCON demonstrated convincingly that FRC composites with sustained strength in tension (as high as the compressive strength of normal concrete) and simultaneously very high ductility could be achieved. SIFCON belonged mostly to the class of strain-hardening composites. Instead of using the terms “strain-hardening” and

“strain softening,” “high-performance” and “conventional fiber reinforced concrete” were used.

Naaman et al. (1987) essentially calculated the critical volume percentage of fibers, resulting in the behavior shown in Fig. 2.15(a), which is essentially a strain-hardening behavior under tension. He established the acronym HPFRCC (high performance fiber reinforced cement composite) to describe this type of behavior. He used the following two equations derived from previous studies (Naaman et al., 1972; Naaman et al., 1973; Naaman et al., 1974) to calculate the critical volume fraction of fibers required to produce that response:

$$\sigma_{cc} = \sigma_{mu}(1 - V_f) + \alpha\tau V_f \frac{L_f}{d_f} \quad (2.11)$$

$$\sigma_{pc} = \lambda\tau \frac{L_f}{d_f} V_f \quad (2.12)$$

Where, σ_{cc} is the strength at first cracking of the composite; σ_{pc} is the post-cracking strength, which represented the peak tensile stress that may be taken by the composite after first cracking; σ_{mu} is the tensile strength of the matrix. V_f is the volume percentage (or fraction) of fibers in the composite; τ is the average bond at the fiber matrix interface; L_f is the fiber length. Also, d_f is the fiber diameter, whereas $\frac{L_f}{d_f}$ is known as the fiber aspect ratio; α and λ are coefficients that results from product of several other factors. Fiber distribution, orientation, bonding efficiency, all play a role.

To characterize a material as tension hardening, Naaman (1987) required that the tensile strength of the composite be greater than, or equal to the initial tensile strength in order to obtain a stress-strain response similar to that shown in Fig. 2.14(b):

$$\sigma_{pc} \geq \sigma_{cc} \quad (2.13)$$

Upon substitution of Eqs. 2.11 and 2.12 into Eq. 2.14 led to the following expression:

$$\sigma_{pc} \geq \sigma_{cc} \rightarrow \lambda\tau V_f \geq \sigma_{mu}(1 - V_f) + \alpha\tau V_f \frac{L_f}{d_f} \quad (2.14)$$

From Eq. 2.14, the following solution for V_f , and the minimum required fiber volume fraction, $V_{f_{min}}$, to ensure strain hardening response in tension after cracking was derived:

$$V_f \geq \frac{1}{1 + \left[\left(\frac{\tau}{\sigma_{mu}} \right) \left(\frac{l}{d} \right)^{\lambda - \alpha} \right]} = V_{f_{min}} \quad (2.15)$$

Equation (2.15) shows the impact of several parameters other than the fiber volume fraction, such as the aspect ratio of the fiber, the matrix tensile strength and the bond at the fiber-matrix interface. The same result can be calculated with the following equation:

$$V_f \frac{\tau}{\sigma_{mu}} \frac{l}{d} \geq \frac{1 - V_f}{\lambda - \alpha} \quad (2.16)$$

Since V_f is relatively small in FRC composites ($1 - V_f \approx 1$) and Eq. (2.17) can then be written as:

$$V_f \frac{\tau}{\sigma_{mu}} \frac{l}{d} \approx \frac{1}{\lambda - \alpha} \quad (2.17)$$

In a 1995 workshop (Naaman et al., 1996) three models were proposed to describe the volumetric distribution of the main fibers, an aspect that was necessary in order to completely characterize the strain-hardening and multiple cracking behavior of HPFRCC and ECC: the first model by Naaman (Naaman et al., 1987) and two other more recent models, one by Li and Wu, 1992 and the second by Tjiptobroto and Hansen (1983). Naaman et al. (1996) examined the similarities and contrasts between these models and provided additional data. Naaman and Reinhardt's 1996 work provides a detailed analysis of the commonalities and differences between these models, as well as other key information. The trade-offs required to achieve strain-hardening are depicted by plotting Equation 2.15 as seen in Fig. 2.15 (b).

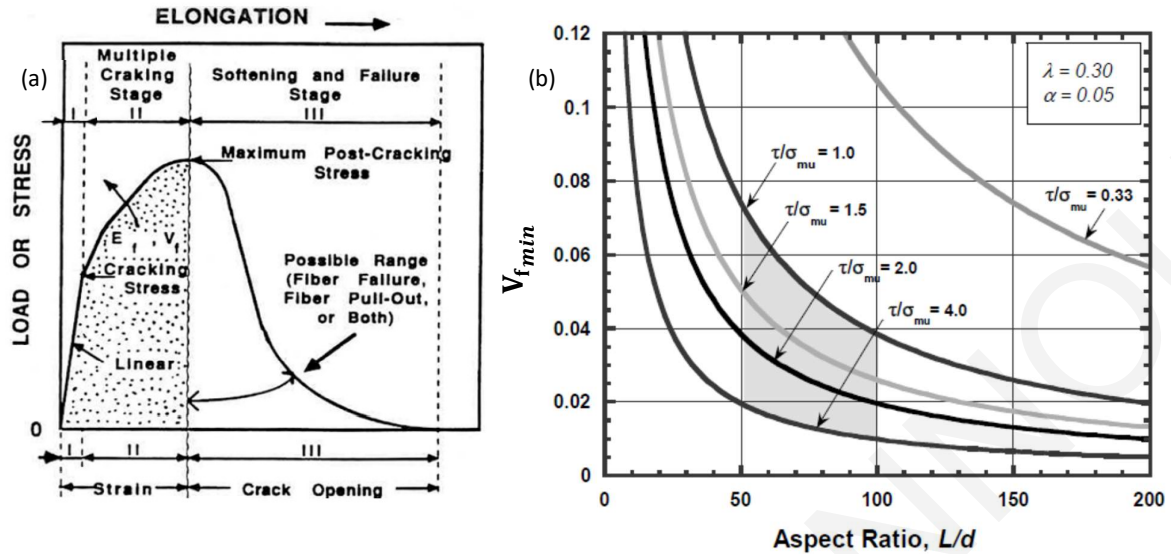


Figure 2.15 : Critical volume percentage of fibers to carry out strain-hardening behavior in tension

2.2.1.2 Replacement of Cement by Fly Ash in Concrete

Fly Ash is a by-product of coal burning in thermal power plants and is therefore considered an Industrial Waste (Ramezani pour et al., 2014). During coal burning, the waste classification system collects volatile waste (fine molecular deposits) before the exhaust gases enter the atmosphere. Most waste particles are round in shape from 1 to 150 microns. Unburned coal collects carbon particles with the fly ash, the amount of which is determined by parameters such as the rate of combustion, the air/fuel ratio, and the degree of pulverization of the coal.

Compared to the combustion of bituminous coal, the fly ash waste generated from the combustion of sub-bituminous coal contains more calcium and less iron. The unburned coal combines with the carbon particles in the fly ash and the amount is determined by the ignition rate, air-fuel ratio and coal size.

By 1930, the term Fly Ash had become popular in the energy sector and in 1937 Davis et al. published the first comprehensive statistics on its specific use in North America. In 1948, the US Bureau of Reclamation published statistics on the use of fly ash in the construction of the Hungry Horse Dam which is in Montana State (U.S.A). This was the first truly widespread use

of this material. Following these early projects, global spread of Fly Ash propagated, but interest in it peaked in the 1970s, when energy (and cement) costs soared.

In recent years, Fly Ash has undergone significant and obvious changes, indicating its combustion and, to some extent, its origin. The Canadian Standards Association (CSA, 1982) and the American Testing and Materials Association (ASTM, 1978) have identified two forms of Fly Ash: Class C is comprised of lignite from sub-bituminous coals whereas Class F is made of bituminous coals.

2.2.1.3 Slanted Shear Test

Figure 2.16 shows the slanted shear test, which is frequently used to assess the interface bond between ECC and Core concrete. It was proposed by Kriegh et al. (1976), and because it was developed at the University of Arizona, it is also known as the Arizona slanted shear test. Several standards, such as EN 12615, 1999 and ASTM C 882, now define it (1999).



Figure 2. 16 : Slanted shear test

The interface is subjected to a stress state of compression and shear in this bond test. The slanted shear test is a consistently reliable approach because it produces a stress condition that simulates the mode of application and failure mode of interfaces. In Kriegh et al. (1976) test, the specimen is a composite concrete cylinder with a bond interface at 30 degrees with the specimen's longitudinal axis of diameter and height 150mm (6in.) and 300mm (12in.)

respectively. As a normal concrete specimen, this composite cylinder is examined under compression.

Prismatic slanted shear specimens can also be utilized as an alternative. According to [Clímaco and Regan \(2001\)](#), one difficulty of this bond test is the difference in standards for specimen dimensions and interface angles, which makes a comparison of obtained results difficult. To better generate interface failure modes, [Zilch and Reinecke \(2000\)](#) proposed an alternate prismatic slant shear specimen with a notch at both ends of the shear plane.

2.2.1.4 Splitting Test

Figure 2.17 shows a splitting test that is performed to define the tensile strength at the interface between two different concretes which created and proposed practically at the same time according to [Thaulow \(1957\)](#), [Carneiro and Barcellos \(1953\)](#), and [Akazawa et al. \(1953\)](#). This test is also known as the Brazilian test, and it is defined in current standards such as [EN 12390-6, 2004](#) and [ASTM C 496, 2004](#).

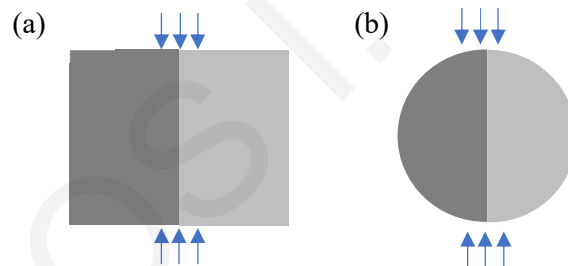


Figure 2. 17 : Splitting Test (a) rectangular shaped specimen; (b) circular shaped specimen

The splitting test is a straightforward procedure. A composite specimen is examined in this test by applying two opposing compressive forces parallel to the contact surface. Due to the Poisson effect, failure occurs in tension normal to the interface surface. For quality control purposes, the formwork used to cast the concrete specimens for normal compressive testing can also be utilized to cast the specimens for the splitting test.

2.2.3 Available Research in the Literature Related to PC and ECC Interface Interaction

Prism samples (100 x 100 x 300 mm) were used to test interface roughness and slope angle effect (Youm et al., 2021). Interface angles of 50, 60 and 70 degrees has been considered with reference to the horizontal axis (Fig. 2.18(a)).

The wedge-shaped substrates concrete specimens were produced ahead of time and cured for two weeks under constant temperature environment ($20 \pm 2^\circ\text{C}$ RH $60 \pm 5\%$). The inclined surfaces of the hardened substrates were next roughened using sandblasting (Fig.2.18(b)), which is the most efficient form of surface preparation (ACI 546.3R-14, 2014). The average depth of the groove recession from the surface of the PC is 0.5 to 1.0 mm, which is in line with the design parameters.

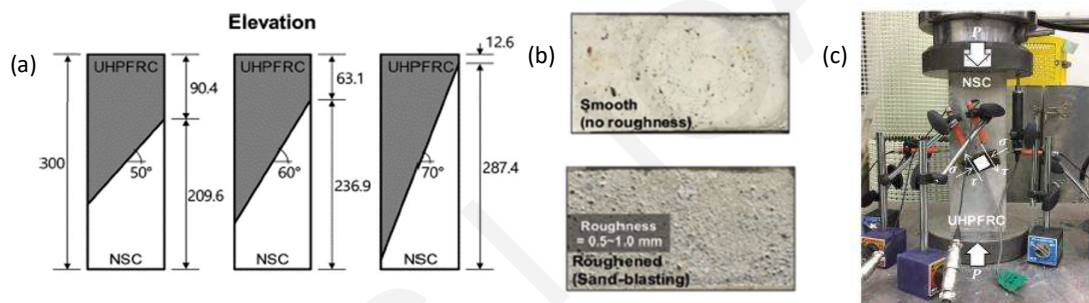


Figure 2.18 : (a) Combined specimens with inclined interface planes of 50°, 60°, 70°; (b) Interface roughness conditions of test samples; (c) Test set up

Therefore, the final mechanism for ECC-PC connection failure can be divided into type-I failure (surface sliding failure), NIC failure (is near-interface concrete cracking), or NSC substrate CC failure (concrete crushing of plain concrete), depending on the test configuration (Fig.2.19). Experimental results show that an ECC-PC composite shear strength prediction model should account for the failure mode transition based on the slope and roughness of the interface.

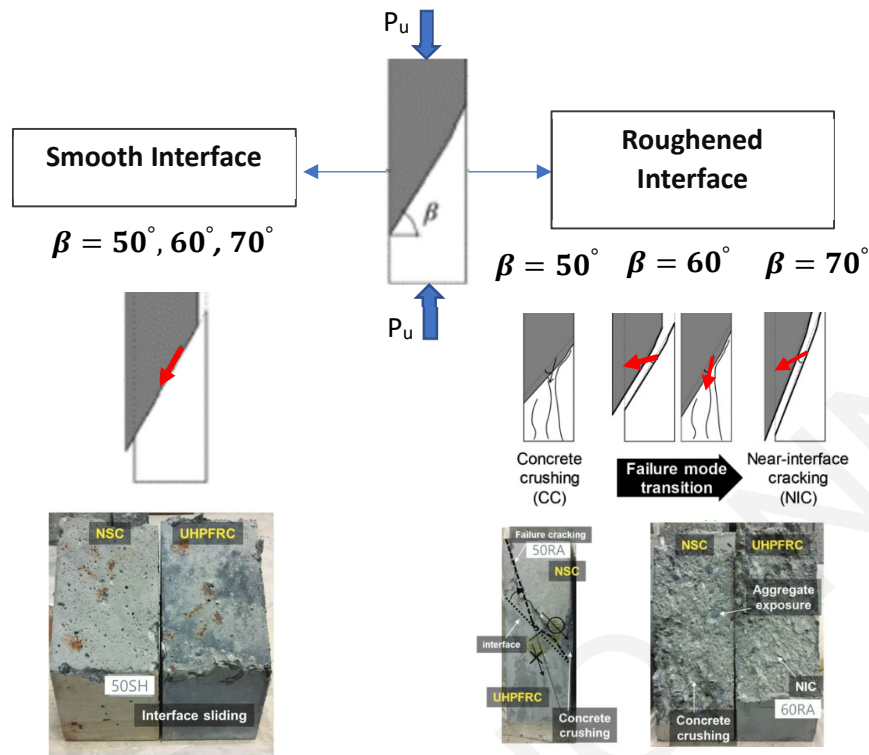


Figure 2. 19 : Specimen failure modes identification

The data obtained from these tests are used to quantify the behavior of the interface of ECC-PC using the theory of plasticity. Figure 2.20 depicts the theoretical fracture zone for a nearly brittle material such as concrete, according to the Mohr-Coulomb theory. Jensen first proposed the concept of interfacial shear strength in 1976. Espeche et al. (2011) performed a series of splitting tests and, based on the work of Jensen (1976) and Carol et al. (1997) a failure criterion was created for the interface between new and old concrete. Youm et al. (2021) continued this work considering the interface under high compression shear conditions as would be induced if the new concrete is in the UHPC class. Zone I and Zone II represent CC failure and interface related (I and NIC) failure, respectively. According to Jensen (1976) and Espeche et al. (2001) Zone III depends on a combination of interface and separation tolerances.

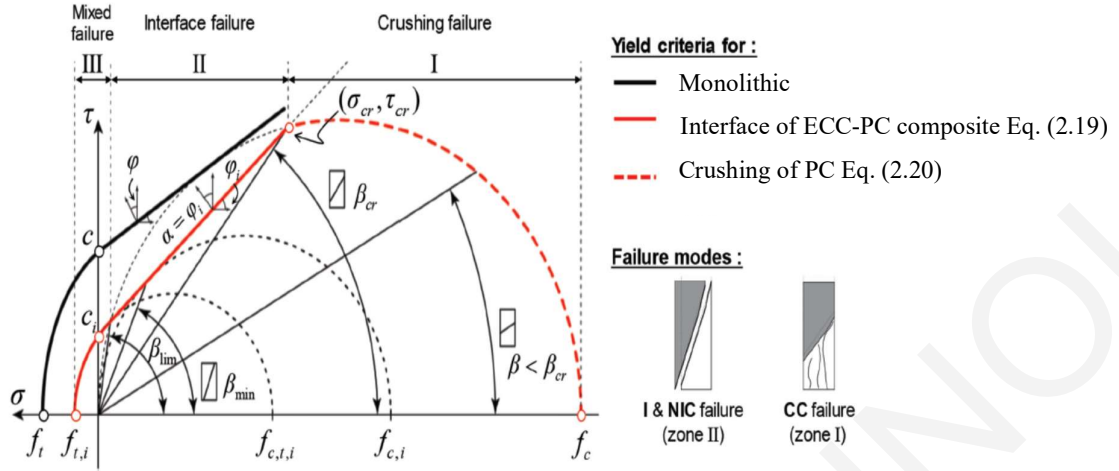


Figure 2. 20: Interface failure by a Mohr-Coulomb type model (proposed by [Espeche et al., 2011](#)).

The limiting state equation $Y(Y(\sigma, \tau))$ is defined in the space of normal and shear stress in the plane of the interface, which satisfies the condition of normality and obeys the Mohr-Coulomb material law. The failure criterion has two characteristic parameters associated with the properties of the interface as follows:

$$Y(\sigma, \tau) = \tau - \sigma \tan \varphi_i \quad (2.18)$$

Adopting this to the failure criteria for ECC-PC composites with sloped interfaces consists of two equations, considering the cohesion, c_i , and the friction angle, φ_i :

$$\frac{\tau}{f_c} = c_i + \frac{\sigma}{f_c} \tan \varphi_i \quad \text{for } \beta \leq \beta_{cr} \quad (2.19)$$

$$\left(\frac{\sigma}{f_c} - \frac{1}{2}\right)^2 + \left(\frac{\tau}{f_c}\right)^2 = \frac{1}{4}, \quad \frac{\tau}{f_c} \leq \frac{1}{2} \quad \text{for } \beta \geq \beta_{cr} \quad (2.20)$$

Considering the failure modes in regions I and II, all possible stress levels at the interface should meet the parameters of the recommended interface failure criteria. Mixed failure that results in concrete crushing in the concrete wedge is not considered in this analysis.

The two failure envelopes intersect at the following point (σ_{cr} , τ_{cr}):

$$\frac{\sigma_{cr}}{f_c} = \frac{1 - 2c_i \tan \varphi_i + \sqrt{1 - 4c_i \tan \varphi_i - 4c_i^2}}{2(1 + \tan^2 \varphi_i)} \quad (2.21)$$

$$\frac{\tau_{cr}}{f_c} = \frac{2c_i + \tan \varphi_i (1 + \sqrt{1 - 4c_i \tan \varphi_i - 4c_i^2})}{2(1 + \tan^2 \varphi_i)} \quad (2.22)$$

The characteristic interface parameters c_i and φ_i can be statistically estimated by linear extrapolation of the test results. Then, depending on the coefficient of cohesion of the interface c_i and the angle of friction of the interface, the critical angle of transition β_{cr} can be calculated φ_i as shown below.

$$\beta_{cr} = (f_c, c_i, \varphi_i) = \tan^{-1} \left(\frac{c_i}{\frac{\sigma_{cr}}{f_c}} + \tan \varphi_i \right) \quad (2.23)$$

In the experiments designed by [Zhang et al. \(2020\)](#), the ECC application is used as a repair material for PC substrates. Surface roughness, ECC aging, substrate moisture, curing conditions, PC strength, and bonding agents are all significant parameters. Six different surface treatments listed in Table 2.2 is used to roughen the PC surface. For each test, plain concrete specimens were roughened to a macro texture depth of 4.0 to 5.0 mm at the interface.

Table 2. 2 : Studied parameters used in experiments

| Parameter | Detailed situation |
|--------------------------|--|
| Moisture degree of | Air surface dry (ASD), air surface wet (ASW), and |
| NSC substrate | Saturated surface dry conditions (SSD) |
| Age of UHPC | 0.5,1,2,3,7,28,90,180 days |
| Treatment of NSC Surface | S _m , WB, LR, HR, RD, and RG |
| Curing condition | Normal-temperature curing, steam curing at 60 °C and 90 °C |
| Strength of NSC | Grade-50, Grade-40 and Grade-30 |
| Adhesive agent | With and without |
| Expansive agent | With and without |

The surface roughness of the plain concrete (PC) substrate was chosen as the main study parameter in this test because it was previously found to be significantly related to the bond strength of the UHPC-PC contact. Surface roughness of PC is determined using the average macrotexture depth (R_t) measured by the so-called sand-pour method and then classified using [fib Model Code for Concrete Structures 2010, 2013](#) where for $R_t < 1.5$ mm smooth surface, $R_t \geq 1.5$ mm - medium roughness surface, $R_t \geq 3.0$ mm - rough surface. The characteristics of the surfaces of the substrate are shown in Figure 2.21 (a) : I Smooth (S_m), which is a horizontal section surface without roughness assessment; (ii) a wire brush (WB) obtained by finishing the grout on the surface of the base without exposing the aggregates, $R_t = 0.6 \sim 1.2$ mm; (iii) low roughness (LR) revealing a partial coarse aggregates and $R_t = 1.0 \sim 3.0$ mm; (iv) High Roughness (HR), (v) roughed and drilled holes (RD) where the substrate surface is roughened to HR and a few drills are added with a distance of 30 mm and a depth of 30 mm opening hole; (vi) Rough + Groove (RG), roughening the substrate surface was classified as HR, adding a groove 20 mm wide and 10 mm deep.

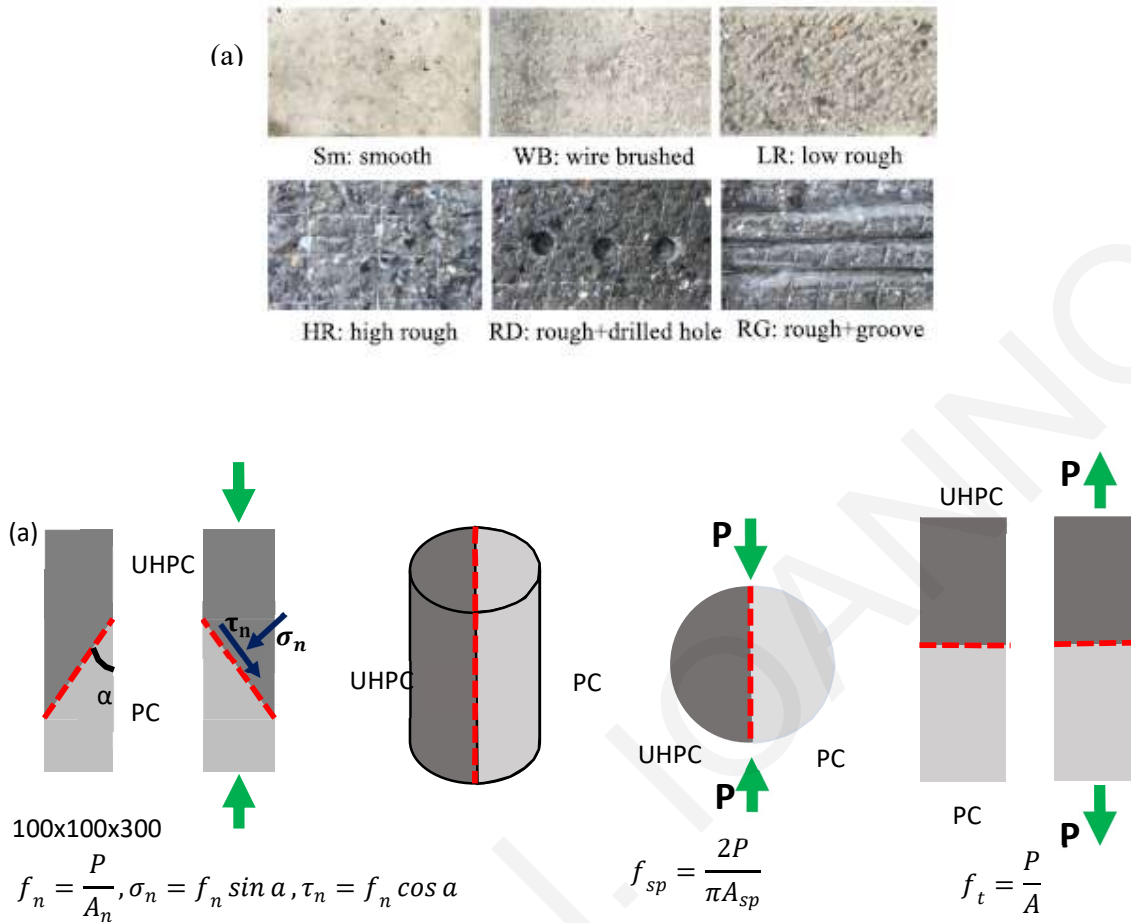


Figure 2. 21 : (a) Different surface treatments for PC substrates and (b) test specimens for slanted shear test, splitting tensile test and direct tensile test.

The typical failure modes of composites obtained from slanted shear, splitting tensile, and direct tensile tests can be classified into three types depending on the characteristics and location of failure plane: (i) Pure interface shear where the failure occurs at the interface, where the surfaces of two materials remained smooth, and neither the PC substrate nor the UHPC overlay showed any cracking or fracturing. (ii) Partial interface failure where the failure occurs in the transition zone, where a partial thin layer of PC substrate material is still bonded to the UHPC surface at the time of failure. (iii) Failure mode C is identified if the UHPC attached a considerable quantity of PC substrate at failure.

The methods for calculating the bonding capacity of the interface in the codes [AASHTO LRFD, 2010](#) and [Fib Model Code for Concrete Structures, 2010](#) are similar, if there is no shear reinforcement at the interface, this can be simplified as follows:

$$\tau_u = c + \mu\sigma_n \quad (2.24)$$

where τ_u is the shear bond strength of the interface (in MPa); c is cohesion which is expressed as τ_a in the Fib Code (in MPa); μ is friction coefficient; and σ_n is compressive stress perpendicular to the shear interface strength (in MPa). [AASHTO, 2010](#) gives c and μ values for the ECC-PC interface with various substrate surface roughness, namely 1.65 MPa and 1.0 for rough surfaces and 0.5 MPa and 0.6 for the smooth surfaces, respectively. When the interface is in tension, σ_n is zero, and Eq. 2.24 gives the failure plane's tensile bond strength. Equation 2.24 can be used to back calculate the friction coefficient μ and the same equation may then be used in processing experimental results to compute the interfacial shear strength τ_u of the interface based on the cohesion c and friction coefficient μ determined by the testing.

Table 2.3 summarizes results from the collection of the available tests. It is noted that the cohesion c and friction coefficient μ are much more pronounced than those recommended by [AASHTO](#). With the exception of the friction coefficient of [Hussein et al. \(2016\)](#), the values of c and μ_n of the ECC-PC interfaces are 4 and 2 times that of the S_m (smooth) surface, and 1.5 and 1.4 times greater than the WB (Wire Brushed) and LR (Low Roughness) surfaces, respectively. The proposed values of c and μ are 2.2 MPa and 1.37 (for rough surfaces) and 2.18 MPa and 1.2 (for smooth surfaces, respectively) based on the baseline results in Table 2.3. The bonding interface of the ECC-PC depends on various aspects such as the roughness of the substrate surface, substrate moisture, curing environment, concrete strength and the stress state at the interface, etc.

Table 2. 3 : Cohesion and friction coefficients obtained by the direct tensile and slant shear tests

| Sources | Roughness | Slanted shear test | | Direct tensile or pull-off test c (MPa) | Friction coefficient μ (MPa) |
|------------------------|--------------|--------------------|------------------|---|----------------------------------|
| | | τ_n (MPa) | σ_n (MPa) | | |
| Zhang et. al., 2020 | Smooth | 12.06 | 6.97 | 2.18 | 1.42 |
| | Wire brushed | 16.09 | 9.29 | 2.5 | 1.46 |
| | Low rough | 21.34 | 12.32 | 2.92 | 1.5 |
| Husan et al., 2020 | Smooth | 4.1 | 2.3 | 3.02 | 0.47 |
| | Mild rough | 13.5 | 7.8 | 5.01 | 1.09 |
| | Rough | 33.1 | 19.1 | 5.63 | 1.44 |
| Tayeth et al., 2012 | Smooth | 7.51 | 4.34 | 2.3 | 1.2 |
| | Wire brushed | 11.04 | 6.38 | 2.32 | 1.37 |
| | Sandblasted | 15.42 | 8.9 | 2.34 | 1.47 |
| Carbonell et al., 2014 | Wire brushed | 16.1 | 9.3 | 2.2 | 1.49 |
| | Sandblasted | 21.7 | 12.3 | 2.3 | 1.58 |

Tayeh et al., (2013) presented and analyzed experimental results regarding the roughness characteristics of the interface behavior using a three-layer (3D) optical surface metrology. Surface roughness is defined as per the ISO 4287, 1997.

The definition of average roughness is illustrated in Fig. 2.23.

$$R_a = \frac{1}{l_m} \int_0^{l_m} |y(x)| dx \quad (2.25)$$

where, l_m is the evaluation length; and $y(x)$ is the profile height at position x .

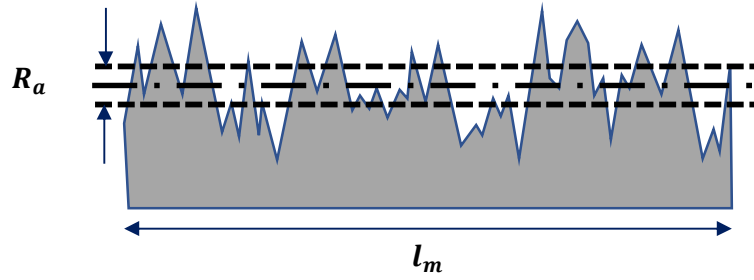


Figure 2. 22: Average roughness, R_a

A parameter R_q is defined as the root-mean-square average roughness of a surface:

$$R_q = \sqrt{\frac{l}{m} \int_0^{l_m} y^2(x) dx} \quad (2.26)$$

Here the peak roughness R_p is the height of the highest peak in the roughness profile over the evaluation length. R_q is a statistical metric that indicates the breadth of the amplitude distribution function (ADF): the broader the ADF, the higher the R_q value, and the rougher the surface. Similarly, R_v is the depth of the deepest valley in the roughness profile over the evaluation length. The total roughness, R_t , is the sum of these two, or the vertical distance from the deepest valley to the highest peak.

$$R_p = |\max [y(x)]| \quad 0 < x < l_m \quad (2.27)$$

$$R_v = |\max [y(x)]| \quad 0 < x < l_m \quad (2.28)$$

$$R_t = R_p + R_v \quad (2.29)$$

With reference to Fig. 2.23, the mean peak-to-valley height of roughness profile is defined, R_z ,

$$R_z = \frac{1}{5} \sum_{i=1}^5 z_i \quad (2.30)$$

where, z_i is the peak-to-valley height in each cut-off length (λ_c).

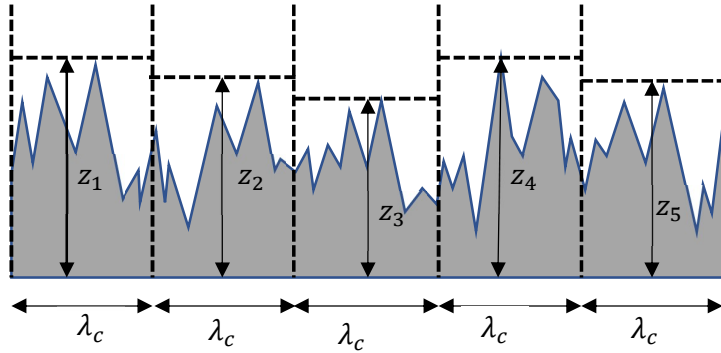


Figure 2. 23 : Mean peak-to-valley height, R_z .

Another criterion that determines the geometry of the ADF is skewness, which is a measure of the ADF's asymmetry and it assesses the symmetry of a profile's fluctuation around its mean line.

$$R_{sk} = \frac{1}{l_m R_q^3} \int_0^{l_m} y^3(x) dx \quad (2.31)$$

Using three types of surface textures for surface roughening (i) as-cast (AC), i.e. without surface preparation as reference, (ii) wire-brushed (WB) without exposing the aggregates; (iii) sand-blasted (SB) with the aggregates purposefully exposed, the following values were obtained for the bond strength of the interface under direct pull-off tension.

Table 2. 4 : Bond quality is measured in terms of bond strength

| Bond Quality | Bond Strength (MPa) |
|--------------|---------------------|
| Excellent | ≥ 2.1 |
| Very Good | 1.7-2.1 |
| Good | 1.4-1.7 |
| Fair | 0.7-1.4 |
| Poor | 0-0.7 |

Linear regression was used between the substrate roughness parameters and bond strength. The roughness of the substrate was used as the independent variable. The substrate roughness characteristics of the AC surface, WB surface, and SB surfaces present high correlation with bond strength in indirect tension and slant shear (Table 2.5). The results of previous researchers [Garbacz et al., 2005; Julio et al., 2004] who indicated that the splitting cylinder tensile test and the slant shear test are sensitive to substrate surface treatment are in general agreement with these findings.

Table 2. 5 : Correlation between substrate roughness parameters and bond strength

| Roughness parameters | | Coefficient of correlation(R^2) | | | | | |
|--|-----------|-------------------------------------|--------|---------|----------------------|--------|---------|
| | | Splitting tensile strength | | | Slant shear strength | | |
| | | 3 days | 7 days | 28 days | 3 days | 7 days | 28 days |
| Average roughness of profile | R_a | 0.945 | 0.855 | 0.865 | 0.945 | 0.919 | 0.89 |
| Root-Mean -Square roughness of profile | R_q | 0.946 | 0.843 | 0.879 | 0.947 | 0.921 | 0.897 |
| Maximum peak -to-valley height of roughness Profile | R_t | 0.932 | 0.819 | 0.924 | 0.935 | 0.913 | 0.809 |
| Mean peak-to-valley height of roughness Profile | R_z | 0.945 | 0.837 | 0.898 | 0.947 | 0.922 | 0.904 |
| Maximum peak -to-valley height of roughness Profile within a sampling length | R_{max} | 0.930 | 0.817 | 0.925 | 0.933 | 0.911 | 0.909 |
| Maximum peak height of roughness profile | R_p | 0.907 | 0.790 | 0.938 | 0.909 | 0.891 | 0.901 |
| Maximum valley height of roughness profile | R_v | 0.946 | 0.840 | 0.891 | 0.948 | 0.922 | 0.902 |
| Mean height of profile irregularities of Roughness profile | R_c | 0.945 | 0.839 | 0.895 | 0.9474 | 0.922 | 0.903 |

2.3 Retrofitting strategies through ECC jacketing of RC Columns

The research community is particularly interested in devising retrofit solutions for structural components that do not comply with current seismic regulations, such as poor detailing, discontinuous load paths, and a lack of capacity design considerations in their design. In response to the new requirements of seismic codes, many of the previous intervention techniques have been adapted and developed, and new techniques have become available, many based on innovative materials (such as FRP and ECC). One of the most popular concrete repair techniques is reinforced concrete jacketing. The main advantage of RC jacket technology is that the lateral load capacity is distributed throughout the structure, eliminating the tendency of localization of deformation demand in stiffness and strength deficient components. Construction is tedious, as this intervention requires extension on the added jacket longitudinal reinforcement from floor to floor, and addition of stirrups. The increased cross-sectional area and longitudinal reinforcement increases the effective stiffness and flexural strength. Additional transverse steel bars play a significant role in shear, buckling and confinement, and contributes to shear strength, deformability, and anchoring or splicing of steel bars. RC Jacketing is therefore considered a global intervention, of the same nature as adding walls, in the sense that this intervention alters the dynamic characteristics of the structure (Thermou and Elnashai, 2006). Several studies have investigated the method's efficiency, which has been supported by experimental work (Rodriguez and Park 1991; Stoppenhagen et al., 1995; Julio et al., 1998). The procedure is adjusted in circumstances when buildings are close to one another, and one-, two-, or three-sided jacketing is used (Tsonos et al., 2007; Fardis et al., 2009).

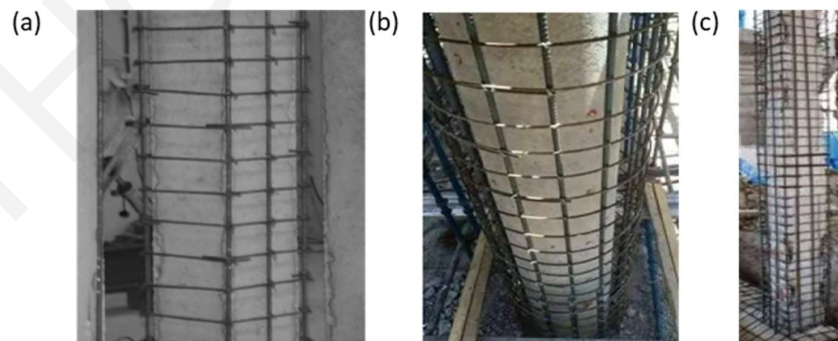


Figure 2. 24 : Reinforced concrete jacketing of different types of existing reinforced concrete columns (Thermou and Elnashai, 2006)

2.3.1 Advantages and Disadvantages of Concrete Jackets

In view of their expense adequacy, concrete jackets are yet the preferable technique for seismic upgrading of individual concrete members. There are a few reasons: Depending on the used reinforcement, a concrete jacket can have several effects, such as increasing stiffness, shear strength, ductility of deformation, anchorage/reinforcement continuity in anchoring or splicing zones, moment resistance (enabling conversion of a weak-column/strong-beam frame to a strong-column/weak-beam frame), shear strength and bond in joints through which the jacket continues, and protection of the old reinforcement against (further) corrosion.

RC jackets also have limitations, such as effecting architectural interventions as they alter the geometry of the members, construction causes disruption of building functionality, whereas they cannot function as local measures for retrofit of individual components (as is, for example, achieved through FRP jackets) without affecting the overall building where such a global change is not desirable.

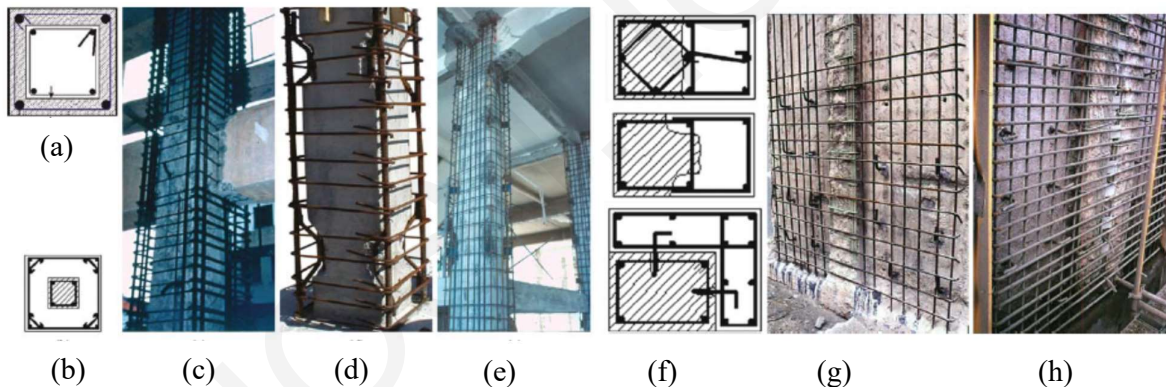


Figure 2. 25 : Concrete jackets in columns (a) the simplest example; (b) jacket bars bundled near corners, engaged by crossties or octagonal tie; (c) jacket bars bundled at corners, dowels at interface with old column; (d) U-bars welded to corner bars; (e) steel plates welded to corner bars; (f), (g), (h) one- or two-sided jackets; (Thermou and Elnashai, 2006)

2.3.2 Jacketing with ECC

ECC has been used alone or in combination with FRP textile or steel rebars to reinforce circular and square RC columns or to reshape the column cross-section after reinforcement, as shown in Fig. 2.26. A strengthening layer is used in this concept to confine the concrete core column

that is subjected to triaxial compressive stresses. By delaying crack growth and expansion and improving brittle fracture behavior, ECC can help concrete columns absorb more deformation energy.

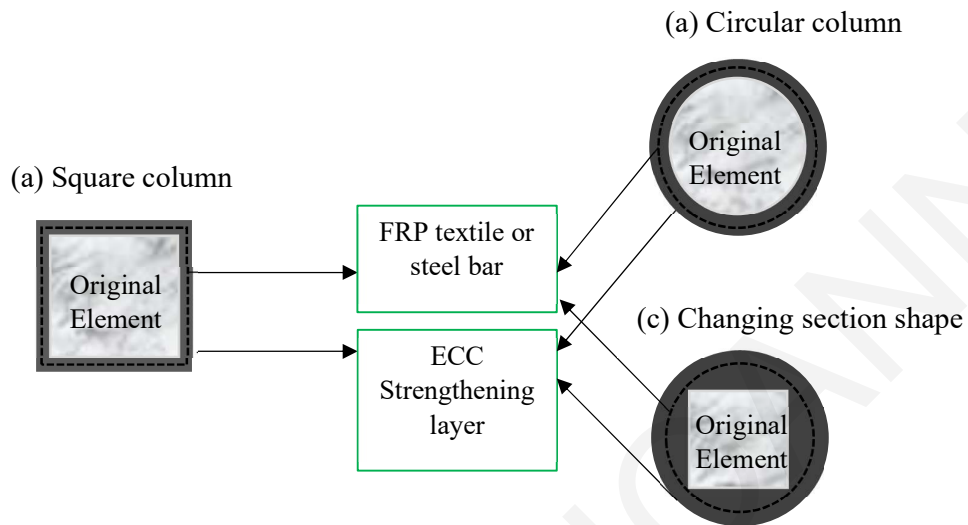


Figure 2. 26 : Strengthening types for RC columns using ECC

[Deng et al. \(2018\)](#) used ECC jackets to strengthen four RC short columns, while a steel reinforced jacket was used to strengthen another. Fig.2.27 depicts the retrofitting details. To replicate seismic excitation, all specimens were exposed to lateral cyclic loading. Different design schemes were tested to see how they affected the performance of RC short columns. As indicated in Table 2.6, compared to control specimens, columns with ECC jackets have more ductile failure mechanisms. The shear strength and deformation capacity of reinforced concrete columns are greatly improved.

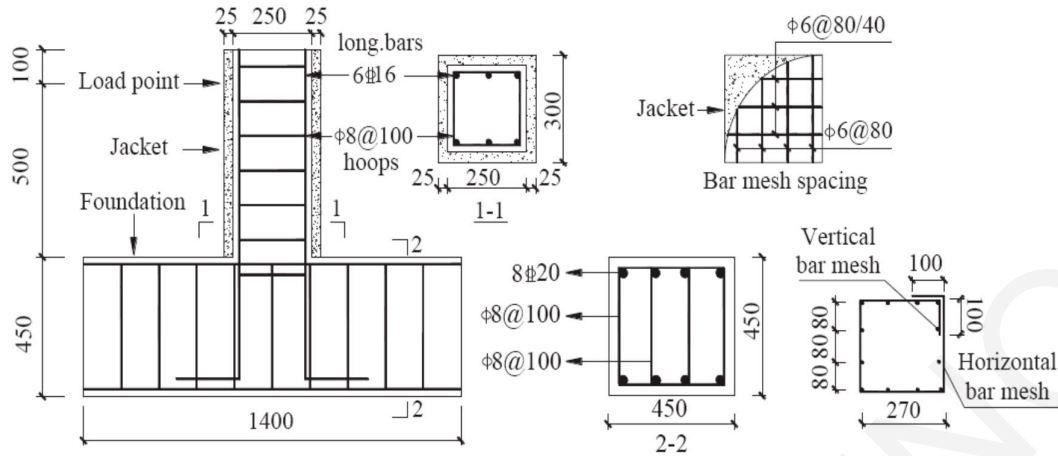


Figure 2. 27 : Retrofitting detailing of RC short columns (Deng et al., 2018)

Table 2. 6 : Specimen details and strengthening effect

| Specimen number | matrix | Reinforcement | Axial load ratio | | Maximum load/KN | Displacement /mm | Failure mode |
|-----------------|--------|--------------------|------------------|--------|-----------------|------------------|---------------------------|
| | | | Design | Tested | | | |
| C-1 | - | - | 0.8 | 0.35 | 212.43 | 6.65 | Shear failure |
| C-2 | Mortar | 80×80mm Ferro-cem. | 0.47 | 0.22 | 317.3 | 5.36 | Brittle flex.-shear fail. |
| C-3 | ECC | 0 | 0.47 | 0.21 | 309.11 | 7.43 | Ductile flex.-shear fail. |
| C-4 | ECC | 80×80mm bar mesh | 0.47 | 0.21 | 318.55 | 5.51 | Ductile flex.-shear fail. |
| C-5 | - | - | 1 | 0.43 | 229.32 | 4.91 | Shear failure |
| C-6 | ECC | 80×80mm bar mesh | 0.58 | 0.26 | 319.43 | 6.31 | Ductile flex.-shear fail. |
| C-7 | ECC | 40x80mm bar mesh | 0.58 | 0.26 | 316.3 | 5.69 | More ductile failure mode |

Zhu and Wang (2016) studied the load and deformation capacities of RC cylindrical columns jacketed with FRP textile and ECC under compression. It was found that all reinforced concrete columns collapsed due to FRP rupture, but when used in combination with a confining ECC layer, the FRP-ECC retrofit showed superior performance in terms of load and deformation capability enhancement. Similarly, AL-Gemeel and Zhuge (2018) examined the confinement effect of basalt fiber textile mixed with ECC, in jacketing square sectioned RC columns. The shape of the cross-section and the brittleness of FRP at the corners reduced the effectiveness of the jacketing when Bassalt-FRP was used alone; by adding ECC the section was converted to a rectangular shape, to address these disadvantages. The matrix type and basalt textile spacing were the test parameters. Test effects showed that this strengthening strategy increased both the load bearing capacity and ductility of RC column.

Considering the sustained tensile strength of the jacket up large strain levels, the shear strength of jacketed reinforced RC columns is estimated from (Deng et al., 2018):

$$V_{mc} = V_c + V_L \quad (2.33)$$

$$V_c = \frac{175}{\lambda+1} f_t b h_0 + f_{yv} \frac{A_{sv}}{s} h_0 + 0.07N \quad (2.34)$$

$$V_L = a_c \frac{1.75}{\lambda+1} f_{tl} A_l + a_s f_{yvl} \frac{A_{svl}}{s_l} h_{01} \quad (2.35)$$

where V_c and V_L , and h_0 and h_1 are the shear contributions and effective heights of the original RC column and the strengthening layer, respectively; $0.07N$ is the shear contribution of the axial load to the shear strength; λ is the shear span ratio of the columns; f_t and f_{tl} are the concrete and ECC tensile strengths, respectively; f_{yv} (f_{yvl}), s (s_l), and A_{sv} (A_{svl}) are the yield strength, the spacing, and the cross-section area of the stirrups (the FRP textiles or steel bars), respectively; and a_c and a_s are the effective strength coefficients of ECC and FRP textiles, respectively.

As noted by Li et al. (2020), it is important to clarify the effect of ECC jacketing on the development of plastic hinges in columns; note that ECC enhances bond of reinforcement and therefore the development of slip that enables strain penetration and spreading of the plastic hinge is restrained, leading to increased danger of local bar fracture. To this end, Lee et al. (2020) conducted an experimental and analytical investigation of the cyclic performance of

scaled bridge column specimens (Fig. 2.28). By establishing equilibrium, the effective confinement pressure was estimated and treated in the same manner as confining stress exerted by ties, in the confinement model of Mander et al. (1988). The two confining contributions, namely the ECC lateral pressure and the confining pressure exerted by ties, were considered additive in this approach. Therefore, with reference to the free body diagram of Fig. 2.28, the lateral pressure provided by the ECC jacket is estimated as:

$$f_{l,ECC} s b_c = f_{t,ECC} A_{ECC} \quad (2.44)$$

$$f_{l,ECC} = \frac{f_{t,ECC} A_{ECC}}{s b_c} \quad (2.45)$$

Where b_c is the sectional dimension of the column core, s the spacing of transverse stirrups, and $f_{l,ECC}$ is the lateral confining pressure provided by the ECC jacket; $f_{t,ECC}$ is the tensile cracking strength of the ECC jacket; and A_{ECC} is the entire area of the ECC jacket in elevation at the height of tie spacing in the y or z direction, which may be calculated using Eq. 2.46:

$$A_{ECC} = 2ts \quad (2.46)$$

where t is the thickness of ECC jacket. Therefore,

$$f_{l,ECC} = \frac{2t f_{t,ECC}}{b_c} \quad (2.47)$$

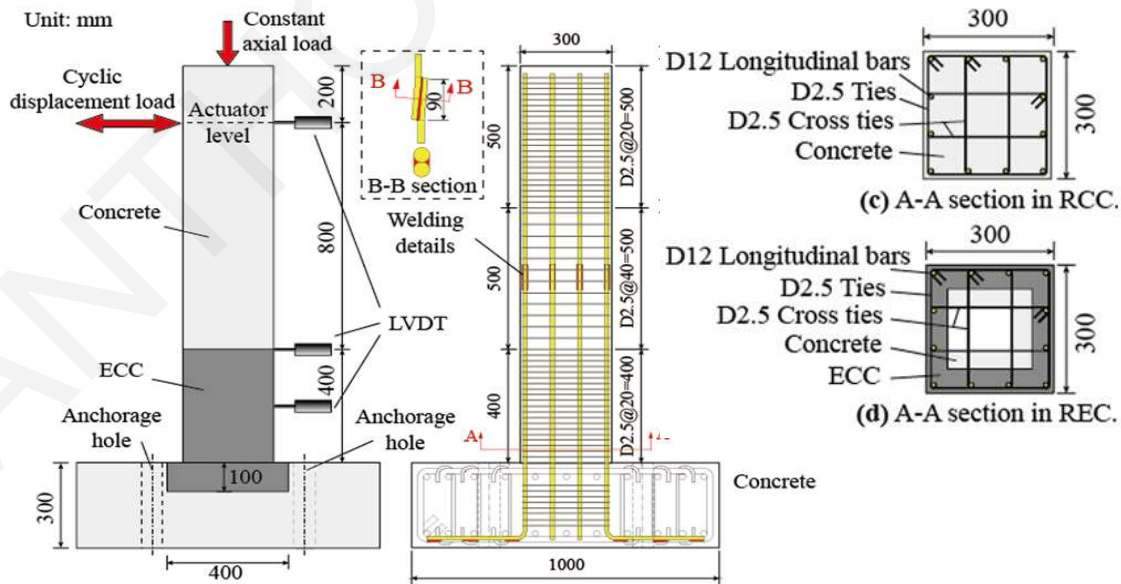


Figure 2. 28: Dimensions and configurations of columns

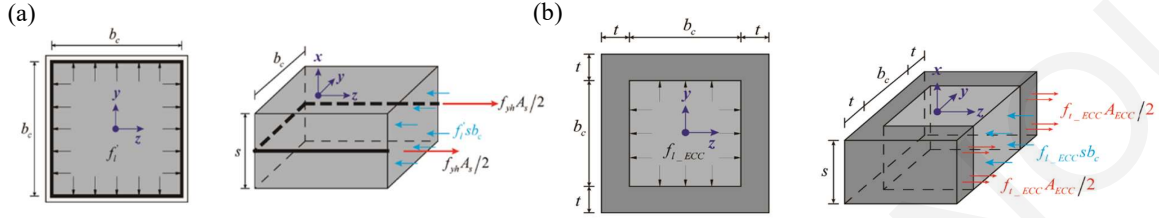


Figure 2. 29: Free-body diagrams of: (a) concrete core confined by stirrups; (b) concrete core confined by ECC jacket

It is noted that while ties and longitudinal bars provide discrete lateral confinement, the ECC jacket provides continuous confinement. The combined effect of the two confining mechanisms while considering their reduced effectiveness when acting on a square section (as compared with the idealized circular section) is reflected below in estimating the encased concrete's compressive strength and deformation capacity:

$$f'_{cc} = f'_c + k_1(f_l + 0.5f_{l,ECC}) \quad (2.48)$$

$$\varepsilon'_{cc} = \varepsilon'_c \left(1 + k_2 \frac{f_l + 0.5f_{l,ECC}}{f'_c} \right) \quad (2.49)$$

Alsomiri et al. (2021) used 600 mm tall, 250 mm diameter concrete cylinders as scaled models of a circular column, as shown schematically in Fig. 2.30. Three cases were examined: one comprising normal or regular concrete (C) whereas the other two were jacketed (J1, J2) with a 25 mm thick UHPFRC jacket. The jacket was overlaid around the cylindrical specimen (Fig. 2.30(a)), but the jacket was slightly shorter than the specimen so that a narrow gap of 10mm was left at the top and bottom ends of the cylinder to prevent direct loading from being applied to the jacket during compression testing. Tables 2.7 and 2.8 show the mechanical properties of conventional and UHPFRC concrete used in the study and the results obtained after compression testing.

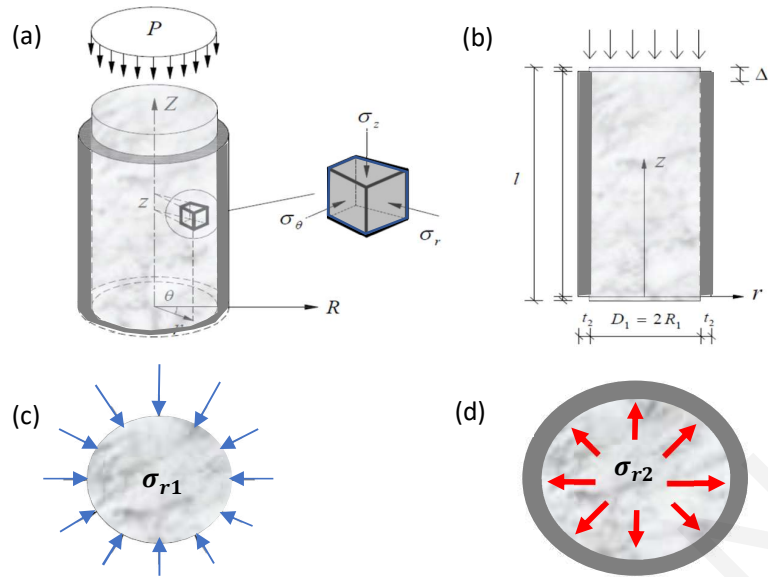


Figure 2. 30 : Schematic diagram of a concrete cylinder with UHPFRC jacket under axial compression (a) three-dimensional view; (b) side view; (c) radial stress of concrete cylinder; (d) radial stress on the jacket

Table 2. 7 : Material properties for normal concrete

| Property | Specimen geometry | Test results |
|----------------------------------|-------------------|--------------|
| Cubic compressive strength (MPa) | 150x150x150 | 44.2 |
| Modulus of elasticity (MPa) | - | 34,500 |
| Tensile strength (MPa) | - | 2.79 |
| Passion's ratio | - | 0.167 |

Table 2. 8 : Material properties for UHPFRC

| Property | Specimen geometry | Test results |
|----------------------------------|-------------------|--------------|
| Cubic compressive strength (MPa) | 100x100x100 | 156.8(MPa) |
| Modulus of elasticity (MPa) | 100x100x100 | 55,468(MPa) |
| Flexural strength (MPa) | 100x100x100 | 17.2(MPa) |
| Poisson's ratio | - | 0.2 |

The C specimen developed an explosive crushing failure under compression; in contrast the jacketed specimens developed cracks parallel to the loading direction, extensive compressive straining (closing the gap at top and bottom in the ends of the test) while at the same time maintaining their original shape. Unlike the C specimen, the damage process was ductile and progressive. Significant lateral dilation was also seen in the jacketed specimens. The response curves were nearly elastic up to large fraction of the applied load (to 55% of the peak); when the jacket material transitioned into the hardening branch (with the formation of multiple cracking), a non-linear stage became more evident. Using these tests, the confined strength increase, reflected by factor K in the relationship: $f_{cc}=K:f_c$ was determined, indicating that its value increases with the jacket thickness, having a more pronounced effect in increasing the axial strain capacity rather than the strength.

The literature, albeit relatively limited with regards to ECC, has been enhanced recently with the addition of more UHPFRC jacketing experiments. Although the technology is in general the same, ECC jacketing seems to be suffering less from problems related to preferential fiber orientation seen when steel fibers are used. This means that the ductility is even greater with the ECC jackets; however, the experimental literature need be enhanced substantially before definitive conclusions can be made regarding the design issues and use limitations of this retrofitting technology. This is explored in the remaining chapters of the present thesis.

2.4 Review on Finite Element Methods / Analyses of Reinforced Concrete Elements

2.4.1 General

The need for experimental research persists within the context of advanced design and analytic techniques for modern structures. Experiments provide to design equations a solid foundation, which is crucial throughout the initial design stages. The fundamental data for finite element models, such as materials mechanical properties, are also provided by experimental study. Finite element analysis results must also be compared to experiments using full-scale models of structural sub assemblages or even entire structures in order to be appraised. Recognizing that tests are time-consuming, expensive, and usually do not accurately reflect the loading and boundary conditions of the actual structure, it is possible to reduce the number of test specimens needed for the solution of a given problem by developing reliable analytical models.

The following factors highlight the difficulty to create analytical models of RC structure response:

- Reinforced concrete is a composite material comprised of two materials with very different physical and mechanical properties: concrete and steel.
- Concrete exhibits nonlinear behavior even under low level loads due to material behavior nonlinearity, environmental conditions, cracking, biaxial stiffening, and strain softening.
- Through bond-slip and aggregate interlock mechanisms, steel reinforcement and concrete interact extensively.

Engineers have historically relied extensively on empirical formulas for the design of concrete structures, which were created from numerous experiments, due to these complicated phenomena. Researchers have made several attempts to produce analytical answers that would reduce the necessity for experiments since the development of digital computers and strong analytical techniques such as the finite element method. Thus, the finite element approach has developed into a sophisticated computational tool that makes it possible to routinely conduct complicated evaluations of the nonlinear behavior of RC structures. This approach allows for the analytical study of the significance and interactions of various nonlinear influences on the response of RC structures (Kwak and Filippou, 1990).

2.4.2 Literature on Finite Element Analysis Algorithm

This section gives an overview of the research that has already been completed concerning the use of the finite element method to model reinforced concrete structures. The American Society of Civil Engineers' outstanding state-of-the-art research findings from 1982 (ASCE 1982) and 1985 provide a more thorough explanation of the theories that have been in existence and the use of the finite element method to analyze linear and nonlinear reinforced concrete structures (Meyer and Okamura, 1985).

Ngo and Scordelis published the first paper in 1967 using the finite element method to examine RC structures. In their investigation of simple beams using a model in which the concrete and steel reinforcement were modeled by constant strain triangular elements, a special bond connector element was employed to connect the steel to the concrete and simulate the bond-slip effect. A linear elastic analysis was performed to identify the main stresses in the concrete, stresses in the steel reinforcement, and bond stresses on beams with predefined cracking patterns. Since the publication of this important paper, there has been an increase in interest in the analysis of reinforced concrete structures, and a lot of studies have been released. The similar methodology was utilized by Scordelis et al. (1974) to examine the shear effect in beams with diagonal stress fractures and took into consideration the stirrup, dowel, aggregate, and horizontal splitting effects along the reinforcing bars close to the support.

Nilson, 1972 utilized an incremental load approach of nonlinear analysis and added nonlinear bond-slip relationships and nonlinear material mechanical properties for concrete and steel to the analysis. By condensing the central node of four triangular components of constant strain, a quadrilateral element was created. The solution was stopped when an element achieved its tensile strength, and progressive reloading was employed to consider cracking after redefining a new cracked structure. Concentric and eccentric reinforced concrete tensile members were subjected to loads imposed at the ends of reinforcing bars, and the method was applied to these members. The results were compared with experimental data.

By establishing a nonlinear analysis that automatically considering cracking inside finite elements and the redistribution of stresses in the structure, Franklin, 1970 improved the capabilities of the analytical method. This enabled for the continuous examination of the behaviour of two-dimensional systems from initial loading through failure. Cracking in the finite elements and nonlinear material behaviour were taken into account using gradual loading

with iterations within each increment. Franklin examined the behaviour of plain RC frames and combined RC frames-shear walls using specific frame-type elements, quadrilateral plane stress elements, axial bar members, two-dimensional bond connections, and tie connectors.

Many researchers have examined the behavior of reinforced concrete frame and wall systems using plane stress elements. Using an initial stress technique, Nayak and Zienkiewicz (1972) conducted two-dimensional stress investigations that included the tensile cracking and the elasto-plastic behavior of compressed concrete. Cervenka (1970) employed an initial stress approach to evaluate shear walls and spandrel beams, using the elastic stiffness matrix at the onset of the analysis in each iteration. For the composite concrete-steel material uncracked, cracked, and plastic stages of behavior, Cervenka proposed a constitutive relationship.

The modified stiffness approach and the layer approach have been employed to date in the study of RC slabs using the finite element method. The former divides the finite element into theoretical layers of concrete and steel with idealized stress-strain relationships for concrete and reinforcing steel, whereas the latter bases its response on an average moment-curvature relationship that depicts the various stages of material behavior.

Rajagopal (1976) created a layered rectangular plate element with axial and bending stiffness in which concrete was considered as an orthotropic material for the analysis of RC beams with material and geometric nonlinearities. Many other researchers have also used similar approaches to solve RC beam and slab problems, including Lin and Scordelis (1975), Bashur and Darwin (1978), Rots et al. (1985), Barzegar and Schnobrich (1986), Adeghe and Collins (1987), Bergmann and Pantazopoulou in 1988, Cervenka et al. (1990), and Kwak (1990).

Recent findings on nonlinear finite element analysis of reinforced concrete slabs can also provide understanding of the behaviour inside the slabs, predicting possible failure mechanisms, validate experimental results, and extend existing findings in situations where test data are unknown. According to Genikomsou (2015) FEA of reinforced concrete slabs have been performed by many researchers (Menétrey, 1994; Hallgren, 1996; Ožbolt et al., 2001; Polak, 2005; Guan and Polak, 2007; Negele et al., 2007; Eder et al., 2010;); with the recent publication by Genikomsou and Polak (2015). Menétrey (1994) and Hallgren (1996) studied reinforced concrete slabs with two dimensional models using rotationally symmetric elements. The findings from Menétrey (1994) and Hallgren (1996) demonstrate that the punching shear failure can be simulated using rotational symmetric continuum elements. The 2D elements,

however, are not suitable for applications where modeling of orthogonal reinforcement or unsymmetrical punching is occurred. As a result, 3D elements became the latest innovative trend in the most recent investigations.

In order to simulate the behaviour of masonry and concrete, [Mavros \(2015\)](#) examined through a modelling scheme that used the smeared-crack and the discrete-crack methods, with constitutive models implemented in shell and interface elements. A uniaxial material law that models truss elements and describes the inelastic behaviour of reinforcing steel under cyclic stress used to describe the behaviour of reinforcing steel. To simulate how the steel reinforcement interacts with the masonry or concrete around it, including bond slip and dowel action, a unique interface element with the suitable material laws has been developed. The interface element formulation was innovative because enabled the connection of steel and shell elements of different sizes. This feature made it possible to greatly reduce the number of shell elements needed for an analysis and, as a result, the amount of computational time needed. The bond slip and dowel action of reinforcement steel might be accurately modeled while allowing for a fine appropriate mesh. To implement the element formulations and the material models the finite element software FEAP ([Taylor, 2014](#)) has been used.

[Jinlong et al. \(2015\)](#) investigated an ECC column under eccentric stress using theoretical and finite element (FE) methods and reported that the maximum error between these techniques was 8.2 %. [Hemmati et al. \(2016\)](#) combined an examination of experimental methods and finite element analysis using ABAQUS software to investigate the contributions of HPFRCC on the lateral resistance of frame structures through the construction of three frames from plain concrete, HPFRCC, and a combined frame from both the materials. With regards to [Hemmati et al. \(2016\)](#) for plain concrete and HPFRCC frames, the discrepancies in the magnitude of lateral load predicted using experimental techniques and FEA were found to be 4.5 and 2.8 %, accordingly. Because of ECC high tensile strength, ductility, and durability (due to the lack of coarse grains) ([Ramadoss et al., 2008](#); [Wanga et al., 2014](#)), it's use as a replacement material in retrofitting techniques replacing normal concrete concrete is grown up rapidly. A strong relationship could also be found between the ECC jacketing and the body of plain concrete since the ECC structure and plain concrete are similar.

Chapter 3: Reinforced Concrete Column Limit States

3.1 Introduction

Following the development of Performance – Based Assessment (PBA) frameworks, between 1995 and 2010, practical evaluation of the seismic behavior of RC became a priority on account of the large number of existing RC buildings in urban centers – several already near or beyond the end of their design service life. Earthquakes that happened in the last 30 years affected urban regions such as Loma-Prieta (1989), Northridge (1994, California), Athens (1999, Parnitha), Izmit (1999, Turkey), ChiChi (1999), L’Aquila (2009, Italy), Haiti (2010), etc., all highlighted the catastrophic potential and risk to human life imparted by old construction. Damage was more intense in RC buildings with soft storeys (also known as pilotis). For the first time in this period, the explicit interest in the literature is focused on the drift capacity of columns at collapse – i.e., the point in the resistance curve of a column beyond which the component can no longer carry its overbearing loads. A big number of studies have been published since then, attempting to quantify the deformation capacity of columns; with reference to the seismic risk presented by existing construction. In particular, crucial parameters that affect the seismic behaviour of this type of element at advanced stages of deformation are of significant importance when it refers to elements with inadequate steel reinforcing configuration that represent old-type practices. On account of the interaction between the loading history and the many response parameters that affect deformation capacity of columns, not surprisingly, a wide dispersion was found in the characteristic values of deformation and failure of R.C columns despite the extent of the relevant literature (Berry et al., 2004; Elwood and Moehle, 2005; Syntzirma and Pantazopoulou, 2007; Inel et al., 2007; Pantazopoulou and Syntzirma, 2010; Biskinis and Fardis, 2010; Grammatikou et al., 2017; Opabola and Elwood, 2021).

An important factor responsible for the dispersion of results is the perceived insensitivity of the analytical models to some critical parameters that control the onset of failure. In columns controlled by flexural yielding before failure (flexure-shear elements), the load carrying capacity against horizontal load is generally controlled by flexure, but the deformation capacity is generally much lower than that specified by the analytical models extracted from fundamental principles – the attenuation relationship discussed in Chapter 2, which superimposes a limiting envelope on the resistance curve, is intended to deal with this by effectively controlling the interplay between shear and flexure in the range after yielding based

on the ratio $V_n(\mu)/V_{flex}$. For example, limiting drift capacity as per the KANEPE 2014 model, where $V_{n,red}=V_n(1 - 0.05 \min(5, \mu_{\theta}^{pl}))$ leads to the following estimation:

$$\mu_{\theta}^{pl} = 20 \cdot \left(1 - \frac{V_{flex}}{V_n}\right) \rightarrow \mu_{\theta} = 1 + 20 \cdot \left(1 - \frac{V_{flex}}{V_n}\right) \quad (3.1)$$

(i.e., for example, for $V_n=1.4V_{flex}$, the implied value of ductility is 7, a value that is seldom supported by experimental evidence). Flexural strength is hardly the only controlling variable; for example, strength loss in lap splices, exacerbated by cyclic deformation reversals may alter the hierarchy expressed by the preceding ratio. To account for the effect of shear strength degradation on deformation capacity estimates [Elwood and Moehle \(2005\)](#) recognized two distinct points of failure in the resistance curve of a structural column – the first, which refers to the loss of lateral load resistance, is distinguished from a point occurring later, at higher drifts, where the load bearing capacity to vertical loads is lost. Their proposal, being an empirical relationship between drift at collapse and axial load magnitude, has been calibrated against a limited number of test specimens where this type of collapse could be observed (i.e. columns under seismic loading through seismic table and not under imposed controlled displacement).

The present chapter aims to investigate the available models in so far as the evaluation of drift capacity of columns under cyclic loading during (a) loss of lateral resistance, and (b) failure under axial load. It is noted for consistency that the shear failure is defined as the point on the post-peak branch of the envelope resistance curve that corresponds to a residual load of 80% of peak. The axial load failure is referred to as the point of the actual collapse.

For the needs of the present work, a dataset was extracted from the PEER database of columns ([Berry et al., 2004](#)) which contained a large volume of tests collected from published experimental literature. In incorporating any specimen in the selected dataset, the type of failure of the RC column specimen was the main criterion. Using the extracted data, the proposed models for shear strength calculation were compared with the reported values, and a specific methodology was followed to determine whether or not the experimental results had been previously corrected for second order effects (i.e., in the original test reports), as well as when assembled in the PEER database of [Berry et al. \(2004\)](#). To improve the investigation, an optimization methodology was used to augment and improve the existing proposed models evaluating the shear strength, i.e. the model included in [EN1998-3, 2005](#) and that proposed by [Pardalopoulos et al., 2013](#). Furthermore, finite element models of specimens with

old-type detailing selected from the database have been studied, with the objective to verify through parametric studies the experimental trends that have been illustrated by the database and to check the validity of the available models used in assessment procedures of existing reinforced concrete elements.

3.2 Significant Behaviour Parameters and Open Issues

A qualifying criterion for the type of failure and the behavior of RC columns is yielding of the longitudinal reinforcement before the occurrence of shear failure. (Shear failure is identified by transverse reinforcement yielding precluding other inadequacies such as lap-splice failure). If longitudinal bar yielding precedes stirrup yielding, the failure is described as of flexure-shear type, whereas if the sequence is reverse, the failure is referred to as brittle-shear. For brittle-shear type of failure the drift capacity is particularly small and in any case is less than the nominal yielding drift of the element θ_y .

Because flexural yielding is the benchmark reference in assessment procedures, the drift at the onset of longitudinal bar yielding is needed to define all other forms of failure by comparison. Thus, θ_y is calculated either by member analysis (i.e., [Response 2000](#)), or according to Greek Standards for Assessment and Retrofitting of Existing Structures ([KA.NE.IIE., 2014](#)) and the [EN 1998-3, 2005](#). Alternatively, mechanics-based relationships may be used (i.e. $\theta_y = \frac{1}{3} \cdot \varphi_y \cdot L_s$, where $\varphi_y = \min \left\{ 2.1 \frac{\varepsilon_y}{h}, \frac{0.75\varepsilon_{co}}{\chi} \right\}$, and χ the height of the compression zone $=\xi d$, L_s is the shear span and h the cross-sectional height). The values of drift where brittle failures are developed are obtained from $\theta = \theta_y \frac{V_n}{V_{flex}}$, where V_n is the member shear strength and V_{flex} , is the flexural strength calculated from the yielding moment of the critical section divided by the shear span ([Pardalopoulos et al., 2011](#)). It is noted that in the case of shear failure before flexural yielding, the ratio $\frac{V_n}{V_{flex}} \leq 1$. The shear strength, V_n for the needs of seismic assessment are obtained from [ASCE/SEI 41, 2017](#) and [EN1998-3, 2005](#) respectively, using mean values for material strengths:

$$V_n^A = V_c + V_w = \eta^A \lambda \left(\frac{0.5 \sqrt{f_c}}{\frac{M}{Vd}} \sqrt{1 + \frac{P}{0.5 \sqrt{f_c} A_g}} \right) 0.8 A_g + \eta^A \frac{A_{s,tr} f_{y,tr,d}}{s} \quad (3.2)$$

$$V_n^E = V_c + V_w + V_N = \eta^E (\mu) \cdot 0.16 \sqrt{f_c} (0.8 A_c) [\max\{0.5, 100 \rho_{tot}\}] \cdot (1 - 0.16 \cdot \min\{5, \frac{L_s}{h}\}) + \eta^E (\mu) \frac{A_{st} f_{tt}(d-d')}{s} + \min\{N, 0.55 A_c f_c'\} \cdot \tan \alpha \quad (3.3)$$

Indices A and E given in the form of superscripts refer to the two reference standards [ASCE/SEI 41, 2017](#) and [EN1998-3, 2005](#) respectively, which are using different approaches for the discussed factor. Angle α in the [EN1998-3, 2005](#) approach refers to the angle of inclination of the diagonal compression with reference to the longitudinal axis of the element as shown in Fig. 3.1; i.e., it is defined by the line that connects the centroids of the compression zones in the opposite ends of the member.

A noteworthy difference of approach is underlying the two empirical models, despite that the expressions have been calibrated against the same database of tests. For one, the ASCE approach accounts for the influence of the axial load within the concrete contribution term, whereas in the EN approach the contribution of the axial load is considered as a standalone independent component – the value of $N \cdot \tan \alpha$ actually represents the horizontal component of the inclined strut that is visualized as transferring the axial load to the support of the column ([Chasioti et al., 2014](#); [Pardalopoulos et al., 2013](#)). Another difference is that whereas in the ASCE approach the axial load component degrades with increasing displacement ductility together with all other terms, its contribution is moderated by the $\frac{1}{2}$ exponent.

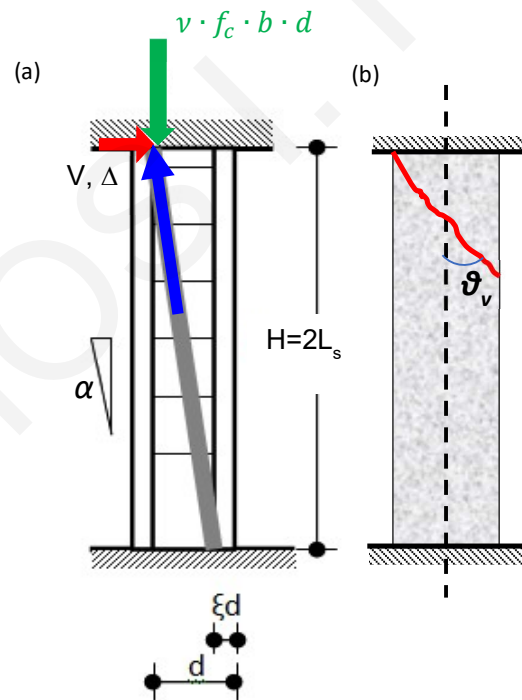


Figure 3. 1: EN model for the contribution of the diagonal strut to shear strength (a) Definition of the strut angle, and (b) definition of the critical crack angle, θ_v .

Relevant studies that have applied the above-mentioned framework have been conducted by [Aschheim and Moehle, 1992](#); [Lynn and Moehle, 1996](#); [Sezen and Moehle, 2004](#); [Elwood and Moehle, 2003](#); [Priestley et al., 1996](#). Regarding Eq. 3.3, for consistency with fundamental principles, a correction has been proposed at a later stage as follows: The effective concrete section area contributing to the shear strength at the critical section is equal to the area of compression zone, and therefore the $0.5\sqrt{f'_c} \cdot (0.8A_c)$ is replaced with $0.4\sqrt{f'_c} \cdot (\chi \cdot b)$ ([Tureyen and Frosch, 2003](#)) – at this point the compression zone height is taken equal to $\chi = \xi d$ ([Berry et al., 2004](#)).

[Ioannou et al. 2018](#) considered the EN expressions with some additional modifications that had been proposed earlier in [Pardalopoulos et al. \(2013\)](#): first, the concrete contribution term is taken as per the [Tureyen and Frosch \(2003\)](#) approach where the underlying assumption is that shear transfer in cracked sections under cyclic loading occurs mainly in the compression zone of the member; second, the axial load contribution is accounted for, provided that the axial load ratio exceeds a lower limit of 0.1 (sign convention used is compression positive), so as to ensure that cracks in the compression zone are closed and the force component transferred may be non-trivial; and third, the number of stirrups activated in the V_w term is determined from the inclination of the critical crack plane measured with reference to the longitudinal axis, θ_v which is usually not taken as 45° as it is assumed from previous available models in the literature [$\cot\theta_v=1$] but rather, it depends on the axial load magnitude acting on the section (Fig. 3.1(b)):

$$V_n = 0.4\xi bd\sqrt{f'_c} + \lambda \cdot v \cdot (bdf_c) \tan \alpha + A_{st}f_{yt} \frac{d(1-\xi)}{s} \cdot \cot \theta_v \quad (3.4)$$

$$\theta_v = 45^\circ \text{ for } v \leq 0.10$$

$$\theta_v = 45^\circ - 15^\circ \cdot \frac{v}{0.25} \geq 30^\circ \text{ for } v \geq 0.25$$

$$\lambda = 1 \text{ if } v \geq 0.1, \text{ otherwise, } \lambda = 0$$

Also, If $\frac{d(1-\xi)}{s} \cdot \cot \theta_v < 1$ then the contribution of transverse reinforcement is ignored

$$\text{Where, } \tan \alpha = \frac{(h-0.8\xi d)}{H}$$

Figure 3.2 plots the normalized depth of the compression zone, ξ , for symmetrically reinforced cross sections, different amounts of (total) longitudinal reinforcement ratios and different axial load ratios.

Consequently, for the model considered, the contribution of the transverse reinforcement (V_w) is taken into consideration as long as it has been confirmed that at least one stirrup meets the critical sliding plane. Last but not least, all terms are reduced with increasing displacement ductility through a postulated reduction factor $0.7 \leq \eta(\mu_\Delta) \leq 1$. The above model is examined through comparison with results from tests and nonlinear F.E. analysis described in the following sections.

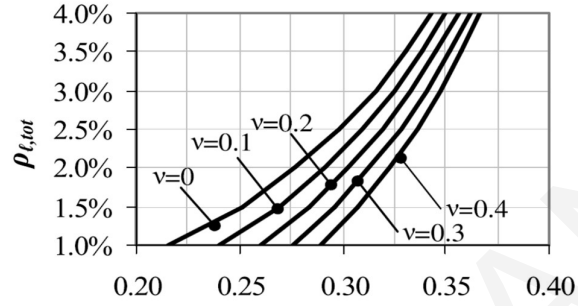


Figure 3. 2: Relationship between ξ , $\rho_{l,tot}$ and normalized axial load ratio, v , for columns at the onset of yielding

Literature regarding the limit states in terms of the deformation capacity is dominated by the simplified mechanistic model of [Elwood and Moechle \(2005\)](#) although in recent years a few attempts at improvement of the expressions though further calibration with tests and different regression analyses have been made ([Matchulat 2008](#); [Azadi et al., 2019](#)). To determine the relative drift at shear failure (at 80% residual strength) the following has been recommended:

$$\theta_{sh,fail} = \max \left(3\% + 4\rho_{st} - \frac{1}{40} \frac{v_{ee}}{\sqrt{f_c}} - \frac{1}{40} v; \frac{1}{100} \right) \quad \text{in MPa} \quad (3.5)$$

where ρ_{st} is the transverse reinforcement ratio ($A_{sw}/b \cdot s$) and v_{ee} is the shear stress ($v = V_{test}/bd$) – it is noted here that the last term, for an axial load ratio of 0.3, reduces the effective drift capacity by 0.0075 radians; higher shear demand also reduces effectively the drift capacity which however increases with shear reinforcement. For calculating the drift capacity at axial load failure, the residual strength along the plane of sliding failure is estimated from the clamping action of stirrups:

$$V_{s,0} = \frac{A_{sw} f_{yw} (d-d')}{s} \cot \theta_v \quad (3.6a)$$

Whereas the relative drift ratio where the loss of axial load bearing capacity takes place is estimated from:

$$\theta_{\alpha, fail} = \frac{4}{100} \frac{1 + (\tan \theta)^2}{\tan \theta + P \left(\frac{s}{A_s w f_y w d_c \tan \theta} \right)} \text{ where } \theta = 65^\circ \quad (3.6b)$$

The inclination θ_v of the failure plane, defined with reference to the element's longitudinal axis, is taken equal to 65° for the calculation of Equation 3.6. The above relationship emerged from correlation of the model with reinforced concrete experimental results with an axial load ratio of 0.5, where a loss of axial load bearing capacity had been reported (e.g., Matchulat et al., 2008).

Actions in a structure are classed as either deformation controlled, or force controlled, according to ASCE/SEI 41, 2017. The identification of linear and nonlinear acceptance criteria of deformation-controlled actions is specified in Table 3.1 and Table 3.2 for beam and column elements respectively. The acceptance criteria are classified according to the limiting structural damage state where IO=intermediate occupancy; LS=Life Safety and CP=Collapse prevention.

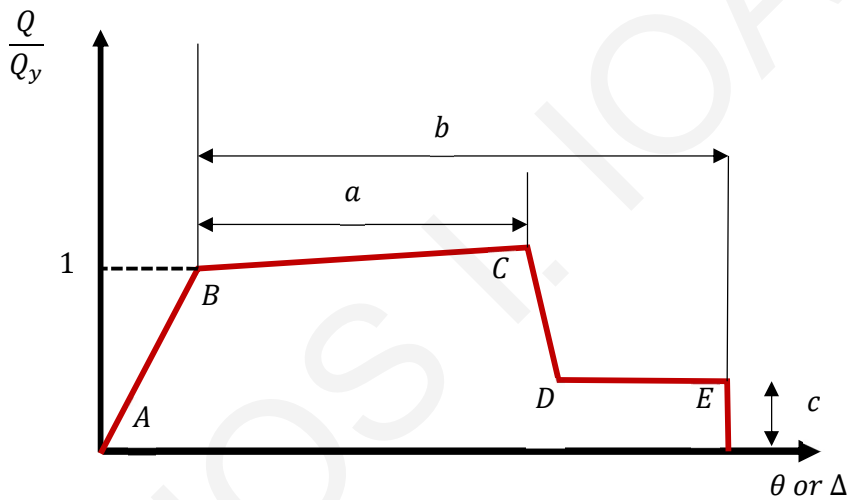


Figure 3. 3: Generalized Force - Deformation Relation for Concrete Elements or Components (ASCE/SEI 41, 2017)

Table 3. 1: Modeling parameters and Numerical Acceptance Criteria for Nonlinear Procedures-Reinforced Concrete Beams according to [ASCE/SEI 41, 2017](#)

| Conditions | | | Modelling Parameters ^a | | | Acceptance Criteria ^a | | |
|---|---------------------------------------|------------------------------------|-----------------------------------|-------------------------|---------------------------------|----------------------------------|--------|--------|
| | | | Plastic Rotation Angle (radians) | Residual Strength Ratio | Plastic Rotation Angle(radians) | Performance Level | | |
| | | | a | b | c | IO | LS | CP |
| Condition i. Beams controlled by flexure^b | | | | | | | | |
| $\frac{\rho - \rho'}{\rho_{bal}}$ | Transverse Reinforcement ^c | $\frac{V^d}{b_w d \sqrt{f'_{CE}}}$ | | | | | | |
| ≤0.0 | C | ≤0.25 | 0.025 | 0.05 | 0.2 | 0.010 | 0.025 | 0.05 |
| ≤0.0 | C | ≥0.5 | 0.02 | 0.04 | 0.2 | 0.005 | 0.02 | 0.04 |
| ≥0.5 | C | ≤0.25 | 0.02 | 0.03 | 0.2 | 0.005 | 0.02 | 0.04 |
| ≥0.5 | C | ≥0.5 | 0.015 | 0.02 | 0.2 | 0.005 | 0.0015 | 0.02 |
| ≤0.0 | NC | ≤0.25 | 0.02 | 0.03 | 0.2 | 0.005 | 0.02 | 0.03 |
| ≤0.0 | NC | ≥0.50 | 0.01 | 0.015 | 0.2 | 0.0015 | 0.01 | 0.015 |
| ≥0.5 | NC | ≤0.25 | 0.01 | 0.015 | 0.2 | 0.005 | 0.01 | 0.0015 |
| ≥0.5 | NC | ≥0.5 | 0.005 | 0.01 | 0.2 | 0.0015 | 0.005 | 0.01 |
| Condition ii. Beams controlled by shear^b | | | | | | | | |
| Stirrup spacing ≤d/2 | | | 0.003 | 0.02 | 0.2 | 0.0015 | 0.01 | 0.02 |
| Stirrup spacing >d/2 | | | 0.003 | 0.01 | 0.2 | 0.0015 | 0.005 | 0.01 |
| Condition iii. Beams controlled by inadequate development or splicing along span^b | | | | | | | | |
| Stirrup spacing ≤d/2 | | | 0.003 | 0.02 | 0.0 | 0.0015 | 0.01 | 0.02 |
| Stirrup spacing >d/2 | | | 0.003 | 0.01 | 0.0 | 0.0015 | 0.005 | 0.03 |
| Condition iv. Beams controlled by inadequate embedment into beam-column joint^b | | | | | | | | |
| | | | 0.0015 | 0.003 | 0.2 | 0.01 | 0.02 | 0.03 |

Note: f'_{CE} in MPa units.

^a Values between those listed in the table should be determined by linear interpolation.

^b Where more than one of conditions i, ii, iii and iv occur for a given component, use the minimum appropriate numerical value from the table.

^c "C" and "NC" are abbreviations for conforming and nonconforming transverse reinforcement, respectively. Transverse reinforcement is conforming, within the flexural plastic hinge region, hoops are spaced at ≤d/3, and if, for components of moderate and high ductility demand, the strength provided by the hoops (V_s) is at least ¾ of the design shear. Otherwise, the transverse reinforcement is considered nonconforming

^d V is the design shear force from NSP or NDP

Table 3. 2 : Modeling Parameters and Numerical Criteria for Nonlinear Procedures – Reinforced Concrete Columns other than Circular with Spiral Reinforcement or Seismic Hoops as Defined in ACI 318 according to [ASCE/SEI 41, 2017](#)

| Modelling Parameters ^a | Acceptance Criteria ^a | | |
|---|----------------------------------|----------|----------|
| | Plastic Rotation Angle(radians) | | |
| | Performance Level | | |
| Plastic Rotation Angles, a and b (radians) | IO | LS | CP |
| Residual Strength Ratio, c | | | |
| Columns not controlled by inadequate development or splicing along the clear height ^a | | | |
| $a = (0.042 - 0.043 \frac{N_{UD}}{A_g f'_{cE}} + 0.63 \rho_t - 0.023 \frac{V_{yE}}{V_{colOE}} \geq 0.0$ | $0.15a \leq 0.005$ | $0.5b^b$ | $0.7b^b$ |
| For $\frac{N_{UD}}{A_g f'_{cE}} \leq 0.5$ $b = \frac{0.5}{5 + \frac{N_{UD}}{0.8 A_g f'_{cE} \rho_t f_{ytE}}} - 0.01 \geq a^a$ | | | |
| $c = 0.24 - 0.4 \frac{N_{UD}}{A_g f'_{cE}} \geq 0.0$ | | | |
| Columns controlled by inadequate development or splicing along the clear height^c | | | |
| $a = \left(\frac{1 \rho_t f_{ytE}}{8 \rho_l f_{ylE}} \right) \begin{cases} \geq 0.0 \\ \leq 0.025^d \end{cases}$ | 0.0 | $0.5b$ | $0.7b$ |
| $b = \left(0.012 - 0.085 \frac{N_{UD}}{A_g f'_{cE}} + 12 \rho_t^e \right) \begin{cases} \geq 0.0 \\ \geq a \\ \leq 0.06 \end{cases}$ | | | |
| $c = 0.15 + 36 \rho_t \leq 0.4$ | | | |
| <p>Notes: ρ_t shall not be taken as greater than 0.0175 in any case nor greater than 0.0075 when ties are not adequately anchored in the core. Equations in the table are not valid for columns with ρ_t smaller than 0.0005</p> <p>$\frac{V_{yE}}{V_{colOE}}$ shall not be taken as less than 0.2</p> <p>N_{UD} shall not be the maximum compressive axial load accounting for the effects of lateral forces as described in $Q_{UD} = Q_G + Q_E$ where Q_{UD} =deformation-controlled action caused by gravity loads and earthquake forces; Q_G= action caused by gravity loads as defined in Paragraph 7.2.2 of ASCE/SEI 41, 2017; Q_E =action caused by the response to selected Seismic Hazard Level calculation using Paragraphs 7.4.1 and 7.4.2 of ASCE/SEI 41, 2017.</p> <p>Alternatively, it shall be permitted to evaluate N_{UD} based on the limit state analysis:</p> <p>^a b shall be reduced linearly for $\frac{N_{UD}}{(A_g f'_{cE})} > 0.5$ from its value at $\frac{N_{UD}}{(A_g f'_{cE})} = 0.5$ to zero at $\frac{N_{UD}}{(A_g f'_{cE})} = 0.7$ but shall not be smaller than a</p> <p>^b $\frac{N_{UD}}{(A_g f'_{cE})}$ shall not be taken as smaller than 0.1</p> <p>^c Columns are considered to be controlled by inadequate development or splices where the calculated steel stress at the splice exceeds the steel stress specified by Eq. (10-1a) and (10-1b) of ASCE/SEI 41, 2017. Modelling parameter</p> | | | |

for columns controlled by inadequate development or splicing shall be taken as zero if the splice region is not crossed by at least two tie groups over its length.

^da for columns controlled by inadequate development or splicing shall be taken as zero if the splice region is not crossed by at least two tie groups over its length

^e ρ_t shall not be taken as greater than 0.0075

The parameters affecting the value of drift at failure are, the aspect ratio, the second-order effects because of the axial load, and the transverse reinforcement ratio. Additionally, it is estimated that the residual shear strength, which may degrade down to 60% - 70% of the design value (EN1998-3, 2005, ASCE/SEI 41, 2017) and applies independently from steel reinforcement details and axial load size, seems to be conservative. In the following, and in order to understand the phenomenon better, a set of experimental data is examined paying special attention to the individual phenomena contributing to the overall loss of resistance.

3.3 Selection of Dataset Entries

The dataset used in the present study comprised 74 specimens containing steel reinforcement configurations that classify as of old type. Before using the data, a correction was considered on account of the apparent loss of strength caused by second order effects which was kept separate from the actual degradation. Through this process, the post peak reduction of the envelope became milder (see Fig. 3.4(b) which illustrates schematically the resulting differentiated envelope resistance curve as modified from the original experimental result). The influence of the correction is negligible for low levels of relative drift (<1%) but it becomes significant at higher levels. The conceptual failure point at 20% loss of shear strength was defined in order to quantify the ductility that led to this degradation (i.e., in 80% residual strength, see Fig. 3.4(c)). This displacement divided by the yielding displacement gives the ductility level at shear failure, $\mu_{\Delta, Sh-fa}$. For this value of ductility, the estimated degradation of the Code models was calculated and compared with the 20% loss that was used as an anchor point reference (nominal shear failure).

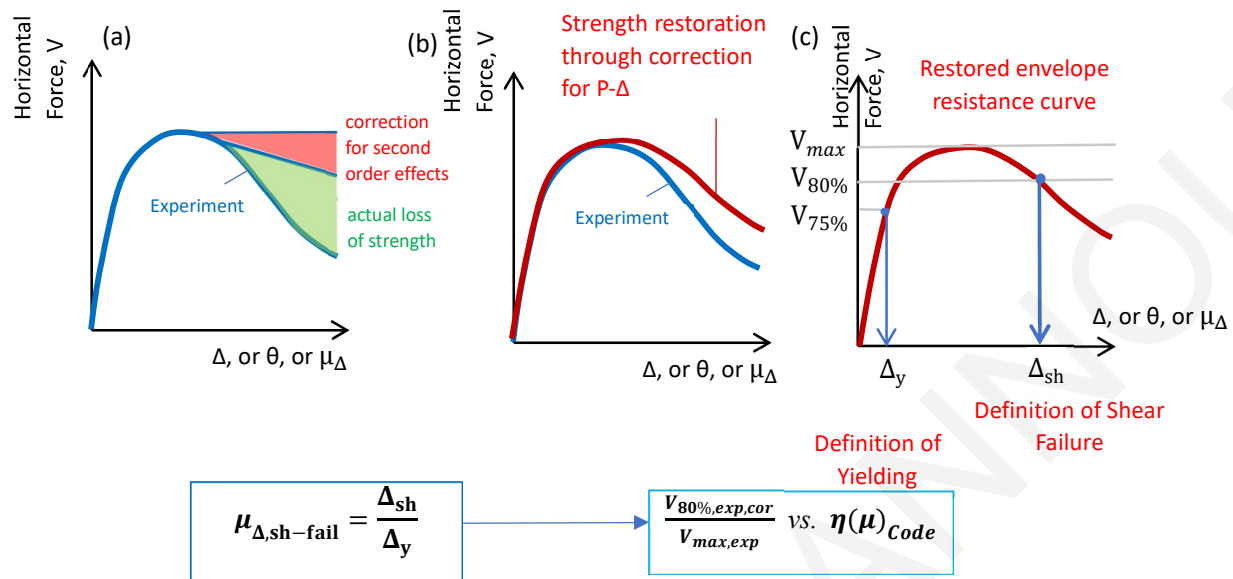


Figure 3. 4 : Schematic representation of the influence of second order effects in the envelope resistance curve

3.4 Description of Data Base Configurations (Data, Parameters and Description of the Procedure Followed for Data Base Composition)

A comprehensive selection and correction of the available experimental results was carried out which aimed to remove any experimental bias and the statically quantifiable effects such as P-Δ from the strength degradation relationships. In the selected dataset, reinforced concrete columns with rectangular cross section, tested under static cyclic loading to single or double curvature were included. Criterion for the specimens' selection was the reporting of a pure shear or a flexure-shear failure, which meant that longitudinal reinforcement yielding preceded the observed shear failure. Several of the specimens were extracted from available databases from [Berry et al. \(2004\)](#) and [Kim et al. \(2018\)](#).

Table 3. 3: Analysis of data base parameters

| Parameter | Definitions⁸ |
|-----------------------|--|
| Test | Identification Code |
| Slippage | if longitudinal bar slippage is possible out of the critical section |
| L_s | Element shear span |
| b | Section Width |
| h | Section Height |
| d | Effective depth from the extreme compression face of a reinforced concrete section to the centroid axis of tensile steel reinforcement |
| L_s/d | Shear span to depth ratio |
| c | Concrete cover |
| ρ_{tot} | Longitudinal reinforcement ratio |
| f_{yt} | Longitudinal reinforcement yielding stress |
| d_{bl} | Longitudinal reinforcement diameter |
| f_c | Concrete compressive strength |
| d_{bw} | Transverse reinforcement diameter |
| s | Transverse reinforcement spacing |
| f_{yw} | Transverse reinforcement yielding stress |
| ρ_{st} | Geometrical transverse reinf. ratio in the direction of seismic action |
| $v=P/f_c A_c$ | Axial load ratio |
| P | Axial load |
| Failure | FS= Flexure-Shear Failure=2 |
| Classification | S=Shear Failure =1 |
| θ_y | Drift at yield point |
| θ_{shear} | Drift at shear failure |

| | |
|----------------------|--------------------------------|
| θ_{axial} | Drift at axial failure |
| θ_{max} | Drift at maximum lateral load |
| $V_{exp,max}$ | Experimental shear force |
| $V_{Response\ 2000}$ | Analytical maximum shear force |

**Notation: For Table 3.3, the drift at shear failure is taken at 80% residual post peak strength after correction of the recorded resistance. Drift at axial failure is associated with the inadequacy to support axial load on the corrected envelope resistance curve.*

Specimens in the dataset are drawn from the experimental studies of, [Lynn et al. 2001](#); [Henkhaus et al. 2013](#); [Zhou et al. 1987](#); [Kim et al. 2018](#); [Nagasaka et al. 1982](#); [Arakawa et al. 1989](#); [Umehara et al. 1982](#); [Aboutaha, 1999](#); [Sokoli and Ghannoum, 2016](#); [Matchulat et al. 2008](#); [Sezen and Moehle 2002](#); [Pujol et al. 2002](#); [Ohue et al. 1985](#); [Amitsu et al. 1991](#); [Martirosyan and Xiao 2001](#); [Zhou et al. 1985](#); [Imai and Yamamoto et al. 1986](#) and [Ono et al., 1989](#). The collection of data is given in Table 3.4

Table 3. 4: Data set with specimen details

| Reference | Test | Member | Loading | L_c (mm) | h_{col} (mm) | b (mm) | h (mm) | a/d | d (mm) | cover(mm) | ρ_{int} (%) | f_{yl} (Mpa) | d_{hl} (mm) | f'_c (Mpa) | d_{hw} (mm) | A_{tr} (mm) | s (mm) | f_{yw} (Mpa) | ρ_w (%) | v max | P(KN) max | Failure Mode |
|-------------------------------|-----------|--------|---------|------------|----------------|--------|--------|-----|--------|-----------|------------------|----------------|---------------|--------------|---------------|---------------|--------|----------------|--------------|-------|-----------|--------------|
| Lynn et al.(1996) | 3SLH18 | Column | Cycling | 1473.0 | 2946.0 | 457.0 | 457.0 | 3.2 | 381.0 | 38.1 | 3.0 | 331.0 | 31.8 | 26.9 | 9.5 | 141.8 | 457.0 | 400.0 | 0.1 | 0.1 | 503.0 | S |
| Lynn et al.(1996) | 3CMD12 | Column | Cycling | 1473.0 | 2946.0 | 457.0 | 457.0 | 3.2 | 381.0 | 38.1 | 3.0 | 331.0 | 31.8 | 27.6 | 9.5 | 241.0 | 305.0 | 400.0 | 0.2 | 0.3 | 1512.0 | S |
| Lynn et al.(1996) | 3CMH18 | Column | Cycling | 1473.0 | 2946.0 | 457.0 | 457.0 | 3.2 | 381.0 | 38.1 | 3.0 | 331.0 | 31.8 | 27.6 | 9.5 | 141.8 | 457.0 | 400.0 | 0.1 | 0.3 | 1512.0 | S |
| Henkhauset al. 2013 | B1 | Column | Cycling | 736.5 | 1473.0 | 457.0 | 457.0 | 1.6 | 401.4 | 35.0 | 1.5 | 455.0 | 22.2 | 20.0 | 9.5 | 141.8 | 457.0 | 490.0 | 0.1 | 0.4 | 1545.5 | S |
| Henkhauset al. 2013 | B2 | Column | Cycling | 736.5 | 1473.0 | 457.0 | 457.0 | 1.6 | 404.6 | 35.0 | 1.5 | 455.0 | 22.2 | 19.3 | 6.4 | 63.3 | 203.0 | 455.0 | 0.1 | 0.4 | 1531.7 | S |
| Henkhauset al. 2013 | B3 | Column | Cycling | 736.5 | 1473.0 | 457.0 | 457.0 | 1.6 | 401.4 | 35.0 | 1.5 | 455.0 | 22.2 | 22.1 | 9.5 | 141.8 | 457.0 | 490.0 | 0.1 | 0.2 | 969.3 | S |
| Henkhauset al. 2013 | B4 | Column | Cycling | 736.5 | 1473.0 | 457.0 | 457.0 | 1.6 | 399.7 | 35.0 | 2.5 | 441.0 | 25.6 | 24.1 | 9.5 | 241.0 | 457.0 | 490.0 | 0.1 | 0.4 | 2164.3 | S |
| Henkhauset al. 2013 | B5 | Column | Cycling | 736.5 | 1473.0 | 457.0 | 457.0 | 1.7 | 399.7 | 35.0 | 2.5 | 441.0 | 25.6 | 23.4 | 9.5 | 241.0 | 457.0 | 490.0 | 0.1 | 0.5 | 2248.1 | S |
| Henkhauset al. 2013 | B6 | Column | Cycling | 1473.0 | 2946.0 | 457.0 | 457.0 | 3.2 | 399.7 | 35.0 | 2.5 | 490.0 | 25.6 | 27.6 | 9.5 | 241.0 | 305.0 | 469.0 | 0.2 | 0.1 | 634.1 | S |
| Henkhauset al. 2013 | B7 | Column | Cycling | 1473.0 | 2946.0 | 457.0 | 457.0 | 3.2 | 399.7 | 35.0 | 2.5 | 490.0 | 25.6 | 28.3 | 9.5 | 241.0 | 305.0 | 469.0 | 0.2 | 0.1 | 650.1 | S |
| Henkhauset al. 2013 | B8 | Column | Cycling | 1473.0 | 2946.0 | 457.0 | 457.0 | 3.2 | 399.7 | 35.0 | 2.5 | 490.0 | 25.6 | 29.0 | 9.5 | 241.0 | 305.0 | 469.0 | 0.1 | 0.1 | 666.2 | S |
| Zhou et al.1987 | 104-08 | Column | Cycling | 160.0 | 320.0 | 160.0 | 160.0 | 1.0 | 137.8 | 12.5 | 2.2 | 341.0 | 9.5 | 19.8 | 5.0 | 39.3 | 40.0 | 599.0 | 0.7 | 0.8 | 406.0 | S |
| Zhou et al.1987 | 114-08 | Column | Cycling | 160.0 | 320.0 | 160.0 | 160.0 | 1.0 | 137.8 | 12.5 | 2.2 | 341.0 | 9.5 | 19.8 | 5.0 | 39.3 | 40.0 | 599.0 | 0.7 | 0.8 | 406.0 | S |
| Kim et al.2018 | Sbd2 | Column | Cycling | 1200.0 | 1200.0 | 400.0 | 400.0 | 3.0 | 334.8 | 40.0 | 2.5 | 571.0 | 25.0 | 32.0 | 12.7 | 253.4 | 165.0 | 500.0 | 0.4 | 0.2 | 870.4 | S |
| Kim et al.2018 | Sbd4 | Column | Cycling | 1200.0 | 1200.0 | 400.0 | 400.0 | 3.0 | 334.8 | 40.0 | 2.5 | 571.0 | 25.0 | 32.0 | 12.7 | 253.4 | 165.0 | 500.0 | 0.8 | 0.2 | 870.4 | S |
| Kim et al.2018 | SCd2 | Column | Cycling | 1200.0 | 1200.0 | 400.0 | 400.0 | 3.0 | 334.8 | 40.0 | 2.5 | 571.0 | 25.0 | 32.0 | 12.7 | 253.4 | 165.0 | 500.0 | 0.4 | 0.2 | 870.4 | S |
| Kim et al.2018 | SDd2 | Column | Cycling | 1200.0 | 1200.0 | 400.0 | 400.0 | 3.0 | 334.8 | 40.0 | 2.5 | 571.0 | 25.0 | 32.0 | 12.7 | 253.4 | 165.0 | 500.0 | 0.4 | 0.1 | 512.0 | S |
| Kim et al.2018 | SDd4 | Column | Cycling | 1200.0 | 1200.0 | 400.0 | 400.0 | 3.0 | 334.8 | 40.0 | 2.5 | 571.0 | 25.0 | 32.0 | 12.7 | 253.4 | 82.0 | 500.0 | 0.8 | 0.2 | 870.4 | S |
| Kim et al.2018 | Rfd2 | Column | Cycling | 1200.0 | 1200.0 | 250.0 | 640.0 | 4.8 | 187.4 | 40.0 | 2.4 | 566.0 | 22.2 | 32.0 | 9.5 | 212.6 | 105.0 | 530.0 | 0.8 | 0.2 | 870.4 | S |
| Nagasaka 1982 | HPRC10-63 | Column | Cycling | 300.0 | 600.0 | 200.0 | 200.0 | 1.5 | 176.2 | 12.0 | 1.3 | 371.0 | 12.7 | 21.6 | 5.5 | 47.5 | 35.0 | 344.0 | 0.7 | 0.2 | 146.9 | S |
| Arakawa et al.1989 | OA2 | Column | Cycling | 225.0 | 450.0 | 180.0 | 180.0 | 1.3 | 132.8 | 10.0 | 3.1 | 340.0 | 12.7 | 31.8 | 4.0 | 25.1 | 64.3 | 249.0 | 0.2 | 0.2 | 189.6 | S |
| Arakawa et al.1989 | OA5 | Column | Cycling | 225.0 | 450.0 | 180.0 | 180.0 | 1.3 | 132.8 | 10.0 | 3.1 | 340.0 | 12.7 | 33.0 | 4.0 | 25.1 | 64.3 | 249.0 | 0.2 | 0.4 | 475.8 | S |
| Umebara and Irsa 1982 | CUS | Column | Cycling | 455.0 | 910.0 | 410.0 | 230.0 | 1.1 | 369.5 | 25.0 | 3.0 | 441.0 | 19.0 | 34.9 | 6.0 | 56.5 | 89.0 | 414.0 | 0.3 | 0.2 | 533.2 | S |
| Umebara and Irsa 1982 | CUW | Column | Cycling | 455.0 | 910.0 | 230.0 | 410.0 | 2.0 | 189.5 | 25.0 | 3.0 | 441.0 | 19.0 | 34.9 | 6.0 | 56.5 | 89.0 | 414.0 | 0.3 | 0.2 | 533.2 | S |
| Umebara and Irsa 1982 | 2CUS | Column | Cycling | 455.0 | 910.0 | 410.0 | 230.0 | 1.1 | 369.5 | 25.0 | 3.0 | 441.0 | 19.0 | 42.0 | 6.0 | 56.5 | 89.0 | 414.0 | 0.3 | 0.3 | 1069.4 | S |
| Bet et al. 1985 | 1-1 | Column | Cycling | 457.0 | 914.0 | 305.0 | 305.0 | 1.5 | 264.5 | 25.0 | 2.4 | 462.0 | 19.0 | 29.9 | 6.0 | 96.1 | 210.0 | 414.0 | 0.2 | 0.1 | 289.3 | S |
| Aboutaha et al.1999 | SC3 | Column | Cycling | 1219.2 | 1219.2 | 457.2 | 914.4 | 2.7 | 397.2 | 38.0 | 1.9 | 434.0 | 25.0 | 21.9 | 9.5 | 354.4 | 406.4 | 400.0 | 0.1 | 0.0 | 0.0 | S |
| Aboutaha et al.1999 | SC9 | Column | Cycling | 1219.2 | 1219.2 | 914.4 | 457.2 | 1.3 | 854.4 | 38.0 | 1.9 | 434.0 | 25.0 | 16.0 | 9.5 | 141.8 | 406.4 | 400.0 | 0.1 | 0.0 | 0.0 | S |
| Sokoli and Ghannoum 2016 | CS-60 | Column | Cycling | 1066.8 | 2133.6 | 457.2 | 457.2 | 2.3 | 419.1 | 38.1 | 4.7 | 464.0 | 32.0 | 26.4 | 16.0 | 804.2 | 140.0 | 472.0 | 1.5 | 0.3 | 290.0 | FS |
| Sokoli and Ghannoum 2016 | CS-100 | Column | Cycling | 1066.8 | 2133.6 | 457.2 | 457.2 | 2.3 | 419.1 | 38.1 | 2.9 | 700.0 | 25.0 | 32.0 | 10.0 | 314.2 | 114.0 | 820.0 | 0.7 | 0.3 | 1806.0 | FS |
| Lynn et al.(1996) | 2CLH18 | Column | Cycling | 1473.0 | 2946.0 | 457.0 | 457.0 | 3.2 | 381.0 | 38.1 | 2.0 | 331.0 | 25.4 | 33.1 | 9.5 | 141.8 | 457.0 | 400.0 | 0.1 | 0.1 | 503.0 | FS |
| Lynn et al.(1996) | 3CLH18 | Column | Cycling | 1473.0 | 2946.0 | 457.0 | 457.0 | 3.2 | 381.0 | 38.1 | 3.0 | 331.0 | 31.8 | 25.6 | 9.5 | 141.8 | 457.0 | 400.0 | 0.1 | 0.1 | 503.0 | FS |
| Lynn et al.(1996) | 2SLH18 | Column | Cycling | 1473.0 | 2946.0 | 457.0 | 457.0 | 3.2 | 381.0 | 38.1 | 2.0 | 331.0 | 25.4 | 33.1 | 9.5 | 141.8 | 457.0 | 400.0 | 0.1 | 0.1 | 503.0 | FS |
| Lynn et al.(1996)(lap splice) | 2CMH18 | Column | Cycling | 1473.0 | 2946.0 | 457.0 | 457.0 | 3.2 | 381.0 | 38.1 | 3.0 | 331.0 | 25.4 | 25.7 | 9.5 | 141.8 | 457.0 | 400.0 | 0.1 | 0.3 | 1512.0 | FS |
| Lynn et al.(1996)(lap splice) | 3SMD12 | Column | Cycling | 1473.0 | 2946.0 | 457.0 | 457.0 | 3.2 | 381.0 | 38.1 | 3.0 | 331.0 | 31.8 | 25.6 | 9.5 | 241.0 | 305.0 | 400.0 | 0.2 | 0.3 | 1512.0 | S |
| Matchulata et al. 2005 | Sp.1 | Column | Cycling | 1473.0 | 2946.0 | 457.0 | 457.0 | 3.2 | 388.8 | 39.7 | 2.5 | 441.3 | 28.6 | 20.7 | 9.5 | 141.8 | 460.0 | 372.3 | 0.3 | 0.5 | 2159.5 | FS |
| Matchulata et al. 2005 | Sp.2 | Column | Cycling | 1473.0 | 2946.0 | 457.0 | 457.0 | 3.2 | 388.8 | 39.7 | 2.5 | 441.3 | 28.6 | 23.4 | 9.5 | 141.8 | 460.0 | 372.3 | 0.3 | 0.3 | 1663.0 | FS |

3.5 Parametric Analysis for Strength and Deformation Parameters

3.5.1 Correction for Second Order Effects According to the PEER (Berry et al., 2004)

Data Base Manual

In order to take into consideration the influence of second order effects, Berry et al. (2004) proposed four types of correction with regards to experiment boundary conditions. It was stated that columns included in the Berry et al. (2004) database needed to be resolved regarding the vertical and lateral components to consider P- Δ effects. The vertical load P is the axial load given by the available data. Depending on the test setup, the contribution of the vertical actuator is added to (or subtracted from) the force applied by the horizontal actuator component to obtain the net horizontal force, F_H .

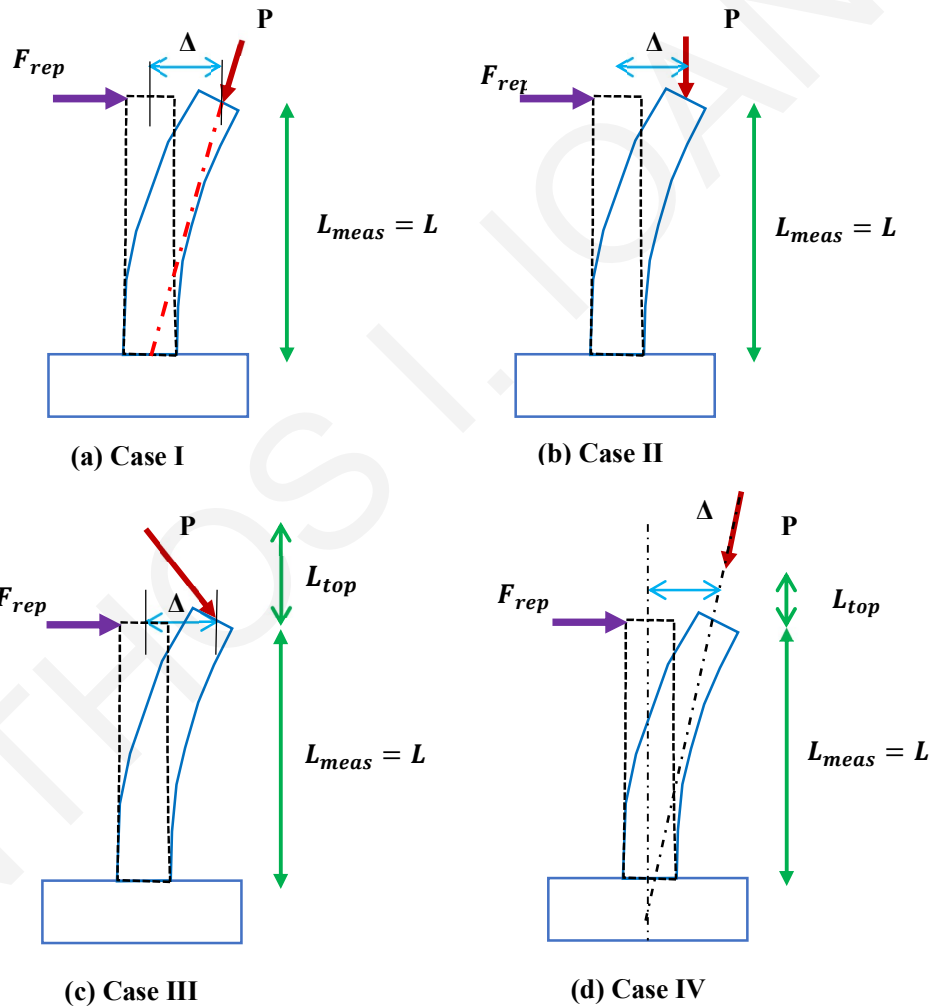


Figure 3. 5: Second order effects incidents according to Berry et.al. 2004

To enable consideration of the P- Δ effects in the reference study, the specimens were organized into four cases of lateral force-displacement application (see Figure 3.5). In the figure, the horizontal force is what is reported from the piston/jack through the data acquisition system (subscript “*rep*”). The schematics of the four cases illustrate how the reported value is used together with the magnitude of the axial load and the lateral drift, in order to calculate the actual horizontal (lateral) force F_H that quantifies the lateral resistance of the specimen.

- **Case I:** The force and displacement data in the source reference is in the format of effective force F_{rep} in a relationship with Δ at L_{meas} . Thus, in this manner of load application, the vertical rods that apply the axial load P on the column via prestressing rods, resist the lateral load, artificially increasing the measured strength. The actual lateral or horizontal resistance of the column is defined according to Equation 3.7.

$$F_H = F_{rep} - \frac{P\Delta}{L_{meas}} \quad (3.7)$$

- **Case II:** Force-displacement data in the source reference is in the format of horizontal piston force, force F_{rep} against the horizontal displacement, Δ .

$$F_H = F_{rep} \quad (3.8)$$

- **Case III:** Force data represent the horizontal load applied by the lateral actuator, but the top support of the vertical hydraulic jack does not move – instead the jack pivots at its top support to follow the specimen at the point of its attachment to it. Here, the lateral component of the vertical load actuator needs to be added to the reported force, F_{Rep} , in order to be included in the combined horizontal force (F_H).

$$F_H = F_{rep} + \frac{PL_{top}}{\Delta} \quad (3.9)$$

- **Case IV:** Force data represent the horizontal load applied by the lateral actuator. Because the axial load ratio is not applied at the same elevation as the lateral force, the horizontal component (P_H) of the vertical load actuator is subtracted from the reported force, F_{rep} , to get the horizontal force (F_H).

$$P_H = P \cdot \sin a \quad (3.10)$$

$$a = \tan^{-1} \left[\frac{\Delta \left[\frac{L+L_{top}}{L} \right]}{L+L_{top}+L_{bot}} \right] \quad (3.11)$$

$$F_H = F_{Rep} - P_H \quad (3.12)$$

When the axis of the axial load application does not pass through the centroid of the base cross section as in cases II and III, then the combined lateral force and the overbearing vertical load contribute to the total base moment as follows:

$$M_{base} = F_H \cdot L + P \cdot \Delta \left(\frac{L_{top} + L}{L_{meas}} \right) \quad (3.13)$$

F_H =net horizontal force (Column Shear)

L =shear span length

P =gravity vertical load

Δ =measured displacement at cantilever elevation L_{meas}

L_{top} =distance from elevation at which lateral force was applied to elevation at which gravity (vertical load) is applied

L_{meas} =elevation at which lateral column displacement was measured

As the flexural moment is the only objective measure of the member strength, the corrected, effective shear force can then be calculated from:

$$F_{eff} = \frac{M_{base}}{L} \quad (3.14)$$

3.5.2 Additional Correction of Second Order Effects

With reference to the primary purpose of this investigation, it is recommended that the actual column shear, V_{actual} be used instead of F_H in each of the cases described in section 3.5.1. This was analyzed in detail in Fig. 2.9; it is noted that even in the case of follower axial loads that are applied through prestressing rods that connect the centroid of the top cross section of a cantilever specimen with the centroid of the base, reportedly so as to eliminate the second order effects, errors are induced as the load cannot follow the trajectory of the deforming specimen. Thus, the top cross section where the axial load is applied, rotates by 1.5θ , where $\theta = \Delta/L$ the column drift – which introduces further errors that are generally not accounted for since it is generally assumed that the vertical follower force acting along the chord of the member makes no contribution to shear. Here the member is analyzed in the deformed configuration to account for these effects, as outlined by the following Equations 3.15, 3.16, 3.17, 3.18 and 3.19 which define the calculation of V_{actual} as per Fig. 3.6:

Case I:

$$V_{actual} = F_H + P \cos \theta_{vp} \frac{\Delta}{L_{meas}} \quad (3.15)$$

Case II:

$$V_{actual} = F_H + P \frac{\Delta}{L_{meas}} \quad (3.16)$$

Case III:

$$V_{actual} = F_H + P \sin \theta_{vp} \frac{\Delta}{L_{meas}} \quad (3.17)$$

Case IV:

$$V_{actual} = F_H + P \frac{\Delta}{L_{meas}} \quad (3.18)$$

Case V:

$$V_{actual} = (F_{rep} - V_{pist,tot}) + P_{test} \cos \theta_{vp} \cdot \frac{\Delta}{H_{col}} \approx (F_{rep} - V_{pist,tot}) + P_{test} \cdot \frac{\Delta}{H_{col}} \approx F_{rep} \quad (3.19)$$

In the above equations, θ_{vp} is the rotation of the piston relative to the vertical axis, in degrees.

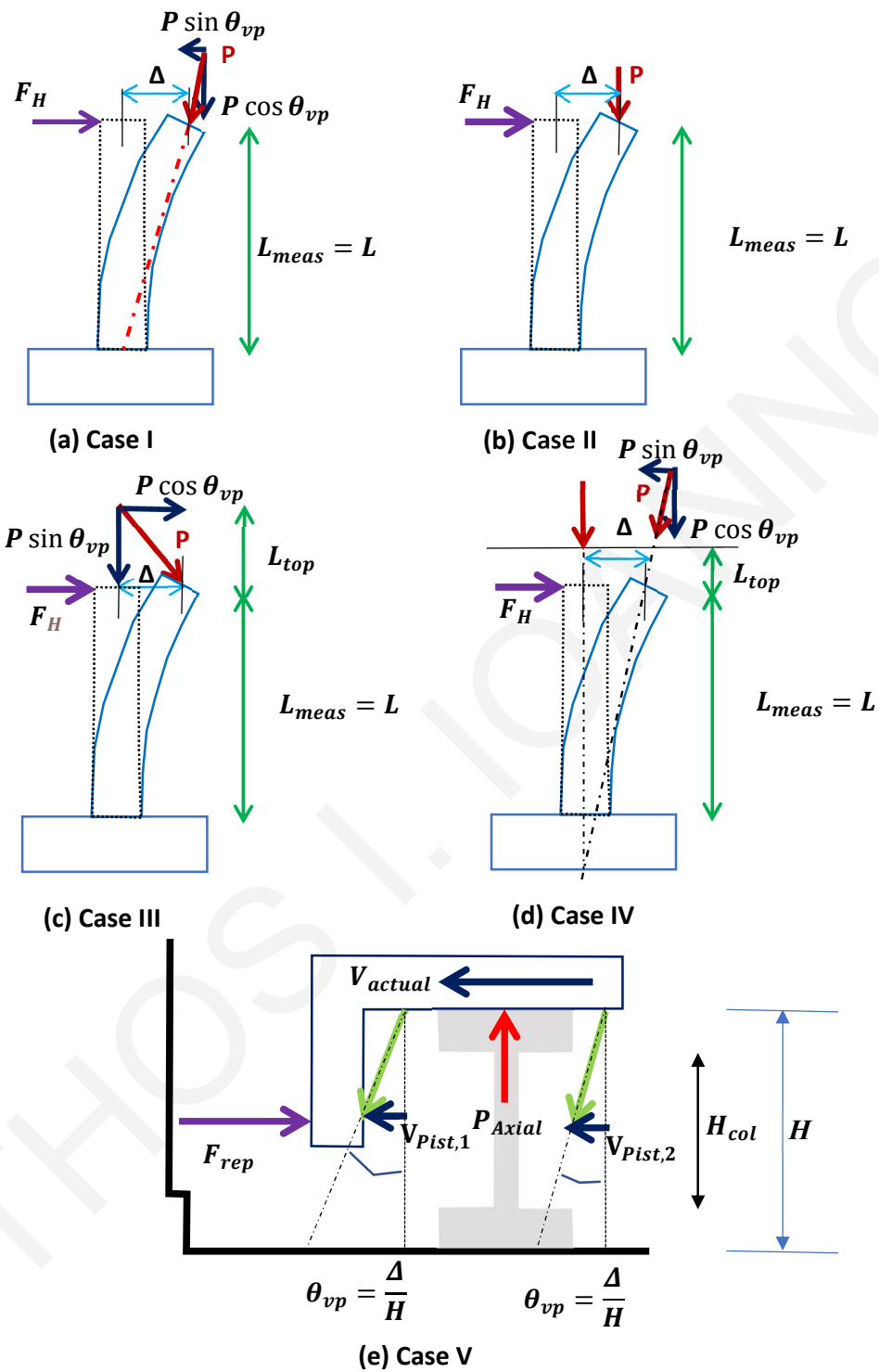


Figure 3. 6: Additional corrections for second order effects for cases I, II, III, IV

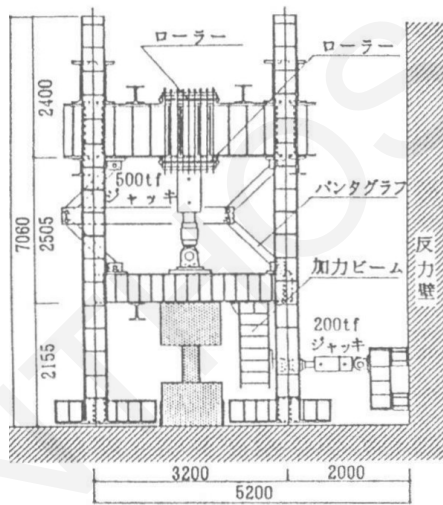
3.6 Methodology Followed for Dataset Processing

3.6.1 Shear Strength Degradation

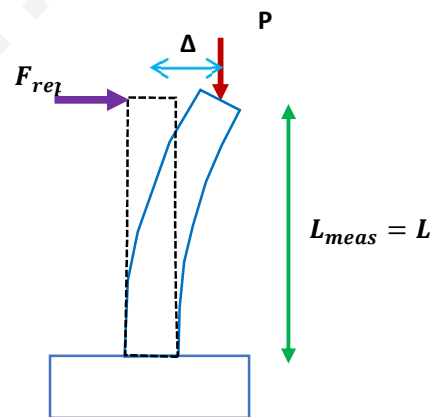
Figure 3.7 summarizes, using as an example case specimen CB060C by Amitsu et al (1991), the steps of systematic processing of the data so as to eliminate contributions of P- Δ effects from the apparent strength degradation with increasing drift demand. Appendix B details the analytical process used on all specimens included in the dataset.

1. Classification of experimental type according to the cases discussed in previous paragraph.
2. Determination of V_{actual} value according to Eq. 3.15, 3.16, 3.17, 3.18 and 3.19
3. Correlation between degradation factor proposed values and the relevant values carried out considering the influence of second order effects
4. Section and member analysis through Response 2000 to evaluate the elements' flexural resistance, V_{flex} considering the influence of shear in the stress and strain analysis
5. Data processing and optimization of proposed and existing relationships concerning the elements' shear strength evaluation.

Failure classification: Flexure-Shear

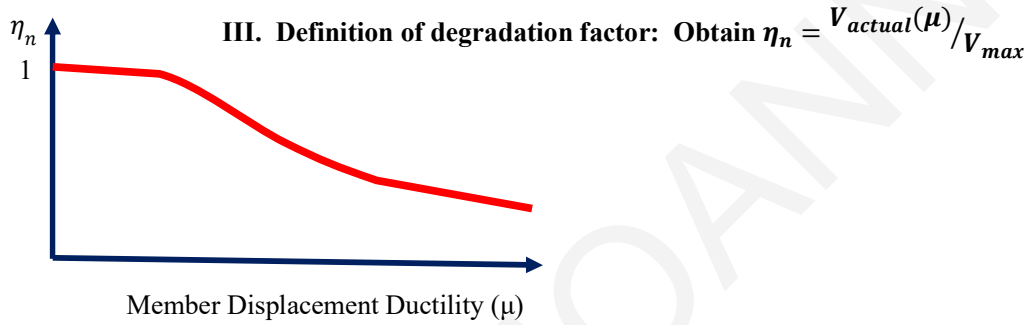
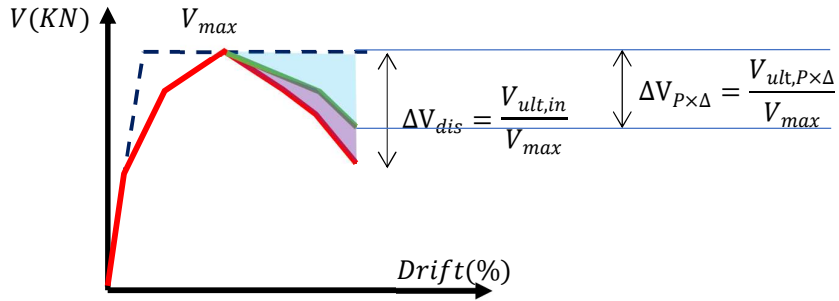


Boundary Conditions
Categorization



Case II

II. Correction of the envelope considering P×Δ



I. Plotting of Resistance Curve in accordance with the source experiment and the data from PEER

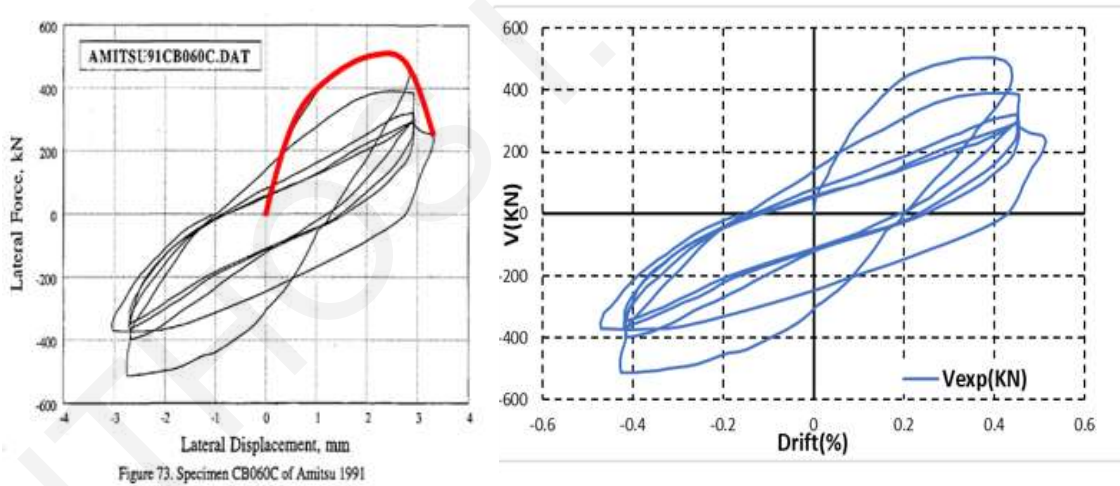


Figure 3. 7 : Procedure followed for second order effects consideration

3.6.1.1 Investigation of Proposed and Existent Equations Related to the Evaluation of the Shear Strength of Reinforced Concrete Elements

Figure 3.8 shows a comparison of the experimental values from the dataset against the proposed model related to shear strength evaluation of Equation 3.4 (Pardalopoulos et al., 2013) and the respective suggested model from EN1998-3, 2005 (Equation 3.3). The purpose of the study was to verify the consistency of the examined models in terms of actual experimental reinforced column shear or flexure-shear failures to propose improved models using an optimization methodology as detailed in the following paragraphs.

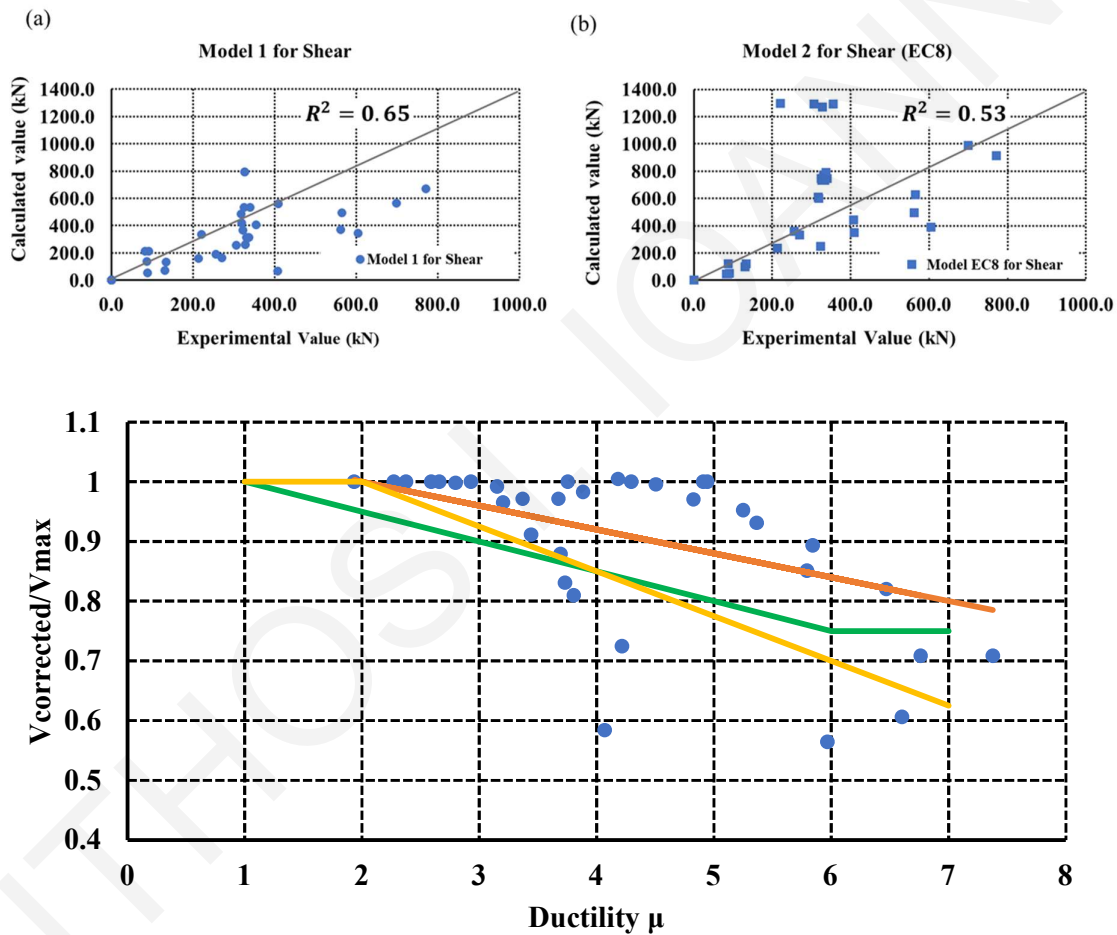


Figure 3. 8: Correlation of data base elements experimental corrected maximum shear strength vs. proposed models (a) Proposed model by Pardalopoulos et al. (2013); (b) Proposed model by EN1998-3, 2005; Degradation models of flexure-shear failures after correction of the data. (Green line: Eurocode; Yellow: ASCE/SEI -41)

The 45° line is the equal value case: points above it are cases where the analytical estimate overestimates the experiment; points below are conservative estimates. Consistent overestimation suggests the need for introduction of a safety factor; distant dispersion from the equal value line suggests poor predictive capacity. It is observed that the model proposed by [Pardalopoulos et al. 2013](#) has a higher correlation value of $R^2 = 0.65$ than the current [EN1998-3, 2005](#) model, that has a correlation coefficient of $R^2 = 0.53$. This result underscores the need for improvement of the maximum shear strength estimate. To achieve this objective, an optimization technique has been used.

Degradation of shear strength with increasing ductility for the experiments that experienced shear failure after correction for the contribution of the axial load in the response is depicted by the orange line in Fig. 3.8(c) below, defined by:

$$V_{red} = (V_{actual})(1 - 0.04 \cdot (\mu_{\theta} - 2)) \quad (3.19)$$

It is noted that this is much milder than the estimated degradation obtained from the current expression ([KA.NE.IIE., 2014](#)).

3.6.1.2 Optimization of Shear Strength Estimation Using an MLA

The Machine Learning Algorithm (MLA) model's basic concepts are focused on the formation of nonlinear terms made up of various combinations of independent variables up to the third degree. The method may choose nonlinear features that correlate to the lowest prediction error automatically.

The algorithm was programmed to analyze 90 percent of the data by discovering relative relationships, which were then utilized to train the system. The remaining 10% of the data was then used to evaluate the performance of the shear strength equations after optimization. This procedure is repeated 100 times, by choosing randomly permuted subsets of the training set, in a cross-validation setting. The algorithm on the next page provides the procedure for generating the formula that has been developed in Julia programming language ([Bezanson et al. 1992; Murphy 2012](#)). It was confirmed that the proposed algorithm is efficient in supplying the necessary tools for constructing the prediction equations based on the numerical inquiry performed for the purposes of this work. However, this is based on a limited dataset, and in our future steps, we will enrich the dataset with more samples, and possibly further refine the resulting expressions.

To build a design formula through training, a large number of data sets was necessary (related to experimental shear strength), and the shear strength experimental results of data base elements were employed as an independent variable. Additionally, the parameters from proposed equations from [Pardalopoulos et al. \(2013\)](#) and [EN1998-3 2005](#) were employed as dependent variables, with the goal of proposing improved models for both Equations 3.3 and 3.4. Figures 3.9 and 3.10 and Equations 3.20 and 3.21 show the results of optimized models, respectively.

$$V_{3,terms} = a \cdot d \cdot f_{yw} \cdot \theta_v + b \cdot f_{yl} \cdot A_{tr} \cdot v + c \cdot s^2 \cdot v \quad \text{all units in mm, MPa and degrees} \quad (3.20)$$

$$\theta_v = 45^\circ \text{ for } v \leq 0.10 \quad \theta_v = 45^\circ - 15^\circ \cdot \frac{v}{0.25} \geq 30^\circ \text{ for } v \geq 0.25$$

$$a = 4 \times 10^{-4}, b = 4.1 \times 10^{-3}, c = 2.87 \times 10^{-2}$$

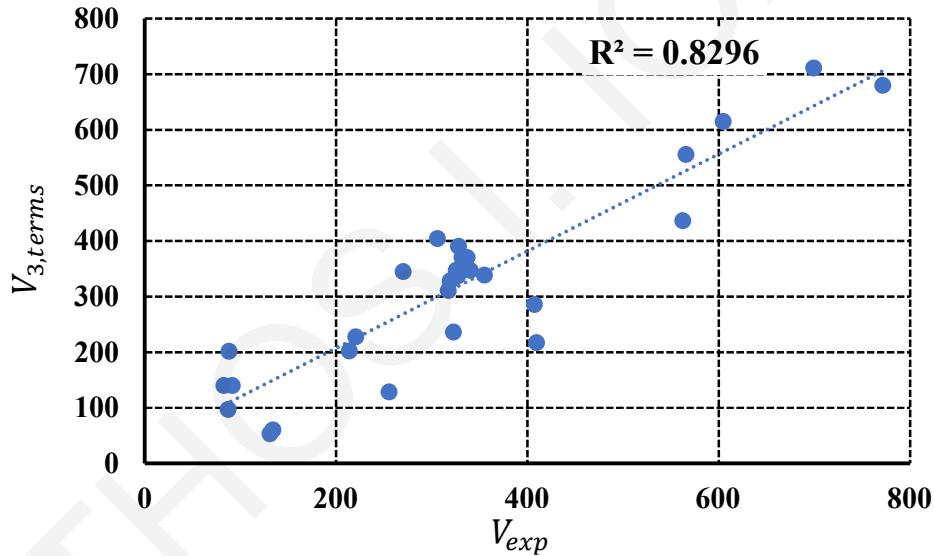


Figure 3. 9: Extra validation data for proposed shear strength model from [Pardalopoulos et al. \(2013\)](#). Correlation of the 3-feature formula.

$$V_{3,terms} = a \cdot \tan a \cdot 0.55 \cdot A_c \cdot f'_c \cdot \sqrt{f'_c} \cdot A_c + b \cdot P^2 \cdot 100 \cdot \rho_{tot} + c \cdot (\sqrt{f'_c} \cdot A_c)^3 \quad (3.21)$$

$$a = 4.47 \cdot 10^{-11}, b = 5.65 \cdot 10^{-11}, c = 1.4 \cdot 10^{-16}$$

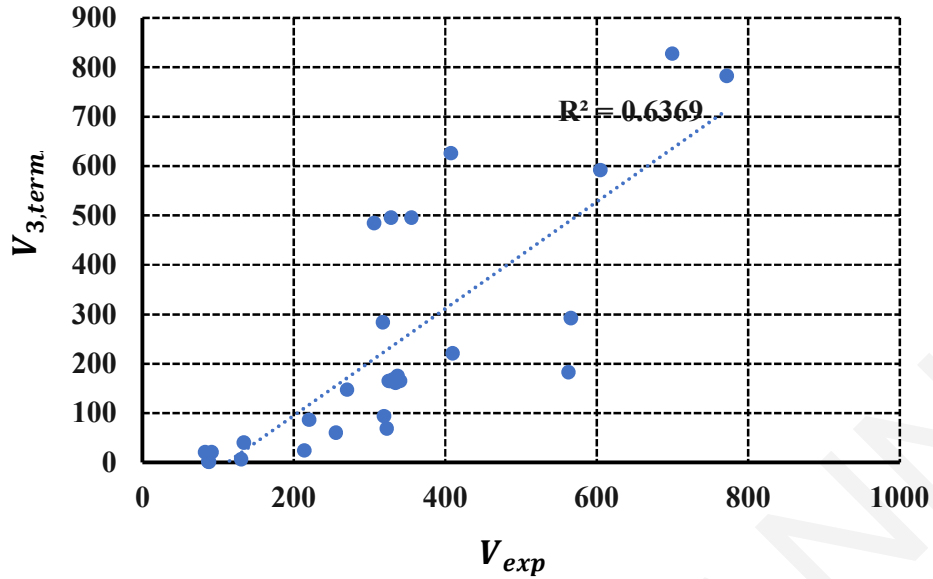


Figure 3. 10: Extra validation data for proposed shear strength model from EN1998-3 2005: Correlation of the 3-feature formula.

3.6.2 Correlation of Experimental Values of Drift at Shear and Axial Failure

The parameters of $\theta_{sh,fail}$ and $\theta_{\alpha,fail}$ have been recorded using the experimental envelope curves of each column from the dataset. The drift at shear failure is measured at a 20 percent reduction of maximum lateral strength, while the drift at axial failure is measured at the 50 percent of the residual load. According to Elwood and Moehle, (2005) in Equations 3.5 and 3.6 (b) and Figure 3.11(c), $\theta_{sh,fail}$ describes the midpoint of the empirical drift capacity model and the idealized flexural response curve. In addition, $\theta_{\alpha,fail}$ denotes the point at which an element can no longer support vertical loads, mainly because experimentally the longitudinal reinforcement capacity cannot be verified. Figures 3.11 (a) and 3.11 (b) show the experimental results of the two limit states as a function of the relevant proposed model (b). To evaluate the accuracy of the suggested equations, the drift capacities for the two failure scenarios are computed (flexure-shear and shear). According to Fig. 3.11(a) and (b) and considering the correlation factor R^2 (with a maximum value of 1), there is a significant scatter of the respective ratios. In general, the analytical findings demonstrate a good correlation, notably for shear and flexure-shear failures for the given shear drift model, and for flexure-shear failures in the case

of the axial drift ratio model. The distribution underscores the need for improvement of the drift capacity estimates.

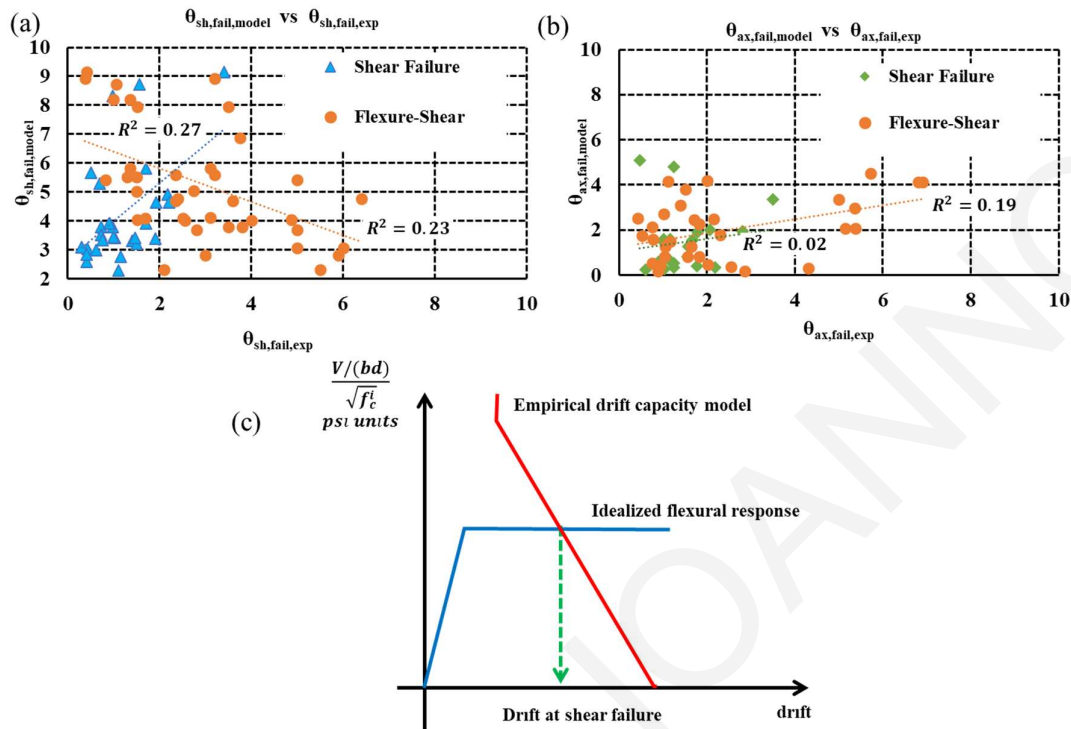


Figure 3. 11: Correlation between analytical vs experimental values: (a) drift at shear failure; (b) drift at axial failure; (c) determination of drift at shear failure according to [Elwood and Moehle, \(2005\)](#).

Additional methods were employed aiming to compare and analyse the envelope resistance curves of data base specimens that developed flexure-shear failure modes. The specimens were split into 3 plot types according on their axial load ratio; type 1: green for $0 < \nu \leq 0.15$; type 2: orange for $0.15 < \nu \leq 0.30$ and type 3: red for $\nu \geq 0.30$. Values in the vertical axis are presented, normalized with respect to the recorded peak strength. Then, in accordance with the [ASCE/SEI 41, 2017](#) standard, the equation of parameter a shown in Figure 3.3 and Table 3.2 was utilized to determine the nonlinear drift capacity of each column. The average values of parameter a were also categorized according to the axial load ratio level, and the corresponding values are given in Figure 3.12 as vertical dashed lines. In contrast to type 2 results, which are shown to be very unconservative and show a large dispersion, type 1 and type 3 results exhibit consistency with the tests. This supports the suggestion that axial load limits the drift capacity

in ways that are not accurately represented by the available drift models in members that develop shear failure after the occurrence of flexural yielding.

The grey arrow illustrates also the increasing degradation intensity of the columns – the phenomenon is much more intense in type 3 columns, whereas it is mild to negligible in type 1 – this finding underscores the need to link the degradation parameter, $\eta(\mu_0)$ to the axial load ratio ν . How strength provided by the stirrups is also affected by the axial load ratio and whether that degrades with drift is an open question that may only be interpreted through numerical simulation.

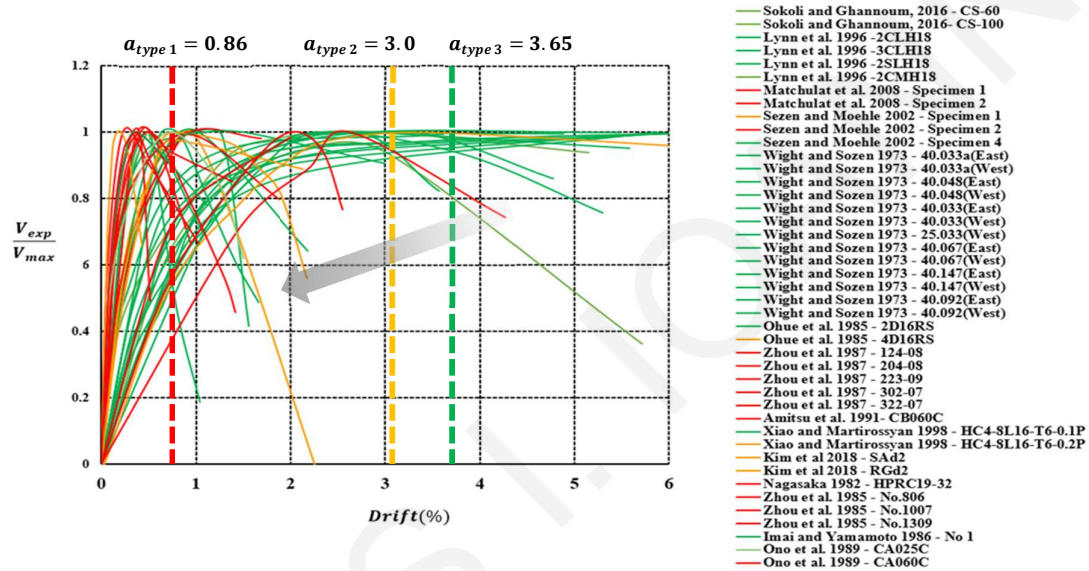


Figure 3.12 : Flexure-shear critical columns classification according to axial load ratio

3.7 Finite Element Analysis

3.7.1 Nonlinear Finite Element Analysis

To investigate the role of axial load ratio ν , and the angle of the failure plane θ_v on the shear failure and deformation mechanisms, a finite element investigation was undertaken to observe the parametric dependency of these phenomena. Through the study, the extent of plastic hinge, l_{pl} , was also monitored, as it affects significantly the theoretical estimates of drift capacity. In the present investigation, the length l_{pl} was determined as the region where bar strains exceed the yielding limit; this definition, originally introduced by [Tastani et al., \(2018\)](#), is meant to account for strain penetration that occurs beyond the region where flexural moment attains its yielding value (which is the conventional definition of the plastic hinge length). Benchmark study for the parametric investigation were the data base specimens of [Matchulat et al. \(2008\)](#) shown in Figure 3.13. Additionally, to the existing levels of axial load ratio ($=0.5$), five different levels of axial load ratio were also considered, i.e., $\nu = 0, \nu = 0.1, \nu = 0.2, \nu = 0.3, \nu = 0.4$. A discretization of eight nodes hexahedral elements of 50mm cubes was used in order to prepare the FEA models. According to [Abaqus Documentation Manual, 1992](#) a static stress analysis was used neglecting inertia effects on account of the pseudostatic application of the load in the actual test. Time-dependent material effects (creep, swelling, viscoelasticity) were also not considered. The longitudinal and transverse reinforcements were simulated as truss elements in full embedment connection with concrete. The columns were subjected to a relative lateral translation of top and bottom cross sections, with the following boundary conditions:

Table 3. 5: Specimen Boundary Conditions

Matchulat et al. 2008 (column bent in double curvature)

1. Bottom: $u_x=0, u_y=0, u_z=0, \theta_x=0, \theta_y=0, \theta_z=0$
 2. Top: $u_x=400\text{mm}, u_y \neq 0, u_z \neq 0, \theta_x \neq 0, \theta_y \neq 0, \theta_z \neq 0$
 3. Symmetry in level $z=0$: $u_z(0) = 0$
-

Material mechanical properties were modelled using: (a) the Concrete-Damaged Plasticity (CDP) model for concrete, and (b) the elastoplastic behavior model (Metal Plasticity Model) with hardening based on the Von Mises failure criterion for the steel

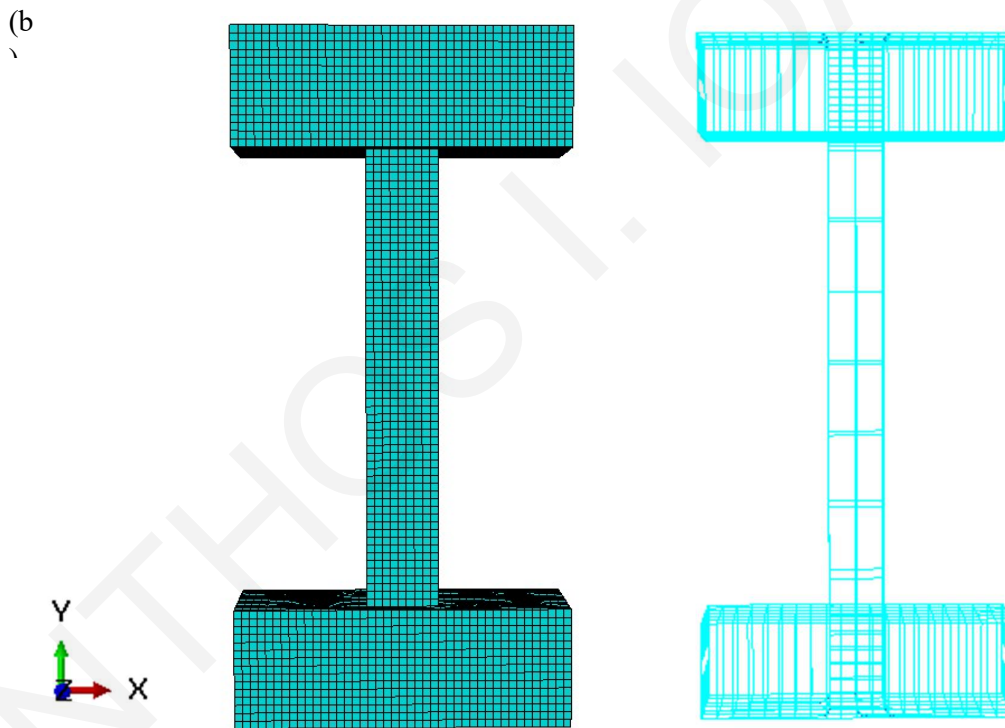
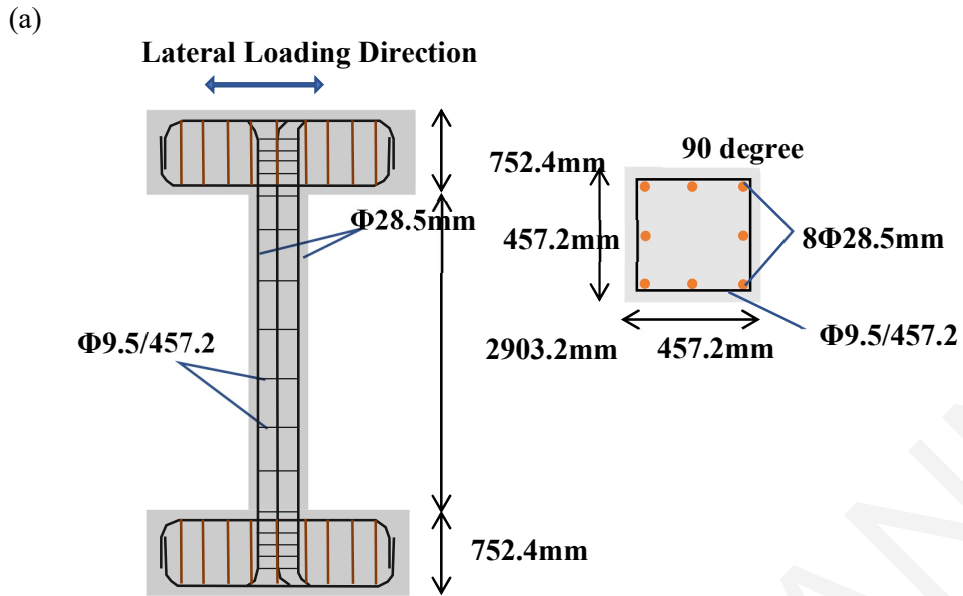


Figure 3. 13: Matchulat et al. (2008) Specimen 1 details: (a) Geometrical properties of examined specimen; (b) Finite elements of concrete parts and steel reinforcement rebar.

3.7.1.1 Concrete Damaged Plasticity Model in ABAQUS

Based on Genikomsou et al. (2015) and Abaqus Documentation Manual, 1992 a brief presentation of the damaged plasticity model is presented. The yield function was proposed by Lubliner et al. (1989) and then modified by Lee and Fenves (1998). It is defined according to Equation 3.24:

$$F = \frac{1}{1-a} (\bar{q} - 3a\bar{p} + \beta(\bar{\varepsilon}^{pl}) \langle \bar{\sigma}_{max} \rangle - \gamma \langle -\bar{\sigma}_{max} \rangle) - \bar{\sigma}_c(\bar{\varepsilon}_c^{pl}) \quad (3.24)$$

In Equation 3.24, \bar{p} is the hydrostatic pressure stress and \bar{q} is the Mises equivalent effective stress. Parameter α is calculated according to Equation 3.25, where (σ_{b0}) is the biaxial compressive strength and (σ_{c0}) is the uniaxial compressive strength. The default value of the biaxial ratio at failure $(\frac{\sigma_{b0}}{\sigma_{c0}})$ is 1.16.

$$a = \frac{(\sigma_{b0}/\sigma_{c0})^{-1}-1}{2(\sigma_{b0}/\sigma_{c0})^{-1}-1} \quad (3.25)$$

Function $\beta(\bar{\varepsilon}^{pl})$ shows up in the yield function, when the algebraically maximum principal effective stress $\bar{\sigma}_{max}$ is positive (the Macauley bracket $\langle . \rangle$ is obtained as: $\langle x \rangle = \frac{1}{2}(|x| + x)$ and it is determined as:

$$\beta(\bar{\varepsilon}^{pl}) = \frac{\bar{\sigma}_c(\bar{\varepsilon}_c^{pl})}{\bar{\sigma}_t(\bar{\varepsilon}_t^{pl})} (1 - a) - (1 + a) \quad (3.26)$$

where $\bar{\sigma}_c(\bar{\varepsilon}_c^{pl})$ and $\bar{\sigma}_t(\bar{\varepsilon}_t^{pl})$ are the effective cohesion stresses for compression and tension respectively. In biaxial compression where $\bar{\sigma}_{max} = 0$, the parameter $\beta(\bar{\varepsilon}^{pl})$ is not active and the only remaining parameter in the equation is α . The shape of the yield surface is defined by parameter γ according to Equation 3.27. Parameter γ is active in Equation 3.24, when the maximum effective principal stress $\bar{\sigma}_{max}$ is negative, a situation that occurs in triaxial compression.

$$\gamma = \frac{3(1-k_c)}{2k_c-1} \quad (3.27)$$

k_c is the ratio of the tensile to the compressive meridian and defines the shape of the yield surface in the deviatoric plane (Fig. 3.14).

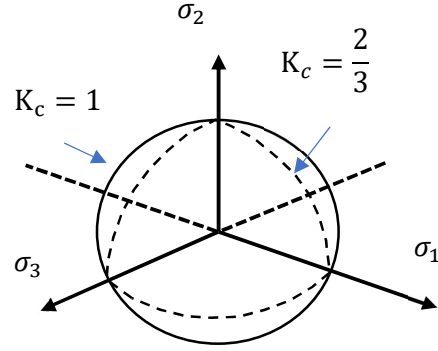


Figure 3.14: Yield surfaces in the deviatoric plane ($K_c = 2/3$ corresponds to the Rankine failure criterion, whereas $K_c = 1$ corresponds to the Drucker–Prager criterion).

The concrete damaged plasticity model uses the flow potential function, $G(\sigma)$, which is a Drucker–Prager hyperbolic function and is defined according to Equation 3.28.

$$G(\sigma) = \sqrt{(\varepsilon\sigma_{t0}\tan\psi)^2 + \bar{q}^2} - \bar{p}\tan\psi \quad (3.28)$$

In Equation 3.28, ε is the eccentricity that gives the rate at which the plastic potential function approximates the asymptote (see Fig. 3.16 (a)), σ_{t0} is the uniaxial tensile stress and ψ is the dilation angle measured in the $p - q$ plane at high confining pressure. Figure 3.1 (a) shows the plastic potential function compared to the yield surface. The plastic strain increment is normalized as for the plastic potential function. Figure 3.16 (b) presents the schematic representation of the dilation angle and the eccentricity. According to the default value, the eccentricity is taken equal to 0.1, showing that the concrete has the same dilation angle through a wide range of confining pressure stresses. The dilation angle shows the direction of the plastic strain increment vector. The non-associated flow rule means that the plastic strain vector is normal to the plastic potential function, which however is different from the yield surface.

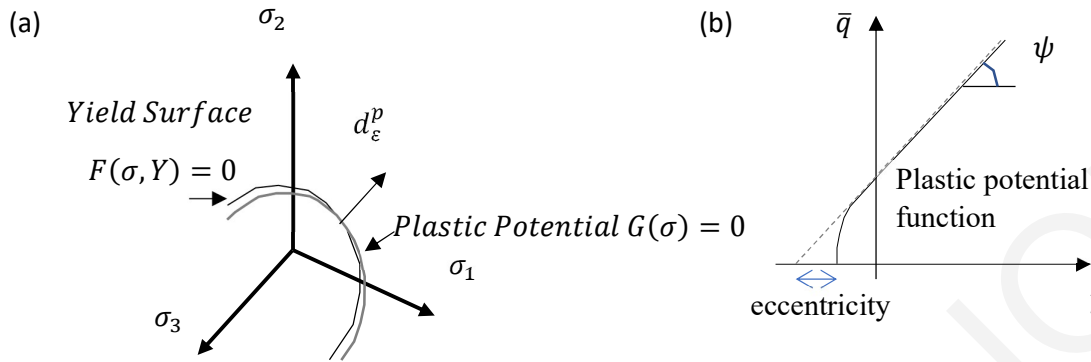


Figure 3. 15: (a) Plastic potential surface and yield surface in the deviatoric plane, (b) Dilation angle and eccentricity in the meridian plane.

Damage is introduced in the model according to Equation (3.28):

$$\sigma = (1 - d)\bar{\sigma} = (1 - d)E_0: (\varepsilon - \varepsilon^{pl}) \quad (3.28)$$

The damage parameter d is defined in terms of compression and tension, d_c and d_t , respectively, as follows:

$$(1 - d) = (1 - s_t d_c)(1 - s_c d_t) \quad (3.29)$$

where s_t and s_c describe the tensile and compressive stiffness recovery.

3.7.1.2 Material Modelling

The concrete material parameters that were used in the presented analyses are: the modulus of elasticity E_0 , the Poisson's ratio ν and the compressive and tensile strengths of the selected material. The concrete damaged plasticity model considers a constant value for the Poisson's ratio, ν , even for cracked concrete. Therefore, in the analyses presented herein, the value $\nu=0$ was assumed, so that the expansive behavior of concrete due to damage is attributed entirely to the elastic response. The dilation angle was taken as 36 degrees, the shape factor, $K_c=0.667$, the biaxial stress ratio, $\sigma_{c0}/\sigma_{b0}=1.16$ and the eccentricity $\varepsilon=0.1$. The uniaxial stress–strain response of concrete in tension was assumed linear elastic up to cracking at attainment of tensile strength, f'_t . After cracking, the descending branch was modelled by a softening process, which ends at a tensile strain ε_u , where residual tensile strength is taken equal to zero (Fig. 3.16 (b)). The concrete's brittle behavior is often characterized by a stress–crack displacement response instead of a stress–strain relationship. The stress–crack displacement relationship can

be defined using various options: linear, bilinear, or exponential tension softening response. In this study, bilinear stiffening response was selected and was calculated according to the Fig. 3.17 (a), where f'_t is the maximum tensile strength and G_f denotes the fracture energy of concrete that represents the area under the tensile stress-crack displacement curve.

The fracture energy G_f depends on the concrete quality and aggregate size and can be obtained from Equation 3.30, obtained from the [CEB-FIP Model Code, 1993](#).

$$G_f = G_{f0} \left(\frac{f_{cm}}{f_{cm0}} \right)^{0.7} \left(\frac{N}{mm} \right) \quad (3.30)$$

where $f_{cm0} = 10MPa$ and G_{f0} is the base fracture energy depending on the maximum aggregate size, d_{max} . The value of the base fracture energy G_{f0} is 0.030 N/mm has been recommended for maximum aggregate size d_{max} equal to 20 mm that was used in the tested specimens.

According to [Model Code, 1990](#) f_{cm} is the mean compressive strength of concrete and its relationship with the characteristic value, f_{ck} , is:

$$f_{cm} = f_{ck} + 8MPa \quad (3.31)$$

In order to minimize the localization of fracture, the tensile strains were used, and they were defined by dividing the cracking displacement (w) by the characteristic length of the element, l_c . For 3D elements the characteristic length can be defined as the cubic root of the element's volume. The adopted critical length l_c in the following simulations was 50 mm. The equivalent tensile stress-strain graph is illustrated in Fig. 3.16(b).

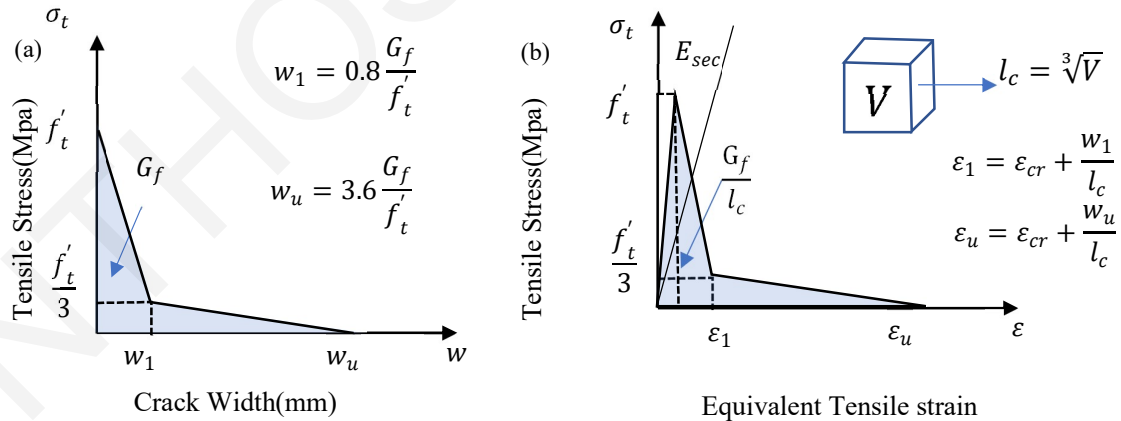


Figure 3. 16: Uniaxial tensile stress-crack width relationship for concrete.

Concrete in compression was modelled using the familiar Hognestad parabola (Fig. 3.18). The assumed stress–strain relation to describe the behavior of the concrete under uniaxial compressive stress was divided into three domains. The first one represents the linear-elastic branch, with initial modulus of Elasticity, $E_0 = 4500\sqrt{f'_c}$. The linear branch ends at the stress level of σ_{c0} that here was taken as: $\sigma_{c0} = 0.4f'_c$. The second segment describes the ascending branch of the uniaxial stress–strain relationship for compression loading to the peak load at the corresponding strain level, $\varepsilon_0 = \frac{2f'_c}{E_{sec}}$. The secant modulus of Elasticity was defined as: $E_{sec} = f'_c/\varepsilon_0$, where $\varepsilon_0=0.00225$. The third part of the stress–strain curve after the peak stress and until the ultimate strain ε_u represents the post-peak branch. The equations for the assumed compressive stress–strain diagram for first, second and third branch of curve are given in Figure 3.18.

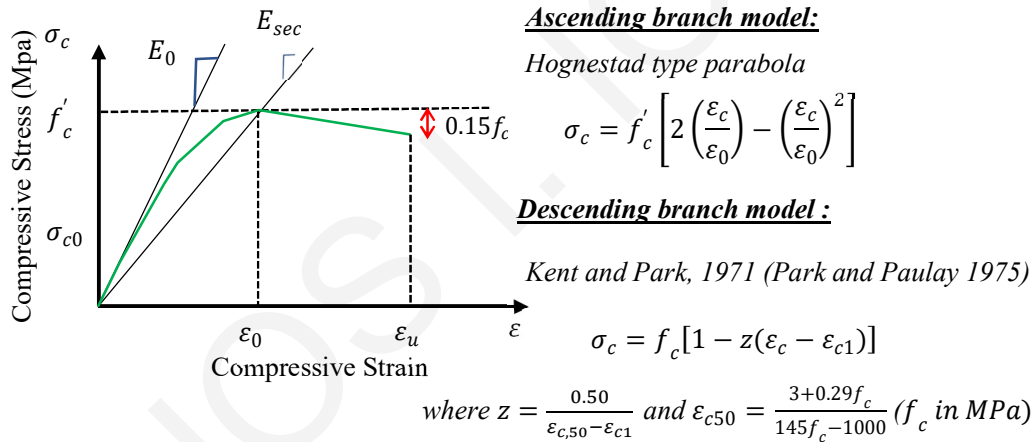


Figure 3. 17: Uniaxial compressive stress–strain relationship for concrete.

Damage was introduced in concrete damaged plasticity model in tension and compression according to Figs. 3.19 (a) and 3.19 (b), respectively. Concrete damage was assumed to occur in the softening range in both tension and compression. In compression the damage was introduced after reaching the peak load corresponding to the strain level, ϵ_0 .

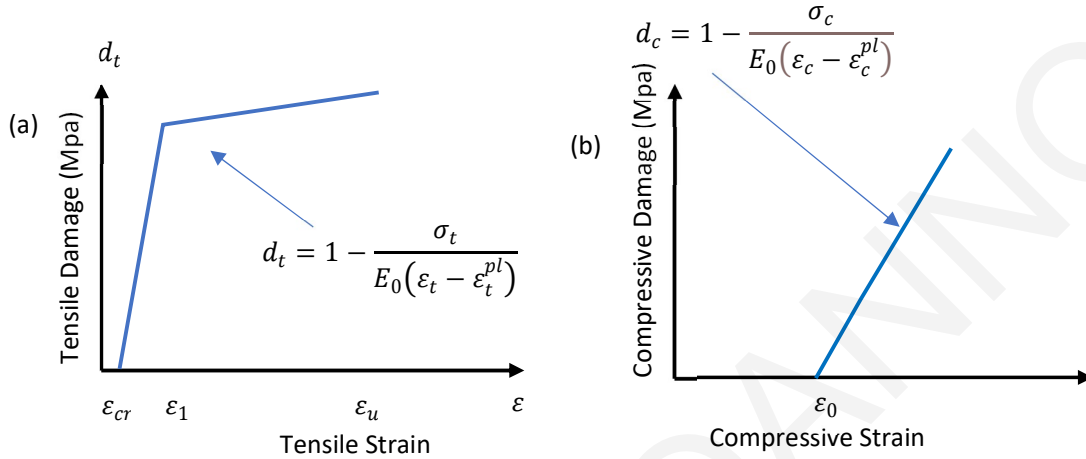


Figure 3. 18: (a) Tensile damage parameter–strain relationship for concrete; (b) Compressive damage parameter–strain relationship for concrete (simplified in linear form).

The uniaxial stress–strain relation of reinforcement was modelled as linear elastic with Young’s modulus E_s and Poisson’s ratio ν of which typical values are 200,000 MPa and 0.3, respectively. Plastic behavior was input in a tabular form, including yield stress and corresponding plastic strain. The plastic properties were defined based on the test results with a bilinear strain hardening yield stress – plastic strain curve obtained from the tensile test performed both on longitudinal and transverse reinforcement by [Matchulat et al. \(2008\)](#). Table 3.7 presents the material properties of the reinforcement. Appendix C contains information on Finite Element Analysis, including the algorithm, type of analysis, type of element, and type of meshing.

Table 3. 1: Material properties of the reinforcement.

| Reinforcement Type | Column Specimen | f_y(MPa) | ϵ_y | f_t(MPa) | ϵ_t |
|---------------------------|-------------------------------------|------------------------------|--------------------------------|------------------------------|--------------------------------|
| Longitudinal | Matchulat et al. (2008), Specimen 1 | 442 | 0.0024 | 442 | 0.01 |
| Transverse | Matchulat et al. (2008), Specimen 1 | 282 | 0.0015 | 376 | 0.0092 |

3.7.1.3 Parametric Analysis

The experimental results regarding the envelope curve and the failure mode of the reference specimens are presented in Fig. 3.19. The results from the monotonic push-over simulation are compared to the envelope resistance curve of the cyclic loading results from the experimental procedure in Fig. 3.20. Results are in good agreement both in relation to the Shear Load as well as the drift of the member.

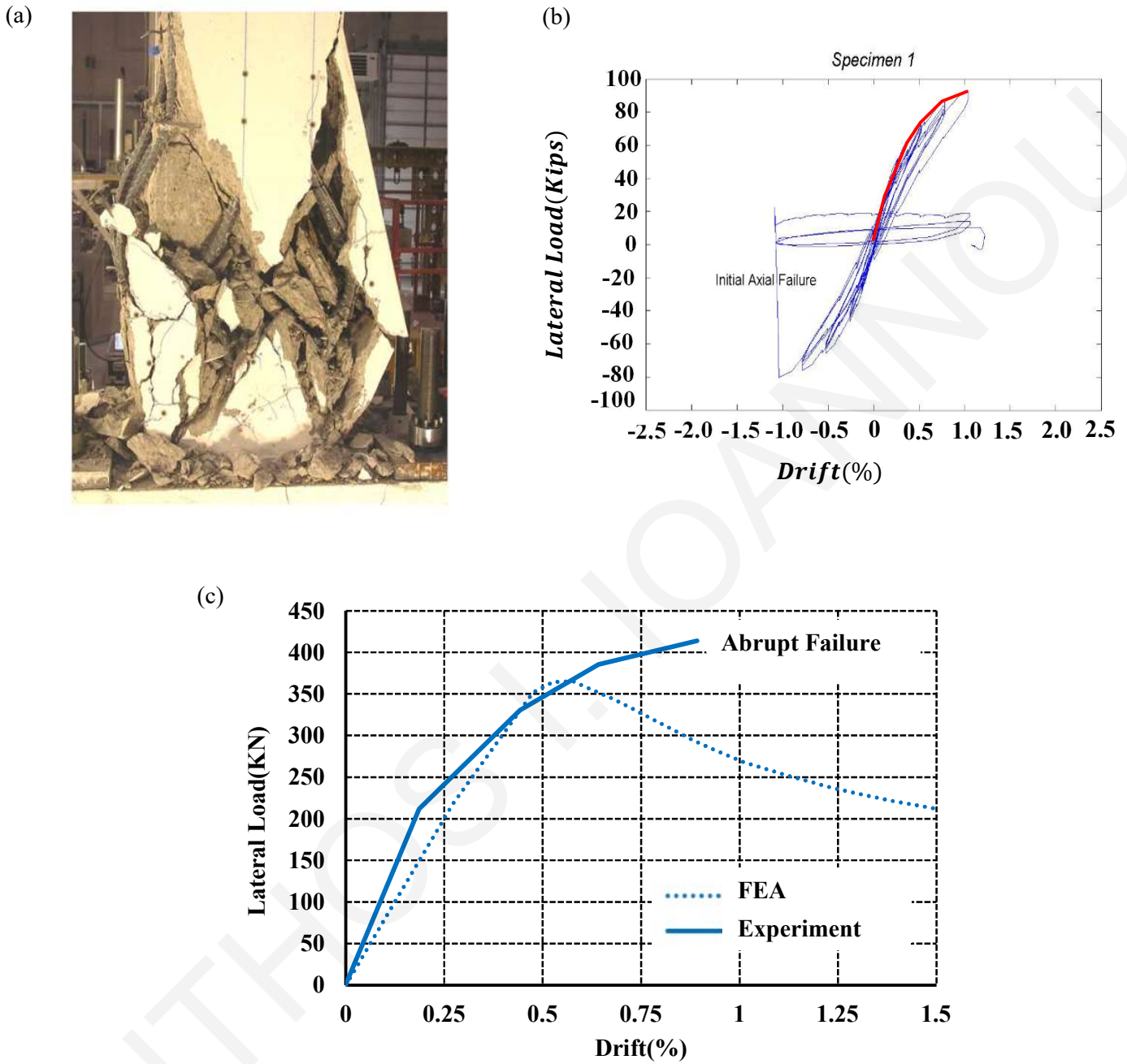


Figure 3. 19: Specimen 1 from [Matchulat et al. \(2008\)](#) experimental results: (a) Failure mode; (b) Cyclic loading curve; (c) Experimental envelope resistance curve

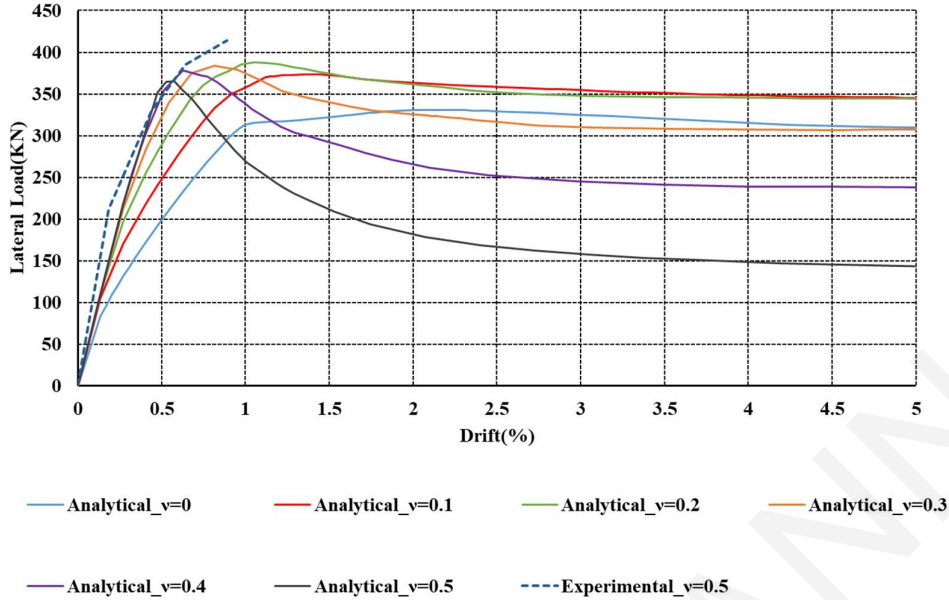


Figure 3. 20: Matchulat et al. (2008) experimental envelope curve vs FEA pushover curve considering different levels of axial load ratio.

Figure 3.20 compares the envelope resistance curves ($V-\theta$) considering the theoretical value of the shear force for the examined different levels of axial load ratio. While the axial load is increasing an immediate decrease is observed in the available deformation capacity and the descending branch falling gradually after maximum value of shear strength. In order to estimate the specimen's lateral load bearing capacity, which was referred to as V_{actual} in the preceding paragraphs, it is important to emphasize the role of second order effects. Comparison of $\frac{V_{max}-V_{ult}}{V_{max}}$ before and after a correction $\frac{V_{max}-V_{ult,Px\Delta}}{V_{max}}$ was the most practical technique to establish the proportion of strength consumption due to axial load additional moments. In Figure 3.21, the findings are compared for different level of axial load ratio and a constant drift level equal to 4%.

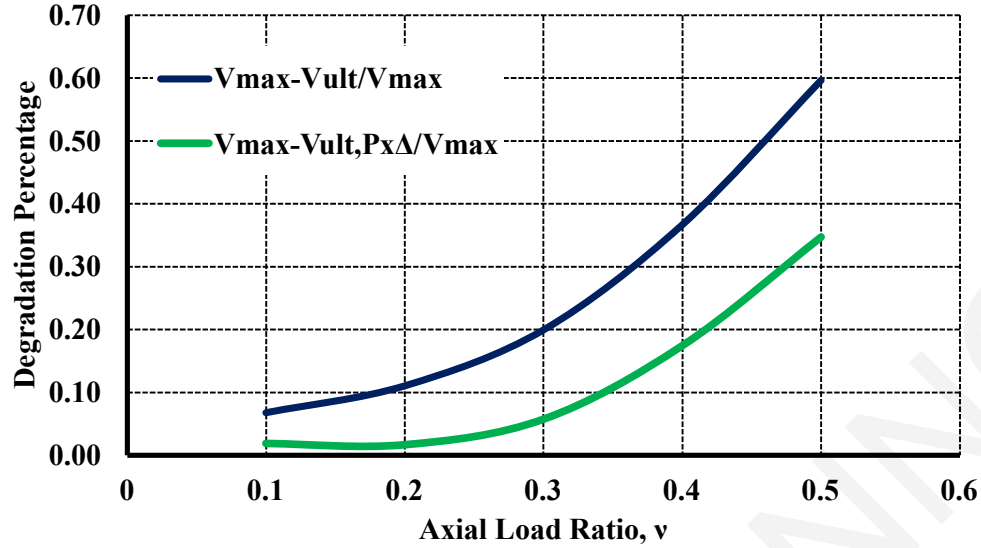


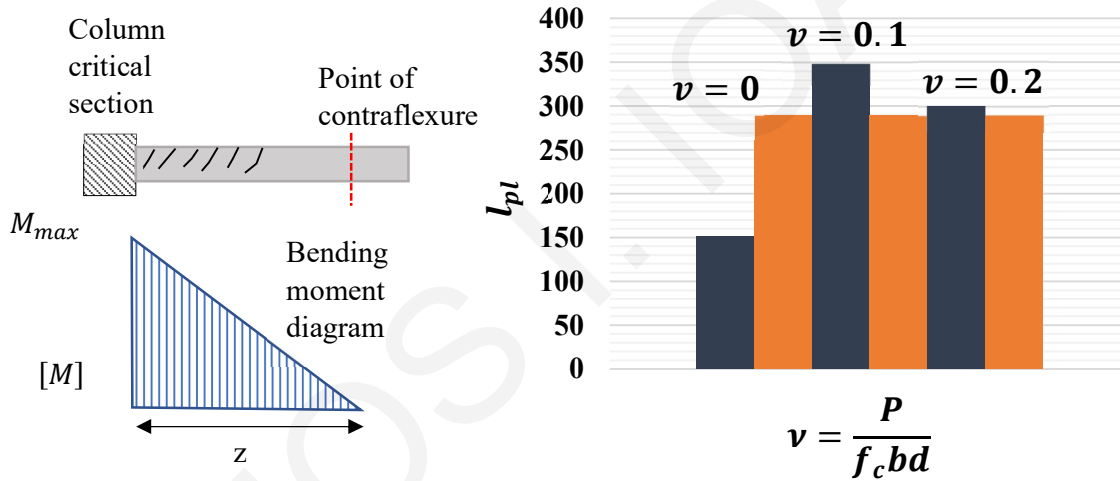
Figure 3. 21 : Comparison of ratios $((V_{max} - V_{ult}) / V_{max})$ vs $((V_{max} - V_{ult, Px\Delta}) / V_{max})$ according to theoretical shear force values taken from Figure 3.20

Figure 3.21 demonstrates that the influence of second order effects on phenomenological shear strength degradation beyond the peak is significant. As a result, any reduction factor employed in assessment methods must be calibrated for second order effects to avoid underestimating the residual shear strength. The parametric investigation yielded also results regarding the relationship between plastic hinge length and axial load ratio. Equation 3.32 is a theoretical estimate of l_{pl} considering the effect of strain penetration (f_b^{res} is the residual bond strength along the bar, inside the footing and along the shear span) (Tastani et al., 2019); this estimate used to determine the plastic hinge length according to FEA models results which was applicable for $\nu < 0.3$, since for $\nu \geq 0.3$ a compression damage failure occurred in the relevant models. The results emerged from Equation 3.32 are compared with the respective values obtained from Equation 3.33 which was proposed by Priestley and Park (1987). Figure 3.23 illustrates that the plastic hinge length grows proportionally with the axial load ratio, a finding that is consistent with the results of Bayrak et al. 2008. Plastic hinge shrinks and diminishes for higher axial load ratios that preclude bar yielding (i.e. when the depth of compression zone exceeds 55% of the section height).

$$l_{pl} = l_{r,span} + l_{r,anch} = (\varepsilon_0 - \varepsilon_{sy}) \cdot \frac{E_{sh} D_b}{4} \left(\frac{1}{f_b^{res,span}} + \frac{1}{f_b^{res,anch}} \right) \quad (3.32)$$

The specimen cross section analyzed in the present study was 457mm square, reinforced with eight $d_b = 28.6mm$ longitudinal reinforcing bars with $f_{yl}=441.3MPa$ and $E_{sh}=0.05E_s$ having a clear cover of $c=39.7mm$. Stirrups had a 9.5mm diameter, spaced at 457mm o.c. (on centres) with yield strength of 372.3 MPa. Concrete strength was $f_c = 20.7MPa$, and the axial load ratio [$v = N/f_cbd$] was 0.16. For the example studied, the residual bond strength for the anchorage was taken equal to $f_{bmax,anch} = 5 \left(\frac{f_{cm}}{25} \right)^{0.25}$ (4.7MPa) according to [Fib Model Code 2010](#). For the shear span the bond strength was calculated using the same model due to the sparse installation of transverse reinforcement $f_{b,max,span} = 4.73MPa$. At ultimate strain cover delamination had already occurred and thus the residual bond strength $f_{b,res,span}$ was calculated as 1.80MPa (this value was also assigned to $f_{b,res,anch}$).

$$l_{pl} = 0.08z + 6d_b \quad (3.33)$$



where z = distance from critical section to point of contraflexure and

d_b = diameter of longitudinal reinforcement

Figure 3.22: Plastic hinge length parameters and results: (a) Cracking in member and bending moment diagram; (b) results obtained from the FE analysis and the theoretical estimate of strain penetration through bond degradation.

Figure 3.23 presents the deformed shapes of the model column for the different levels of axial loads considered in the parametric FEA analysis. It is observed that with an increase in the axial load, the length of the damaged area also increases. Using the length of the damaged

region and dividing with the effective depth of the cross section, the angle θ_v of the sliding plane is defined, by which the number of stirrups intersecting that failure plane can be calculated, thereby determining the V_w contribution in the present study.

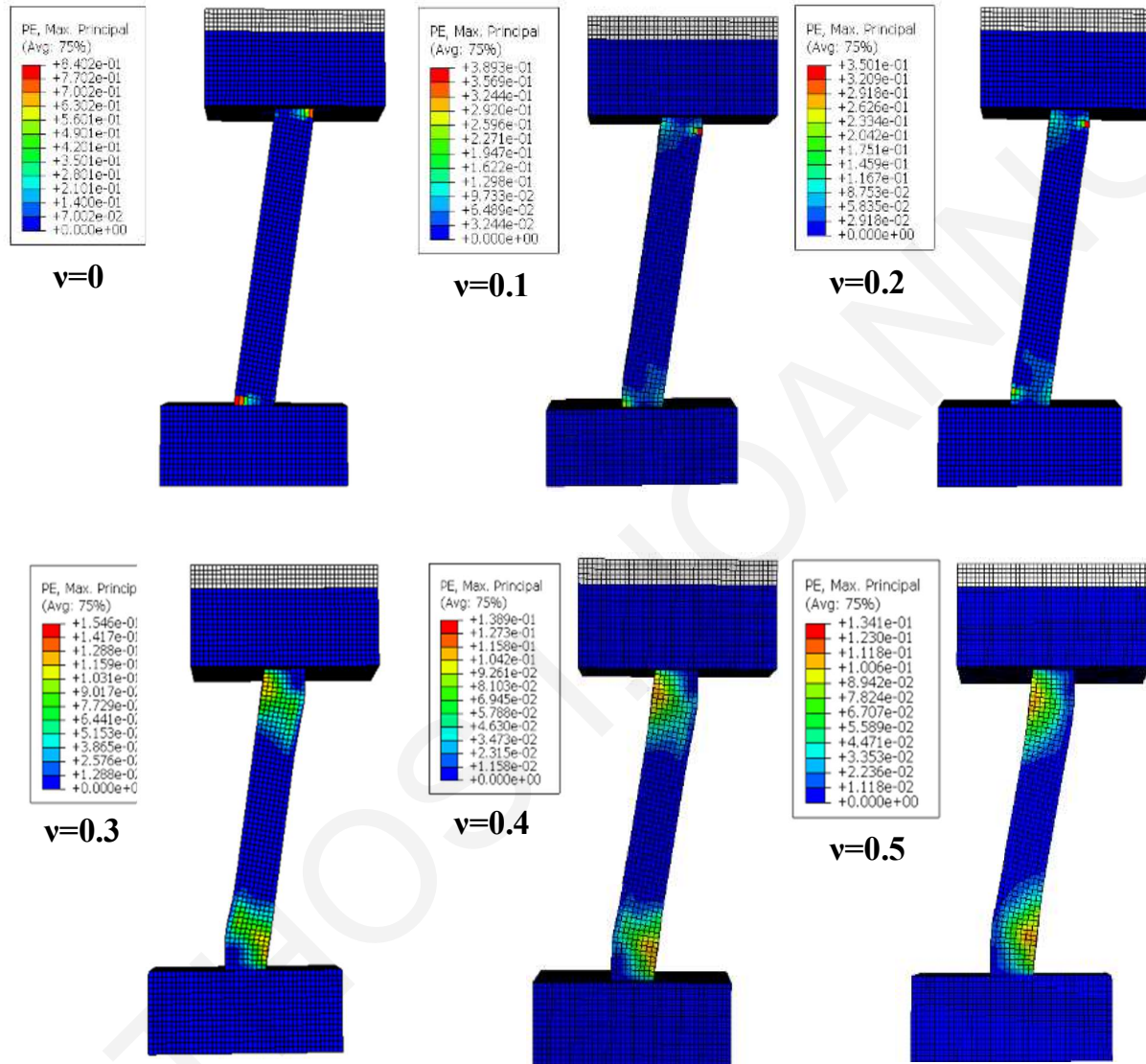


Figure 3.22 : FEA models failure modes for different levels of axial load ratios

3.4. Conclusions

The present study investigated the strength and deformation parameters defining the mechanical behavior of columns under lateral sway such as what is occurring during seismic loading, focusing into the details of failure mechanisms of columns. A carefully chosen collection of specimens from the experimental database that experimentally highlight the behavior of columns experiencing shear failure after flexural yielding was assembled in order to study the parametric sensitivity of the examined data, while at the same time an evaluation of the proposed relationships for the limit state failure in displacements and strength terms was carried out (shear mechanism failure and bearing capacity at failure). It was seen that a fraction of the apparent strength degradation of columns is really a manifestation of second order effects; the remaining fraction of shear strength reduction, which is an effect of internal damage of the shear resisting mechanism, although significant, is relatively milder than originally accounted for in terms of ductility. The influence of the axial load ratio in the development of the observed failures and in terms of the formation of the plastic hinge length was studied using the finite model of a benchmark example that represented a full-scale column with brittle details that was tested to failure under a high axial compression. It was found that the length of plastic hinge, when defined with reference to steel strains accounting for strain penetration, is consistent with the Finite Element results, and this measure is significant in determining the the failure plane of the component.

Chapter 4: Interface interaction between ECC and Normal-Strength Concrete

4.1 Introduction

The observed degradation in structural performance of existing concrete structures subjected to extreme mechanical and environmental actions, which has prevailed in the last few years as the older building stock exceeds the 50-year service-life mark, raises the importance and prioritizes the development of pertinent repair and retrofitting methodologies (Hyun-Soo Youm et al., 2021). Over the years two retrofit methods have gained popularity and are recognized by practitioners as the main available options for rehabilitation of frame components: One is the traditional jacketing, whereby a layer of reinforced concrete, about 70 to 150 mm thick is overlaid on the member cross section; the other is through wrapping of FRP layers comprising glass or carbon fibers. Of these two methods, the first is classified as a global intervention (Thermou et al., 2006) because it increases significantly the flexural strength and therefore the flexural stiffness of the retrofitted member from its original state. The second is considered a local intervention only (Pantazopoulou et al., 2016) because although it alters the deformation capacity by suppressing the brittle modes of failure, it cannot affect the member stiffness. The latter has received criticism, over the recent years, because it locks inside the member moisture and reactive agents that may lead to anaerobic corrosion of the reinforcement that is not externally detectable until it is too late, whereas in the former case the concerns are of a different type: the change in the cross section size is an important architectural intervention, whereas the effect of the stiffness addition of the rehabilitation need be seen in the context of the entire structural system response (Youm et al., 2021).

With the emergence of ECC, new opportunities have emerged to mitigate these two problems of the jacketing retrofits: (Tayeh et al., 2013; Momayez et al., 2004; Mu et al., 2002; Ali et al., 1999). Because of the significant tension force resultant that strain hardening cementitious materials can develop in tension, the same result in terms of confinement can be achieved with a much thinner jacket than conventional concrete, while mitigating the problems of permeability of the FRP jackets. A sustainable ECC mix (whereby 60% of the reactive powders are Fly-ash) containing PVA fibers was developed at UCY (Georgiou, 2017) and has been shown to have significant tensile ductility. This material is used in the present study as a means of retrofitting through jacketing (Ioannou et al., 2021).

Cementitious jackets applied on concrete structural members have a critical plane of weakness, at the interface of existing and new material. The cohesion and strength between the two

surfaces is yet to be determined (Momayez et al., 2004). As indicated by Youm et al. (2021) the genuine investigation of interface examination can be executed through at least three experimental tests using different combinations of effectively induced stress at the interface specifically, a shear slant test, a pure shear test, and the direct tensile test; the upper limit is defined by monolithic compression tests. The stress conditions of interfaces for each applicable experimental test strategy are shown in Fig. 4.1.

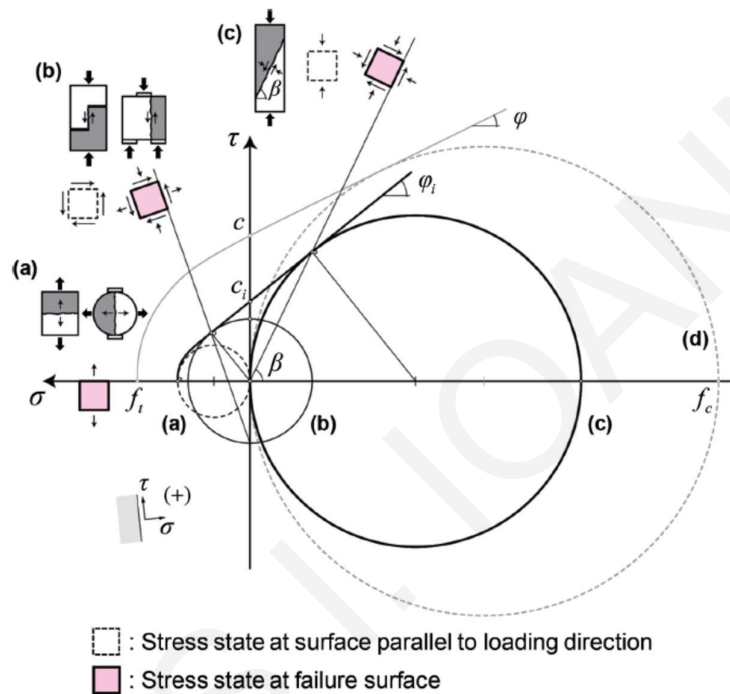


Figure 4. 1: Interface stress states for various test methods: (a) direct tension;(b) pure shear; (c) shear slanted and (d) monolithic compression (Youm et al., 2021)

Therefore, the interface of two bonded semi-prisms of concrete and repair system should be examined through tests of the type listed above, by subjecting specimens containing interfaces of ECC and plain concrete to loading combinations of shear and compression or tension, to simulate the state of stress that occurs at the interface in the jacket of a typical real structure. As per ACI 546.3R-1413, 2014 the interface bond performance between two different concretes is required to be evaluated using the slant shear test, conforming to ASTM C882.14, 2013. Thus, to define the failure envelope shown above, the angle of inclination of the interface is an important variable.

As the jacketing is applied in retrofitting after removal of cover, the interface in such applications is a very anomalous surface – this to a certain extent is expected to enhance the

interface properties, through interlocking and friction (Naderi, 2009). The roughness is therefore an important parameter in defining the failure surface of Fig. 4.1.

Several studies aiming to investigate the bond of the ECC-PC interface have been already published [Youm et al., 2021; Tayeh et al., 2013; Momayez et al., 2004]. Parameters such as a roughness index of the interface and the moisture content of the PC (Plain Concrete) substrate, as well as the PC strength which are the most important factors for the bonding strength at the PC substrate and ECC (Engineered Cementitious Composite) interface have been examined (Zhang et al., 2020). Harris et al. (2014) found that the experimental results prove a strong bonding between ECC and PC and this can succeed with limited surface preparation and without the use of bonding agents such as epoxies or latex emulsions that are commonly used in overlays. It was shown that the bond of ECC with the old concrete is adequate and restores the structural integrity and it is durable having the ability to tolerate (withstand) severe climatic conditions. Finally, it was found that it has a chemical, electrochemical, permeability, and dimensional compatibility with the old substrate being repaired (Harris et al., 2014).

The studies cited focused on the evaluation of interface interaction between plain and fiber reinforced concrete which consider various parameter ranges, but only a small number tried to describe the failure envelope characteristics. The main objective of the present study is the experimental investigation of bond stress level in the interface of the two materials through pure tension and shear slanted tests. The examined variables were the inclination angle, the interface roughness and the plain concrete mix design. Two cycles of tests were conducted, where the failure modes were studied through comparison between the instrumentation system recordings and the digital image correlation methodology.

4.2. The Aim of the Experiment

4.2.1 Experimental Procedure

Regarding the experimental investigation of ECC jackets for the repair of damaged R.C. members under monotonic and cyclic loading which are examined in the next chapters, the experimental study conducted to characterize the interface properties between plain concrete (PC) and ECC is presented. To this end, series of slanted shear, direct tensile and compression tests were carried out. Parameters of the investigation was the inclination of the interface with respect to the longitudinal axis of the member, the mix design which affected the compressive

strength of the plain concrete, and the roughness of surface substrate [Youm et al., 2021; Tayeh et al., 2013; Zhang et al., 2020; Banthia et al., 2014]. Therefore, as shown in Figure 4.2, four types of experiments were executed. The compressive test (Fig.4.2 (a)) was used to characterize the basic strength of the individual materials (as per the ASTM C39-21, 2021 standard). Four-point bending tests on prismatic specimens of ECC were used to measure the tensile strength according to the Canadian Standard (Fig. 4.2 (b)) as described in Annex U of CSA-A23.1 2019; characteristic points of the tensile stress strain response were obtained through inverse analysis of the test results according with the method of Lopez (2017). Splitting tests (Fig.4.2 (c)) used to test the tensile strength of combined specimens in the interface as specified in ASTM C496/C496M-17, 2017 and slanted shear tests (Fig. 4.2 (d)) as per ASTM C882/C882M, 2013 were used to investigate the interface interaction between PC and ECC.

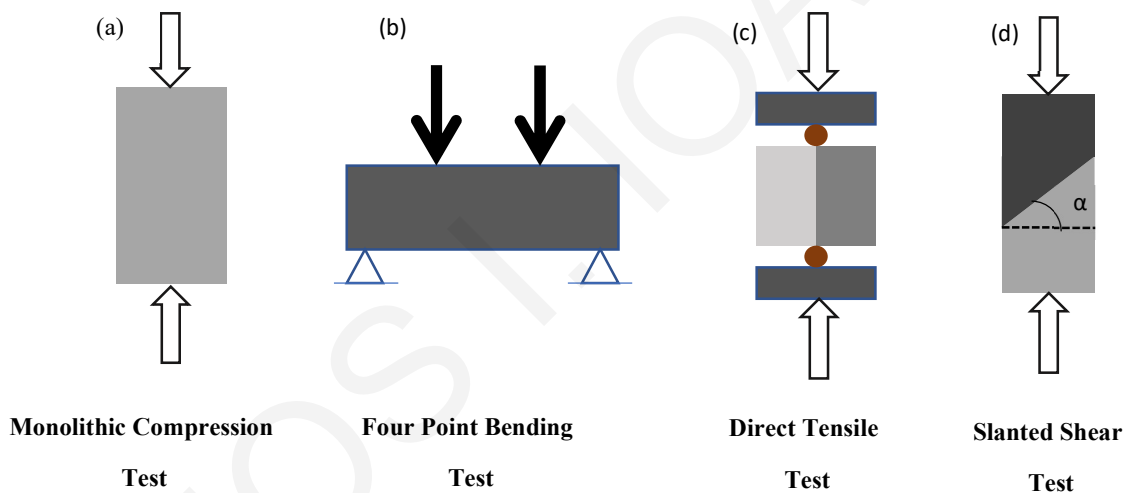


Figure 4. 2: Types of experiments: (a) compression test (b) four-point bending test for ECC tensile strength evaluation; (c) splitting test for interface tensile strength evaluation; and (d) combined compression - shear test to define the failure surface model of the interface.

4.2.2 Materials – PC and ECC Mix Designs

With regards to the construction of experimental specimens for the needs of the investigation, two similar test series were carried out, the only difference between the two groups of experiments being the free surface roughness of the PC material, which controls the aggregate interlock at the ECC-PC interface. To achieve this goal the concrete mix designs differed in the volume of sand (<4mm).

4.2.2.1 Plain Concrete

The mix designs are given in Table 4.1 for plain concrete production of category C20/25 for experimental cycles 1 and 2 respectively. Pure calcite limestone aggregates (Mitsero) were used, having diameter of 0-4 mm for the sand, and 4-10mm for the gravel. Composite Portland Cement of type [EN 197-1 CEM II / A-M 29 \(L-S\) 42.5 R, 2011](#) was used. This type of Blended Cement is produced using pure calcite limestone and it is more impermeable and denser as compared to OPC, with a higher degree of workability and reduced plastic shrinkage. The compressive strength of this particular cement at 28 days is equivalent to that of 42.5 R OPC and superior at 2 and 7 days.

Sand comprised pure calcite limestone of 0-4mm size (Fig. 4.3 (a)) with the grain size distribution shown in Fig 4.3 (a). Pure calcite limestone gravel was used having 4-10mm grain size (Fig. 4.3 (b)). The grain size distribution is illustrated in Fig. 4.3(b).

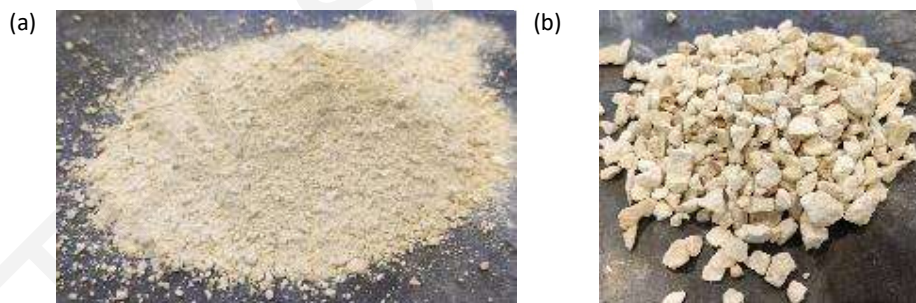


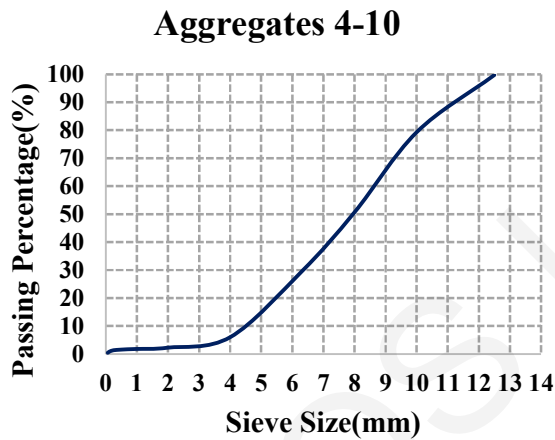
Figure 4. 3 : (a) Limestone sand of 0-4mm size; (b) limestone gravel used of 4-10mm grain size

Sika ViscoCrete Techno-10+ was used as superplasticizer; the admixture comprised aqueous solution of polycarboxylate polymers and is produced according to [EN 934.02:2009+A1,2012](#).

Table 4. 1: Plain concrete mix design of experimental cycle 1

| Mix Design #1 | | Mix Design #2 | |
|------------------|------------------------------|------------------|------------------------------|
| Materials | Quantity(kg/m ³) | Materials | Quantity(kg/m ³) |
| Cement | 352 | Cement | 432 |
| Water | 211 | Water | 288 |
| Sand(0-4mm) | 828 | Sand(0-4mm) | 600 |
| Gravel (4-10mm) | 1004 | Gravel (4-10mm) | 1080 |
| Superplasticizer | 6 | Superplasticizer | 12 |

(a)



(b)

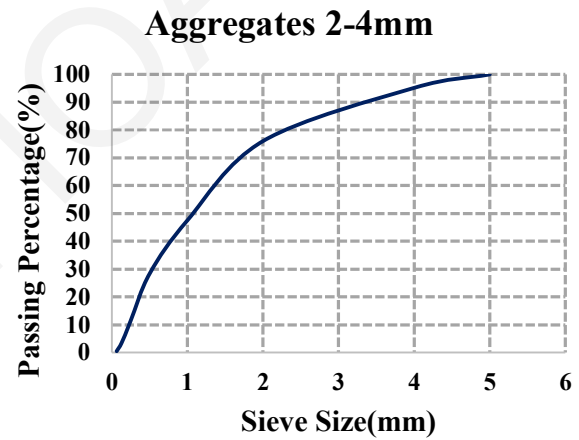


Figure 4. 4: Grain sizes granulation for aggregates (Mitsrou) (a) Gravel 4-10mm and (b) Sand 0-4mm

4.2.2.2 Fiber Reinforced Concrete

The ECC material mix design which used was adopted from [Georgiou \(2017\)](#). The mix design is detailed in Table 4.2 and batching is described below. In summary the composition of ECC material comprised Cement [EN 197-1 CEM II / A-M \(L-S\) 42.5 R, 2011](#) silica sand, fly-ash, Polyvinyl alcohol fibers (PVA); the same superplasticizer as in mixing PC was used.

Silica Sand:

It comprises spherical crystal quartz particles with a very narrow grain size distribution (see Fig. 4.5), it has a high SiO₂ content as well as a very special light color. The sand particles vary from 0.06 to 0.3 mm. The percentage of silica oxide is in the order of 98.6%, while small quantities of Al₂O₃, Fe₂O₃ and TiO₂ are contained. The Mohs Hardness of this product is 7, while raw density is 2.65 gr/cm³ and bulk density is 1.35 gr/cm³.

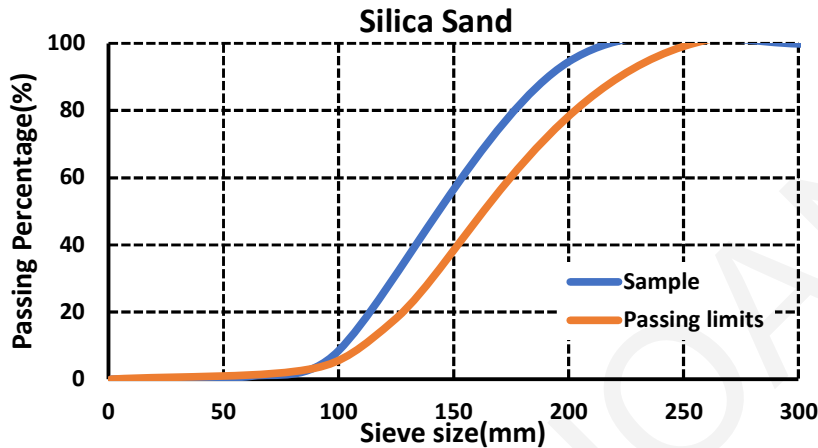


Figure 4. 5: Grain size distribution for silica sand

Fly Ash

A-type Fly Ash (FA) was used. This fly ash is intended as partial cement replacement as well as aggregate for cement slurries and mortars. The pozzolanic and physical properties enhance the performance of concrete and it complies fully with [EN 450-1:2012P, 2012](#). It contains extremely fine latently reactive silicon dioxide of fineness category N (30±10%). The presence of this substance gives greatly improved internal cohesion and water retention. The cohesiveness of concrete becomes extremely strong and the pumping properties are substantially improved. In the set concrete the latently reactive silicon dioxide forms a chemical bond with free lime. The fly ash is categorized to class F according to the certificate of conformity ([Szczerbiak, 2015](#)). Class F fly ash chemical composition properties are specified in [ASTM C618](#) and are shown in Table 4.2.

Table 4. 2: Fly ash declared performance

| Basic Characteristics | Performance | Harmonised Technical Specification |
|---|---|------------------------------------|
| Activity index | | EN 450-1:2012 |
| After 28 days | ≥ 75% | |
| After 90 days | ≥ 85% | |
| Ignition loss: Category A | ≤ 5% | |
| Fineness: Category N | 30 ± 50% | |
| Constancy of Volume | ≤ 10mm | |
| Initial Setting Time: | No more than a double value of the initial setting time of concrete slurry made in 100% of comparative cement | |
| Sulfuric acid anhydride (as SO ₃) | ≤ 3% | |
| Chloride Content | ≤ 0.1% | |
| Specific Density | 2100 kg/m ³ | |
| Free Calcium oxide CaO | ≤ 1.5% | |
| Reactive Calcium Oxide | ≤ 10.0% | |
| Reactive silicon dioxide SiO _{2reactive} | ≥ 25.0% | |
| Sum of content of oxides SiO ₂ , Al ₂ O ₃ , Fe ₂ O ₃ | ≥ 70.0% | |
| Total content of alkalis | ≤ 5.0% | |
| Magnesium oxide MgO | ≤ 4.0% | |
| Soluble phosphates P ₂ O ₅ | ≤ 100mg/Kg | |
| Phosphates P ₂ O ₅ | ≤ 5.0% | |
| Durability | Fulfilled in accordance with PN-EN-450-1 point 5.4.1 | |

| | | |
|---|--|--|
| Release of hazardous substances and radioactivity | PL, fulfilled, see, 'Substance Information Sheet'-Cinder (residua), carbon | |
|---|--|--|

When used in production of concrete, Class F fly ash is often mixed as Portland cement replacement in the range of 20-30% of the mass of the reactive powders; in ECC as in the present case the cement replacement ratio is in the order of 60%. The advantages derived by cement substitution with class F fly ash are:

- Increased late compressive strength (beyond the 28 days)
- Increased resistance to alkali silica reaction (ASR)
- Increased resistance to sulfate attack
- Less heat generation during hydration
- Increased pore refinement
- Decreased permeability
- Decreased water demand
- Increased workability
- Decreased cost (\$80/ton for Portland cement vs. \$30/ton for fly ash).

It is noted that when Class F fly ash is used as a Portland cement replacement, the setting time may be delayed, and the early compressive strengths (before 28 days) may be decreased. Additionally, the fine aggregate fraction of the concrete mix will need to be modified because fly ash has a lower bulk specific gravity than Portland cement, and therefore a greater volume is needed for the same mass. If using any organic admixtures such as air entrainment, the amount added must be modified since the carbon (LOI) in the fly ash adsorbs organic compounds. Moreover, if the fly ash has a high calcium content, it should not be used in hydraulic applications.

Polyvinyl alcohol fibers (PVA)

In the present investigation PVA fibers having 12 mm length and 39 μm diameter were used. The nominal tensile strength was 1600 MPa, the Young's Modulus was 40 GPa, the fibers' strain capacity was 6.5% and the density was 1300 kg/m^3 . The fibers were procured from KURARAY-Japan, and the product chemical name is Kuralon K-II, based on polyvinyl alcohol (PVOH) resin.

Table 4. 3: Engineered Cementitious Composite Mix Design

| <i>Materials</i> | <i>Quantity(kg/m³)</i> |
|-----------------------|-----------------------------------|
| Cement | 530 |
| Fly Ash | 636 |
| Silica Sand | 425 |
| PVA Fibers | 25 |
| (SP) Superplasticizer | 13 |

4.3. Specimen Fabrication

4.3.1 Plain Concrete Preparation

To batch the plain concrete mix, firstly sand, gravel and cement in dry conditions were mixed in the pan-type mixer for two minutes (Fig. 4.6 (a)). Half of the total quantity of water was added into the mixer and after 3 minutes of continuous mixing the remaining water was gradually added (Fig. 4.6(b)). After 3 minutes of mixing if the concrete slump test control was less than 18 cm (Fig. 4.6(c)) a small dosage of superplasticizer poured into the mixing composition for keeping and maintaining an adequate concrete workability required for concrete casting into the molds.



Figure 4. 6: (a) Dry Aggregates; (b) Mixing after water addition; (c) Concrete slump test

4.3.2. Fiber Reinforced Concrete Preparation

4.3.2.1 ECC Strength Confirmation

Several trial procedures were used for production of the ECC-FRC, the objective being to achieve flowability during the pour, but also adequate strength; this investigation was necessary as the fly ash used was sourced from a different supplier than what had been used in the original development of the mix design (Georgiou, 2017). In order to ascertain the ECC mechanical properties a final trial batch was executed prior to fabrication of the specimens, where totally six prismatic samples were examined in tension and compression (see details in Table 4.4). The testing method was in accordance with EN 196-1 2016 and the samples were tested at 90 days under laboratory conditions ($(20 \pm 2) ^\circ\text{C}$ and $(50 \pm 3) \% \text{RH}$).

Table 4. 4: Experimental specimens coding and dimensions for flexural and compression strength determination

| Specimen | Dimensions | Type of Experiment |
|----------|-----------------|----------------------|
| FRC-T1 | 40×40×160mm | Flexural Strength |
| FRC-T2 | 40 × 40 × 160mm | Flexural Strength |
| FRC-T3 | 40 × 40 × 160mm | Flexural Strength |
| FRC-C1 | 40 × 40 × 80mm | Compressive Strength |
| FRC-C2 | 40 × 40 × 76mm | Compressive Strength |
| FRC-C3 | 40 × 40 × 76mm | Compressive Strength |

4.2.2.2 ECC Mixing Procedure

During the FRC production, firstly powders in dry condition of ECC (cement, fly ash and silica sand) were mixed in the planetary mixer for 2 minutes. Then half of the total water and superplasticizer were added and mixing continued. Finally, PVA fibers were added and then the rest of water and superplasticizer volume mixed independently and gradually added into the mixer until an adequate workability got in the mixture. (See Figure 4.7 (a) and 4.7 (b))

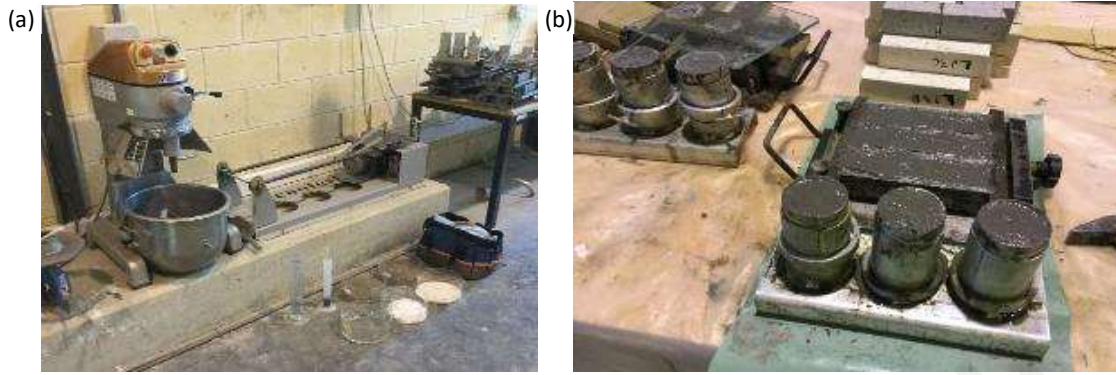


Figure 4. 7: (a) FRC trial production and mixing procedure in planetary mixer; (b) FRC specimens for tensile and compressive strength tests

4.3.2.3 ECC Tensile and Compression Tests and Experimental Results

To determine the tensile strength of ECC, experimental tests were executed under three-point bending tests according to [EN 196-1 2016](#) and tensile stress and strain relationships were exported (Fig. 4.8 (a)). Compression tests ([EN 196-1 2016](#)) were done on rectangular prisms with a 1:2 aspect ratio with dimensions of 40×40×80mm. Tests were executed under displacement control to obtain the compression stress and strain relationship; strain rate used in the compression test was 0-60 $\mu\epsilon$ /s. Strain gauges were applied in the three sides of specimens, i.e., on two opposite sides to record the vertical strain and a third strain gauge installed in the horizontal axis to record transverse strains (Fig. 4.8(b) and (c)). Experimental results are presented in Figure 4.9 (a) and (b).

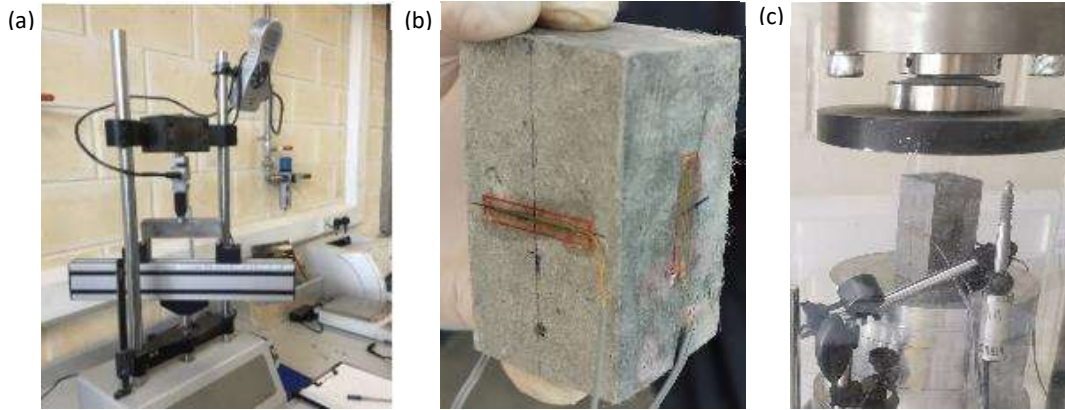


Figure 4. 8: (a) Three point bending experimental lay out; (b) Installation of strain gauges on rectangular shaped prisms; (c) Compression test under displacement control

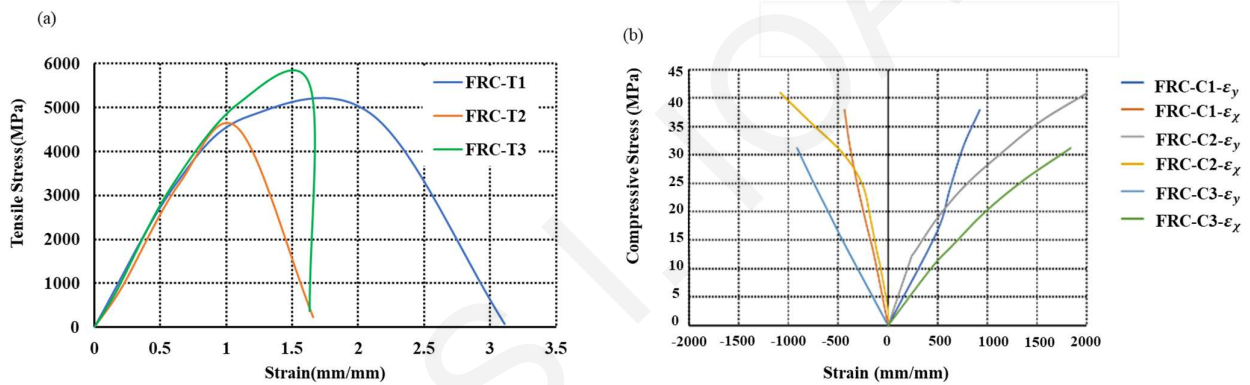


Figure 4. 9; (a) Three-point bending test Force vs. Displacement result (b) Compression test results

After ascertaining the tensile and compressive strength levels the procedure described in Paragraph 4.3.2.2 was applied for upscaling the production of ECC batch in the pan-mixer. Preparation of materials (Fig. 4.10 (a)), powder mixing in dry condition (Fig. 4.10 (b)), and after water and SP addition in Fig. 4.10 (c) and (d) PVA fibers were added last and final mixing continued in order to get the specified ECC mix design flow consistency (Figure 4.10 (e) and (f)).

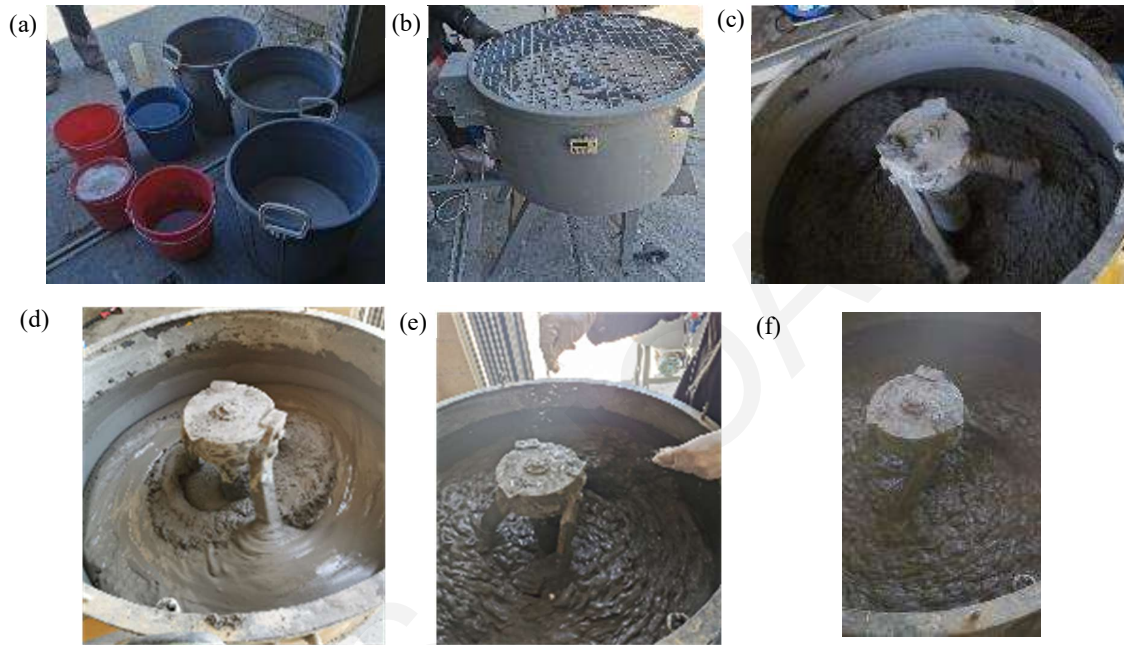


Figure 4. 10: (a) Weighed quantities (b) Mixing of powders in dry condition (c) Mixing of powders with half the water volume (d) Mixing of powders with half the SP volume (e) PVA fibers' addition (f) Addition of remaining water and final mixture consistency

4.3.3 Specimen Production Procedure

Specimen identification used illustrates the values of the main parameters varied in the interface characterization study, namely the inclination of the interface with respect to the longitudinal axis and surface roughness. Specimen coding is analyzed in Table 4.5.

Table 4. 5: Specimen coding scheme and dimensions for flexural and compression strength determination

| Specimen* | Dimensions | Type of Experiment |
|--------------|------------------|--------------------|
| PC-CYL-N | D=100mm, H=200mm | CT |
| ECC-CYL-N | D=75mm, H=200mm | CT |
| SP-N-A | 100×100×200mm | SST |
| SP-N-SPLIT | 100×100×200mm | ST |
| FRC-SPN-BEAM | 100×60×280mm | FPBT |

*Notation: CYL=Cylinder; SP=Specimen; N= ID number of the specimen; A = inclination of interface; CT=compression test; SST=slant shear test; ST=splitting test; FPBT=four-point bending test

4.3.3.1 PC Specimen casting

In total 18 specimens of type SP-N-A and 3 specimens of type PC-CYL-N were made. First the PC part of the specimen was cast. To ensure the inclination level of interface special wooden stepwise structures were prepared, where each step had a different angle with the horizontal plane. After filling the molds exactly at 50% of the total volume with fresh PC, they were placed on the steps as shown on Fig. 4.11. Thus, when placed on the inclined steps the free surface of the fresh concrete leveled along the horizontal, thereby creating an angle of inclination with the longitudinal axis of the mold, that was equal to the angle of the supporting wooden step. After hardening in that position, molds were removed and specimens were cured immersed in the laboratory water tanks under stable temperature of 20°C for 28 days. Specimens PC-CYL-N were tested at that point in compression to measure the PC compressive strength.

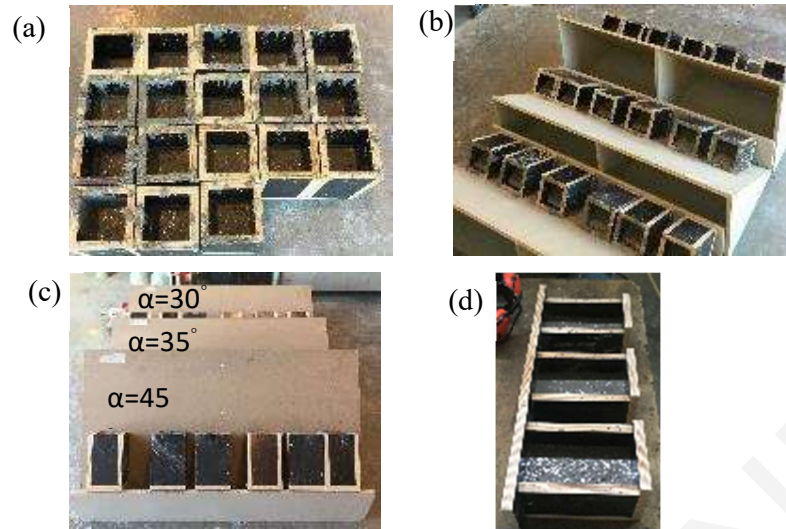


Figure 4. 11: (a) Casting of slanted shear specimens in horizontal position; (b), (c) Positioning of SP-N-A specimens for configuration of the free surface (d) Casting of SP-N-SPLIT series

Records of the specimens' dimensions are given in Table 4.6 in order to accurately determine the actual inclination of the interface. The roughness factor of all free surfaces was measured through the use of Gwydion software with a simple methodology. Gwydion is a modular program for SPM (scanning probe microscopy) data visualization and analysis. Primarily it is intended for the analysis of height fields obtained by scanning probe microscopy techniques (AFM, MFM, STM, SNOM/NSOM) and it supports various SPM data formats (Petr K et al., 2004).

4.3.3.1 Roughness Parameters

The estimation of standardized one-dimensional roughness parameters was evaluated through Gwyddion software with the Roughness tool. The one-dimensional texture is split into waviness (the low-frequency components defining the overall shape) and roughness (the high-frequency components) at the cut-off frequency. This frequency is specified in the units of the Nyquist frequency, that is value 1.0 corresponds to the Nyquist frequency. The Nyquist frequency is a signal processing sampling frequency that is defined as "half the rate" of a discrete signal processing system. The Nyquist frequency denotes the point at which a visual model of a signal can be constructed. This is related to the concept of "aliasing" in discrete time sampling. Two samples each cycle is required to adequately establish a signal, according to

this theory. It is the maximum frequency that can be coded for a given sample rate in order to reconstruct the signal. It is also displayed as the corresponding real-space wavelength.

A few parameters were used to quantify the surface roughness and are presented in the following according to ISO 4287 4 by Equations 4.1– 4.2. These parameters may be considered individually or combined.

4.3.2.1.1 Roughness amplitude parameter

Roughness Average R_a Standards: Represents the arithmetic mean deviation. The average deviation of all points of the roughness profile from a mean line over the evaluation length

$$R_a = \frac{1}{l_m} \int_0^{l_m} |y(x)| dx \quad (4.1)$$

Where, l_m is the evaluation length; and $y(x)$ is the profile height at position x

4.3.2.1.2 Statistical parameters

Skewness R_{sk} : Skewness is an additional parameter that describes the amplitude distribution function (ADF) which is a function that gives the probability that a profile of the surface has a certain height y at any position x . Skewness is a measure of the symmetry of the ADF. It measures the symmetry of variation of a profile about its mean line.

$$R_{sk} = \frac{1}{l_m R_q^3} \int_0^{l_m} y^3(x) dx \quad (4.2)$$

R_{sk} greater than about 1.5 in magnitude (positive or negative) indicates that the surface does not have a simple shape and a simple parameter such as R_a is probably not adequate to characterize the quality of the surface (Tayeh et al., 2013).

4.3.3.3 PC Specimen Parts' Roughness Factor Measurements

After 28 days of wet curing, PC specimens were removed from the water storage tank and measurements referred to in the previous paragraph were taken or recorded. All specimens related to slanted shear and splitting tests were stored for three days in the laboratory ambient conditions (Fig. 4.12 (a)) and widescreen photos were taken (Fig. 4.12(b)) for each specimen in order to record roughness average and skewness (Fig. 4.12 (c) and (d)). Results related to roughness parameters are given in Table 4.7.

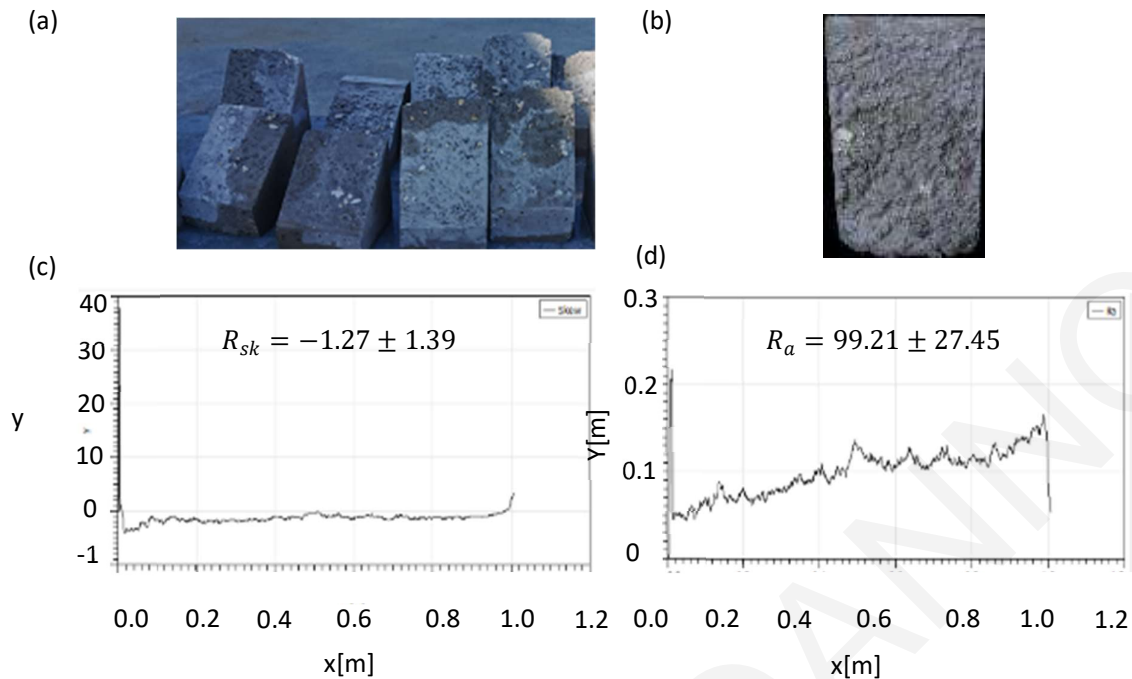


Figure 4. 12: (a) Specimens in laboratory environmental conditions; (b) Sample specimen wire screen for roughness parameter processing; (c) Roughness average and (d) Skewness

4.3.3.4 Concrete Surface Profiles Quantification

The most well-known qualitative method for estimating a quantitative measure of the texture of a concrete surface was proposed by the [International Concrete Repair Institute \(ICRI\) \(1997\)](#). In this method, the concrete surface to be characterized is visually compared with nine *concrete surface profiles (CSP)* of increasing roughness, Figure 4.13. The advantages and disadvantages are clear: rapid method, yielding subjective results that are user-sensitive ([Santos and Santos, 2009](#)).

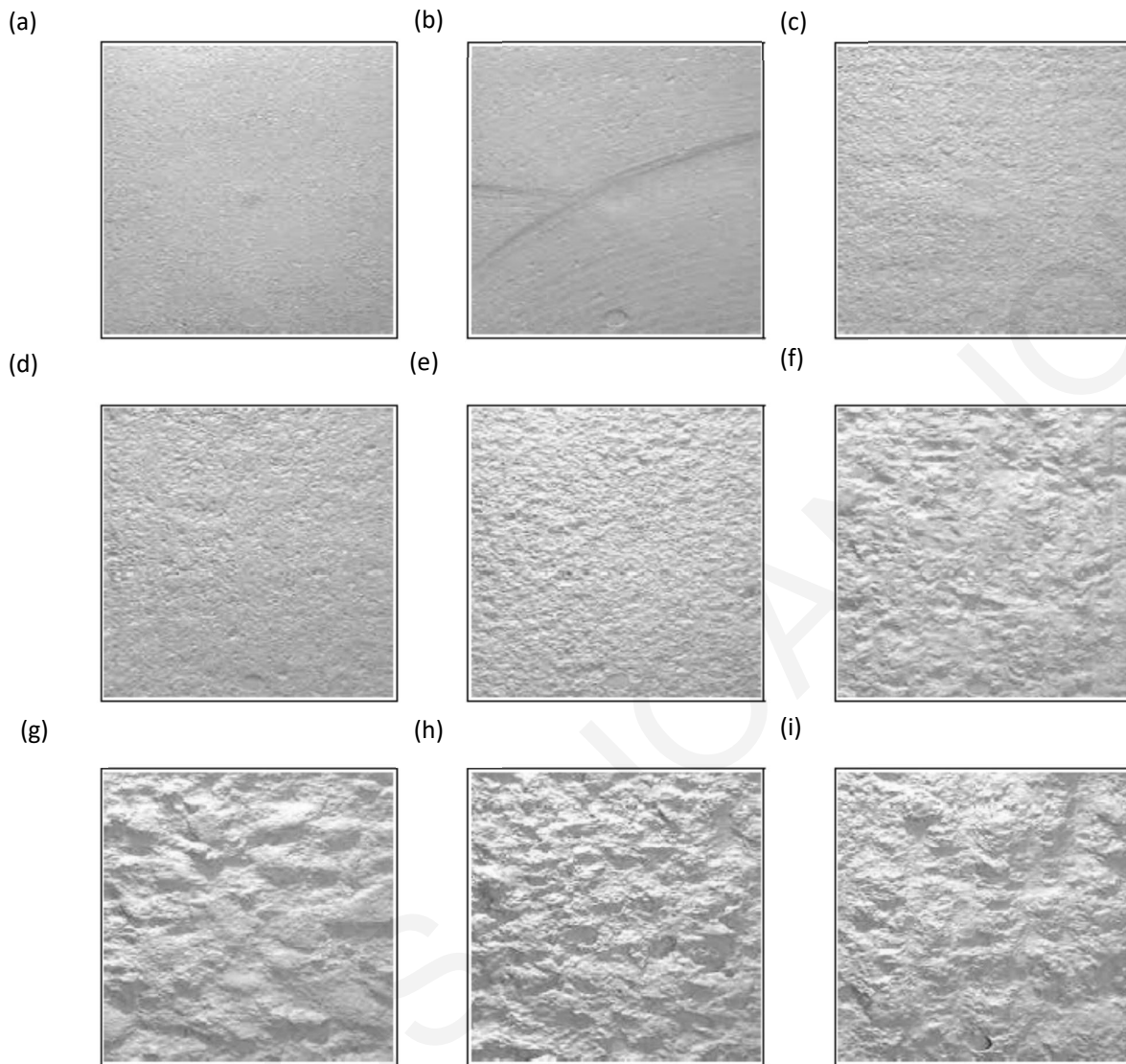


Figure 4. 13: Concrete Surface Profiles (a) CSP 1; (b) CSP 2; (c) CSP 3; (d) CSP 4; (e) CSP 5; (f) CSP 6; (g) CSP 7; (h) CSP 8; (i) CSP 9 (pictures extracted from [Maerz and Myers \(2001\)](#))

4.3.3.5 ECC Specimen Casting

For the completion of specimens' fabrication, the production of ECC was necessary. Specimens shown in Fig. 4.14 (a) and (b) were once again installed inside the moulds, including the cylindrical and rectangular prism specimens that were intended for ECC mechanical properties' determination (tensile and compressive strength, see Fig 4.14 (a) and (b)). The

production of ECC according to the specified mix design was executed and specimens casting completed by filling the molds, standing upwards, to the rim (4.14 (a), (c), (d)).

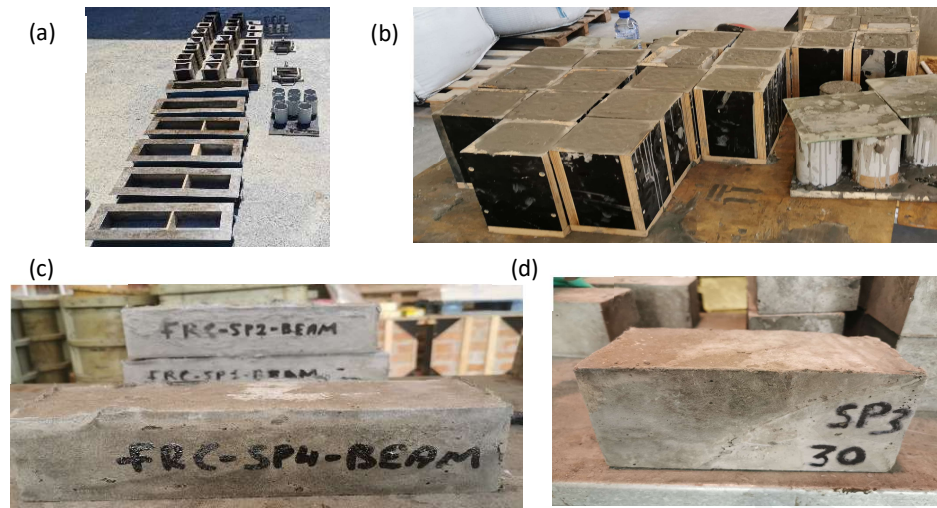


Figure 4. 14: (a) PC parts placement into the molds; (b) Casting of ECC; (c) and (d) experimental specimens

4.3.3.6 Combined Specimen Dimensions and Roughness Parameters

After casting and setting, the composite PC-ECC specimens were maintained in the water tank for a period of 90 days, after which point, they were tested. All measurements regarding combined specimens and roughness parameters recordings and representative samples of the results are listed in Tables 4.6, 4.7 for both the first and second experimental cycles, respectively.

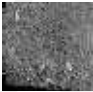
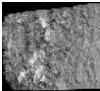


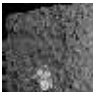
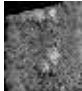


Table 4. 6: First experimental cycle specimens' reference coding and dimensions

| First Experimental Cycle | | |
|---------------------------------|------------------------|---------------------------|
| Element Code[♠] | Experiment Type | Dimensions |
| PC-CYL-1 | CT | H=200mm, D=100mm |
| PC-CYL-2 | CT | H=200mm, D=100mm |
| PC-CYL-3 | CT | H=200mm, D=100mm |
| ECC-CYL-1 | CT | H=150mm, D=75mm |
| ECC-CYL-2 | CT | H=150mm, D=75mm |
| ECC-CYL-3 | CT | H=150mm, D=75mm |
| FRC-SP1-BEAM | FPBT | L=200mm, B=100mm, H=60mm |
| FRC-SP2-BEAM | FPBT | L=200mm, B=100mm, H=60mm |
| FRC-SP3-BEAM | FPBT | L=200mm, B=100mm, H=60mm |
| I or II-SP-4-A(A>30) | SST | H=200mm, B=100mm, W=100mm |
| I or II-SP-5- A(A>30) | SST | H=200mm, B=100mm, W=100mm |
| I or II-SP-6- A(A>30) | SST | H=200mm, B=100mm, W=100mm |
| I or II-SP-1- A(A>35) | SST | H=200mm, B=100mm, W=100mm |
| I or II-SP-5- A(A>35) | SST | H=200mm, B=100mm, W=100mm |
| I or II-SP-6- A(A>35) | SST | H=200mm, B=100mm, W=100mm |
| I or II-SP-1- A(A>45) | SST | H=200mm, B=100mm, W=100mm |
| I or II-SP-2-A(A>45) | SST | H=200mm, B=100mm, W=100mm |

| | | |
|-----------------------|-----|---------------------------|
| I or II-SP-4- A(A>45) | SST | H=200mm, B=100mm, W=100mm |
| I or II-SP-1-SPLIT | ST | H=200mm, B=100mm, W=100mm |
| I or II-SP-2-SPLIT | ST | H=200mm, B=100mm, W=100mm |
| I or II-SP-3-SPLIT | ST | H=200mm, B=100mm, W=100mm |

♦ Notation: *I*=First experimental cycle; *II*=Second experimental cycle; *N*=Sample type number; *A* = inclination angle of interface measured with respect to the horizontal axis.

Table 4. 7: Substrate level inclination and roughness parameters of PC - first batch of specimens

| | Substrate Level inclination | Mean Roughness Factor | Skewness | Concrete Surface Profiles | Surface Profile |
|-------------|--|--------------------------------------|---------------------------|--|---|
| I-SP-4-51 | 51 ° | 87.82 $\pm 29.15\mu m$ | -0.96 $\pm 0.51\mu m$ | CSP 6 |  |
| I-SP-5-50-1 | 50 ° | 115 $\pm 28.84\mu m$ | -1.084 $\pm 0.80\mu m$ | CSP7 |  |
| I-SP-6-56 | 56 ° | 99.21 $\pm 27.45\mu m$ | -1.274 $\pm 1.39\mu m$ | CSP5 |  |
| I-SP-1-53 | 53 ° | 113.2 $\pm 28.52\mu m$ | -0.87 $\pm 1.066\mu m$ | CSP8 |  |
| I-SP-5-50-2 | 50 ° | 95.44 $\pm 22.5\mu m$ | -0.77 $\pm 1.15\mu m$ | CSP6 |  |
| I-SP-6-49 | 49 ° | 105 $\pm 27.17\mu m$ | -0.72 $\pm 0.65\mu m$ | CSP7 |  |
| I-SP-1-45 | 45 ° | 99.25 $\pm 29.6\mu m$ | -0.921 $\pm 1.89\mu m$ | CSP9 |  |
| I-SP-2-45 | 45 ° | 98.16 $\pm 32.63\mu m$ | $-0.76 \pm 1.5\mu m$ | CSP9 |  |





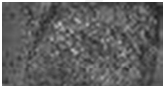
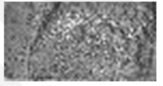
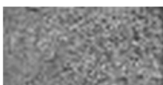



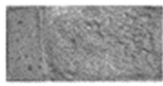
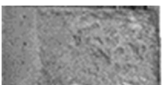
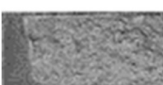
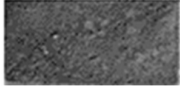
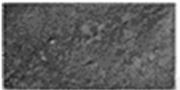

| | | | | | |
|--------------|------|---------------------------|----------------------------|------|---|
| I-SP-4-42 | 42 ° | 98.19 $\pm 21.73\mu m$ | -0.87 $\pm 1.612\mu m$ | CSP9 |  |
| I-SP-1-SPLIT | - | 190.7 $\pm 125.9\mu m$ | $0.18 \pm 0.53\mu m$ | CSP4 |  |
| I-SP-2-SPLIT | - | 202.4 $\pm 118.6\mu m$ | -0.22 $\pm 0.9125\mu m$ | CSP4 |  |
| I-SP-3-SPLIT | - | 162.9 $\pm 114.1\mu m$ | 0.067 $\pm 0.65\mu m$ | CSP5 |  |

Table 4. 8: Substrate level inclination and roughness parameters of PC second experimental cycle specimens

| | Substrate Level inclination | Mean Roughness Factor | Skewness | | Surface Profile |
|------------|--|--------------------------------------|--------------------------|------|---|
| II-SP-1-51 | 51 ° | 229.9 $\pm 89.22\mu m$ | 0.50 $\pm 0.20\mu m$ | CSP6 |  |
| II-SP-3-50 | 50 ° | 189 $\pm 12.51\mu m$ | $1.03 \pm 0.1\mu m$ | CSP6 |  |
| II-SP-4-57 | 57 ° | 206.1 $\pm 112.4\mu m$ | 0.44 $\pm 0.305\mu m$ | CSP5 |  |
| II-SP-1-58 | 58 ° | 180.1 $\pm 126.7\mu m$ | 0.077 $\pm 0.65\mu m$ | CSP5 |  |
| II-SP-2-53 | 53 ° | 236.244 $\pm 110\mu m$ | 0.20 $\pm 0.39\mu m$ | CSP5 |  |
| II-SP-3-56 | 56 ° | 185.8 $\pm 129.6\mu m$ | 0.055 $\pm 0.67\mu m$ | CSP4 |  |
| II-SP-1-46 | 46 ° | 187.5 $\pm 131\mu m$ | 0.18 $\pm 0.58\mu m$ | CSP5 |  |
| II-SP-2-45 | 45 ° | 205.9 $\pm 93.44\mu m$ | 0.62 $\pm 0.20\mu m$ | CSP5 |  |
| II-SP-3-42 | 42 ° | 186.7 $\pm 130.4\mu m$ | 0.18 $\pm 1.58\mu m$ | CSP5 |  |

| | | | | | |
|-------------------|---|---------------------------|--------------------------|------|---|
| II-SP-1- SPLIT | - | 244.6 $\pm 170.5\mu m$ | 0.24 $\pm 0.530\mu m$ | CSP4 |  |
| II-SP-2- SPLIT | - | 244.8 $\pm 171.2\mu m$ | 0.25 $\pm 0.53\mu m$ | CSP4 |  |
| II-SP-3- SPLIT | - | 231.7 $\pm 161\mu m$ | 0.25 $\pm 0.51\mu m$ | CSP4 |  |

4.4 Experiments - Instrumentation Layout

In this section the layout of instrumentation is specified for the four types of experiments executed to characterize the interfacial properties of PC-ECC composite specimens; these include tests of the individual materials in compression (100×200mm PC cylinders, 75×150 ECC cylinders), ECC tensile strength, slanted shear tests to characterize the interface shear under combined shear-compression, and the resistance of the interface to direct tension through splitting tests. The stress-strain response in compression was recorded using cylinder specimens, instrumented with four 30mm-long strain gauges, two along the horizontal axis and two along the vertical axis (Fig 4.15 (a) and (b)). ECC tensile strength was characterized through flexural prism tests where the properties were extracted from the resistance curve by conducting inverse analysis (presented in the following paragraphs). As shown in Figure 4.15 (c), two pairs of displacement transducers were used to record the relative displacement of the midspan with regards to the support rollers (the pairs were used in the front and the back of the specimen, respectively). For the slanted shear tests, two displacement transducers were placed in the vertical direction on PC and ECC parts (Fig. 4.15 (d) and (e)). Additionally, for interface splitting tests, a pair of horizontal displacement transducers were used in the horizontal direction (Fig. 4.15 (f)).

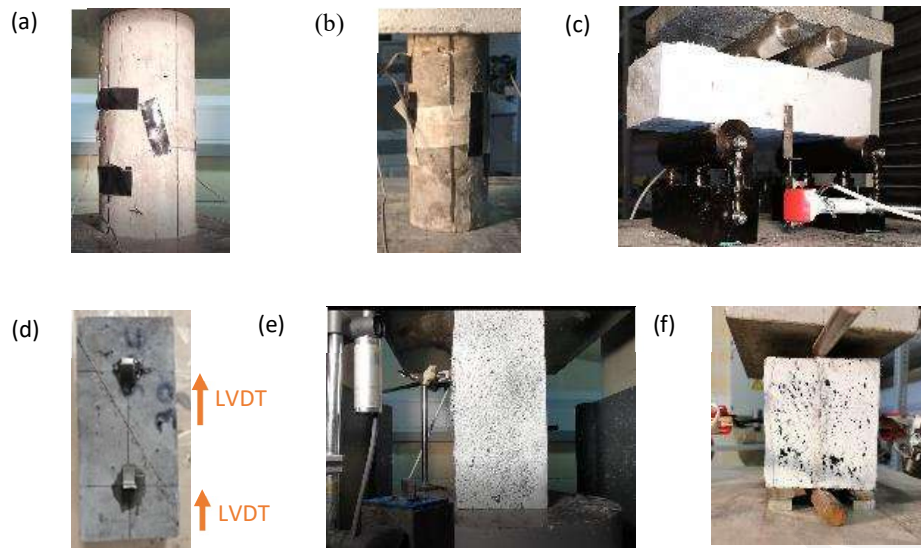


Figure 4.15: Instrumentation lay out of (a) PC cylinder; (b) ECC cylinder; (c) Rectangular prismatic ECC specimen; (d), (e) Combined (slanted) prismatic specimen (ECC and PC) under compression, and (f) splitting test on combined prism.

In a parallel manner with the traditional monitoring system, digital image correlation (DIC) was also used to record the specimen deformations. DIC uses image processing techniques; specimens are speckled, and sequential images are taken during the loading, which are used as input to the DIC algorithm (here, a Matlab based open software was used, known as [ncorr](https://ncorr.com/) (<https://ncorr.com/>)). The algorithm determines a one-to-one correspondence between speckles in the reference and the current configurations, (i.e., initial to subsequent deformed specimen condition.) DIC does this by taking small subsections of the reference picture, called subsets, and deciding their particular areas in the current state. For every subset, the program acquires dislocations and strain data through the change used to coordinate with the area of the subset in the current configuration. Numerous subsets are picked in the reference arrangement, regularly with a separating parameter to lessen computational expense (note that subsets commonly cross-over also). The final product is a framework containing displacement and strain data concerning the reference condition (Lagrangian strains, Blabber, 2021).

4.5 Analysis and Discussion of Results

4.5.1 PC and ECC Cylinders under Uniaxial Compression

Uniaxial compression tests were performed well into the post-peak range under displacement control using a closed-loop, servo hydraulic controlled testing machine at a loading rate of 1.50 $\mu\text{m/s}$. An additional LVDT measured the deformation over the entire length of the specimen, through the displacement of the platens. The displacement control of the machine was based on this LVDT.

Compressive stress-axial strain-lateral strain curves extracted from the experimental measurements are plotted in Figure 4.16. Axial stress was computed by dividing the recorded load by the area of the cross section while axial and lateral strains were obtained as the average of the two strain gauges' records. Lateral dilation was a very important parameter that was required for the analysis of ECC and PC behavior under compression since softening of the compressive strength is directly related to cracking parallel to the direction of loading and lateral expansion (Pantazopoulou and Mills, 1992; Pantazopoulou, 1995).

From comparison of the PC and ECC uniaxial compression experimental results shown in Figure 4.16 (a), (b), the dramatic improvement in ductility effected by the fibers is noted (relatively milder post-peak stress-strain envelope). Response curves are terminated where strain gauge failure occurred.

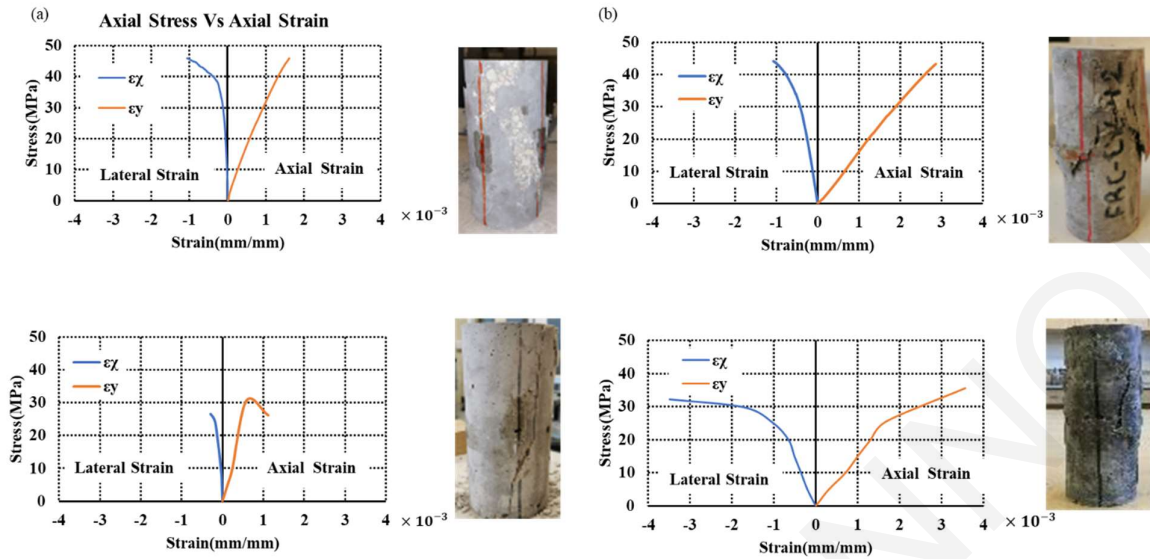


Figure 4. 16: Average compression stress and stain envelopes for PC-CYL-N and ECC-CYL-N series of (a) first experimental cycle and (b) second experimental cycle.

4.5.2 Four Point Bending Tests

Four-point bending tests for both cycles of experiments were carried out to determine the tensile stress and cracking mechanical properties of the proposed ECC mix design. Three prismatic rectangular shaped specimens were prepared to for each batch and the experimental set up was discussed in Section 4.4. The experiments were conducted under displacement control. Specimens were more than 90 days when tested, to evaluate the deformation capacity in the end of the pozzolanic activity of the FA powders which could enhance fiber bond thereby compromising ductility.

The experimental envelope curves of load-deflection curves of the four-point bending results are given in Figure 4.17 (a), (b) accompanied by the most characteristic failure mode. The tested specimens developed flexural ductile response, marked by multiple cracking in the constant moment zone. Failure occurred by localization of deformation along an inclined single crack that developed after maximum load either under the load application points or in the constant moment region.

Yang et al. (2020) used the inverse analysis method to determine the critical points of the tension stress-strain response of the material using the approach adopted by the CSA-S6 (2019) Canadian bridge code as described in the (tension hardening) THFRC Annex 8, that originally was developed and proposed by Lopez (2017). The procedure requires the resistance curve

from four point loading as depicted in Fig. 4.18a, where the total applied vertical load is P , and the midspan displacement is δ . Note here that the midspan displacement must be measured with reference to the chord of the deformed specimen (i.e., with reference to the chord of the member, which is the line that connects the midpoints of the sections directly above the supports). This is achieved either using a yoke mounted on the specimen that supports the linear variable differential transducers (LVDTs) in order for the relative displacement to be obtained directly, or three LVDTs are used in order to measure both the midspan deflection and the support displacements from a stationary reference, so that the relative displacement δ may be obtained (the latter approach was used in this study).

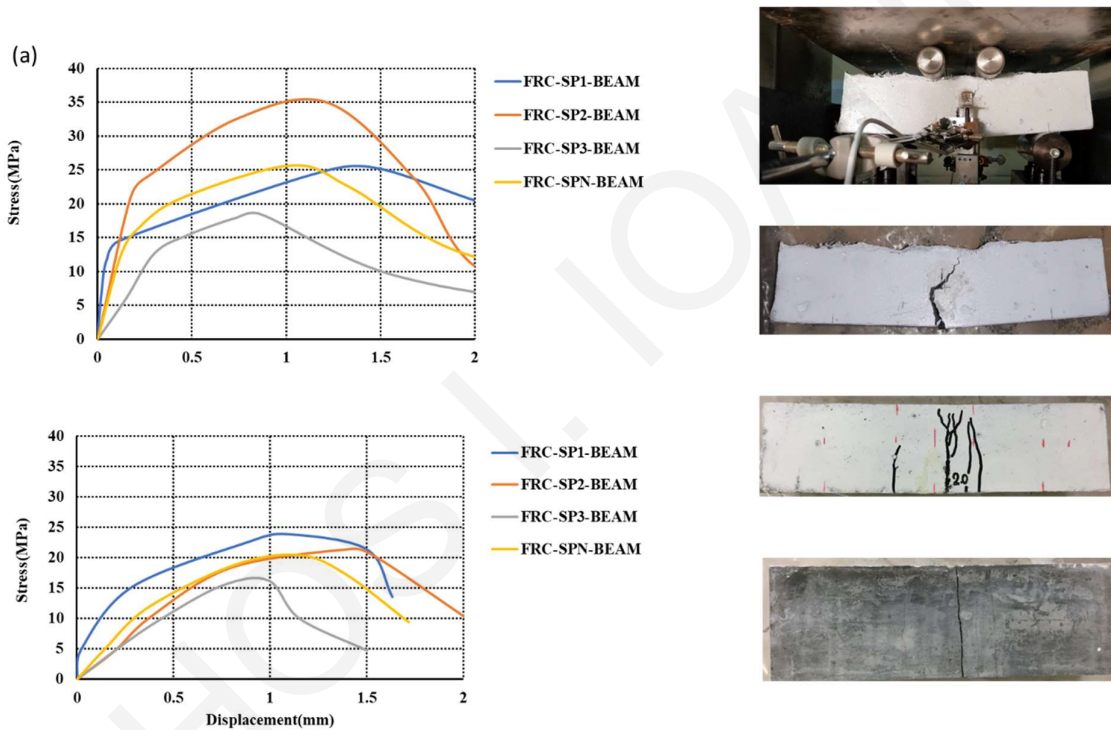


Figure 4. 17: Load - Deflection response curves and failure modes of FRC-SPN-BEAM series of (a) first experimental cycle and (b) second experimental cycle.

The procedure used for inverse analysis is outlined with reference to Fig. 4.18. The slope of the ascending branch of the curve, s_o , defines the point (P_o, δ_o) and the intersection of the straight lines from $(0,0)$ with inclination 75% and 40% of s_o , which are denoted as s_{75} and s_{40} , with the envelope curve, determines the points (P_1, δ_1) and (P_2, δ_2) . Additionally, (P_3, δ_3) and

(P_4, δ_4) correspond to the 97% of maximum load and 80% of P_3 in the post-peak range, respectively.

Using the coordinates of these points from the resistance curve of the prism specimens, the milestone points of the tensile stress–strain response of the material are obtained, as shown in Figure 4.18 (b). Note that the obtained tensile behavior comprises a stress–strain relationship that describes the ascending and strain-hardening part of the response (f - ε), which is followed by a stress-crack opening displacement (f - w), where the maximum crack width, w , is limited by half the length of fiber used, l_f (i.e., here $w_{max} = 6$ mm).

A summary of the inverse analysis steps and the related mathematical relationships which are used in conducting the calculations is provided in Appendix A. Following the application of this procedure, the results obtained for the characteristic tensile stress – strain response of the ECC material are given in Table 4. 9.

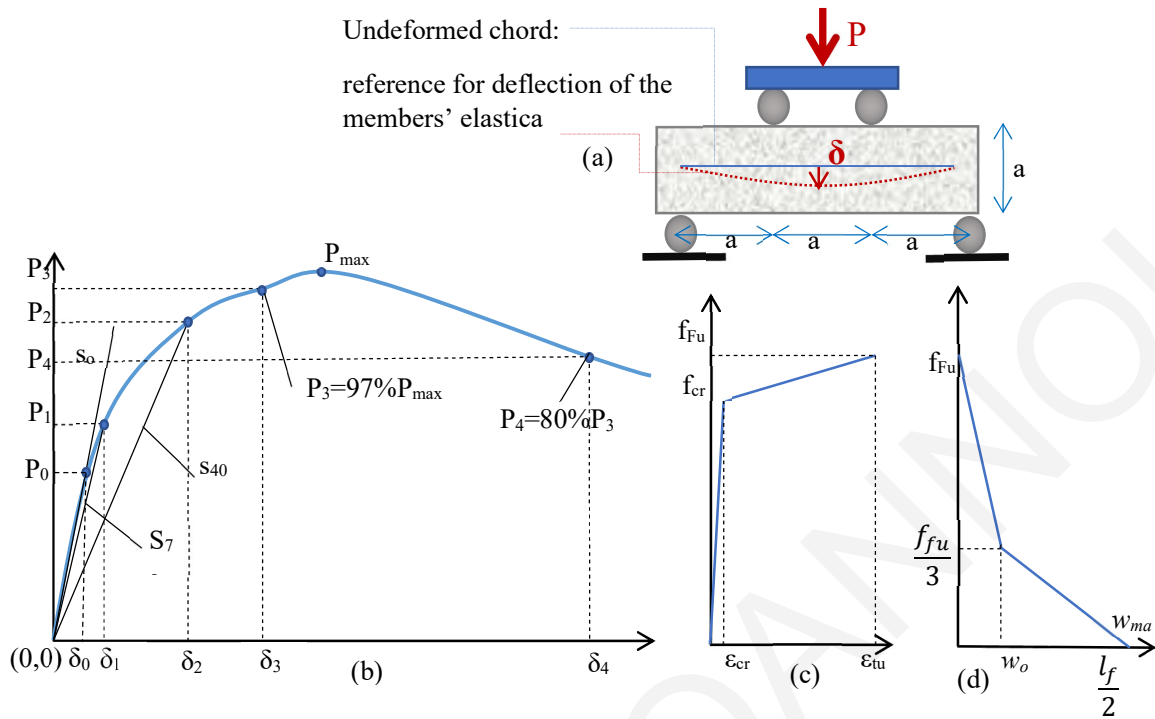


Figure 4.18: Third Point Loading of Prism to obtain the resistance curve shown in (b) and from there, through inverse analysis the stress-strain curve shown in (c) and the stress-crack opening displacement in (d).

Table 4.9: Inverse analysis results of first and second experimental procedures

| First Cycle | Second Cycle |
|---------------------------|---------------------------|
| $f_{cr} = 4.65\text{MPa}$ | $f_{cr} = 4.00\text{MPa}$ |
| $f_{Fu} = 5.00\text{MPa}$ | $f_{Fu} = 5.00\text{MPa}$ |
| $E_c = 18300\text{MPa}$ | $E_c = 1800\text{MPa}$ |
| $\epsilon_{tu} = 0.0092$ | $\epsilon_{tu} = 0.0044$ |

4.5.3 Slanted Shear Tests and Direct Tensile Tests

In the following paragraph the failure modes and ultimate strengths of combined specimens under slanted shear and direct tension tests are presented. The influence of the main parameters affecting the interface response, such as the simultaneously acting compressive stress and the resulting displacement(slip) are additionally examined and discussed.

4.5.3.1 Interface bond strength

At the point of interface, the vertical and transverse stresses can be determined by resolving the applied uniaxial compression force P on the inclined sliding plane of the slanted specimen. If α is the angle of inclination of the plane relative to the horizontal axis, the axial load P results in a normal and a shear force as shown in Fig. 4.19 (a), equal to $P \cdot \cos\alpha$ and $P \cdot \sin\alpha$, respectively. These are divided by the area of the sliding plane, $A/\cos\alpha$ to produce normal and shear stresses as depicted in Fig. 4.19 (b), where A is the normal cross-sectional area of the prism; therefore, these stresses may be obtained from the normal stress, $\sigma_c = P/A$, that is applied at the top through compression as,

$$\sigma_n = \frac{P \cdot \cos^2 \alpha}{A} = \sigma_c \cdot \cos^2 \alpha \quad (4.2)$$

$$\tau_n = \frac{P \cdot \sin \alpha \cdot \cos \alpha}{A} = \sigma_c \cdot \sin \alpha \cdot \cos \alpha \quad (4.3)$$

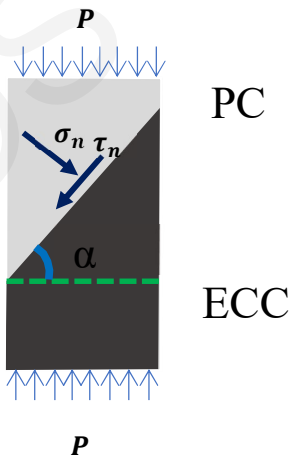


Figure 4. 19: Slanted shear test method for evaluating the repair/concrete bond strength with applied forces

The interface bond strength is determined at peak load, denoted here as P_u beyond which failure by sliding occurs. Concerning the interface bond strength, the minimum requirements, regarding the test methods and curing periods of the concrete according to [ACI 546.3R-1413, \(2014\)](#) are presented in Table 4.10.

Table 4. 10: Minimum requirements for interface bond strength of repair material and substrate plain concrete ([ACI 546.3R-1413, 2014; Youm et al., 2021](#))

| Test Method | Bond Strength, MPa | | |
|-----------------------|--------------------|------------|------------|
| | 1 day | 7 days | 28 days |
| Slanted Shear | 2.8 to 6.9 | 6.9 to 12 | 14 to 21 |
| Direct Tension | 0.5 to 1 | 1 to 1.7 | 1.7 to 2.1 |
| Direct Shear | 1.0 to 2.1 | 2.1 to 2.8 | 2.8 to 4.1 |

The results emerged from the slanted shear tests are illustrated in Table 4.11 for both batches of specimens which were tested at greater age than the 28 days. In comparison with the above values most specimens satisfied the minimum requirements of [ACI 546.3R-14.13](#) with the exception of II-SP-1-58, II-SP-3-56, II-SP-4-57 of the second batch. As it can be seen from the results, increasing angle of substrate plan with respect to the horizontal led to reduced bond strength at the interface. Mechanisms such as aggregate interlock, increased roughness of the examined surface and higher concrete compression strength contributed to enhancing the bond value.

Table 4. 11: Summary of test results at the ultimate

First Experimental Cycle

| Specimen Code | α | σ_c (vertical compressive stress) | τ_u | $\sigma_{n,u}$ |
|----------------------|----------------------------|--|----------------------------|----------------------------------|
| I-SP-4-51 | 51.0 | 57.0 | 27.9 | 22.6 |
| I-SP-5-50-1 | 50.0 | 46.0 | 22.7 | 19.0 |
| I-SP-6-56 | 56.0 | 59.0 | 27.4 | 18.4 |
| I-SP-1-53 | 53.0 | 54.0 | 26.0 | 19.6 |
| I-SP-5-50-2 | 50.0 | 38.0 | 18.7 | 15.7 |
| I-SP-6-49 | 49.0 | 70.0 | 34.7 | 30.1 |
| I-SP-1-45 | 45.0 | 70.0 | 35.0 | 35.0 |
| I-SP-2-45 | 45.0 | 70.0 | 35.0 | 35.0 |
| I-SP-4-45 | 42.0 | 59.0 | 29.3 | 32.6 |

Second Experimental Cycle

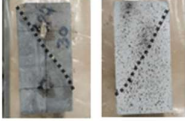

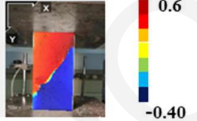
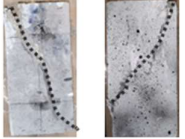
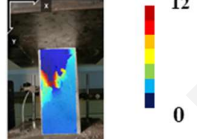
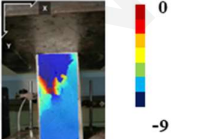

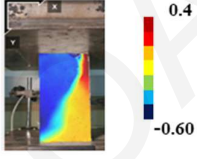
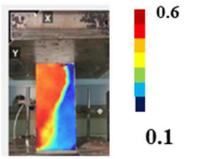
| Specimen Code | α | σ_c (vertical compressive stress) | τ_u | σ_u |
|----------------------|----------------------------|--|----------------------------|------------------------------|
| II-SP-1-58 | 58.0 | 27.0 | 12.1 | 7.6 |
| II-SP-2-53 | 53.0 | 36.0 | 17.3 | 13.0 |
| II-SP-3-56 | 56.0 | 30.0 | 13.9 | 9.4 |
| II-SP-1-51 | 51.0 | 29.0 | 14.2 | 11.5 |
| II-SP-3-50 | 50.0 | 36.0 | 17.7 | 14.9 |
| II-SP-4-57 | 57.0 | 23.0 | 10.5 | 6.8 |
| II-SP-1-46 | 46.0 | 35.0 | 17.5 | 16.9 |
| II-SP-2-45 | 45.0 | 34.0 | 17.0 | 17.0 |
| II-SP-3-42 | 42.0 | 39.0 | 19.4 | 21.5 |

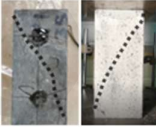
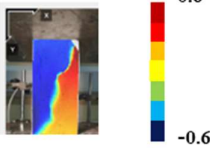
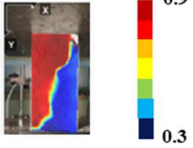

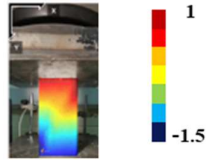
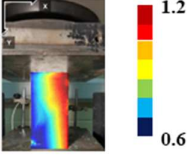
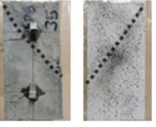
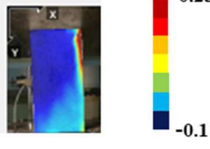
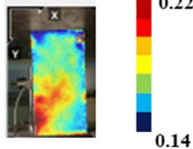
4.5.3.3.2 Failure modes


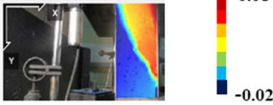
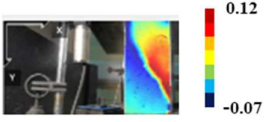

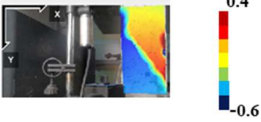
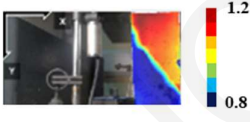
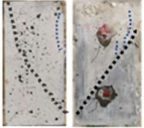
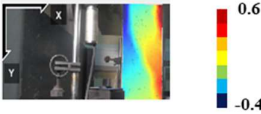
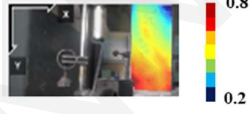
Most of the specimens with greater roughness surface and compressive strength showed brittle behaviors with a sudden drop in load-bearing capacity after the peak, resulting in cracks extending from the part of PC before an interface sliding failure, irrespective of the interface inclination angle and the curing condition of the ECC. In some cases, the damage level penetrated into the ECC. In the meantime, the samples with a less roughened interface area failed directly at the substrate level due to the absence of aggregates with diameter greater than 4-10mm, where the aggregate interlocking mechanism could not be developed. It is clearly shown from the results that the contribution of PC mix design (volume of greater size aggregates → greater roughness) and the compressive strength contributed to the shear transfer mechanism at the interface. It is furthermore seen that compressive strength at the interface exceeded the compressive strength of PC as it has been reported by [Youm et al. \(2021\)](#); [Austin et al. \(1999\)](#) and [Randl et al. \(2016\)](#). Failure modes are shown in Table 4.12.

Table 4. 12: Failure modes identified through DIC


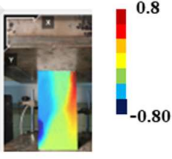
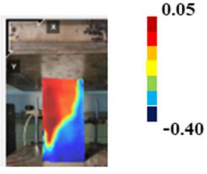

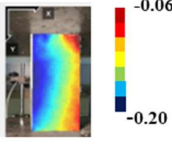
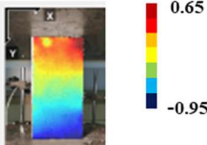

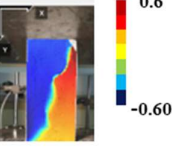
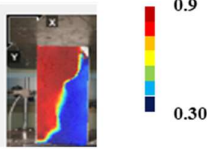
First Experimental Cycle

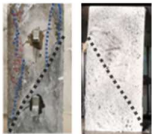
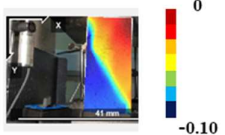
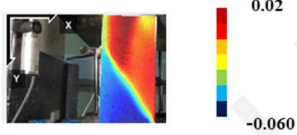
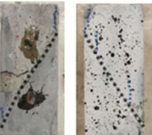
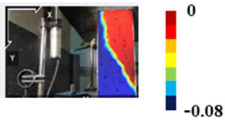
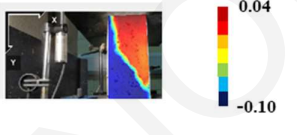

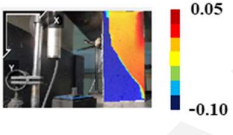
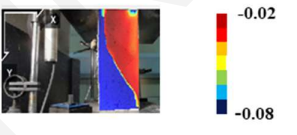
| Specimen Code | Failure Type | Horizontal Displacement | Vertical Displacement |
|---------------|---|--|---|
| I-SP-1-51 |  |  |  |
| I-SP-5-50-1 |  |  |  |
| I-SP-6-56 |  |  |  |


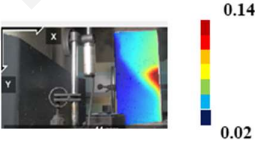
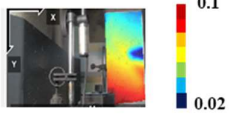
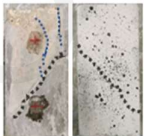
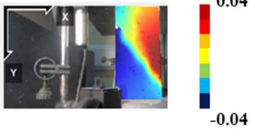
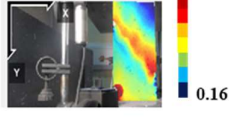

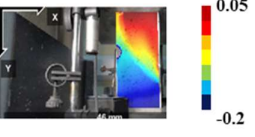
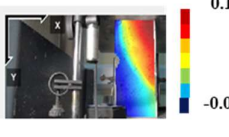
| Specimen Code | Failure Type | Horizontal Displacement | Vertical Displacement |
|---------------|---|--|---|
| I-SP-1-53 |  |  |  |
| I-SP-5-50-2 |  |  |  |
| I-SP-6-49 |  |  |  |

| Specimen Code | Failure Type | Horizontal Displacement | Vertical Displacement |
|---------------|---|--|---|
| II-SP-1-58 |  |  |  |
| II-SP-2-53 |  |  |  |
| II-SP-3-56 |  |  |  |

Second experimental cycle

| Specimen Code | Failure Type | Horizontal Displacement | Vertical Displacement |
|---------------|---|--|---|
| I-SP-1-45 |  |  |  |
| I-SP-2-45 |  |  |  |
| I-SP-4-45 |  |  |  |

| Specimen Code | Failure Type | Horizontal Displacement | Vertical Displacement |
|---------------|---|--|---|
| II-SP-1-51 |  |  |  |
| II-SP-3-50 |  |  |  |
| II-SP-4-57 |  |  |  |

| Specimen Code | Failure Type | Horizontal Displacement | Vertical Displacement |
|---------------|---|--|---|
| II-SP-1-46 |  |  |  |
| II-SP-3-45 |  |  |  |
| II-SP-4-42 |  |  |  |

4.3.3.2 Splitting Tensile Test

According to [ASTM C496, 2017](#) the splitting tensile test - which is an indirect tensile test, was carried out to evaluate the tensile bond strength between the PC substrate and ECC. After casting of PC, ECC was cast and bonded to the PC substrate specimens to form a rectangular shaped prismatic composite sample (100 mm height, 100mm width and 200 mm length). The splitting tensile strength was calculated using Equation 6.

$$\sigma_{split} = \frac{2P}{\pi BD} = \left[\frac{D^2}{z(D-z)} \right] - 1 = \frac{2P}{\pi BD} \quad (4.4)$$

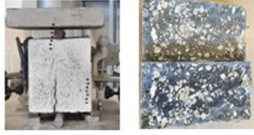
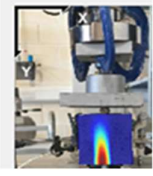

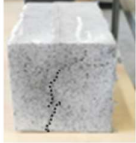
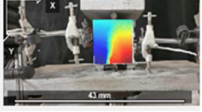
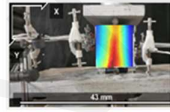


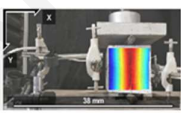
where σ_{split} is the splitting tensile strength (in MPa); P is the maximum applied load (in N); B is the length of the specimen and D the height of the specimen. In this case the bonded area was taken equal to the nominal value of $200 \times 100 = 20,000 \text{ mm}^2$. The splitting test results for both the first and second experimental cycle are shown in Table 4.13. The relevant failure modes are listed in Table 4.14. As it may be seen most of the tensile strengths obtained from the first experimental cycle are following the minimum requirements according to Table 4.10 except of specimen SP-1-SPLIT. In the case of the second batch none of the tensile strength results met the minimum requirement.

Table 4. 13: Splitting tensile strength results


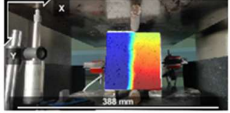
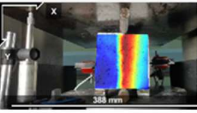
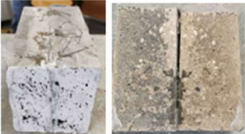
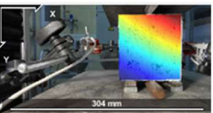
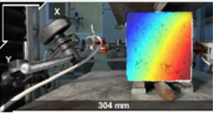
| First Experimental Cycle -Direct Tensile Test | | |
|---|------------------|----------|
| Specimen Code | σ_{split} | τ_u |
| SP-1-SPLIT | 1.6 | 0 |
| SP-2-SPLIT | 3.5 | 0 |
| SP-3-SPLIT | 2.3 | 0 |
| Second Experimental Cycle -Direct Tensile Test | | |
| Specimen Code | σ_{split} | τ_u |
| SP-2-SPLIT | 0.6 | 0 |
| SP-3-SPLIT | 0.3 | 0 |

Table 4. 14: DIC from first and second experimental batches

First experimental cycle

| Specimen Code | Failure Type | Horizontal Displacement | Vertical Displacement |
|---------------|---|---|---|
| I-SP-1-SPLIT |  |  0.14 0.02 |  0.14 0.020 |
| I-SP-2-SPLIT |  |  0.02 -0.08 |  0.02 -0.01 |
| I-SP3-SPLIT |  |  0.20 0.050 |  0.010 -0.030 |

Second experimental cycle

| Specimen Code | Failure Type | Horizontal Displacement | Vertical Displacement |
|---------------|---|--|--|
| II-SP-1-SPLIT |  |  0.4 -0.2 |  -0.05 -0.15 |
| II-SP-2-SPLIT |  |  0.70 0.30 |  0.5 0.10 |

4.5.4 Parameters affecting the interface

In most of the cases of slanted shear tests, the specimens showed higher interface bond performance than the minimum requirements of [ACI 546.3R-1413](#). However, splitting test results of batch 2 where the interfaces were smoothed were below limits – no cohesion could be supported between the PC and the ECC parts of the specimen. A large fraction of tests failed directly at the interface and another large group failed in the plain concrete part of the specimen. For a small number of specimens, the failure penetrated into the ECC part of the specimen. Adequate strength was developed at the interfaces of the first batch of specimens where the roughness was higher. High roughness increases both the contact surface and the frictional resistance due to mechanical interlocking at the interface. In the tests, this improvement depended on the concrete mix design and the relevant slump test (Fig. 4.20). It is concluded that interface roughness is crucial in the success of the strengthening by ECC jackets over PC surfaces.

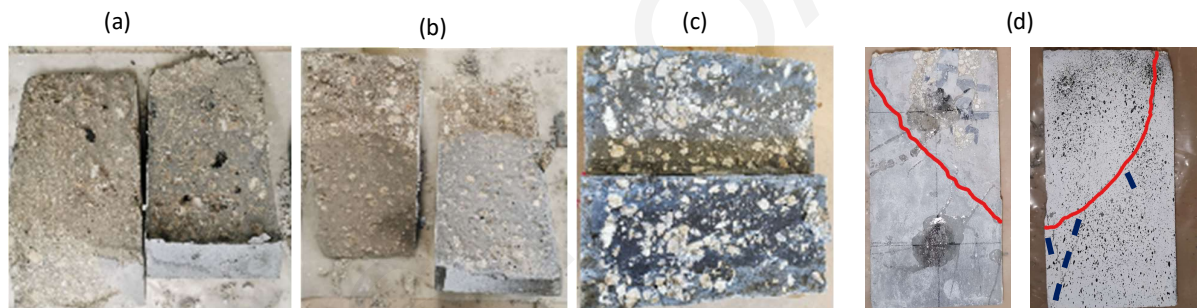


Figure 4. 20: Types of failure modes (a) Direct interface failure; (b) and (c) PC cracking and failure; (d) Failure penetration in ECC

Another fundamental parameter influencing the magnitude of shear strength in the interface was the inclination angle. According to the experimental results most of the specimens with higher angles failed in lower levels of shear strength independently of the interface roughness. In a real circumstance this can be interpreted as the lower the angle of interface, the higher the shear to normal stress ratio can be achieved according to [Youm et al. 2021](#). Normal stress clamps the interface providing greater robustness and resistance to crack growth at the interface and contributes to the development of a micro-crack mechanism. With a high inclination angle, the interface has relatively low resistance as the normal stress acting in the role of clamping is small, whereas the applied shear stress is high.

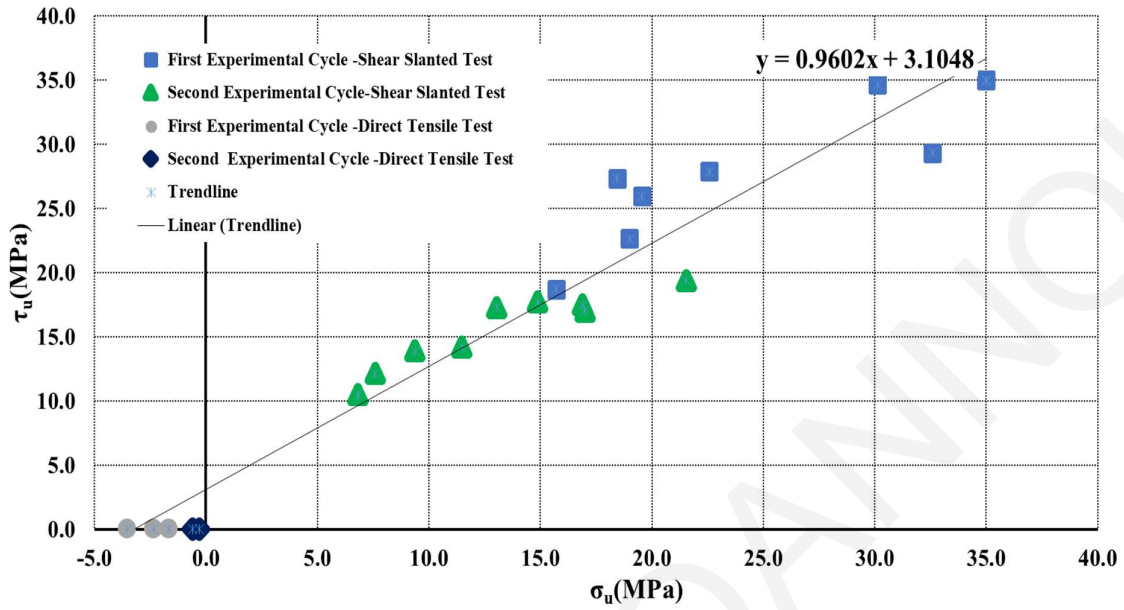
4.5.4.1 Mohr Coulomb Failure Criterion for the ECC-PC interface

With reference to shear and tensile strengths results from the tests presented in the preceding sections have clearly shown that interface strength depends on its roughness. The effect of the interface roughness on shear and tensile strength of the specimens is presented in Figures 14.21 (a) and (b) where the envelope curve between normal (i.e., clamping) and shear (i.e., sliding) stress could be described by the Mohr–Coulomb failure criterion using a linear relationship of the type (Labuz et al. 2012, Heyman 1972):

$$|\tau_u| = s_0 + \sigma_u \tan \varphi \quad (4.5)$$

where s_0 is the inherent shear strength, also known as cohesion c , and φ is the angle of internal friction, with the coefficient of internal friction $\mu = \tan \varphi$. The criterion contains two material constants s_0 and φ as opposed to one material constant for the Tresca criterion (Nadai 1950). The representation of the equation in the Mohr diagram is a straight line inclined to the σ_u -axis by the angle φ (Figure 4.21 (b)). All the results are following a clear linear correlation, i.e., a failure surface that presents the characteristics of a frictional material. For the experimental results these constants are, $c=0.96\text{MPa}$ and $\varphi=43.83^\circ$.

(a)



(b)

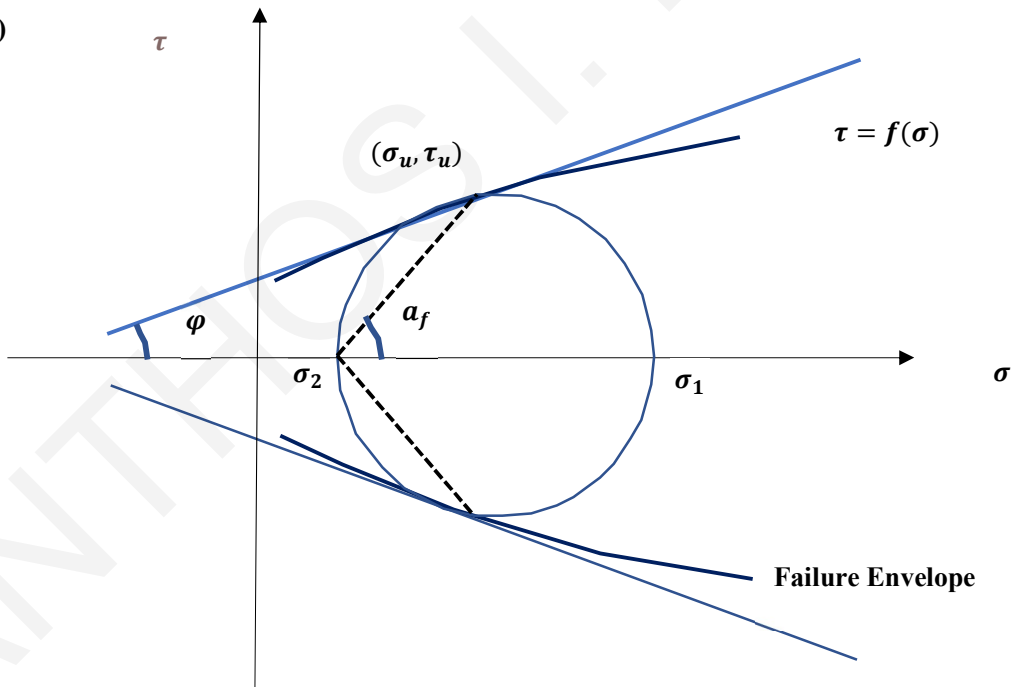


Figure 4. 21: (a) Normal vs shear stress at the interface plane for first and second experimental batch; (b) Mohr diagram and failure envelopes.

4.3.5.4.2 Three Parameter Failure Criterion

In order to determine the behavior of combined specimens at the interface, a criterion for the failure mode marking the beginning of fracture ought to be determined. By the use of this boundary, the incremental stress-strain relationship for concrete in the plastic range can be established. While the Mohr-Coulomb criterion could be used for this purpose, a number of disadvantages such as the fact that the intermediate stress is not considered, is contrary to the experimental results, whereas the fact that the failure surfaces are straight lines with corners is difficult to handle in numerical analysis. In order to express the failure criterion, the octahedral stresses τ_{oct} and σ_{oct} , were used to develop a three-parameter criterion, while the influence of J_3 or θ were neglected. The relationship between the octahedral stresses is represented by a nonlinear envelope which is consistent with the experimental evidence.

Therefore, the experimental results were used to calibrate the failure criterion that included: uniaxial compression and the splitting test. The relation between the octahedral stresses are approximated by a quadratic parabola of the form (Georgiou et al., 2021) (σ_c positive when tensile and f_c always positive):

$$\frac{\tau_{oct}}{f_c} = a + b \frac{\sigma_{oct}}{f_c} + c \left(\frac{\sigma_{oct}}{f_c} \right)^2 \quad (4.6)$$

Parameters a, b and c are established by curve fitting of the available experimental test data. The equations that were used to derive the octahedral stresses of the experimental set are as follows:

$$\tau_{oct} = \sqrt{\left(\frac{2}{3}J_2\right)} \text{(octahedral shear stress)} \quad (4.7)$$

$$\sigma_{oct} = \frac{1}{3}I_1 \text{ (octahedral normal stress)} \quad (4.8)$$

$$I_1 = \sigma_1 + \sigma_2 + \sigma_3 \text{ (first invariant of stress tensor)} \quad (4.9)$$

$$J_2 = \frac{1}{6} \left[(\sigma_x - \sigma_y)^2 + (\sigma_y - \sigma_z)^2 + (\sigma_z - \sigma_x)^2 \right] + \tau_{xy}^2 + \tau_{yz}^2 + \tau_{zx}^2 \text{ (second invariant)} \quad (4.10)$$

The complete set of octahedral stresses of all the experiments are plotted in Fig. 4.22 (a) and (b).

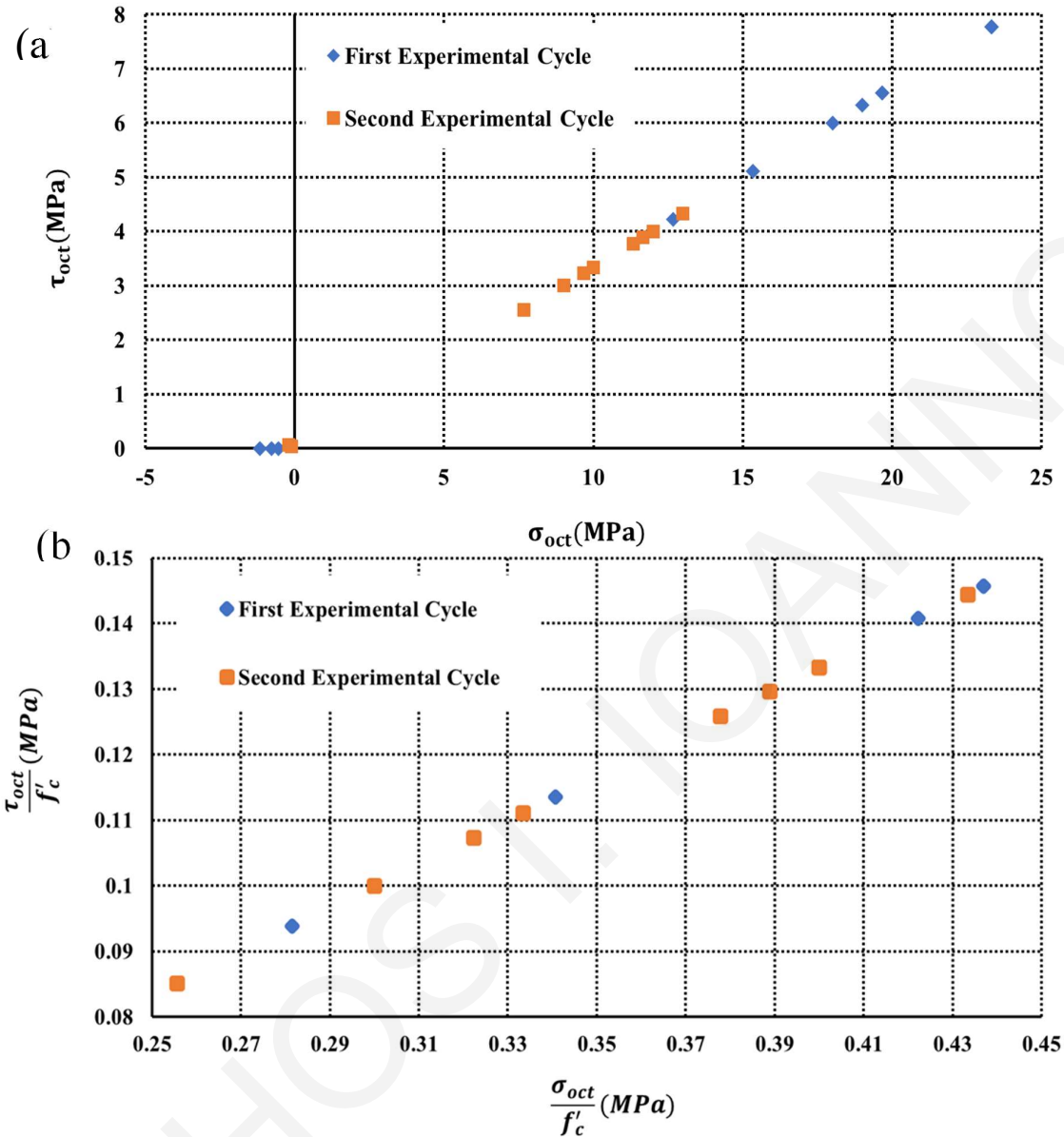


Figure 4.22: (a) Octahedral stresses according to experimental data; (b) Normalized octahedral stresses

4.6. Conclusion

Through a set of slanted shear and splitting tests in this study the interface shear strength and ultimate failure modes of the interface between PC and ECC was experimentally studied. The most important parameters that controlled the bond strength of the interface were, interface roughness, the PC and ECC compressive strengths, the inclination angle, the curing condition

and the aggregate interlocking mechanism. Interface failure criteria for the ECC-PC composites have been discussed by determining the parameters of a Mohr-Coulomb failure criterion and a Bresler-Pister type three-parameter failure criterion (Brestler and Pister, 1985).

The following conclusions were drawn:

- The ultimate failure modes of the ECC-PC interface were classified into three different types, i.e., direct interface failure, the direct PC cracking and the combination of PC and ECC cracking. The first failure mode was observed in the samples with a low level of roughness, whereas the second failure mode occurred in specimens with a medium level of roughness and the third occurred in specimens where the PC surface roughness was high.
- Failure criteria based on a three-parameter envelope was used to model the strength at failure of the interface between ECC and PC components.
- The combination of the two failure criteria for ECC-PC components interprets the transitions between the failure modes exploiting the interface characteristic parameters from the experimental results.
- Results of the slanted shear test method depend on the strengths of repair and concrete as well as on the bond and friction between the two. Increasing the interface angle increases the possibility of sliding failure with limited resistance in the absence of clamping pressure.

Chapter 5: Members under Monotonic Loading

5.1 Introductions

Several retrofitting methods have been developed for the repair and strengthening of deficient structural elements, a prominent concept being the various forms of jacketing. Such include concrete and steel jacketing (Thermou and Pantazopoulou, 2007; Rodriguez and Park, 1991; Chai et al., 1994; Vadoros and Dritsos, 2008; Raza et al., 2019), fiber-reinforced polymer (FRP), SRP and SRG jacketing, either fully wrapped around rectangular section (for strengthening of plastic hinge regions) or in U-shaped layers (for shear strength enhancement) (Parvin and Wang, 2001; Thermou and Pantazopoulou, 2009; Funari et al., 2020; Funari et al., 2021). A disadvantage of concrete jackets is the need to provide a layer of external reinforcement in order to mitigate the lack of stirrups, which leads to a minimum jacket thickness in the range of 70 to 100 mm; the increased thickness in some situations is considered a disadvantage, as it interferes with the architectural function of the retrofitted member, while the jacketing scheme takes on the role of a global intervention (Thermou et al., 2007), since it affects significantly the stiffness of the member. Thin jackets (SRP and SRG) are an effective method to reduce the geometric alteration of the member; their strength is controlled by the anchorage of the metallic wires and the adhesion of the grout layer on the (Parvin A. and Wang W., 2001; Thermou, G.E. and Pantazopoulou, S.J., 2009, Funari et al. 2020; Funari et al., 2021). FRP jackets represent a well-documented, effective, and quick solution to recover or enhance deformation capacity, mitigating brittle failures without altering the member stiffness; a disadvantage is the cost, the susceptibility to fire, and the decreasing efficiency as more and more FRP layers are added to the jacket. Steel jackets are a very robust option, their only disadvantage being that they are rather expensive and difficult to apply, and for this reason, this solution is only used in high importance structures, such as critical highway bridge piers.

This chapter explores the use of Strain-Hardening Cementitious Composites (SHCC) for replacement of concrete cover as a means of retrofitting damaged reinforced concrete structural members. Cover replacement means that the external dimensions of the retrofitted member remain unaltered; the fiber-reinforced cover sustains its tensile strength up to very large levels of tensile deformation, which, in the role of an encasing jacket of the existing member, functions as a confinement mechanism (Figure 5.1).

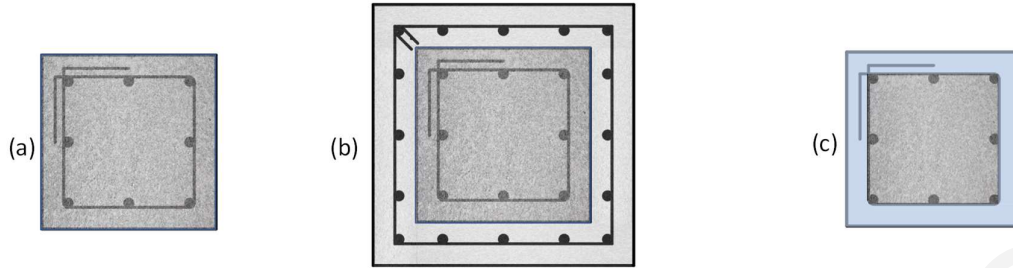


Figure 5. 1 : (a) Deficient cross-section; (b) Retrofit with reinforced concrete jacket; (c) Retrofit with cover replacement using SHCC.

The higher the tensile strength and the strain hardening properties of the SHCC material, the greater the intensity of the effected jacket confinement. Depending on the type of fiber, a high tensile deformation capacity, durability, and reinforcement protection may be achieved; the method of application is simple and can provide an alternative solution for use in the repair and strengthening of reinforced concrete members either as web concrete replacement or as concrete jacket in the areas of plastic hinges of columns ([Massicotte and Boucher-Proulx, 2009](#)).

In the present research, an Engineered Cementitious Composite (ECC) reinforced with 12 mm long, 0.039 mm diameter PVA fibers was used to retrofit the cover of four beam–column elements with different types of substandard reinforcement details, which had been previously damaged through the application of monotonically increasing lateral displacement to failure. This material has a very resilient strain-hardening response in direct tension, marked by fine, multiple cracking—therefore, it is an SHCC material. The specimens had been designed using the minimum requirements of [EN 1992-1-1, 2004](#) for lap-splicing of longitudinal reinforcement and for transverse steel reinforcement detailing. Transverse reinforcement comprised smooth bars to simulate old type (pre-1980s) detailing practices. The SHCC material used for cover replacement had already been investigated in Cyprus ([Georgiou, 2017](#)) with demonstrated advantages in terms of ductility and tensile strength. Through testing of the retrofitted components, it was found that the cover replacement is a very effective means of strengthening, enabling a significant increase of deformation capacity and recovery of resistance.

The objective of the present chapter is to investigate a new form of jacketing of reinforced concrete members with inadequate transverse reinforcement details, where the cover is replaced with a tension-hardening cementitious composite with significant tensile strain resilience after cracking. The contribution of the new cover material to the shear strength and confinement of existing, damaged reinforced concrete columns through concrete cover replacement is investigated through testing. In the following sections, the experimental program, the material laws, the primary loading results, and the application of the retrofit are described in detail, including reference to the observed failure modes, and specimens' section analysis, as well as the overall performance and efficacy of the retrofit methodology.

5.2 Experimental Program

5.2.1. Experimental Setup

To evaluate the effectiveness of cover replacement with SHCC, four pre-damaged structural components were tested under monotonically increasing lateral displacement. The objective of the tests was to determine whether the thin cover layers comprising strain hardening fiber-reinforced cementitious (FRC) material may effectively provide the benefits of a jacket in confining the structural member, particularly in recovering part of the deformation capacity in the critical regions of the components tested and to quantify the FRC cover contribution to the shear strength of the repaired components. To this end, four specimens of beam/column type were constructed and subjected to monotonic lateral displacement using the setup illustrated in Figure 5.2a. The experimental testing in the reaction frame using a servo-hydraulic piston, depicted in Figure 5.2b, was adopted from an older investigation for specimens of similar geometry (Georgiou and Pantazopoulou, 2018). Overall, the test setup resembles a simply supported system of a beam–column subassembly loaded at midspan with a point load, which generates the moment and shear diagrams shown in Figure 5.2c.

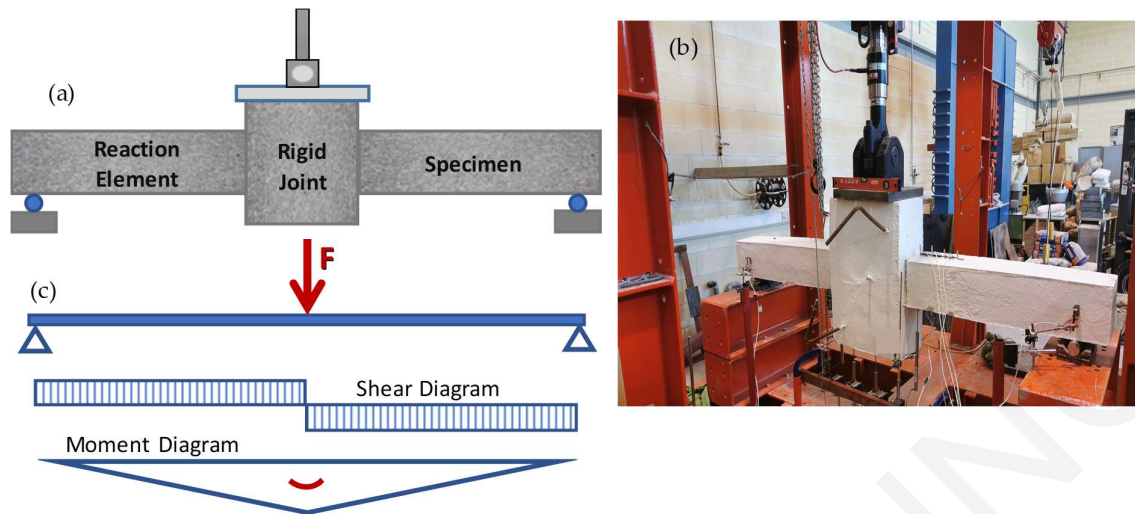


Figure 5. 2: (a) Test setup; (b) Picture of actual setup; (c) Moment and shear diagrams of the simply supported assembly.

Two equal length beam-columns were connected back-to-back in the central stub, which served as the midspan support of the piston. Roller supports were provided at the ends of the subassembly. The load was applied monotonically under displacement control. The central stub modeled the foundation part of a half column subjected to constant shear. The two sides of the subassembly adjacent to the stub represent two half beam-columns; of those, the one shown on the right-hand side is the test specimen, where specific reinforcing details and retrofit measures are studied. The one on the left hand-side of the central stub is a much stronger element (heavily reinforced), which is designed to serve as the reaction specimen. The longitudinal reinforcement of each prismatic member was anchored in the central stub with 90° hooks; the stub was confined with significant amounts of transverse reinforcement (Figure 5.2).

5.3. Parameters of the Test Specimens

Four specimens were constructed, having a 200 mm square cross-section and a length of the test element equal to 1000 mm, whereas the shear span (distance from the face of the stub to the roller support) was $L_s = 890$ mm. Thus, the moment diagram created resembles the pattern occurring in a structural member that belongs to a lateral load resisting system undergoing lateral sway (i.e., constant shear in the shear span, linearly varying moment from the face of

the support to the roller). All test specimens had smooth stirrups comprising 6 mm diameter bars spaced at 120 mm and tied with 90° hooks, as would occur in older construction. Of the four specimens, two had continuous longitudinal reinforcement, whereas the other two had lap spliced longitudinal reinforcement in the critical region extending over a length of 35Φ , where Φ is the longitudinal bar diameter. This was intended to test the influence of an inadequately tied lap-splice on the deformation capacity of the member before and after the retrofit.

Another parameter studied was the magnitude of shear demand in the plastic hinge region, which is affected through adjustment of the longitudinal reinforcement ratio. Thus, by changing the longitudinal bar diameter (Φ , either 10 or 14 mm), the longitudinal reinforcement ratio was altered from 1.6% to 3.1% (note that a $\Phi 10$ has a bar area $A_b = 78.5 \text{ mm}^2$, whereas a $\Phi 14$ has $A_b = 154 \text{ mm}^2$). Following the monotonically increasing displacement of the central stub, all columns developed the expected damage in the critical region. A repairing procedure was applied (ECC jacketing by cover replacement), and the specimens were re-examined under monotonic loading to assess the repair material's contribution to the lateral load resistance and deformation capacity. Therefore, the results for eight tests are examined in the present study (initial and repaired condition). Specimens are identified by a code name as depicted in Table 5.1, referring to the layout of reinforcement depicted in Figure 5.3.

Table 5. 1: Specimen parameters' identification code.

| Specimen Code | Condition | | Long. Reinf. Ratio, ρ | Bar Diameter Φ (mm) | No Lap- Splice (NL) | w/ Lap- Splice ℓ_0 (in Φ Mult.) |
|--------------------|-----------|----------|----------------------------------|--------------------------------|---------------------------|---|
| | Initial | Repaired | | | | |
| M1.6 Φ 10NL | ✓ | | 1.6% | 8- Φ 10 | ✓ | |
| RM1.6 Φ 10NL | | ✓ | 1.6% | 8- Φ 10 | ✓ | |
| M1.6 Φ 10L35 | ✓ | | 1.6% | 8- Φ 10 | | 35· Φ |
| RM1.6 Φ 1035 | | ✓ | 1.6% | 8- Φ 10 | | 35· Φ |
| M3.1 Φ 14NL | ✓ | | 3.1% | 8- Φ 14 | ✓ | |
| RM3.1 Φ 14NL | | ✓ | 3.1% | 8- Φ 14 | ✓ | |
| M3.1 Φ 14L35 | ✓ | | 3.1% | 8- Φ 14 | | 35· Φ |
| RM3.1 Φ 14L35 | | ✓ | 3.1% | 8- Φ 14 | | 35· Φ |

5.4. Specimen Design

The reference specimen that was used as a benchmark for the geometry layout and reinforcement detailing was the ECC specimen tested in (Georgiou and Pantazopoulou, 2018). In the reference study, a comparison between two test specimens was made, whereby in one case, the steel reinforcement was configured for Ductility Class M according to EN 1998-1, 2004, whereas in the second case, the minimum transverse reinforcement was provided; however, a fiber-reinforced ECC material was used in the latter case, while the same matrix but without the fibers was used in the former.

Figures 5.3, 5.4 illustrate the geometry of experimental specimens accompanied by the steel reinforcement detailing. The elements' axial load ratio was $\nu = 0$. All specimens and reaction members have cross-sectional dimensions $200 \times 200 \text{ mm}^2$, with eight bars symmetrically placed on the cross-section, i.e., three bars per side, as shown in Figure 5.3. While specimens were reinforced with 10- or 14-mm bars (Table 5.1), the reaction members were all reinforced with eight, symmetrically placed, 16 mm bars. Clear cover was 25 mm in all cases. During testing, a constant shear force acted in the specimen, equal to $\frac{1}{2}$ of the applied total force at the midspan stub; flexural moment at the critical section was calculated from the product of the shear force times the shear span.

In the present study, emphasis is placed on the development capacity of longitudinal reinforcement over the lap length. Pairs of specimens were designed to have either continuous reinforcement or with lapped bars over a length measured from the face of the central stub, which is equal to 35Φ . The required lap length was calculated as per EN 1992-1-1, 2004, assuming a bond strength $f_b = 5 \text{ MPa}$, as follows.

The required lap-splice length was obtained from:

$$l_o = a_1 l_{b,net} \geq \max(0.3a_1 l_b, 15\Phi, 200 \text{ mm}), \quad (5.1)$$

where $l_b = l_{b,net}$. In Equation (5.1), coefficient a_1 is a factor that depends on the geometric conditions of the lap-splice, whereas the required anchorage length is obtained from:

$$l_{b,net} = \alpha \cdot \left(\frac{\Phi}{4} \cdot \frac{f_{yd}}{f_{bd}} \right) \geq l_{b,min} \quad (5.2)$$

Here, $\alpha = 1$ for a straight anchorage and $\alpha = 0.7$ if (a) hooks are formed and the bars are stressed in tension or if (b) transverse bars have been welded on the anchored bar. Length $l_{b,min} =$

$\max(0.3l_b \text{ or } 0.6l_b)$ for bars in tension or compression, respectively. Upon substitution, it was found that $l_o = 2 \cdot (0.25 \cdot \Phi \cdot 500/5) = 50\Phi$ (with $a_1 = 2$). In the present investigation, the estimated required lap-slice lengths for anchorage are shown in the insert table of Figure 5.3c. Where lap-splicing has been used, a shorter lap than the required value was provided (i.e., 35Φ as compared to 50Φ) to represent older practices of construction. The lapped bar-pairs were placed side by side at the top and bottom sides of the cross-section, as depicted in Figure 5.3f, g to further emulate old reinforcing practices, stirrups were spaced at distances of 120 mm, i.e., 12Φ and 8.5Φ for the two utilized sizes of longitudinal bars, respectively. Pictures of specimens' actual steel reinforcement configurations are provided in Figure 5.4.

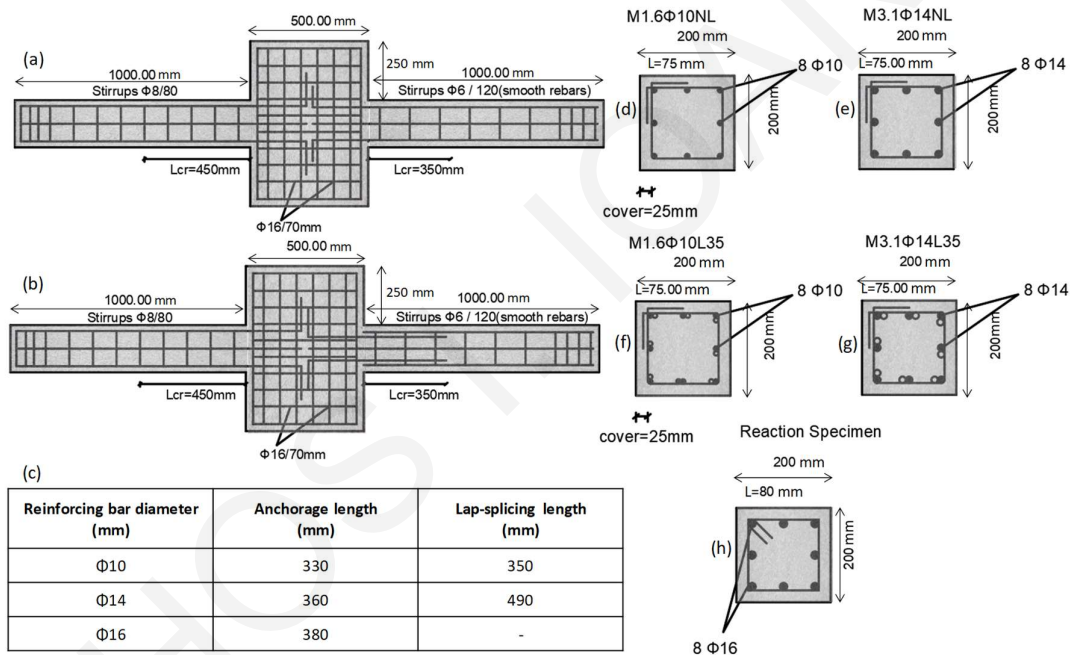


Figure 5. 3: (a) M1.6Φ10NL steel reinforcement; (b) M1.6Φ10L35 steel reinforcement; (c) Table of lap-splicing and anchorage lengths; (d) M1.6Φ10NL section; (e) M3.1Φ14NL section; (f) M1.6Φ10L35 section; (g) M3.1Φ14L35 section; (h) Reaction element section.



Figure 5. 4: Specimens' molds and steel reinforcement configuration: (a) with continuous longitudinal bars; (b) with lap-spliced bars.

5.5. Material Properties

Table 5.2 presents the mix design for standard concrete and the resulting average compressive strengths obtained after 28-day testing of 100 mm diameter by 200 mm height cylinders in uniaxial compression. The corresponding axial compressive stress vs. axial and lateral strain diagrams are plotted in Figure 5.5a. The uniaxial tensile stress-strain diagrams of steel reinforcement (all bar sizes) are plotted in Figure 5.5b.

Table 5. 2: Standard concrete mix design and concrete compressive strengths.

| Materials | Quantity (kg/m ³) | Specimen ID | f_c' (MPa) |
|------------------|-------------------------------|-------------|--------------|
| Cement | 352 | M1.6Φ10NL | 61.20 |
| Water | 211 | M3.1Φ14NL | 54.75 |
| Sand (0–4 mm) | 828 | M1.6Φ10L35 | 61.45 |
| Gravel (4–10 mm) | 1004 | M3.1Φ14L35 | 58.30 |
| Superplasticizer | 6 | | |

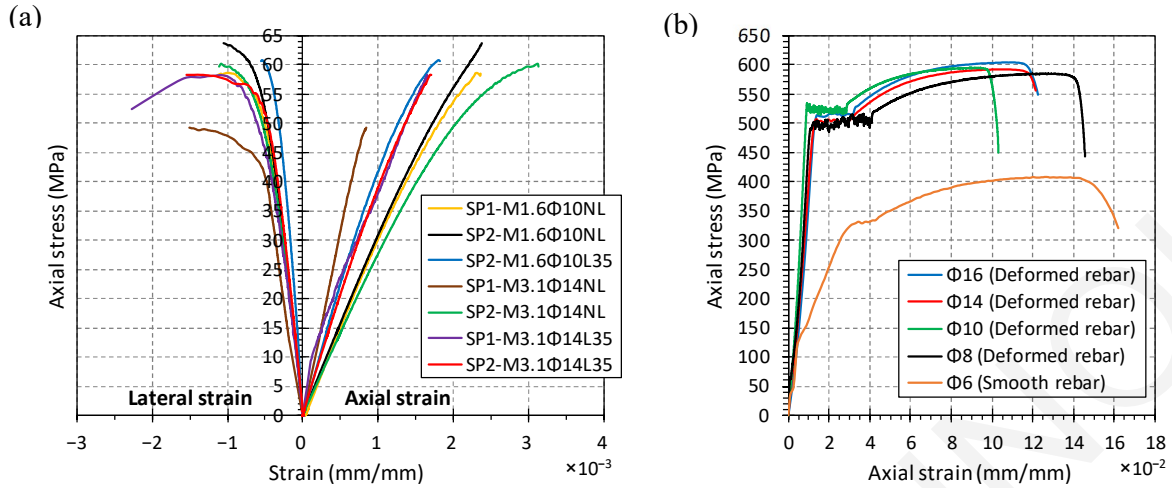


Figure 5. 5: (a) Cylinder's compression stress vs. lateral and axial strain curves for normal concrete; (b) Steel reinforcement tensile stress–strain curves.

Figure 5.6 illustrates the crack pattern of specimens after monotonic loading up to an advanced level of damage or failure, whichever occurred first. Tests of specimens with continuous reinforcement were terminated at a nominal drift ratio of 5%; specimens with lap-spliced reinforcement failed at a corresponding nominal drift ratio of 3%. As shown in Figure 5.6a, a through vertical crack developed at the face of the support of specimen M1.6 Φ 10NL, combined with flexure and shear-flexure cracks. Specimen M3.1 Φ 14NL also developed flexure-shear cracking, but eventually tensile reinforcement pullout from the central stub dominated the response, as may be observed from the initiating horizontal crack on the adjacent stub at this point. For both specimens M1.6 Φ 10L35 and M3.1 Φ 14L35, where reinforcement was lap-spliced in the critical zone, a brittle shear failure was observed, which was accompanied by shear cracks starting from the overlapping endpoint.

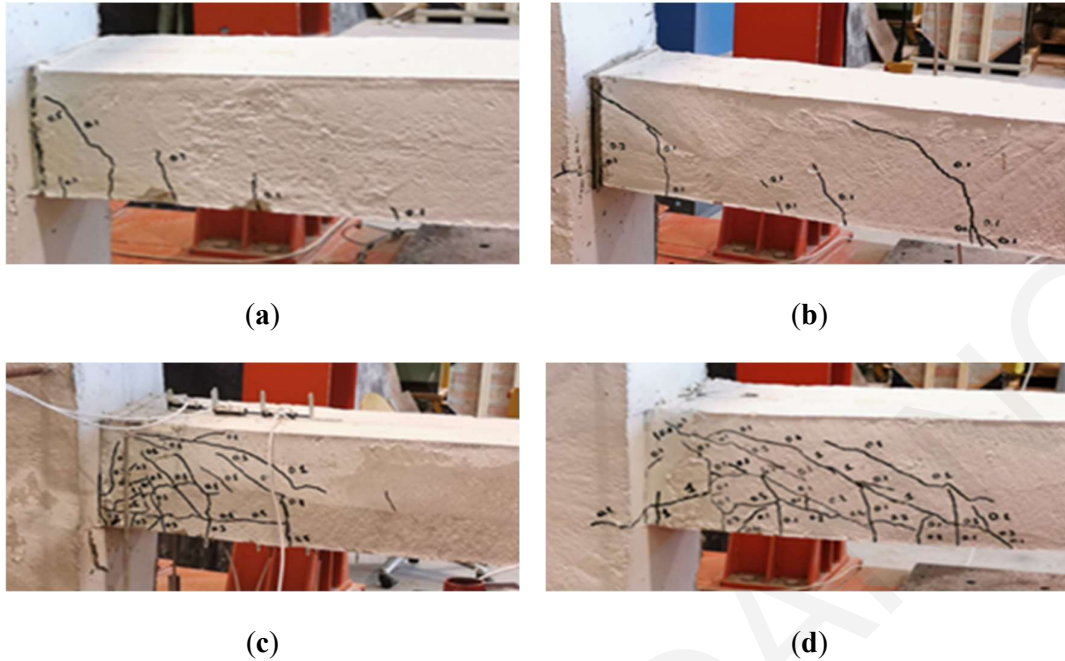


Figure 5. 6: Failure patterns of specimens under monotonic loading: (a) M1.6Φ10NL; (b) M3.1Φ14NL; (c) M1.6Φ10L35; (d) M3.1Φ14L35.

The response curves obtained are presented together with those of the retrofitted counterparts in later sections of this paper. The response was marked by an almost linear ascending branch up to a drift ratio of about 1% for M1.6Φ10NL and M1.6Φ10L35, and up to about 1.5% for specimens M3.1Φ14NL and M3.1Φ14L35; peak strengths were attained roughly at 3% drift ratio for the specimens with continuous reinforcement, but strength degradation started earlier (at about 2.5% drift ratio) for the lap-spliced specimens. The drift level where each specific crack occurred is shown in Figure 5.6 (numerals on the specimen faces near the cracks represent the drift level at which the crack had propagated up to the point that is adjacent to the numeral). A brittle failure was observed in the lap-spliced specimens, which was marked by dense diagonal cracking, with a clear splitting crack propagating along the lap splice. No reinforcement ruptures were observed; longitudinal reinforcement yielded extensively with yield penetration into the central stub and significant pullout slip at the support, whereas, owing to the poor anchorage of the stirrups, the transverse reinforcement did not reach the yield point.

5.6. Retrofitting Procedure

The procedure for repair and strengthening was carried out after completion of the monotonic tests. All tested specimens were retrofitted in the critical region (starting from the face of the support, the repair length was $h_{cr} = 2b_w$) after removal of the damaged cover, as depicted in Figure 5.7a, using a small electric concrete hammer until all the reinforcement was revealed. Where the damaged region extended into the central stub, this was also included in the retrofit. The removed concrete cover was replaced using an inhouse-made ductile, fiber-reinforced cementitious composite (ECC) material, which was placed to also function in the role of a jacket. The mix design of the ECC material is listed in Table 5.3. The material was workable, self-consolidating with a pot life that extended to about 40 min after mixing.

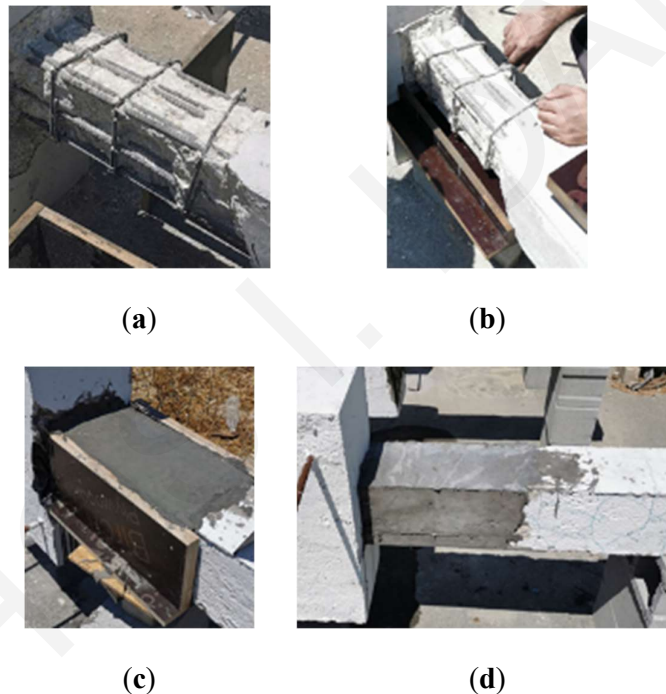


Figure 5. 7: **(a)** Removal of damaged cover to full revelation of the bars; **(b)** Bottom extendable form for lower cover cast; **(c)** Side forms for side and top cover cast; **(d)** Final result of cover replacement.

Figures 5.7b, c depict the placement of the ECC material in the cover of the specimen, lying in the horizontal direction during repair as during testing. To facilitate placement, an extendable form was used; first, the lower layer (bottom cover) was cast, as shown in Figure 5.7b, with the sides of the form extending upwards only 40 mm. Then, the extensions to the side forms

were placed as shown in Figure 5.7c, and the side cover was cast, whereas the top cover and finishing of the free surface followed. Where cracking had been detected in the reaction members, they were strengthened with high strength repair mortar and CFRP wraps, in order to enhance their reacting capacity to the repaired study specimens.

Table 5. 3: Strain-hardening ECC mix design. Compressive strength and corresponding compressive strain at peak: $f_{c,ECC} = 45$ MPa, $\epsilon_{co} = 0.0027$.

| Materials | Quantity (kg/m ³) |
|----------------------------|-------------------------------|
| Cement | 530 |
| Water | 372 |
| Fly Ash | 636 |
| Silica Sand | 425 |
| PVA Fibers (12 mm, d=39µm) | 16.25 |
| Superplasticizer | 13 |

5.7 Repair Material

The mix design for the repair ECC material used for cover replacement is listed in table 5.3 PVA fibers having a tensile strength of 1600 MPa, a Young's Modulus of 40 GPa, density of 1300 kg/m³, length of 12 mm, and diameter of 39 µm were added at a volumetric ratio of 1.25%. Then, 75 mm in diameter by 150 mm-high ECC cylinders were tested in compression under displacement control in order to characterize the compressive stress–strain properties of the cementitious repair material. Figure 5.8 presents the average axial compressive strain vs. axial and circumferential strain of the tested specimens. Flexural prisms having a cross-section of 60 × 100 mm² and a span of 180 mm were tested under four-point loading (with the applied loads acting at the third points of the span). The objective of these tests was to obtain the tensile stress–strain response of the material through inverse analysis as discussed in Chapter 4; the detailed description of the procedure used is provided in the following paragraphs and Appendix A.

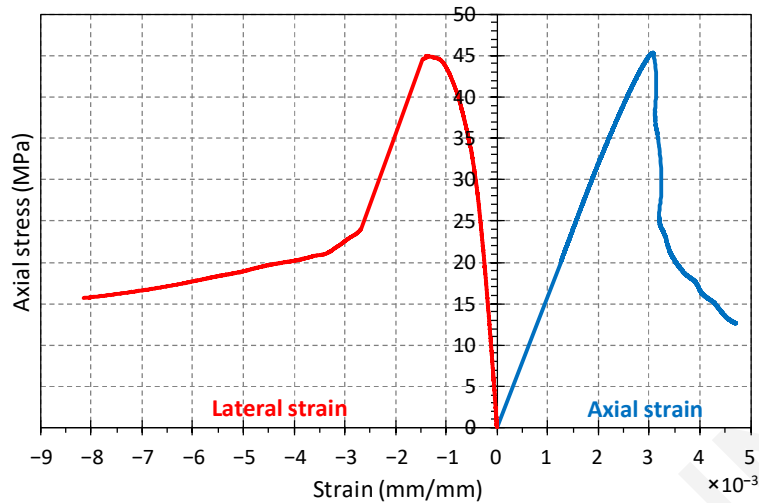


Figure 5. 8: Cylinder’s compression stress vs. lateral and axial strain curves for fiber-reinforced concrete.

A summary of the inverse analysis steps and the related mathematical relationships, which are used in conducting the calculations, is provided in Appendix A. Following the application of this procedure, the results obtained for the characteristic tensile stress–strain response of the ECC material are given in Table 5.4.

Table 5. 4: Inverse analysis results.

| |
|-----------------------------|
| $f_{cr} = 4.65\text{MPa}$ |
| $f_{Fu} = 5.00\text{MPa}$ |
| $E_C = 18300\text{MPa}$ |
| $\varepsilon_{tu} = 0.0092$ |

5.8 Instrumentation

The instrumentation layout included five LVDTs (defined earlier) and eight displacement transducers (DTs) of different nominal gauge lengths (see Figure 5.9) to record the specimens’ deformations and displacements during the experiment. The positioning of the whole instrumentation equipment is depicted in Figure 5.9. For monitoring of the vertical deflection, five LVDTs were installed at the bottom center point of the element. DTs 7 and 8 were positioned at the ends of shear spans to measure the centroidal axis’s vertical displacement,

and DTs 1 to 6 were installed at the top and the bottom sides of experimental specimens at the areas where the development of plastic hinge was expected. All measuring instruments were supported on an independent steel beam without having any contact with the reacting steel frame that supported the hydraulic piston.

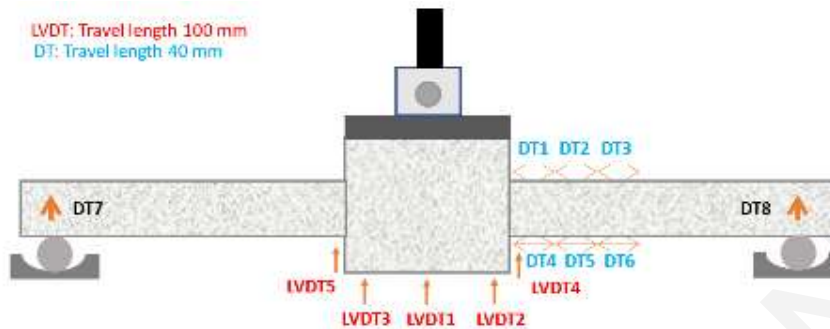


Figure 5. 9: Instrumentation layout.

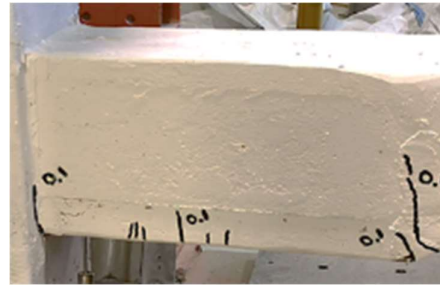
5.9 Observed Experimental Response

5.9.1 Damage Profiles and Resistance Curves

The responses of the retrofitted specimens obtained after monotonically increasing midspan load applied under displacement control are compared with the original specimens in Figure 5.10 and figure 5.11. The failure modes are compared for the original and the retrofitted specimens placed side by side in Figure 5.10. Figure 5.11 plots the experimentally obtained resistance curves for the original and the retrofitted specimens; the vertical axis plots the shear force developed in the shear span of the specimen (i.e., it is half the total applied load), whereas the drift ratio plotted in the horizontal axis is the nominal chord rotation of the deforming member, which is calculated as the ratio of midspan displacement divided by the deformable length of the member from the face of the support to the end roller.



(a.1)



(a.2)



(b.1)



(b.2)



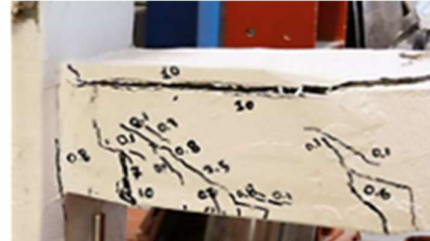
(c.1)



(c.2)



(d.1)



(d.2)

Figure 5. 10: Failure modes of specimens: (a.1) M1.6Φ10NL vs. (a.2) RM1.6Φ10NL; (b.1) M3.1Φ14NL vs. (b.2) RM3.1Φ14NL; (c.1) M1.6Φ10L35 vs. (c.2) RM1.6Φ10L35; (d.1) M3.1Φ14L35 vs. (d.2) RM3.1Φ14L35.

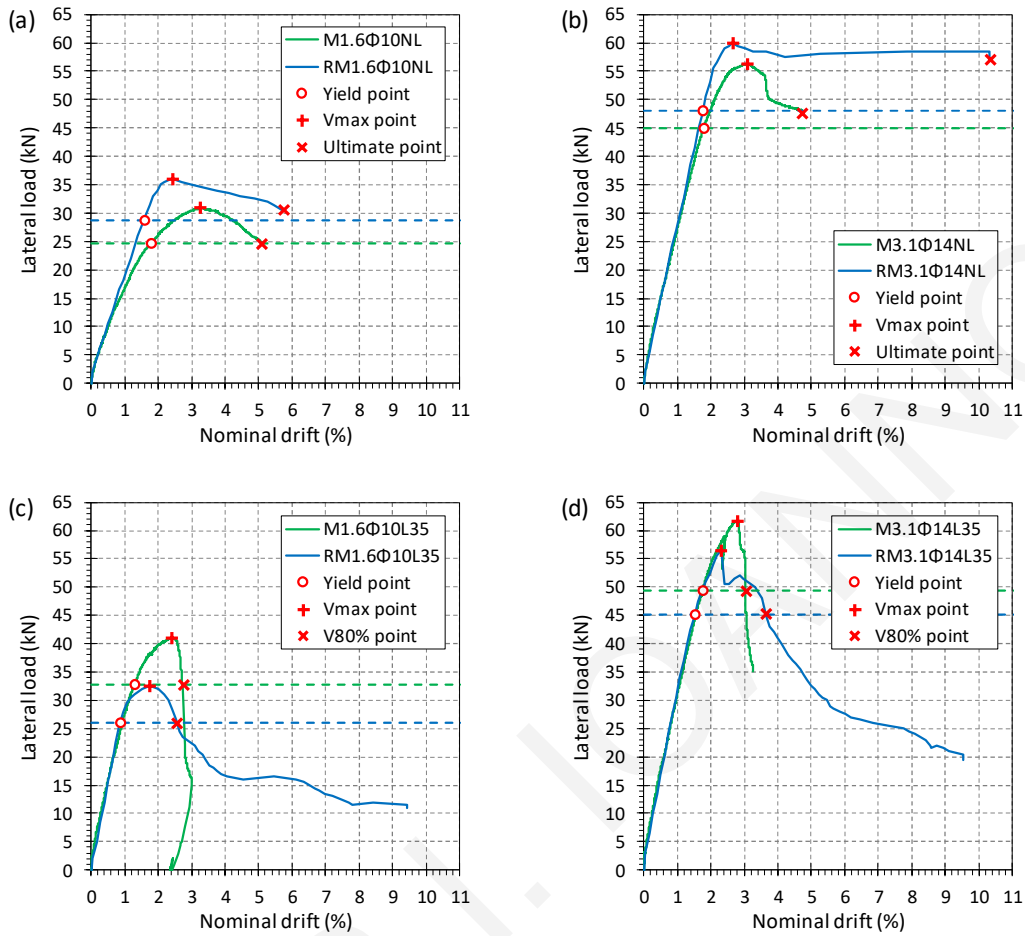


Figure 5. 11: Envelope curves of specimens: (a) M1.6Φ10NL vs. RM1.6Φ10NL; (b) M3.1Φ14NL vs. RM3.1Φ14NL; (c) M1.6Φ10L35 vs. RM1.6Φ10L35; (d) M3.1Φ14L35 vs. RM3.1Φ14L35.

Note that all specimens in the original condition developed a brittle response after attainment of the peak load. On the contrary, retrofitted specimens with continuous reinforcement attained their peak load at a drift ratio of about 3% and showed spectacular deformation capacity and resilience up to nominal drift levels that exceeded the limit of 5% (Figure 5.11). For example, specimen RM1.6Φ10NL, containing a low reinforcing ratio and continuous bars extending into the central stub, developed a purely flexural response marked by cracks oriented normal to the neutral axis of the element; the same behavior was observed in the case of specimen RM3.1Φ14NL, despite the very high shear demand effected by the larger size of longitudinal bars; however, in this case, diagonal cracking did occur particularly beyond a drift ratio of 1.5%.

During primary loading, specimens with continuous longitudinal reinforcement had developed shear and shear-flexure cracks of maximum length 200 mm and width 0.2–0.3 mm. Lap-splicing specimens had shown densely combined diagonal and horizontal crack patterns of length and width 300 mm and 1–2 mm, respectively. On the other hand, failure modes of retrofitted elements showed a lighter crack profile, with cracks extending to shorter lengths and with smaller crack width openings in the critical region. A wide vertical crack that pre-existed from the first phase of loading at the face of the support, owing to the anchorage slip from the footing, which occurred in the primary loading phase, persisted in the post-repair phase.

It is noted that the contribution of the ECC cover in both cases is significant, despite the fact that the average compressive strength of the ECC material was inferior to that of the original specimens; the improved behavior is evidently owing to the confining contribution of the jacket material in the compression zone, but also it is due to the contribution of the tensile strength of the material beyond cracking in the section equilibrium (a resultant tensile force develops in the concrete tension zone).

The specimens containing lap splices showed inferior performance to those with continuous reinforcement when tested in the original condition (see Figure 5.10c.1, d.1, and the green lines in the resistance envelopes of Figure 5.11c, d). Although the replacement of the cover could not fully recover the original strength of the specimens due to permanent damage in the joint region (anchorage), a much more resilient response was obtained after retrofit; the extent of cracking was also less after retrofit, underscoring the strain hardening response of the cover material in tension.

The compressive layer of the replaced cover spalled off in the cases of RM1.6 Φ 10L35 and RM3.1 Φ 14L35 at relatively large levels of drift, which was dominated by reinforcement pullout from the anchorage (a damage caused in the first phase of loading, which could not be repaired without invasive operation in the rigid side of the stub; this was not done because it was deemed to be beyond the scope of the study, which focused on cover replacement only).

To illustrate the strength recovery that was affected by the retrofit procedure, sectional analysis of the specimen cross-sections shown in Figure 5.12, considering the original condition of the cover, as well as its replaced condition as per Figure 5.12c, is pursued in the following section.

5.9.2 Evaluation of the Flexural Strength of the Specimens

Calculation of the flexural moment vs. curvature of the cross-sections of the specimens with continuous reinforcement was conducted using the basic concepts of the theory of flexure (plane sections remaining plane, discretization of the cross-section in layers and numerical integration). Material stress-strain laws were as follows: (a) for concrete and ECC concrete in compression, a basic Hognestad-type parabola 195 was used to describe the ascending branch, each material attaining its respective peak compressive strengths (as per Tables 38 and 40) at a compressive strain of 0.002 and 0.0027 for plain and ECC concretes, respectively; the Kent and Park, (1982) model was used for the post-peak descending branch, using strain values of $\varepsilon_{c,50} = 0.003$ and 0.004, respectively (this is the strain in the post-peak range where compressive strength has been degraded to 50% of peak). The tensile strength of plain cover was neglected in the analysis of the original sections. However, the tensile strength of the ECC cover was accounted for in calculating the forces developed in the sectional layers that fell within the tension zone of the repaired sections using a bilinear, elastic–perfectly plastic stress–strain diagram for the tensile response prior to crack localization (at $\varepsilon_{tu} = 0.0092$, see Table 4). The slope of the ascending branch was set equal to the elastic modulus of the ECC (= 18300 MPa). A bilinear elastic–perfectly plastic diagram of stress and strain curve for steel reinforcement was considered, the yield point being defined as per Figure 5.12b.

The calculated moment–curvature diagrams are plotted in Figure 5.12 for the typical cross-sections of specimens M1.6 Φ 10NL, RM1.6 Φ 10NL, M3.1 Φ 14NL, and RM3.1 Φ 14NL. The strength obtained in the respective test is plotted as well. It is noted that strength values are approximated closely by the flexural theory. Evidently, the actual influence of the ECC cover replacement is remarkable, underscoring the confining effectiveness of the jacket as well as its sustained tensile resilience to large strain levels, which was also sufficient to compensate for the initial stiffness loss of the damaged specimens (the retrofitted specimens were stiffer than the original cases).

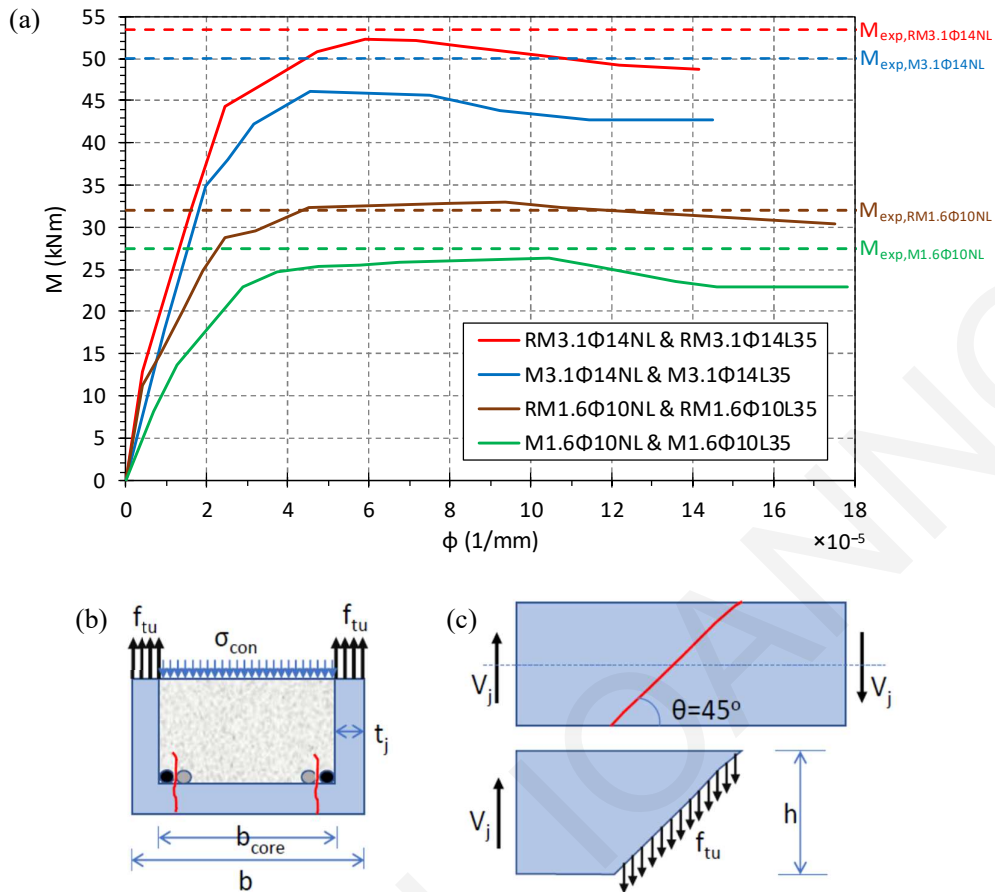


Figure 5.12: (a) Moment vs. curvature relationships: M1.6 Φ 10NL vs. RM1.6 Φ 10NL, and M3.1 Φ 14NL vs. RM3.1 Φ 14NL. (b) Estimation of confinement stress, and (c) shear stress contribution provided by the ECC jacket.

5.9.3. Envelope Resistance Curves

The improvements attained in terms of lateral load resistance and deformability by means of cover replacement are summarized in Table 5.5 both for the original as well as the retrofitted components. Values reported include the coordinates of nominal yielding (V_y and θ_y , defined by the point in the ascending branch of the response curve that corresponds to 80% of strength), peak resistance (V_{max} and θ_{max}), as well as the point in the post-peak branch at a residual strength equal to 80% of the peak, or the last point in the experimental curve if degradation did not occur (V_u , θ_u); these points are also marked on the response curves of Figure 5.11. In all cases, the ECC-retrofitted specimens developed a more ductile or resilient response curve than the corresponding control specimens. The post-peak strength reduction was more gradual, and a greater energy dissipation was achieved by means of the retrofit.

Table 5. 5: Characteristic points of the retrofitted envelope curves and ductility μ .

| Specimens | V_y (kN) | θ_y (%) | V_{max} (kN) | θ_{max} (%) | $V_{80\%}$ (kN) | θ_{80} (%) | μ | θ_{80}/θ_y |
|--------------------|------------|----------------|----------------|--------------------|-----------------|-------------------|-------|------------------------|
| M1.6 Φ 10NL | 24.7 | 1.8 | 30.9 | 3.3 | 24.7 | 5.1 | 2.8 | - |
| RM1.6 Φ 10NL | 28.8 | 1.6 | 36.0 | 2.4 | 30.5 | 5.7 | 3.6 | - |
| M3.1 Φ 14NL | 45.0 | 1.8 | 56.2 | 3.1 | 47.6 | 4.7 | 2.6 | - |
| RM3.1 Φ 14NL | 48.0 | 1.8 | 60.0 | 2.6 | 57.0 | 10.3 | 5.7 | - |
| M1.6 Φ 10L35 | 32.8 | 1.3 | 41.0 | 2.4 | 32.8 | 2.7 | 2.3 | 2.1 |
| RM1.6 Φ 10L35 | 26.0 | 0.9 | 32.5 | 1.7 | 26.0 | 2.6 | 10.5 | 2.9 |
| M3.1 Φ 14L35 | 49.4 | 1.7 | 61.7 | 2.8 | 49.4 | 3.0 | 1.9 | 1.8 |
| RM3.1 Φ 14L35 | 45.2 | 1.5 | 56.5 | 2.3 | 45.2 | 3.6 | 6.4 | 2.4 |

The experimental results confirmed older investigations where traditional jacketing approaches had been applied without dowelling (Deng et al., 2018), provided the member was fully encased by the jacket as in the present case. In these studies, lateral load resistance and deformation capacity were improved as a result of the high tensile properties of the retrofitting material. In a state-of-the art review of strengthening applications with ECC, Shang et al. (2019) concluded that the strain-hardening property of ECC renders it an ideal retrofitting material; the interfacial resistance is adequate to ensure monolithic behavior between core and jacket, which is a finding that is also supported by inclined interface shear tests between plain and ECC concrete, particularly if the substrate is roughened prior to the strengthening application. It is also worth mentioning that the results of the present work are in line with the findings of Papavasileiou et al. (2020), who demonstrated that implementing a thin jacket layer to a deficient member is an effective retrofit technique that can be competitive to other strengthening methods (such as conventional thicker jackets or bracings at frame bays), provided that the thin jacket is composed of appropriate material(s) to develop sufficient confinement of the core and the additional strength required for the retrofitted member.

To assess the jacket effectiveness in enhancing all the mechanisms of resistance (apart from flexural strength which is depicted in Figure 5.12a), the contribution of the 25 mm jacket layer provided to shear and lap splice strength of the member was calculated with reference to Figure

5.12b, c. First, the average confining stress in the remaining core concrete (after cover replacement) is estimated from equilibrium of normal stresses through a cut in the cross-section:

$$\sigma_{con} = \frac{2 \cdot t_j \cdot f_{tu}}{b_{core}} = \frac{2 \cdot 25 \text{mm} \cdot 5 \text{MPa}}{200 \text{mm} - 2 \cdot 25 \text{mm}} = 1.67 \text{MPa}. \quad (5.3)$$

Shear strength contribution is obtained with reference to the shear sliding plane inclined at an angle $\theta = 45^\circ$ (Figure 5.12c) with respect to the longitudinal axis of the member (since there is no axial load present) and assuming isotropic development of tensile strength in the jacket (on account of the random distribution of the fibers) as:

$$V_j = 2 \cdot t_j \cdot f_{tu}(h - t_j) \cdot \tan \theta = 2 \cdot 25 \text{mm} \cdot 5 \text{MPa} \cdot (200 - 25) \text{mm} \cdot \tan 45^\circ = 43.7 \text{kN} \quad (107)$$

It is noted that the contribution to shear is substantial and increases with the depth of cross-section, whereas the effective core confinement is inversely proportional to the section width, so the effect of confinement on the compression zone may be neglected. On the other hand, the jacket force normal to the splitting plane (see the red lines representing splitting cracks through the lap splices in Figure 5.12b) multiplied by the length of lap splice quantifies the tension development capacity increase for each of the spliced longitudinal bar pairs (assuming a coefficient of friction of 1 over the bars), which is estimated here as $\Delta T = \mu \cdot (t_j \cdot f_{tu}) \cdot 35\Phi$, which is equal to 43 kN for 10 mm diameter bars and 61.2 kN for 14 mm bars. Note that even with a safety factor of 2, the jacket contribution to both shear and lap-splice development capacity remains significant.

5.10. Conclusions

A retrofit scheme of reinforced concrete structural members with old-type detailing, comprising replacement of conventional concrete cover with a ductile, tension hardening engineered cementitious composite (ECC) was studied in the present work. Based on the experimental results, the following conclusions are drawn.

The ECC-cover replacement acted as a confining jacket, mitigating the brittle characteristics of the response of inadequately tied structural elements. The tension-hardening characteristic of the new cover material participated in flexural response through the development of tensile stresses over the height of the tension zone, thereby enhancing the flexural strength by more

than 17% and 9%, respectively, for flexure and shear dominated members that had been originally damaged under lateral sway. It also recovered the lap-splice resistance of members controlled by failure in lap splices due to inadequate transverse confinement and enhanced their post-peak resilience.

By the retrofitting application of ECC jackets in the plastic hinge zone, significant rotation capacity was attained: retrofitted specimens with continuous reinforcement exceeded a drift ratio of 5.5%; lap-spliced specimens exceeded a drift capacity ratio of 2.5% after retrofit of the lap-splice zone. Where reinforcement anchorage was not severely damaged during the previous loading application, the cementitious material's contribution in the increase of lateral load resistance was significant. Where damage outside the critical region (in the footing) had occurred, cover replacement was still able to retrofit the critical region recovering a significant fraction of strength (90% of maximum) and imparting notable strain energy absorption capacity and resilience. The contribution of the ECC jacket to confinement of the encased core, to the member's web shear strength, and to the lap-splice development capacity through clamping action was quantified, using established mechanistic models. It was found that this contribution can be substantial and can alter the critical mode of failure of the structural member while at the same time enhancing the component's strain energy dissipation and resilience. Thus, for a layer of 25 mm of strain-hardening jacket material with a uniaxial tensile strength of 5 MPa, it was found that the confining pressure exerted on the encased core was 1.65 MPa, the shear strength increase was 43.7 kN (i.e., an average shear stress of 5 MPa developing in the vertical segments of the jacket), whereas the clamping force enhancing the development capacity by an equal amount due to friction was 125 N per mm of lap length and for each bar pair (i.e., a total of 43 kN and 61.2 for a 10 mm and 14 mm diameter lapped bar, i.e., it was adequate to support yielding of the longitudinal reinforcement).

The experimental program confirms that the replacement cover developed sufficient bond at the interface with normal concrete, to the extent that stress transfer was possible in order to engage the section in a monolithic response.

Chapter 6: Cyclic Testing of RC Elements Repaired with ECC Cover Replacement

6.1 Introduction

Recent earthquakes have revealed time and again the vulnerability of older reinforced concrete (R.C.) construction by the extensive damage of structural components especially in columns and in the critical regions of beam-column connections. Poor structural performance was due to brittle structural details, such as light transverse reinforcement, smooth reinforcing bars, insufficient longitudinal reinforcement, and poor anchorage and lap splicing length. Many of these structural details are critical causes of brittle failure (shear, flexure-shear) that lead to degradation of the elements' structural strength and ductility.

To improve the lateral load resistance of R.C. beam-column elements, a new and innovative methodology using Engineered Cementitious Composites (ECC) was proposed by [Ioannou et al. \(2021\)](#) according with the developed technique, the damaged concrete cover of R.C. elements is replaced by ECC to a depth of about 25-30 mm. Four prismatic members that had been retrofitted using ECC jackets for cover replacement following preliminary damage were tested under monotonically increasing lateral drift. Through the tests it was illustrated that the thin ECC jacket suffices to successfully recover the damaged lateral strength of the element, enhance its deformation capacity, while preserving the geometric dimensions of the original component.

In this chapter the proposed retrofit methodology is examined under cyclic displacement reversals simulating earthquake effects. Four new beam-column elements were fabricated with varied steel reinforcement details representing old-type detailing practices. In fabricating the R.C. specimens, the minimum [DIN 1045, 1972](#) prescribed requirements of longitudinal, transverse, and lap-splicing reinforcement detailing were used. The reinforcement detailing and the concrete mix design are typical of R.C. structures built approximately in the latter half of the 20th century. The specimens were first damaged through testing under a cyclic history of displacement reversals, and were subsequently retrofitted with the cover replacement technique, using a moderate strength ECC ([Georgiou and Pantazopoulou, 2018](#); [Li, 2003](#), [Xu and Pan et al., 2017](#)). Because of the high degree of compactness of ECC material which is reinforced with PVA fibers, this cementitious material provides a very resilient strain-hardening direct tensile response, marked by fine and multiple cracking.

Cover replacement with a ductile ECC composite is used as the retrofitting strategy in order to remedy the existing damage but also to compensate for the brittle details along the member length. The underlying concept of the retrofit method is that the ECC thin layer on the perimeter of the member will arrest crack formation and will contribute to the response through an effective confining mechanism, as the material behavior in tension is characterized by post-cracking tension hardening up to significant levels of tensile strain capacity. The contribution of ECC material in confinement and shear strength of the structural component is investigated by testing the repaired components under a reversed cyclic displacement history of gradually increasing intensity. The mechanics of this response is further explored through detailed finite element simulations. In the following the experimental program, material laws, the main experimental findings, and the finite element analysis results are discussed in detail including the observed specimen's failure modes as well as the overall performance and efficiency of the retrofitting methodology.

6.2 Specimen preparation and experimental testing

Four beam-column specimens were constructed in total. Fig. 6.1 depicts the geometry and test setup of the typical specimen. It is noted that the present specimens have the same geometry with other previously tested beam-columns under monotonic loading, in order to enable comparison of the retrofit response between monotonic and cyclic load conditions. Specimens were designed to be tested using the available reacting frame of the lab in a horizontal layout with a servo-hydraulic piston loading in the vertical orientation. To enable this type of a test setup, each complete test unit has the layout shown in Fig. 5.11a, so that the full assembly may be tested as a simply supported beam with a point load at the center; the actual setup is shown in Fig. 6.1b. Double direction rollers are provided in the ends of the span to support the reversal of the load, as depicted in the detail of Fig. 6.1c. To enable the load application, a central stub is formed in the middle, which also serves as a footing for the anchorage of the longitudinal reinforcement of the left and the right parts of the specimen – the moment and shear diagrams thus generated by application of the mid-span cyclic load are depicted in Fig. 6.1c. Reversal of the load is achieved by anchoring the piston head to a steel plate under the footing, with through threaded rods. The right part of the test unit shown in Fig. 6.1 is the study region: here the reinforcing details are varied according with the experimental study objectives. The left

part is oversized in order to ensure that failure would occur in the study region. The length from the face of the footing to the roller support (Fig. 6.1a) is referred to henceforth as the shear span of the element; in modelling a swaying component of an actual frame structure, this corresponds to the length from the inflection point to the location of peak moment, so it represents half the height (or length) of a swaying column (or beam) respectively (Fig. 6.1d).

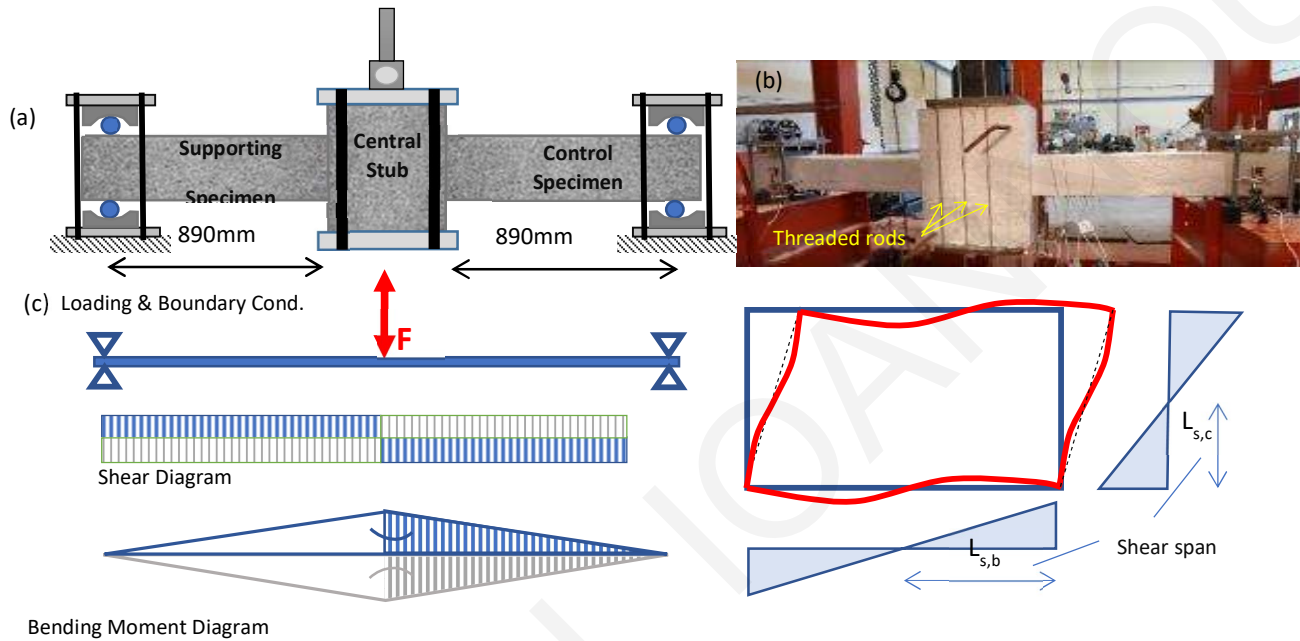


Figure 6. 1: (a) Test setup; (b) Picture of actual setup; (c) Moment and shear diagrams of the simply supported assembly (blue: loading downwards, gray: upwards) (d) Schematic representation of shear span

Fig. 6.2 depicts the geometry and reinforcing details of the specimens tested. The specimens' cross section outside the central stub region was 200×200mm with a total length of control and test segments equal to 1000 mm each (so the total length of a typical unit was 2.5m including the length of the stub and the length of the beam-columns extending beyond the supports). The typical shear span from the face of the stub to the double-direction roller supports was $L_s = 890\text{mm}$. Note the similarity of the moment and shear diagram in the shear span of the test specimen (Fig. 6.1c) with the triangular moment distribution that occurs in the shear span of the swaying frame elements of Fig. 6.1d. Sparse transverse reinforcement in the form of perimeter stirrups was used for the test specimens; stirrups were smooth 6mm diameter bars,

spaced at 120mm on centers (o.c.) and having 90° anchorage hooks, as would occur in old practices.

Parameters of the study were the presence or not of a lap splice in the critical region of the test-span and the amount of longitudinal reinforcement used in the cross section in order to vary the intensity of the shear demand as compared to the shear strength. All test specimens were reinforced with 8 bars equally spaced on the perimeter of the cross section. The support segment of the test unit was reinforced with 8 – 16 mm diameter bars. Of the four test units, two had 10mm diameter longitudinal bars in the test span, whereas the other two were reinforced with 14mm diameter bars. (Note that the individual bar areas are as follows: $A_{16}=200\text{mm}^2$; $A_{14}=150\text{mm}^2$; $A_{10}=78.5\text{mm}^2$; $A_6=30\text{mm}^2$). These reinforcement arrangements correspond to 1.6% and 3.2% longitudinal reinforcement ratio, calculated over the element cross section respectively. Cover was 25mm in all cases. For each pair of specimens reinforced with identical bars, one had lap-spliced longitudinal reinforcement in the critical region extending to 35Φ length where Φ is the longitudinal bar diameter (Fig. 6.2(b)). Where lap-splicing has been used, it was set as per the requirements of [DIN 1045, 1972](#)– this length would be shorter than what is required by modern standards such as [EN 1992-1-1, 2004](#) (i.e., 35Φ as compared to 50Φ) to represent older practices of construction. Cross sectional reinforcement arrangement is depicted in Fig. 6.2(c). Bars were anchored with 90° hooks inside the stub. The total anchorage length of the bars (including the hook) was 35Φ also, so as to model old detailing practices; this length may be adequate to support bar yielding in one cycle, however swift degradation is expected to follow after yielding. In the remainder of this work specimens are referred to with the following code: after the letter C (for cyclic), the numeral indicates the percentage of the longitudinal reinforcement ratio (C1.6 and C3.2); followed by the longitudinal bar diameter used ($\Phi 10$ and $\Phi 14$), and by the length of the lap splice (NL means no lap, and L35 means a lap length of 35 times the bar diameter). Letter R in the beginning of the specimen identification code identifies the repaired specimen.

Reinforcement yield strength values of the longitudinal and transverse bars were: $f_{y,\Phi 6} = 330$ MPa, $f_{y,\Phi 10} = 520$ MPa, $f_{y,\Phi 14} = 505$ MPa, $f_{y,\Phi 16} = 510$ MPa. For the fabrication of the specimens, plain concrete was batched in the Reinforced Concrete Laboratory of the University of Cyprus using a mix design of C20/25 concrete (ASTM C94/C94M-04; which would correspond to Bn250 in [DIN 1045, 1972](#) or B300 in South European practice of the time (Beton Kalender 1970). The workability category was S3 according to [EN 1992-1-1, 2004](#). Average

compressive strengths obtained from standard 100×200 mm cylinder tests at 28 days are listed in Table 6.1.

Table 6. 1: Cylinder specimens' compressive strengths

| Specimen ID | 28-day Cylinder Strength, f_c' (MPa) [▲] |
|-------------|---|
| C1.6Φ10NL | 33 |
| C1.6Φ10L35 | 43 |
| C3.1Φ14NL | 38 |
| C3.1Φ15L35 | 40 |

[▲]Average of 3 identical tests

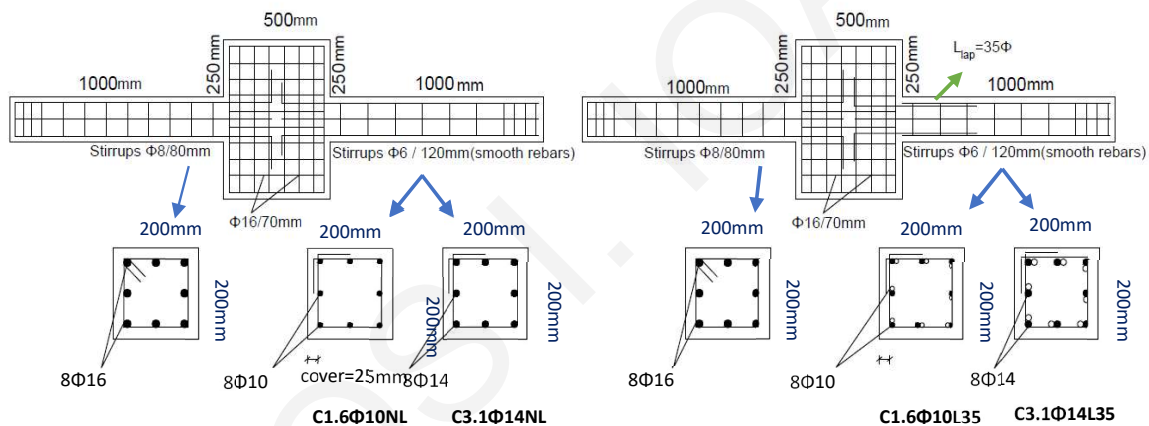


Figure 6. 2: (a) C1.6Φ10NL and C3.1Φ14NL steel reinforcement and specimens' section; (b) C1.6Φ10L35 and C3.1Φ14L35 steel reinforcement and specimens' section.

6.3 Calculation of Member Resistance Values

The characteristic strengths of all the specimens that are reported in the present study are calculated considering the initial and the retrofitted condition. The mechanistic model establishes the shear force V_{min} that may occur in the test specimen when (a) flexural strength of the member develops at the face of the support, V_{flex} ; (b) The anchorage or the lap splice of

the specimen attains its development capacity, V_a ; and (c) The shear reinforcement attains its yield strength, V_s .

Nominal yield values are listed in Tables 43 and 44. These were calculated using the intended characteristic strength of concrete ($f_{ck}=20\text{MPa}$). The flexural strength of the cross section, M_y , was calculated from layered sectional analysis using the material properties for steel and concrete for the original and the retrofitted condition: it is noted here that after cover replacement with ECC, the contribution of the cover's tensile strength which is supported by the material up to large levels of tensile strain, was considered in establishing sectional equilibrium. The corresponding value of the shear force required to support nominal flexural yielding at the critical section of the test specimen was obtained from (Table 6.3),

$$V_{flex} = \frac{M_y}{L_s} \quad (6.1)$$

The recommended bond model from [Fib Model Code, 2010](#) for Concrete Structures was used to calculate the available bond and lap splicing strength. For the anchorage, the pullout strength in good bond conditions was considered with:

$$\tau_{bmax} = 2.5\sqrt{f_{ck}} \quad (6.2)$$

where f_{ck} is the characteristic compressive strength of concrete (here the design was 20/25), which corresponds to $\tau_{bmax} = 11 \text{ MPa}$. The anchoring force was then produced by Eqn. 6.3, where L_b is the straight length of the anchorage.

$$F_{b,anch} = \tau_{bmax}(L_b\pi\Phi + 60A_b) \quad (6.3)$$

Where, the second component in the right-hand side is owing to the contribution of the hook. Similarly, the lap splice length is likely to develop splitting type of bond failure where the peak bond strength is estimated from,

$$f_b = 7.0 \cdot (f_{ck}/20)^{0.25}, \text{ with } F_{b,lap} = f_b(L_{lap}\pi\Phi) \quad (6.4)$$

Based on Eqns. (6.3) and (6.4) the shear force of the structural component at Anchorage or Lap Failure is obtained from (also listed in Table 6.3),

$$V_a = \min\{F_{b,anch}, F_{b,lap}, F_y\} \cdot [n_{b,t} \cdot jd + n_{b,m} \cdot (jd - 0.5h)]/L_s \quad (6.5)$$

Here $n_{b,t}$ is the number of longitudinal bars in the remotest tension layer (here $n_{b,t}=3$), $n_{b,m}$ is the number of intermediate bars in the cross section (here $n_{b,m}=2$), jd is the internal lever arm in flexure (estimated as $0.85d$, where h and d is the total and the effective depths of the member

cross section respectively (here, $h=200mm$, and $d=200-25mm=175mm$, and $L_s=890mm$), and F_y is the nominal yield force of the bar. Resulting values for $\min\{F_{b,anch}, F_{b,lap}, F_y\}$ are listed in Table 6.2: it is noted that yielding controls, and therefore, the values for V_a in Table 6.3 for the original specimens are identical to V_{flex} which is obtained from flexural analysis of the cross section of the member considering the theoretical yielding of longitudinal reinforcement.

Table 6. 2: Bond and lap-splicing strength parameters

| Bar Diameter, ϕ | Lap Splicing Length (mm) | $\text{Min}\{F_{b,anch}, F_y\}$ [kN] | $\text{Min}\{F_{b,lap}, F_y\}$ [kN] |
|-------------------------|-----------------------------|---|--|
| $\Phi 10$ | 350 | $\min\{82.0, 39.25\}$ | $\min\{76.9, 39.25\}$ |
| $\Phi 14$ | 490 | $\min\{158.37;76.9\}$ | $\min\{150.78;76.9\}$ |

The nominal shear strength contribution of the transverse reinforcement V_s for specimens in their original condition was calculated using Eqn. 6.6, and values are summarized also in Table 6.3.

$$V_s = A_{s,tr} \cdot \frac{d_v}{s} \cdot f_{y,\Phi 6} \quad (6.6)$$

In Eqn. (6.6), $A_{s,tr}$ is the area of stirrup legs intersecting a diagonal crack (here $2 \times 30mm^2 = 60mm^2$); d_v is the effective depth of the idealized Ritter Mörsh truss ($d_v = 200 mm - 2 \times 25mm$) and s is the longitudinal spacing of stirrups (Beton Kalender 1970). It is noted here that the above calculation was based on assumption of a 45°-angle diagonal struts, and that the nominal values listed in the table for the original specimens do not account for the concrete contribution. For the repaired condition the jacket contribution is accounted for, considering the tensile strength of the ECC material in the cover, according with the model proposed by Ioannou et al. (2021) i.e.,

$$\Delta V_s = 2t_j f_{t,ECC} (h - t_j) \tan \frac{\pi}{4} \quad (6.7)$$

Where t_j is the jacket thickness for cover replacement (here $t_j=25mm$), and $f_{t,ECC}$ is the tensile strength of the material. For the nominal tensile strength of the ECC used herein ($f_{t,ECC} = 4MPa$), the expected shear strength increase owing to the ECC jacket through cover replacement is 35 kN.

Table 6. 3: Specimen parameters' identification code. (Letter R stands for repaired)

| Specimen ID | Long. | Φ (mm) & # of bars | Lap-Splice ℓ_o (in Φ Mult.) | V_{flex} [kN] | V_s [kN] | V_a [kN] |
|--------------------|-------|-------------------------|--|-----------------|------------|---------------|
| C1.6 Φ 10NL | 1.6% | 8- Φ 10 | NL | 24.2 | 24.75 | 24.2 |
| RC1.6 Φ 10NL | 1.6% | 8- Φ 10 | NL | 36.60 | 59.75 | 36.6 |
| C1.6 Φ 10L35 | 1.6% | 8- Φ 10 | 35- Φ | 24.2 | 24.75 | 24.2 |
| RC1.6 Φ 1035 | 1.6% | 8- Φ 10 | 35- Φ | 36.80 | 59.75 | 36.8 |
| C3.1 Φ 14NL | 3.1% | 8- Φ 14 | NL | 47.5 | 24.75 | 47.5 |
| RC3.1 Φ 14NL | 3.1% | 8- Φ 14 | NL | 55.75 | 59.75 | 55.75 |
| C3.1 Φ 14L35 | 3.1% | 8- Φ 14 | 35- Φ | 47.5 | 24.75 | 47.5 |
| RC3.1 Φ 14L35 | 3.1% | 8- Φ 14 | 35- Φ | 55.75 | 59.75 | 55.75 |

6.4 Instrumentation and Experimental testing procedure

Eight displacement transducers (DTs) with various nominal gauge lengths and five linear variable differential transducers (LVDTs) were used in the experimental setup to provide insights into the behavior of the specimens. Figure 6.3 depicts the instrumentation equipment configuration. LVDT 1 to 5 were installed at the bottom of the specimen for vertical deflection monitoring.

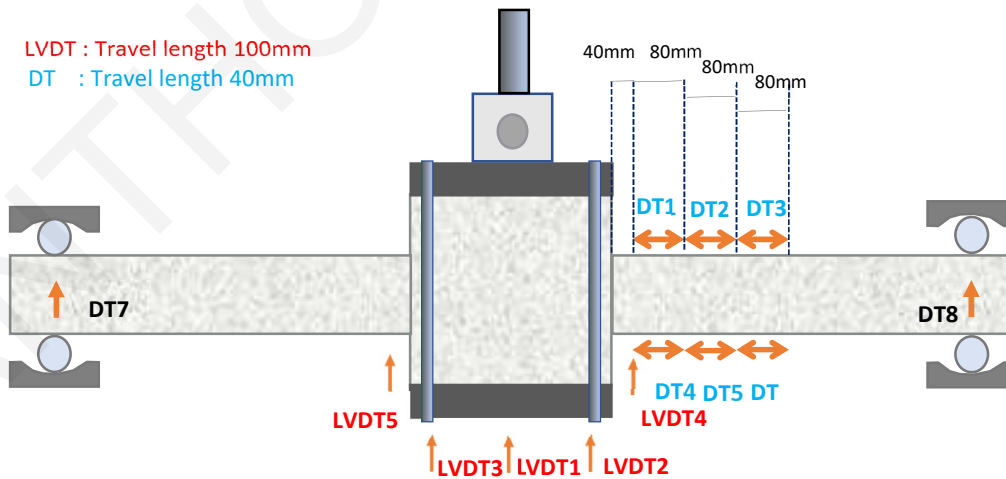


Figure 6. 3: Outline of the instrumentation equipment

Six DTs were installed symmetrically at the top and bottom part of the test specimen for monitoring the deformation and curvature along with the height of the specimen. To measure the vertical displacement of the centroidal axis, DTs 7 and 8 were placed at the ends of the shear spans over the roller supports. Figure 6.4 (a) presents the displacement load history applied on the central stub of the specimens during both test phases (initial damage and post-repair). Displacement histories are corrected for the support displacement (provided by the DTs at the roller supports) – however, the difference is negligible as depicted in the comparison shown in Fig. 6.4 (b).

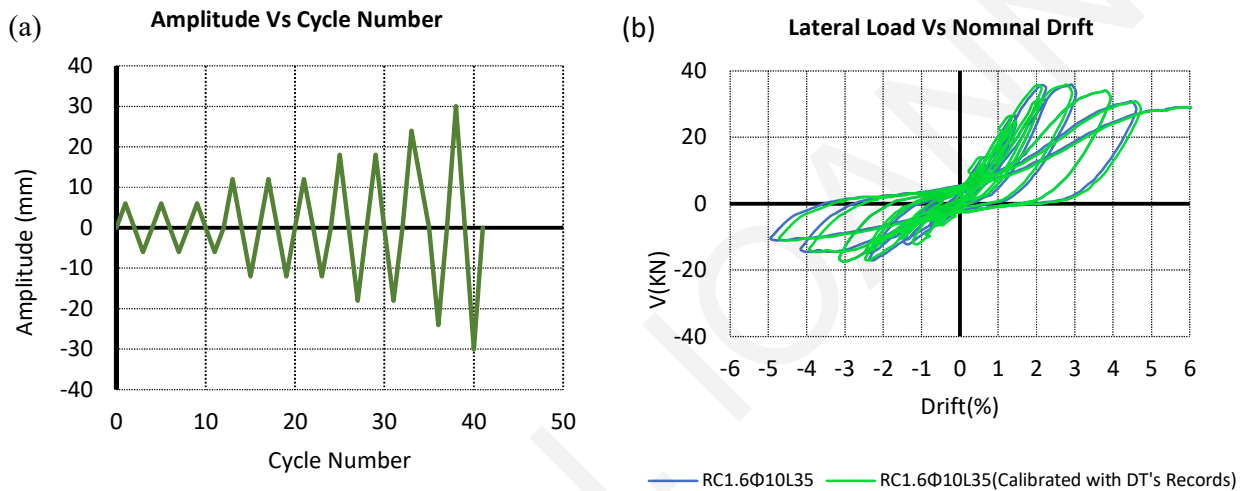


Figure 6. 4: Cyclic displacement history of the central stub used in all tests (specimens in original and in repaired condition)

6.5 Experimental Results of the Initial Testing Phase

During testing all specimens developed a plastic hinge in the critical region of the test span and strain penetration in the footing stub. In the initial phase of testing ten cycles of displacement with increasing amplitude were applied to each specimen, following the history of Fig. 6.4. Each test was continued up to a drift ratio of 4% (40mm central displacement, which was the limit of the hydraulic actuator). As it may be observed from the experimental results which are presented in Fig. 6.5, the response was characterized by an envelope curve with a linear ascending branch up to 1.15% and 1.10% for C1.6Φ10NL and C1.6Φ10L35 and up to 1.6% and 1.15% for specimens C3.1Φ14NL and C3.1Φ14L35 respectively. The significant

compliance was a result of pullout activity in the anchorage and lap splices of the specimens, as evidenced also by the severe pinching of the response hysteretic loops near the zero-displacement value. As expected, the peak strength was greater for the specimens having a higher longitudinal reinforcement ratio ($8\Phi 14$ bars), but because the shear contribution of the stirrups was insufficient to support the flexural strength (see the comparison of the V_s and V_{flex} values in Table 6.3 lines corresponding to the $\Phi 14$ cases) these specimens developed intensive shear cracking (Fig. 6.6(c) and (d)). Both tests with 10 mm diameter longitudinal bars showed early flexural cracks in the specimen length after the third cycle (see Fig. 6.6). As the response envelope degraded, cracks continued to penetrate both along the length of the test unit towards the support but also in the central stub, marked by splitting of cover, due to the limited length of anchorage and lap splice. It is noted that the splice length could not suffice for bond redistribution as strain penetration occurred after load reversals in the anchorage and lap splices, although it was able to support development of first yielding. In all cases the nominal flexural strength calculated in Table 6.3 (V_{flex} value) was attained, but begun to degrade after few cycles only, marked by bar pullout from the footing stub and the lap splices in all cases.

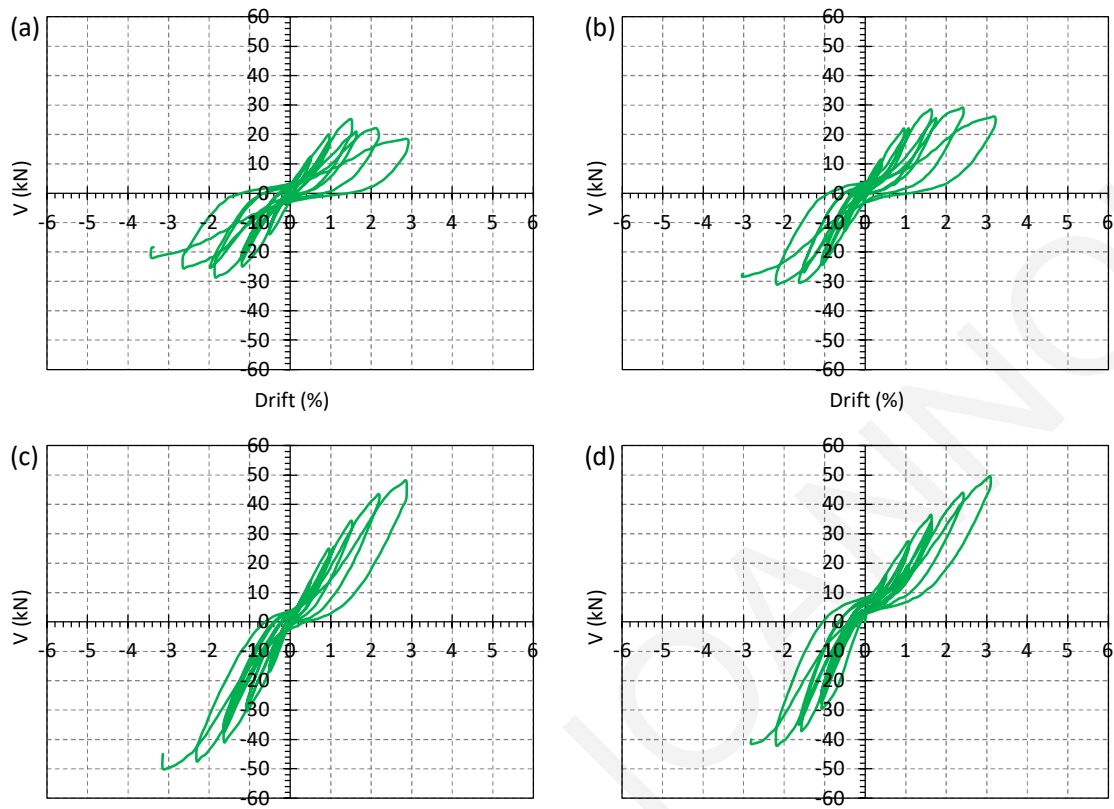


Figure 6.5: Cyclic loading curves of specimens: (a) C1.6Φ10NL; (b) C1.6Φ10L35; (c) C3.1Φ14NL; (d) C3.1Φ14L35.

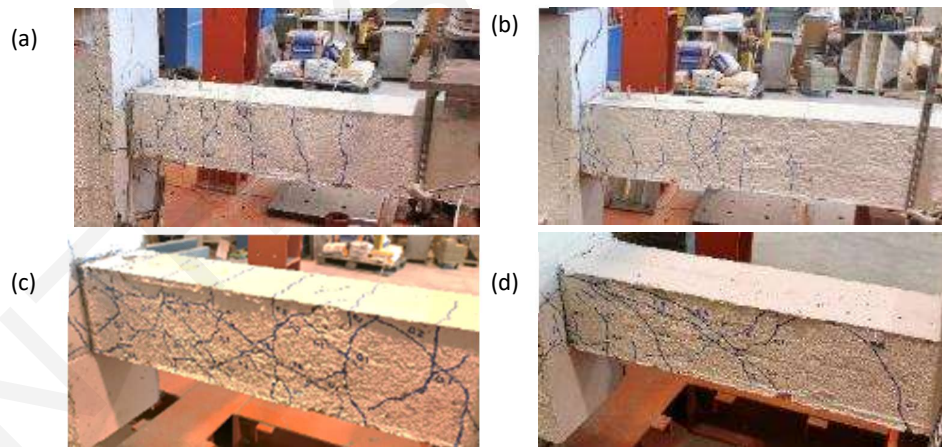


Figure 6.5: Failure modes of specimens before retrofit: (a) C1.6Φ10NL; (b) C1.6Φ10L35; (c) C3.1Φ14NL; (d) M3.1Φ14L35

6.6 Retrofitting Procedure and Repair Material

Engineered Cementitious Composites (ECCs) can be used effectively for retrofitting of the critical regions of RC columns (Li, 2003). Their advantage over conventional concrete rides on the ability to sustain tensile stresses up to large levels of tensile deformation, due to development of multiple fine cracks. ECCs as a retrofitting material may contribute effectively to control of cracking, attenuate stiffness reduction, and may actually enhance the energy dissipation and improve the characteristics of the element's resistance curve. This was demonstrated experimentally by the authors (Ioannou et al., 2021), where the amount of confining strength enhancement and contribution to shear strength by the ECC jacket was quantified and related to the ultimate tensile strength of the ECC material, f_{tu} .

In the present study the ECC material used contained a large fraction of Fly Ash (see Table 6.4) and was reinforced with 1.25% by volume of PVA fibers, having the following fiber properties: tensile strength of 1600MPa, density of 1300Kg/m³, a Young's Modulus of 40GPa, length of 12mm and diameter of 39μm. The compressive strength of the ECC material, measured on cylinders 75 mm× 150 mm at 28 days from casting was 45MPa (Fig. 6.7(a)). Tensile strength was determined from four-point bending tests conducted on prisms having a square cross-section of 100mm width by 60 mm height, and a total span of 3×60 mm (loads were applied at the third points of the span). An inverse analysis procedure was applied on the experimental data (CSA S6-Annex 8, 2019; Yang et. al., 2020) originally proposed by Lopez (2017). The milestone points of the tension stress-strain response of ECC material were as follows (Fig. 6.7(b)): cracking strength $f_{cr} = 4.65$ MPa, ultimate tensile resistance, $f_{fu} = 5.0$ MPa, secant modulus of elasticity (slope of the compressive stress strain response to 40% of peak compressive stress) $E_c = 18300$ MPa, ultimate tensile strain capacity at peak tensile strength, $\varepsilon_{tu} = 0.0092$ and the maximum crack width $w_{max}=6$ mm.

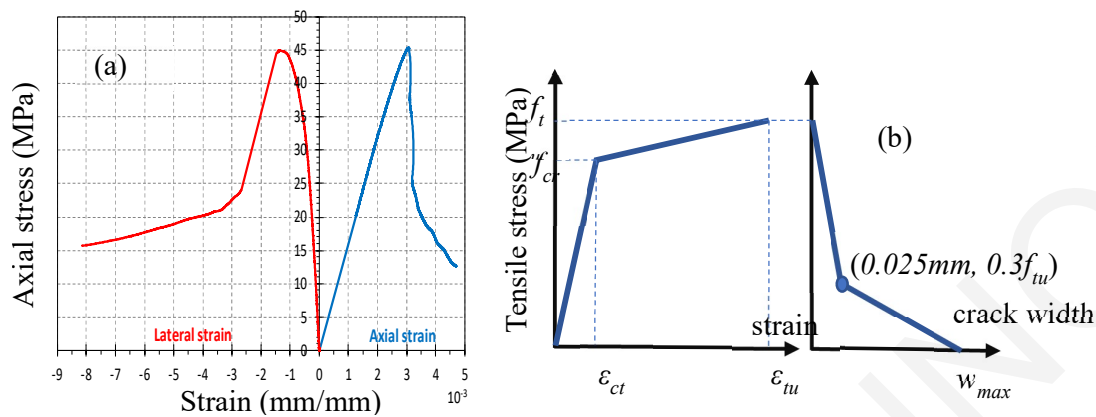


Figure 6.7 (a) Tensile stress and strain response of ECC material; (b) Cylinder's compression stress vs. lateral and axial strain curves for fibers e reinforced concrete

The retrofitting application includes the production (according to [ACI PRC-544.1R-96](#), see 6.8) and application of the ECC jacket [[Ioannou et al., 2021](#), [Georgiou and Pantazopoulou, 2018](#)] to the pre-damaged control specimens maintaining the same geometry and construction detailing. To achieve this goal the cracked concrete was removed over the length of the critical region (in the present work this was taken, $h_{cr}=2b_w$) as per Fig. 6.8 until all transverse and longitudinal reinforcement was fully exposed in the length of interest (see specimen in Fig. 6.8a). Jacketing was applied in phases using easy to assemble, modular forms as depicted in the sequence of Fig. 6.8a-c, after removal of the damaged, cracked cover.

Table 6. 4: ECC material mix design

| <i>Materials</i> | <i>Quantity (kg/m³)</i> |
|------------------|------------------------------------|
| Cement | 530 |
| Water | 372 |
| Fly Ash | 636 |
| Silica Sand | 425 |
| PVA Fibers | 16.25 |
| Superplasticizer | 13 |

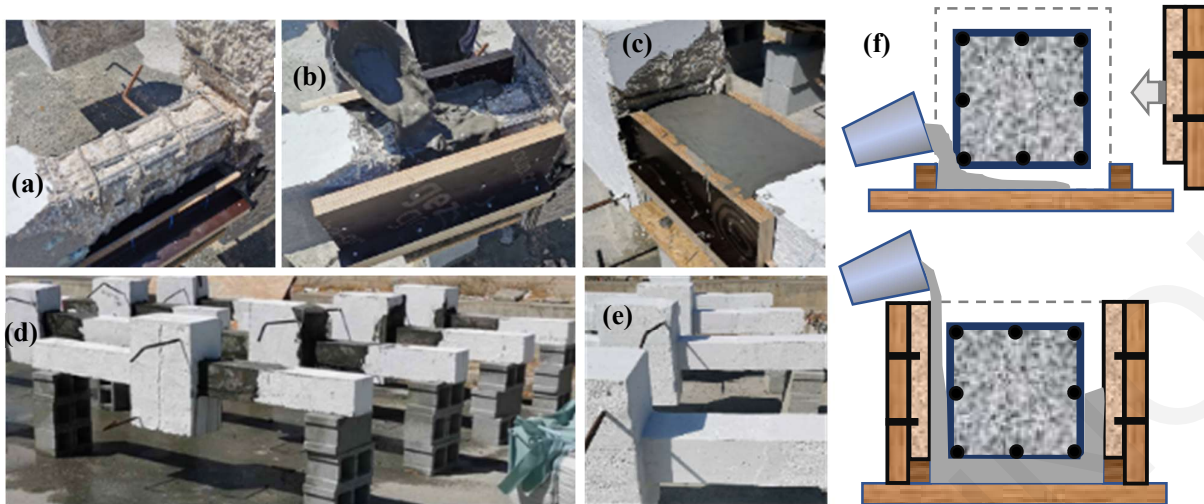


Figure 6. 6: A modular form is used to cast the jacket: (a) lower cover cast from the side; (b) Side forms are placed for casting of the sides; (c) Leveling of top cover; (d) After formwork removal; (e) retrofitted specimens ready for testing; (f) Sectional detail of the modular form.

It should be noted at this point that additional retrofit measures were used in cases where damage to the central rigid stub and supporting specimen had occurred during the initial phase, to avoid further localization of damage in these areas. Any cracked concrete was removed from the central stub and was replaced with a high strength cementitious repair grout as per class R4 of EN 1504-3. The supporting segments were also retrofitted using ultra high cement grout according to EN 1504-06 to prepare for the increased demands of the second test phase where it was expected that the repaired test spans could exhibit increased strength. Following the repair of the stub and supporting segment, the sharp corners were smoothed so that a unidirectional woven carbon fiber fabric with mid-range strength FRPs could be placed to ensure further confinement (Figure 6.9).



Figure 6. 7: Additional retrofitting of central stub and supporting part of the specimen

6.7 Observed Response of Retrofitted Specimens

Figure 6.10 plots the cyclic shear force vs - drift experimental curves attained by the retrofitted test specimen after loading with the displacement history of Fig. 6.4. With the exception of specimen RC3.1 Φ 14NL, which had experienced irrecoverable damage in the anchorage inside the stub, the peak load matched the theoretical values listed in Table 6.3 for the ECC-retrofitted components. The cracking patterns that developed in the specimens near the end of testing are shown in Fig. 6.11. Specimens that attained a higher load developed intensive cracking over the test length whereas those experiencing lower loads exhibited transfer of damage in the region near the end of the repaired segment.

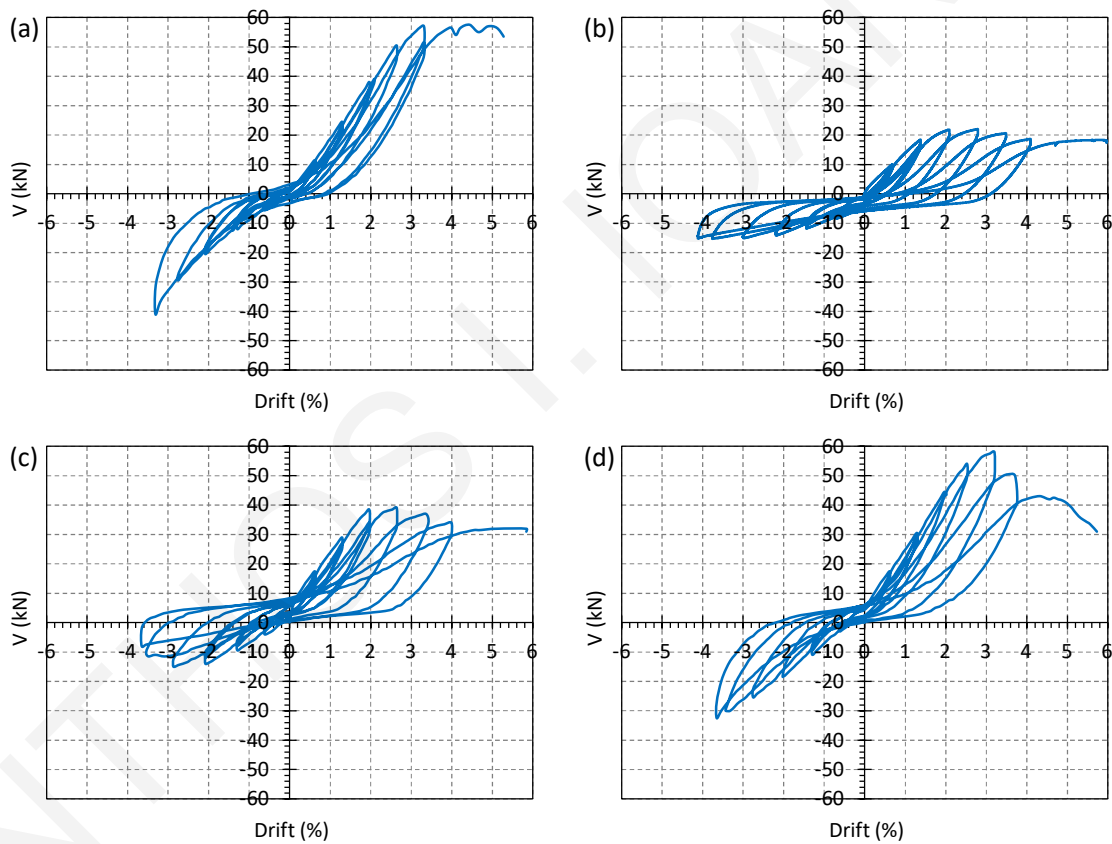


Figure 6. 8: Cyclic loading curves of specimens: (a) RC1.6 Φ 10NL; (b) RC3.1 Φ 14NL; (c) RC1.6 Φ 10L35; (d) RC3.1 Φ 14L35.

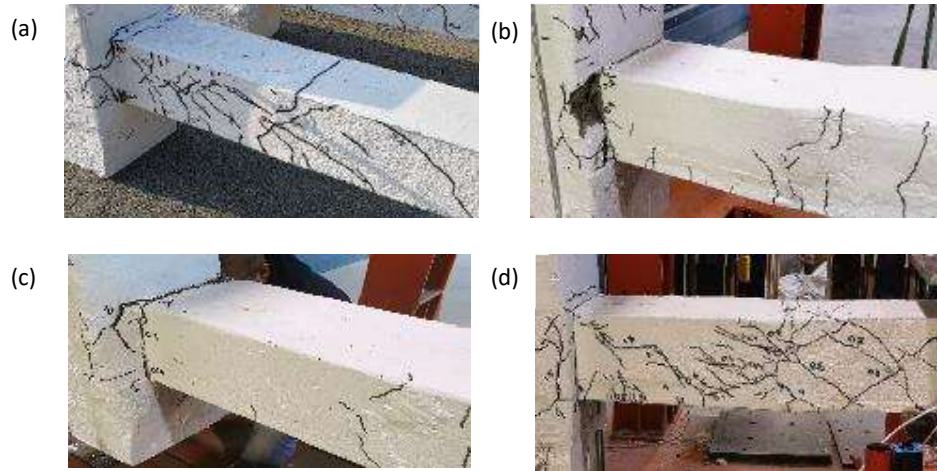


Figure 6. 9: Failure modes of specimens after retrofitting: (a) RC1.6Φ10NL; (b) RC1.6Φ10L35; (c) RC3.1Φ14NL; (d) RC3.1Φ14L35

The characteristic points of the hysteresis load–drift curves are illustrated in Table 6.5. Yielding is defined as the point corresponding to 75% of the peak in the ascending branch. Original specimens exhibited a stable behavior up to 2-2.5% but retrofitted specimens presented an ascending branch of greater stiffness up to 3% drift. In general, specimens with lap spliced reinforcement attained higher resistance than their counterparts with continuous reinforcement – this is most likely owing to the fact that in the lap-spliced specimens damage during the first phase occurred mostly in the plastic hinge zone which was repaired after the cover replacement; whereas in the continuous reinforcement case, the hooks were deformed out of shape at large drifts – a damage pattern that could not be recovered with replacement of the damaged concrete. As was seen in the case also of the monotonic tests, the ECC jacketing through cover replacement was able to fully recover the strength and mitigate shear failure under cyclic displacement reversals (an exception was the case where the damage in the anchorage occurred outside the ECC-repair region, which limited the resistance of the unit).

Table 6. 5: Characteristic points of cyclic loading tests under vertical displacement of the central stub*

| Specimen | V_{max} | V_y | Θ_y % | V_u | Θ_u % |
|-------------|-----------|--------|--------------|-------|--------------|
| C1.6Φ10NL | 28.5 | 21.30 | 0.8 | 20.50 | 3.0 |
| | -26.0 | -19.5 | -1.0 | -17.0 | -3.48 |
| RC1.6Φ10NL | 54.0 | 40.50 | 2.25 | 50.50 | 2.28 |
| | -46.5 | -34.90 | -3.0 | -46.0 | -3.40 |
| C3.1Φ14NL | 50.0 | 37.50 | 1.0 | 51.0 | 2.92 |
| | -45.0 | -33.75 | -1.25 | -43.5 | -2.35 |
| RC3.1Φ14NL | 21.6 | 16.20 | 1.25 | 18.0 | 5.95 |
| | -15.0 | -11.25 | -1.50 | -15.0 | -4.0 |
| C1.6Φ10L35 | 32.0 | 24.0 | 0.75 | 29.0 | 3.25 |
| | -28.0 | -21.0 | -1.1 | -25.0 | -3.0 |
| RCΦ10L35 | 36.0 | 27.0 | 1.25 | 28.0 | 5.85 |
| | -17.0 | -12.75 | -1.40 | -11.0 | -3.70 |
| C3.1Φ14L35 | 47.5 | 36.0 | 1.25 | 48.0 | 3.10 |
| | -42.0 | -31.50 | -1.0 | -42.5 | -2.80 |
| RC3.1Φ14L35 | 55.0 | 41.25 | 1.90 | 30.0 | 5.75 |
| | -33.5 | -25.10 | -2.40 | -34.0 | -3.70 |

* (Positive value is down / negative is up)

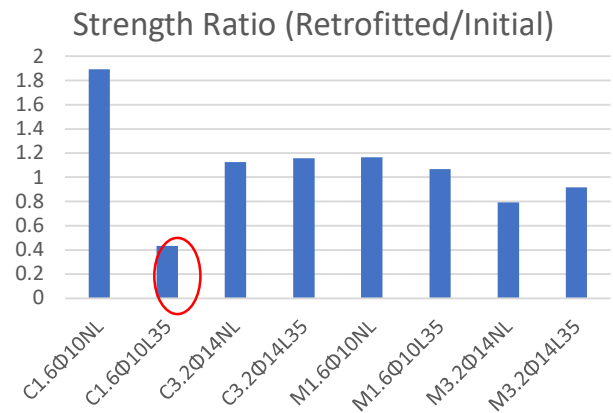
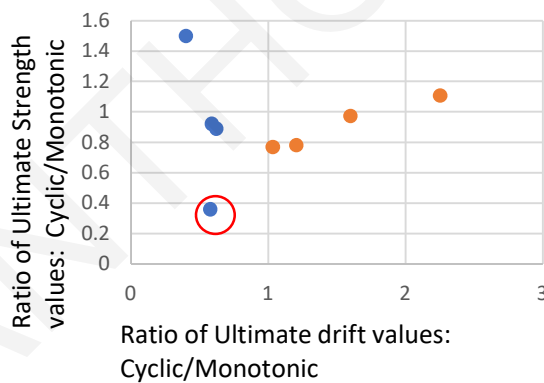


Figure 6. 10: (a) Comparison between monotonically and cyclically loaded specimen pairs.
(b) Ratio of retrofitted to initial specimen strength

The ultimate drift values of the cyclically loaded specimens and the corresponding strength values (defined at the point in the post-peak range of the resistance curve envelope at a resistance equal to 80% of the peak value) are compared in Fig. 6.12(a). The blue dots refer to specimens with 10mm diameter longitudinal bars, whereas the orange dots refer to specimens with 14mm bars. It is noted that in most cases cyclic loading reduced the resistance and effectiveness of the strength recovery. This is shown more clearly in Fig. 6.12(b) which gives the strength ratio of retrofitted over the original specimen; with the exception of C1.6Φ10L35 which is marked with the red circles in Fig. 6.12b, that had endured significant damage in the anchorage (i.e. outside the range of the ECC retrofit) all specimens recovered at least 80% of their resistance. It was seen that the most critical aspect that determined the applicability of the retrofit scheme with ECC cover replacement was whether the anchorage had developed permanent deformation during previous loading (i.e., strength was non-recoverable) or not, (in which case strength was recoverable through retrofit).

With regards to the cracking patterns, it was found that in the initial state, specimens with continuous reinforcement had developed flexure and shear-flexure cracks extending to a plastic hinge zone of 300mm reaching crack widths of 0.1-0.3mm. The extent of the cracked region was smaller (50 mm) and cracks larger (0.1-0.5mm respectively) in the case of the lap-spliced cases. However, the failure modes of retrofitted elements developed firstly flexural cracks, whereas shear cracks were observed at advanced stages of loading, especially near the end of the cover replacement length. The response of the retrofitted specimens show that cover replacement may fully mitigate the effects of damage over the critical length (plastic hinge), however it cannot eliminate the implications of prior damage to the anchorage of the reinforcement if it has occurred beyond the length of cover replacement; thus the methodology should be ideally used to retrofit members where shear strength deficiency has precluded the occurrence of extensive flexural yielding that could lead to strain penetration in the footing. Note that the same limitation had been reported with regards to the effectiveness of FRP jacketing for retrofitting of columns ([Thermou and Pantazopoulou, 2009](#)).

6.8 Numerical Modeling to Determine Cover Replacement Effectiveness

To explore further the mechanics of cover replacement as a retrofit methodology a selected number of cases was analyzed in detail using advanced nonlinear finite element simulation in ABAQUS (Georgiou and Pantazopoulou, 2018; Chu and Wu, 2019; Oucif et al., 2017; Abaqus Manual 2010; Sakr et al., 2020). Eight nodes solid elements were used to model concrete and the ECC cover. Longitudinal steel reinforcement was modeled using beam elements with linear elastic-plastic stress-strain laws. Truss elements were used to model stirrups. Accounting for the increased slip of the reinforcement in the specimens, the load-displacement response of the beam elements representing the embedded bar in the anchorage was calibrated in a separate investigation in order to match the compliance by reducing the effective bar stiffness for that bar segment. Material stress and strain laws were modelled as follows: (a) Concrete Damage Plasticity Model was used for both confined and unconfined concrete; the ascending envelope of the uniaxial stress-strain law was modelled with a basic Hognestad parabola (1951) attaining the respective peak compressive strength at a compressive strain of 0.002. The Kent and Park (1981) model was used for the post-peak descending branch using values of $\varepsilon_{c,50}=0.003$ and 0.004 respectively, for plain and confined concrete. The experimental uniaxial compression and tension stress versus strain curve was used to define the input stress-strain response for the ECC jacketing. Concrete model parameters used in the study are listed in Table 6.6. Plain and ECC concrete had elastic properties with a tangent modulus of $E_{PC0}=21000\text{MPa}$, $E_{ECC,0}= 20000\text{MPa}$ and Poisson's ratio of 0.2, respectively. Appendix C contains information on Finite Element Analysis, including the algorithm, type of analysis, type of element, and type of meshing.

Table 6. 6 Concrete Damage Plasticity Model Parameters

| Dilation Angle | Eccentricity | f_{b0}/f_{c0} | K | Viscosity Parameter |
|----------------|--------------|-----------------|------|---------------------|
| 36 | 0.1 | 1.16 | 0.67 | 0 |

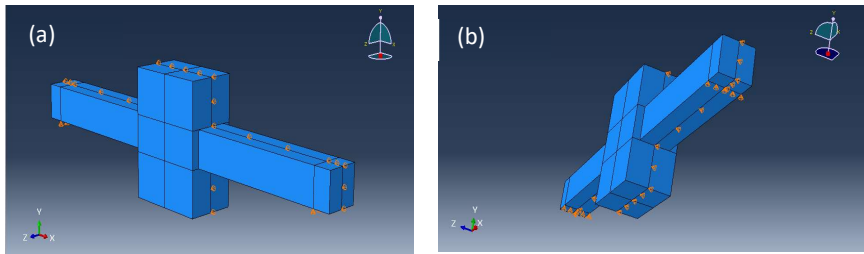


Figure 6.11: Finite element model: (a) Partitioning; (b) Boundary conditions

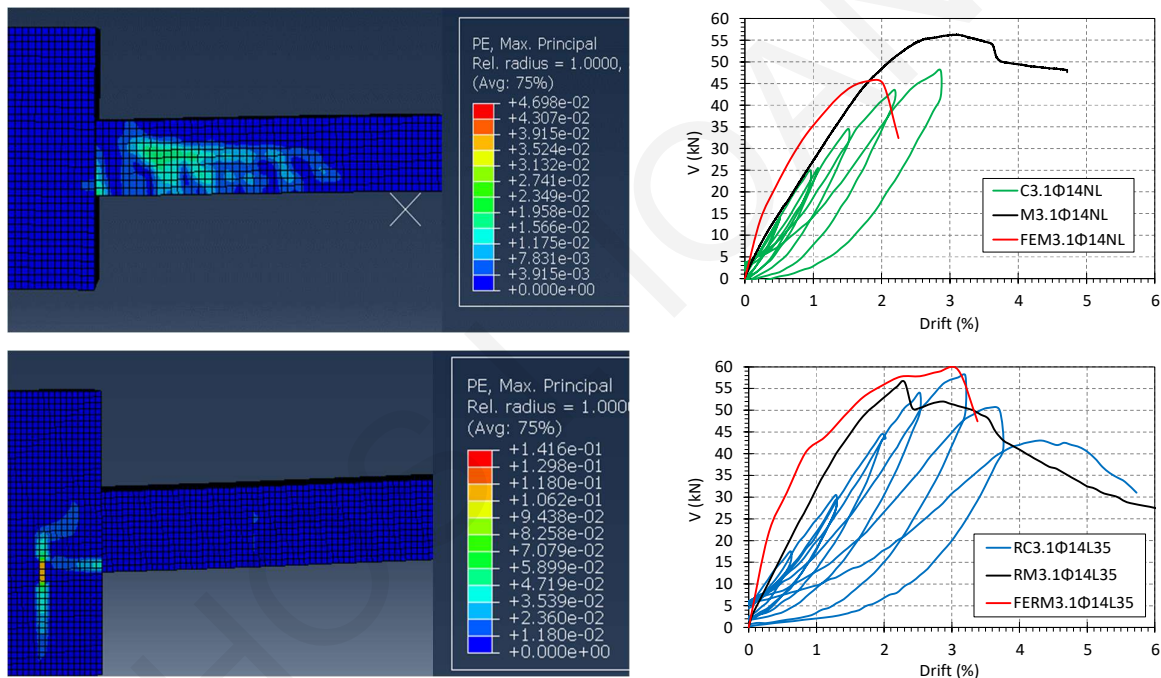


Figure 6.12: (a) C1.6Φ10NL crack patterns and Monotonic response envelopes; (b) same for RC3.6Φ14L35.

Table 6.7 compares the results of finite element modeling normalized with the relevant experimental data. Good agreement is found in terms of both strength and deformation capacity of the specimens in the initial testing phase; for the retrofitted estimates, the F.E. results show a stiffer ascending envelope. The performance of the models for the retrofitted specimens overestimates the resistance only in those cases where significant yield penetration and

deformation of the anchorages had taken place in the initial testing phase – these are the specimens with continuous reinforcement (i.e., both C1.6Φ10NL and C3.1Φ14NL. For these cases, the difference between analytical and experimental strength values is attributed to the prevalence of pre-existing reinforcement pullout from the anchorage which is not accounted for in the model.

Table 6. 7: Normalization of FEA Characteristic points of finite element analysis models under monotonic loading with the respective points emerged from experimental cyclic loading tests

| <i>Specimen</i> | $\frac{V_{max,FEA}}{V_{max,EXP}}$ | $\frac{V_{y,FEA}}{V_{y,EXP}}$ | $\frac{\theta_{y,FEA}}{\theta_{y,EXP}}$ |
|-----------------|-----------------------------------|-------------------------------|---|
| C1.6Φ10NL | 1.10 | 1.10 | 1.07 |
| RC1.6Φ10NL | 0.67 | 0.67 | 0.27 |
| C3.1Φ14NL | 0.91 | 0.91 | 0.50 |
| RC3.1Φ14NL | 2.89 | 2.89 | 1.25 |
| C1.6Φ10L35 | 1.32 | 1.32 | 0.80 |
| RCΦ10L35 | 1.23 | 1.23 | 0.80 |
| C3.1Φ14L35 | 1.26 | 0.82 | 0.56 |
| RC3.1Φ14L35 | 1.10 | 1.01 | 0.4 |

6.8.1 Finite Element Analysis Models Parametric Investigation

Since the best correlation of the retrofitted models matched the responses of those specimens that had lap splices (i.e. such members did not develop permanent damage in the anchorages in the footing due to extensive yield penetration), the corresponding model of C3.1Φ14L35 was used as a point of reference in order to conduct a parametric investigation. This was intended to supplement the findings of the experimental study in quantifying and interpreting the effectiveness of the cover replacement. To this end, the performance after cover-replacement jacketing was compared with the initial response of the R.C. member. For the

theoretical cases that were included in the parametric study and for clarity of illustration, extensive anchorage length was provided inside the stub so as to eliminate the likelihood of early anchorage failure outside the jacketed region. Using as benchmark cases the reinforcement arrangement of experimental cases C3.1Φ14NL and C3.1Φ14L35 in defining the theoretical examples T3.1Φ14NL and T3.1Φ14L35, the parameters varied were the length from the support where the cover was replaced with ECC, and the effective depth of the cross-section (so as to study the possible reduction of the effectiveness in a deeper cross-section). Cases with R in the identification code are retrofitted examples of the otherwise identical cases comprising common concrete (e.g., RT3.1Φ14NL has ECC material in the cover over a length equal to $2b_w$ measured from the face of the support but is otherwise identical to T3.1Φ14NL). In cases with the extension *Full* in their identification code, the cover has been replaced with ECC over the entire length of span, e.g., RT3.1Φ14NL-Full has identical geometry as T3.1Φ14NL but with ECC cover).

Another group of cases considered have the same pattern of reinforcement arrangement (i.e. 8-14mm diameter continuously anchored bars continuous identified by NL), same spacing of rectangular stirrups and cover with the square sections shown in Fig. 6.2, but having a deeper cross-section ($h_b=400$ mm and $b_w=250$ mm). Following the same scheme of identification as before, these cases are identified with D in lieu of T in the identification code. (For example, D8Φ14NL represents the deeper section with 8Φ14 bars comprising normal concrete; RD8Φ14NL is retrofitted over a length of 500mm with cover replacement, and RD8Φ14NL-Full has cover replaced with ECC over the entire length). In this manner, a total of nine theoretical examples were considered in three triplets as depicted in the resistance curves obtained from finite element analysis plotted in Fig. 6. 13.

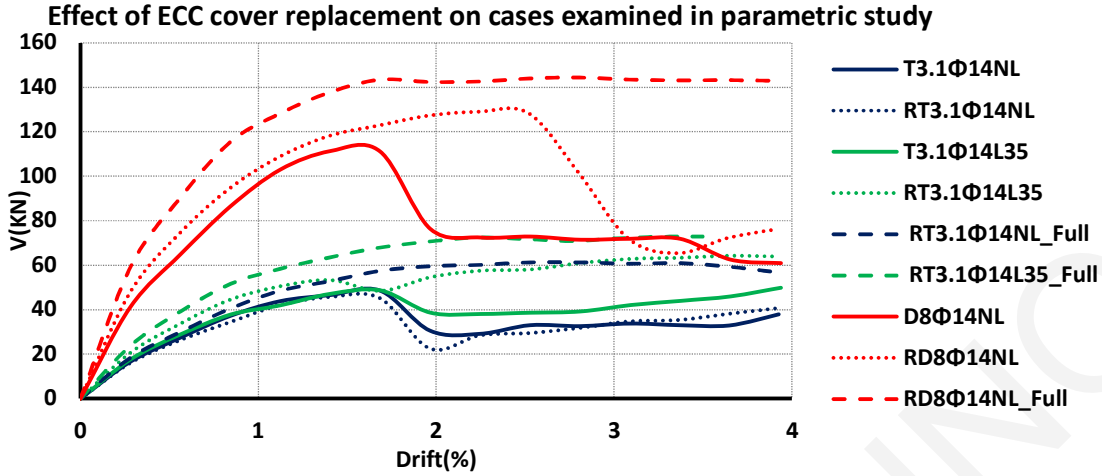


Figure 6. 13: Comparison of the response curves obtained from the parametric investigation

Figures 6.15 and 6.16 summarize the results of the parametric investigation. It is noted that as was observed in the experiment, partial replacement of the cover (i.e. over a critical length measured from the face of the support) does increase the strength of the member up to drift levels between 1.5% and 2%. Beyond this limit, the discontinuous nature of the jacket controls, localizing the failure at the endpoint of the retrofitted zone where the limited number of available stirrups is insufficient to resist the higher shear demand which is affected by the increased flexural strength of the retrofitted member cross-section. Cases with full cover replacement show superior performance in all examples considered. The margin of strength increase was maintained in the case of the deeper member although the cover was the same. It is concluded that the tensile strength contributed by the cover in the tension zone as well as through its contribution in resisting shear is sufficient for the range of sectional dimension increase (doubling the section height) considered. It is noted that based on the derivations by [Ioannou et al. \(2021\)](#) shear strength contribution by the ECC cover jacket equals,

$$V_j = 2 \cdot t_j \cdot f_{tu} \cdot (h - t_j) \cdot \tan \theta \quad (6.8)$$

therefore, the jacket's contribution is proportional to the section height and is not likely to be diminished due to size effects, as illustrated here in the finite element cases of RD8ΦNL and RD8ΦNL-Full which were used to explore the effect of size on the jacketing effectiveness.

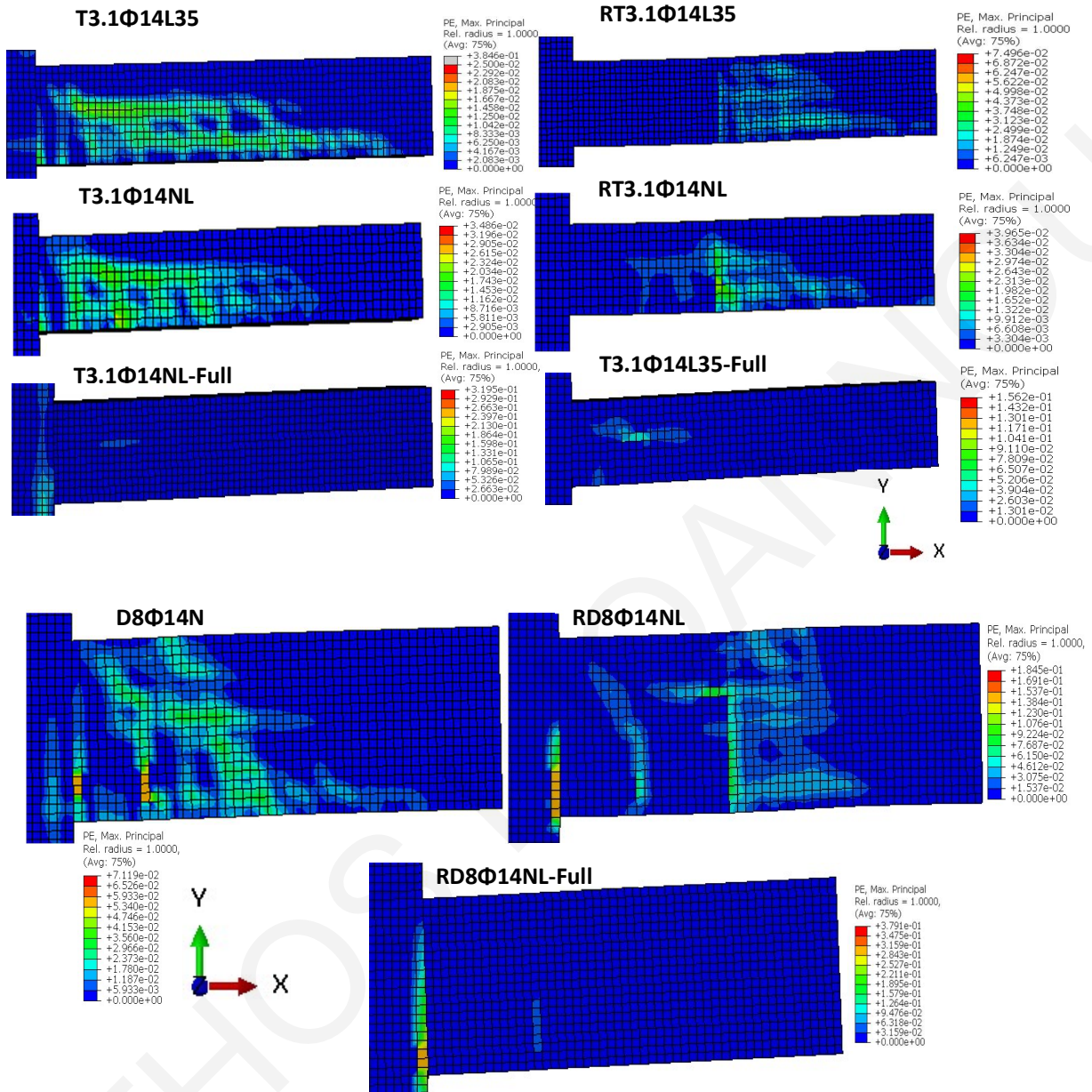


Figure 6. 14: Cracking patterns (Ultimate limit state) obtained for the parametric cases studied

6.9 Conclusions

The experimental results confirmed the seismic vulnerability of lightly reinforced concrete prismatic members, designed with details typical of the European construction practice of the 1960s–1970s, characterized by inadequate lap-splicing lengths of reinforcement, and sparse transverse links. The experimental results of four specimens representing these detailing practices under cyclic load demonstrated a significant loss of lateral strength due to the slip of longitudinal rebars on the support accompanied by flexure–shear cracks along with the specimens. Retrofitting was considered using the replacement of the damaged cover with a strain hardening Engineered Cementitious Composite, extending over a critical region that was about twice the cross-sectional dimension. The proposed retrofitting technique was relatively simple since the material can sustain its tensile strength well beyond cracking and over a large range of strain, whereas being flowable and self-consolidating, it can be cast in thin layers. Experimental results demonstrated that this appears to be an effective technique for strength recovery of severely damaged components, whereas, in the absence of prior damage in the anchorage through yield penetration and bar deformation, it may retrofit existing detailing inadequacies mitigating shear failure and enhancing the flexural strength of components. Therefore, it was concluded that the effectiveness of the approach is hampered if previous flexural yielding has caused the spread of inelastic strain into the support, whereas members with deficiencies that would cause brittle failure along the length of the member may be mitigated effectively through cover replacement with the ECC. Retrofitting effectiveness was studied further through finite-element complementary investigations where it was shown that jacket effectiveness was maintained even after doubling the member section height since the shear strength contribution of the jacket increases proportionally with the member depth.

Chapter 7: Conclusions and Future Work

7.1 Conclusions

The use of eco-materials in building projects is a design framework that combines criteria and methodologies in structural design aiming to extend the life of structures. To this end, the main objective of material design is to limit the resource exploitation while also assisting towards improving the service life and safety of existing construction. Structures with a shorter life expectancy are more expensive and resource intensive, especially when maintenance costs are considered. The present study demonstrated how to optimize the evaluation of elements failing in shear or shear-flexure (sparse transverse reinforcement, inadequate anchorage and lap-splicing length of longitudinal reinforcement) demonstrating via the development of data processing and finite element numerical models that axial load ratio impacts and accelerates the and shear failure mechanism. ECC materials compared to plain concrete, provide extensive ductility in tension, compression, shear, flexure and may be employed in retrofitting approaches with extraordinary results. The strength and ductility of an element can be improved without having a significant impact on the element's geometry and stiffness or mass. Before applying the jacketing retrofitting technique, it was assumed crucial to conduct a number of interface interaction experiments in order to better understand the magnitude and transfer mechanism of shear strength at the interface.

Through a data base development, the current research seeks to investigate the proposed models for assessing the strength and drift capacity of columns under monotonic and cyclic loading conditions. In terms of providing improved expressions for shear strength evaluation, an artificial intelligent algorithm through machine learning was employed to check the shear strength of data base elements that undergone shear failure, considering expressions of relevant standards that were already proposed. Moreover, finite element models of specific specimen from the database were developed in order to validate the experimental findings from the database and the accuracy of the models that were used in the assessment procedures. In order to understand how second order effects affect an element's shear strength mechanism, this interaction was further investigated. When bonding on existing substrates the investigation of the bond stress level at the interface of the repair materials was another primary objective of this study. This was accomplished without the use of an epoxy adhesive at the interface utilizing pure slanted shear and direct tensile tests. The plain concrete mix designs, interface

inclination level and roughness, and other critical parameters were investigated. Another important goal of the current study was the application of Engineered Cementitious Composites (ECC) for concrete cover replacement as a method of rehabilitating damaged reinforced concrete structural members. It was shown through FEA numerical models' parametric investigation that the fiber-reinforced cover maintains its tensile strength up to large prominent levels of tensile deformation, acting as a confinement mechanism in the role of an encasing jacket for the existing member.

The following are some of the most important findings:

Through nonlinear FEA analysis using three-dimensional volume type finite elements, the current work examined the mechanical behavior of columns under horizontal translation, focusing on the developed failure mechanisms (shear), the plastic hinge length and the diagonal cracking inclination. The effect of the axial load was investigated using simulation in order to determine the parametric sensitivity of the analyzed data, while also evaluating the proposed relationships for limit state failures in terms of shear strength. In conclusion, with an emphasis on second order effects, the influence of failure plane and the axial load ratio on the development of plastic hinge length and mode failures has been studied, and improved models for shear strength evaluation during assessment have been provided.

The interface shear strengths and ultimate failure mechanisms of PC and ECC were examined experimentally using a series of slanted shear and direct tensile tests. Surface roughness, PC and ECC compressive strength, inclination angle, curing condition, and aggregate interlocking mechanism are the most critical characteristics that influence shear stress mechanism at the interface. The ultimate failure modes of ECC-PC may be classified into three separate categories: direct interface failure, direct PC cracking, and a combination of PC and ECC cracking. To study the interface of ECC-PC composites, the Coulomb criteria were combined with a three parameters failure criterion. The slanted shear test method's results are dependent on the compressive strengths of on the ECC and normal concrete's, as well as the bond and friction mechanisms within the two materials. The failure is getting vulnerable when the angle of the interface is increased.

Using established mechanistic models, the contribution of the ECC jacket to confinement of the encased core, web shear strength, and lap-splice formation capacity via clamping action was assessed. It was discovered that this contribution might be significant, influencing the structural member's critical mode of failure while also improving the component's strain energy

dissipation and durability. The efficiency of retrofitting was investigated using finite-element supplementary studies, which revealed that jacket effectiveness was maintained even after doubling the member section height since the jacket's shear strength contribution increased proportionately with member depth.

7.2 Future Research Plans

Prequalifying the procedures developed for characterization of the interface of ECC vs PC, the proposed retrofitting techniques of reinforced concrete elements, and the improvement of the procedure proposed for existing reinforced concrete elements assessment through further testing and authentication studies is a next step in the direction of promoting and advancing the research of the current study. The nonlinear finite element code will be quite useful in this respect since it is designed to examine the sensitivity of the design approaches and performance requirements created. The following are some of the longer-term research plan:

Additional research investigation are required to resolve various issues that arose over the process of the current study's development. Alternative surface preparation methods shall be investigated for their impact on the bond strength of concrete-to-concrete interfaces, as well as the variability of the roughness degree obtained using the same preparation method, which can be caused by exposition time, applied pressures, and other factors. It is important to note that this research was conducted without steel reinforcement crossing the interfaces. It's necessary to look into the impact of steel reinforcing bars or connections across the interface. The dowel action ought to be examined and evaluated.

To fully assess the material's various properties of durability, an extended program of accelerated tests exposing elements to severe conditions (fire, chloride-induced corrosion, and freeze-thaw) would be required.

According to previous studies, research gaps with regards to seismic upgrading of RC structures with novel techniques needed. An area, which is certainly worth receiving further attention by the scientific community, is the development of the proposed retrofitting technique not only in linear structural members such as beams but also an investigation needed for applying the proposed technique to other structural members (walls, foundations, structural joints).

Appendix A

A.1 Inverse Analysis

The tensile properties of the strain-hardening, fiber reinforced cementitious material are derived from the resistance curve of a prismatic specimen loaded at the third-points along its span as depicted in Figure 4.18(a) (Lopez, 2017). The dimensions of the specimen are, L , h , and b (clear span, section height and width); in the present study, these values were, 180mm, 60mm, and 100mm, respectively. The tensile modulus of elasticity is E_{co} , and the effective strain value is ε_{t0} . Taking into consideration that after localization (at the peak point) the crack occurs at a horizontal distance d_o from the mid-span in the constant moment region, where the peak displacement actually occurs, the corrected displacement of that midpoint is determined, δ_4^* . Next, the normalized parameters K_1 to K_5 are defined.

Table A. 1 : Inverse analysis parameters

| | |
|---|---|
| $E_{co} = \frac{7.2}{b} s_o$ | $K_1 = \frac{\left(\frac{P_1}{P_2}\right)^{0.19}}{1.63}$ |
| $f_{cr} = K_1 \frac{P_1 L}{bh^2}$ | |
| $\varepsilon_{cr} = \frac{f_{cr}}{E_{co}}$ | $K_2 = 7.65 \frac{\delta_3}{\delta_1} - 10.53$ |
| $\varepsilon_{tu} = K_2 \varepsilon_{cr}$ | |
| $f_{Fu} = K_3 f_{cr}$ | $K_3 = K_2^{-0.18} \left(2.46 \frac{P_3}{P_1} - 1.76\right)$ |
| $\delta_4^* = K_5 \delta_4$ | $K_5 = 1 + \frac{0.6}{L} d_0$ |
| $\varepsilon_{to} = K_4 \varepsilon_{cr}$ | $K_4 = K_3^{-0.37} K_2^{0.88} \left(3 \frac{\delta_4^*}{\delta_3} - 1.8\right)$ |
| $w_o = \left(\varepsilon_{to} - \varepsilon_{tu} + \frac{10 f_{Fu}}{3 E_{co}}\right) 1.5 h$ | |

The inverse analysis method summarized herein determines the milestone points in the tensile stress-strain, and tensile stress-crack opening displacement w , as per the idealized bilinear shapes adopted in Figure 4.18(c) and d: f_{cr} represents the cracking strength and f_{Fu} the ultimate tensile resistance after strain hardening; the respective strains are the ε_{cr} and ε_{tu} . The magnitude of crack opening after failure w_o is measured in mm, whereas l_F is the fiber length used in the mix (here PVA fibers, 12 mm long).

Appendix B

ANTHOS I. IOANNOU

B.1 Shear critical columns

Lynn et al. (1998)

Specimen 3CMH18

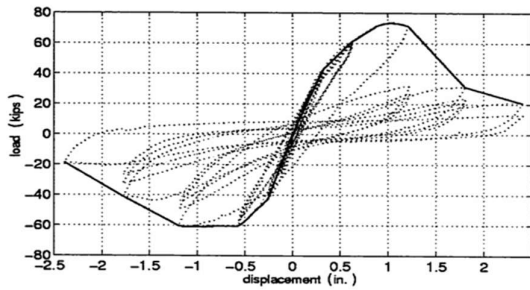
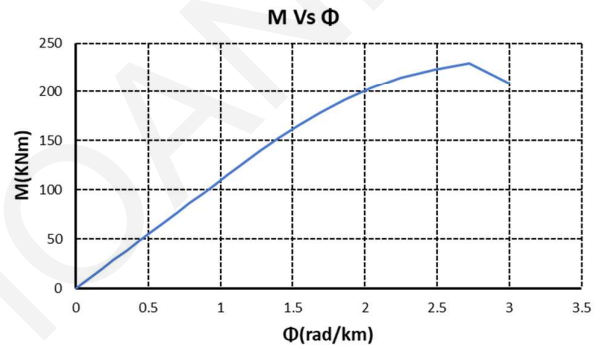
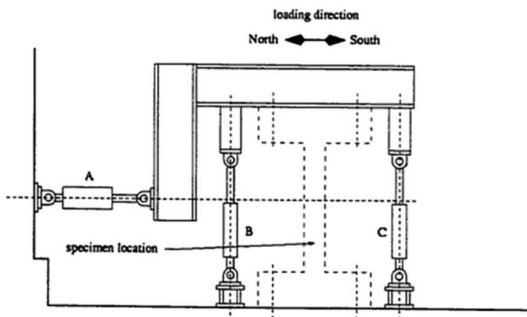
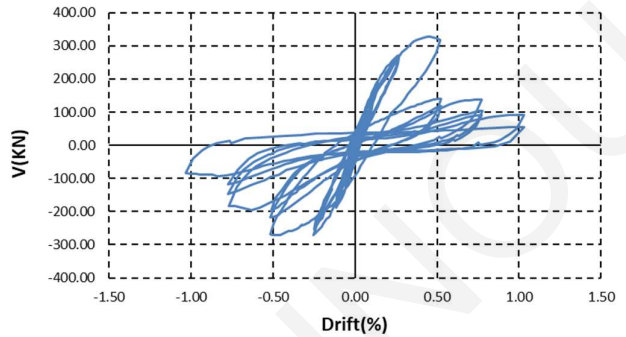


Figure 3.67: Load-displacement history, Specimen 3CMH18



Member Response

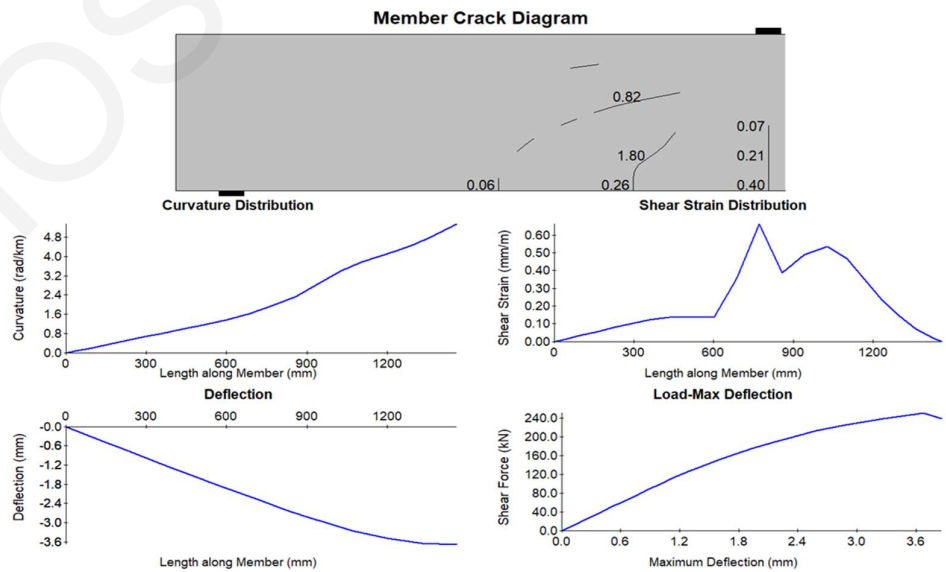
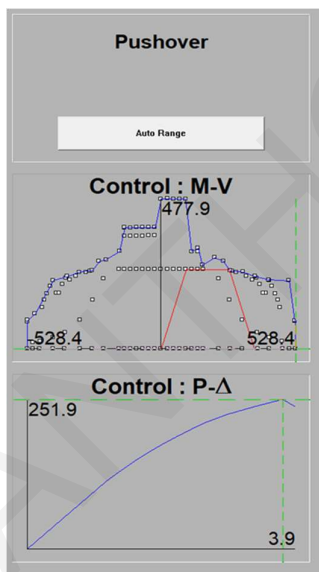


Figure B. 1: Specimen SCD2 experimental envelope curve and response 2000 section and member analysis (Lynn et al., 1998).

Wight and Sozen (1971)
Specimen 25.033(East)

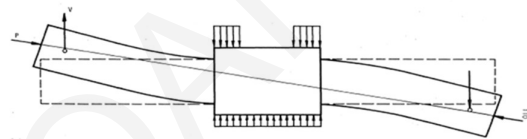
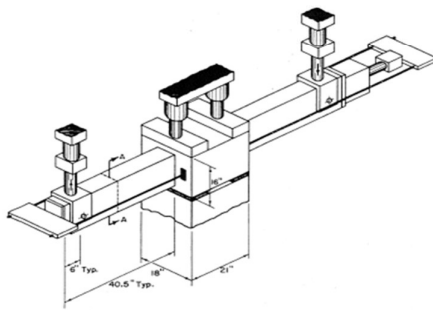
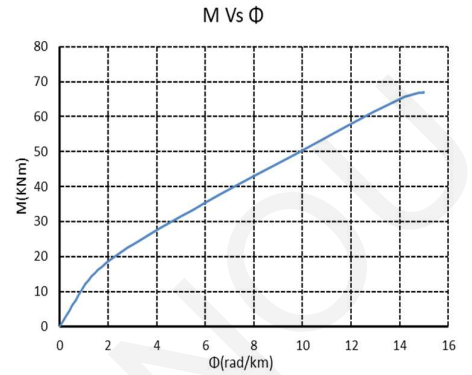
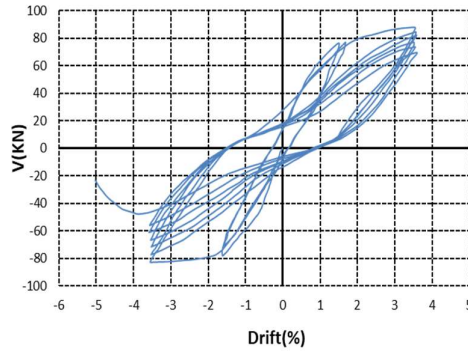
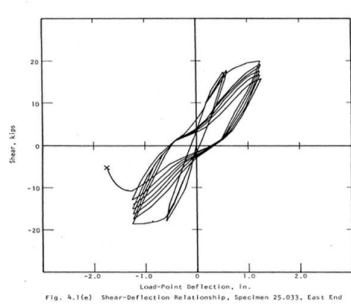


Fig. 2.3 Type of Loads Applied to Test Specimens

Member Response

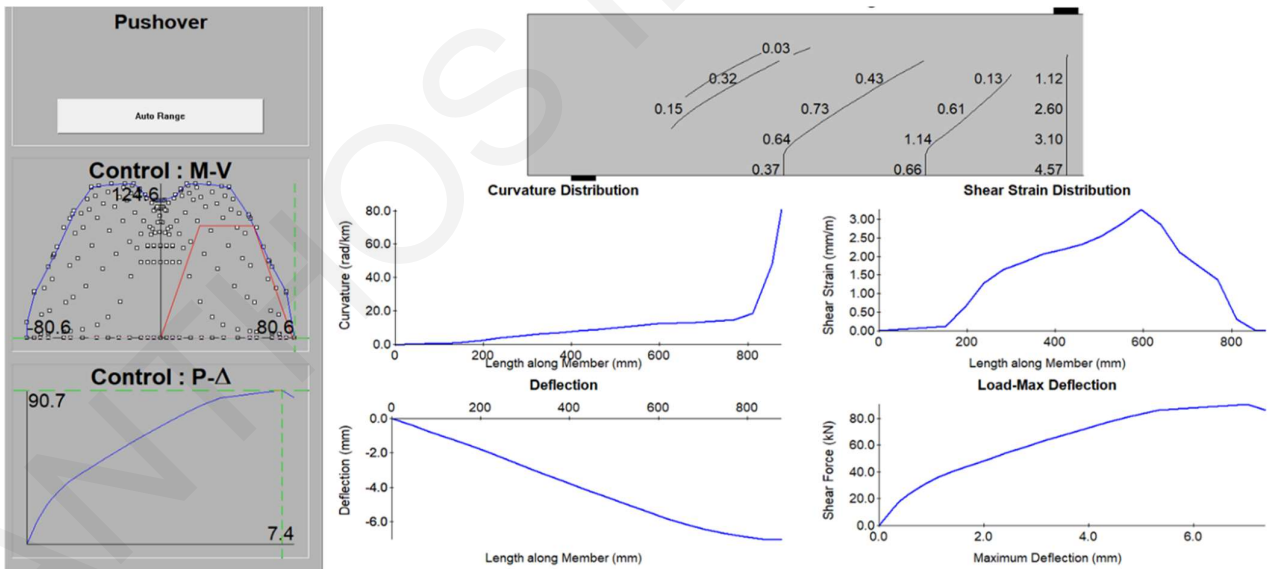


Figure B. 2: Specimen 25.033(East) experimental envelope curve and response 2000 section and member analysis (Wight and Sozen, 1971).

Wight and Sozen (1971)

Specimen 25.033(West)

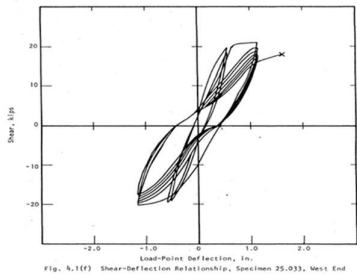


Fig. 4.1(f) Shear-Deflection Relationship, Specimen 25.033, West End

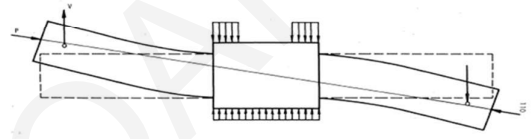
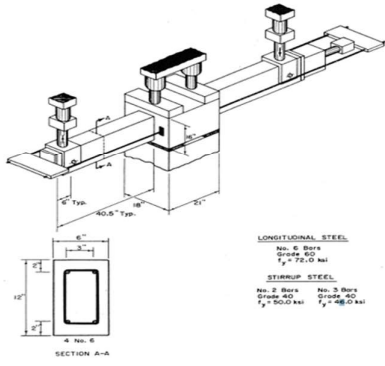
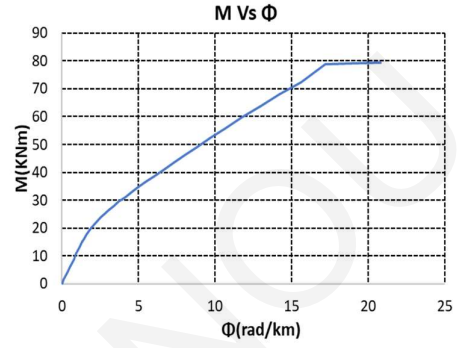
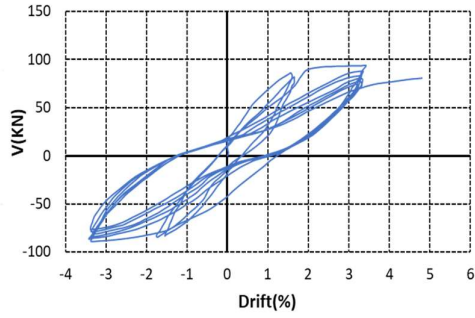


Fig. 2.3 Type of Loads Applied to Test Specimens

Member Response

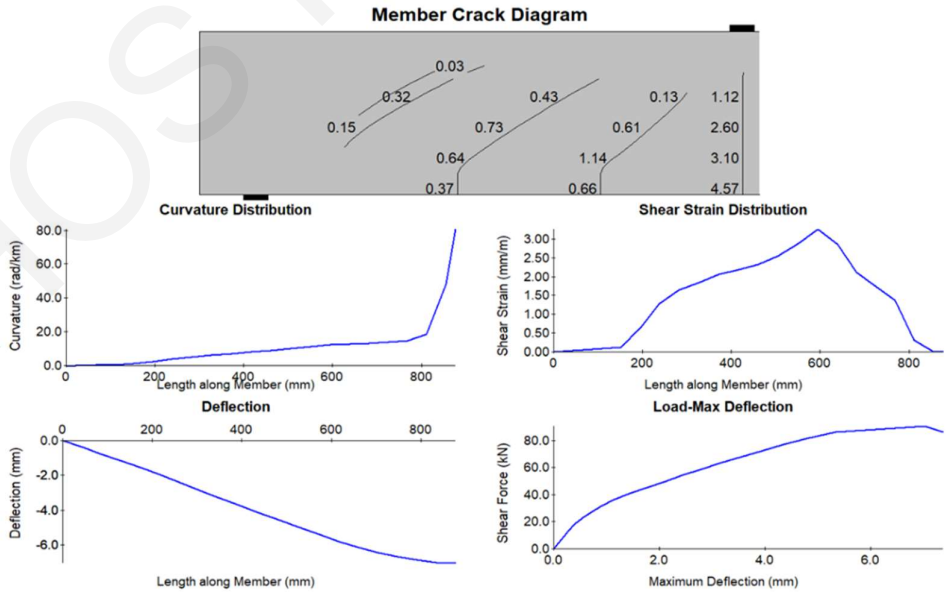
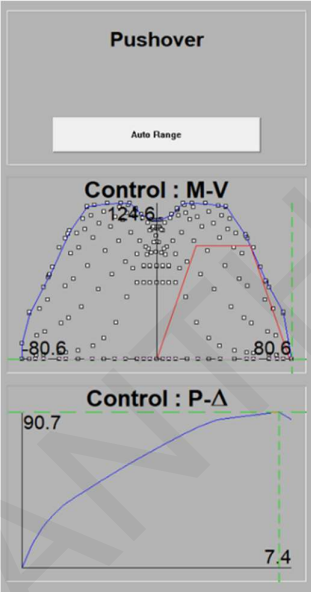


Figure B. 3: Specimen 25.033(West) experimental envelope curve and response 2000 section and member analysis (Wight and Sozen, 1971).

Arakawa (1989)

Specimen OA2

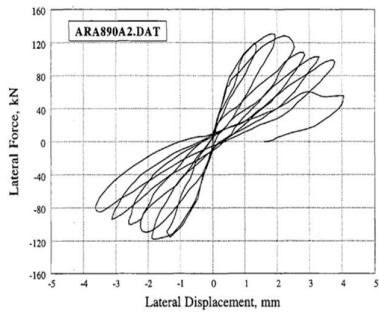
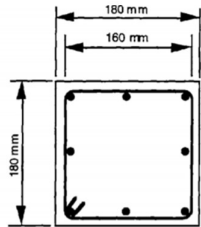
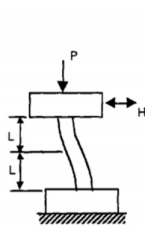
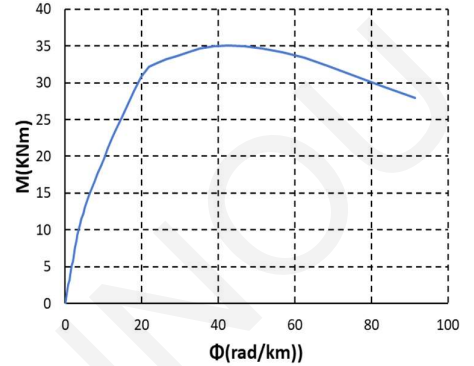
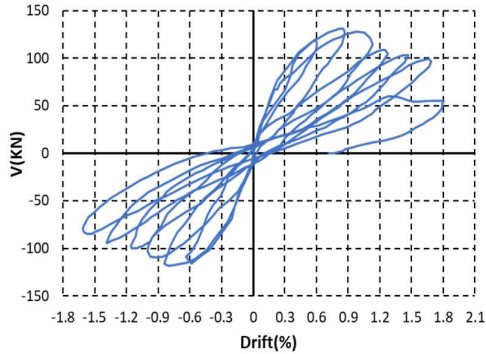


Figure 54. Specimen OA2 of Arakawa 1989



Specimens OA2 and OA5

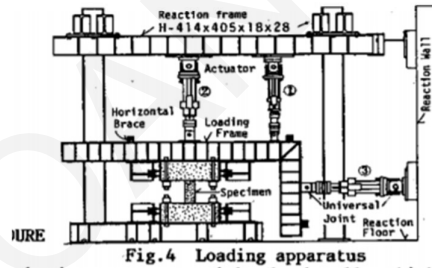


Fig.4 Loading apparatus

Member Response

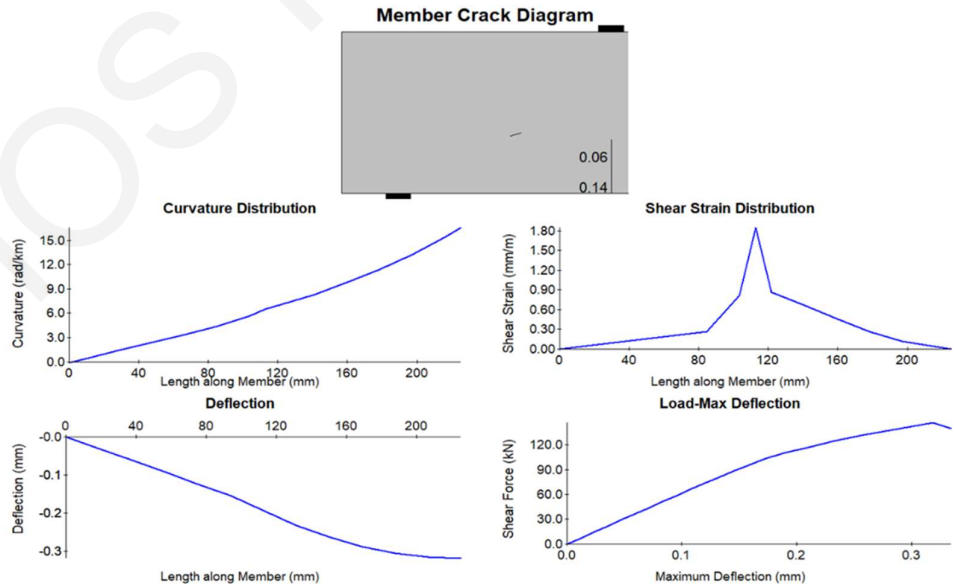
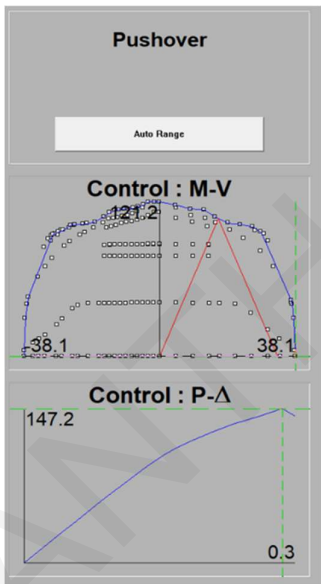


Figure B. 4: Specimen OA2, experimental envelope curve and response 2000 section and member analysis (Arakawa et al., 1989).

Arakawa 1989

Specimen OA5

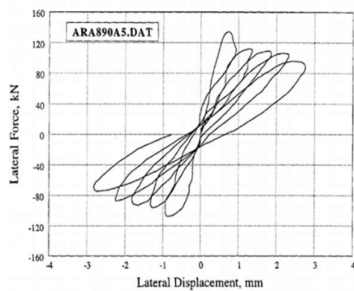


Figure 55. Specimen OA5 of Arakawa 1989

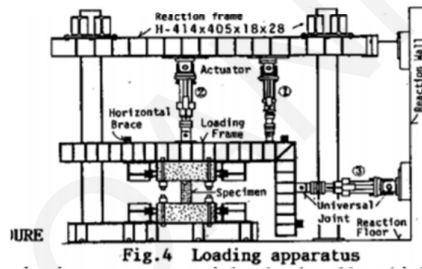
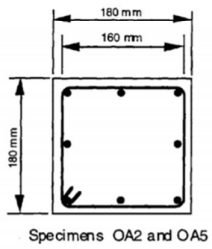
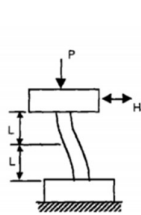
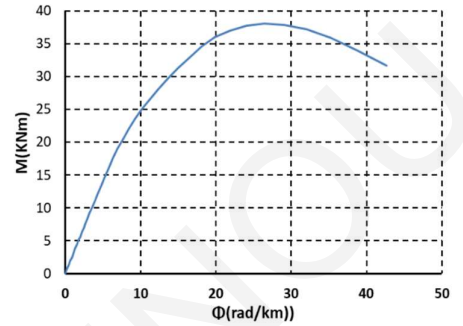
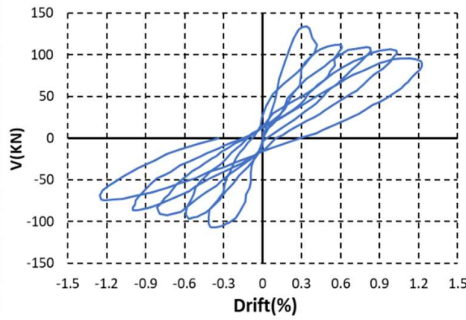
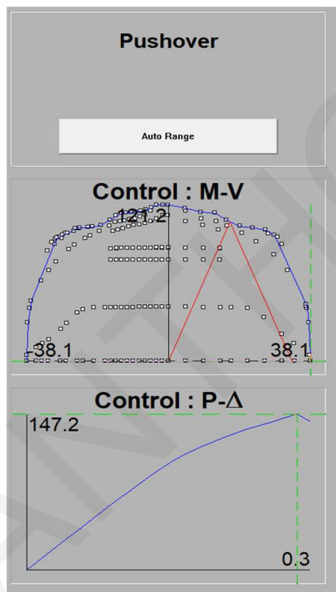


Fig.4 Loading apparatus

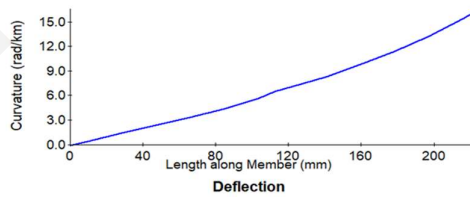
Member Response



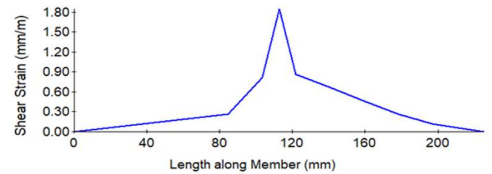
Member Crack Diagram



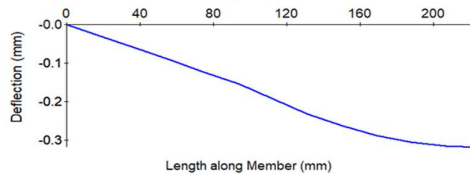
Curvature Distribution



Shear Strain Distribution



Deflection



Load-Max Deflection

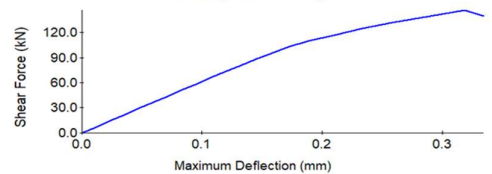


Figure B. 5: Specimen OA5, experimental envelope curve and response 2000 section and member analysis (D).

Umehara and Jirsa (1982)

Specimen CUS

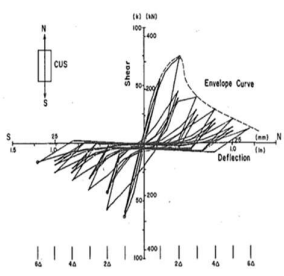
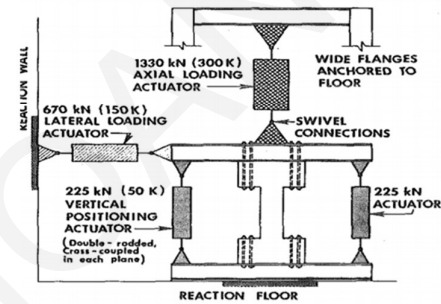
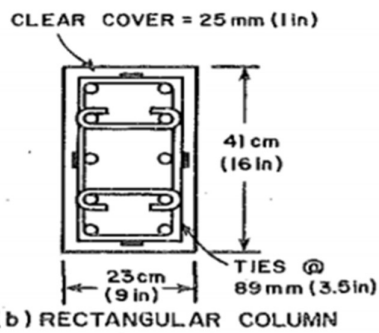
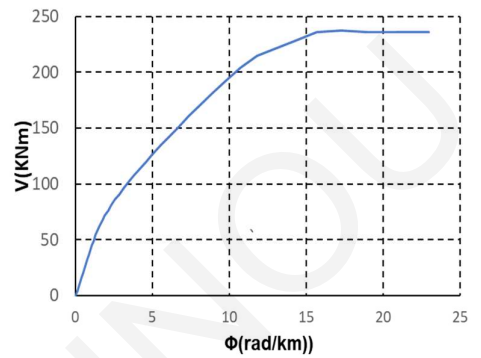
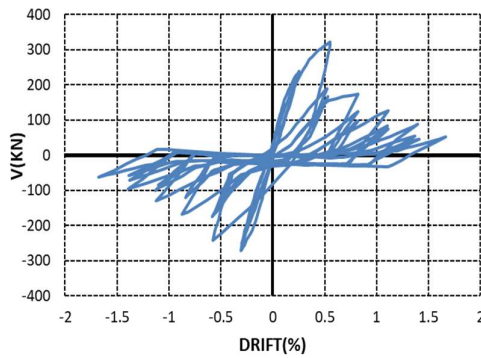


FIG. 6.—Load-Deflection Curves—CUS



Member response

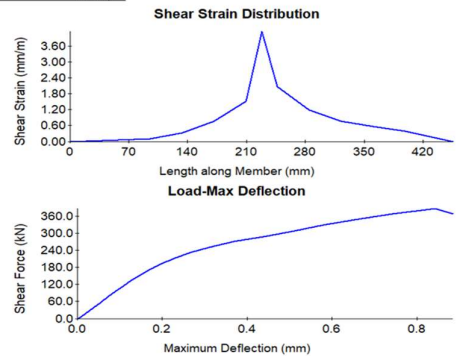
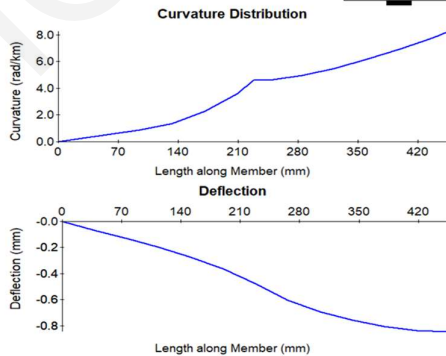
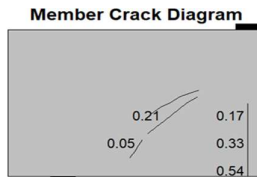
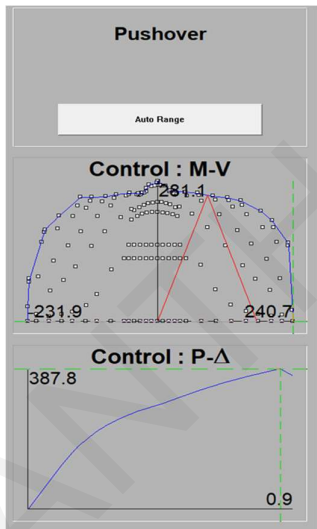
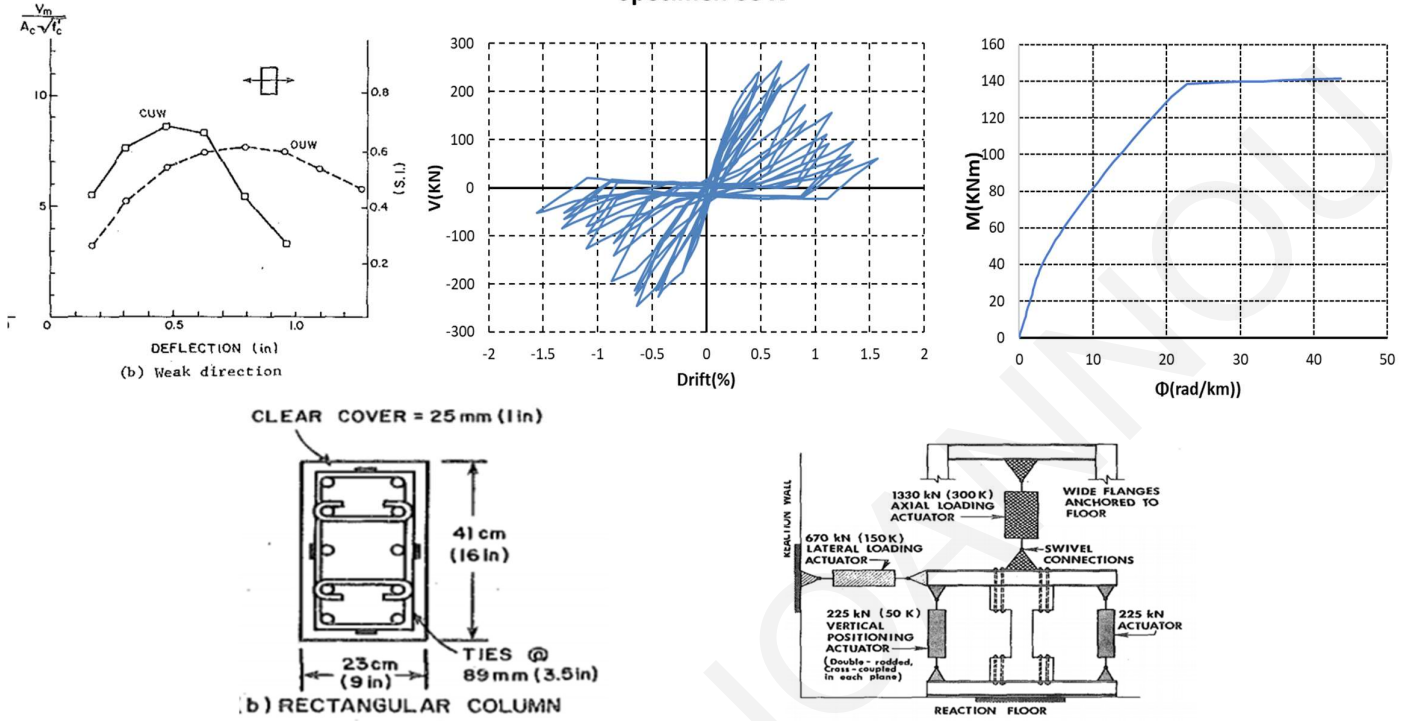


Figure B. 6: Specimen CUS, experimental envelope curve and response 2000 section and member analysis (Umehara and Jirsa, 1982).

Umehara and Jirsa (1982)

Specimen CUW



Member Response

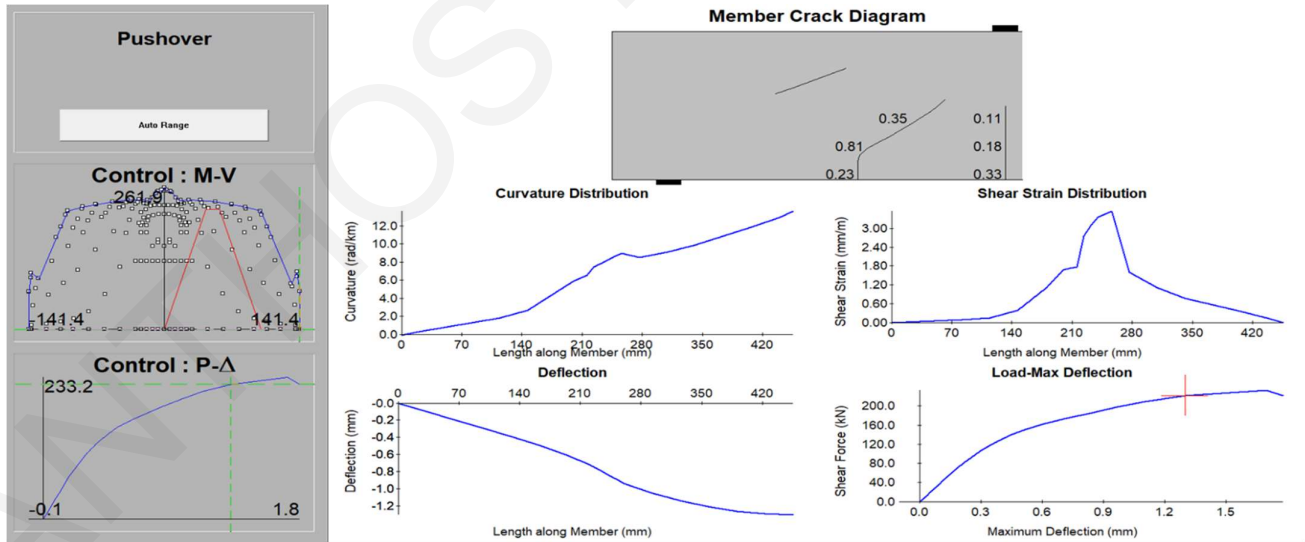
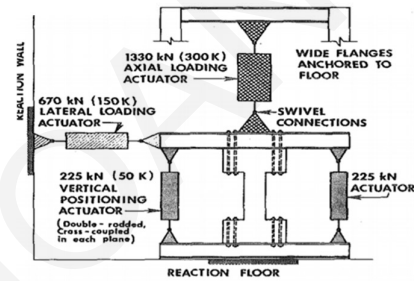
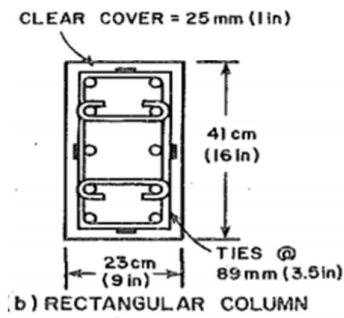
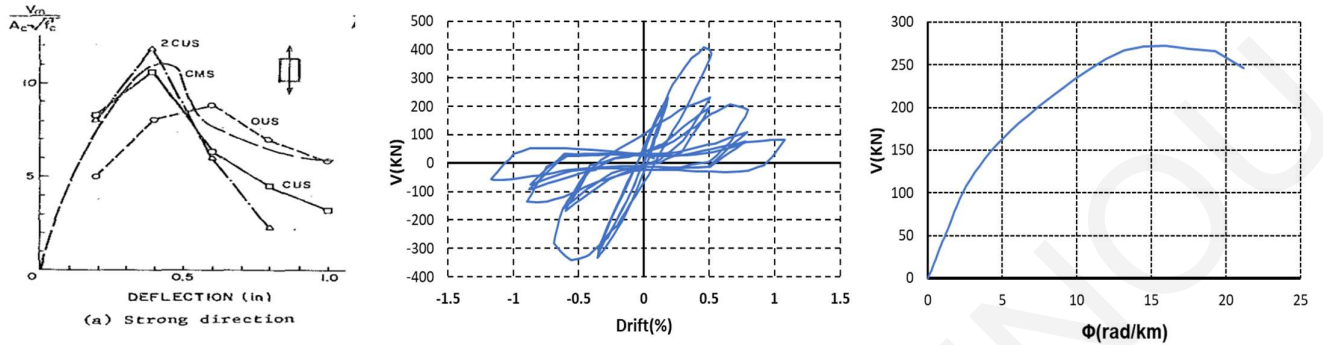


Figure B. 6: Specimen CUW, experimental envelope curve and response 2000 section and member analysis (Umehara and Jirsa, 1982).

Umehara and Jirsa (1982)

Specimen 2CUS



Member Response

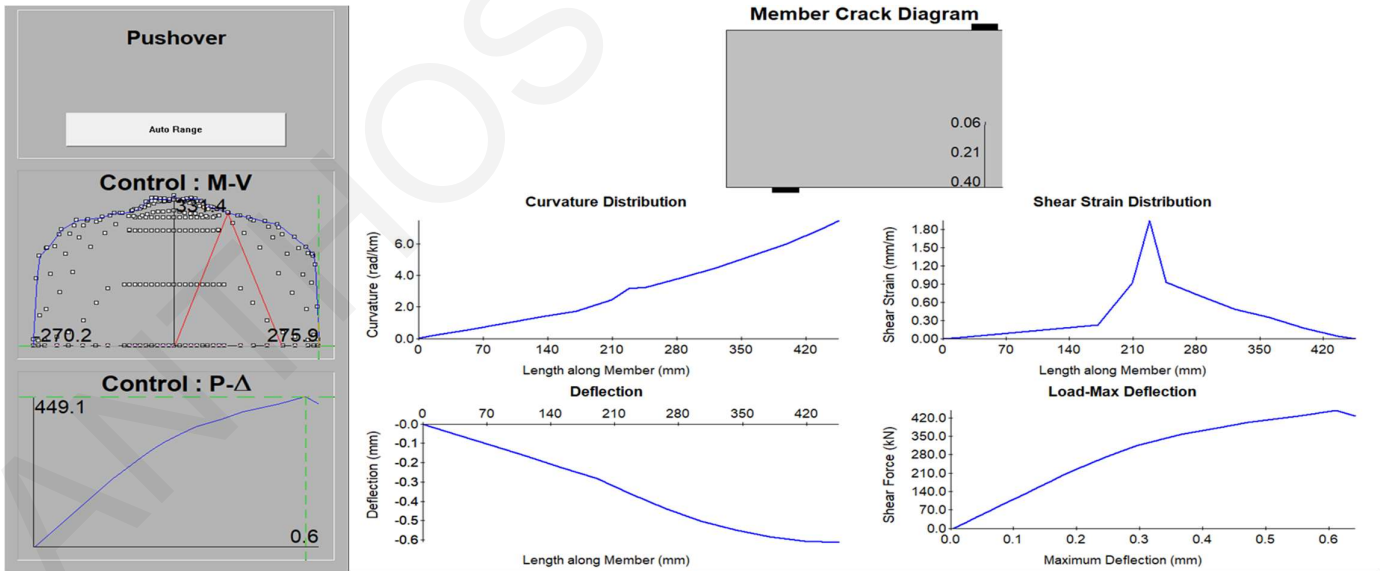


Figure B. 7: Specimen 2CUS, experimental envelope curve and response 2000 section and member analysis (Umehara and Jirsa, 1982).

Bett et al. (1985)

Specimen 1-1

43

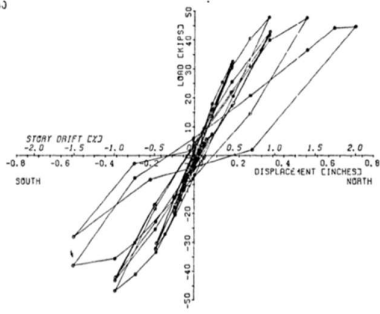
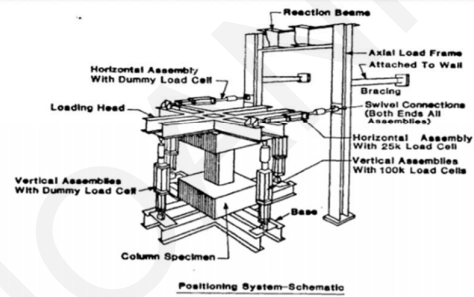
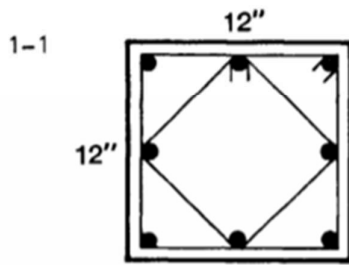
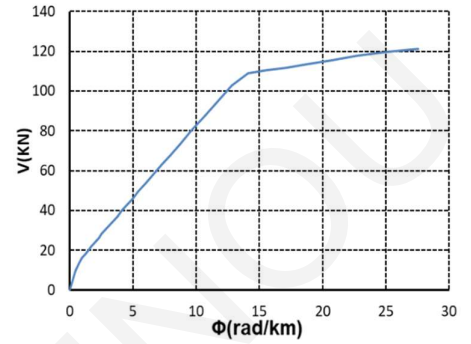
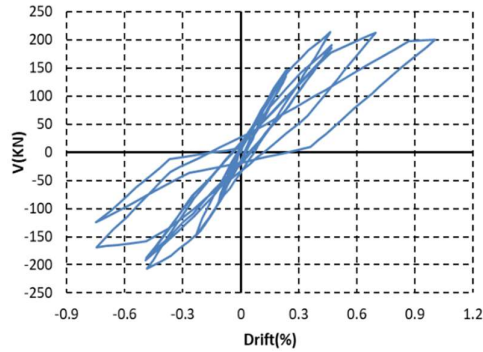
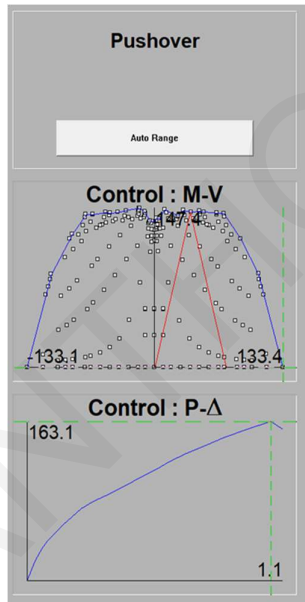


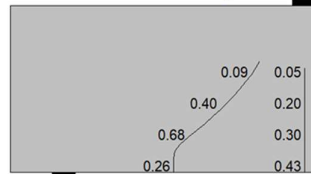
Fig. 4.1 Load-deflection curve, Specimen 1-1



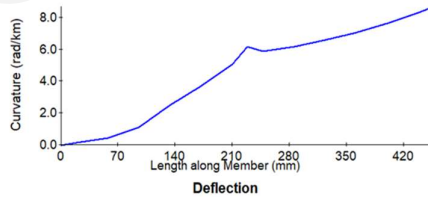
Member Response



Member Crack Diagram



Curvature Distribution



Shear Strain Distribution

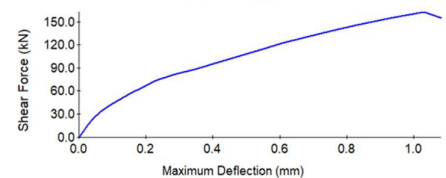
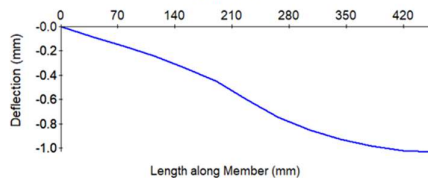
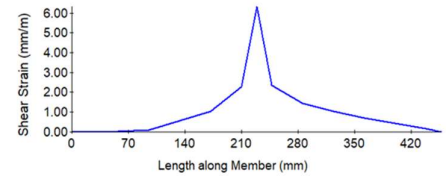
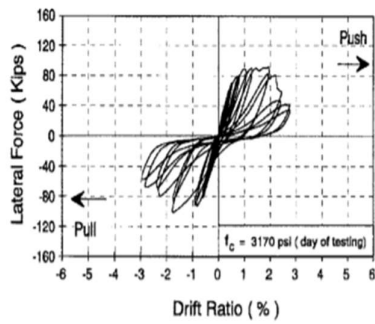


Figure B. 8: Specimen 1-1, experimental envelope curve and response 2000 section and member analysis (Bett et al., 1985).

Aboutaha (1999)

Specimen SC3



(a) Basic Unstrengthened Column SC3

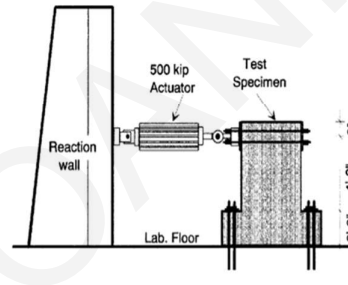
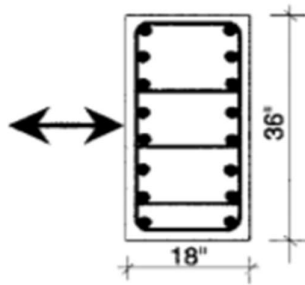
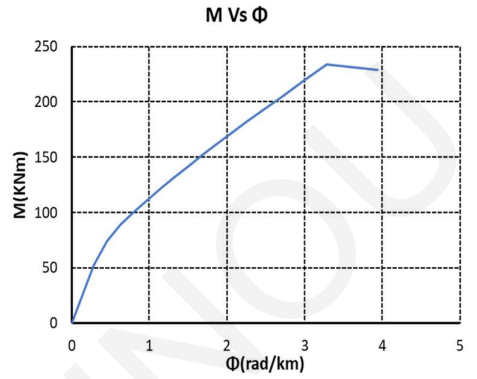
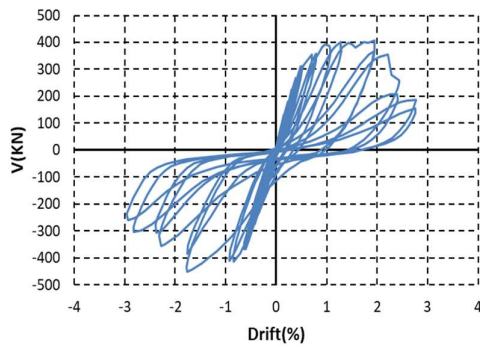


Fig. 1—Test setup.

Member Response

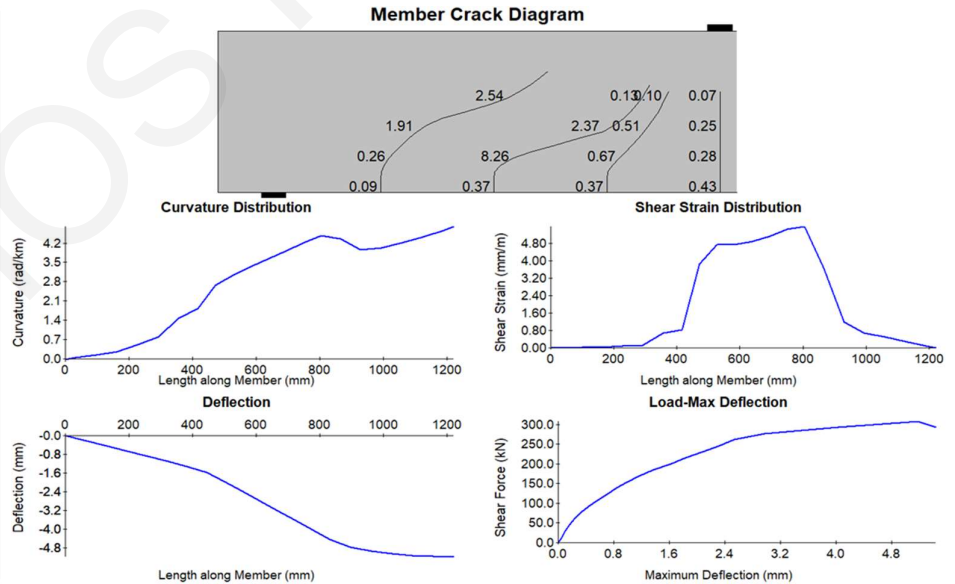
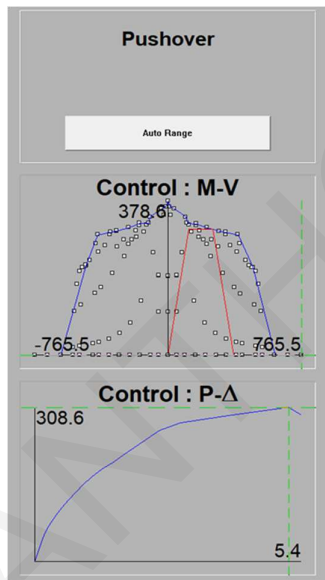
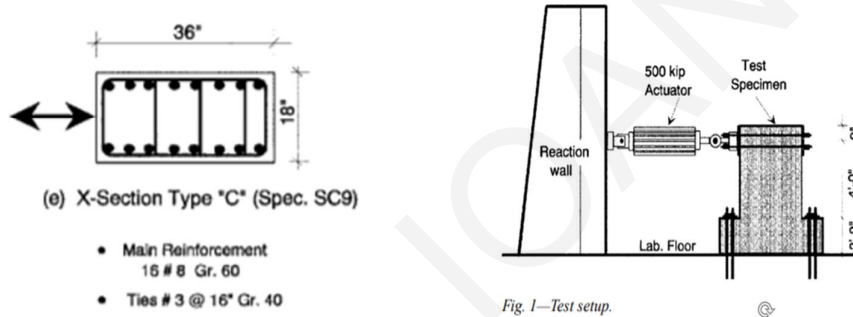
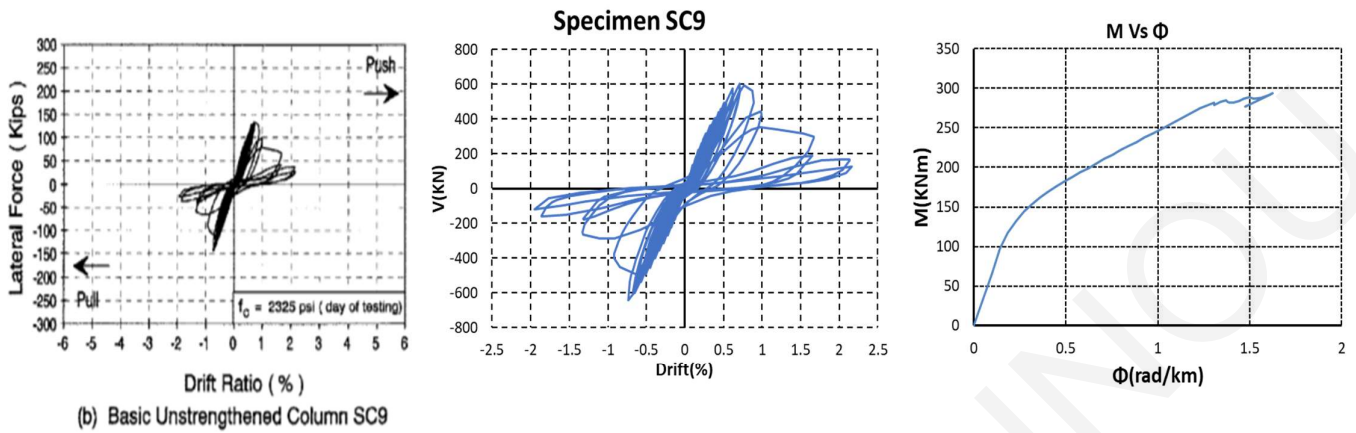


Figure B. 9: Specimen SC3, experimental envelope curve and response 2000 section and member analysis (Aboutaha et al., 1999).

Aboutaha (1999)



Member Response

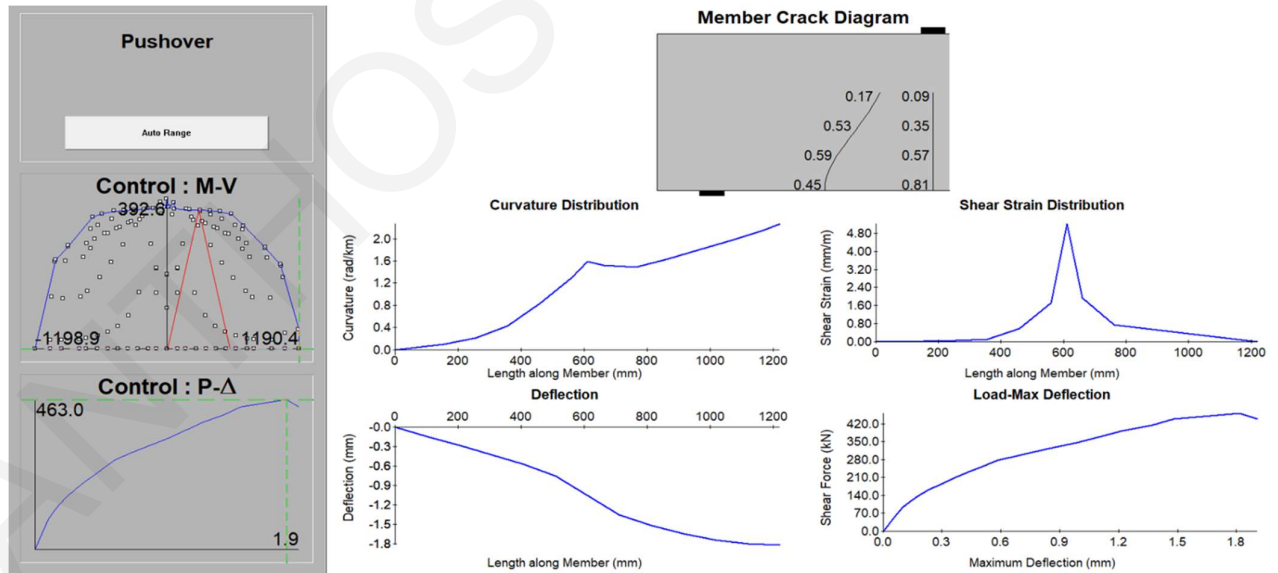


Figure B. 10: Specimen SC9, experimental envelope curve and response 2000 section and member analysis (Aboutaha et al., 1999).

Zhou et al. (1987)

Specimen 104-08

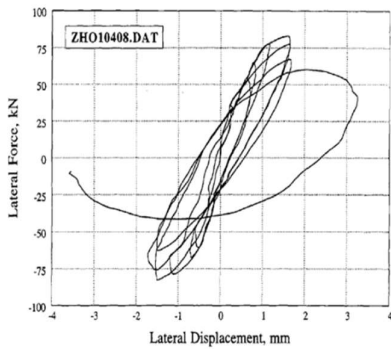
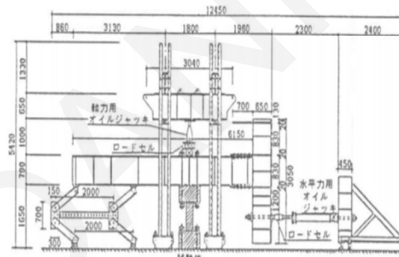
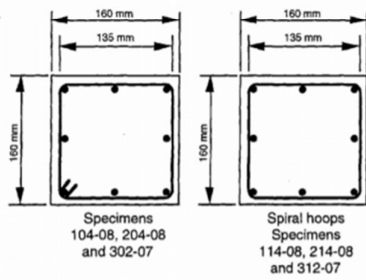
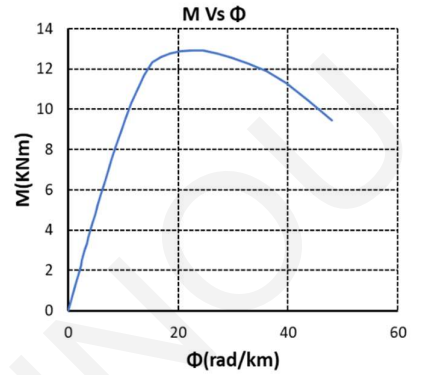
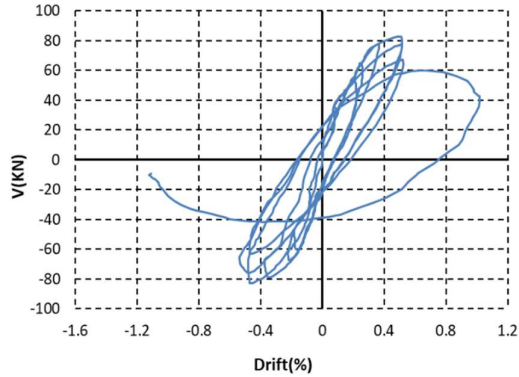
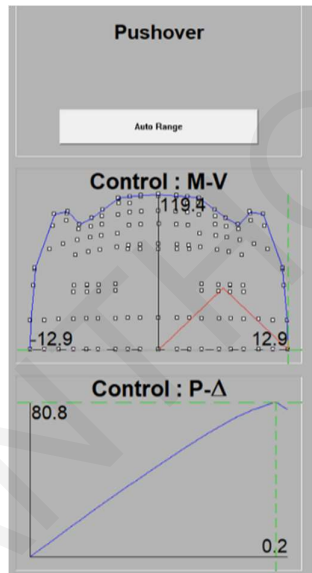


Figure 39. Specimen 104-08 of Zhou et al. 1987



Member Response



Member Crack Diagram

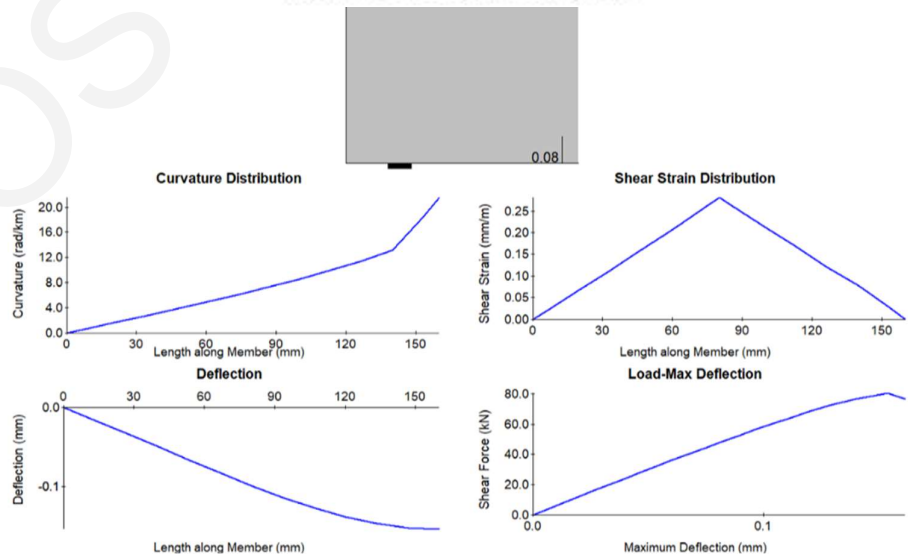


Figure B. 11: Specimen 104-08, experimental envelope curve and response 2000 section and member analysis (Zhou et al., 1987).

Zhou et al. (1987)

Specimen 114-08

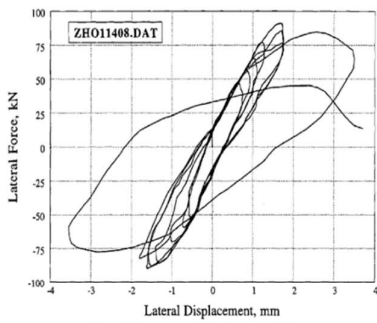


Figure 40. Specimen 114-08 of Zhou et al. 1987

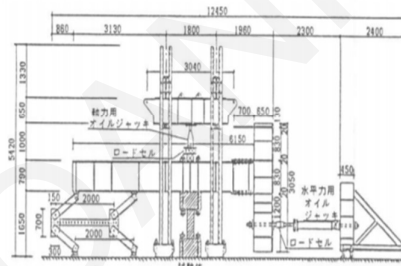
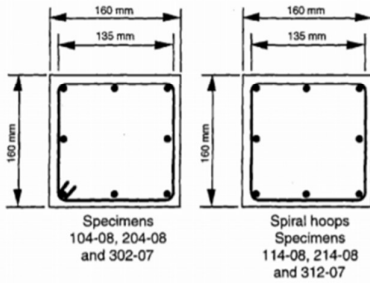
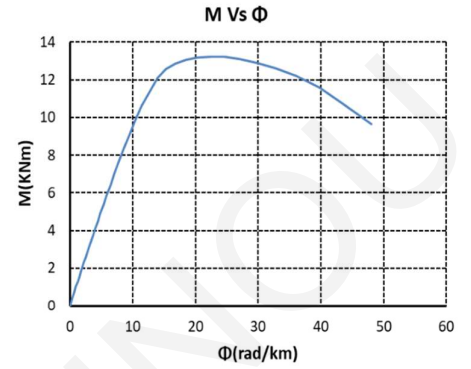
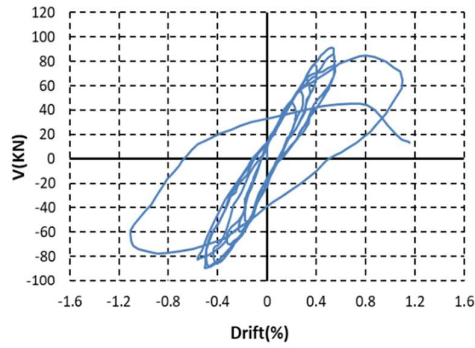


図2 加力装置

Member Response

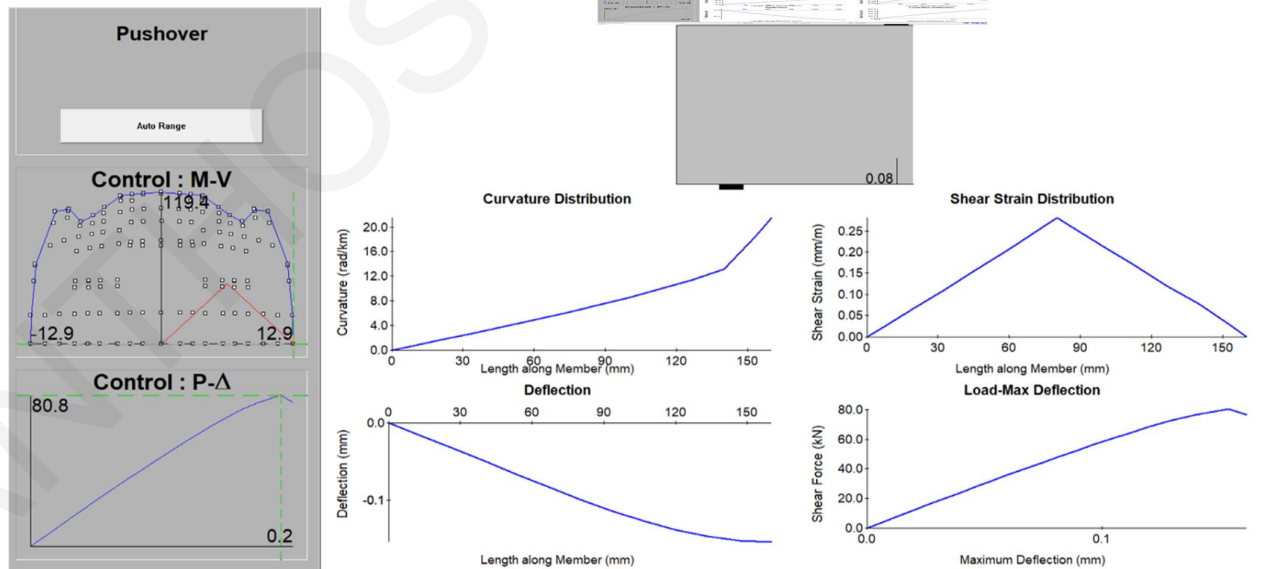


Figure B. 12: Specimen 114-08, experimental envelope curve and response 2000 section and member analysis (Zhou et al., 1987).

Heankhaus et al. (2013)

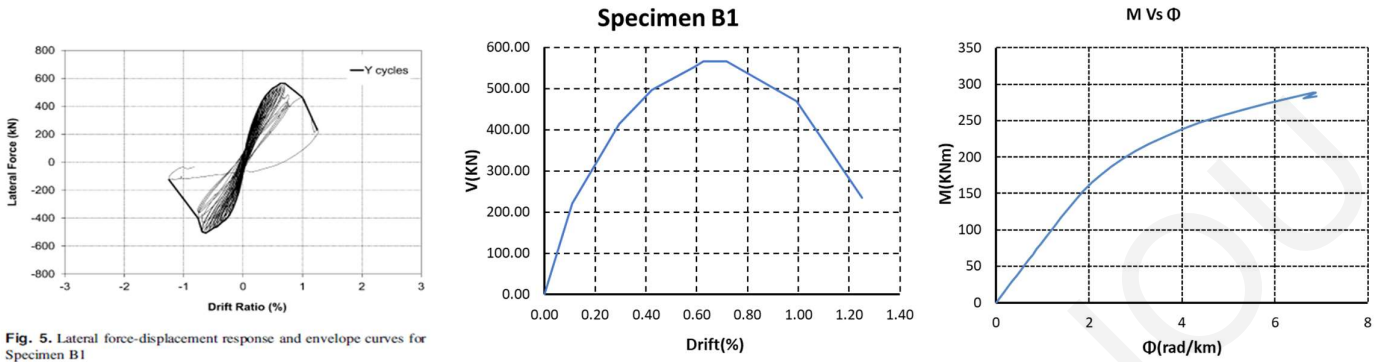


Fig. 5. Lateral force-displacement response and envelope curves for Specimen B1

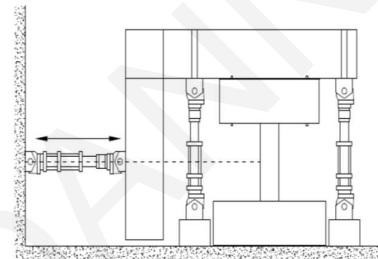
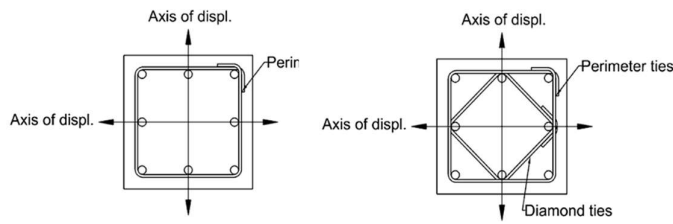


Figure A-32 Elevation view of test setup used at Bowen Laboratory for Specimens #1 and #2

Member Response

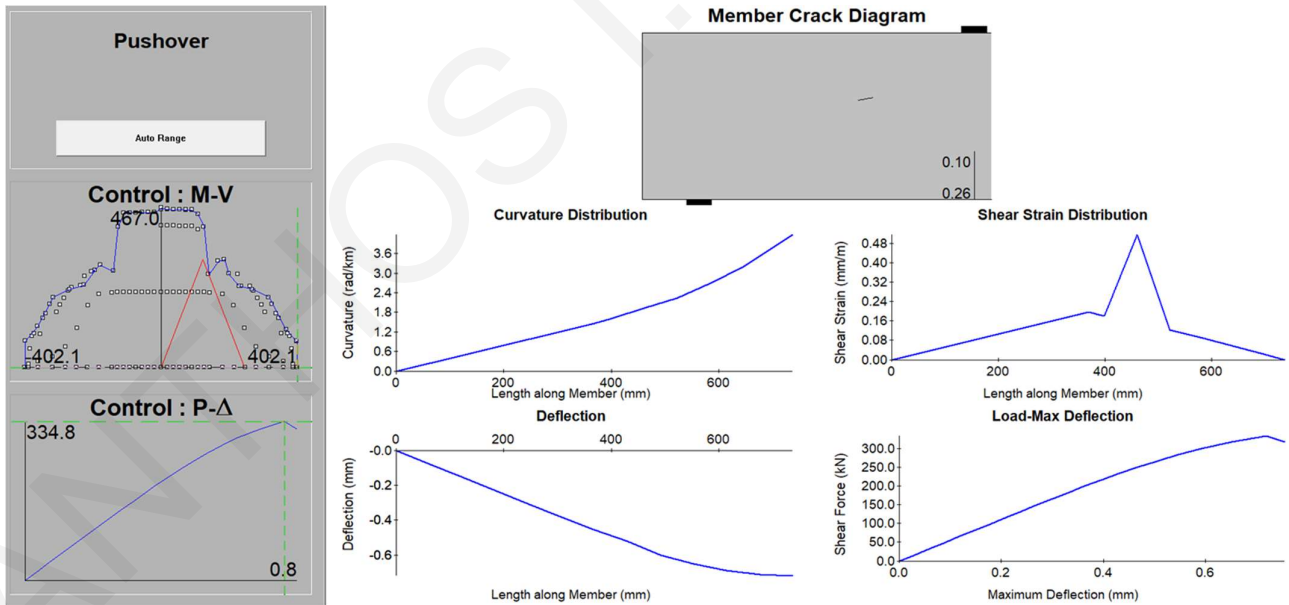


Figure B.13: Specimen B1, experimental envelope curve and response 2000 section and member analysis (Heankhaus et al., 2013).

Specimen B2

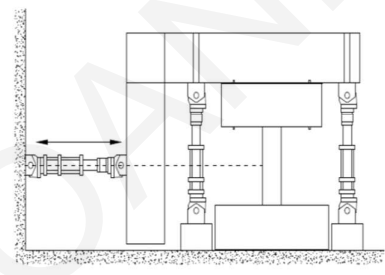
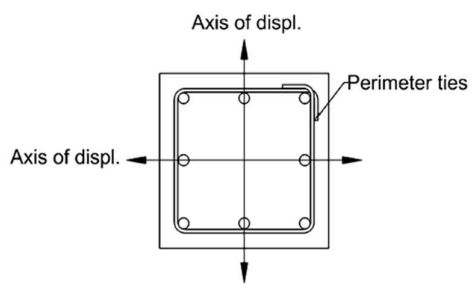
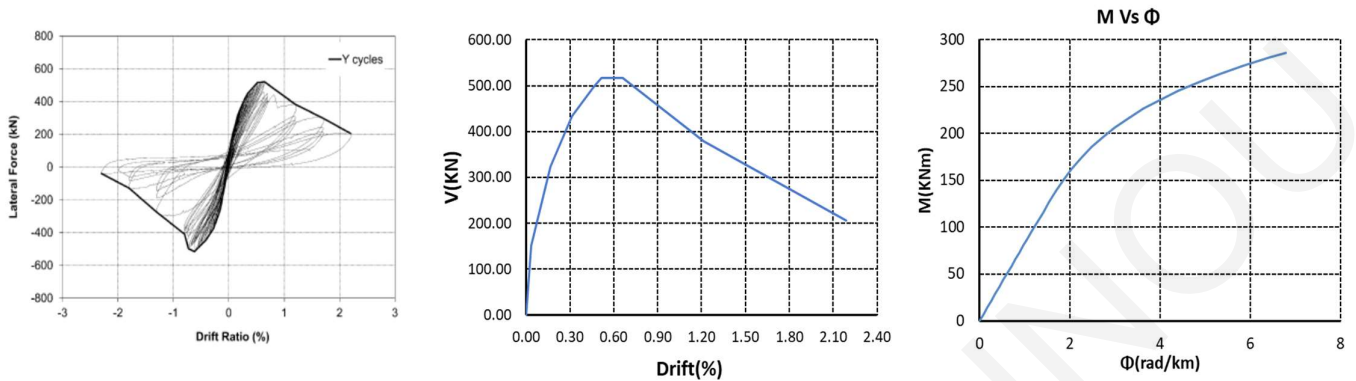


Figure A - 32 Elevation view of test setup used at Bowen Laboratory for Specimens #1 and #2

Member Response

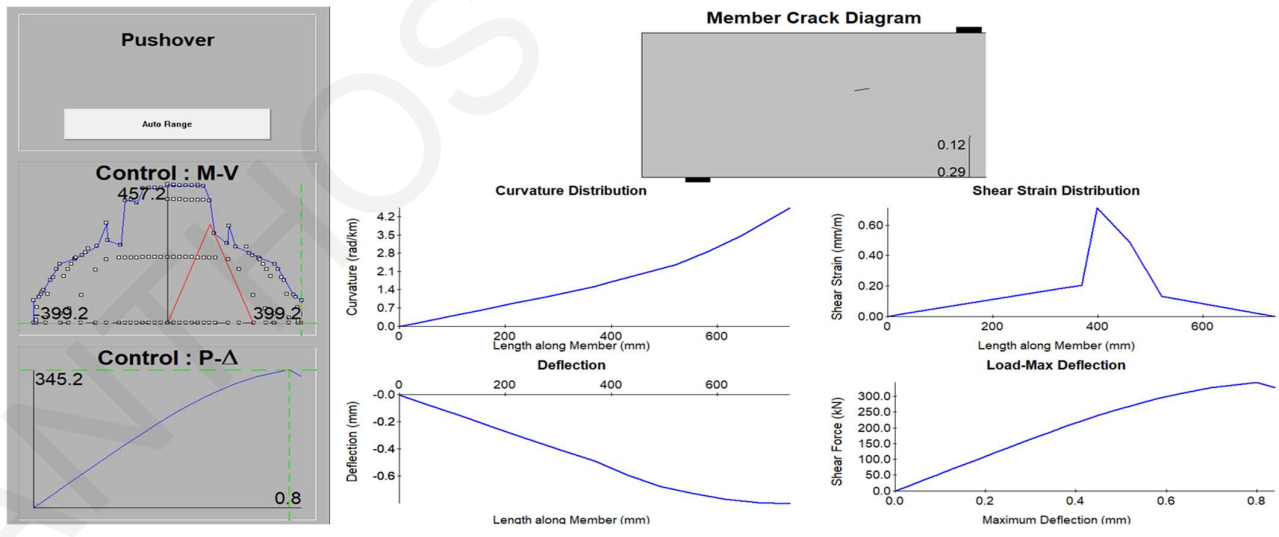
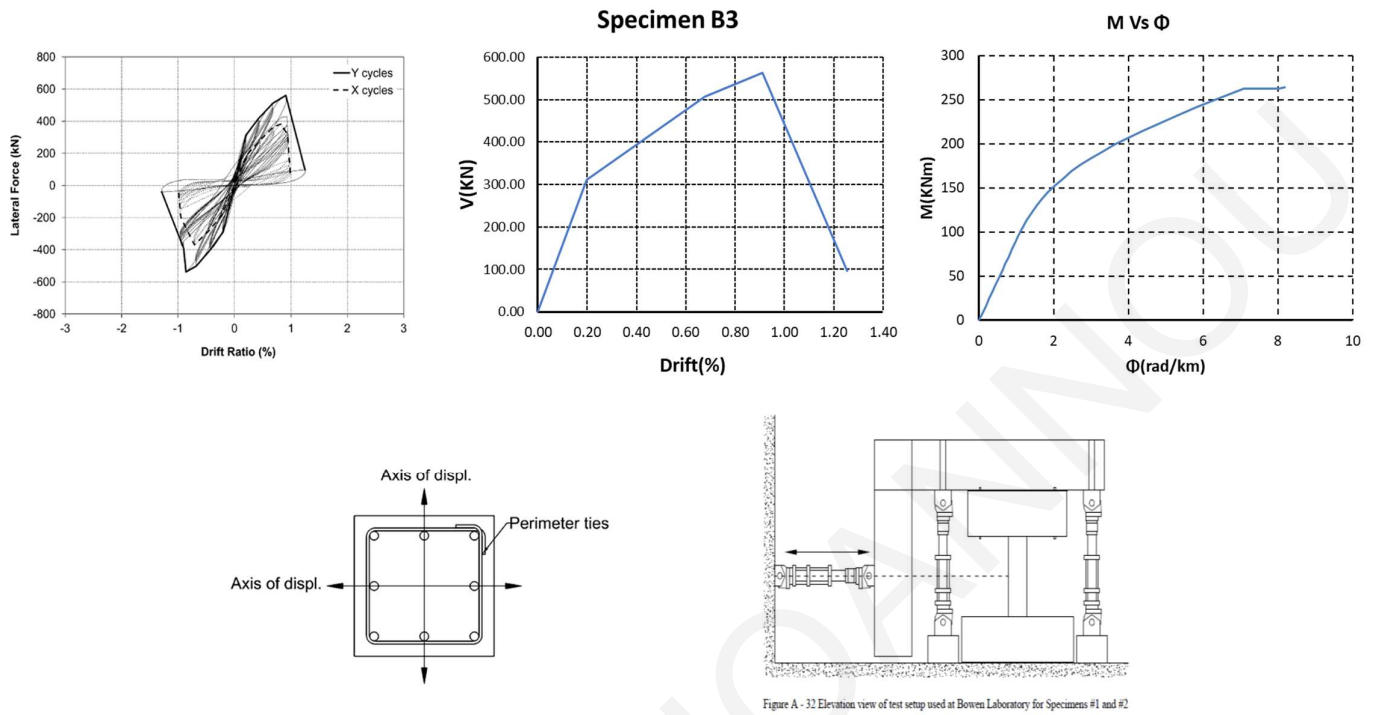


Figure B. 14: Specimen B2, experimental envelope curve and response 2000 section and member analysis (Heankhaus et al., 2013).

Heankhaus et al. (2013)



Member Response

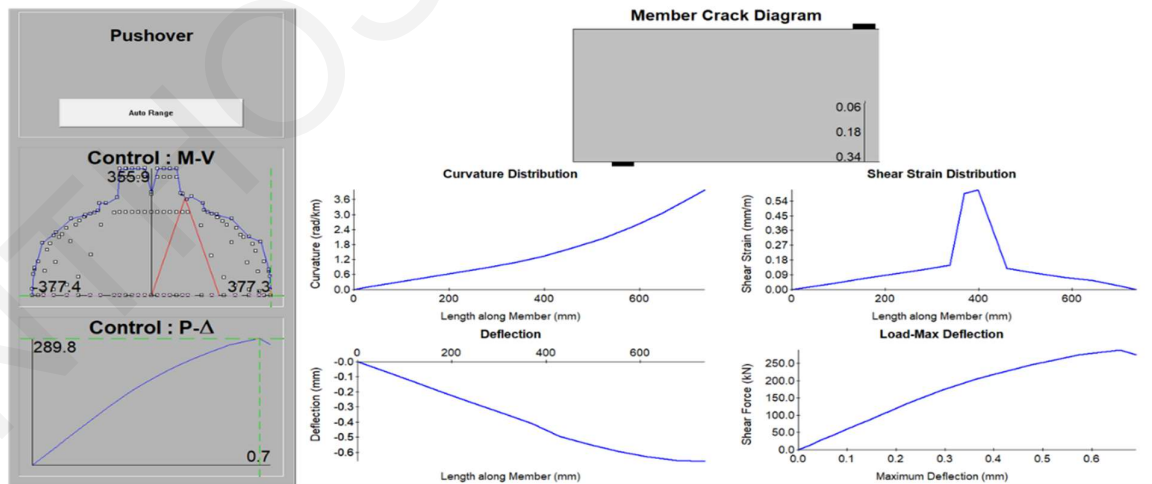


Figure B. 15: Specimen B3, experimental envelope curve and response 2000 section and member analysis (Heankhaus et al., 2013).

Heankhaus et al. (2013)

Specimen B4

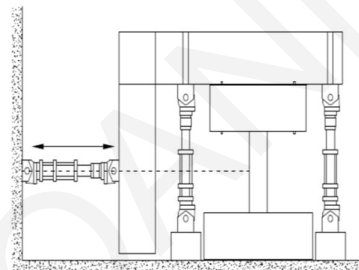
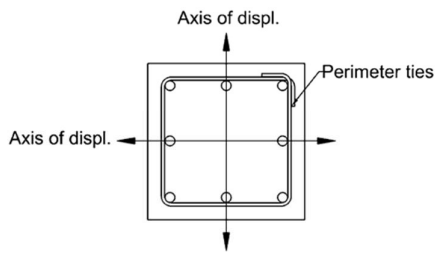
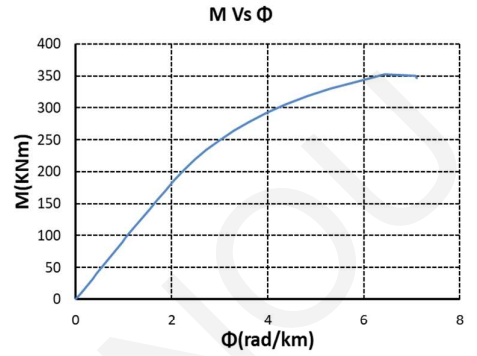
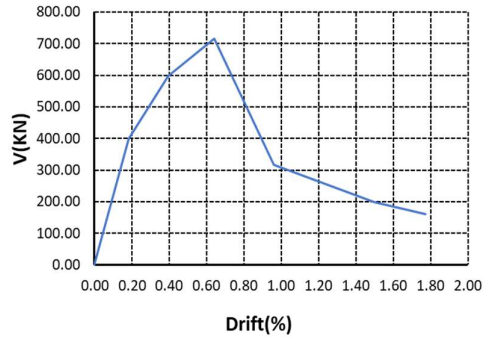
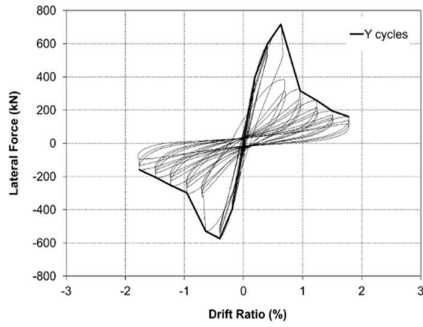
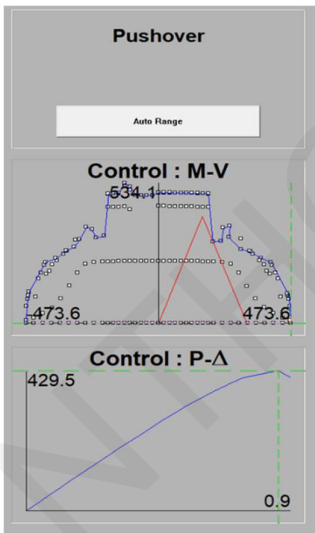


Figure A - 32 Elevation view of test setup used at Bowen Laboratory for Specimens #1 and #2

Member Response



Member Crack Diagram

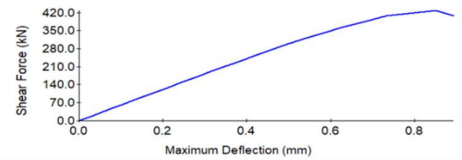
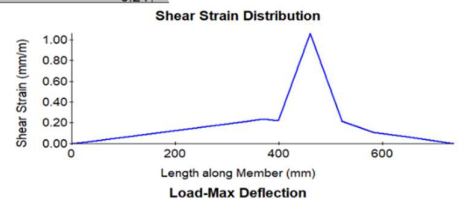
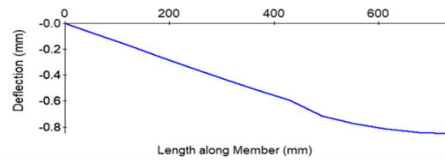
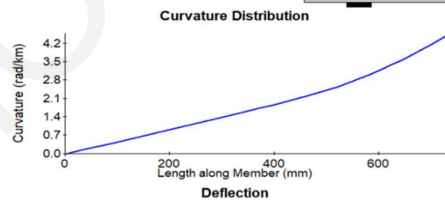


Figure B. 16: Specimen B4, experimental envelope curve and response 2000 section and member analysis (Heankhaus et al., 2013).

Heankhaus et al. (2013)

Specimen B5

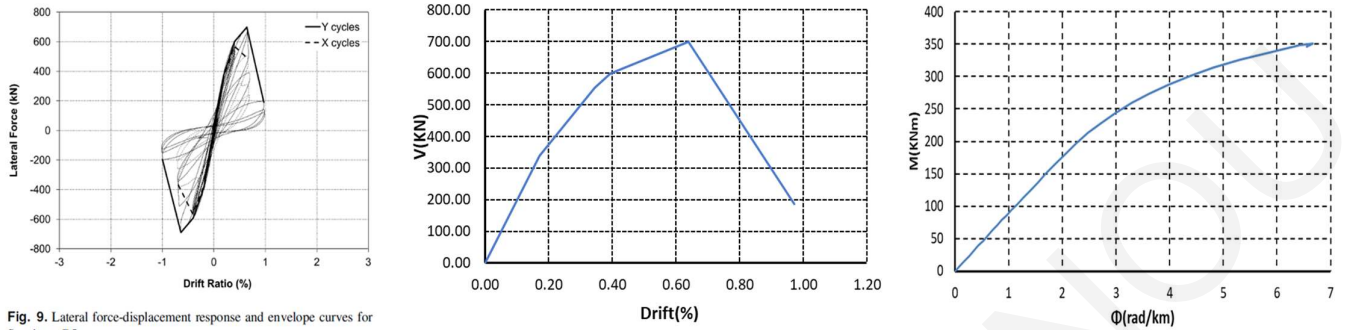


Fig. 9. Lateral force-displacement response and envelope curves for Specimen B5

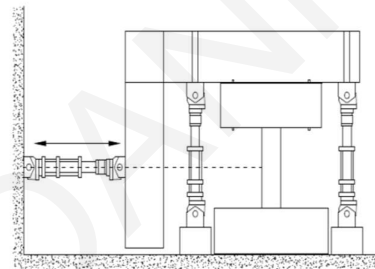
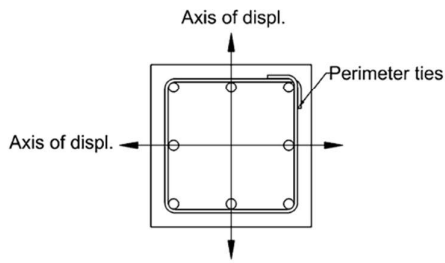


Figure A-32 Elevation view of test setup used at Bowen Laboratory for Specimens #1 and #2

Member Response

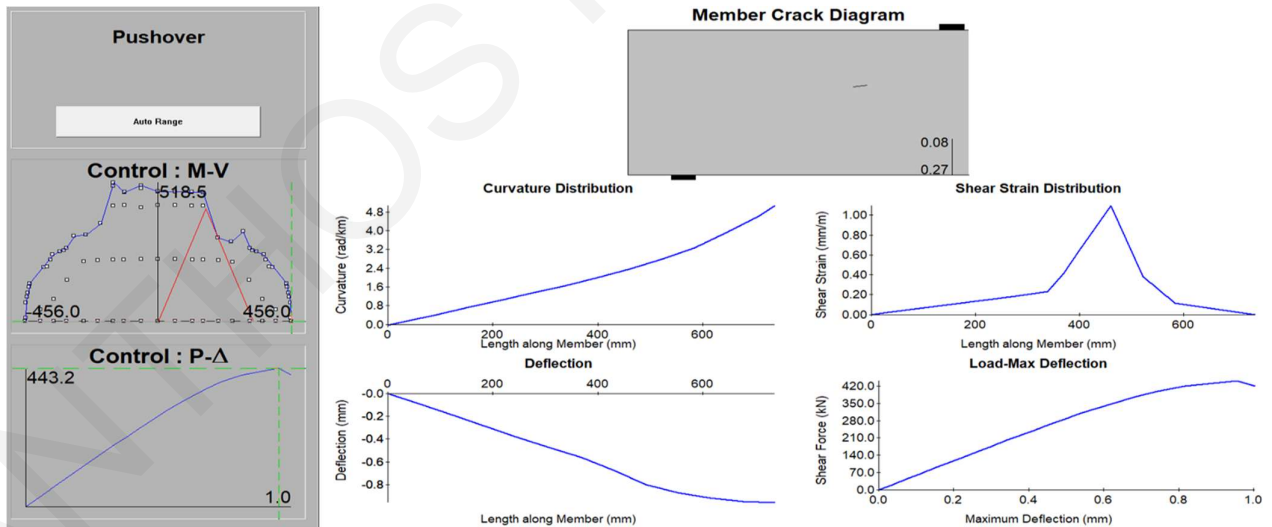


Figure B. 17: Specimen B5, experimental envelope curve and response 2000 section and member analysis (Heankhaus et al., 2013).

Heankhaus et al. (2013)

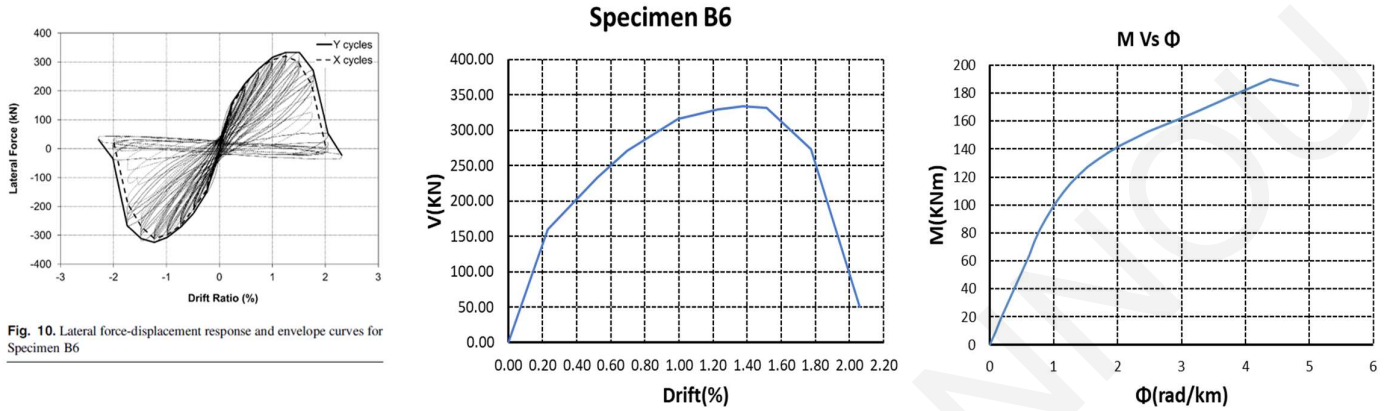
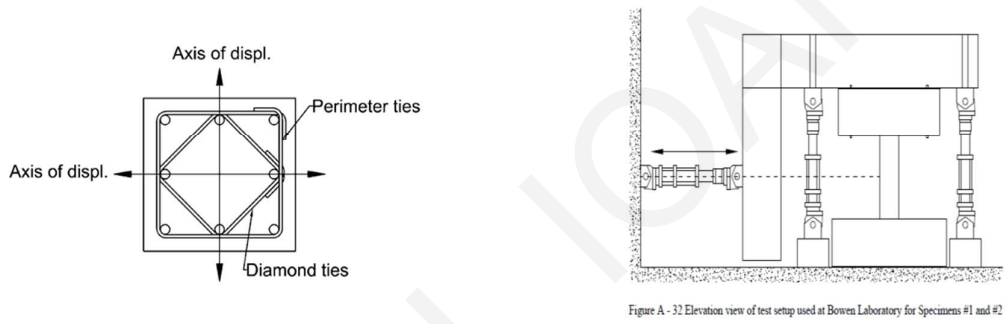


Fig. 10. Lateral force-displacement response and envelope curves for Specimen B6



Member Response

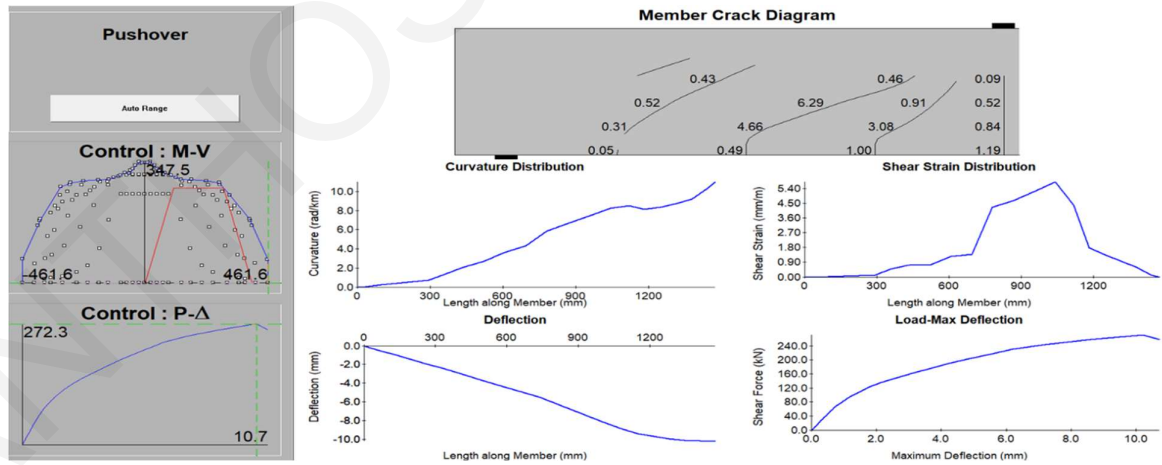


Figure B. 18: Specimen B6, experimental envelope curve and response 2000 section and member analysis (Heankhaus et al., 2013).

Heankhaus et al. (2013)

Specimen B7

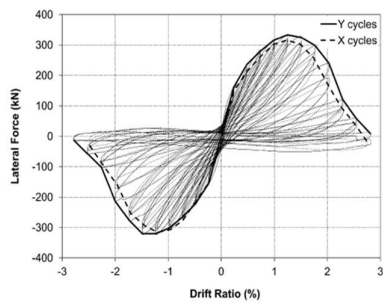


Fig. 11. Lateral force-displacement response and envelope curves for Specimen B7

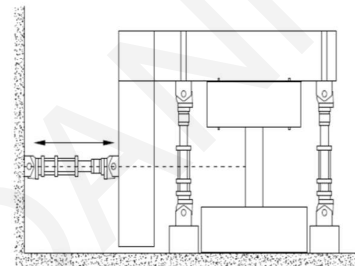
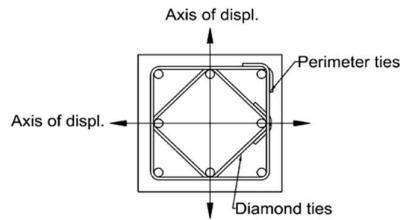
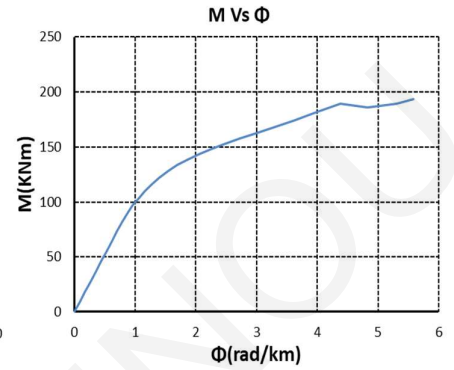
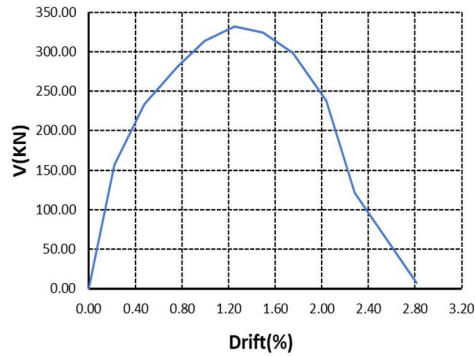


Figure A-32 Elevation view of test setup used at Bowen Laboratory for Specimens #1 and #2

Member Response

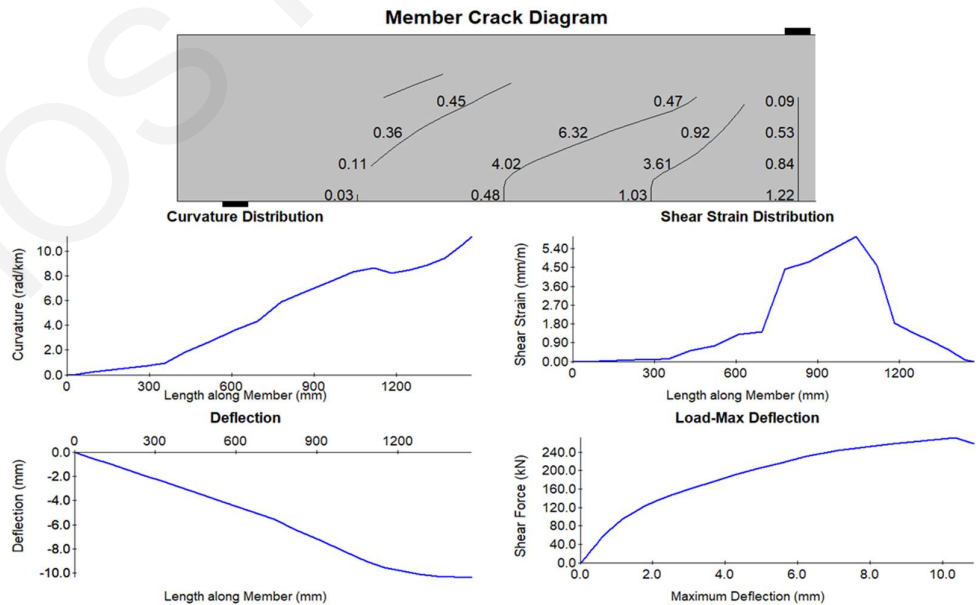
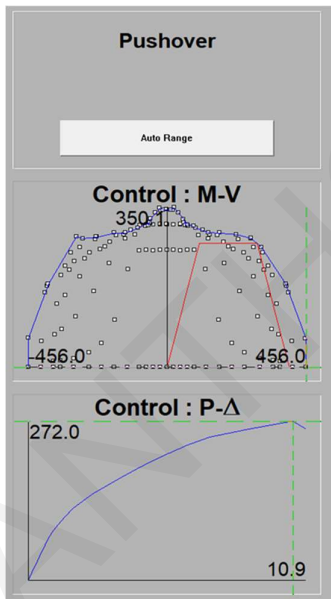


Figure B. 19: Specimen B7, experimental envelope curve and response 2000 section and member analysis (Heankhaus et al., 2013).

Heankhaus et al. (2013)

Specimen B8

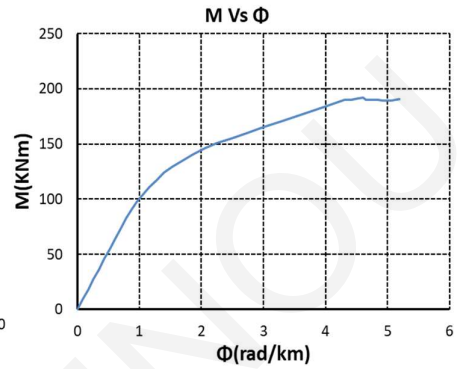
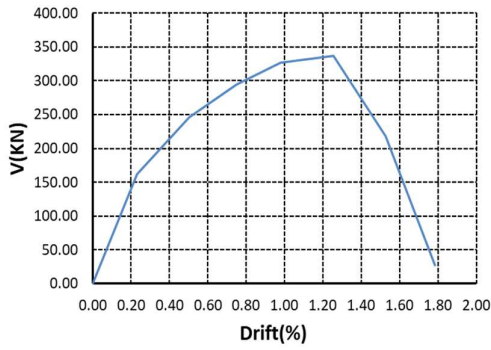
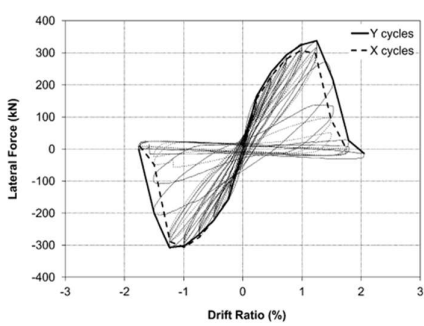


Fig. 12. Lateral force-displacement response and envelope curves for Specimen B8

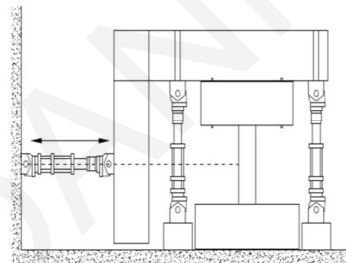
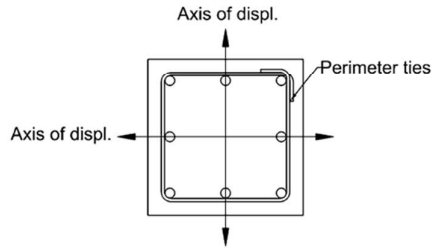


Figure A - 32 Elevation view of test setup used at Bowen Laboratory for Specimens #1 and #2

Member Response

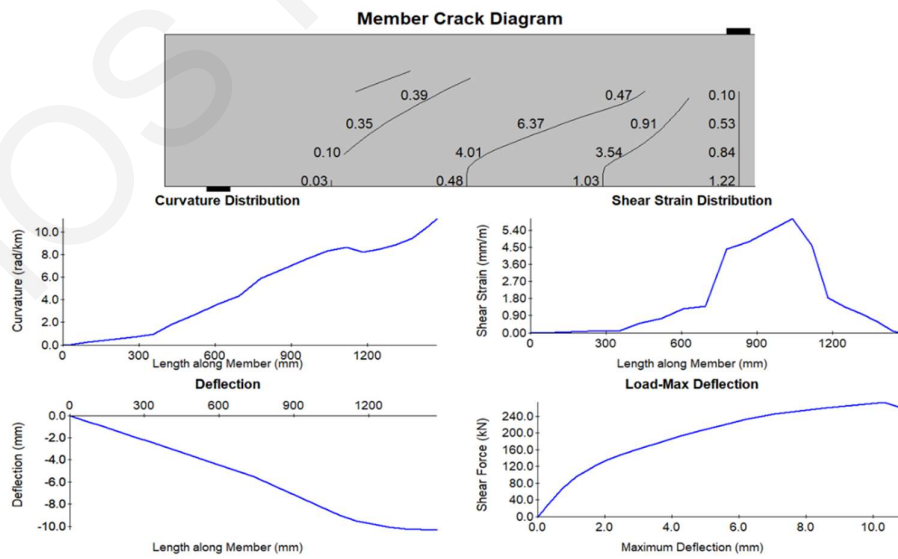
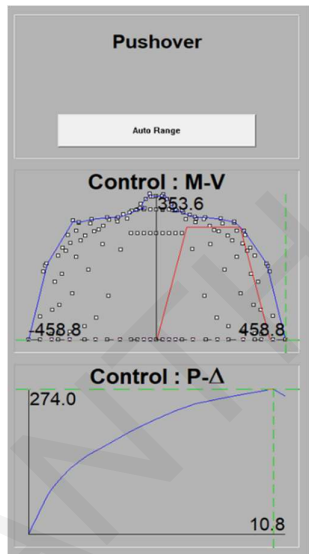


Figure B. 20: Specimen B8, experimental envelope curve and response 2000 section and member analysis (Heankhaus et al., 2013).

Kim et al. (2018)

Specimen SBd2

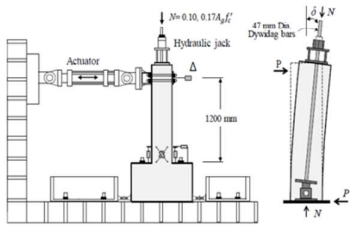
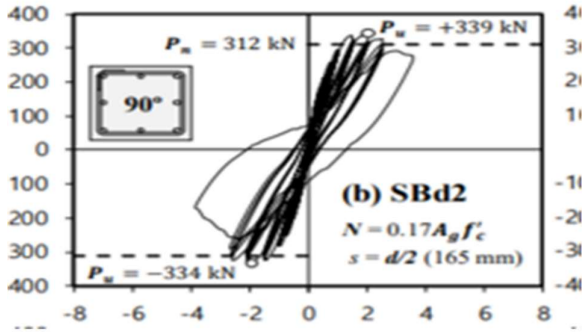
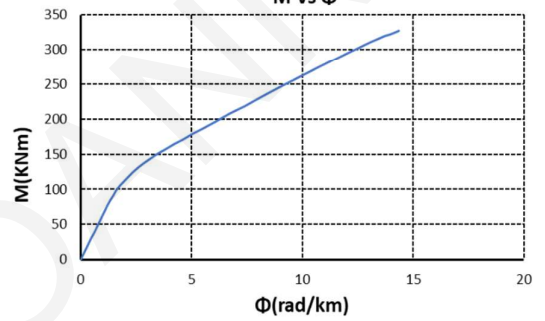
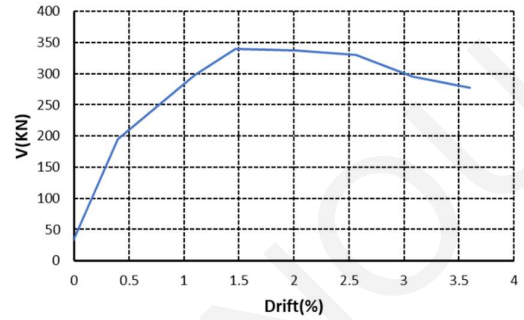


Fig. 4. Test setup



Member response

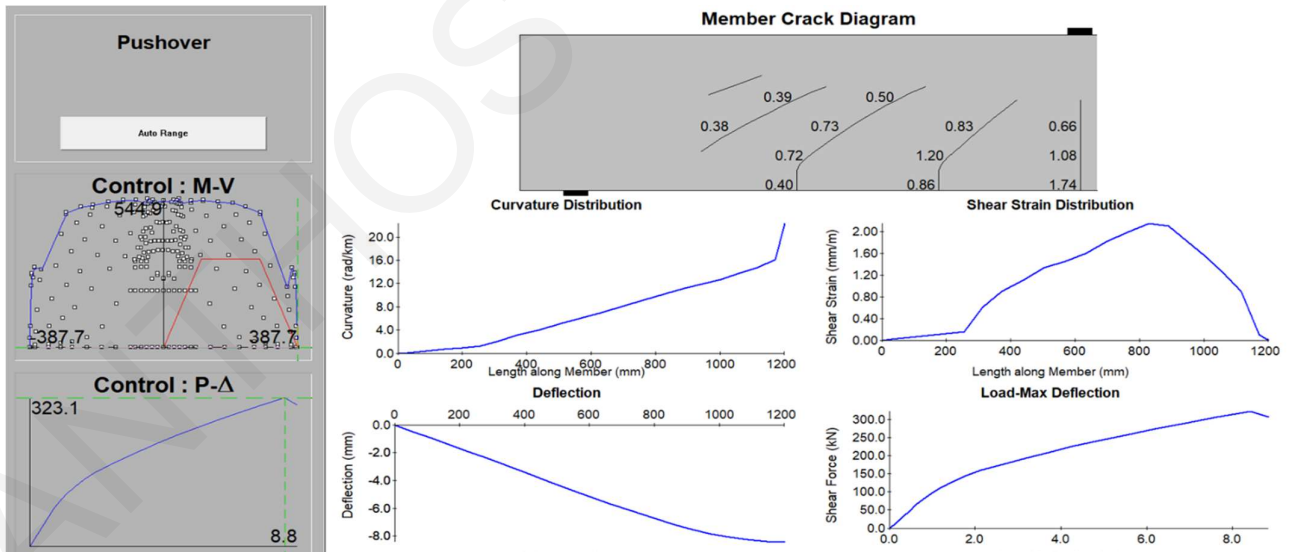


Figure B. 21: Specimen SBd2, experimental envelope curve and response 2000 section and member analysis (Kim et al., 2018).

Kim et al. (2018)

Specimen SBd4

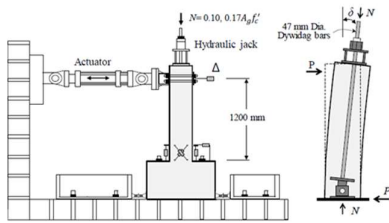
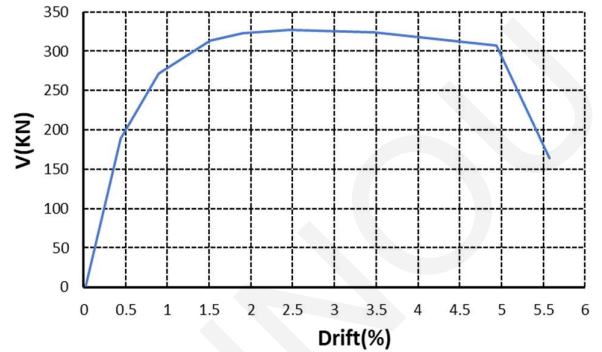
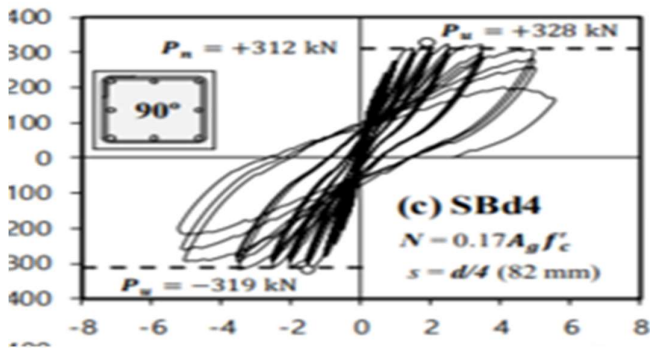
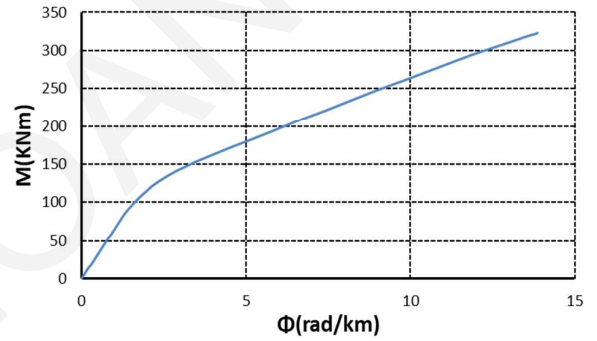


Fig. 4. Test setup



Member Response

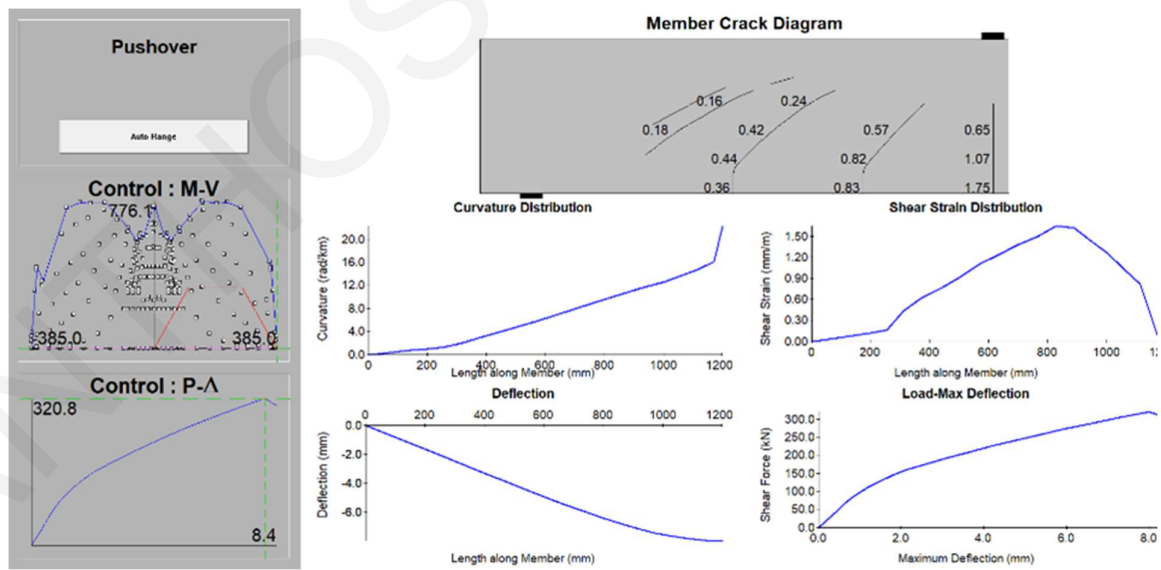


Figure B. 22: Specimen SBd4, experimental envelope curve and response 2000 section and member analysis (Kim et al., 2018).

Kim et al. (2018)

Specimen SCd2

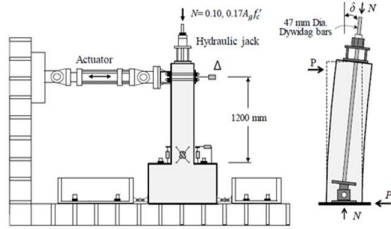
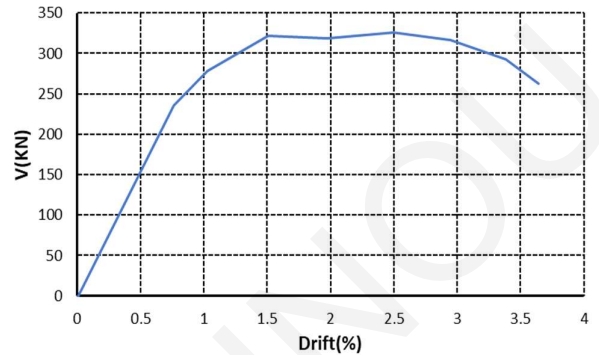
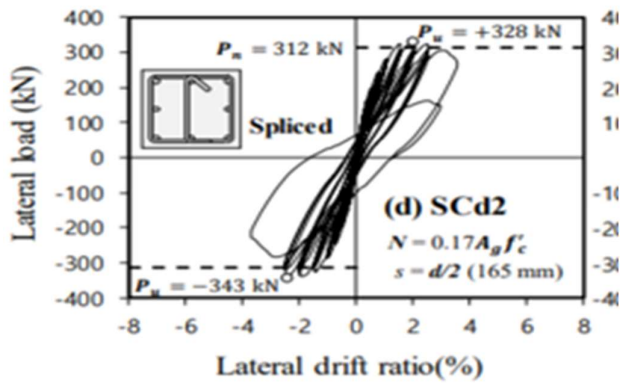
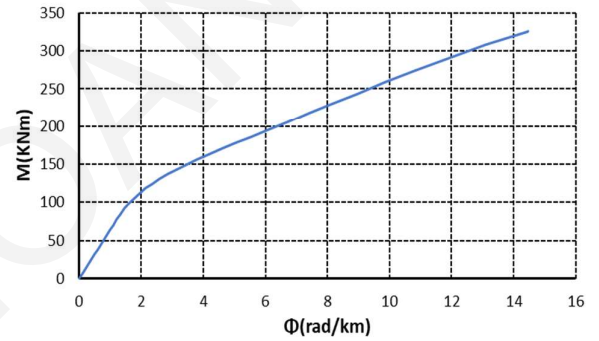


Fig. 4. Test setup



Member Response

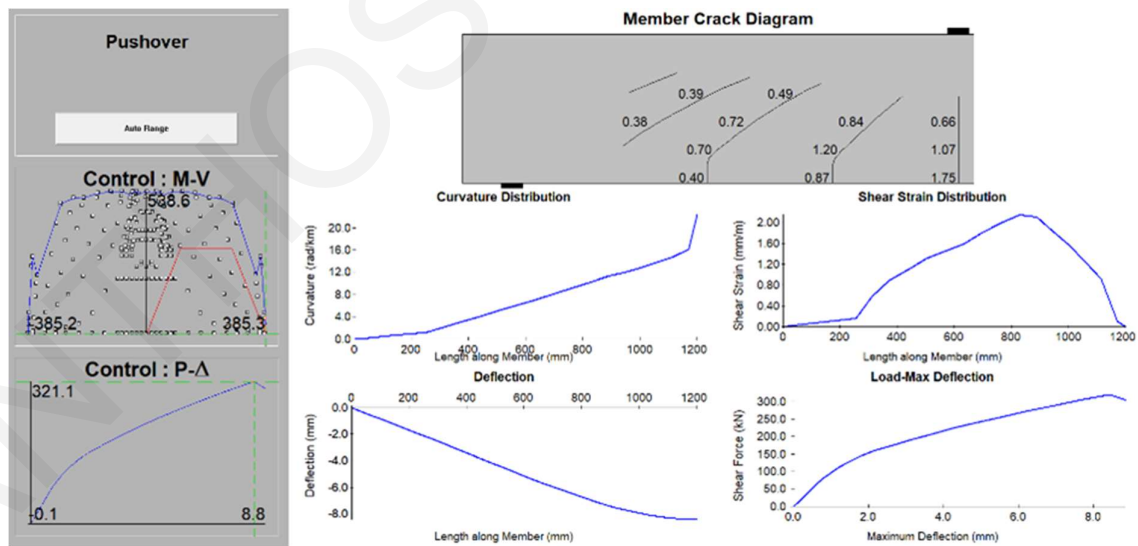


Figure B. 23: Specimen SCd2, experimental envelope curve and response 2000 section and member analysis (Kim et al., 2018).

Kim et al. (2018)

Specimen SDd2

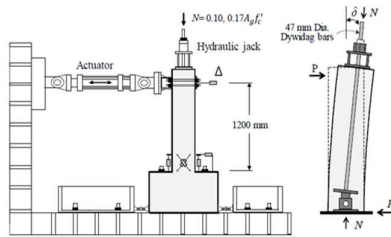
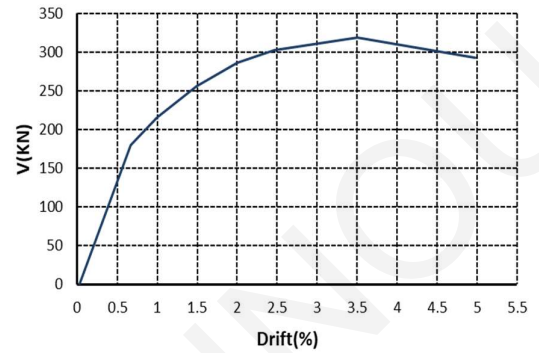
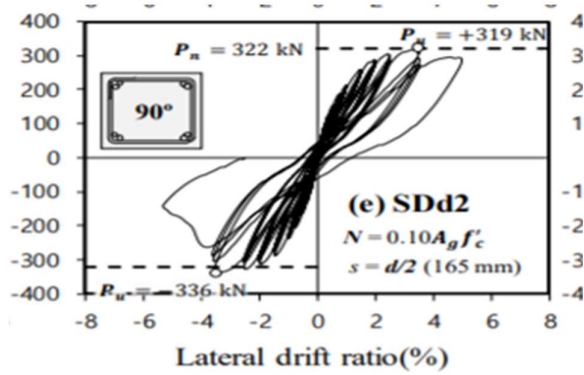
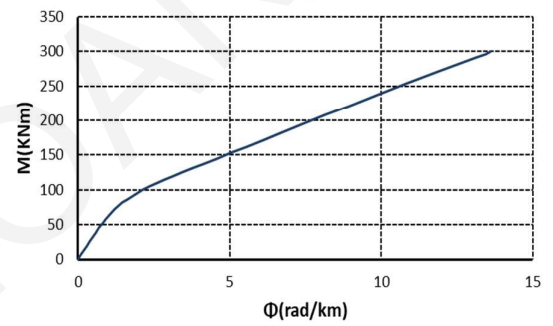


Fig. 4. Test setup



Member Response

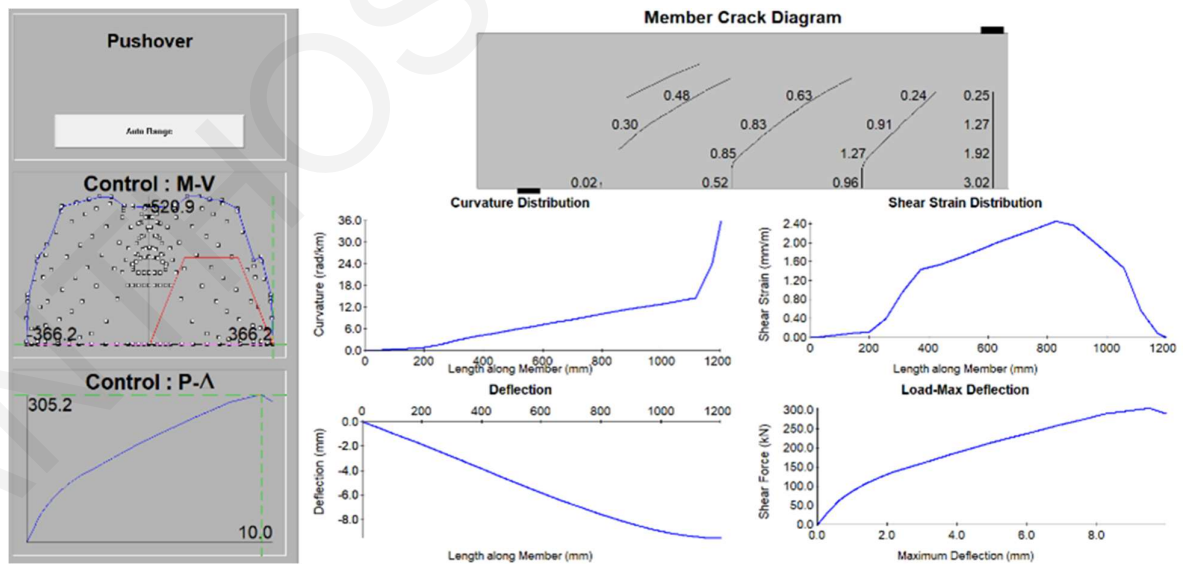


Figure B. 24: Specimen SDd2, experimental envelope curve and response 2000 section and member analysis (Kim et al., 2018).

Kim et al. (2018)
Specimen SDd4

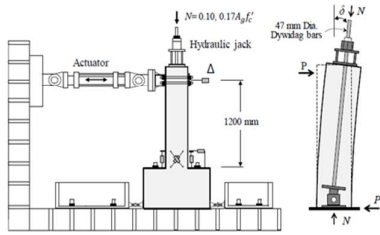
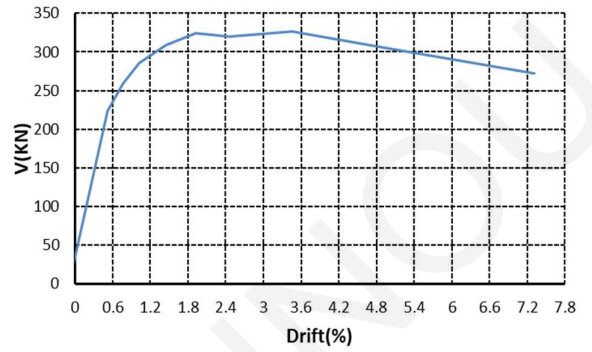
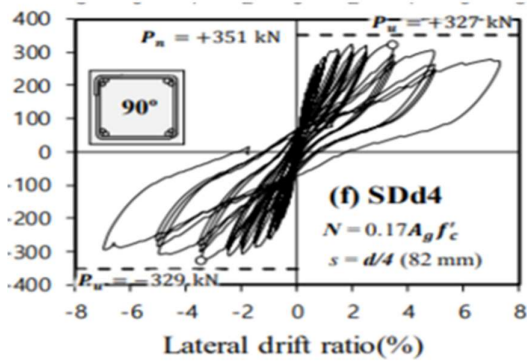
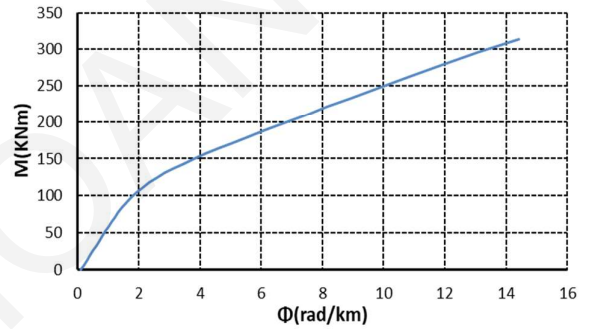


Fig. 4. Test setup



Member Response

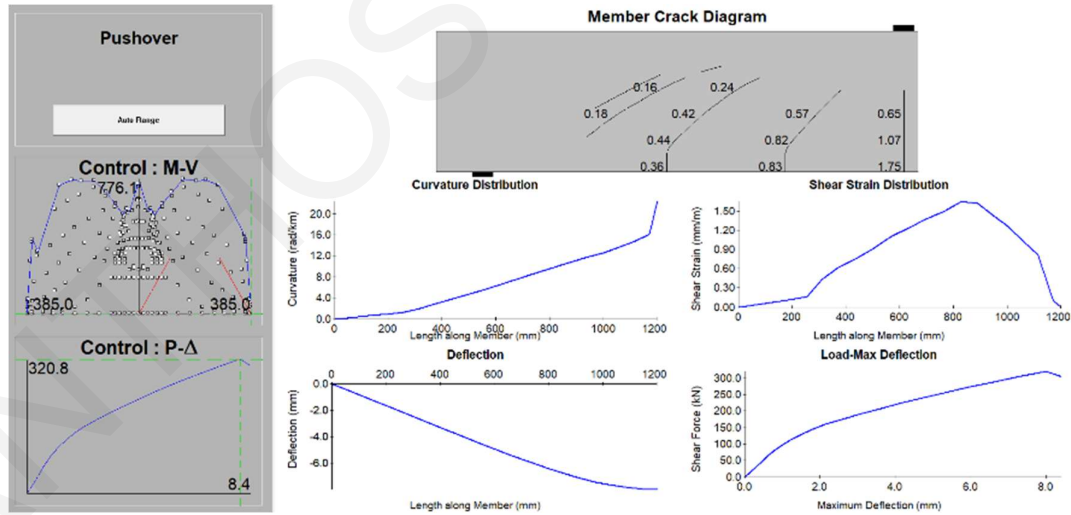


Figure B. 25: Specimen SDd4, experimental envelope curve and response 2000 section and member analysis (Kim et al., 2018).

Kim et al. (2018)
Specimen RFd2

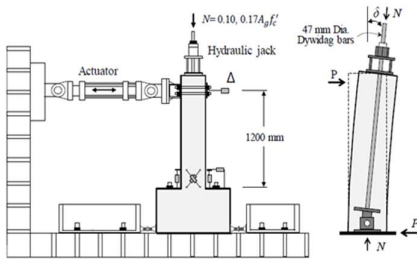
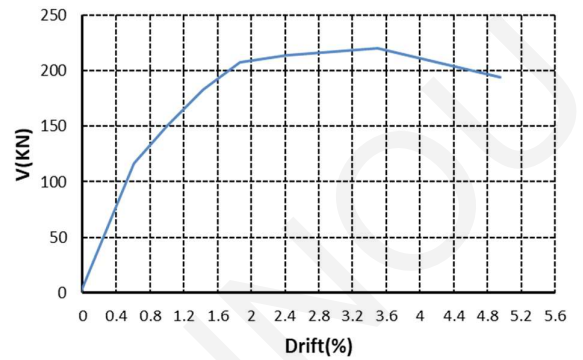
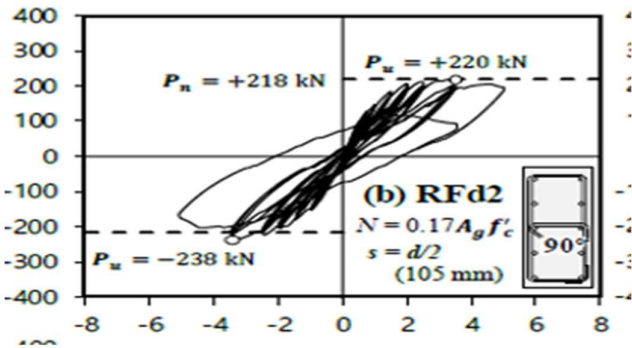
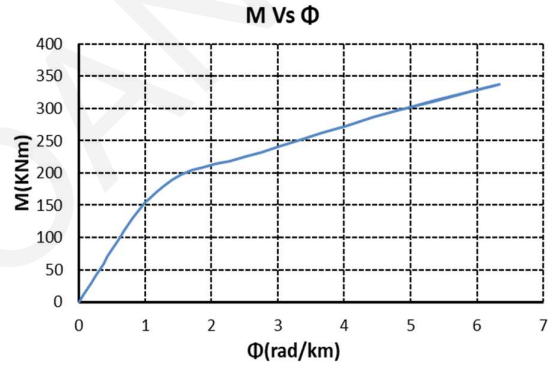


Fig. 4. Test setup



Member Response

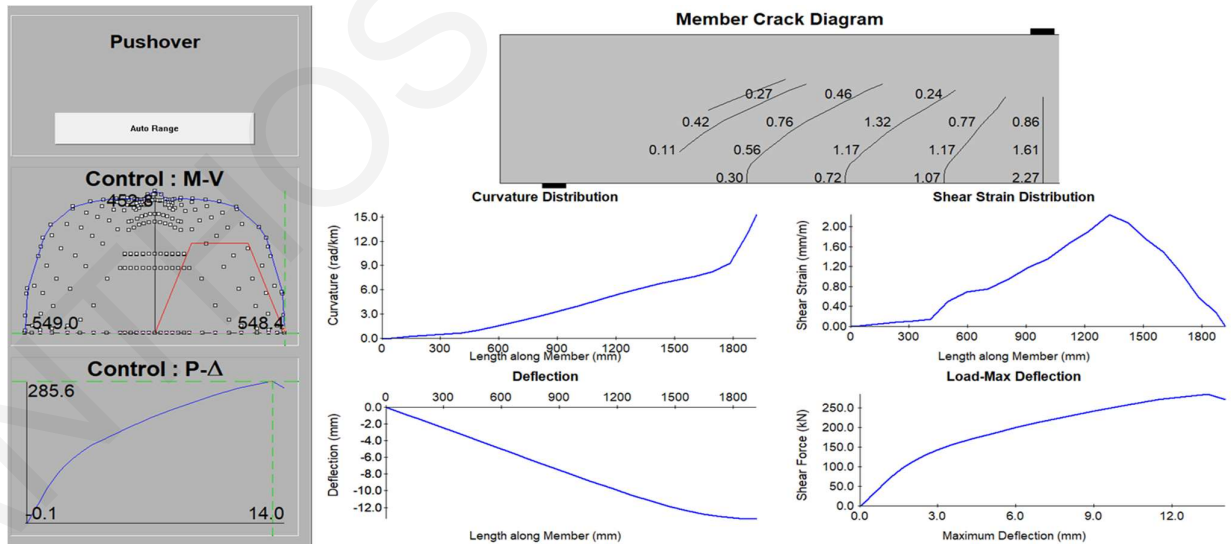
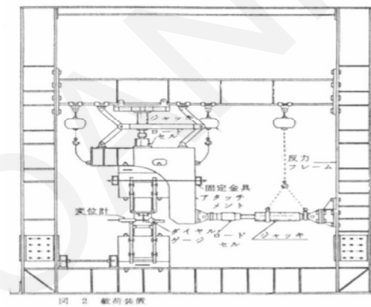
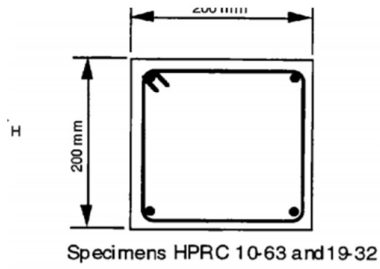
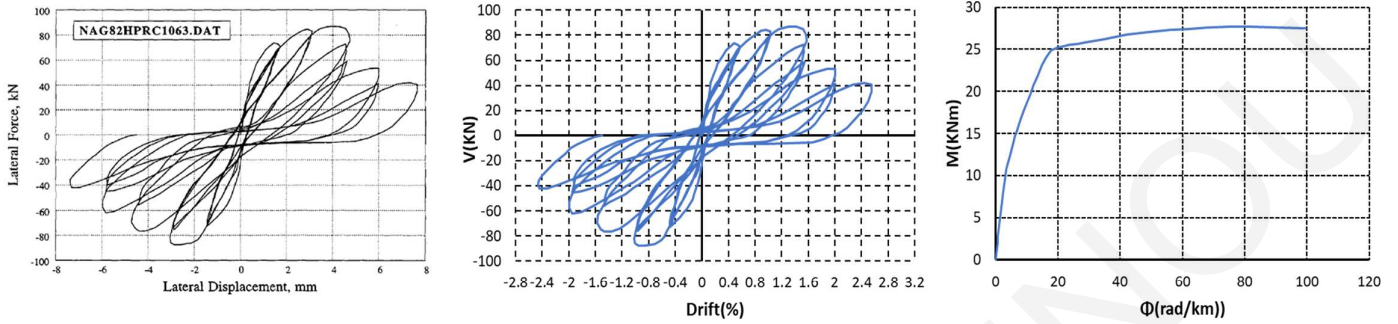


Figure B. 26: Specimen RFd2, experimental envelope curve and response 2000 section and member analysis (Kim et al., 2018).

Nagasaka (1982)

Specimen HPRC10-63



Member Response

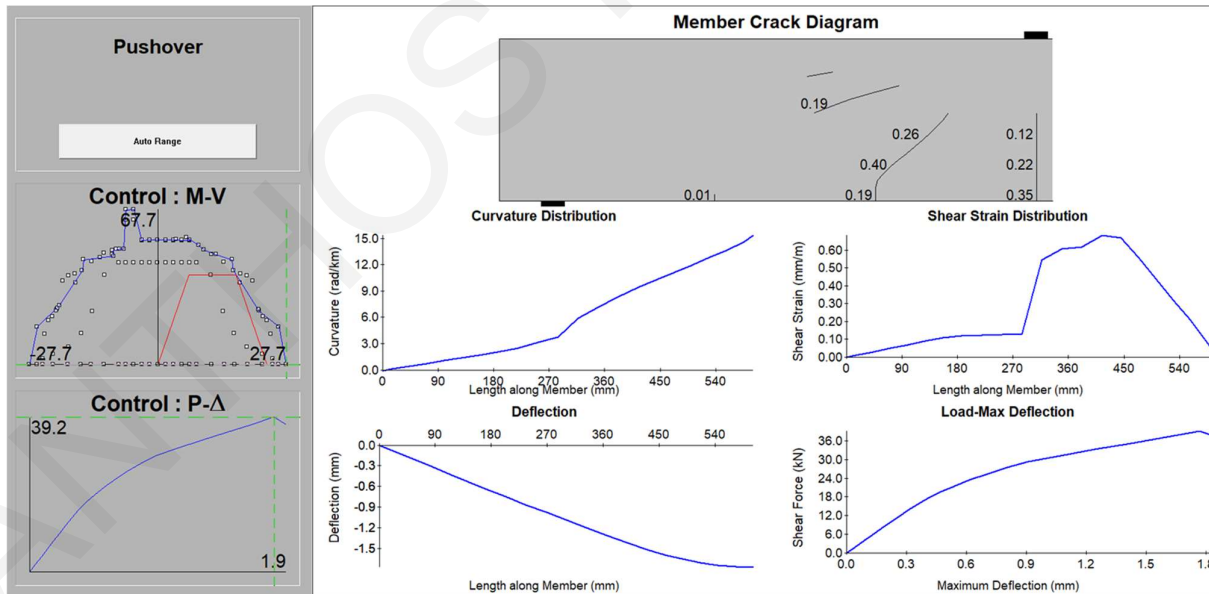


Figure B. 27: Specimen HPRC10-63 experimental envelope curve and response 2000 section and member analysis (Nagasaka., 1982).

Lynn et al. (1998)

Specimen 3SLH18

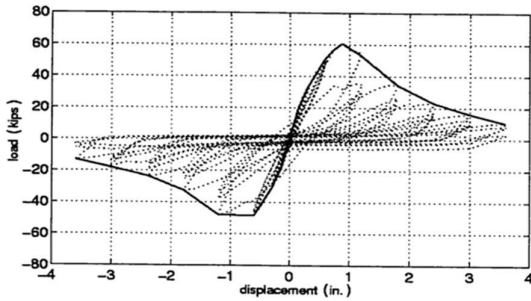
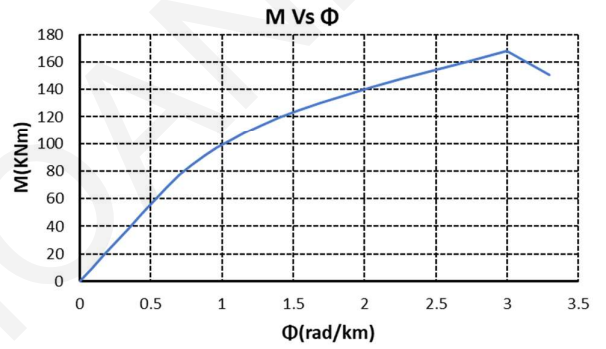
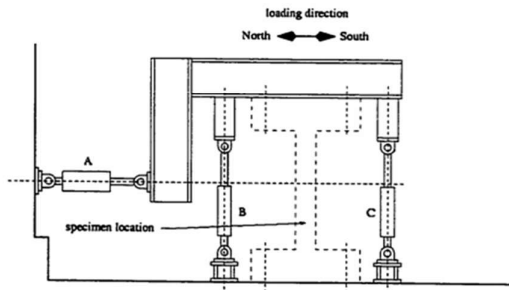
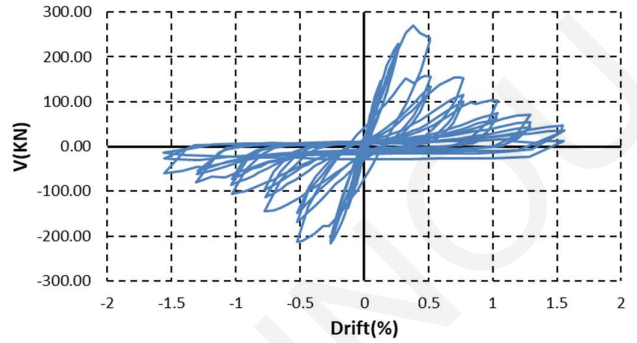


Figure 3.37: Load-displacement history, Specimen 3SLH18



Member Response

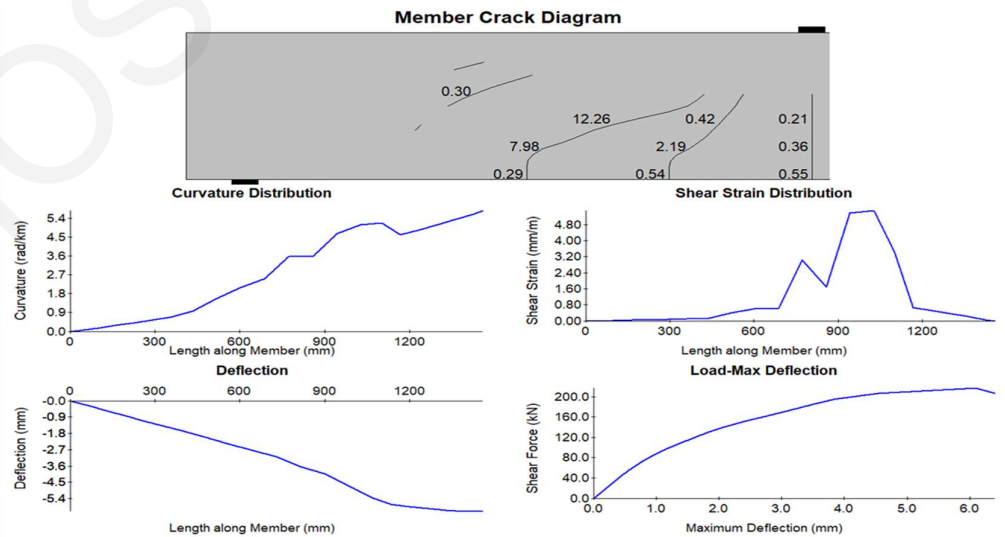
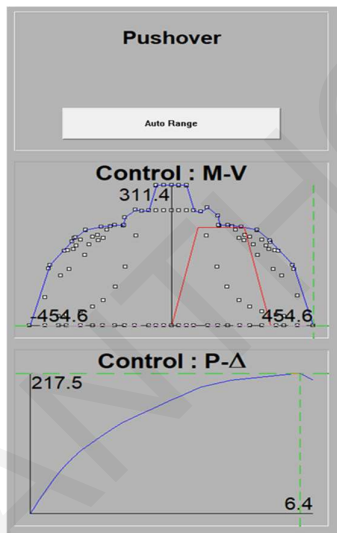


Figure B. 28: Specimen 3SLH18, experimental envelope curve and response 2000 section and member analysis (Lynn et al., 1998).

Lynn et al. (1998)

Specimen 3CMD12

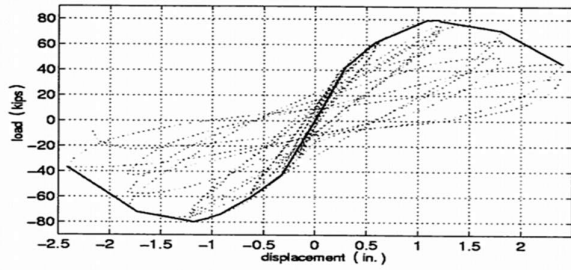
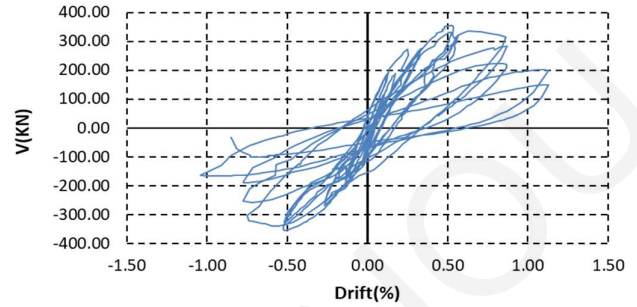
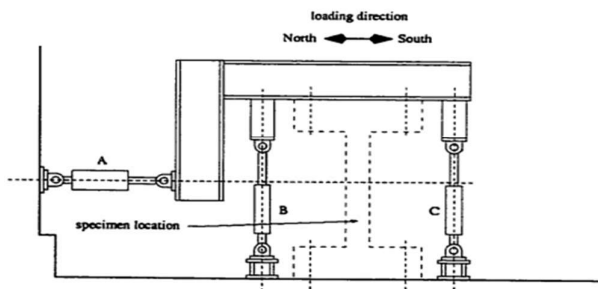
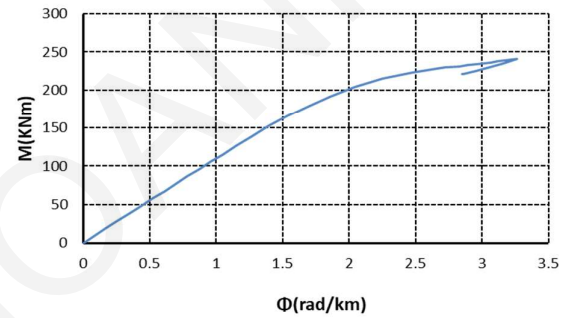


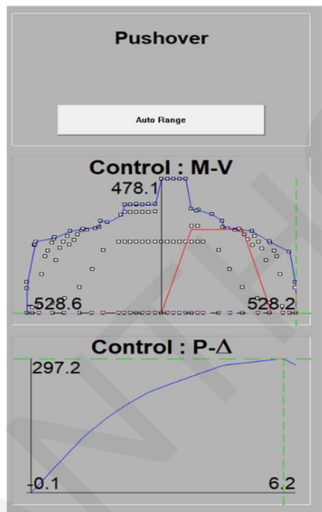
Figure 3.76: Load-displacement history, Specimen 3CMD12



M Vs Φ



Member Response



Member Crack Diagram

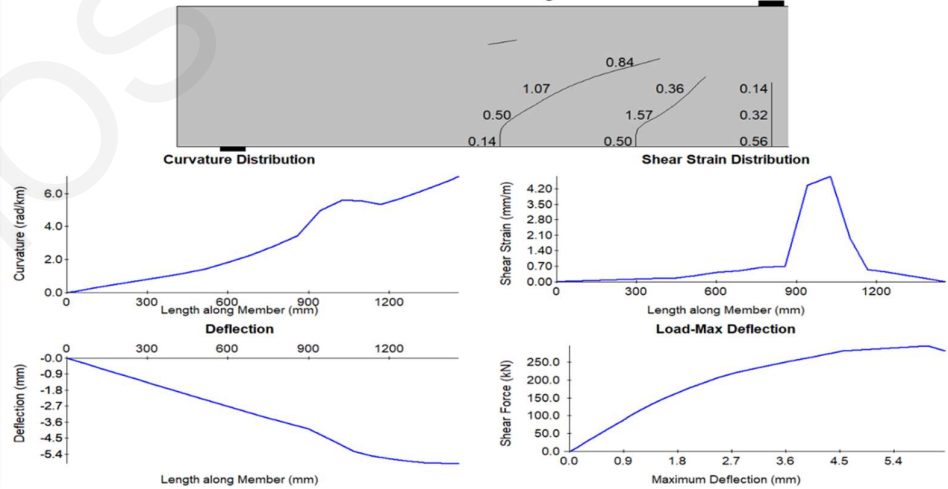


Figure B. 29: Specimen 3CMD12, experimental envelope curve and response 2000 section and member analysis (Lynn et al., 1998).

Lynn et al. (1998)

Specimen 3CMH18

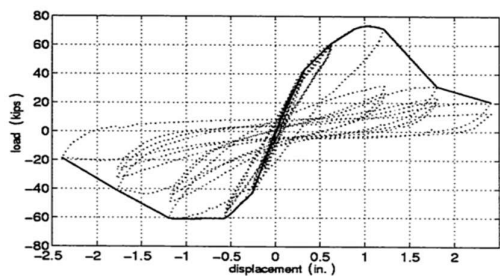
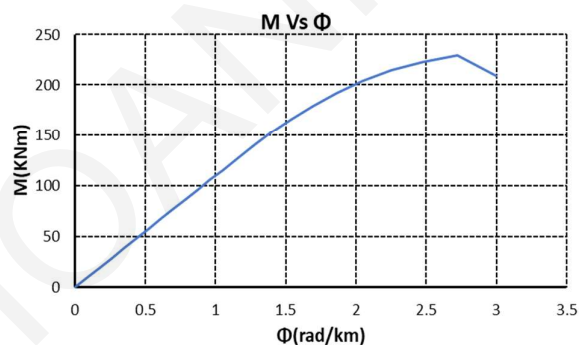
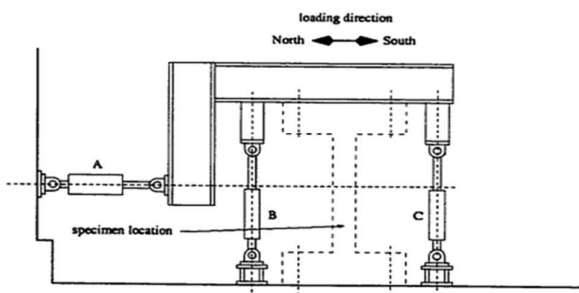
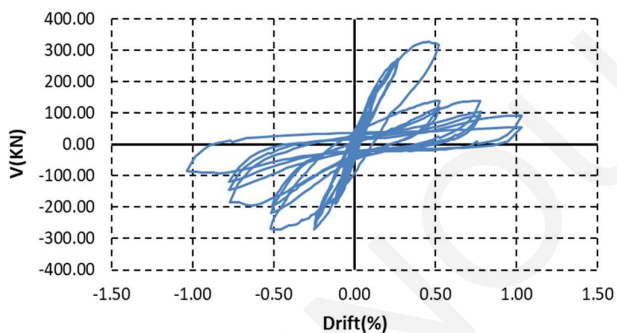


Figure 3.67: Load-displacement history, Specimen 3CMH18



Member Response

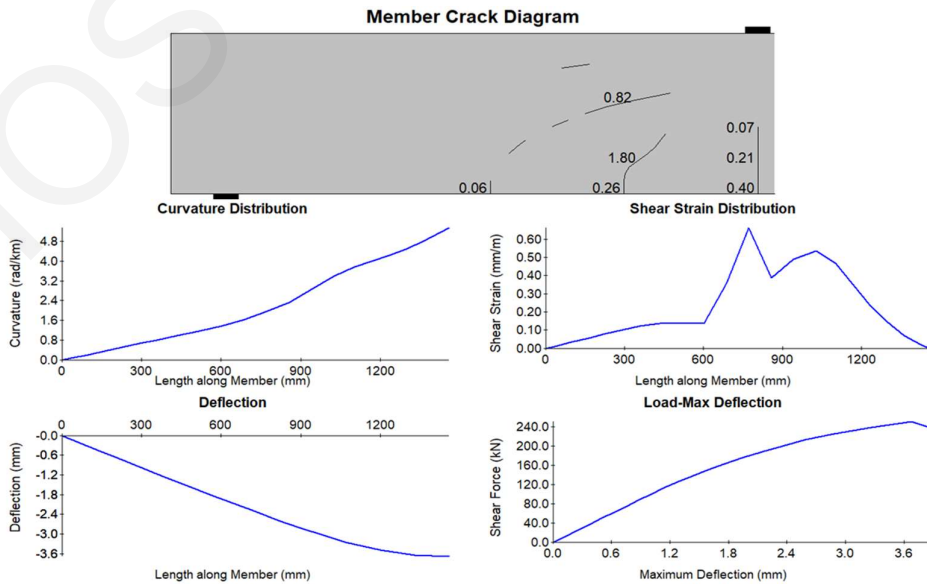
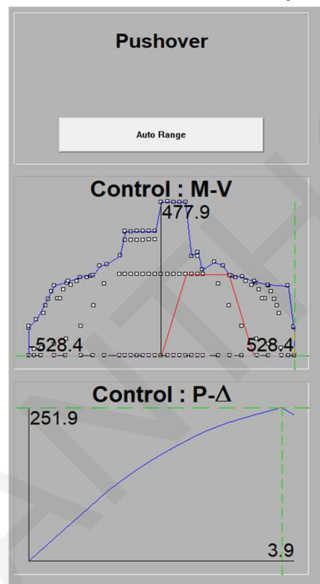


Figure B. 30: Specimen 3CMH18, experimental envelope curve and response 2000 section and member analysis (Lynn et al., 1998).

B.2 Flexure-Shear critical columns

ANTHOS I. IOANNOU

Nagasaka (1982)

Specimen HPRC19-32

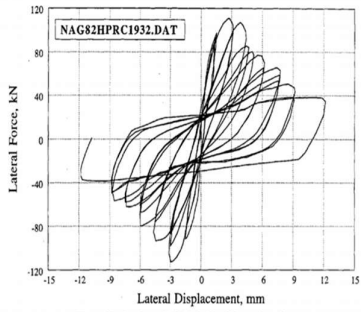
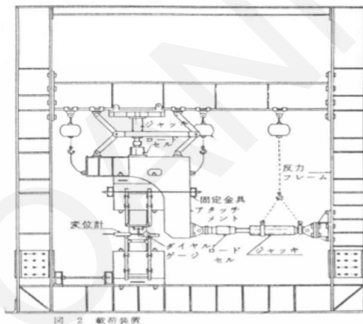
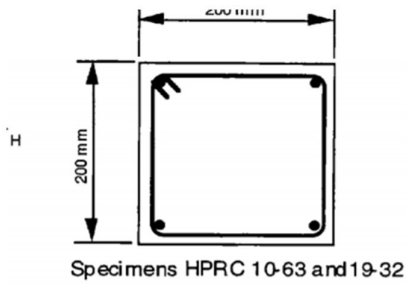
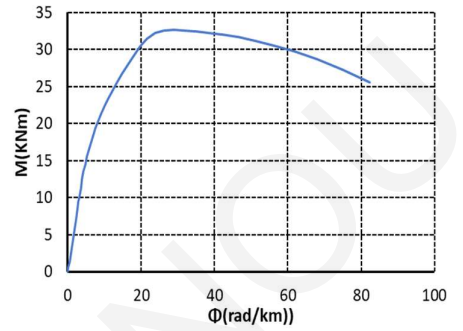
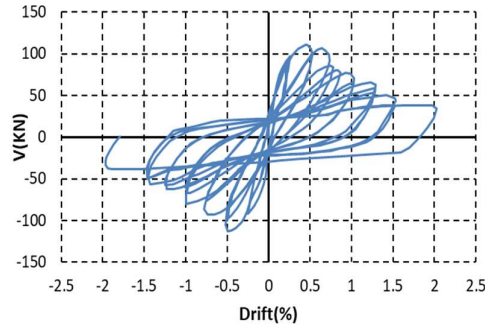


Figure 29. Specimen HPRC 19-32 of Nagasaka 1982



Member Response

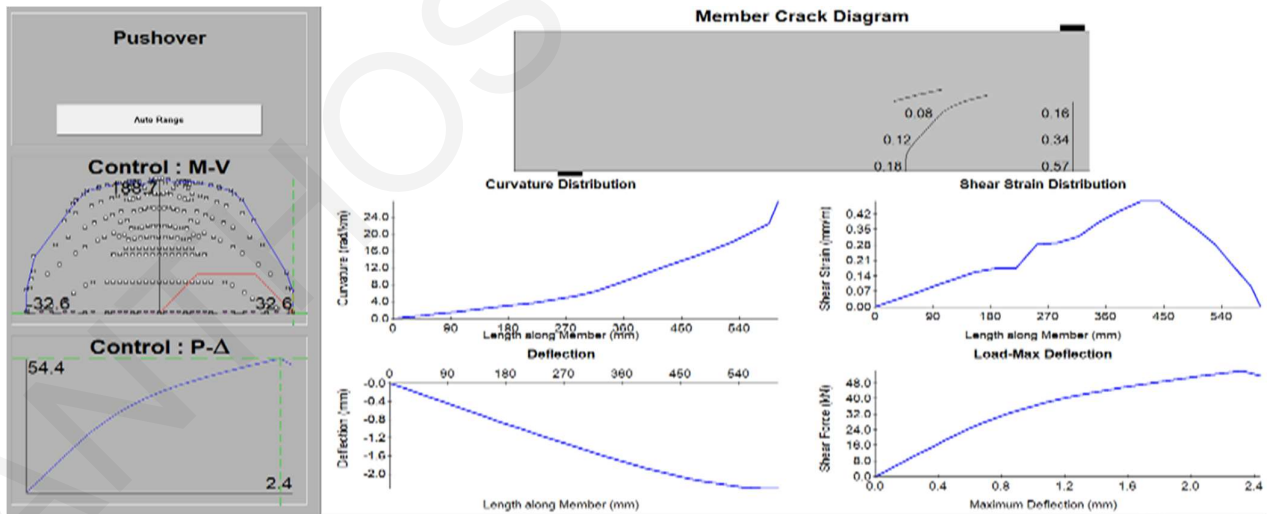
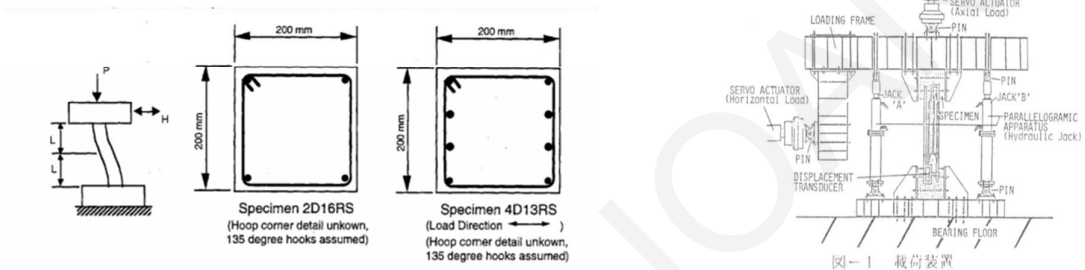
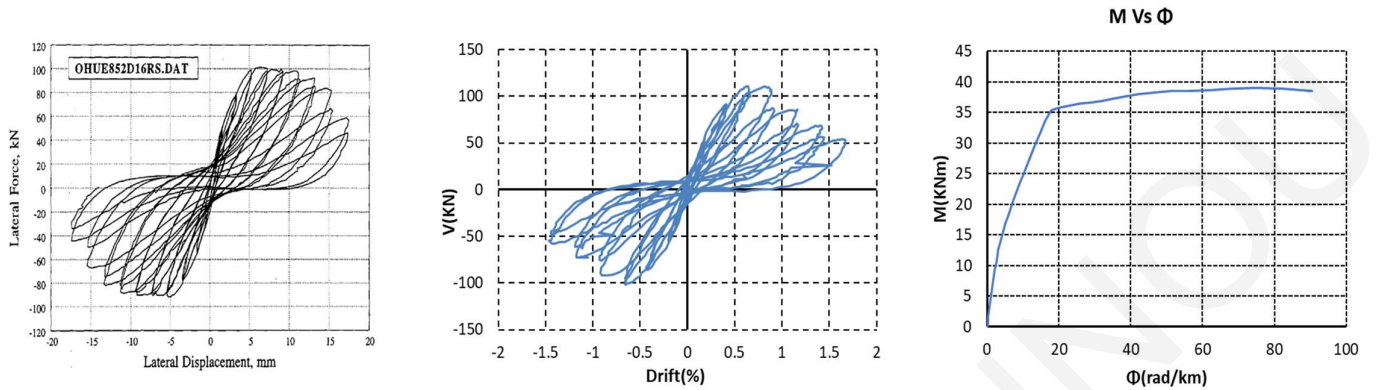


Figure B. 31: Specimen HPRC19-32, experimental envelope curve and response 2000 section and member analysis (Nagasaka., 1982).

Ohue et al. (1985)

Specimen 2D16RS



Member Response

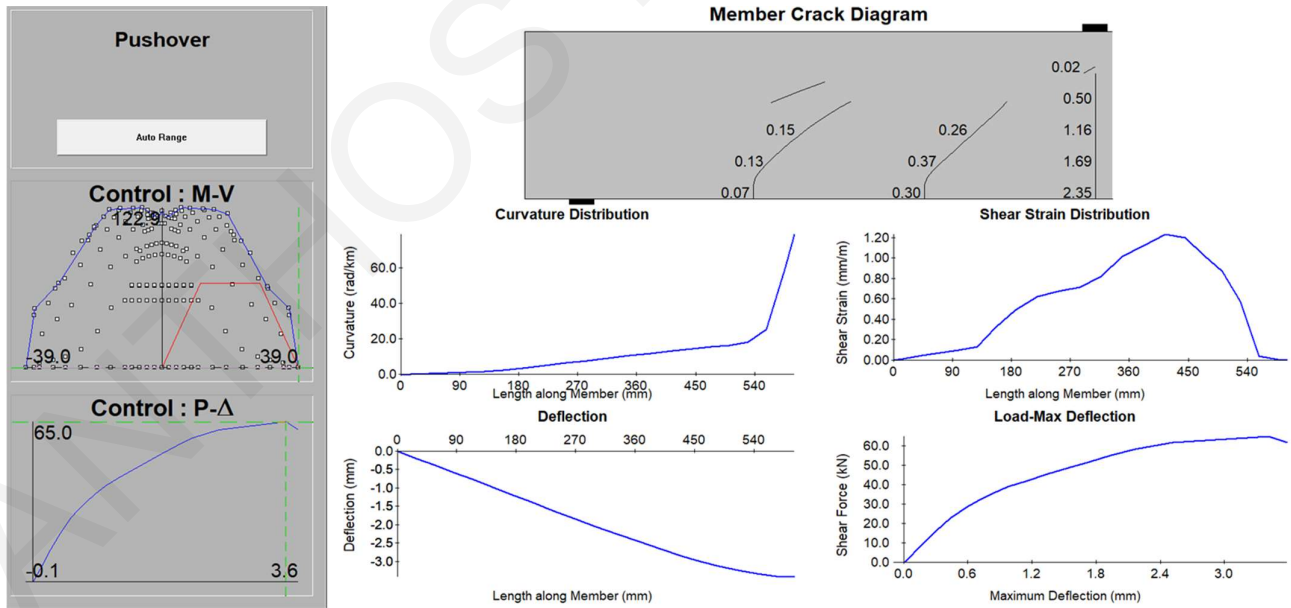
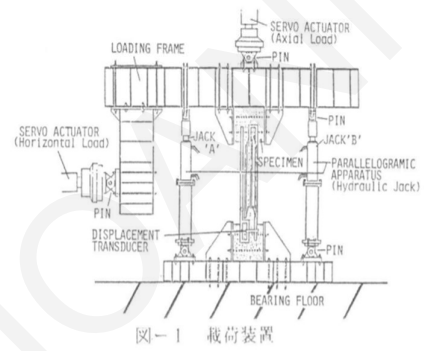
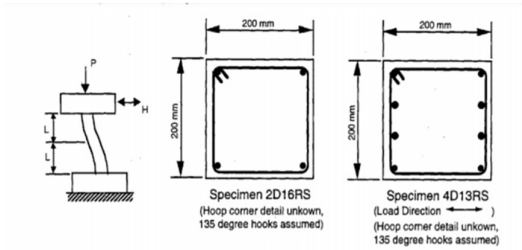
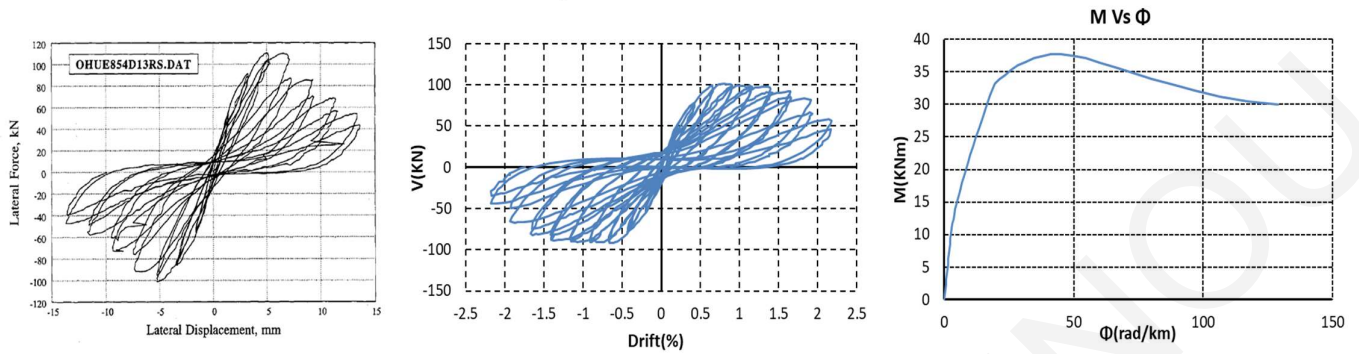


Figure B. 32: Specimen 2D16RS, experimental envelope curve and response 2000 section and member analysis (Ohue et al., 1985).

Ohue et al. (1985)

Specimen 4D13RS



Member Response

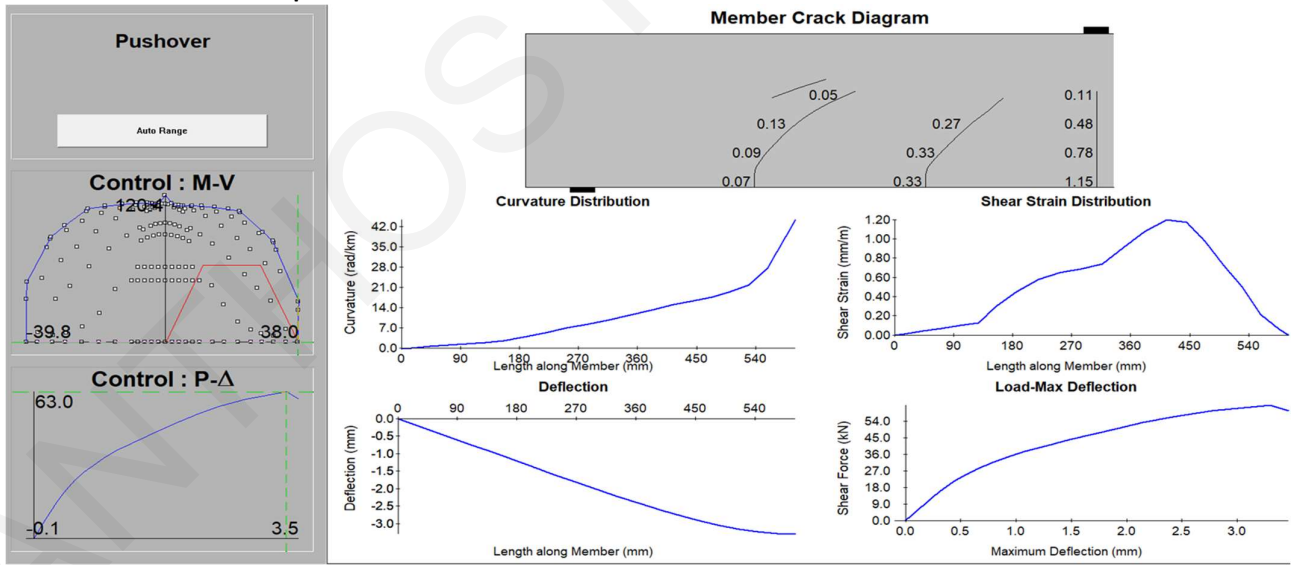


Figure B. 33: Specimen 4D13RS, experimental envelope curve and response 2000 section and member analysis (Ohue et al., 1985).

Zhou et al. (1985)

Specimen No 806

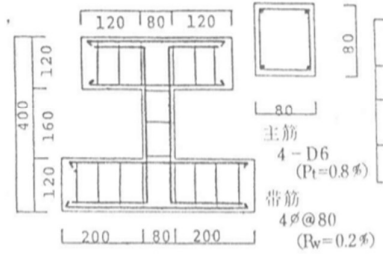
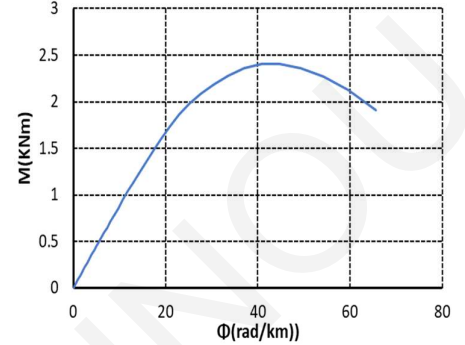
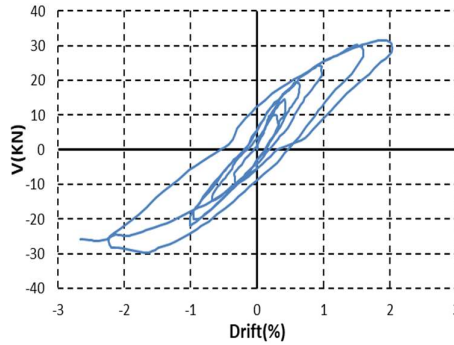
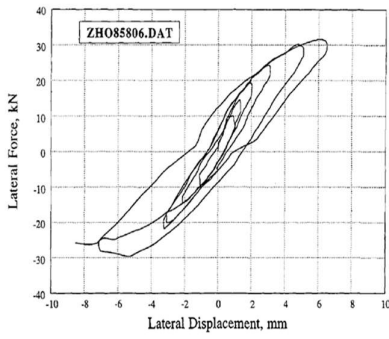


图 1. 试验体配筋图

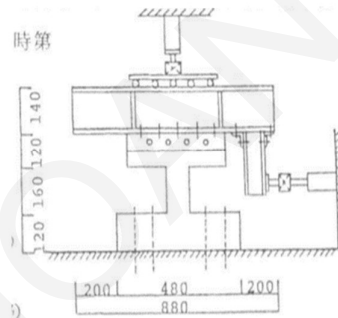


图 2. 加力装置

Member Response

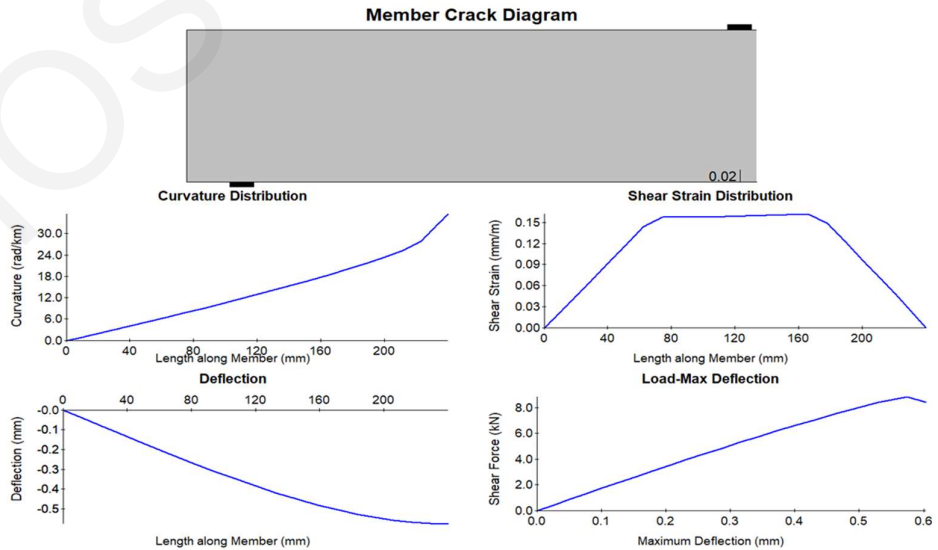
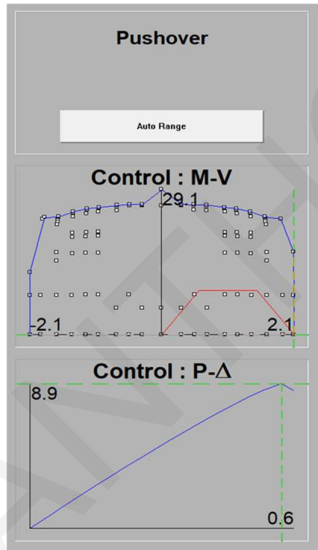


Figure B. 34: Specimen No 806, experimental envelope curve and response 2000 section and member analysis (Zhou et al., 1985).

Zhou et al. (1985)

Specimen No 1007

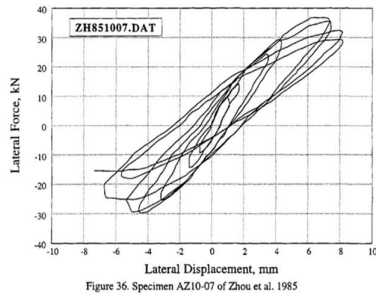


Figure 36. Specimen AZ10-07 of Zhou et al. 1985

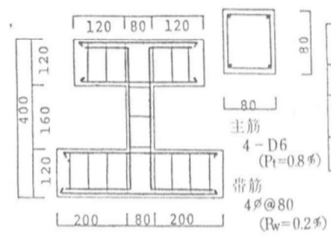
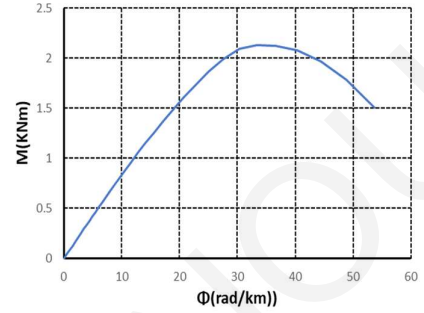
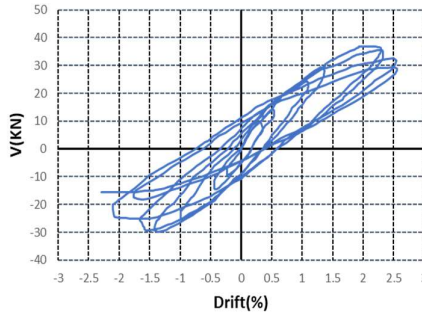


图 1. 試驗体配筋图

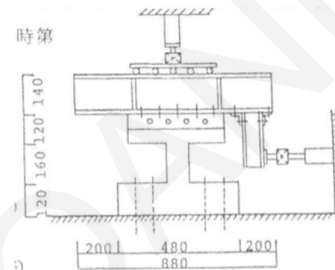


图 2. 加力装置

Member Response

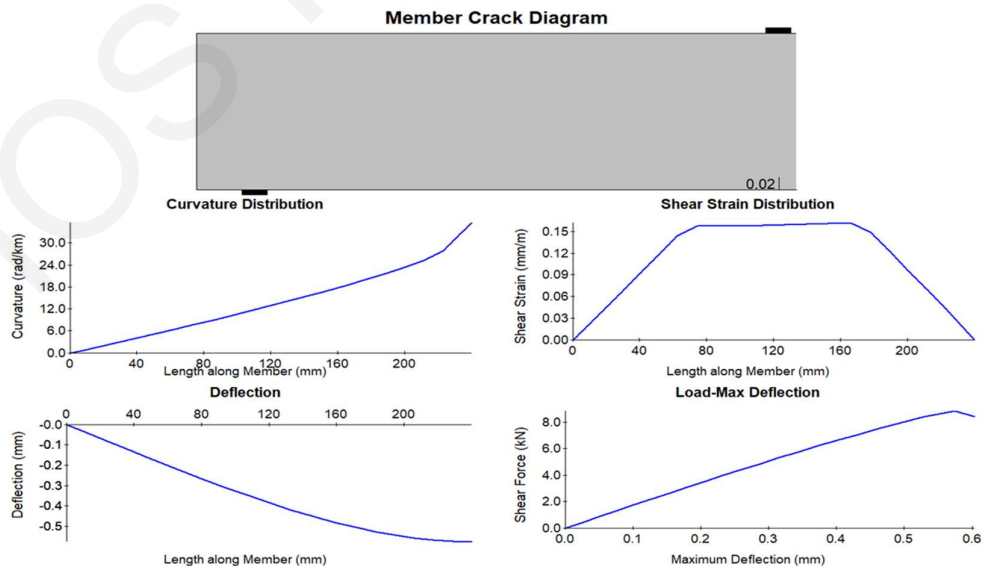
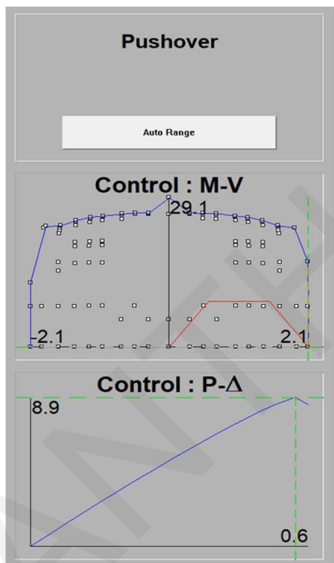
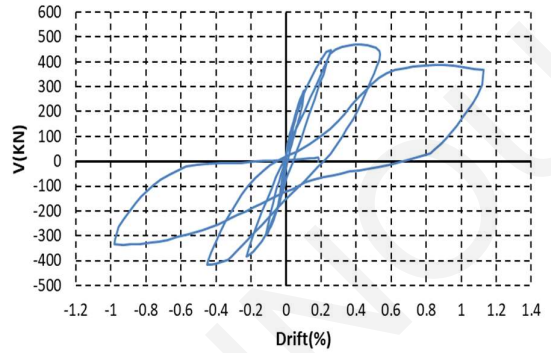
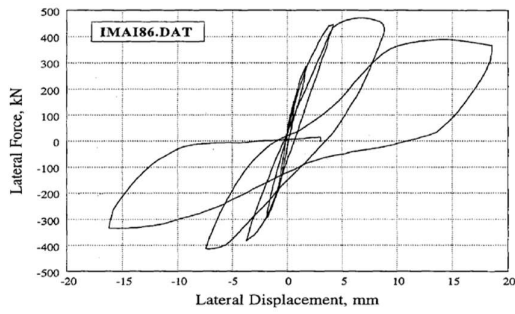


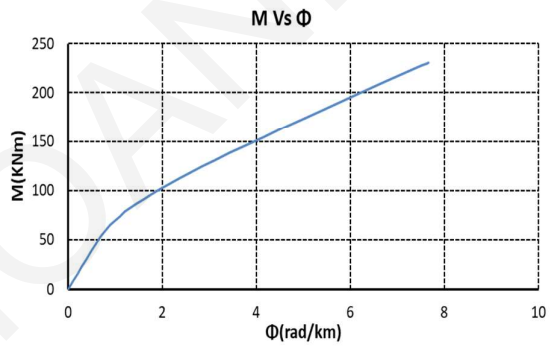
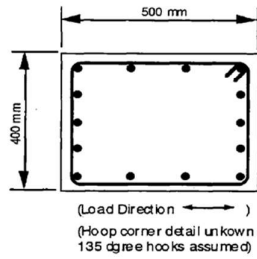
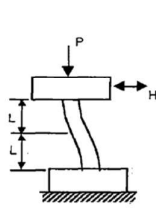
Figure B. 35: Specimen No 1007, experimental envelope curve and response 2000 section and member analysis (Zhou et al., 1985).

Imai and Yamamoto (1986)

Specimen No 1



1986 Imai and Yamamoto



Member Response

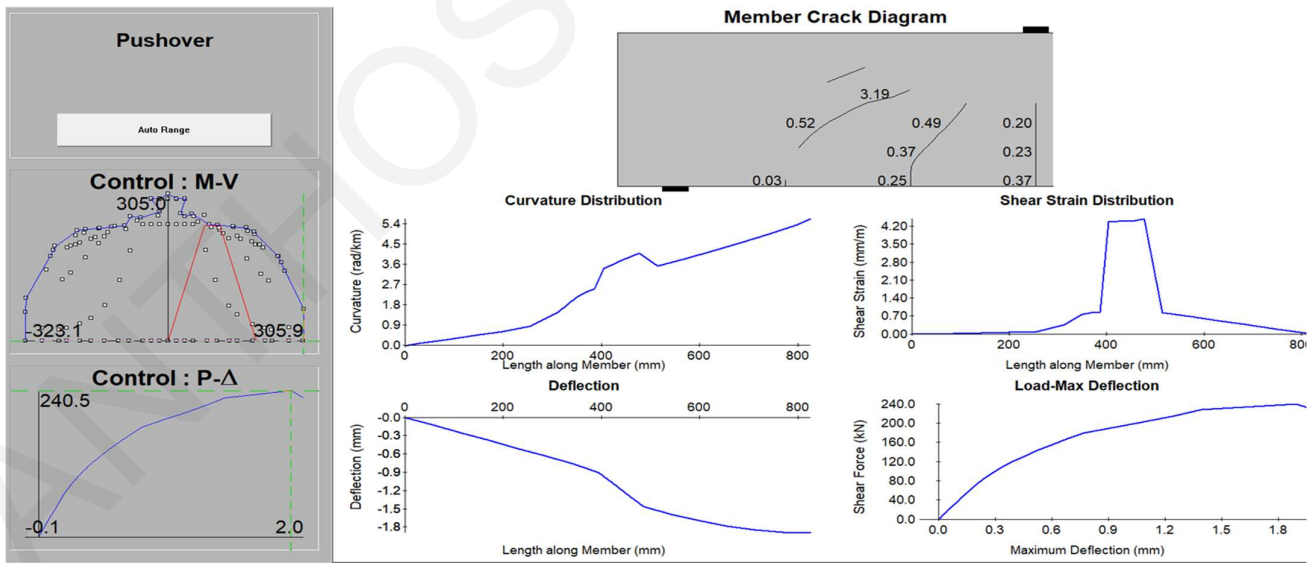


Figure B. 36: Specimen No 1, experimental envelope curve and response 2000 section and member analysis (Imai and Yamamoto, 1986).

Zhou et al. (1985)

Specimen No 1309

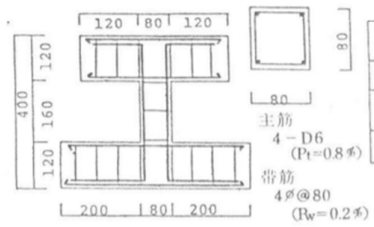
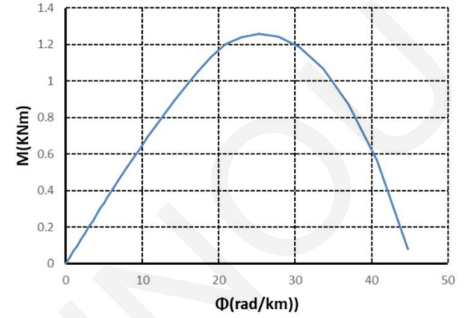
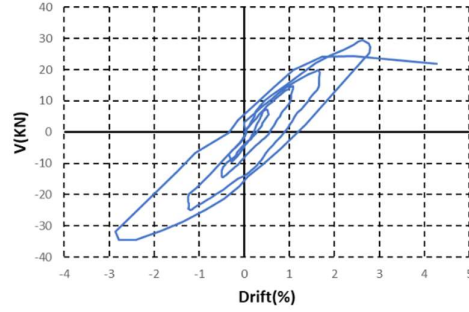
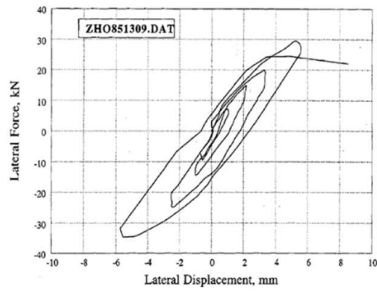


图 1. 試驗体配筋圖

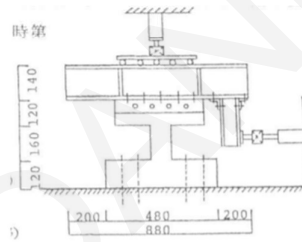


图 2. 加力裝置

Member Response

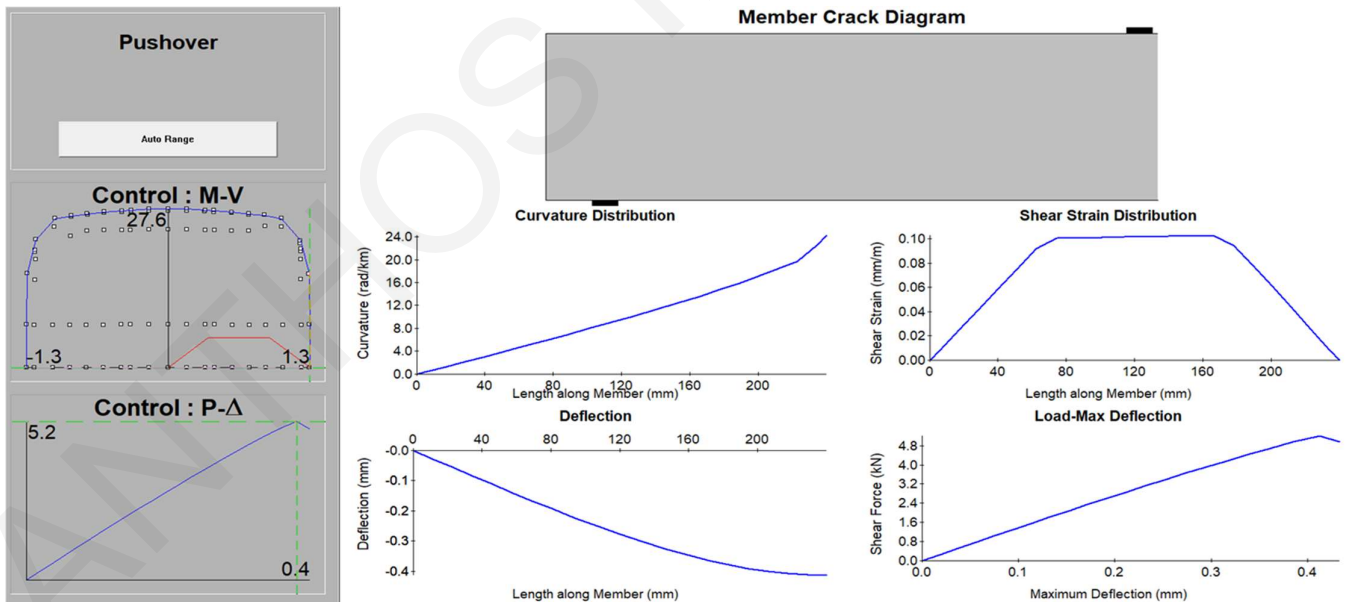
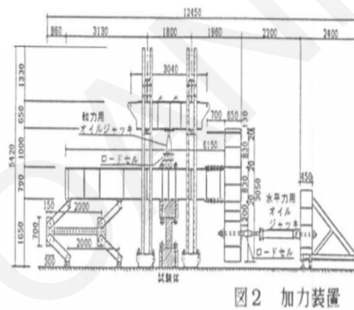
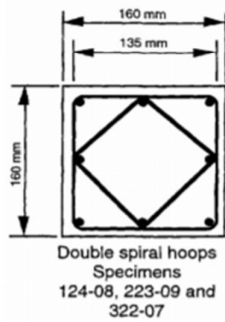
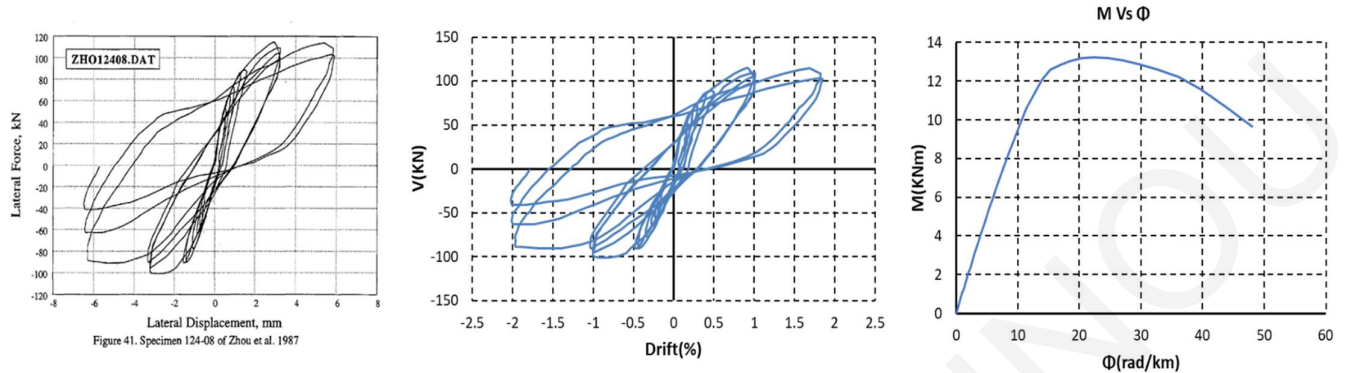


Figure B. 37: Specimen No 1309, experimental envelope curve and response 2000 section and member analysis (Zhou et al., 1985)

Zhou et al. (1987)

Specimen 124-08



Member Response

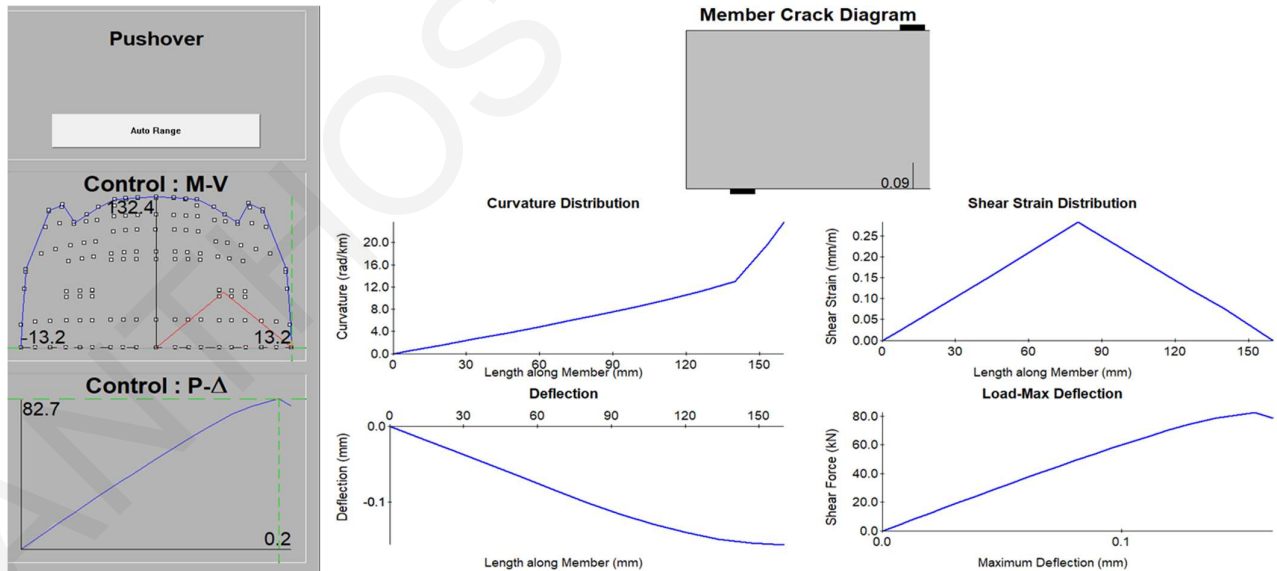


Figure B. 38: Specimen 124-08, experimental envelope curve and response 2000 section and member analysis (Zhou et al., 1987).

Zhou et al. (1987)

Specimen 204-08

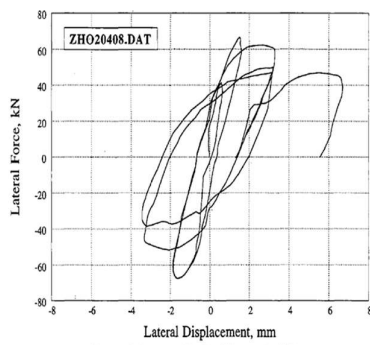
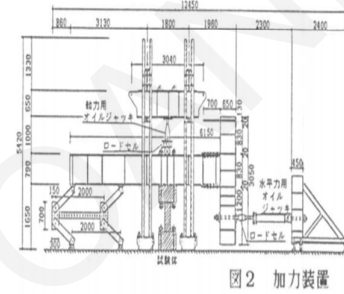
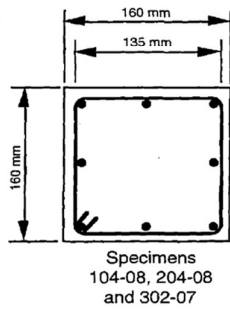
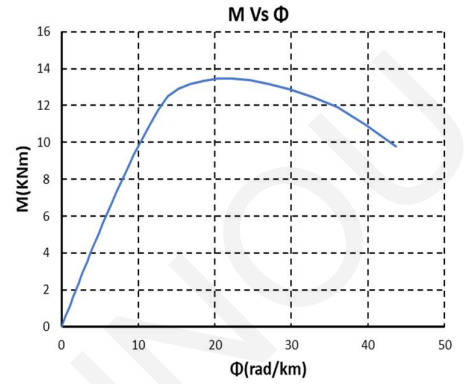
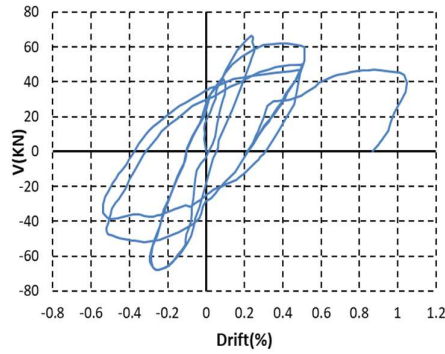


Figure 42. Specimen 204-08 of Zhou et al. 1987



Member Response

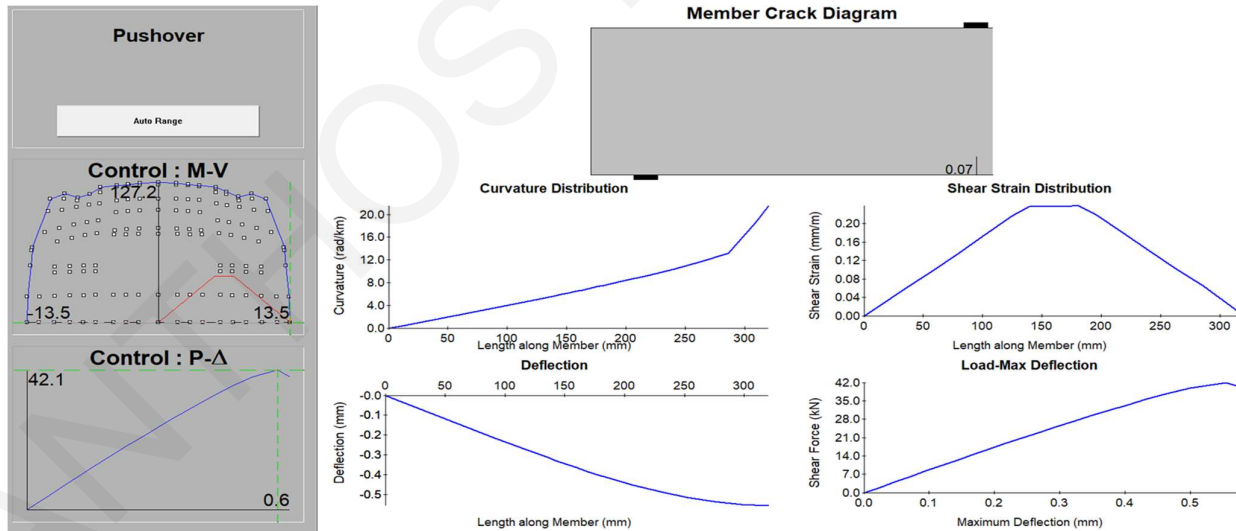
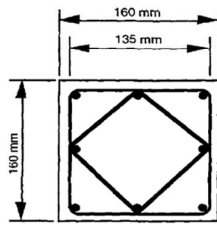
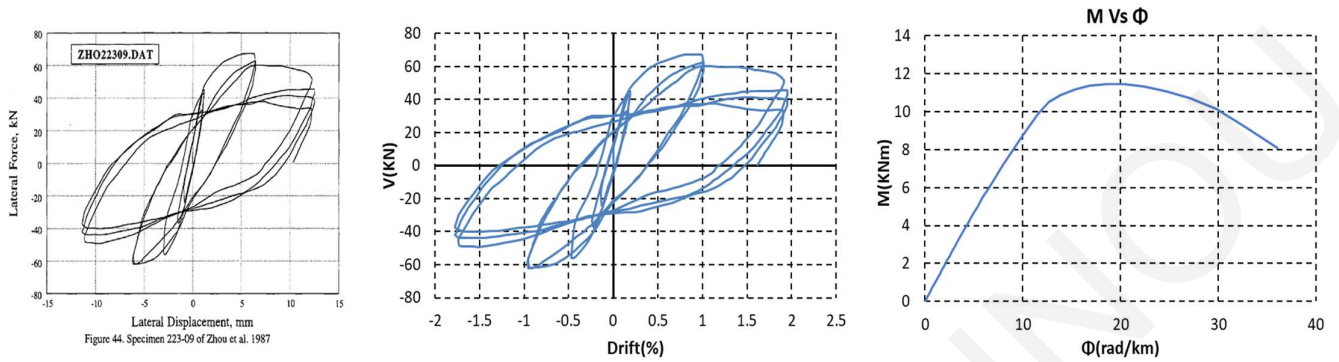


Figure B. 39: Specimen 204-08, experimental envelope curve and response 2000 section and member analysis (Zhou et al., 1987).

Zhou et al. (1987)

Specimen 223-09



Double spiral hoops
Specimens
124-08, 223-09 and
322-07

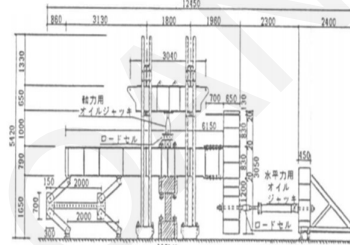


図2 加力装置

member Response

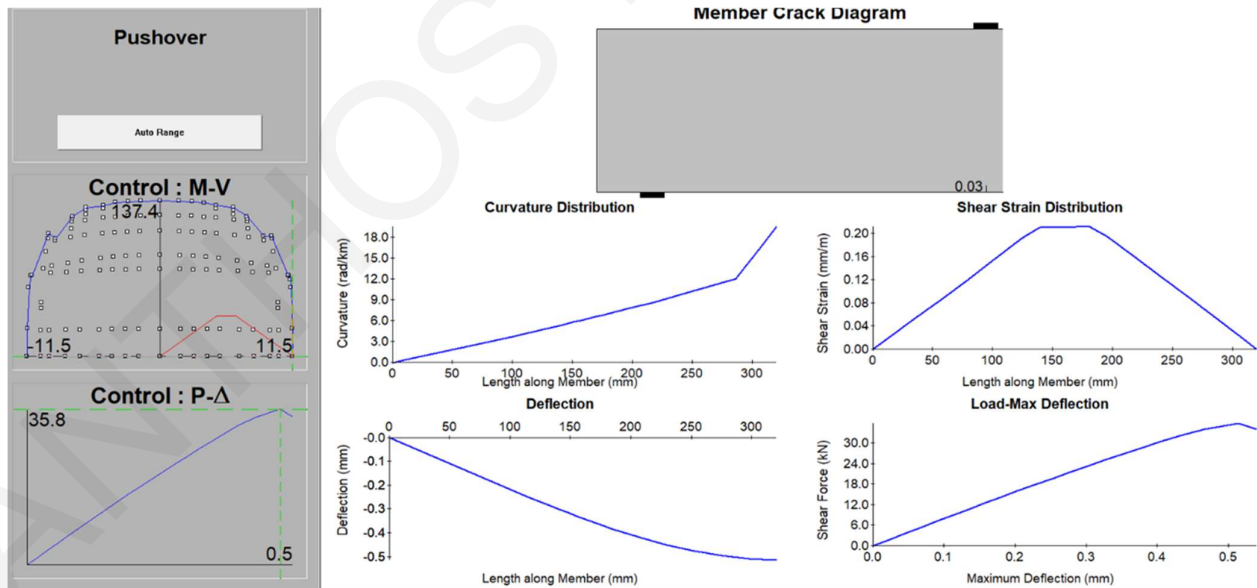
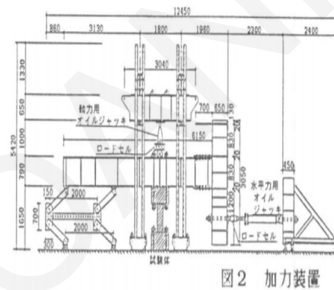
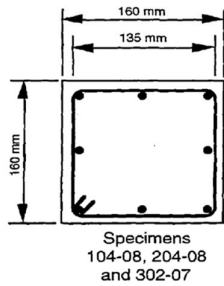
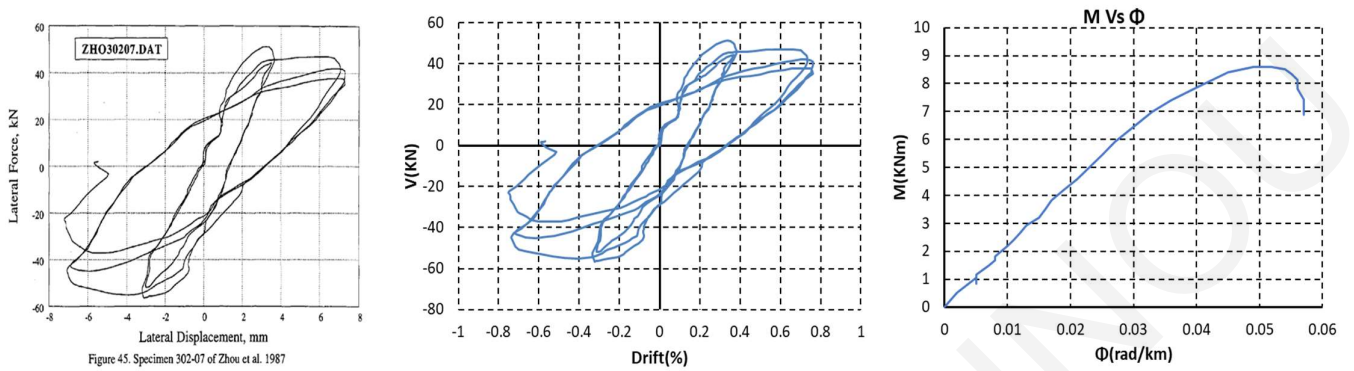


Figure B. 40: Specimen 223-09, experimental envelope curve and response 2000 section and member analysis (Zhou et al., 1987).

Zhou et al. (1987)

Specimen 302-07



Member Response

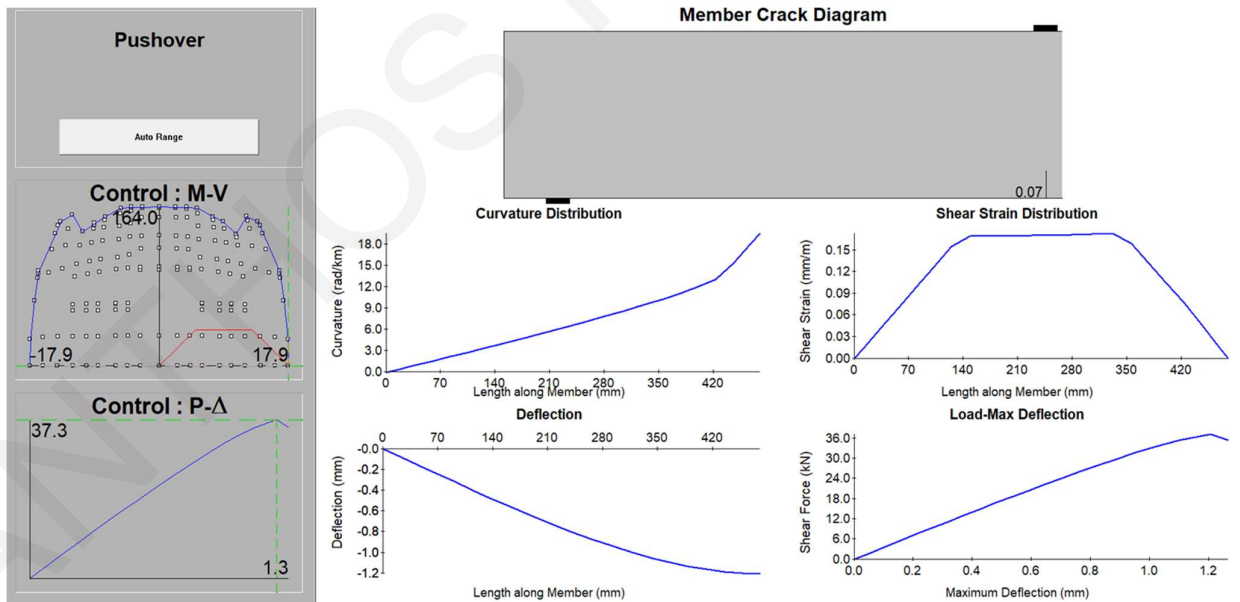


Figure B. 41: Specimen 302-07, experimental envelope curve and response 2000 section and member analysis (Zhou et al., 1987).

Zhou et al. (1987)

Specimen 312-07

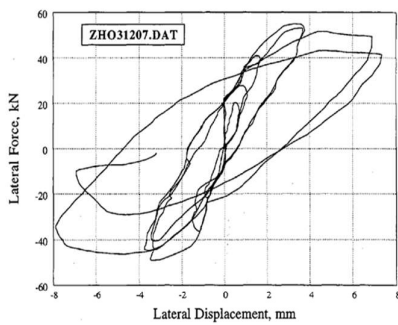


Figure 46. Specimen 312-07 of Zhou et al. 1987

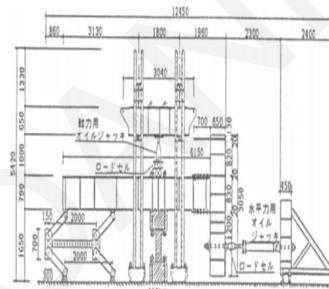
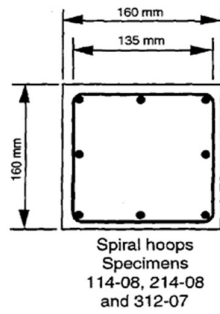
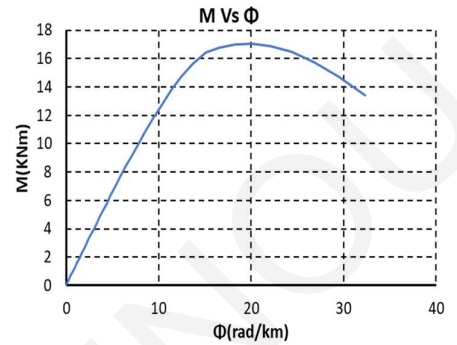
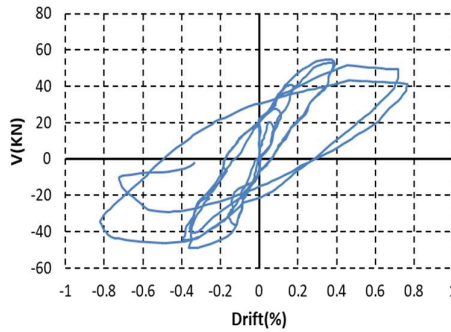


图2 加力装置

Member Response

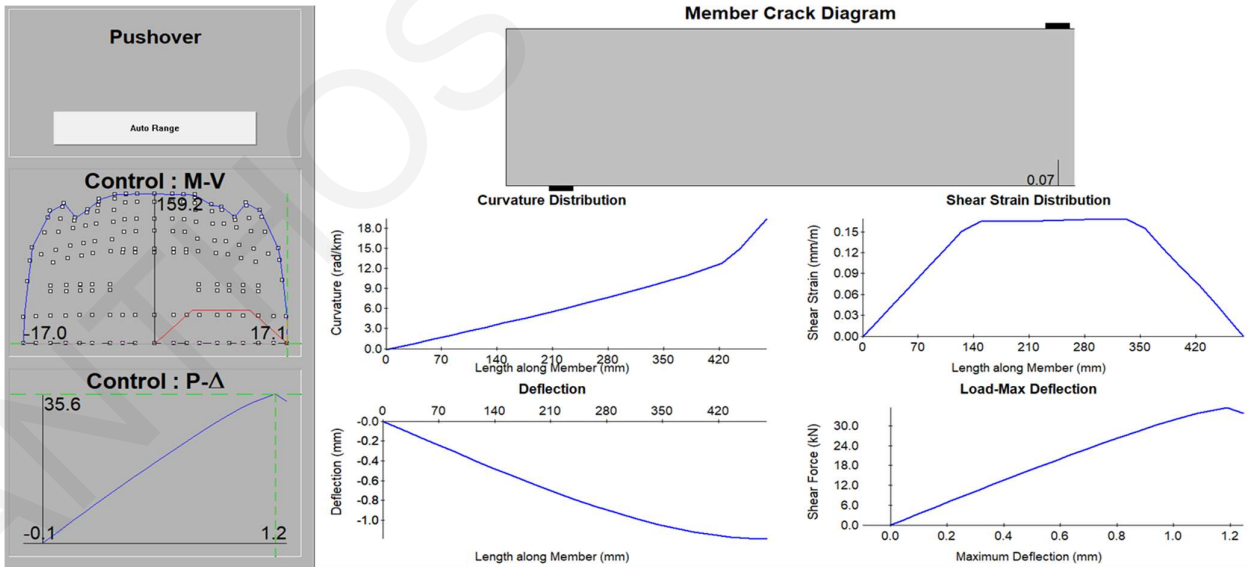


Figure B. 42: Specimen 312-07, experimental envelope curve and response 2000 section and member analysis (Zhou et al., 1987).

Zhou et al. (1987)

Specimen 322-07

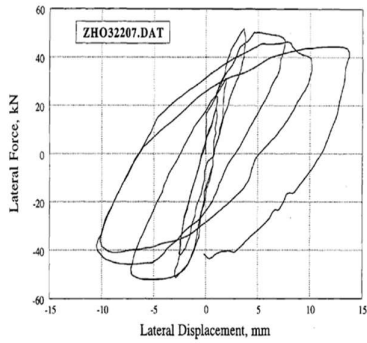


Figure 47. Specimen 322-07 of Zhou et al. 1987

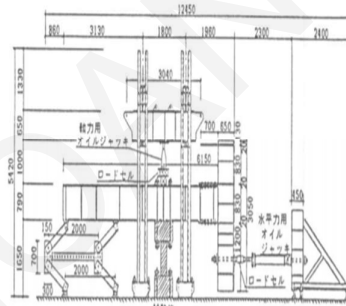
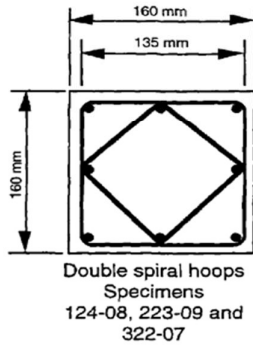
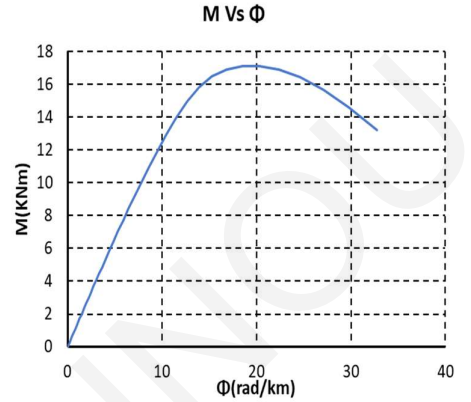
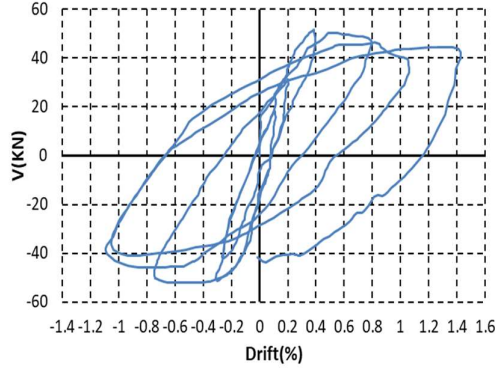


図2 加力装置

Member Response

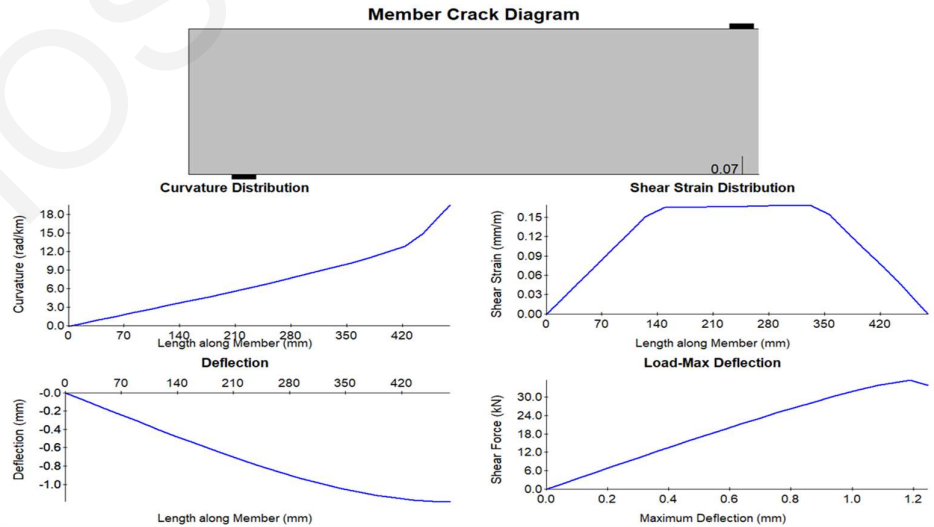
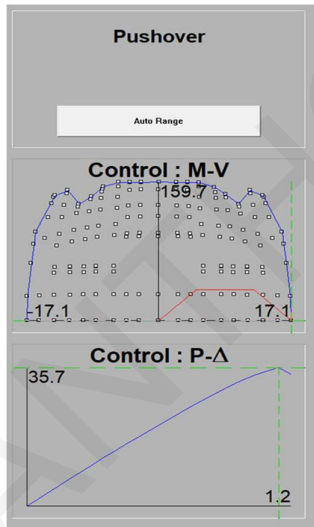


Figure B. 43: Specimen 322-07, experimental envelope curve and response 2000 section and member analysis (Zhou et al., 1987).

Ono et al. (1989)

Specimen CA025C

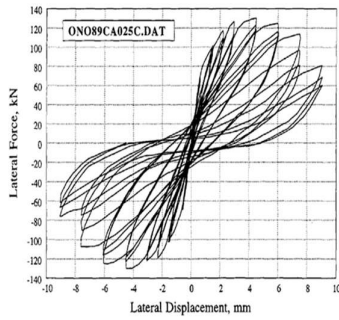
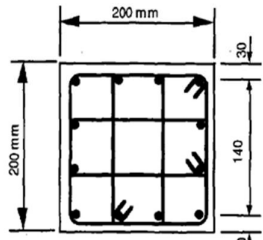
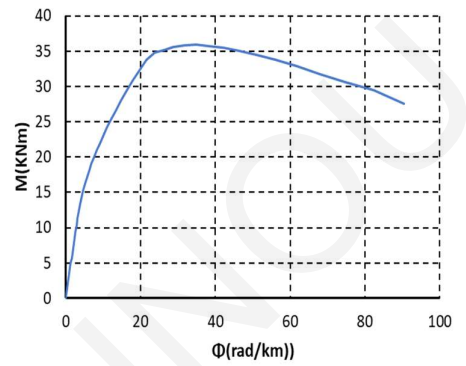
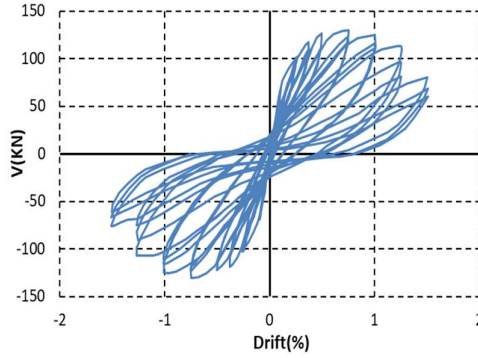
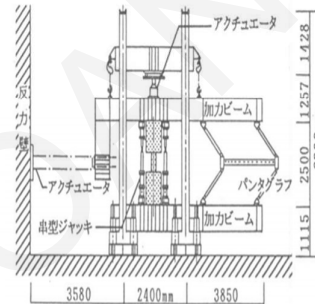


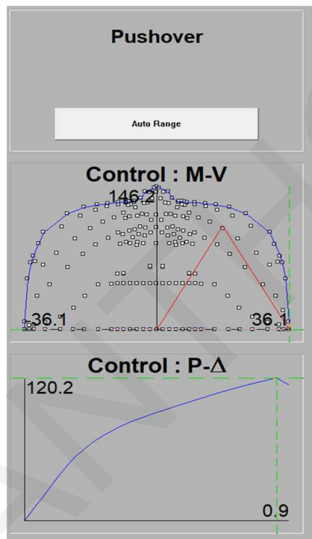
Figure 64. Specimen CA025C of Ono 1989



Specimens CA025C and CA060C



Member Response



Member Crack Diagram

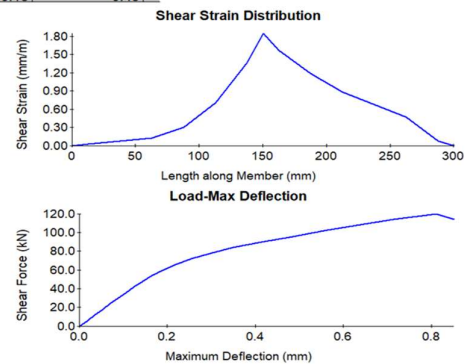
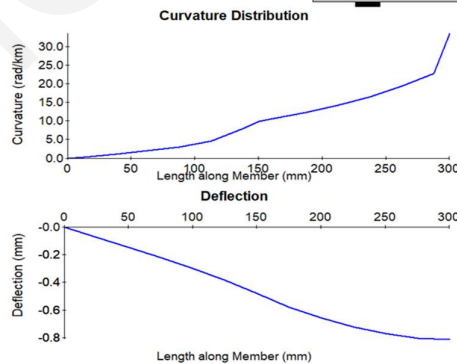
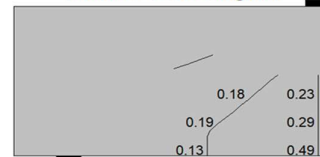


Figure B. 44: Specimen CA025C, experimental envelope curve and response 2000 section and member analysis (Ono et al., 1989).

Ono et al. (1989)

Specimen CA060C

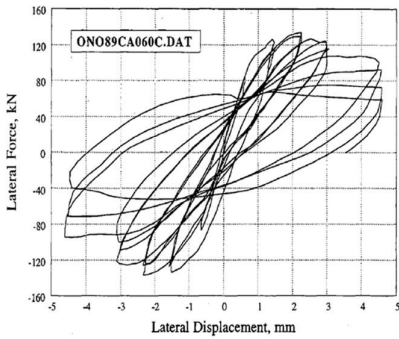
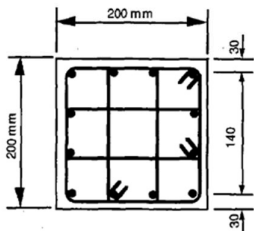
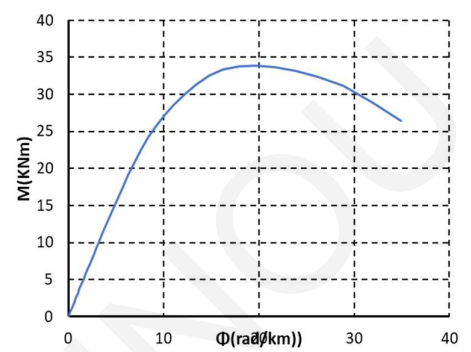
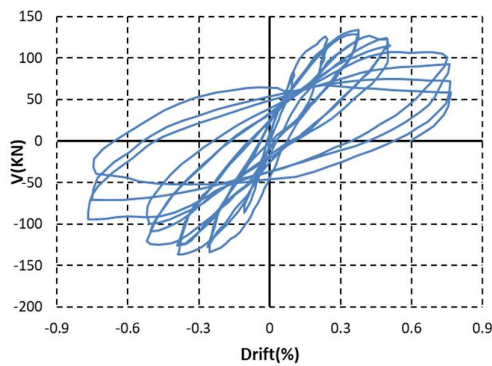
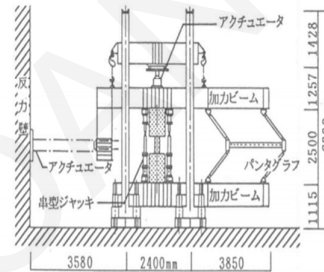


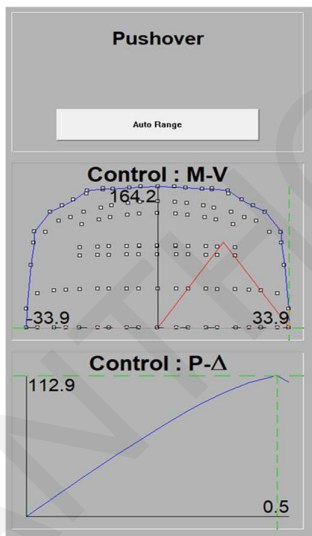
Figure 65. Specimen CA060C of Ono 1989



Specimens CA025C and CA060C



Member Response



Member Crack Diagram

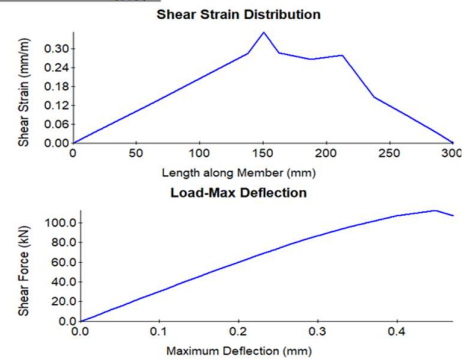
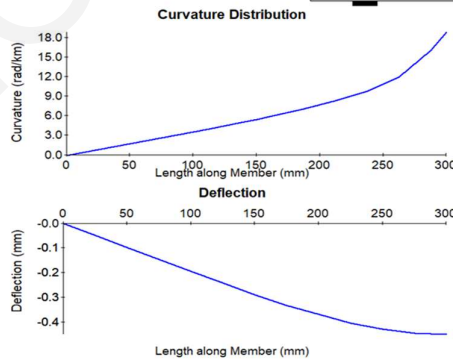


Figure B. 45: Specimen CA060C, experimental envelope curve and response 2000 section and member analysis (Ono et al., 1989).

Amitsu (1991)

Specimen CB060C

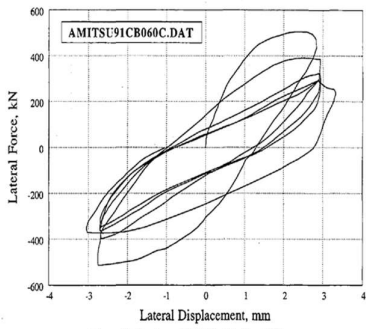
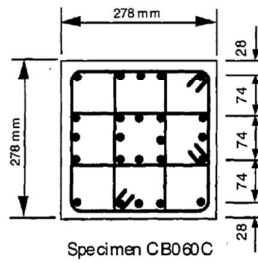
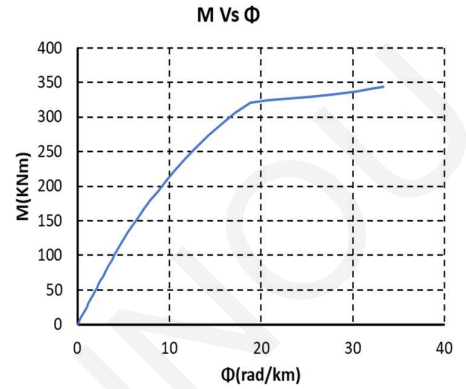
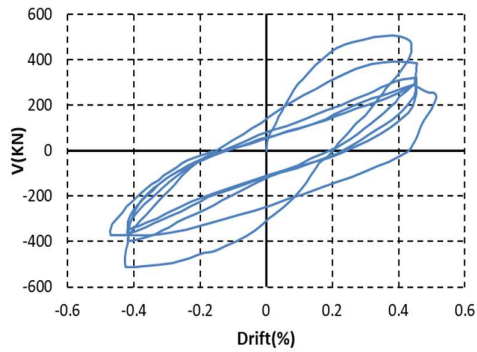
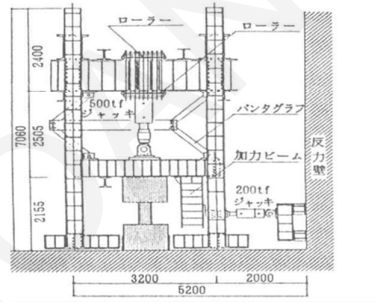


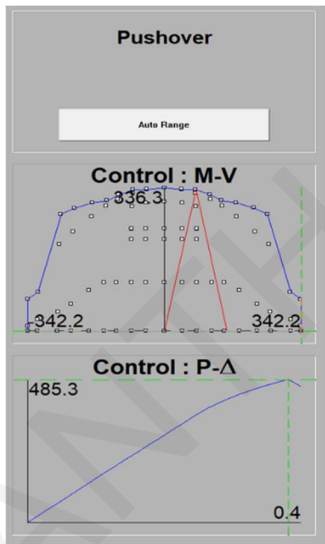
Figure 73. Specimen CB060C of Amitsu 1991



Specimen CB060C



Member Response



Member Crack Diagram

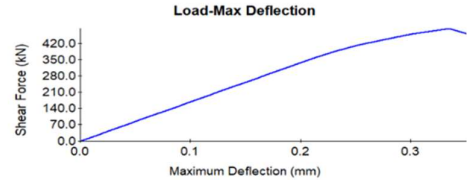
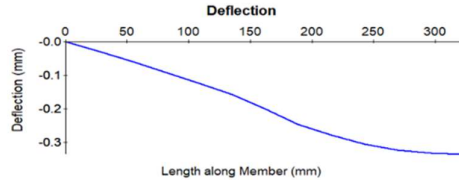
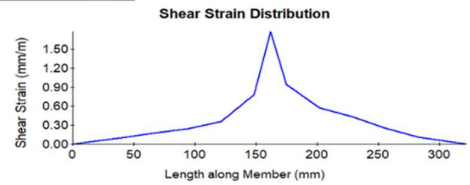
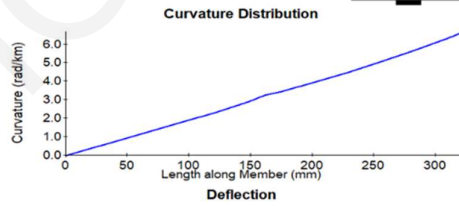


Figure B. 46: Specimen CB060C, experimental envelope curve and response 2000 section and member analysis (Amitsu, 1991).

Wight and Sozen (1973)
Specimen 40.033a(East)

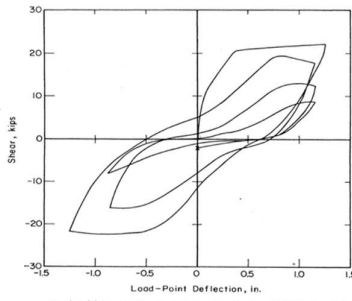


Fig. 4-1 (a) Shear-Drift Relationship, Specimen 40.033a, East End

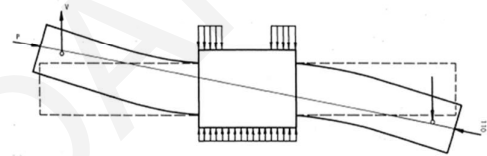
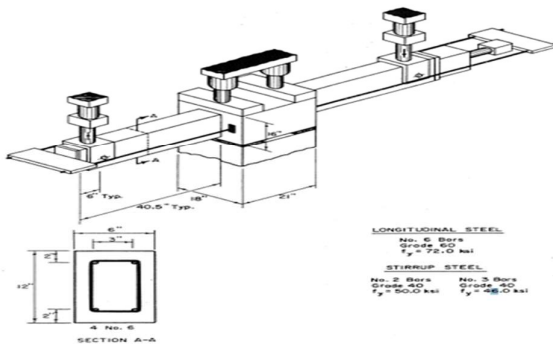
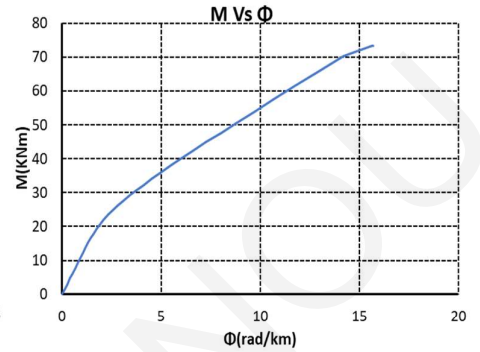
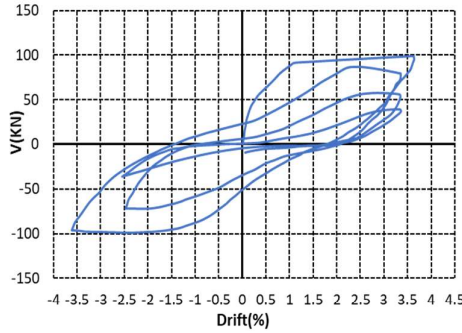


Fig. 2-3 Type of Loads Applied to Test Specimen

Member Response

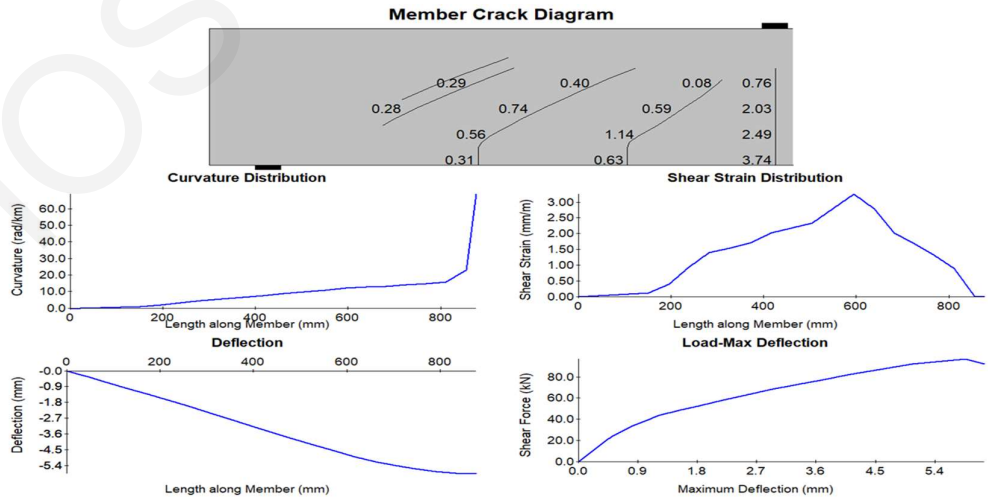
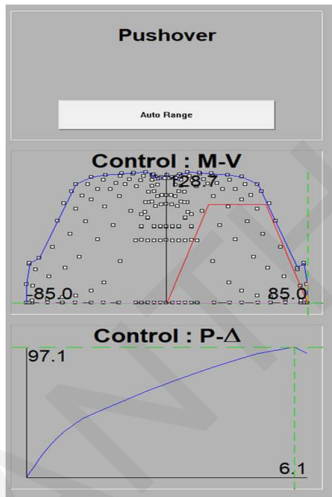


Figure B. 47: Specimen 40.033a(East) , experimental envelope curve and response 2000 section and member analysis (Wight and Sozen, 1971).

Wight and Sozen (1971)

Specimen 40.033a(west)

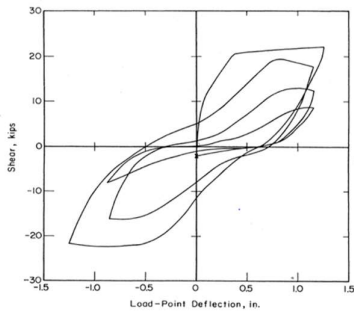


Fig. 4.1 (a) Shear-Deflection Relationship, Specimen 40.033a, Test End

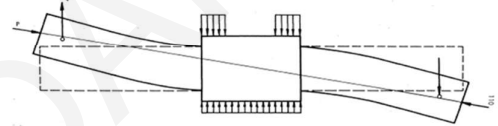
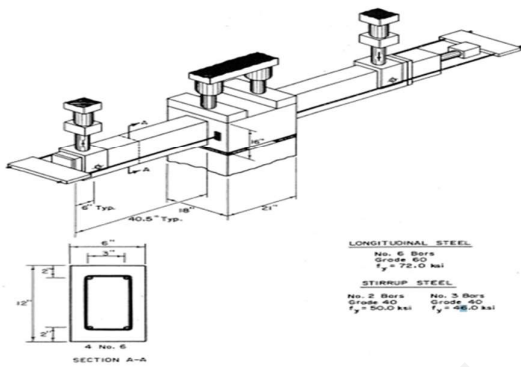
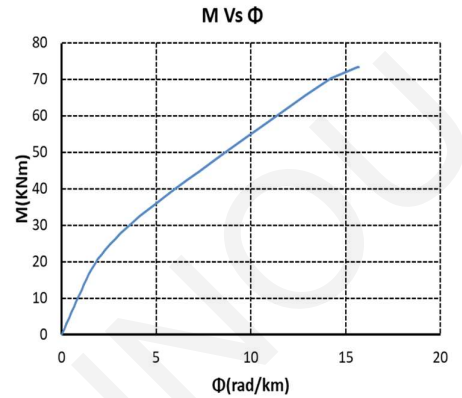
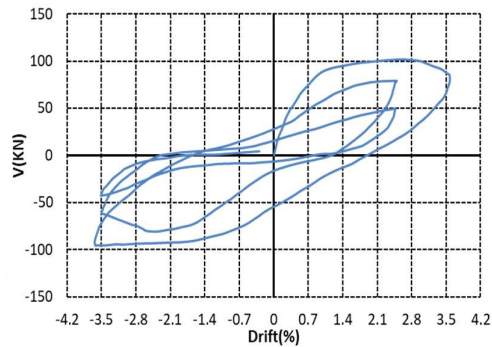


Fig. 2.3 Type of Loads Applied to Test Specimens

Member Response

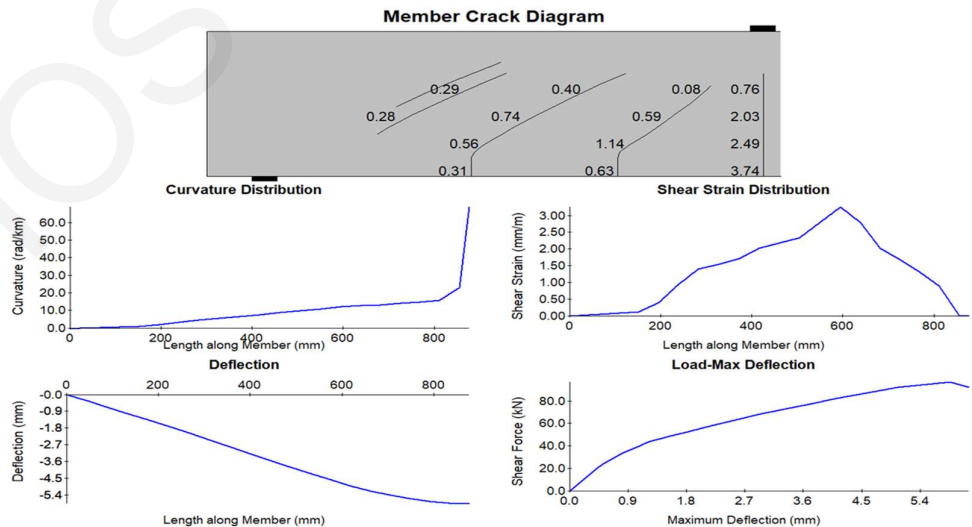
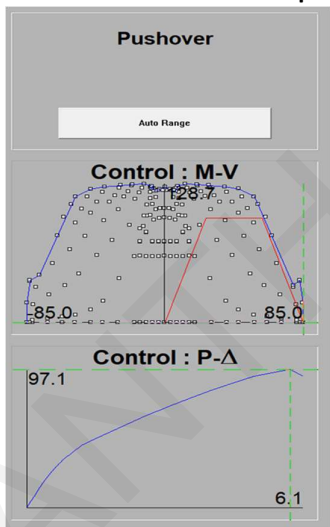


Figure B. 48: Specimen 40.033a(West), experimental envelope curve and response 2000 section and member analysis (Wight and Sozen, 1971).

Wight and Sozen (1971)

Specimen 40.048.(East)

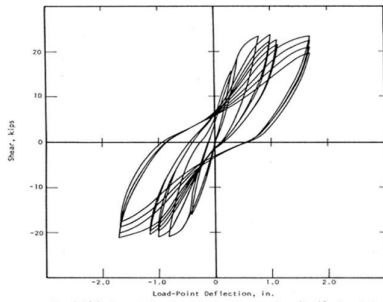


Fig. 4.1(j) Shear-Deflection Relationship, Specimen 40.048, East End

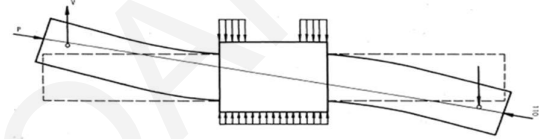
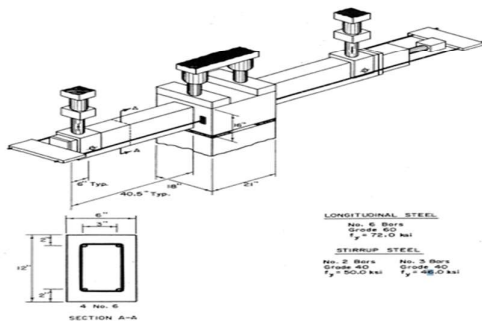
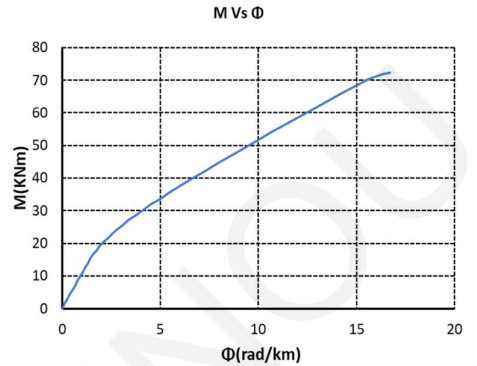
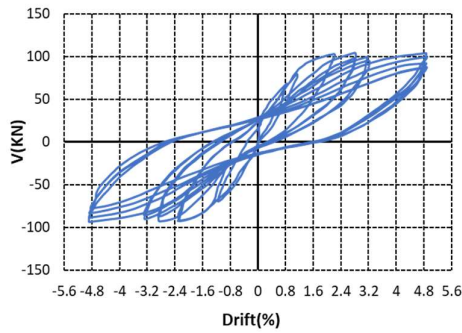


Fig. 2.3 Type of Loads Applied to Test Specimens

Member Response

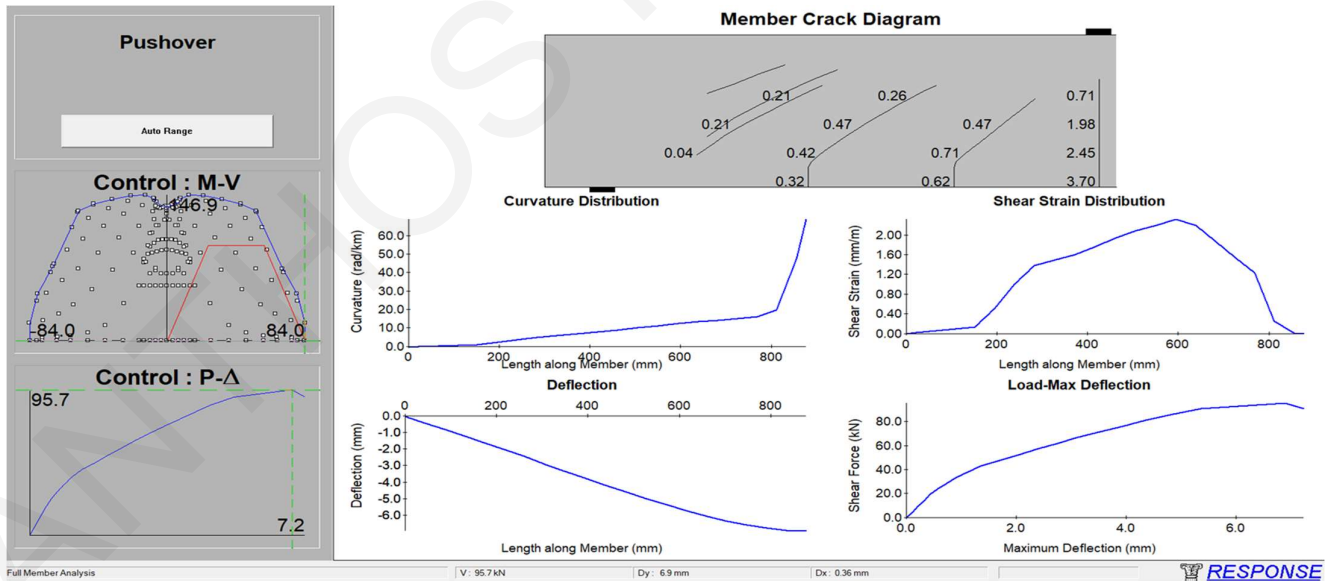


Figure B. 49: Specimen 40.048(East), experimental envelope curve and response 2000 section and member analysis (Wight and Sozen, 1971).

Wight and Sozen (1971)

Specimen 40.048(West)

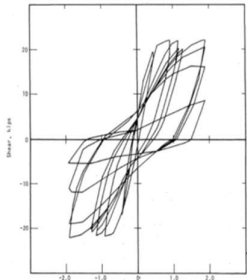


Fig. 4.1(3) Shear-Deflection Relationship, Specimen M.048, West End

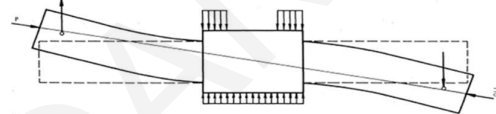
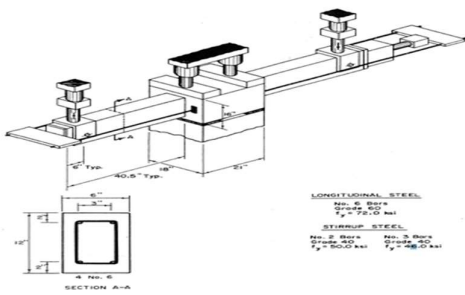
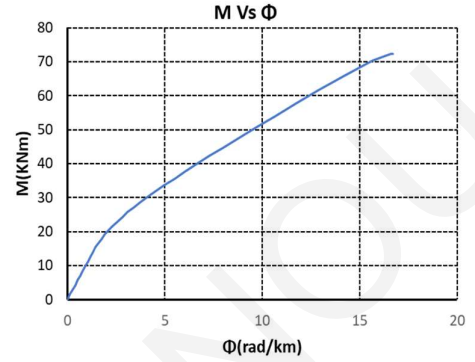
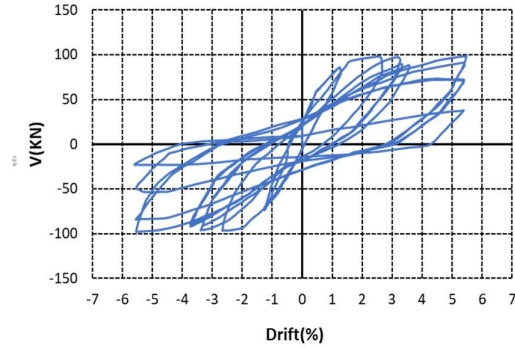


Fig. 2.3 Type of Loads Applied to Test Specimens

Member Response

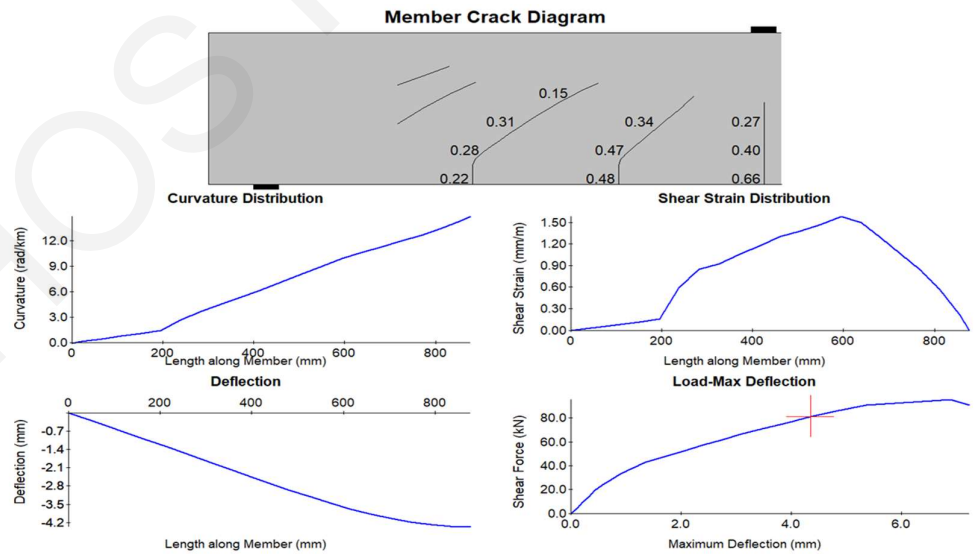
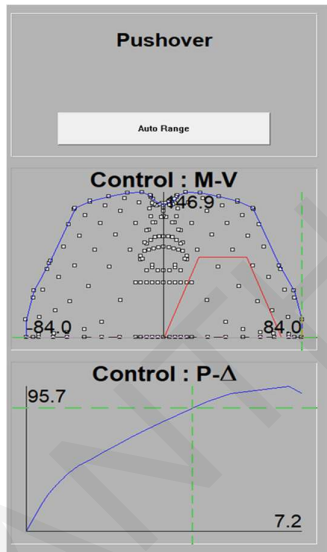


Figure B. 50: Specimen 40.048(West), experimental envelope curve and response 2000 section and member analysis (Wight and Sozen, 1971).

Wight and Sozen (1971)

Specimen 40.033(East)

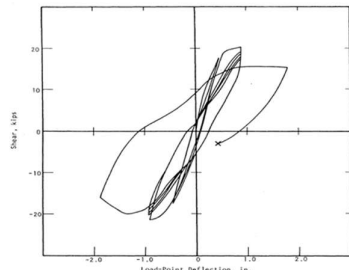


Fig. 4.1(c) Shear-Deflection Relationship, Specimen 40.033, East End

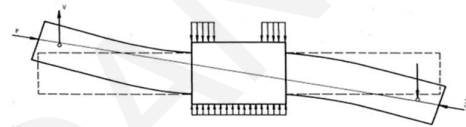
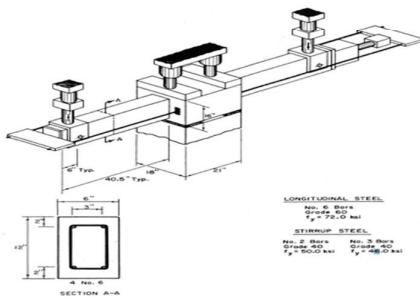
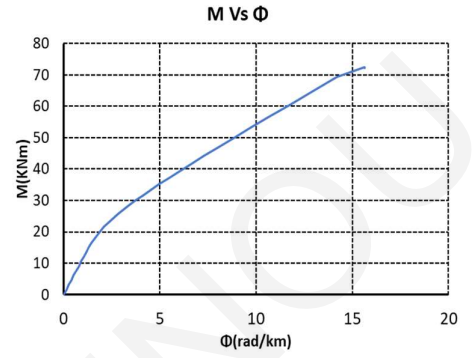
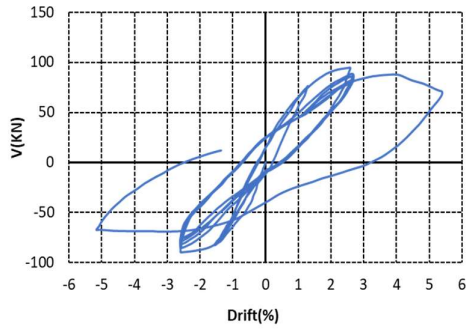


Fig. 2.3 Type of Load Applied to Test Specimen

Member Response

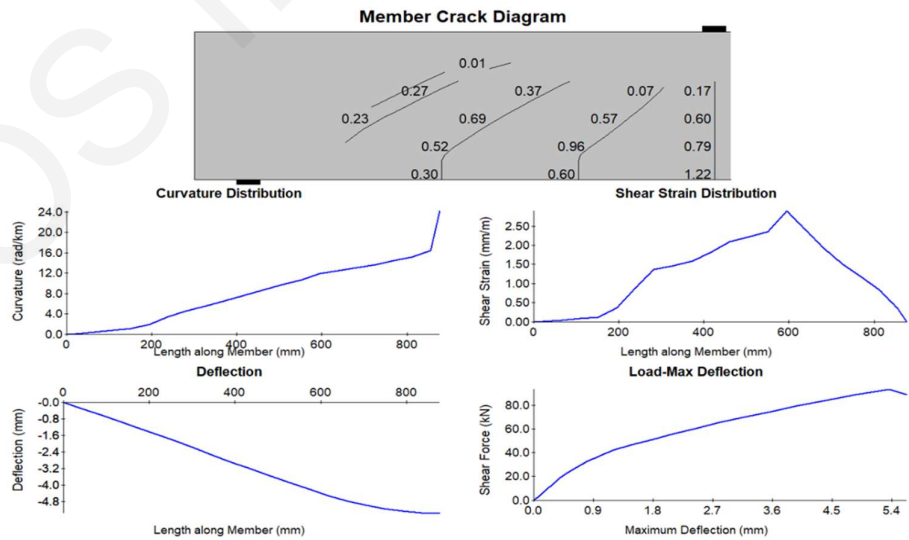
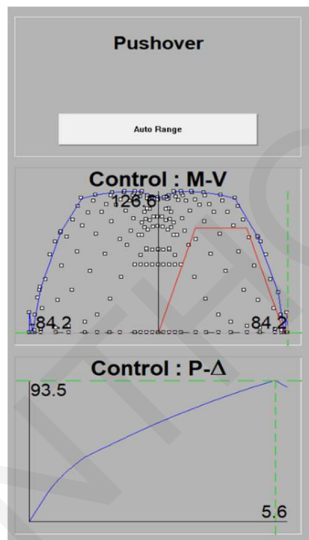


Figure B. 51: Specimen 40.033(East), experimental envelope curve and response 2000 section and member analysis (Wight and Sozen, 1971).

Wight and Sozen (1971)

Specimen 40.033(West)

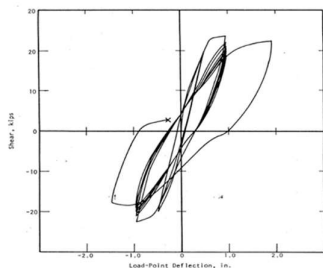


Fig. 4.16(a) Shear-Deflection Relationship for Specimen 40.033, West End

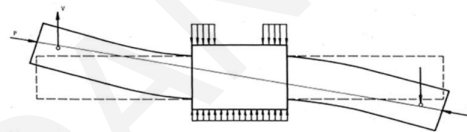
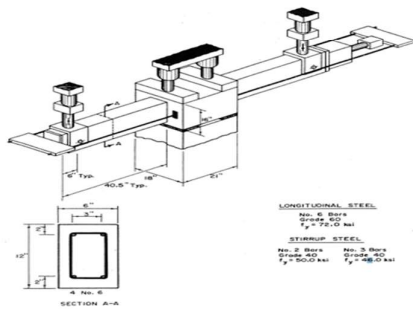
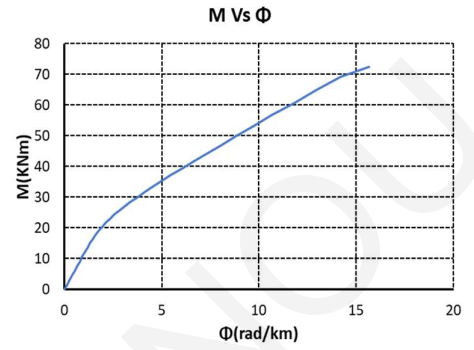
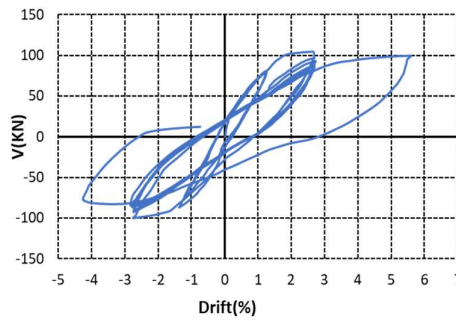


Fig. 2.3 Type of Load Applied to Test Specimens

Member Response

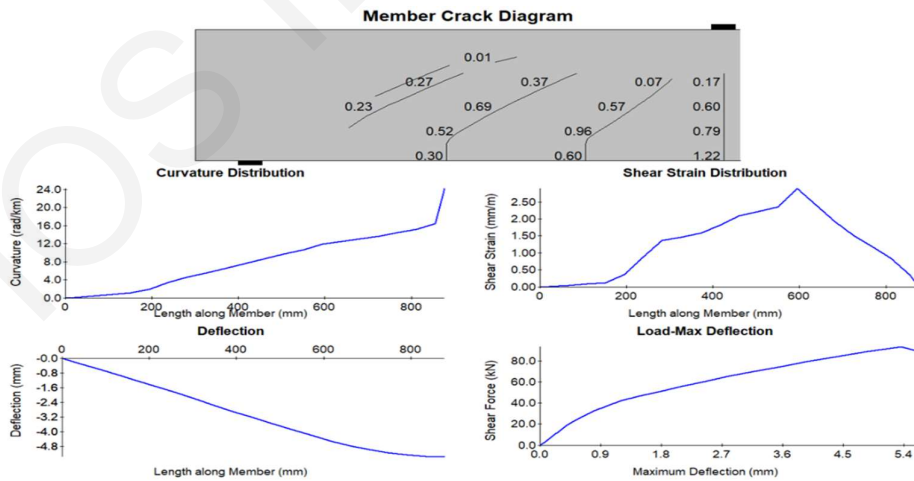
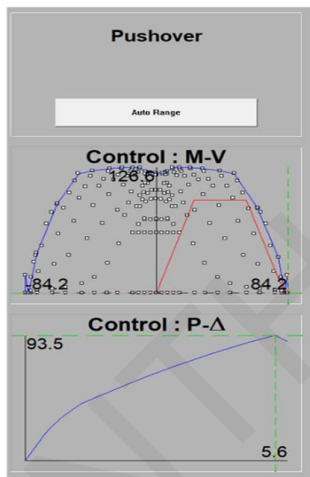


Figure B. 52: Specimen 40.033(West), experimental envelope curve and response 2000 section and member analysis (Wight and Sozen, 1971).

Wight and Sozen (1971)

Specimen 40.067(East)

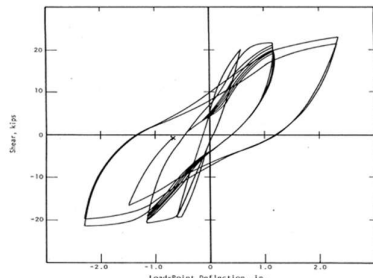


Fig. 4.16(a) Shear-Deflection Relationship, Specimen 40.067, East End

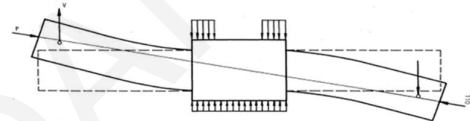
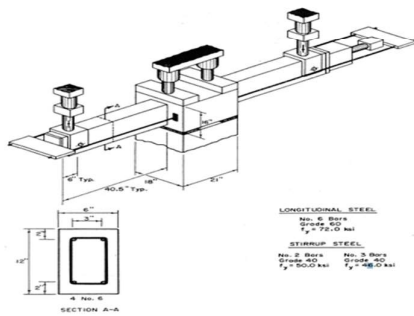
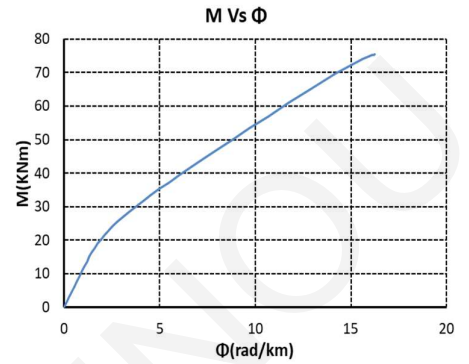
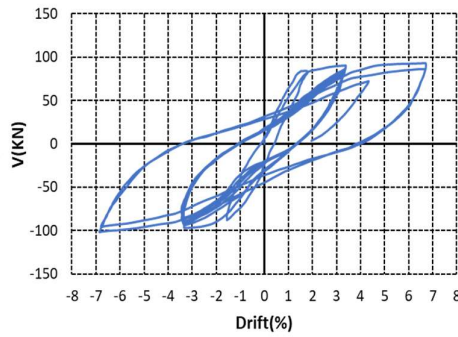


Fig. 2.3 Type of Loads Applied to Test Specimen

Member Response

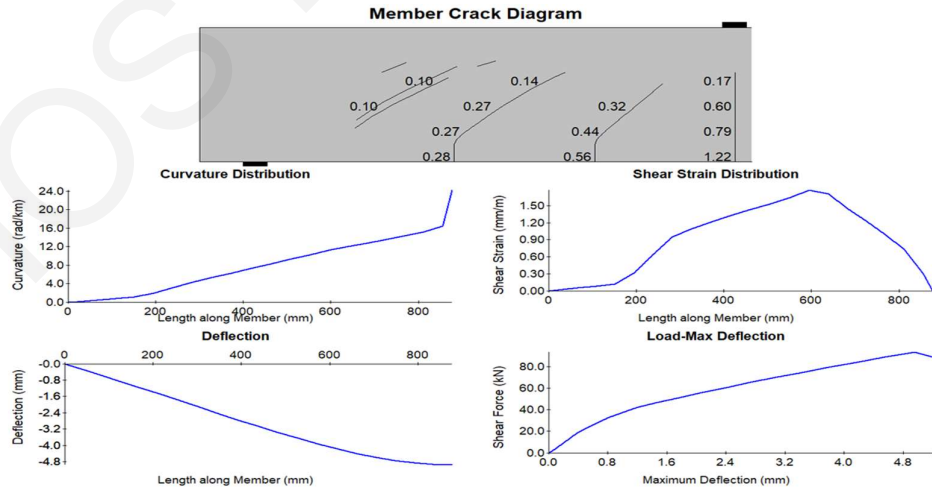
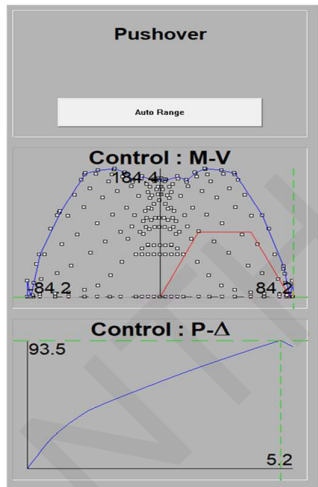


Figure B. 53: Specimen 40.067(East), experimental envelope curve and response 2000 section and member analysis (Wight and Sozen, 1971).

Wight and Sozen (1971)

Specimen 40.067(West)

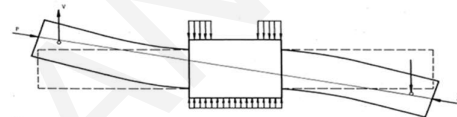
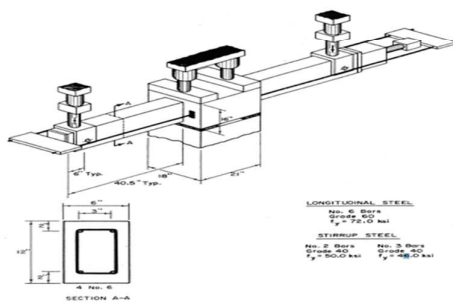
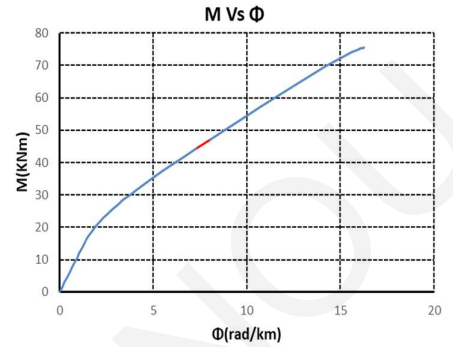
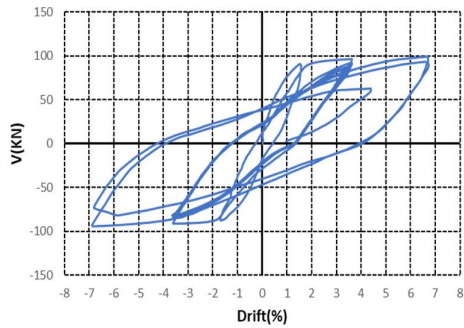
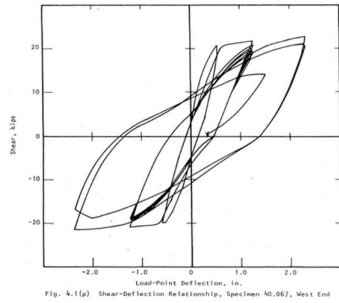


Fig. 2.3 Type of Load Applied to Test Specimen

Member Response

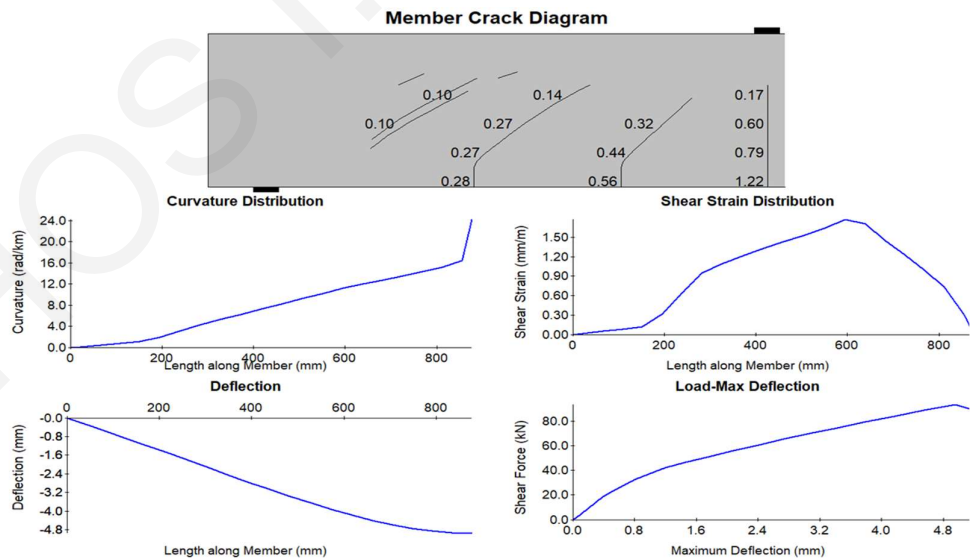
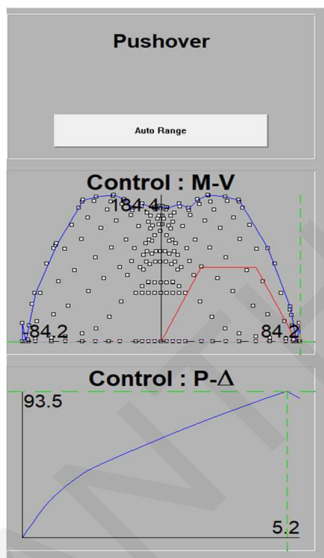


Figure B. 54: Specimen 40.067(West), experimental envelope curve and response 2000 section and member analysis (Wight and Sozen, 1971).

Wight and Sozen (1971)

Specimen 40.147(East)

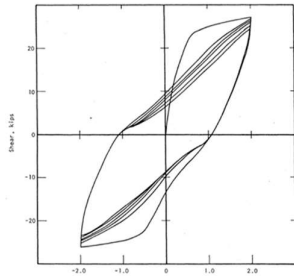


Fig. 4.16a Shear-Deflection Relationship, Specimen 40.147, East End

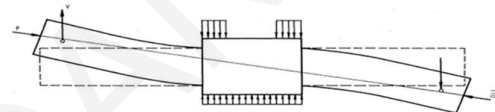
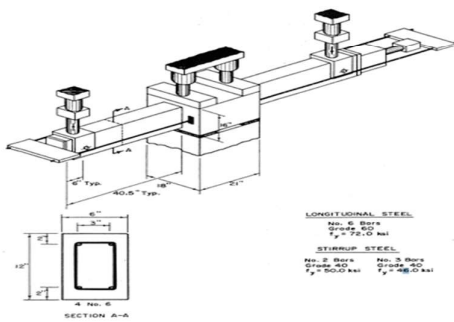
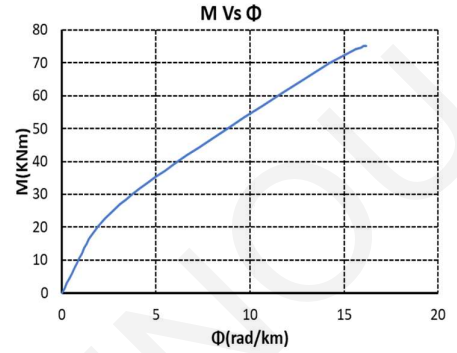
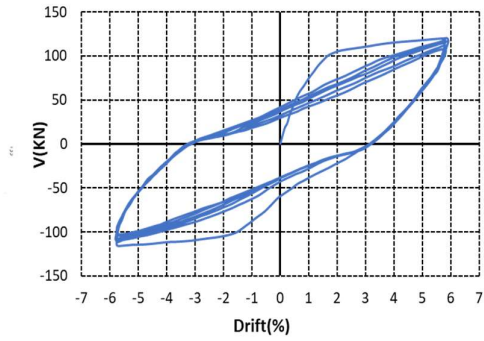


Fig. 2.3 Type of Load Applied to Test Specimen

Member Response

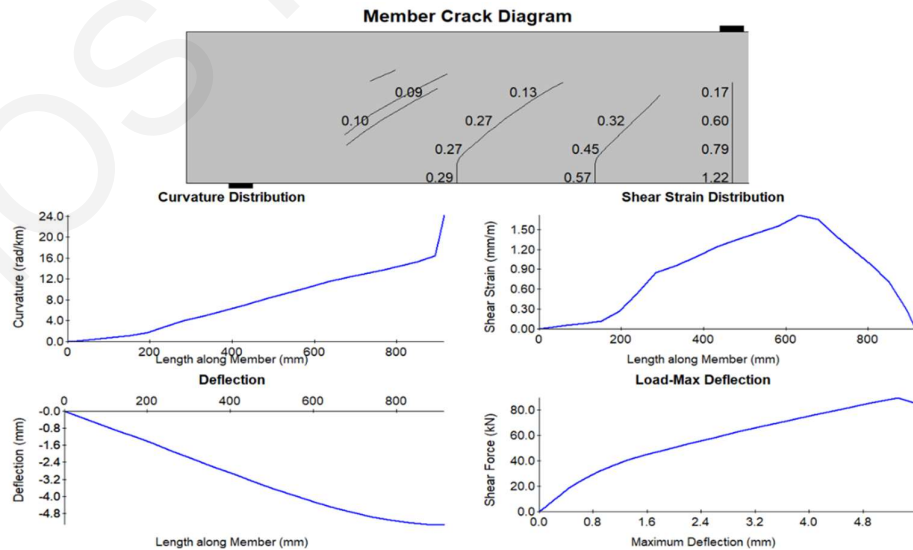
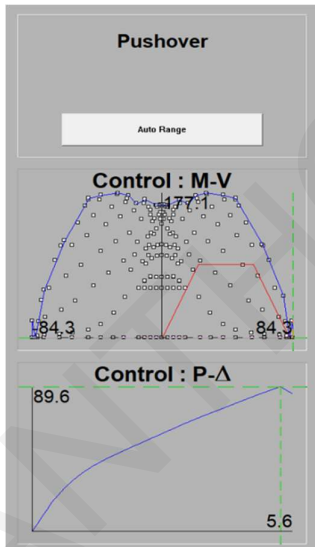


Figure B. 55: Specimen 40.147(East), experimental envelope curve and response 2000 section and member analysis (Wight and Sozen, 1971)

Wight and Sozen (1971)

Specimen 40.147(West)

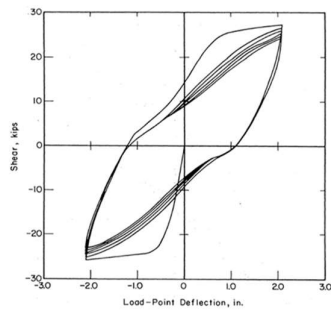


Fig. 4.1 (a) Shear-Deflection Relationship, Specimen 40.147, West End

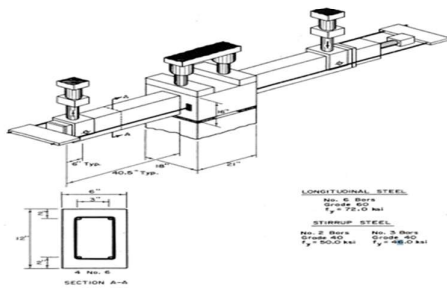
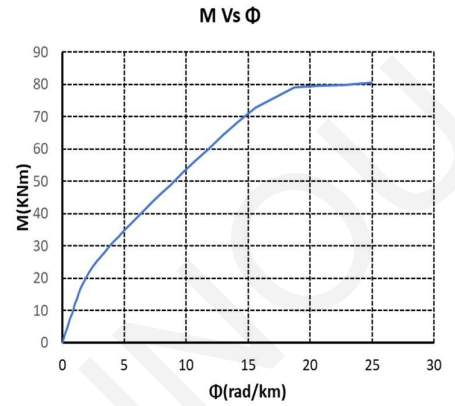
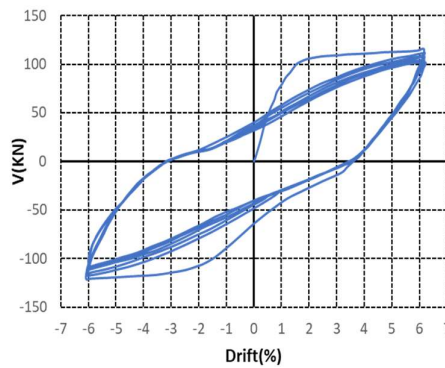


Fig. 2.3 Type of Loads Applied to Test Specimens

Member Response

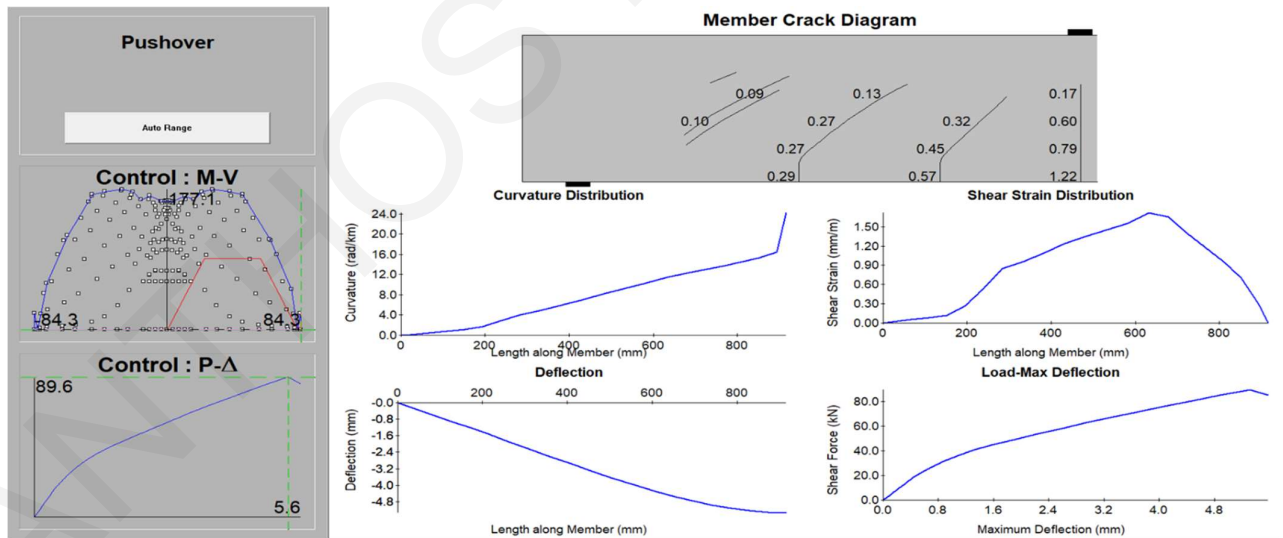


Figure B. 56: Specimen 40.147(West), experimental envelope curve and response 2000 section and member analysis (Wight and Sozen, 1971).

Wight and Sozen (1971)

Specimen 40.092(East)

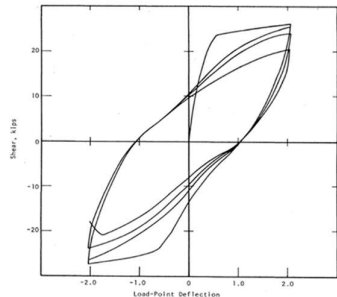


Fig. 4.16a Shear-Deflection Relationship, Specimen 40.092, East End

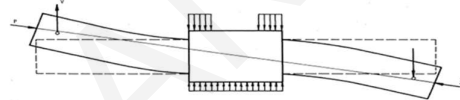
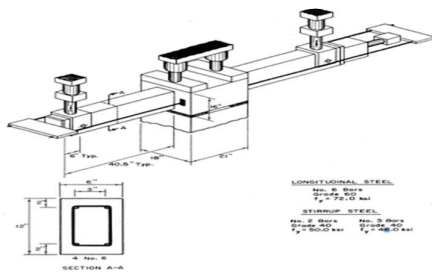
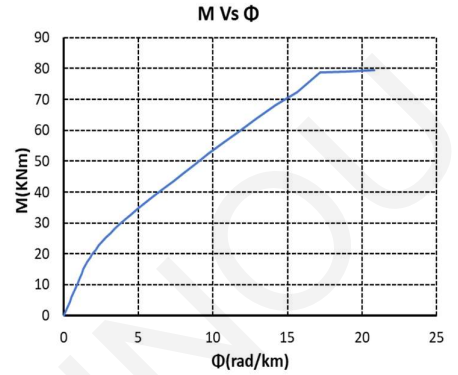
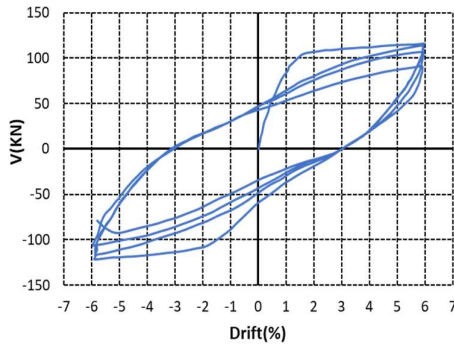


Fig. 2.3 Type of Loads Applied to Test Specimen

Member Response

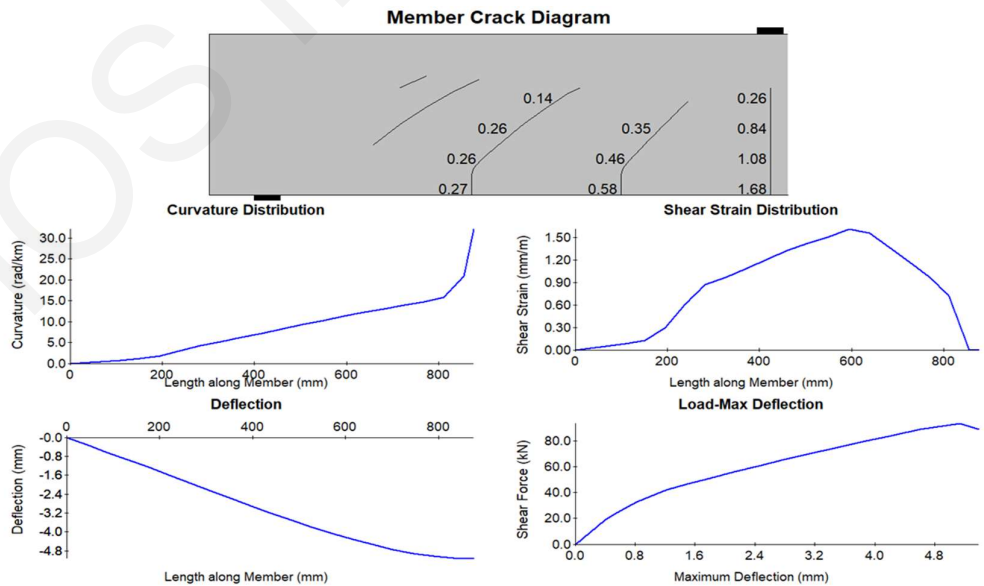
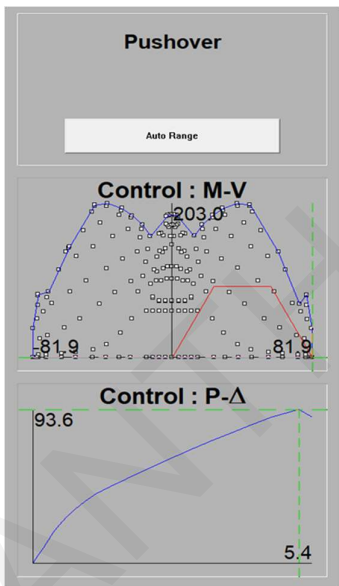


Figure B. 57: Specimen 40.082(East), experimental envelope curve and response 2000 section and member analysis (Wight and Sozen, 1971).

Wight and Sozen (1971)

Specimen 40.092(West)

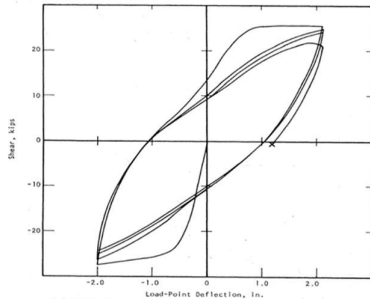


Fig. 4-1(1) Shear-Deflection Relationship, Specimen 40.092, West End

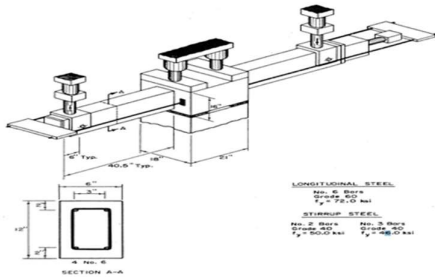
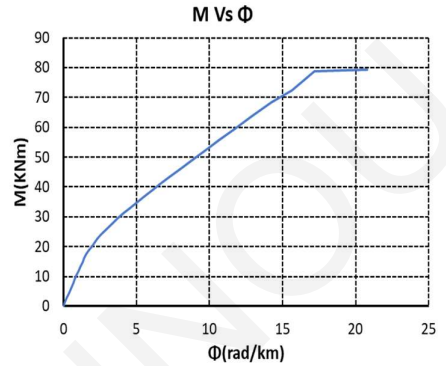
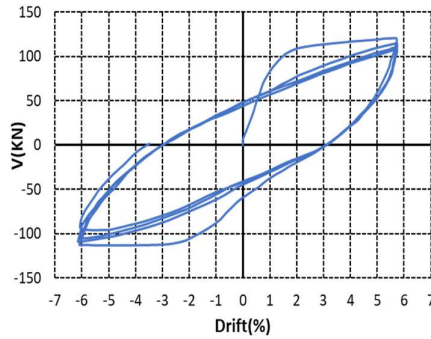


Fig. 2.3 Type of Loads Applied to Test Specimen

Member Response

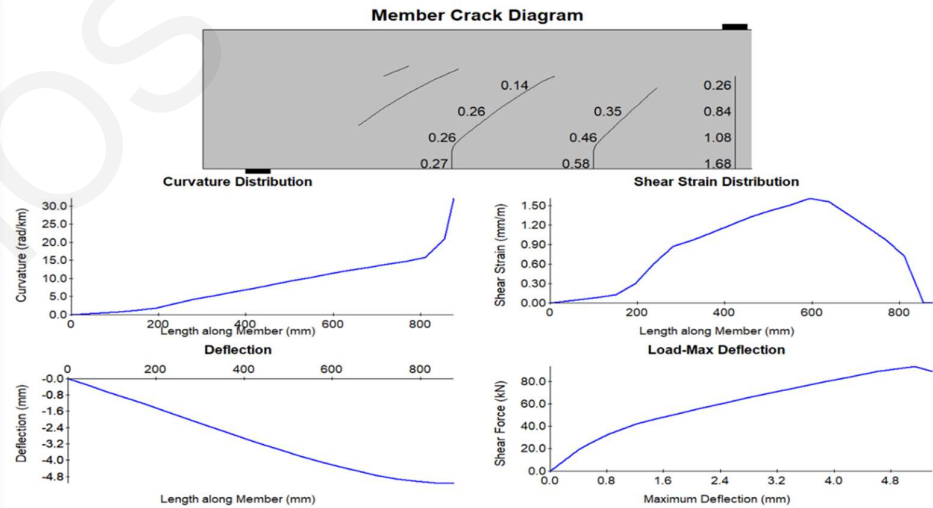
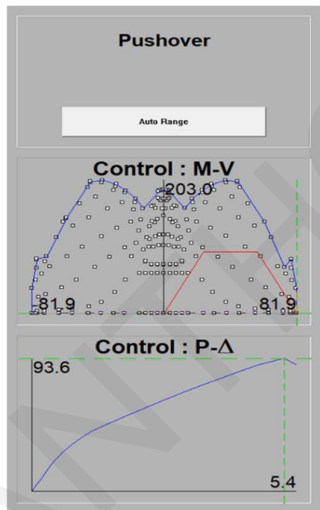


Figure B. 58: Specimen 40.082(West), experimental envelope curve and response 2000 section and member analysis (Wight and Sozen, 1971).

Lynn et al. (1998)

Specimen 2CLH18

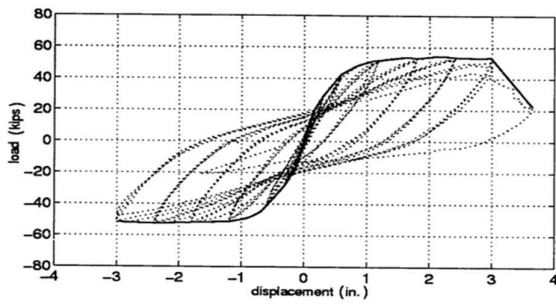
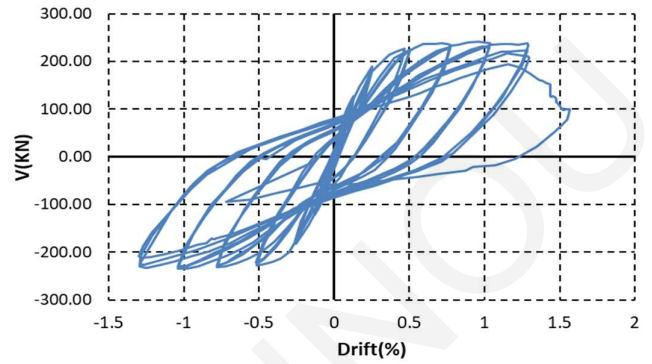
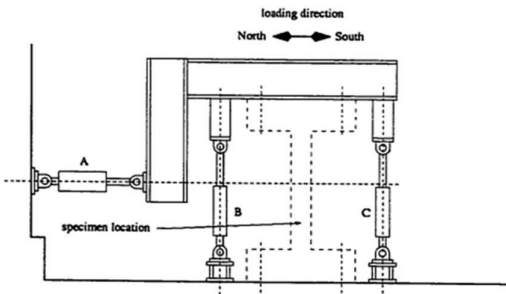
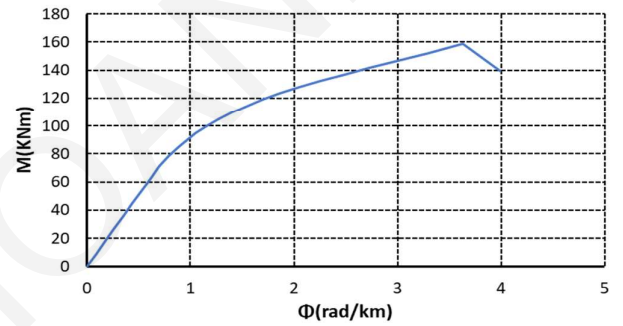


Figure 3.27: Load-displacement history, Specimen 2CLH18



M Vs Φ



Member Response

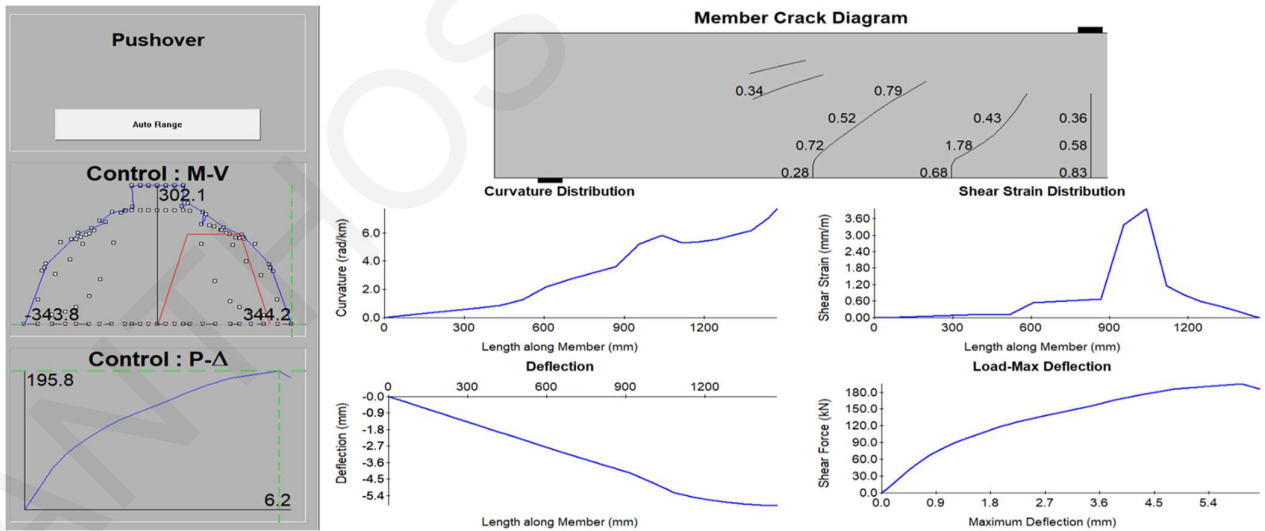


Figure B. 59: Specimen 2CLH18, experimental envelope curve and response 2000 section and member analysis (Lynn et al., 1998).

Lynn et al. (1998)
Specimen 3CLH18

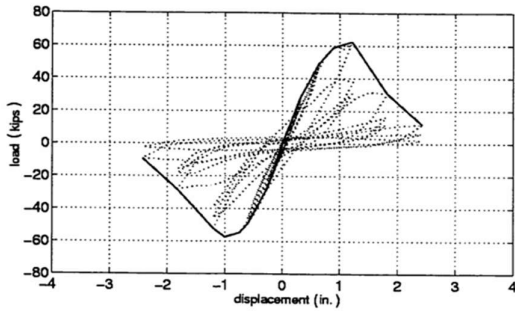
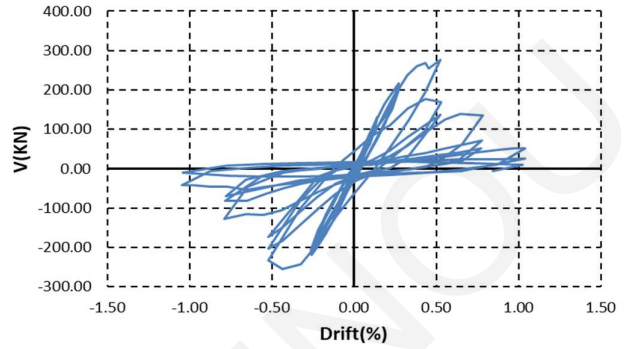
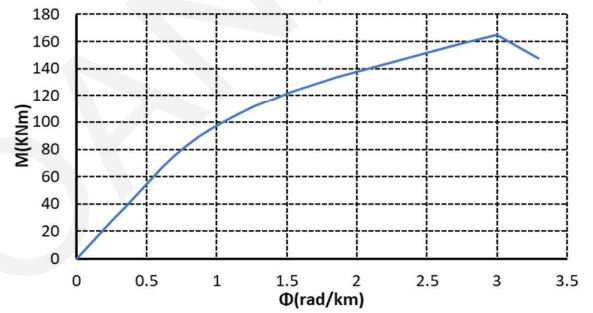
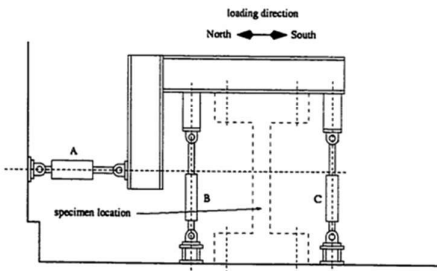


Figure 3.17: Load-displacement history, Specimen 3CLH18



M Vs Φ



Member Response

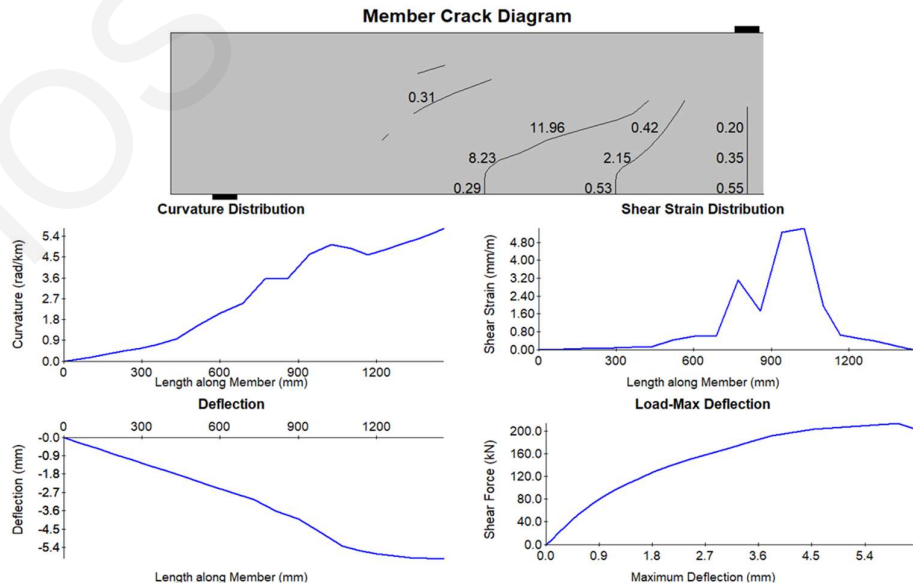
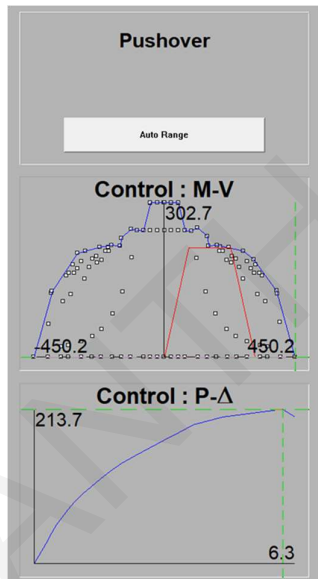


Figure B. 60: Specimen 3CLH18 experimental envelope curve and response 2000 section and member analysis (Lynn et al., 1998).

Lynn et al. (1998)

Specimen 2SLH18

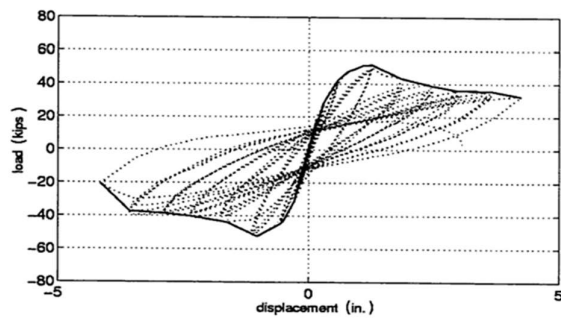
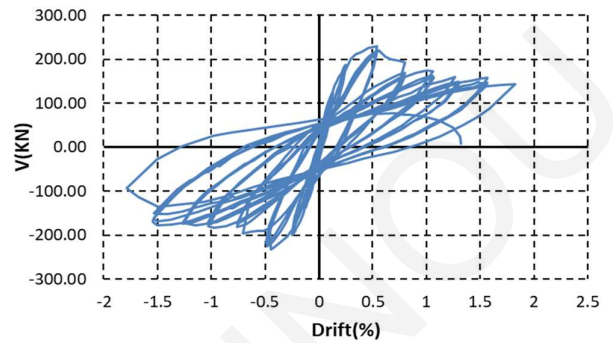
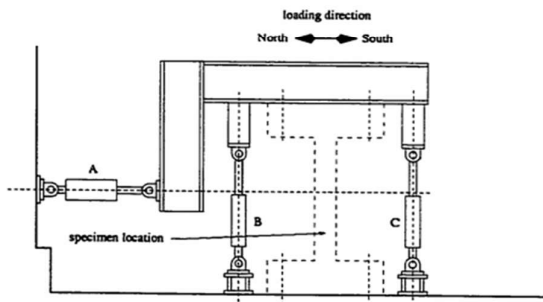
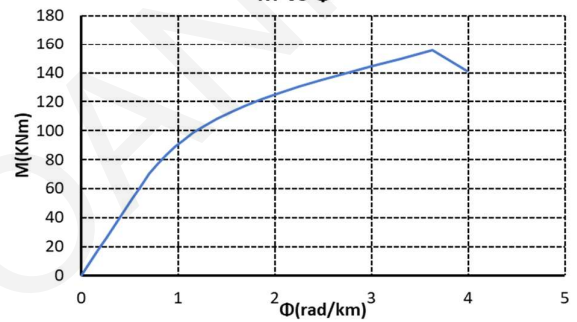


Figure 3.44: Load-displacement history, Specimen 2SLH18



M Vs Φ



Member Response

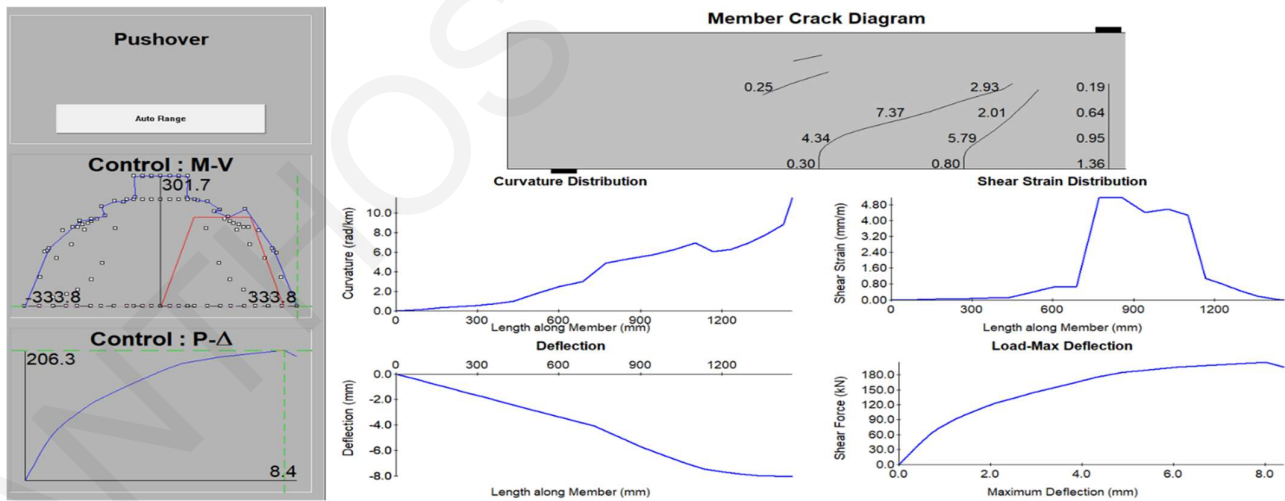


Figure B. 61: Specimen 2SLH18 experimental envelope curve and response 2000 section and member analysis (Lynn et al., 1998).

Lynn et al. (1998)

Specimen 3SMD12

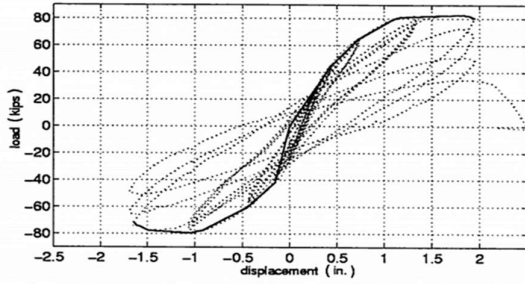
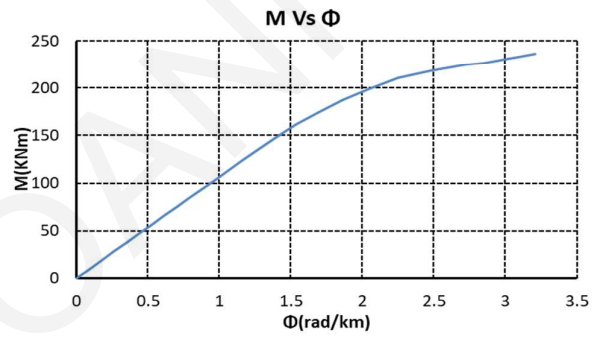
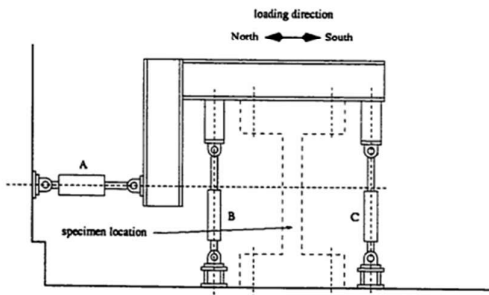
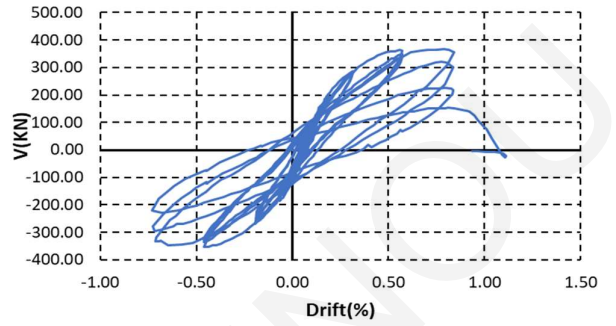


Figure 3.86: Load-displacement history, Specimen 3SMD12



Member Response

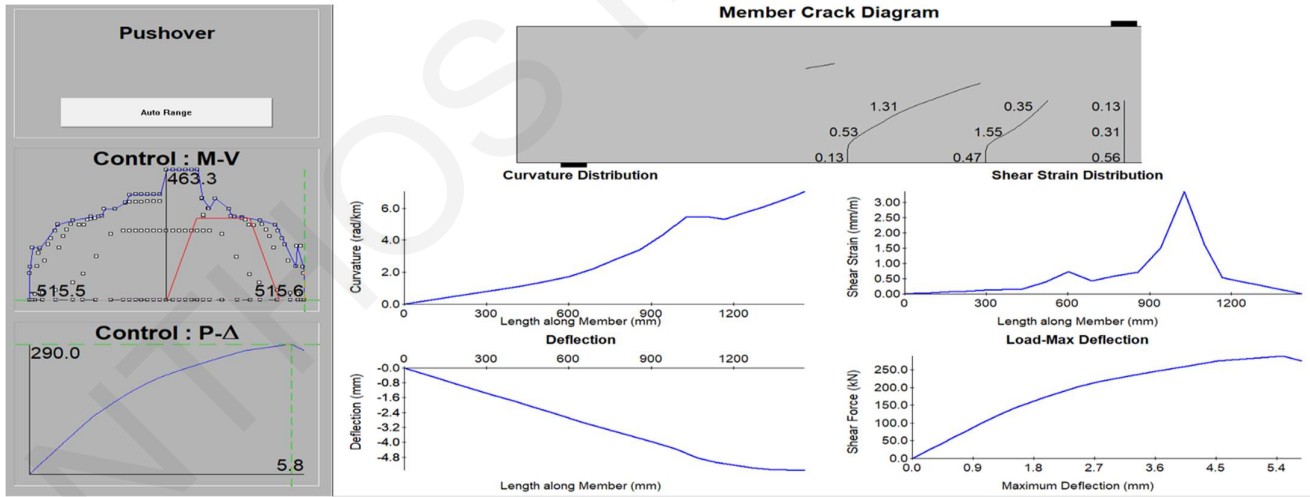


Figure B. 62: Specimen 3SMD12 experimental envelope curve and response 2000 section and member analysis (Lynn et al., 1998).

Lynn et al. (1998)

Specimen 2CMH18

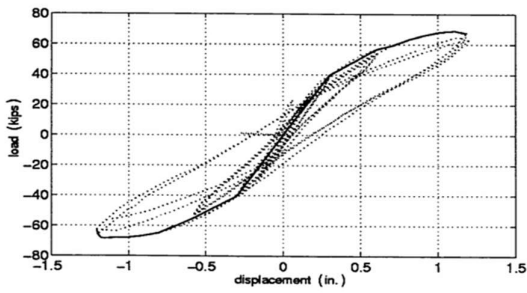
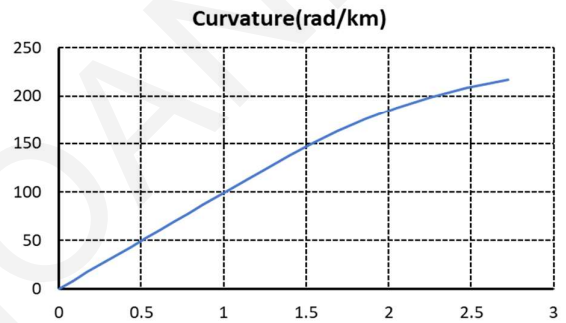
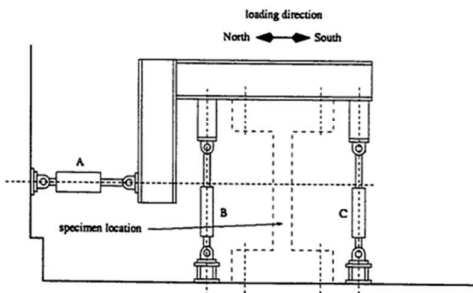
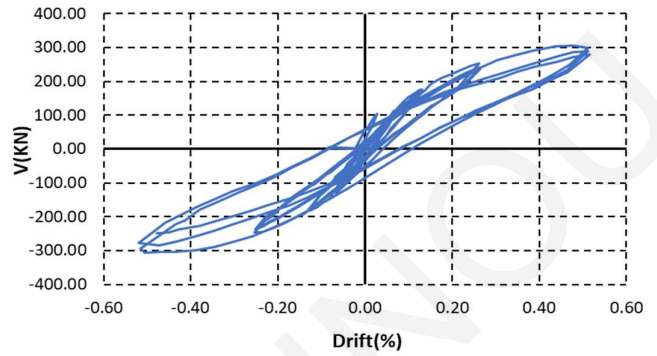


Figure 3.57: Load-displacement history, Specimen 2CMH18



Member Response

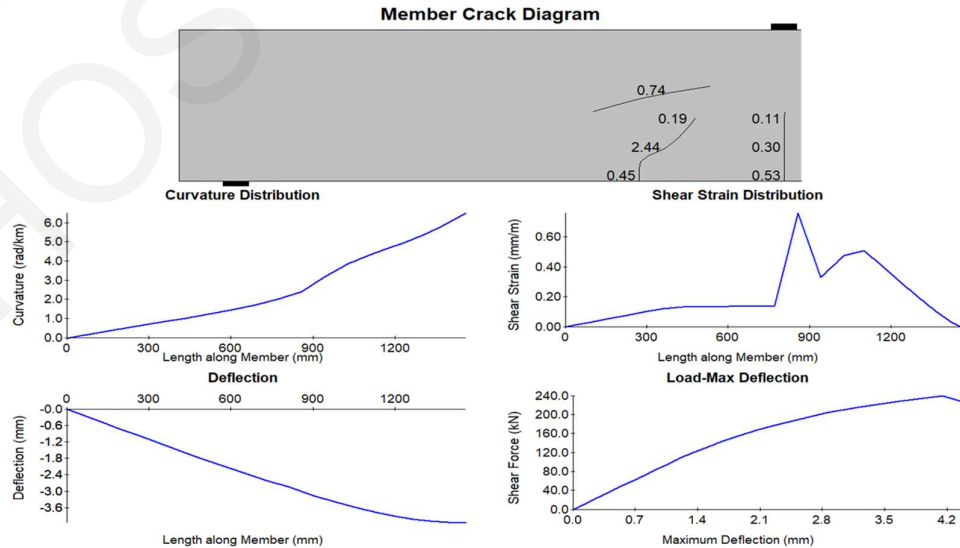
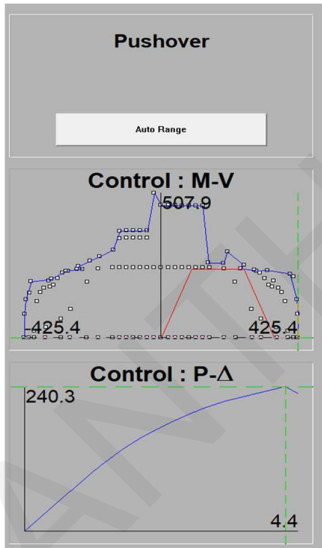
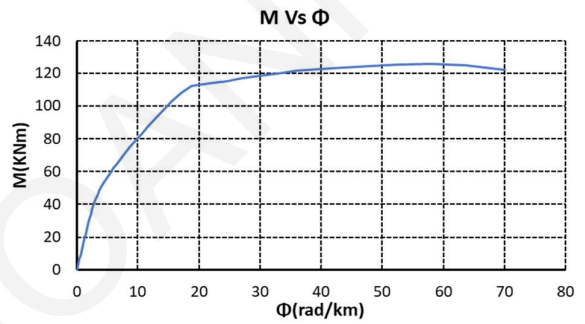
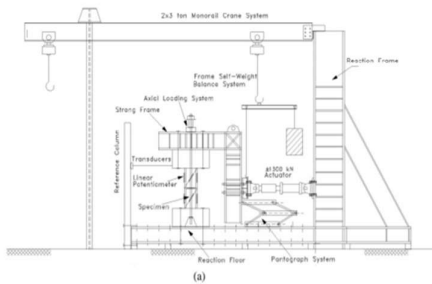
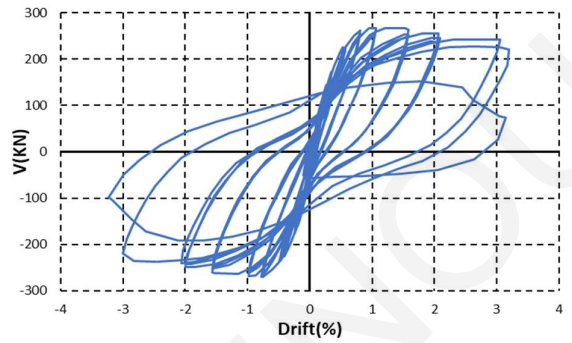
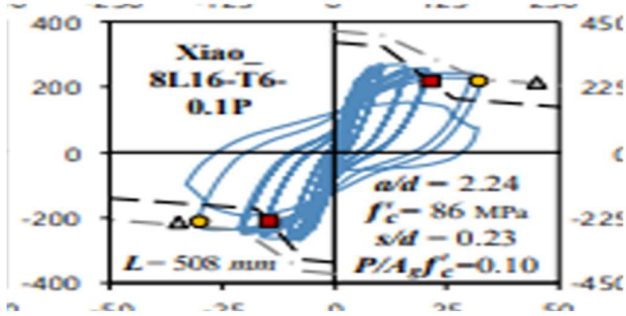


Figure B. 63: Specimen 2CMH18 experimental envelope curve and response 2000 section and member analysis (Lynn et al., 1998).

Xiao and Martirosyan (1998)

Specimen HC4-8L16-T6-0.1P



Member Response

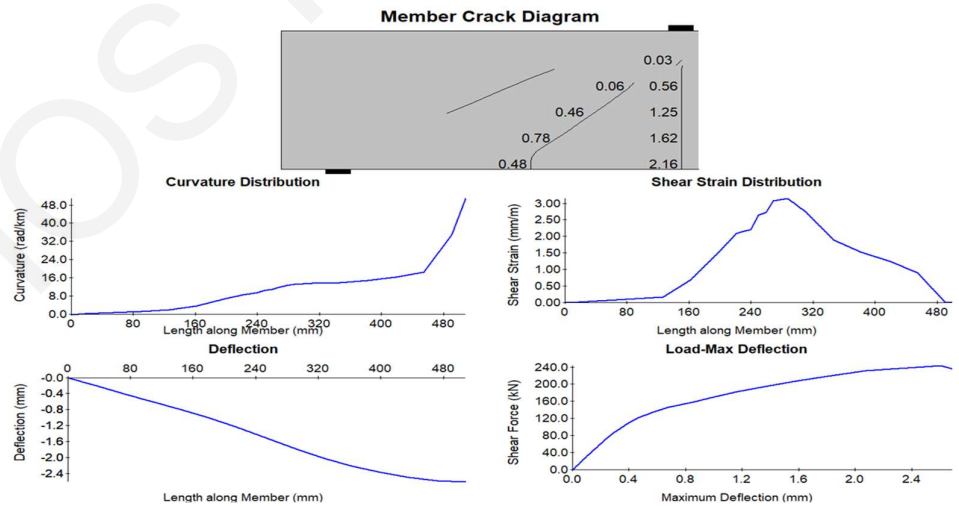
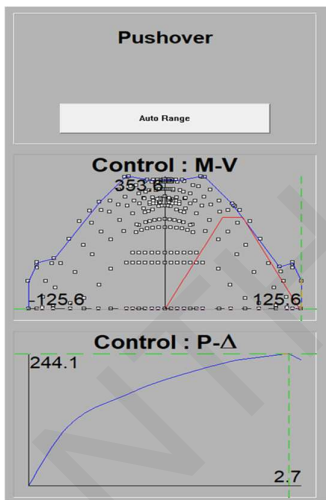
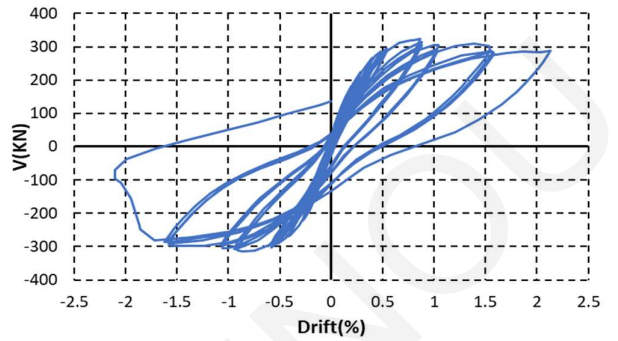
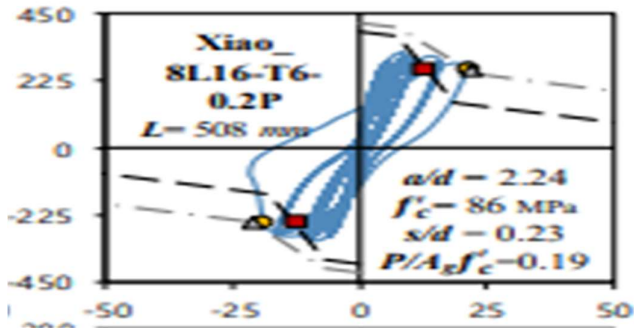


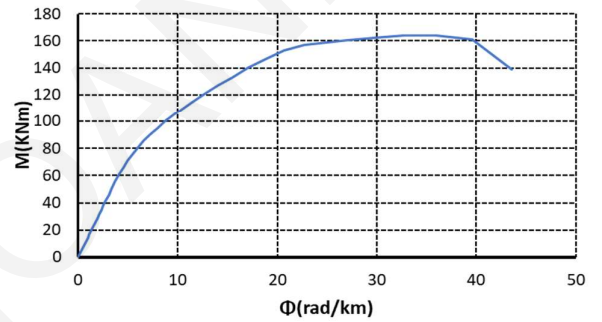
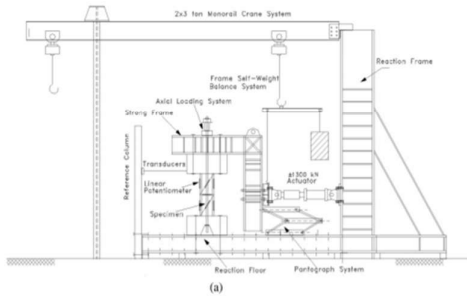
Figure B. 64: Specimen HC4-8L16-T6-0.1P experimental envelope curve and response 2000 section and member analysis (Xiao and Martirosyan, 1998).

Xiao and Martirosyan (1998)

Specimen HC4-8L16-T6-0.2P



M Vs Φ



Member Response

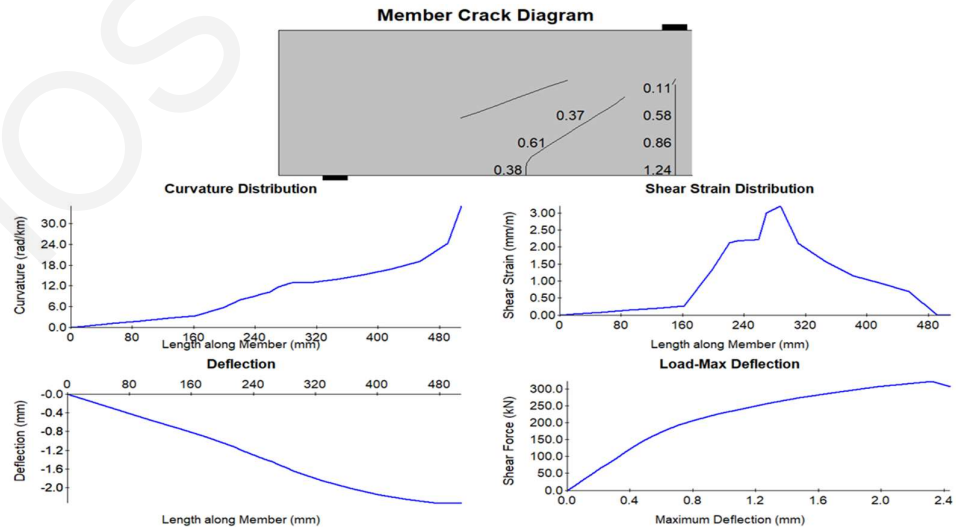
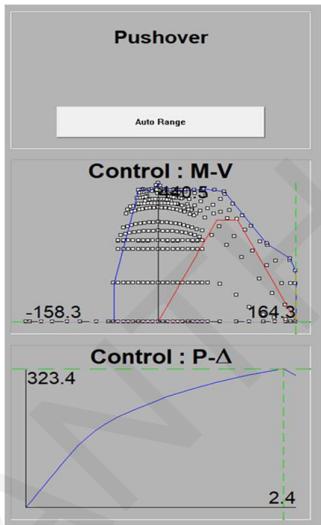


Figure B. 65: Specimen HC4-8L16-T6-0.2P experimental envelope curve and response 2000 section and member analysis (Xiao and Martirosyan, 1998).

Sezen and Moehle (2002)

Specimen 4

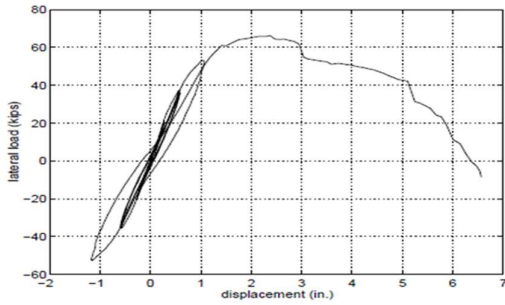
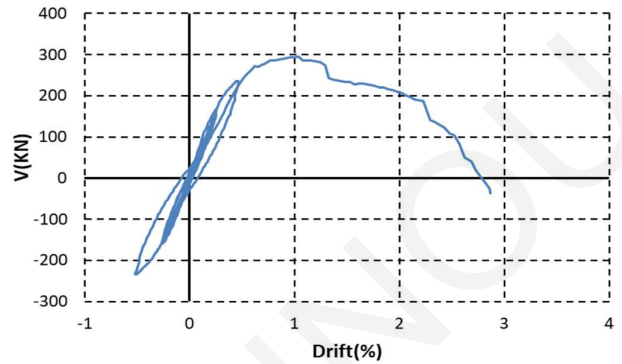


Figure 4.27 Lateral load-displacement relation for Specimen-4



M Vs Φ

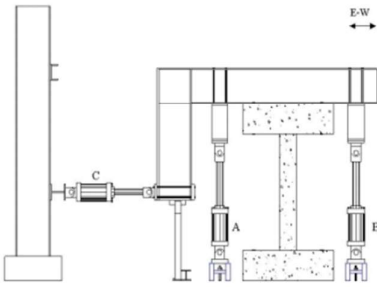
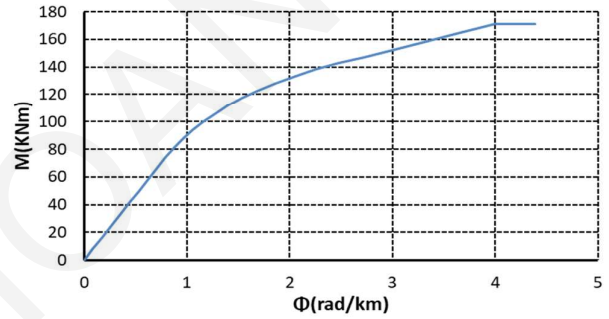
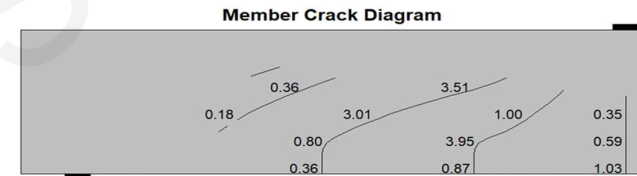
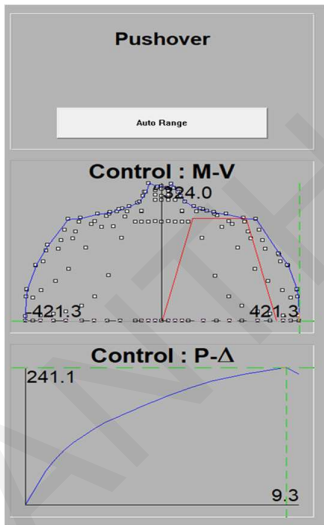


Figure 3.16 Loading frame elevation in the east-west direction

Member Response



Curvature Distribution

Shear Strain Distribution

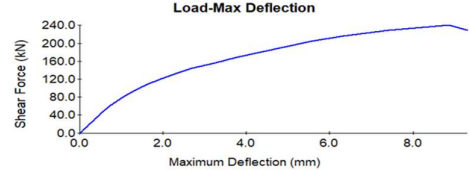
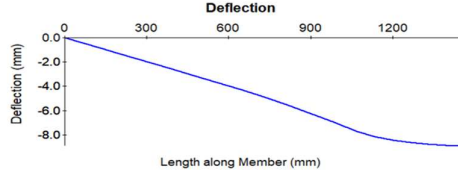
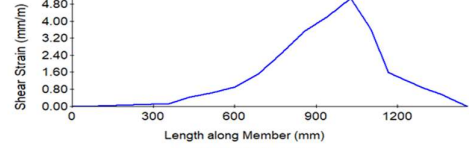
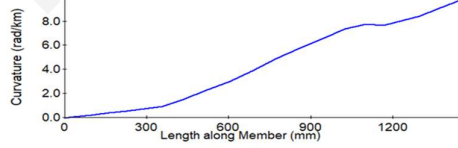


Figure B.66: Specimen 4 experimental envelope curve and response 2000 section and member analysis (Sezen and Moehle, 2002).

Sezen and Moehle (2002)

Specimen 1

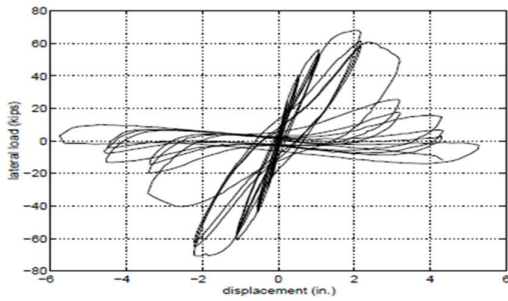


Figure 4.6 Lateral load-displacement relation for Specimen-1

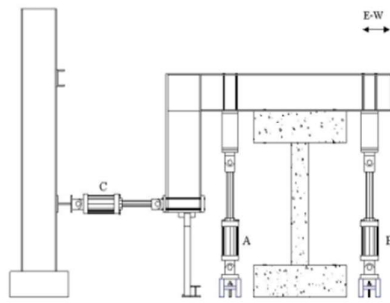
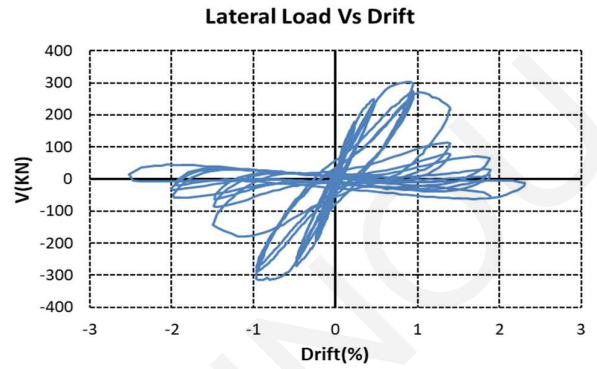
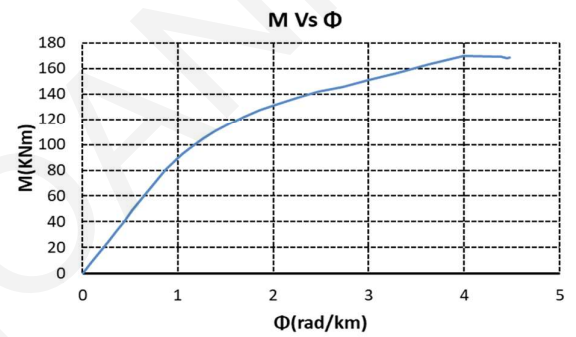


Figure 3.16 Loading frame elevation in the east-west direction



Member Response

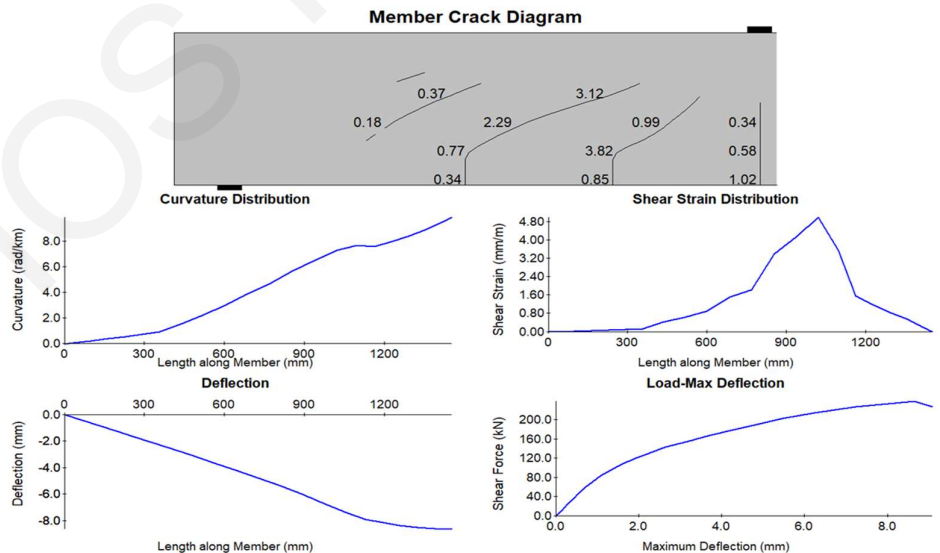
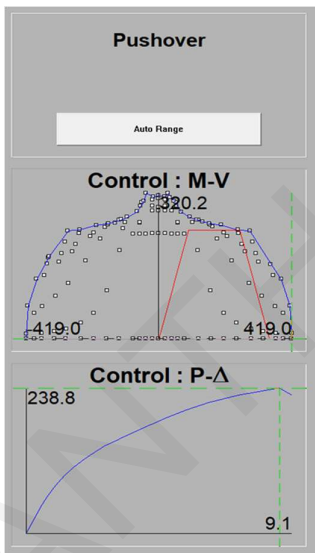


Figure B. 67: Specimen 1 experimental envelope curve and response 2000 section and member analysis (Sezen and Moehle, 2002).

Sezen and Moehle (2002)

Specimen 2

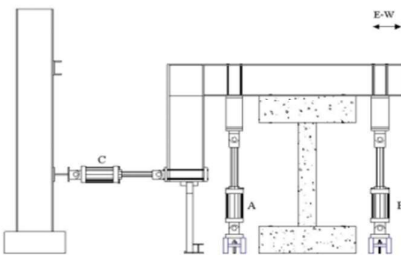
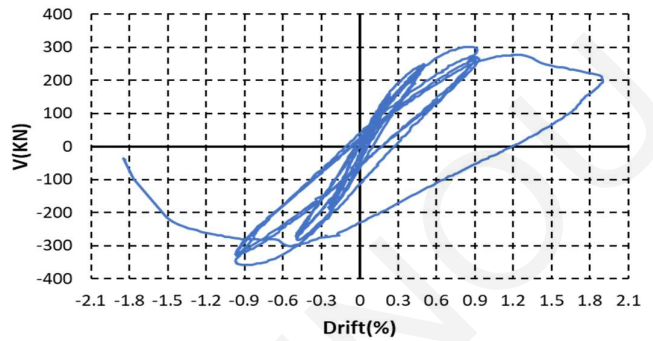
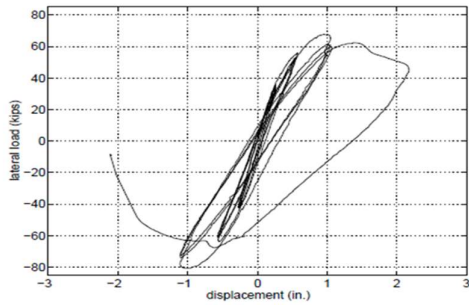
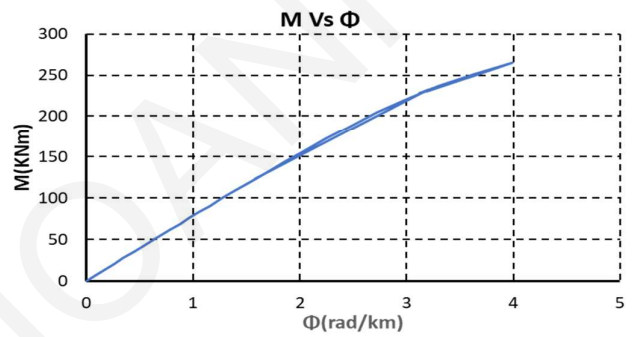


Figure 3.16 Loading frame elevation in the east-west direction



Member Response

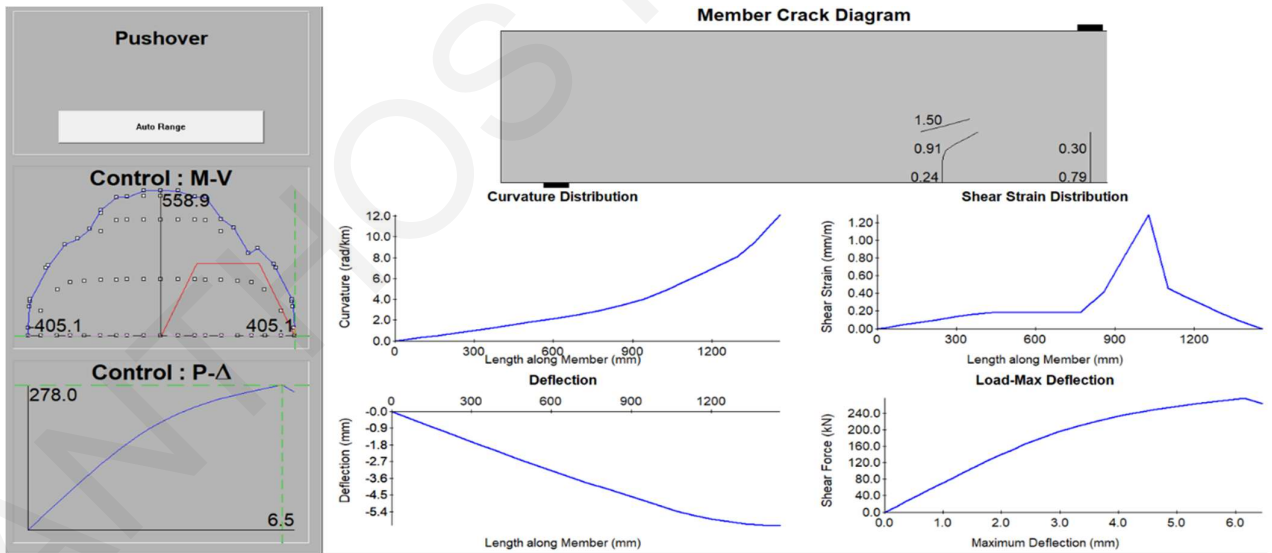
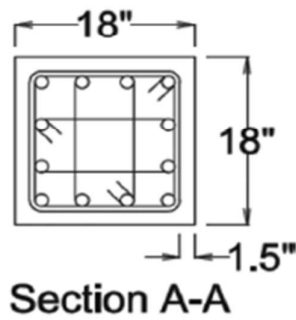
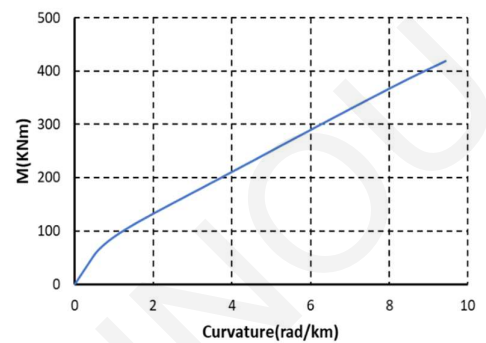
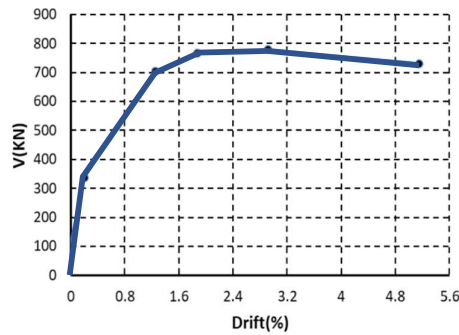
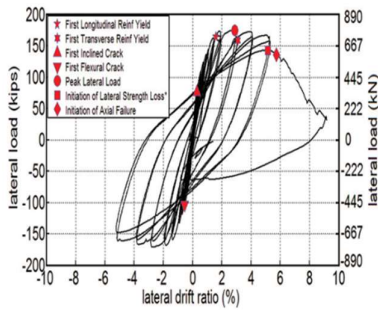


Figure B. 68: Specimen 2 experimental envelope curve and response 2000 section and member analysis (Sezen and Moehle, 2002).

Sokoli and Ghannoum (2016)

Specimen CS-60

Moment Curvature Diagram - Specimen CS60



Member Response

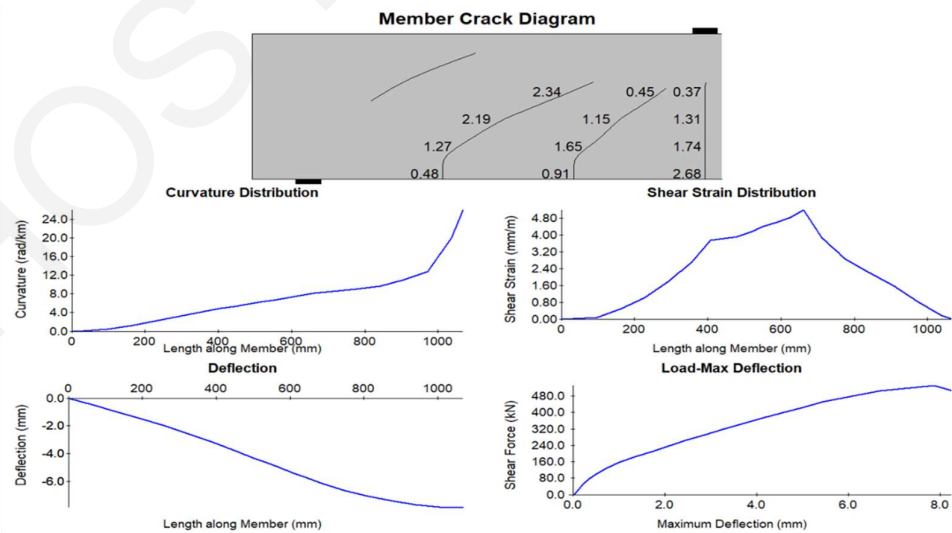
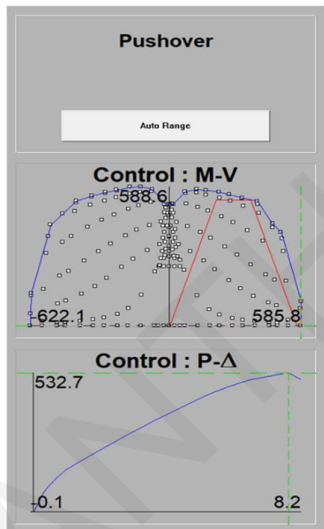
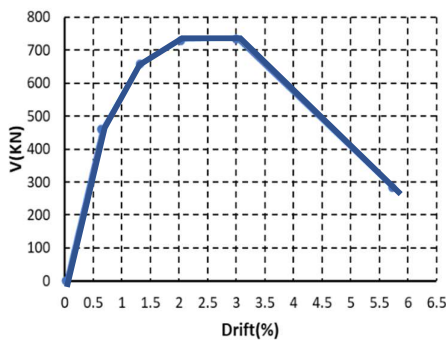
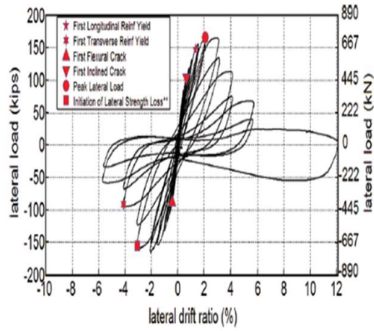


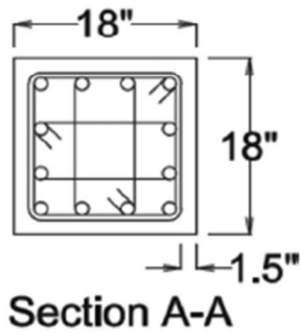
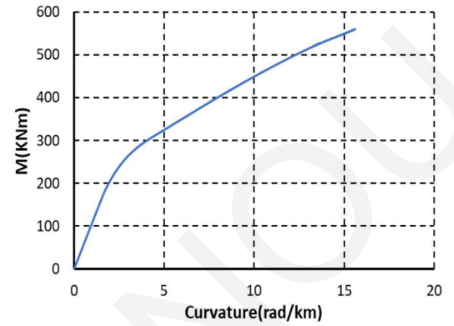
Figure B. 69: Specimen CS-60 experimental envelope curve and response 2000 section and member analysis (Sokoli and Ghannoum, 2016)

Sokoli and Ghannoum (2016)

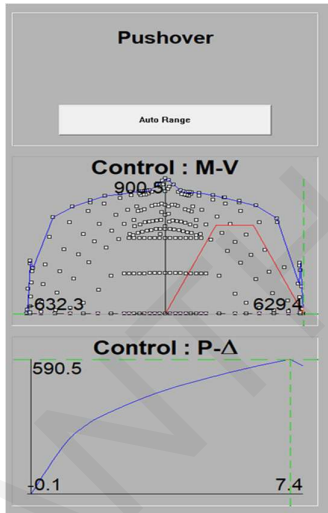
Specimen CS-100



Moment Curvature Diagram - Specimen CS100



Member Response



Member Crack Diagram

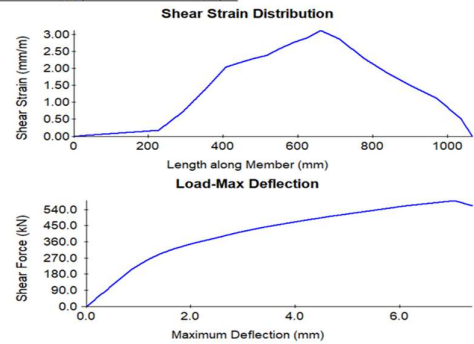
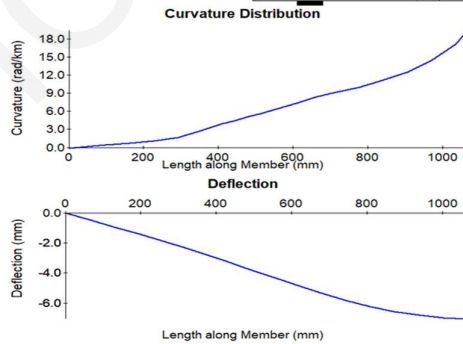
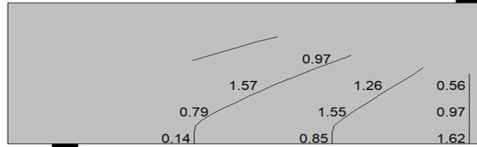


Figure B. 70: Specimen CS-100 experimental envelope curve and response 2000 section and member analysis (Sokoli and Ghannoum, 2016).

Matchulat et al. (2005)

Specimen 1

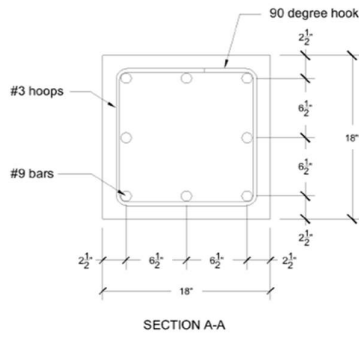
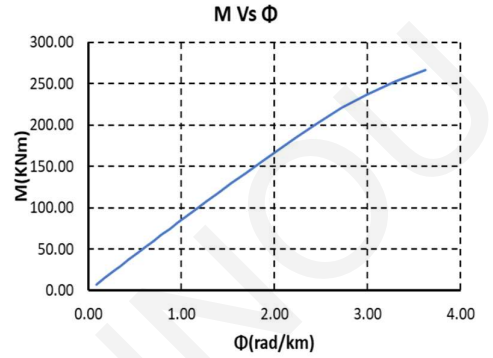
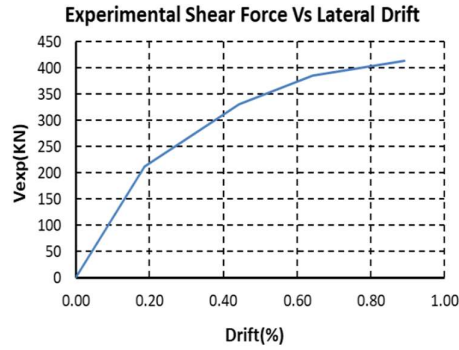
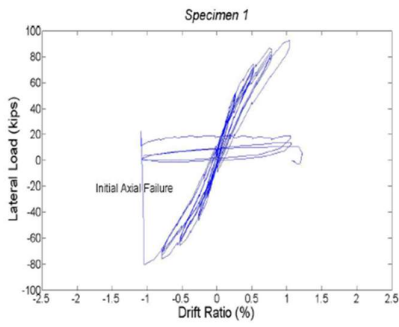
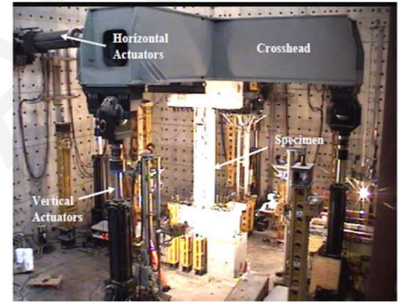
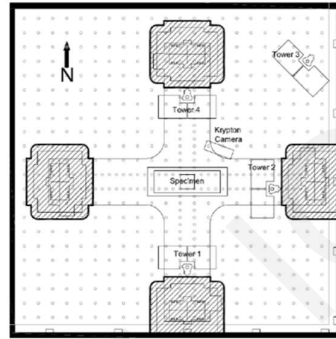


Figure 2.2: Column cross-section



Member Response

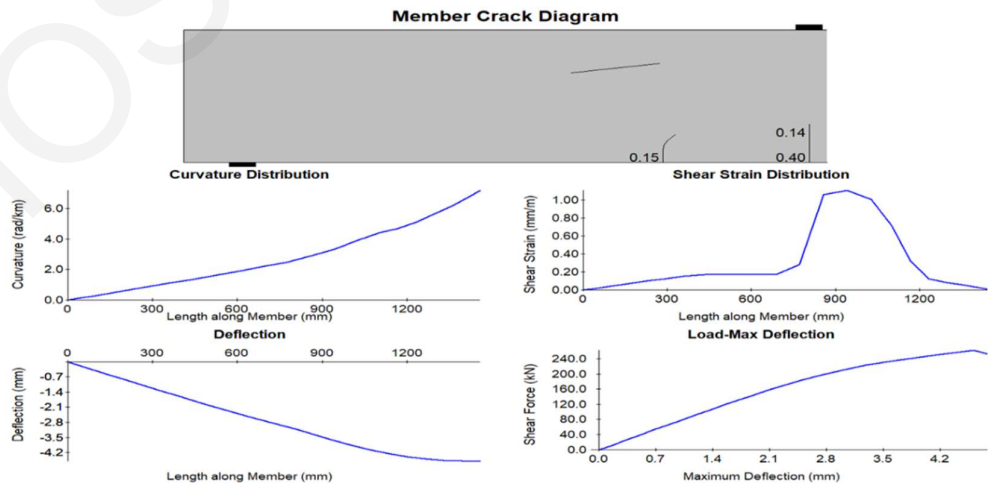
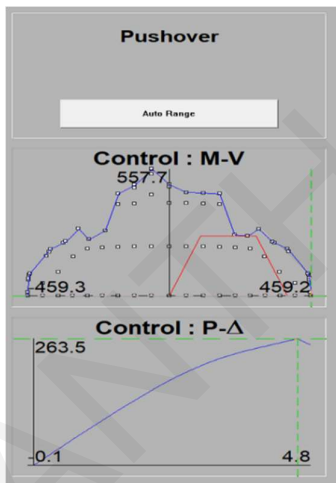


Figure B. 71: Specimen 1 experimental envelope curve and response 2000 section and member analysis (Matchulat et al., 2005).

Matchulat et al. (2005)

Specimen 2

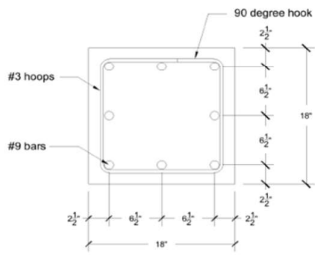
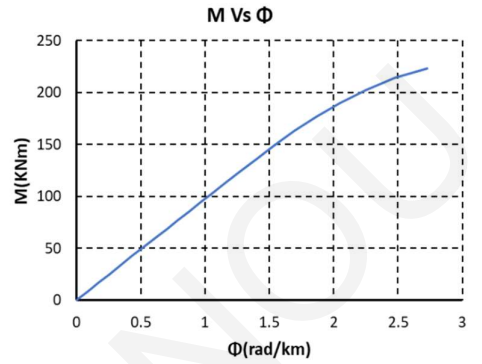
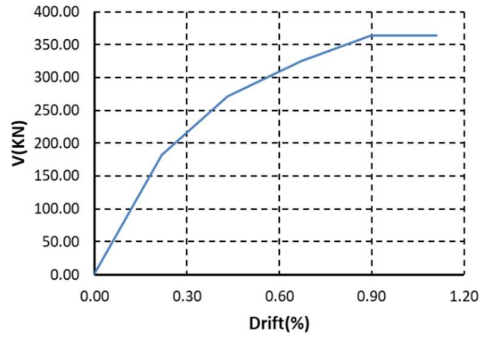
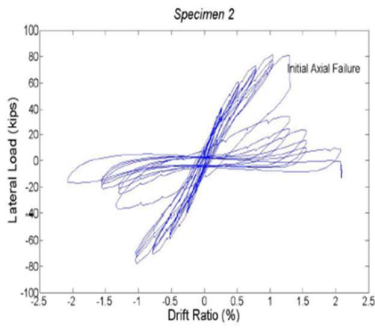
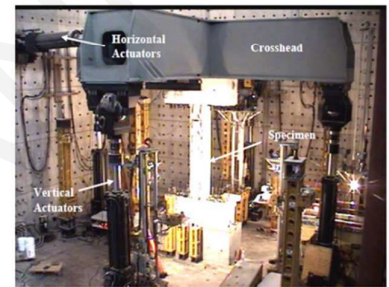
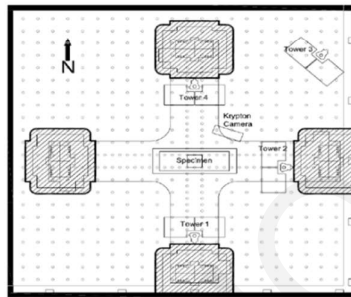


Figure 2.1: Column cross-section



Member Response

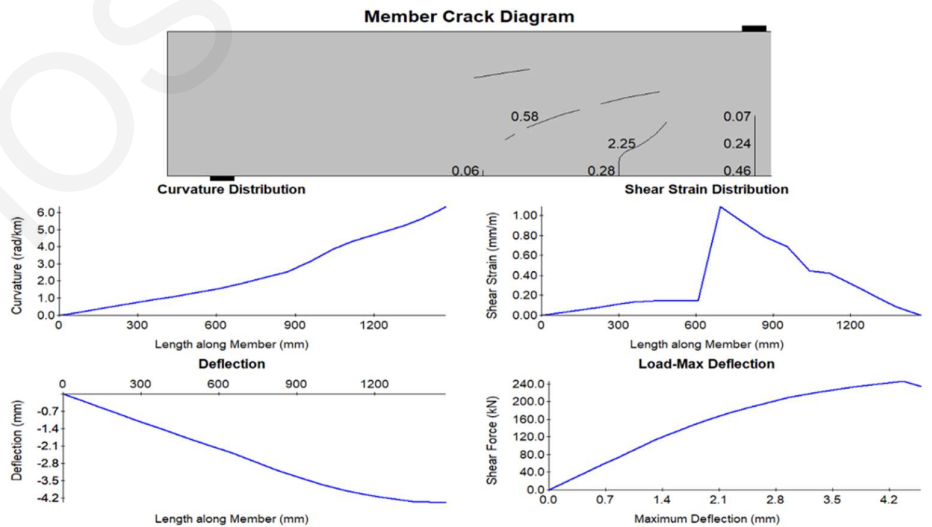
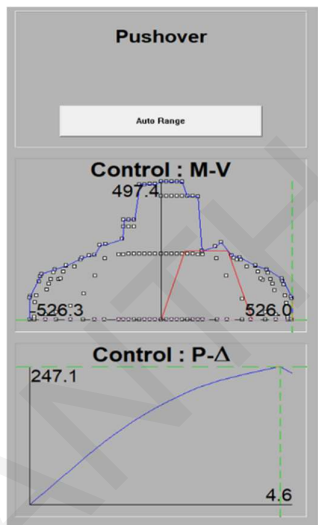


Figure B. 72: Specimen 2 experimental envelope curve and response 2000 section and member analysis (Matchulat et al., 2005).

Kim et al. (2018)
Specimen SAd2

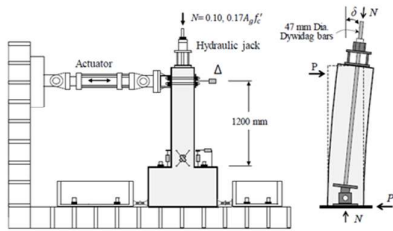
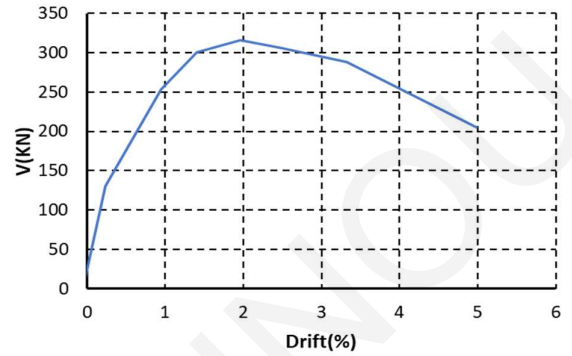
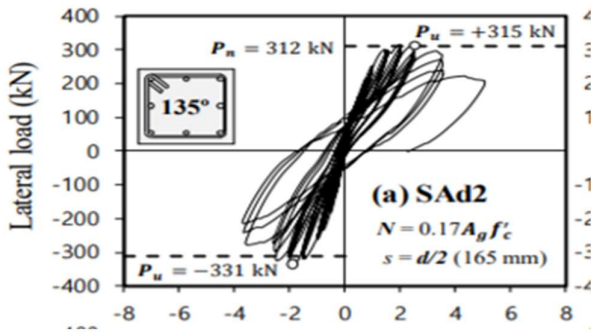
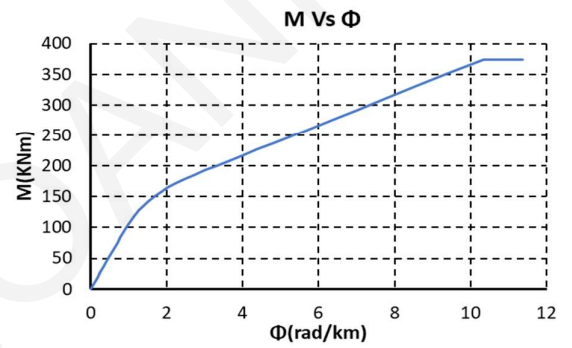


Fig. 4. Test setup



Member Response

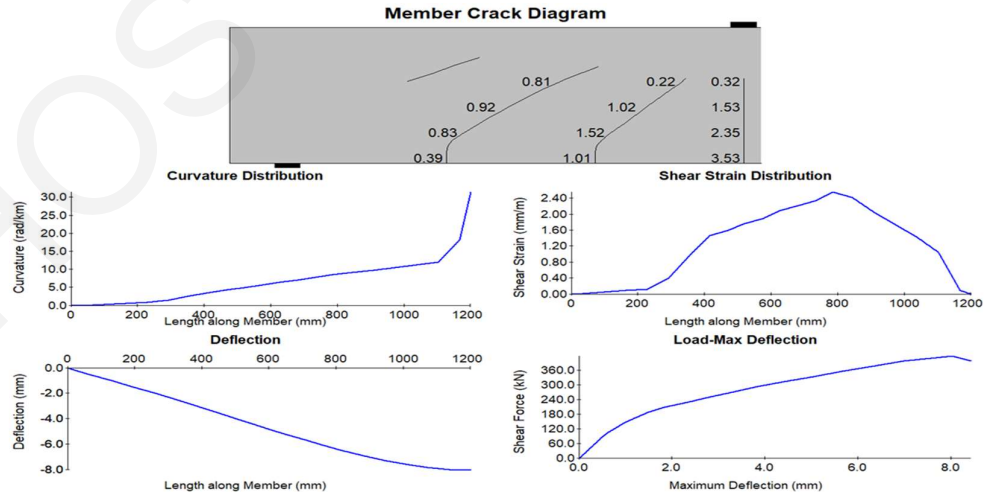
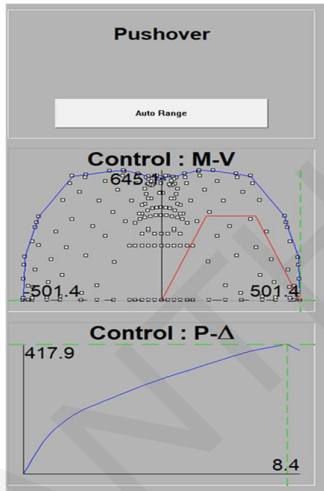


Figure B. 73: Specimen SAd2 experimental envelope curve and response 2000 section and member analysis (Kim et al., 2018).

Kim et al. (2018)

Specimen RGd2

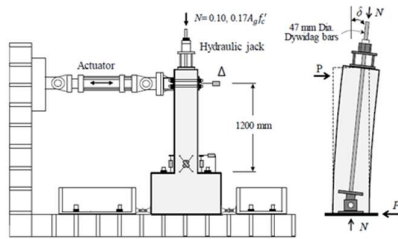
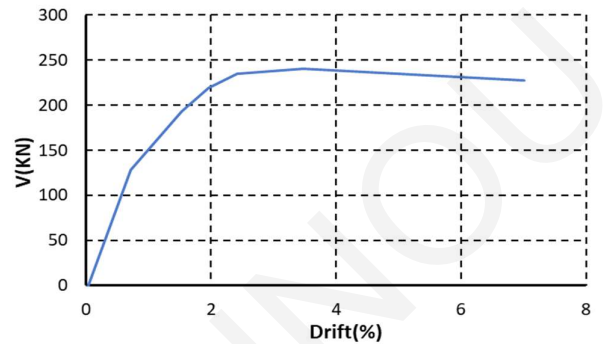
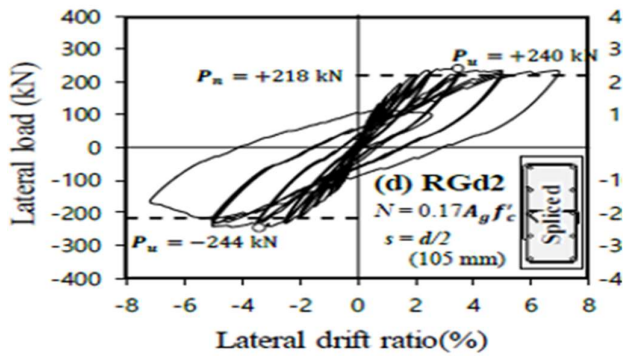
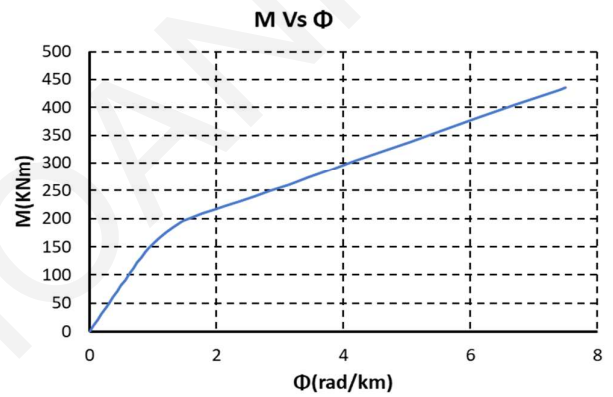


Fig. 4. Test setup



Member Response

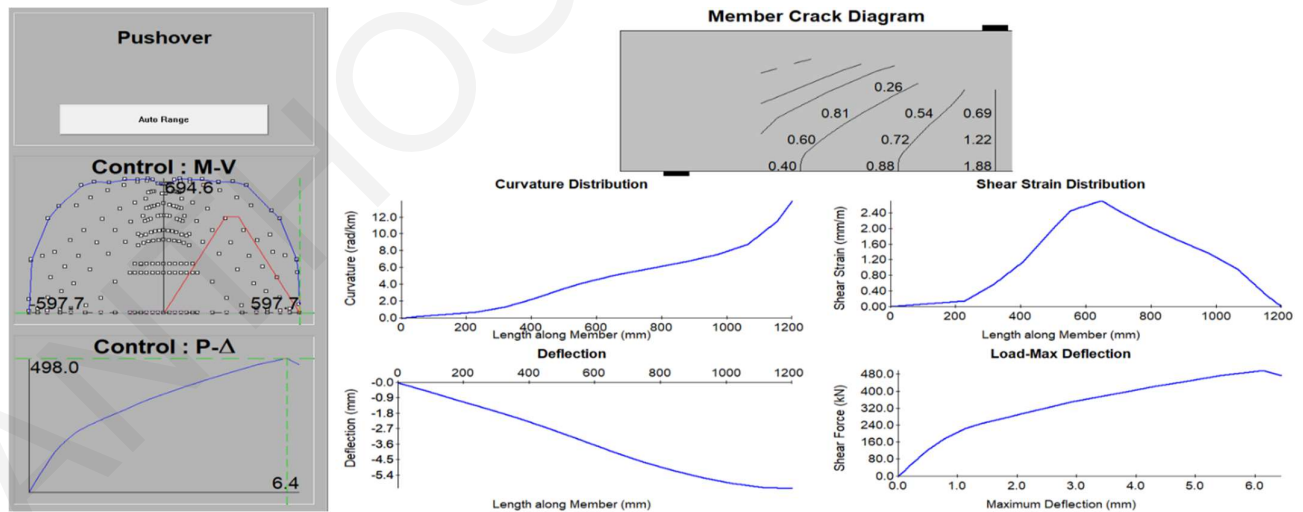


Figure B. 74: Specimen RGd2 experimental envelope curve and response 2000 section and member analysis (Kim et al., 2018)

Appendix C

Table C. 1 : Matchulat et al. (2008) Finite Element Analysis Algorithm Details

| | | | |
|--|------------------------------|----------------|--|
| Analysis Type: | Static, General | | |
| Maximum Number of Increments: | 100000 | | |
| | Incrementation | | |
| | Increment Size | | |
| Initial | Minimum | Maximum | |
| 0.01 | 1e-20 | 0.1 | |
| Matrix storage: | Solver Default | | |
| Solution Technique: | Full Newton | | |
| Convert Severe Discontinuity Iterations: | Propagate from previous step | | |
| Default Load Variation with Time: | Ramp linearly overstep | | |
| Extrapolation of previous state at start of each increment: | Linear | | |

Table C. 2 : Matchulat et al. (2008) Finite Element Analysis Element Types for Solid Parts

| | | | |
|---|---|--|--|
| Element Library: | Standard, 3D stress | | |
| Geometric Order: | Linear | | |
| Element Type: | Hex | | |
| Integration: | Reduced | | |
| Viscosity: | Default | | |
| Kinematic Split: | Average Strain | | |
| Second Order Accuracy: | No | | |
| Distortion Control: | No | | |
| Hourglass Control: | Default | | |
| Stiffness viscous weight-factor: | 0.5 | | |
| Element Deletion: | Default | | |
| Max Degradation: | Default | | |
| | Scaling Factors | | |
| Displacement Hourglass: | 1 | | |
| Linear Bulk Viscosity: | 1 | | |
| Quadratic Bulk Viscosity: | 1 | | |
| Element Description: | C3D8R, An 8-node linear brick, reduced integration, hourglass control | | |
| Mesh Technique: | Structured | | |

Table C. 3 : Matchulat et al. (2008) Finite Element Analysis Types for Truss Elements (Longitudinal and Transverse Reinforcement)

| | |
|-----------------------------|---------------------------|
| Element Library: | Standard |
| Geometric Order: | Linear |
| Element Type: | Truss |
| | Line |
| Element Description: | A 2-node linear 3-D truss |
| Mesh Technique: | - |

Table C. 4 : C1.6Φ10NL and RC3.6Φ14L35 Finite Element Analysis Algorithm Details

| | |
|--|-----------------------|
| Analysis Type: | Dynamic Explicit |
| Time Period: | |
| | Incrementation |
| Type: | Automatic |
| Stable Increment Estimator: | Global |
| Max Time Increment: | Unlimited |
| Time Scaling Factor: | 1 |
| Linear Bulk Viscosity Parameter: | 0.06 |
| Quadratic Bulk Viscosity Parameter: | 1.2 |

Table C. 5 : C1.6Φ10NL and RC3.6Φ14L35 Finite Element Analysis Element Types for Solid Parts

| | |
|---|---|
| Element Library: | Explicit, 3D stress |
| Geometric Order: | Linear |
| Element Type: | Hex |
| Integration: | Reduced |
| Viscosity: | Default |
| Kinematic Split: | Average Strain |
| Second Order Accuracy: | No |
| Distortion Control: | No |
| Hourglass Control: | Default |
| Stiffness viscous weight-factor: | 0.5 |
| Element Deletion: | Default |
| Max Degradation: | Default |
| | Scaling Factors |
| Displacement Hourglass: | 1 |
| Linear Bulk Viscosity: | 1 |
| Quadratic Bulk Viscosity: | 1 |
| Element Description: | C3D8R, An 8-node linear brick, reduced integration, hourglass control |
| Mesh Technique: | Structured |

Table C. 6 : C1.6Φ10NL and RC3.6Φ14L35 Finite Element Analysis Types for Truss Elements (Longitudinal Reinforcement)

| | |
|-----------------------------|-------------------------------|
| Element Library: | Explicit |
| Geometric Order: | Linear |
| Element Type: | Beam |
| | Line |
| | Scaling Factors: |
| Element Description: | A 2-node linear beam in space |
| Mesh Technique: | - |

Table C. 7: C1.6Φ10NL and RC3.6Φ14L35 Finite Element Analysis Types for Truss Elements (Transverse Reinforcement)

| | |
|-----------------------------|---------------------------|
| Element Library: | Standard |
| Geometric Order: | Linear |
| Element Type: | Truss |
| | Line |
| | Scaling Factors: |
| Element Description: | A 2-node linear 3-D truss |
| Mesh Technique: | - |

References

1. Abaqus/CAE User's Manual. Dassault Systems Simulia Corp., Providence, RI, USA 2010, 1174.
2. ABAQUS: Theory Manual; Providence, R. I.: Hibbitt, Karlsson & Sorensen. , 1992.
3. Abee, S. H.; Str, P. Sika® ViscoCrete® Techno-10+. **2019**, 3.
4. ACI Committee 318; American Concrete Institute; International Organization for Standardization. Building Code Requirements for Structural Concrete (ACI 318M-08) and Commentary; American Concrete Institute: Farmington Hills, Mich., 2008.
5. ACI Committee 544. ACI PRC-544. 1R-96: Report on Fiber Reinforced Concrete (Reapproved 2009); 2002.
6. Adege, L.N.; Collins, M. P. A Finite Element Model for Studying Reinforced Concrete Detailing Problems; Publication No. 86-12; Department of Civil Engineering, University of Toronto, 1986.
7. Advances in Construction Materials 2007: With 80 Tables; Grosse, C. U., Reinhardt, H. -W., Grobe, C. U., Eds. ; Springer: Berlin Heidelberg, 2007.
8. Akazawa, T. Tension Test Method for Concretes, Bulletin No. 16; International Association of Testing and Research Laboratories: Paris, 1953; pp 11–23.
9. Al-Gemeel, A. N. Experimental Investigation of Textile Reinforced Engineered Cementitious Composite (ECC) for Square Concrete Column Confinement. Construction and Building Materials 2018, 9.
10. Al-Hamaydeh, M.; Markou, G.; Bakas, N.; Papadrakakis, M. AI-Based Shear Capacity of FRP-Reinforced Concrete Deep Beams without Stirrups. Engineering Structures 2022, 264, 114441. <https://doi.org/10.1016/j.engstruct.2022.114441>.
11. Ali Yaz and Ambalavanan R., Flexural behaviour of reinforced concrete beams repaired with styrene-butadiene rubber latex, silica fume and methylcellulose repair formulations. Mag Concrete Res 1999; 51:113–20.
12. Alsomiri, M.; Jiang, X.; Liu, Z. Elastic Restraint Effect of Concrete Circular Columns with Ultrahigh-Performance Concrete Jackets: An Analytical and Experimental Study. Materials 2021, 14 (12), 3278. <https://doi.org/10.3390/ma14123278>.

13. Alvarez, J. C. Seismic Behavior of Concrete Frames with Jacketed Columns. Ph. D. Dissertation, University of Massachusetts Amherst, 2017.
14. American Association of State Highway and Transportation Officials. Load and Resistance Factor Design (AASHTO, LRFD). Bridge Design Specifications; Washington, 2010.
15. American Society for Testing and Materials. Specification for Fly Ash and Raw of Calcined Natural Pozzolan for Use as a Mineral Admixture in Portland Cement Concrete; ASTM: Philadelphia, PA, 1978; Vol. ASTM C618-78.
16. American Society of Civil Engineers, 2017. Seismic Evaluation and Retrofit of Existing Buildings (41-17).
17. American Society of Civil Engineers. Seismic Evaluation and Retrofit of Existing Buildings, 41st ed.; American Society of Civil Engineers: Reston, VA, 2017. <https://doi.org/10.1061/9780784414859>.
18. Arakawa, T.; Arai, Y.; Mizoguchi, M.; Yoshida, M. Shear Resisting Behavior of Short Reinforced Concrete Columns Under Biaxial Bending-Shear. Transactions of the Japan Concrete Institute, 1989.
19. ASCE Task Committee on Finite Element Analysis of Reinforced Concrete Structures. State-of-the-Art Report on Finite Element Analysis of Reinforced Concrete; ASCE Special Publications UCB/SEMM-90/14; 1982.
20. ASCE/SEI 41. Seismic Rehabilitation of Existing Buildings, American Society of Civil Engineers. American Society of Civil Engineers, Reston, VA 2007.
21. ASCE/SEI 41-13. Seismic Evaluation and Retrofit of 5 Existing Buildings. ASCE (American Society of Civil Engineers), Reston, VA. 2014.
22. Aschheim, M.; Moehle, J. P. Shear Strength and Deformability of RC Bridge Columns Subjected to Inelastic Cyclic Displacements. California Department of Transportation March 1992.
23. ASTM C 496. Standard Test Method for Splitting Tensile Strength of Cylindrical Concrete Specimens; American Society for Testing Materials: 100 Barr Harbor Dr., West Conshohocken, PA 19428, USA, 2004.
24. ASTM C 882. Standard Test Method for Bond Strength of Epoxy-Resin Systems Used with Concrete by Slant Shear; American Society for Testing Materials: Barr Harbor Dr., West Conshohocken, PA 19428, 1999.

25. ASTM C39 / C39M-21, Standard Test Method for Compressive Strength of Cylindrical Concrete Specimens, ASTM International, West Conshohocken, PA, 2021, www.astm.org
26. ASTM C496 / C496M-17, Standard Test Method for Splitting Tensile Strength of Cylindrical Concrete Specimens, ASTM International, West Conshohocken, PA, 2017, www.astm.org
27. ASTM C618-19, Standard Specification for Coal Fly Ash and Raw or Calcined Natural Pozzolan for Use in Concrete, ASTM International, West Conshohocken, PA, 2019, www.astm.org
28. ASTM C882/C882M-12. C882/C882M-12 Standard Test Method for Bond Strength of Epoxy-Resin Systems Used with Concrete by Slant Shear; 2013.
29. ASTM. C94/C94M-04-Standard Specification for Ready-Mixed Concrete. 04. 02. https://doi.org/DOI:10.1520/C0094_C0094M-04.
30. ASTM. Standard Test Method for Measuring Pavement Macrotexture Depth Using a Volumetric Technique; E965-96, West Conshohocken, PA, 2006.
31. ASTM-C4541. Standard Test Method for Pull-off Strength of Coatings Using Portable Adhesion Testers. West Conshohocken (; American Society for Testing and Materials, 1992; pp 19428–2959.
32. Austin, S.; Robins, P.; Pan, Y. Shear Bond Testing of Concrete Repairs. *Cement and Concrete Research* 1999, 29 (7), 1067–1076. [https://doi.org/10.1016/S0008-8846\(99\)00088-5](https://doi.org/10.1016/S0008-8846(99)00088-5).
33. Azadi, K.; Mohammad, R.; Allahvirdizadeh, R. Enhanced Empirical Models for Predicting the Drift Capacity of Less Ductile RC Columns with Flexural, Shear, or Axial Failure Modes. *Front. Struct. Civ. Eng.* 2019, 13 (5), 1251–1270. <https://doi.org/10.1007/s11709-019-0554-2>.
34. Bae, S.; Bayrak, O. Plastic Hinge Length of Reinforced Concrete Columns. *ACI Structural Journal* 2008, 105 (3), 291–300.
35. Bakas, N.; Makridakis, S.; Papadrakakis, M. Torsional Parameters Importance in the Structural Response of Multiscale Asymmetric-Plan Buildings. *Coupled systems mechanics* 2017, 6 (1), 55–74. <https://doi.org/10.12989/CSM.2017.6.1.055>.
36. Banthia, N.; Zanotti, C.; Sappakittipakorn, M. Sustainable Fiber Reinforced Concrete for Repair Applications. *Construction and Building Materials* 2014, 67, 405–412. <https://doi.org/10.1016/j.conbuildmat.2013.12.073>

37. Barzegar, F.; Schnobrich, W.C. Nonlinear Finite Element Analysis of Reinforced Concrete under Short Term Monotonic Loading; Civil Engineering Studies; SRS No. 530; Univ. of Illinois at Urbana: Illinois, 1986.
38. Bashur, F.K.; Darwin, D. Nonlinear Model for Reinforced Concrete Slabs. *Journal of Structural Division, ASCE* **1978**, *104* (ST1), 157–170.
39. Bentz, E. C.; Collins, P. C. ACI Shear Provisions Based on the Fib Model Code 2010, 2014.
40. Bentz, E.; Collins, M. P., Response 2000 User's Manual, Version 1. 1., September 2001
41. Berard, A. Artificial Stone. 157 903.
42. Bergmann, R., P., V. A. Finite Element for R/C Shear Walls Under Cyclic Loads; UCB/SEMM-88/09; University of California, Berkeley, 1988.
43. Berry, M.; Parrish, M.; Eberhard, M. PEER Structural Performance Database User's Manual (Version 1. 0). 2004, 44.
44. Beton-Kalender 1970. Taschenbuch für Beton- und Stahlbetonbau, sowie die verwandten Facher, W. Ernst & Sohn, Berlin-München.
45. Bezanson, J.; Edelman, A.; Karpinski. S., S., V. B. Julia: A Fresh Approach to Numerical Computing. 59 (1), 65–98. <https://doi.org/10.1137/141000671>.
46. Biskinis D.; Fardis, M. N.; Flexure-Controlled Ultimate Deformations of Members with Continuous or Lap-Spliced Bars. ICE Publishing 11 (Structural Concrete). <https://doi.org/10.1680/stco.2010.11.2.93>.
47. Biskinis D.; Roupakias G. K.; Fardis M. N. Degradation of Shear Strength of RC Members with Inelastic Cyclic Displacements. ACI Structural Journal 2004, 101 (6), 773–783.
48. Blaber, J., 2021. DIC Algorithms. Ncorr. com. http://www.ncorr.com/index.php/dic-algorithms#1_1
49. Bowman, S. A. Regional Seismic Interpretation of the Hydrocarbon Prospectivity of Offshore Syria. GeoArabia 2011, 16 (3), 95–124. <https://doi.org/10.2113/geoarabia160395>.
50. Bresler, B.; Pister, K. S. Strength of Concrete under Combined Stresses. ACI Journal 1985, 551 (9), 321–345.
51. Burgueño, R.; Babazadeh, A.; Fedak, L. K.; Silva, P. F. Second-Order Effects on Seismic Response of Slender Bridge Columns. ACI Structural Journal 2016, 113 (4). <https://doi.org/10.14359/51688751>.

52. Canadian Highway Bridge Design Code 2019, 12th ed.; CSA Group: Toronto, ON, Canada, 2019; p. 1185.
53. Canadian Highway Bridge Design Code 2019, 12th ed; CSA Group: (15) Toronto, ON. Canada, 2019; p. 1185
54. Canadian Standards Association. Supplementary Cementing Materials and Their Use in Concrete Construction; CSA, Rexdale, ON, 1982; Vol. CAN-A23. 5-M82.
55. Carneiro, F. L. L. B., B., A. Concrete Tensile Strength, Bulletin No. 13; International Association of Testing and Research Laboratories for Materials and Structures: Paris, 1953; pp 97–123.
56. Carol, I.; Prat, P. C.; López, C. M. Normal/Shear Cracking Model: Application to Discrete Crack Analysis. *Journal of Engineering Mechanics* 1997, 123 (8), 765–773. [https://doi.org/10.1061/\(ASCE\)0733-9399\(1997\)123:8\(765\)](https://doi.org/10.1061/(ASCE)0733-9399(1997)123:8(765)).
57. CEN (2004) European Standard EN 1998-1-4, 1996: Eurocode 8: Design of Structures for Earthquake Resistance-Part 3: Assessment and Retrofitting of Buildings. European Committee for Standardization. Brussels, Belgium, 2005
58. CEN (2004a) European Standard EN 1998-1. Eurocode 8: Design of Structures for Earthquake Resistance, Part 1: General rules, Seismic Actions and Rules for Buildings. Committee for Standardization, Design, European Committee for Standardization, Brussels, Belgium
59. CEN (2004b) European Standard EN 1992-1-1. Eurocode 2: Design of Concrete Structures, Part1-1: General Rules and Rules for Buildings, Committee for Standardization. Brussels, Belgium.
60. Cervenka, V. Inelastic Finite Element Analysis of Reinforced Concrete Panels. Ph.D. Dissertation, University of Colorado, Boulder, 1970.
61. Cervenka, V.; Eligehausen, R.; Pukl, R. "SBETA-Computer Program for Nonlinear Finite Element Analysis of Reinforced Concrete Structures; Report 90/1; Institute of Building Materials, University of Stuttgart, 1990.
62. Chai, Y. H.; Priestley, M. J. N.; Seible, F. Analytical Model for Steel-Jacketed RC Circular Bridge Columns. *J. Struct. Eng.* 1994, 120, 2358–2376.
63. Chang J. B. M. G. A. Chang-Fatigue-Damage-Part1-with-Cover-Page-v2. Pdf. National Center for Earthquake Engineering Research - State University of New York at Buffalo March 14, 1994.
64. Chasioti, S.; Megalooikonomou, K.; Pantazopoulou, S. Shear Strength Assesment Of Reinforced Concrete Columns. In *Proceedings of the 4th International*

- Conference on Computational Methods in Structural Dynamics and Earthquake Engineering (COMPDYN 2013); Greece: Kos Island, Greece, 2014; pp 927–940. <https://doi.org/10.7712/120113.4567.C1506>.
65. Chou, C. -C.; Wu, S. -C. Cyclic Lateral Load Test and Finite Element Analysis of High-Strength Concrete-Filled Steel Box Columns under High Axial Compression. *Engineering Structures* 2019, 189, 89–99. <https://doi.org/10.1016/j.engstruct.2019.03.052>.
 66. Clímaco, J. C. T. S.; Regan, P. E. Evaluation of Bond Strength between Old and New Concrete in Structural Repairs. *Thomas Telford, Magazine of Concrete Research* 2001, Vol. 53 (No. 6), 377–390. <https://doi.org/0.1680/mac.53.6.377.40800>.
 67. Comité Euro-International Du Béton, CEB-FIB-Model Code 1990: Design Code.; Thomas Telford: London, 1993.
 68. CYS EN 196-1:2016, Methods of testing cement-Part 1: Determination of strength, European Committee for Standardization, April 2016
 69. CYS EN 450 1:2012, Fly Ash for Concrete, Part 1: Definition, specifications and conformity criteria, European Committee for Standardization, August 2012
 70. CYS EN 934-2:2009 + A1:2012, Admixtures for concrete mortar and grout, Part 2 Concrete Admixtures-Definitions, requirements, conformity, marking and labelling, European Committee for Standardization, June 2012
 71. D. E. Lehman; A. C. Lynn; M. A. Aschheim; J. P. Moehle. *Evaluation Methods for Reinforced Concrete Columns And Connections*; Elsevier Science Ltd: Acapulco, Mexico, 1996.
 72. Davis R. E.; Carlson R. W.; Kelly J. W.; H. E. Davis. Properties of Cements and Concretes Containing Fly Ash. *J. Am. Concr.* 1937, 33, 577–612.
 73. Deng, M.; Zhang, Y.; Li, Q. Shear Strengthening of RC Short Columns with ECC Jacket: Cyclic Behavior Tests. *Engineering Structures* 2018, 160, 535–545. <https://doi.org/10.1016/j.engstruct.2018.01.061>.
 74. Design Team for the Composition of Greek Regulations for Assessment, Retrofit and Strengthening of Existing Reinforced Concrete Structures, Harmonization of KA. NE. IIE. with Eurocodes, Athens, 2017
 75. DIN 1045:1972-01, Reinforced Concrete Structures; Design and Construction; 1972.

76. Eder, M.A; El Ghazouli, A.Y.; Abdel-Fattah, T.; Vollum, R.L. Modelling and Experimental Assessment of Punching Shear in Flat Slabs with Shearheads. *Eng. Structures* 2010, 32 (12), 3911–3924.
77. Elwood, K. J.; Matamoros, A. B.; Wallace, J. W.; Lehman, D. E.; Heintz, J. A.; Mitchell, A. D.; Moore, M. A.; Valley, M. T.; Lowes, L. N.; Comartin, C. D.; Moehle, J. P. Update to ASCE/SEI 41 Concrete Provisions. *Earthquake Spectra* 2007, 23 (3), 493–523. <https://doi.org/10.1193/1.2757714>.
78. Elwood, K. J.; Moehle, J. P. Axial Capacity Model for Shear-Damaged Columns. *ACI Structural Journal* 2005, 10.
79. Elwood, K. J.; Moehle, J. P. Axial Capacity Model for Shear-Damaged Columns. *ACI Structural Journal* 2005, 10.
80. Elwood, K. Shaking Table Tests and Analytical Studies on the Gravity Load Collapse of Reinforced Concrete Frames. Ph. D. Dissertation, University of California, Berkeley, 2003.
81. EN 12390-6. Testing Hardened Concrete. Part 6: Tensile Splitting Strength of Test Specimens; Portuguese Institute for Quality, 2004; p 14.
82. EN 12615. Determination of Slant Shear Strength. In *Products and systems for the protection and repair of concrete structures. Test methods.* ; European Committee for Standardization, 1999.
83. Espeche, A. D.; León, J. Estimation of Bond Strength Envelopes for Old-to-New Concrete Interfaces Based on a Cylinder Splitting Test. *Construction and Building Materials* 2011, 25 (3), 1222–1235. <https://doi.org/10.1016/j.conbuildmat.2010.09.032>.
84. European Committee for Standardization. CYS EN 1504-3:2005: *Products and Systems for the Protection and Repair of Concrete Structures-Definitions, Requirements, Quality Control and Evaluation of Conformity-Part 3: Structural and Non-Structural Repair.* December 2005.
85. European Committee for Standardization. EN 1504-6:2006-*Products and Systems for the Protection and Repair of Concrete Structures - Definitions, Requirements, Quality Control and Evaluation of Conformity - Part 6: Anchoring of Reinforcing Steel Bar.* July 2006.
86. European Committee for Standardization. CYS EN 197-1:2011 - *Cement - Part 1: Composition, Specifications and Conformity Criteria for Common Cements;* 2011.

87. Evan C. B.; Frank J. V.; Michael P. C. Simplified Modified Compression Field Theory for Calculating Shear Strength of Reinforced Concrete Elements. *SJ* 2006, 103 (4). <https://doi.org/10.14359/16438>.
88. F. Raba Jr, S. L. S.; M. Mearing. Subbituminous Fly Ash Utilization in Concrete, in *Proceedings of Symposium on Fly Ash Incorporation in Hydrated Cement Systems*; Materials Research Society, 1981; pp 296–306.
89. Fardis, M. N. *Seismic Design, Assessment and Retrofitting of Concrete Buildings; Geotechnical, Geological, and Earthquake Engineering*; Springer Netherlands: Dordrecht, 2009; Vol. 8. <https://doi.org/10.1007/978-1-4020-9842-0>.
90. Fardis, M. N. *Seismic Design, Assessment and Retrofitting of Concrete Buildings; Geotechnical, Geological, and Earthquake Engineering*; Springer Netherlands: Dordrecht, 2009; Vol. 8. <https://doi.org/10.1007/978-1-4020-9842-0>.
91. FEMA 461. *Interim Testing Protocols for Determining the Seismic Performance Characteristics of Structural and Non-structural Components*. June 2007.
92. *Fib Model Code for Concrete Structures 2010*, International Federation for Structural Concrete (Fib), Federal Institute of Technology Lausanne-EPFL, 2013.
93. *Fibre Reinforced Concrete: Improvements and Innovations: RILEM-Fib International Symposium on FRC (BEFIB) in 2020*; Serna, P. , Llano-Torre, A. , Martí-Vargas, J. R. , Navarro-Gregori, J. , Eds. ; RILEM Bookseries; Springer International Publishing: Cham, 2021; Vol. 30. <https://doi.org/10.1007/978-3-030-58482-5>.
94. Fiebrich, M. H. *Influence of the Surface Roughness on the Adhesion between Concrete and Guniting Mortars Overlays*; Unterengstringen, Switzerland, 1994; pp 107–114.
95. Frank J. V; Michael P. Collins. The Modified Compression-Field Theory for Reinforced Concrete Elements Subjected to Shear. *ACI Structural Journal* 1986, 219–231.
96. Frosch, R. J. *Unified Design of Concrete Shear Strength*. 18.
97. Funari, M. F.; Spadea, S.; Fabbrocino, F.; Luciano, R. A. Moving Interface Finite Element Formulation to Predict Dynamic Edge Debonding in FRP-Strengthened Concrete Beams in Service Conditions. *Fibers* **2020**, *8*, 42.
98. Funari, M. F.; Verre, S. The Effectiveness of the DIC as a Measurement System in SRG Shear Strengthened Reinforced Concrete Beams. *Crystals* 2021, *11*, 265.

99. Garbacz, A.; Górka, M.; Courard, L. Effect of Concrete Surface Treatment on Adhesion in Repair Systems. *Magazine of Concrete Research* 2005, 57 (1), 49–60. <https://doi.org/10.1680/macr.2005.57.1.49>.
100. Genikomsou, A. Nonlinear Finite Element Analysis of Punching Shear of Reinforced Concrete Slab-Column Connections. Ph.D. Dissertation, University of Waterloo, 2015. <https://doi.org/10.12681/eadd/50321>.
101. Genikomsou, A. S.; Polak, M. A. Finite Element Analysis of Punching Shear of Concrete Slabs Using Damaged Plasticity Model in ABAQUS. *Engineering Structures* 2015, 98, 38–48. <https://doi.org/10.1016/j.engstruct.2015.04.016>.
102. Georgiou, A. Characterization of the Structural Performance of Strain-Hardening Fiber Cementitious Composites. Ph. D. Thesis, University of Cyprus, Nicosia, Cyprus, May 2017.
103. Georgiou, A.; Najmeh, E; Pantazopoulou, S. J., “Experimental Calibration of a Failure Criterion for Strain Hardening Cementitious Composites”. *Construction and Building Materials*, August 2021
104. Georgiou, A.; Pantazopoulou, S. J. Performance of Ductile FRCC under Cyclic Loads and Non-Linear FE Simulation. In *Proceedings of the FRC2018: Fibre Reinforced Concrete: from Design to Structural Applications Joint ACI-fib-RILEM International Workshop*, Desenzano, Italy, 27–30 June 2018; pp. 310–320.
105. Georgiou, A.; Pantazopoulou, S. Performance of SHFRCC-RC Concrete Members Under Cyclic Displacement Reversals. In *Earthquake Engineering Thessaloniki*; Thessaloniki, 2018; p 12.
106. Ghannoum, W. M. Experimental and Analytical Dynamic Collapse Study of a Reinforced Concrete Frame with Light Transverse Reinforcement. Ph. D. Dissertation, University of California, Berkeley, 2007.
107. Ghannoum, W. M; Matamoros, A. B. Nonlinear Modeling Parameters and Acceptance Criteria for Concrete Columns. In *SP-297: Seismic Assessment of Existing Reinforced Concrete Buildings*; American Concrete Institute, 2014. <https://doi.org/10.14359/51686898>.
108. Gomes A. M.; Appleton J. *Repair and Strengthening of Reinforced Concrete Elements under Cyclic Loading*. ; Paris, France, 1998.

109. Grammatikou, S.; Biskinis, D. B.; Fardis, M. N.;. Flexural Rotation Capacity Models Fitted to Test Results Using Different Statistical Approaches. International Federation for Structural Concre. <https://doi.org/10.1002/suco.201600238>.
110. Guan, H., Polak, M. A. Finite Element Studies of Reinforced Concrete Slab-Edge Column Connections with Opening. Canadian J. of Civil Engineering 34 (8), 952–965.
111. Guide to Materials Selection for Concrete Repair (ACI 546. 3R-14); American Concrete Institute, Ed.; ACI Committee 546; American Concrete Institute: Farmington Hills, Mich, 2014.
112. Hallgren M. Punching Shear Capacity of Reinforced High Strength Concrete Slabs. Ph.D. Dissertation, Bulletin No. 23, Department of Structural Engineering, Royal Institute of Technology, Stockholm, 1996.
113. Haroun, M. A.; Elsanadedy, H. M. Fiber-Reinforced Plastic Jackets for Ductility Enhancement of Reinforced Concrete Bridge Columns with Poor Lap-Splice Detailing. J. Bridge Eng. 2005, 10 (6), 749–757. [https://doi.org/10.1061/\(ASCE\)1084-0702\(2005\)10:6\(749\)](https://doi.org/10.1061/(ASCE)1084-0702(2005)10:6(749)).
114. Helal, Y.; Garcia, R.; Pilakoutas, K.; Guadagnini, M.; Hajirasouliha, I. Strengthening of Short Splices in RC Beams Using Post-Tensioned Metal Straps. Mater Struct 2016, 49 (1–2), 133–147. <https://doi.org/10.1617/s11527-014-0481-6>.
115. Hellenic Standards of Reinforced Concrete 2000. Hellenic Association of Seismic Design and Protection and Hellenic Association of Civil Engineers October 2000.
116. Hemmati, A., Kheyroddin, A.; Sharbatdar, M., Purk, Y.; Abolmali, A. Ductile Behavior of High-Performance Fiber Reinforced Cementitious Composite (HPFRCC) Frames, Construction and Building Materials 2016, 115, 681–689.
117. Henkhaus, K.; Pujol, S.; Ramirez, J. Axial Failure of Reinforced Concrete Columns Damaged by Shear Reversals. J. Struct. Eng. 2013, 139 (7), 1172–1180. [https://doi.org/10.1061/\(ASCE\)ST.1943-541X.0000673](https://doi.org/10.1061/(ASCE)ST.1943-541X.0000673).
118. Heyman J. Coulomb's Memoir on Statics. Cambridge University Press, London (1972).
119. Hindo K. R. In-Place Bond Testing and Surface Preparation of Concrete. Concr. Int. 1990, 12:46.

120. Hognestad, E. Study of Combined Bending and Axial Load in Reinforced Concrete Members; Technical Report of an Investigation; University of Illinois at Urbana Champaign Bulletin: Champaign, IL, USA, 1951.
121. Homrich, J. R.; Naaman, A. E. Stress-Strain Properties of SIFCON in Compression. Fibre Reinforced Concrete: Properties and Applications, American Concrete Institute 1987, SP-105, 283–304.
122. Hong, S. -G.; Lee, J. -H.; Choi, Y.; Gu, I. -Y. Seismic Strengthening of Concrete Columns by Ultrahigh-Performance Fiber-Reinforced Concrete Jacketing. *J. Struct. Eng.* 2021, 147 (10), 04021157. [https://doi.org/10.1061/\(ASCE\)ST.1943-541X.0003111](https://doi.org/10.1061/(ASCE)ST.1943-541X.0003111).
123. Huang S.; Guo X.; Zhang M. Study of Design Method and Similitude for Small-scale Reinforced Concrete Structural Models. *China Civil Eng. J* 45 (7), 32-8(in Chinese).
124. Hussein, H. H.; Walsh, K. K.; Sargant, S. M.; Steinberg, E. P. Interfacial Properties of Ultrahigh-Performance Concrete and High-Strength Concrete Bridge Connections. *J. Mater. Civ. Eng.* 2016, 28 (5), 04015208. [https://doi.org/10.1061/\(ASCE\)MT.1943-5533.0001456](https://doi.org/10.1061/(ASCE)MT.1943-5533.0001456).
125. Imai; Hiroshi; Yamamoto; Yoshie. A Study on Causes of Earthquake Damage of Izumi High School Due to Miyagi-Ken-Oki Earthquake in 1978. *Transactions of the Japan Concrete Institute* 1986.
126. Inel, M., A., M. A.; Pantazopoulou, S. J. Seismic Deformation Capacity Indices for Concrete Columns: Model Estimates and Experimental Results. *Magazine of Concrete Research.* <https://doi.org/10.1680/macr.2007.59.4.297>.
127. Ioannou, A. I.; Pantazopoulou, S. J.; Petrou, M. F.; Charmpis, D. C. Experimental Investigation of ECC Jackets for Repair of Pre-Damaged R. C. Members under Monotonic Loading. *Buildings* 2021, 11 (5), 180. <https://doi.org/10.3390/buildings11050180>.
128. Ioannou, A.; Pantazopoulou, S. J., G., S.; Illampas, R. Limit States Behaviour (or Failure) of Reinforced Concrete Columns; Hellenic Concrete Conference, 2018.
129. ISO 4287:1997 Geometrical Product Specifications (GPS) — Surface texture: Profile method — Terms, definitions and surface texture parameters
130. ISO BS. Geometrical Product Specifications (GPS) – Surface Texture: Profile Method – Terms, Definitions and Surface Texture Parameters. ; 1997.

131. James K. Wight; Mete A. Sozen. Shear Strength Decay in Reinforced Concrete Columns Subjected to Large Deflections Reversals. The National Science Foundation, University of Illinois, Urbana, Illinois August 1973.
132. James M. Wight; James G. Macgregor. Reinforced Concrete Mechanics and Design, 6th ed.; Pearson.
133. Jensen, B. C. Nogle Plasticitetsteoretiske Beregninger Af Beton Og Jernbeton,. PhD thesis, Technical University of Denmark, Copenhagen, Denmark, 1976.
134. Jinlong, P., Jie, G.; Junhun, C. Theoretical Modeling of Steel Reinforced ECC Column under Compressive Loading, *Science China Technological Sciences* 2015, 58, 889–898.
135. Júlio, E. N. B. S.; Branco, F. A. B.; Silva, V. D. Concrete-to-Concrete Bond Strength. Influence of the Roughness of the Substrate Surface. *Construction and Building Materials* 2004, 18 (9), 675–681. <https://doi.org/10.1016/j.conbuildmat.2004.04.023>.
136. Júlio, E.S.; Branco, F.; Silva, V. D. Structural Rehabilitation of Columns with Reinforced Concrete Jacketing: Column Rehabilitation with RC Jacketing. *Prog. Struct. Engng Mater.* 2003, 5 (1), 29–37. <https://doi.org/10.1002/pse.140>.
137. Kanda, T.; Li, V. C. Interface Property and Apparent Strength of High-Strength Hydrophilic Fiber in Cement Matrix. *Journal of Materials in Civil Engineering* 1998, 10 (1), 5–13. [https://doi.org/10.1061/\(ASCE\)0899-1561\(1998\)10:1\(5\)](https://doi.org/10.1061/(ASCE)0899-1561(1998)10:1(5)).
138. Kawashima, K. Damage of Bridges Due to the 2011 Great East Japan Earthquake. 20.
139. Kawashima, K.; Takahashi, Y.; Ge, H.; Wu, Z. ; Zhang, J. Reconnaissance Report on Damage of Bridges in 2008 Wenchuan, China, Earthquake. *Journal of Earthquake Engineering* 2009, 13 (7), 965–996. <https://doi.org/10.1080/13632460902859169>.
140. Keuser, M., M., G. Finite Element Models for Bond Problems. *Journal of Structural Engineering*, ASCE 113 (10), 2160–2173.
141. Kim, C. -G.; Park, H. -G.; Eom, T. -S. Cyclic Load Test and Shear Strength Degradation Model for Columns with Limited Ductility Tie Details. *J. Struct. Eng.* 2019, 145 (2), 04018249. [https://doi.org/10.1061/\(ASCE\)ST.1943-541X.0002254](https://doi.org/10.1061/(ASCE)ST.1943-541X.0002254).
142. Kim, C. G.; Park, H. G.; Eom, T. S. Cyclic Load Test and Shear Strength Degradation Model for Columns with Limited Ductility Tie Details. *J. Struct. Eng.*

- 2019, 145 (2), 04018249. [https://doi.org/10.1061/\(ASCE\)ST.1943-541X.0002254](https://doi.org/10.1061/(ASCE)ST.1943-541X.0002254).
143. Kriegh, J. D. Arizona Slant Shear Test: A Method to Determine Epoxy Bond Strength. *Journal of the American Concrete Institute* 1976, 73 (3), 372–373.
144. Kuo, W. W. Study on the Collapse Behavior of Nonductile Reinforced Concrete Frames Subjected to Earthquake Loading. Ph. D. Dissertation, Department of Construction Engineering, National Taiwan University of Science and Technology, Taipei, Taiwan, 2008.
145. Kwak, H. G.; Filippou, F.C. Finite Element of Reinforced Concrete Structures Under Monotonic Loading; UCB/SEMM-90/14; Structural Engineering, Mechanics and Materials Department of Civil Engineering University of California, Berkeley, 1990.
146. Labuz, J. F.; Zang, A. Mohr–Coulomb Failure Criterion. *Rock Mech Rock Eng* 2012, 45 (6), 975–979. <https://doi.org/10.1007/s00603-012-0281-7>.
147. Lankard, D. R.; Newell, J. K. Preparation of Highly Reinforced Steel Fibre Reinforced Concrete Composites; American Concrete Institute: Detroit, 1984; Vol. SP-81, p 277–306.
148. Lee, J.; Fenves, G. L. Plastic-Damage Model for Cyclic Loading of Concrete Structures. *Journal of Engineering Mechanics* 1998, 124 (8), 892–900. [https://doi.org/10.1061/\(ASCE\)0733-9399\(1998\)124:8\(892\)](https://doi.org/10.1061/(ASCE)0733-9399(1998)124:8(892)).
149. Lee, M. -G.; Wang, Y. -C.; Chiu, C. -T. A Preliminary Study of Reactive Powder Concrete as a New Repair Material. *Construction and Building Materials* 2007, 21 (1), 182–189. <https://doi.org/10.1016/j.conbuildmat.2005.06.024>.
150. Leung, C. K. Y.; Cao, Q. Development of Pseudo-Ductile Permanent Formwork for Durable Concrete Structures. *Mater Struct* 2010, 43 (7), 993–1007. <https://doi.org/10.1617/s11527-009-9561-4.1>
151. Li, M. Engineered Cementitious Composites for Bridge Decks. In *Advanced Composites in Bridge Construction and Repair*; Elsevier, 2014; pp 177–209. <https://doi.org/10.1533/9780857097019.2.177>.
152. Li, V. C. On Engineered Cementitious Composites (ECC). 2003, 1 (3), 16.
153. Li, V. C.; Wu, H. C. Conditions for Pseudo Strain Hardening in Fibre Reinforced Brittle Matrix Composites. *Journal of Applied Mechanics Review* 1992, 45 (8), 390–398.

154. Li, X.; Chen, K.; Hu, P.; He, W.; Xiao, L. ; Zhang, R. Effect of ECC Jackets for Enhancing the Lateral Cyclic Behavior of RC Bridge Columns. *Engineering Structures* 2020, 219, 110714. <https://doi.org/10.1016/j.engstruct.2020.110714>.
155. Li, Y.; Elwood, K. J. Assessment of ASCE/SEI 41 Concrete Column Provisions Using Shaking Table Tests. 23.
156. Li, Y. The Shaking Table Tests Column Database and Evaluation of Drift Capacity Models for Non-Ductile Columns. **2012**, 227.
157. Lin, C.S.; Scordelis, A.C. Nonlinear Analysis of RC Shells of General Form. *Journal of Structural Division, ASCE* 101 (ST3), 523–538.
158. Lubliner, J.; Oliver, J.; Oller, S.; Oñate, E. A Plastic-Damage Model for Concrete. *International Journal of Solids and Structures* 1989, 25 (3), 299–326. [https://doi.org/10.1016/0020-7683\(89\)90050-4](https://doi.org/10.1016/0020-7683(89)90050-4).
159. Lynn, A. C.; Moehle, J.; Mahin, S.; Holmes, W. Seismic Evaluation of Existing Reinforced Concrete Building Columns. *Earthquake Spectra* 1996, 12, 715–739. <https://doi.org/10.1193/1.1585907>.
160. Maalej, M.; Li, V. C. Introduction of Strain-Hardening Engineered Cementitious Composites in Design of Reinforced Concrete Flexural Members for Improved Durability. *ACI Struct. J* 1995, 92 (2), 167–176.
161. Mander, J. B.; Priestley, M. J. N.; Park, R. Theoretical Stress-Strain Model for Confined Concrete. *J. Struct. Eng.* 1988, 114 (8), 1804–1826. [https://doi.org/10.1061/\(ASCE\)0733-9445\(1988\)114:8\(1804\)](https://doi.org/10.1061/(ASCE)0733-9445(1988)114:8(1804)).
162. Martínez, J. Á. L. Characterization of the Tensile Behaviour of UHPFRC By Means of Four-Point Bending Tests. Ph. D. Thesis, Polytechnical School of Valencia, Valencia, Spain, March 2017.
163. Martín-Pérez, B.; Pantazopoulou, S. J. Mechanics of Concrete Participation in Cyclic Shear Resistance of RC. *J. Struct. Eng.* 1998, 126 (4), 633–641.
164. Martirosyan, A.; Xiao, Y. Flexural-Shear Behavior of High-Strength Concrete Short Columns. *Earthquake Spectra* 2001, 17 (4), 679–695. <https://doi.org/10.1193/1.1423656>.
165. Massicotte, B.; Boucher-Proulx, G. Seismic Retrofitting of Bridge Piers with UHPFRC Jackets. *Des. Build. UHPFRC* 2009, 531–540, doi:10.1002/9781118557839.ch35.
166. Matchulat, L.; Adolfo Matamoros. Mitigation of Collapse Risk in Vulnerable Concrete Buildings. Master of Science, University of Kansas 2008.

167. Mavros, M. Experimental and Numerical Investigation of the Seismic Performance of Reinforced Masonry Structures. Ph.D. Dissertation, University of California, San Diego, California, U.S.A., 2015.
168. Megalooikonomou, K. G.; Tastani, S. P.; Pantazopoulou, S. J. Effect of Yield Penetration on Column Plastic Hinge Length. Elsevier Ltd 2018, 156, 161–174. <https://doi.org/10.1016/j.engstruct.2017.11.003>.
169. Menétrey. Numerical Analysis of Punching Failure In Reinforced Concrete Structures. Master of Science, University of Colorado, Boulder.
170. Meyer, C; Okamura, H. Finite Element Analysis of Reinforced Concrete Structures. In Proceedings of the US-Japan Joint Seminar on Finite Element Analysis of Reinforced Concrete; Tokyo, Japan., 1985.
171. Michael M. Sprinkel, P. E.; Celik Ozyildirim, Ph. D. Evaluation of High-Performance Concrete Overlays Placed On Route 60 over Lynnhaven Inlet in Virginia; Technical; Virginia Transportation Research Council: Virginia United States, 2000.
172. Miguel A. Carbonell Munoz; Devin K. Harris, Ph. D.; A. M. ASCE; Theresa M. Ahlborn, Ph. D. ; P. E. , M. ASCE; David C. Froster. Bond Performance between Ultrahigh-Performance Concrete and Normal-Strength Concrete. J. Mater. Civ. Eng. 2014, 26 (8), 04014031-1: 04014031-9. [https://doi.org/10.1061/\(ASCE\)MT.1943-5533.0000890](https://doi.org/10.1061/(ASCE)MT.1943-5533.0000890).
173. Miguel, R. Ilgi Moble Building; Concrete Buildings Damaged in Earthquakes; Case Study; EERI, 2013.
174. Ministry of Transport of People’s Republic of China. Guidelines for Seismic Design of Highway Bridges (JTG/TB02-01-2008) [S]; Beijing, 2008.
175. Mircea, A. C.; Toader, T. P. Fracture Energy of Engineered Cementitious Composites. Proceedings 2020, 63, 8. <https://doi.org/10.3390/proceedings2020063008>
176. Moehle, J. P.; Eberhard, M. O. Bridge Engineering Handbook. 2000, 34.
177. Moersch E. Concrete-Steel Construction; McGraw-Hill, New York (English translation by E. P. Goordich), 1909.
178. Momayez; M. R. Ehsani; A. A. Ramezani pour; H. Rajaie. Comparison of Methods for Evaluating Bond Strength between Concrete Substrate and Repair Materials. Cement and Concrete Research 2004, 35, 748–757. <https://doi.org/10.1016/j.cemconres.2004.05.027>.

179. Mu B, Meyer C, Shimanovich S. Improving the interface bond between fiber mesh and cementitious matrix. *Cement Concrete Res* 2002;32(5):783–7.
180. Murphy, K. P. *Machine Learning: A Probabilistic Perspective*; Adaptive computation and machine learning series MIT Press: Cambridge, MA, 2012
181. Naaman, A. E. *A Statistical Theory of Strength for Fiber Reinforced Concrete*. Ph. D. Thesis, Massachusetts Institute of Technology, 1972.
182. Naaman, A. E. Advances in High Performance Fibre Reinforced Cement Based Composites. In *Proceedings of the International Symposium on Fibre Reinforced Concrete*; V. S. Parameswaran and T. S. Krishnamurti, Editors, Oxford IBH Publishing Ltd.: New Delhi, India, 1987; p 7. 87–7. 98.
183. Naaman, A. E. High Performance Fibre Reinforced Cement Composites. In *Proceedings of the IABSE Symposium on Concrete Structures for the Future*; Paris, France, 1987; p 371–376.
184. Naaman, A. E.; Argon, A.; Moavenzadeh, F. A Fracture Model for Fiber Reinforced Cementitious Materials. *Cement and Concrete Research* 1973, 3 (4), 397–411.
185. Naaman, A. E.; F. Moavenzadeh; F. J. McGarry. Probabilistic Analysis of Fiber Reinforced Concrete. *Journal of the Engineering Mechanics's Division, ASCE* 1974, 100 (EM2), 397–413.
186. Naaman, A. E.; Reinhardt, H. W. Characterization of High-Performance Fibre Reinforced Cement Composites. In *Proceedings of High-Performance Fibre Reinforced Cement Composites: HPFRCC 2, RILEM; E. & FN Spon: London, 1996; Vol. 31, pp 1–31.*
187. Naaman, A. E.; Reinhardt, H. W. High Performance Fibre Reinforced Cement Composites: HPFRCC 2, RILEM; E. & FN Spon: London, 1996; Vol. 31, p 505.
188. Nadai A. *Theory of flow and fracture of solids*. McGraw Hill, New York (1950)
189. Naderi, M. Analysis of the Slant Shear Test. *Journal of Adhesion Science and Technology* 2009, 23 (2), 229–245. <https://doi.org/10.1163/156856108X369589>.
190. Nagasaka, T. Effectiveness of Steel Fiber as Web Reinforcement in Reinforced Concrete Columns. *Transactions of the Japan Concrete Institute* 1982.
191. Naik, T. Personal Communication from Dr. T. Naik; University of Wisconsin: Milwaukee, WI, 1985.
192. Nayak, G.C.; Zienkiewicz, O.C. Elasto-Plastic Stress Analysis. *International Journal of Numerical Methods in Engineering* 5, 152–163.

193. Negele, A., Eligehausen., R.; Eligehausen, Ožbolt, J., Polak, M. A. Finite-Element Simulations on Punching Tests of Shear Retrofitted Slab-Column Connections. In Proc., IA-FraMCoS-6: International Association of Fracture Mechanics for Concrete and Concrete Structures; Catania, Italy, 2007; pp 911–918.
194. Ngo, D.; Scordelis, A.C. Finite Element Analysis of Reinforced Concrete Beams,. Journal of ACI 1967, 64 (3), 152–163.
195. Nilson, A.H. Internal Measurement of Bond Slip. Journal of ACI 1972, 69 (7), 439–441.
196. Ož bolt, J.; Li, Y.-J.; Kozar, I. Microplane Model for Concrete with Relaxed Kinematic Constraint. International Journal of Solids and Structures, in press. 2001..
197. Ohue, M.; Morimoto, H.; Fujii, S.; Morita, S. The Behavior of R. C. Short Columns Failing in Splitting Bond-Shear Under Dynamic Lateral Loading. Transactions of the Japan Concrete Institute 1985.
198. Ono, A.; Shirai, N.; Adachi, H.; Sakamaki, Y. Elasto-Plastic Behavior of Reinforced Concrete Column with Fluctuating Axial Force. 1989.
199. Opabola, E. A.; Elwood, K. J. Seismic Assessment of Reinforced Concrete Columns with Short Lap Splices. Earthquake Spectra 2021, 37 (3), 1726–1757. <https://doi.org/10.1177/8755293021994834>.
200. Oucif, C.; Ouzaa, K.; Mauludin, L. M. Cyclic and Monotonic Behavior of Strengthened and Unstrengthened Square Reinforced Concrete Columns. J. Appl. Comput. Mech. 2017, No. Online First. <https://doi.org/10.22055/jacm.2017.23514.1159>
201. Pantazopoulou, S. J. Role of Expansion on Mechanical Behavior of Concrete. Journal of Structural Engineering 1995, 121 (12), 1795–1805. [https://doi.org/10.1061/\(ASCE\)0733-9445\(1995\)121:12\(1795\)](https://doi.org/10.1061/(ASCE)0733-9445(1995)121:12(1795)).
202. Pantazopoulou, S. J.; Tastani, S. P.; Thermou, G. E.; Triantafillou, T.; Monti, G.; Bournas, D.; Guadagnini, M. Background to the European Seismic Design Provisions for Retrofitting RC Elements Using FRP Materials. Structural Concrete 2016, 17 (2), 194–219. <https://doi.org/10.1002/suco.201500102>.
203. Papavasileiou, G. S.; Charmpis, D. C.; Lagaros, N. D. Optimized Seismic Retrofit of Steel-Concrete Composite Buildings. *Eng. Struct.* **2020**, *213*, 110573.
204. Pardalopoulos, S. J.; Thermou, G. E.; Pantazopoulou S. J. Preliminary Seismic Assessment Method for Identifying R. C. Structural Failures. In Computational

Methods in Earthquake Engineering; Springer Dordrecht Heidelberg New York London, 2013; Vol. 2.

205. Pardalopoulos, S. J.; Thermou, G. E.; Pantazopoulou, S. J. Rapid Preliminary Seismic Assessment Methodology for Non-Conforming Reinforced Concrete Buildings. 2011, 17
206. Park, H. G.; Choi, K. K.; Kim, J. C. Shear Strength Model Based on Compression Zone Failure Mechanism, 2014.
207. Park, R.; Paulay, T. Reinforced Concrete Structures; J. Wiley & Sons: New York, 1975.
208. Park, R.; Priestley, M. N.; Gill, W. D. Ductility of Square-Confined Concrete Columns. J. Struct. Div. 1982,108, 929–950.
209. Parra-Montesinos, G. J.; Chompreda, P. Deformation Capacity and Shear Strength of Fiber-Reinforced Cement Composite Flexural Members Subjected to Displacement Reversals. J. Struct. Eng. 2007, 133 (3), 421–431. [https://doi.org/10.1061/\(ASCE\)0733-9445\(2007\)133:3\(421\)](https://doi.org/10.1061/(ASCE)0733-9445(2007)133:3(421)).
210. Parvin, A.; Wang, W. Behavior of FRP Jacketed Concrete Columns under Eccentric Loading. J. Compos. Constr. 2001, 5, 146–152.
211. Paultre, P.; Calais, É.; Proulx, J.; Prépetit, C. ; Ambroise, S. Damage to Engineered Structures during the 12 January 2010, Haiti (Léogâne) Earthquake. Can. J. Civ. Eng. 2013, 40 (8), 777–790. <https://doi.org/10.1139/cjce-2012-0247>.
212. Penelis, G. G.; Penelis, G. G. Concrete Buildings in Seismic Regions. 856.
213. Petr K.; David N. and Christopher A. Gwyddion user guide, Copyright © 2004–2007, 2009–2019
214. Polak, M. A. Shell Finite Element Analysis of RC Plates Supported on Columns for Punching Shear and Flexure. International J. for Comp.-Aided Eng. and Software 2005, 22 (4), 409–428.
215. Priestley, M. J. N.; Verma, R.; Xiao, Y. Seismic Shear Strength of Reinforced Concrete Columns. Journal of Structural Engineering 1994, 120 (8), 2310–2329. [https://doi.org/10.1061/\(ASCE\)0733-9445\(1994\)120:8\(2310\)](https://doi.org/10.1061/(ASCE)0733-9445(1994)120:8(2310)).
216. Pujol, S. Drift Capacity of Reinforced Concrete Columns Subjected to Displacement Reversals, Purdue University, 2002.
217. Ramadoss, P. and N Nagamani, K. Tensile Strength and Durability Characteristics of High-Performance Fibre Reinforced Concrete. Arabian Journal for Science and Engineering 2008, 33 (2B), 307–319.

218. Ramezaniapour, A. A. Cement Replacement Materials; Springer Geochemistry/Mineralogy; Springer Berlin Heidelberg: Berlin, Heidelberg, 2014. <https://doi.org/10.1007/978-3-642-36721-2>.
219. Randl, N.; Peyerl, M.; and Steiner, M., “Investigations on Adhesive Bond between High Performance Concrete Overlays and NSC Substrates,” Proceedings of fib Symposium 2016: Performance-Based Approaches for Concrete Structures, Cape Town, South Africa, 2016, 11 pp.
220. Raza, S.; Khan, M. K. I.; Menegon, S. J.; Tsang, H. -H. ; Wilson, J. L. Strengthening and Repair of Reinforced Concrete Columns by Jacketing: State-of-the-Art Review. Sustainability 2019, 11, 3208.
221. Reineck, K. H. Shear Design Integrated in The Design Concept of Strut-and-Tie Models for Structural Concrete; Universitas Pelita Harapan, Indonesia, 2007.
222. Richart F.E.; Brandtzaeg A.; Brown R. A Study of the Failure of Concrete under Combined Compressive Stresses. University of Illinois Engineering Experiment Station 1928.
223. Riyad S. Aboutaha, M. D. E.; James O. Jirsa, M. E. K. Rehabilitation of Shear Critical Concrete Columns by Use of Rectangular Steel Jackets. SJ 1999, 96 (1). <https://doi.org/10.14359/597>.
224. Riyad, A.; Fares, J.; Sara, S.; Mucip T. Final Report - Seismic Evaluation and Retrofit of Deteriorated Concrete Bridge Component; Syracuse University, 2013.
225. Rodriguez M; Park R. Repair and Strengthening of Reinforced Concrete Buildings for Seismic Resistance. Earthquake Spectra (EERI) 1991, 7 (3), 439–459.
226. Romualdi, J. P.; Mandel, J. A. Tensile Strength of Concrete Affected by Uniformly Distributed Closely Spaced Short Length of Wire Reinforcement. ACI Structural Journal 1964.
227. Rots, J.G.; Nauta, P.; Kusters, G.M.A.; Blaauwendraad, J. Smearred Crack Approach and Fracture Localization in Concrete. *HERON* 1985, 30 (1), 3–48.
228. S. J. Pantazopoulou; R. H. Mills. Microstructural Aspects of the Mechanical Response of Plain Concrete. Materials Journal, American Concrete Institute (ACI) 1995, Vol. 92 (6), 605–616.
229. Saad; Tom; Maswoswe; Justice; Derrell Manceaux. FHWA Seismic Retrofitting Seminar, 2010.
230. Santos, P. D. M. Assessment of the Shear Strength between Concrete Layers. PhD thesis, University of Coimbra-Department of Civil Engineering, 2009.

231. Scordelis, A.C.; Ngo, D.; Franklin, H.A. Finite Element Study of Reinforced Concrete Beams with Diagonal Tension Cracks. In Proceedings of Symposium on Shear in Reinforced Concrete; ACI Publication SP-42., 1974.
232. Scribner, C. F.; Wight, J. K. Strength Decay in R. C. Beams under Load Reversals. *J. Struct. Div* 1980, 106 (4), 861–876.
233. Sezen H.; Moehle, J. P.; Mosalam K. M. Seismic Behavior and Modeling of Reinforced Concrete Building Columns, University of California, 2002.
234. Sezen, H.; Moehle, J. P.; Mosalam, K. M. Seismic Behavior and Modeling of Reinforced Concrete Building Columns, University of California, 2002.
235. Shang, X.; Yu, J.; Li, L.; Lu, Z. Strengthening of RC Structures by Using Engineered Cementitious Composites: A Review. *Sustainability* 2019, 11 (12), 3384. <https://doi.org/10.3390/su11123384>.
236. Shang, X.; Yu, J.; Li, L.; Lu, Z. Strengthening of RC Structures by Using Engineered Cementitious Composites: A Review. *Sustainability* 2019, 11 (12), 3384. <https://doi.org/10.3390/su11123384>.
237. Shigeyuki, S.; Shirai, N.; Adachi, H.; Ono, A. Deformation of Reinforced Concrete Column with High or Fluctuating Axial Force. *Transactions of the Japan Concrete Institute* 1991.
238. Shin, Y. B. Dynamic Response of Ductile and Non-Ductile Reinforced Concrete Columns, University of California, Berkeley, 2007.
239. Sokoli, D.; Ghannoum, W. M. High-Strength Reinforcement in Columns under High Shear Stresses. *ACI Structural Journal* 2016, 113 (3). <https://doi.org/10.14359/51688203>.
240. Stoppenhagen DR; Jirsa JO; Wylie Jr. LA. Seismic Repair and Strengthening of a Severely Damaged Concrete Frame. *ACI Structural Journal* 1995, 92 (2), 177–187.
241. Su, R. S. Shake Table Tests on Reinforced Concrete Short Columns Failed in Shear. Master thesis, Department of Construction Engineering, National Taiwan University of Science and Technology, National Taiwan University of Science and Technology, 2007.
242. Syntzirma D. V.; Pantazopoulou S. J. Deformation Capacity of RC Members with Brittle Details Under Cyclic Loads. *ACI Special Publication* 2007, ACI-ASCE Committee 445 (Seismic Shear).

243. Syntzirma, D. V.; Pantazopoulou, S. J.; Aschheim, M. Load-History Effects on Deformation Capacity of Flexural Members Limited by Bar Buckling. *J. Struct. Eng.* 2010, 136 (1), 1–11. [https://doi.org/10.1061/\(ASCE\)ST.1943-541X.0000088](https://doi.org/10.1061/(ASCE)ST.1943-541X.0000088).
244. Szczerbiak, A. I. Declaration of Performance, 2015.
245. Taljaard, V. -L.; Gravett, D. Z.; Mourlas, C.; Markou, G.; Bakas, N.; Papadrakakis, M. Development of a New Fundamental Period Formula by Considering Soil-Structure Interaction with the Use of Machine Learning Algorithms; Athens, Greece, 2021; pp 3801–3809. <https://doi.org/10.7712/120121.8748.18534>.
246. Tasios P. T.; Dritsos S. E.; Kappos E. I.; Fardis M. N.; Chronopoulos M. Greek Standards for Assessment and Retrofit of Existing Structures. Athens February 2017.
247. Tastani, K. G. M.; S. J. Pantazopoulou. Reinforcement to Concrete Bond in Inelastic Regions of RC Frame Members. In *fib Bulletin “Advances on Bond in Concrete”*; The International Federation for Structural Concrete (fib); p 12.
248. Tastani, S. P.; Pantazopoulou, S. J. Direct Tension Pullout Bond Test: Experimental Results. *J. Struct. Eng.* 2010, 136 (6), 731–743. [https://doi.org/10.1061/\(ASCE\)ST.1943-541X.0000159](https://doi.org/10.1061/(ASCE)ST.1943-541X.0000159).
249. Tayeh, B. A.; Abu Bakar, B. H.; Megat Johari, M. A.; Voo, Y. L. Mechanical and Permeability Properties of the Interface between Normal Concrete Substrate and Ultra High-Performance Fiber Concrete Overlay. *Construction and Building Materials* 2012, 36, 538–548. <https://doi.org/10.1016/j.conbuildmat.2012.06.013>.
250. Tayeh, B. A.; Bakar, B. H. A.; Johari, M. A. M.; Ratnam, M. M. The Relationship between Substrate Roughness Parameters and Bond Strength of Ultra-High-Performance Fiber Concrete. *Journal of Adhesion Science and Technology* 2013, 27 (16), 1790–1810. <https://doi.org/10.1080/01694243.2012.761543>.
251. Taylor, R. L. FEAP - Finite Element Analysis Program, 2014.
252. Thaulow, S. Tensile Splitting Test and High Strength Concrete Test Cylinders. American Concrete Institute, *Journal of the American Concrete Institute* 1957, 53 (1), 699–706.
253. Thermou, G. E.; Elnashai, A. S. Seismic Retrofit Schemes for RC Structures and Local-Global Consequences. *Prog. Struct. Engng Mater.* 2006, 8 (1), 1–15.

254. Thermou, G. E.; Pantazopoulou, S. J. Fiber-Reinforced Polymer Retrofitting of Predamaged Substandard RC Prismatic Members. *J. Compos. Constr.* 2009, 13, 535–546.
255. Thermou, G. E.; Pantazopoulou, S. J. Metallic Fabric Jackets: An Innovative Method for Seismic Retrofitting of Substandard RC Prismatic Members. *Struct. Concr.* 2007, 8, 35–46.
256. Thermou, G. E.; Pantazopoulou, S. J.; Elnashai, A. S. Design Methodology for Seismic Upgrading of Substandard Reinforced Concrete Structures. *J. Earthq. Eng.* 2007, 11, 582–606.
257. Thermou, G. E.; Pantazopoulou, S. J.; M. ASCE; Elnashai, A. S.; F. ASCE. Analytical Modeling of Interface Behavior in Reinforced Concrete Jacketed Member; ASCE (American Society of Civil Engineers), Reston, VA., 2004.
258. Thermou, G., and Pantazopoulou, S. J. “Fiber – reinforced polymer retrofitting of substandard RC prismatic members”, *ASCE J. of Composites for Construction*, **13**(6):535-546, (Nov. (2009)).
259. Tjiptobroto, P.; Hansen, W. Model for Prediction of the Elastic Strain of Fibre Reinforced Composites Containing High Volume Fractions of Discontinuous Fibres. *ACI Materials Journal* 1983, 90 (2).
260. Tsonos, A. G. Effectiveness of CFRP-Jackets and RC-Jackets in Post-Earthquake and Pre-Earthquake Retrofitting of Beam–Column Subassemblages. *Engineering Structures* 2008, 30 (3), 777–793. <https://doi.org/10.1016/j.engstruct.2007.05.008>
261. Tureyen, A. K. and Robert, J. F. Concrete Shear Strength: Another Perspective. *ACI Structural Journal* 2003, 100 (5). <https://doi.org/10.14359/12802>.
262. Umehara, H.; Jirsa, J. O.; ASCE, M. Short Rectangular RC Columns Under Bidirectional Loadings. *Journal of Structural Engineering* 110(3), 605–618.
263. UNIDO. Building Construction Under Seismic Conditions in the Balkan Region. Post-Earthquake Damage Evaluation and Strength Assessment of Buildings under Seismic Conditions., Project REP/79/015. ; United Nations Industrial Developing Organization, UNDP/ UNIDO: Vienna, Austria, 1983; Vol. 4.
264. Vandoros, K. G.; Dritsos, S. E. Concrete jacket construction detail effectiveness when strengthening RC columns. *Constr. Build. Mater.* 2008, 22, 264–276.

265. Wang, W.; Liub, J.; Agostini, F., Davy., C. A.; Skoczylas, F.; Corvez, D. Durability of an Ultra High Performance Fibre Reinforced Concrete (UHPFRC) under Progressive Aging,. *Cement and Concrete Research*, 2014, 55, 1–13.
266. Webster, M. *The Assessment of Corrosion-Damaged Concrete Structures*. 318.
267. Wu C. L.; Su R. S; Hwang S. J.; Yang Y. S. Shake Table Tests on Reinforced Concrete Short Columns Failing in Shear; 2008.
268. Wu, C. L.; Loh, C. H.; Yang, Y. S. Shaking Table Tests on Gravity Load Collapse of Low-Ductility RC Frames under near-Fault Earthquake Excitation. *Advances in Experimental Structural Engineering* 2006, 725–732.
269. Wu, Y. -F.; ASCE, M.; Hu, B. Shear Strength Components in Reinforced Concrete Members. *J. Struct. Eng.* 2017, 16.
270. Xie, J.; Fu, Q.; Yan, J. -B. Compressive Behaviour of Stub Concrete Column Strengthened with Ultra-High-Performance Concrete Jacket. *Construction and Building Materials* 2019, 204, 643–658. <https://doi.org/10.1016/j.conbuildmat.2019.01.220>.
271. Xu, L.; Pan, J.; Chen, J. Mechanical Behavior of ECC and ECC/RC Composite Columns under Reversed Cyclic Loading. *J. Mater. Civ. Eng.* 2017, 29 (9), 04017097. [https://doi.org/10.1061/\(ASCE\)MT.1943-5533.0001950](https://doi.org/10.1061/(ASCE)MT.1943-5533.0001950).
272. Yang, Y.; Massicotte, B. ; Genikomsou, A. S. ; Pantazopoulou, S. J. ; Palermo, D. Comparative Investigation on Tensile Behaviour of UHPFRC. *Mater Struct* 2021, 54 (4), 147. <https://doi.org/10.1617/s11527-021-01747-1>.
273. Yavari, S.; Elwood, K. J.; Wu, C. L. 2009. Collapse of a Non-Ductile Concrete Frame: Evaluation of Analytical Models. *Earthquake Engineering & Structural Dynamics* No. 38, 225–241.
274. Youm H. S; Lim, W. Y.; Hong, S. G.; Joh, C. Interface Shear Strength between Ultra-High-Performance Concrete and Normal-Strength Concrete. *SJ* 2021, 118 (2). <https://doi.org/10.14359/51729350>.
275. Yuan, F.; Pan, J.; Dong, L.; Leung, C. K. Y. Mechanical Behaviors of Steel Reinforced ECC or ECC / Concrete Composite Beams under Reversed Cyclic Loading. *J. Mater. Civ. Eng.* 2014, 26 (8), 04014047. [https://doi.org/10.1061/\(ASCE\)MT.1943-5533.0000935](https://doi.org/10.1061/(ASCE)MT.1943-5533.0000935).
276. Yuan, R. L.; Cook, J. E. Study of a Class C Fly Ash Concrete. In *Proceedings of 1st International Conference on the Use of Fly Ash, Silica Fume, Slag, and Other*

Mineral Byproducts in Concrete; American Concrete Institute, Detroit, Special Publication: Montebello, PQ, 1983; Vol. SP-79, pp 307–319.

277. Zhang, Y.; Zhu, P.; Liao, Z.; Wang, L. Interfacial Bond Properties between Normal Strength Concrete Substrate and Ultra-High-Performance Concrete as a Repair Material. *Construction and Building Materials* 2020, 235, 117431. <https://doi.org/10.1016/j.conbuildmat.2019.117431>.
278. Zhao, X.; Wu, Y.-F.; Leung, A. Yt.; Lam, H. F. Plastic Hinge Length in Reinforced Concrete Flexural Members. *Procedia Engineering* 2011, 14, 1266–1274. <https://doi.org/10.1016/j.proeng.2011.07.159>.
279. Zhou, X.; Higashi; Yoichi, J.; Weishan, S.; Yasushi. Behavior of Reinforced Concrete Column Under High Axial Load. 1985.
280. Zhou, X.; Satoh, T.; Jiang, W.; Ono, A.; Shimizu, Y. Behavior of Reinforced Concrete Short Column Under High Axial Load. Transactions of the Japan Concrete Institute 1987.
281. Zhu, Z. F.; Wang, W. W. Experimental Study on Mechanical Behaviour of Circular Reinforced Concrete Columns Strengthened with FRP Textile and ECC. *J. Southeast Univ.* 2016, 46, 1082–1087.
282. Zilch, K.; Reinecke, R. Capacity of Shear Joints between High-Strength Precast Elements and Normal-Strength Cast-in-Place Decks; Orlando, USA, 2000.

ANTHOS I. IOANNOU

References

1. Abaqus/CAE User's Manual. Dassault Systems Simulia Corp., Providence, RI, USA 2010, 1174.
2. ABAQUS: Theory Manual; Providence, R. I.: Hibbitt, Karlsson & Sorensen. , 1992.
3. Abee, S. H.; Str, P. Sika® ViscoCrete® Techno-10+. **2019**, 3.
4. ACI Committee 318; American Concrete Institute; International Organization for Standardization. Building Code Requirements for Structural Concrete (ACI 318M-08) and Commentary; American Concrete Institute: Farmington Hills, Mich., 2008.
5. ACI Committee 544. ACI PRC-544. 1R-96: Report on Fiber Reinforced Concrete (Reapproved 2009); 2002.
6. Adeghe, L.N.; Collins, M. P. A Finite Element Model for Studying Reinforced Concrete Detailing Problems; Publication No. 86-12; Department of Civil Engineering, University of Toronto, 1986.
7. Advances in Construction Materials 2007: With 80 Tables; Grosse, C. U., Reinhardt, H. -W., Grobe, C. U., Eds. ; Springer: Berlin Heidelberg, 2007.
8. Akazawa, T. Tension Test Method for Concretes, Bulletin No. 16; International Association of Testing and Research Laboratories: Paris, 1953; pp 11–23.
9. Al-Gemeel, A. N. Experimental Investigation of Textile Reinforced Engineered Cementitious Composite (ECC) for Square Concrete Column Confinement. *Construction and Building Materials* 2018, 9.
10. Al-Hamaydeh, M.; Markou, G.; Bakas, N.; Papadrakakis, M. AI-Based Shear Capacity of FRP-Reinforced Concrete Deep Beams without Stirrups. *Engineering Structures* 2022, 264, 114441. <https://doi.org/10.1016/j.engstruct.2022.114441>.
11. Ali Yaz and Ambalavanan R., Flexural behaviour of reinforced concrete beams repaired with styrene-butadiene rubber latex, silica fume and methylcellulose repair formulations. *Mag Concrete Res* 1999; 51:113–20.
12. Alsomiri, M.; Jiang, X.; Liu, Z. Elastic Restraint Effect of Concrete Circular Columns with Ultrahigh-Performance Concrete Jackets: An Analytical and Experimental Study. *Materials* 2021, 14 (12), 3278. <https://doi.org/10.3390/ma14123278>.

13. Alvarez, J. C. Seismic Behavior of Concrete Frames with Jacketed Columns. Ph. D. Dissertation, University of Massachusetts Amherst, 2017.
14. American Association of State Highway and Transportation Officials. Load and Resistance Factor Design (AASHTO, LRFD). Bridge Design Specifications; Washington, 2010.
15. American Society for Testing and Materials. Specification for Fly Ash and Raw of Calcined Natural Pozzolan for Use as a Mineral Admixture in Portland Cement Concrete; ASTM: Philadelphia, PA, 1978; Vol. ASTM C618-78.
16. American Society of Civil Engineers, 2017. Seismic Evaluation and Retrofit of Existing Buildings (41-17).
17. American Society of Civil Engineers. Seismic Evaluation and Retrofit of Existing Buildings, 41st ed.; American Society of Civil Engineers: Reston, VA, 2017. <https://doi.org/10.1061/9780784414859>.
18. Arakawa, T.; Arai, Y.; Mizoguchi, M.; Yoshida, M. Shear Resisting Behavior of Short Reinforced Concrete Columns Under Biaxial Bending-Shear. Transactions of the Japan Concrete Institute, 1989.
19. ASCE Task Committee on Finite Element Analysis of Reinforced Concrete Structures. State-of-the-Art Report on Finite Element Analysis of Reinforced Concrete; ASCE Special Publications UCB/SEMM-90/14; 1982.
20. ASCE/SEI 41. Seismic Rehabilitation of Existing Buildings, American Society of Civil Engineers. American Society of Civil Engineers, Reston, VA 2007.
21. ASCE/SEI 41-13. Seismic Evaluation and Retrofit of 5 Existing Buildings. ASCE (American Society of Civil Engineers), Reston, VA. 2014.
22. Aschheim, M.; Moehle, J. P. Shear Strength and Deformability of RC Bridge Columns Subjected to Inelastic Cyclic Displacements. California Department of Transportation March 1992.
23. ASTM C 496. Standard Test Method for Splitting Tensile Strength of Cylindrical Concrete Specimens; American Society for Testing Materials: 100 Barr Harbor Dr., West Conshohocken, PA 19428, USA, 2004.
24. ASTM C 882. Standard Test Method for Bond Strength of Epoxy-Resin Systems Used with Concrete by Slant Shear; American Society for Testing Materials: Barr Harbor Dr., West Conshohocken, PA 19428, 1999.

25. ASTM C39 / C39M-21, Standard Test Method for Compressive Strength of Cylindrical Concrete Specimens, ASTM International, West Conshohocken, PA, 2021, www.astm.org
26. ASTM C496 / C496M-17, Standard Test Method for Splitting Tensile Strength of Cylindrical Concrete Specimens, ASTM International, West Conshohocken, PA, 2017, www.astm.org
27. ASTM C618-19, Standard Specification for Coal Fly Ash and Raw or Calcined Natural Pozzolan for Use in Concrete, ASTM International, West Conshohocken, PA, 2019, www.astm.org
28. ASTM C882/C882M-12. C882/C882M-12 Standard Test Method for Bond Strength of Epoxy-Resin Systems Used with Concrete by Slant Shear; 2013.
29. ASTM. C94/C94M-04-Standard Specification for Ready-Mixed Concrete. 04. 02. https://doi.org/DOI:10.1520/C0094_C0094M-04.
30. ASTM. Standard Test Method for Measuring Pavement Macrottexture Depth Using a Volumetric Technique; E965-96, West Conshohocken, PA, 2006.
31. ASTM-C4541. Standard Test Method for Pull-off Strength of Coatings Using Portable Adhesion Testers. West Conshohocken (; American Society for Testing and Materials, 1992; pp 19428–2959.
32. Austin, S.; Robins, P.; Pan, Y. Shear Bond Testing of Concrete Repairs. *Cement and Concrete Research* 1999, 29 (7), 1067–1076. [https://doi.org/10.1016/S0008-8846\(99\)00088-5](https://doi.org/10.1016/S0008-8846(99)00088-5).
33. Azadi, K.; Mohammad, R.; Allahvirdizadeh, R. Enhanced Empirical Models for Predicting the Drift Capacity of Less Ductile RC Columns with Flexural, Shear, or Axial Failure Modes. *Front. Struct. Civ. Eng.* 2019, 13 (5), 1251–1270. <https://doi.org/10.1007/s11709-019-0554-2>.
34. Bae, S.; Bayrak, O. Plastic Hinge Length of Reinforced Concrete Columns. *ACI Structural Journal* 2008, 105 (3), 291–300.
35. Bakas, N.; Makridakis, S.; Papadrakakis, M. Torsional Parameters Importance in the Structural Response of Multiscale Asymmetric-Plan Buildings. *Coupled systems mechanics* 2017, 6 (1), 55–74. <https://doi.org/10.12989/CSM.2017.6.1.055>.
36. Banthia, N.; Zanotti, C.; Sappakittipakorn, M. Sustainable Fiber Reinforced Concrete for Repair Applications. *Construction and Building Materials* 2014, 67, 405–412. <https://doi.org/10.1016/j.conbuildmat.2013.12.073>

37. Barzegar, F.; Schnobrich, W.C. Nonlinear Finite Element Analysis of Reinforced Concrete under Short Term Monotonic Loading; Civil Engineering Studies; SRS No. 530; Univ. of Illinois at Urbana: Illinois, 1986.
38. Bashur, F.K.; Darwin, D. Nonlinear Model for Reinforced Concrete Slabs. *Journal of Structural Division, ASCE* **1978**, *104* (ST1), 157–170.
39. Bentz, E. C.; Collins, P. C. ACI Shear Provisions Based on the Fib Model Code 2010, 2014.
40. Bentz, E.; Collins, M. P., Response 2000 User's Manual, Version 1. 1., September 2001
41. Berard, A. Artificial Stone. 157 903.
42. Bergmann, R., P., V. A. Finite Element for R/C Shear Walls Under Cyclic Loads; UCB/SEMM-88/09; University of California, Berkeley, 1988.
43. Berry, M.; Parrish, M.; Eberhard, M. PEER Structural Performance Database User's Manual (Version 1. 0). 2004, 44.
44. Beton-Kalender 1970. Taschenbuch für Beton- und Stahlbetonbau, sowie die verwandten Facher, W. Ernst & Sohn, Berlin-München.
45. Bezanson, J.; Edelman, A.; Karpinski. S., S., V. B. Julia: A Fresh Approach to Numerical Computing. 59 (1), 65–98. <https://doi.org/10.1137/141000671>.
46. Biskinis D.; Fardis, M. N.; Flexure-Controlled Ultimate Deformations of Members with Continuous or Lap-Spliced Bars. ICE Publishing 11 (Structural Concrete). <https://doi.org/10.1680/stco.2010.11.2.93>.
47. Biskinis D.; Roupakias G. K.; Fardis M. N. Degradation of Shear Strength of RC Members with Inelastic Cyclic Displacements. ACI Structural Journal 2004, 101 (6), 773–783.
48. Blaber, J., 2021. DIC Algorithms. Ncorr. com. http://www.ncorr.com/index.php/dic-algorithms#1_1
49. Bowman, S. A. Regional Seismic Interpretation of the Hydrocarbon Prospectivity of Offshore Syria. GeoArabia 2011, 16 (3), 95–124. <https://doi.org/10.2113/geoarabia160395>.
50. Bresler, B.; Pister, K. S. Strength of Concrete under Combined Stresses. ACI Journal 1985, 551 (9), 321–345.
51. Burgueño, R.; Babazadeh, A.; Fedak, L. K.; Silva, P. F. Second-Order Effects on Seismic Response of Slender Bridge Columns. ACI Structural Journal 2016, 113 (4). <https://doi.org/10.14359/51688751>.

52. Canadian Highway Bridge Design Code 2019, 12th ed.; CSA Group: Toronto, ON, Canada, 2019; p. 1185.
53. Canadian Highway Bridge Design Code 2019, 12th ed; CSA Group: (15) Toronto, ON. Canada, 2019; p. 1185
54. Canadian Standards Association. Supplementary Cementing Materials and Their Use in Concrete Construction; CSA, Rexdale, ON, 1982; Vol. CAN-A23. 5-M82.
55. Carneiro, F. L. L. B., B., A. Concrete Tensile Strength, Bulletin No. 13; International Association of Testing and Research Laboratories for Materials and Structures: Paris, 1953; pp 97–123.
56. Carol, I.; Prat, P. C.; López, C. M. Normal/Shear Cracking Model: Application to Discrete Crack Analysis. *Journal of Engineering Mechanics* 1997, 123 (8), 765–773. [https://doi.org/10.1061/\(ASCE\)0733-9399\(1997\)123:8\(765\)](https://doi.org/10.1061/(ASCE)0733-9399(1997)123:8(765)).
57. CEN (2004) European Standard EN 1998-1-4, 1996: Eurocode 8: Design of Structures for Earthquake Resistance-Part 3: Assessment and Retrofitting of Buildings. European Committee for Standardization. Brussels, Belgium, 2005
58. CEN (2004a) European Standard EN 1998-1. Eurocode 8: Design of Structures for Earthquake Resistance, Part 1: General rules, Seismic Actions and Rules for Buildings. Committee for Standardization, Design, European Committee for Standardization, Brussels, Belgium
59. CEN (2004b) European Standard EN 1992-1-1. Eurocode 2: Design of Concrete Structures, Part1-1: General Rules and Rules for Buildings, Committee for Standardization. Brussels, Belgium.
60. Cervenka, V. Inelastic Finite Element Analysis of Reinforced Concrete Panels. Ph.D. Dissertation, University of Colorado, Boulder, 1970.
61. Cervenka, V.; Eligehausen, R.; Pukl, R. "SBETA-Computer Program for Nonlinear Finite Element Analysis of Reinforced Concrete Structures; Report 90/1; Institute of Building Materials, University of Stuttgart, 1990.
62. Chai, Y. H.; Priestley, M. J. N.; Seible, F. Analytical Model for Steel-Jacketed RC Circular Bridge Columns. *J. Struct. Eng.* 1994, 120, 2358–2376.
63. Chang J. B. M. G. A. Chang-Fatigue-Damage-Part1-with-Cover-Page-v2. Pdf. National Center for Earthquake Engineering Research - State University of New York at Buffalo March 14, 1994.
64. Chasioti, S.; Megalooikonomou, K.; Pantazopoulou, S. Shear Strength Assesment Of Reinforced Concrete Columns. In *Proceedings of the 4th International*

- Conference on Computational Methods in Structural Dynamics and Earthquake Engineering (COMPDYN 2013); Greece: Kos Island, Greece, 2014; pp 927–940. <https://doi.org/10.7712/120113.4567.C1506>.
65. Chou, C. -C.; Wu, S. -C. Cyclic Lateral Load Test and Finite Element Analysis of High-Strength Concrete-Filled Steel Box Columns under High Axial Compression. *Engineering Structures* 2019, 189, 89–99. <https://doi.org/10.1016/j.engstruct.2019.03.052>.
 66. Clímaco, J. C. T. S.; Regan, P. E. Evaluation of Bond Strength between Old and New Concrete in Structural Repairs. *Thomas Telford, Magazine of Concrete Research* 2001, Vol. 53 (No. 6), 377–390. <https://doi.org/0.1680/mac.53.6.377.40800>.
 67. Comité Euro-International Du Béton, CEB-FIB-Model Code 1990: Design Code.; Thomas Telford: London, 1993.
 68. CYS EN 196-1:2016, Methods of testing cement-Part 1: Determination of strength, European Committee for Standardization, April 2016
 69. CYS EN 450 1:2012, Fly Ash for Concrete, Part 1: Definition, specifications and conformity criteria, European Committee for Standardization, August 2012
 70. CYS EN 934-2:2009 + A1:2012, Admixtures for concrete mortar and grout, Part 2 Concrete Admixtures-Definitions, requirements, conformity, marking and labelling, European Committee for Standardization, June 2012
 71. D. E. Lehman; A. C. Lynn; M. A. Aschheim; J. P. Moehle. *Evaluation Methods for Reinforced Concrete Columns And Connections*; Elsevier Science Ltd: Acapulco, Mexico, 1996.
 72. Davis R. E.; Carlson R. W.; Kelly J. W.; H. E. Davis. Properties of Cements and Concretes Containing Fly Ash. *J. Am. Concr.* 1937, 33, 577–612.
 73. Deng, M.; Zhang, Y.; Li, Q. Shear Strengthening of RC Short Columns with ECC Jacket: Cyclic Behavior Tests. *Engineering Structures* 2018, 160, 535–545. <https://doi.org/10.1016/j.engstruct.2018.01.061>.
 74. Design Team for the Composition of Greek Regulations for Assessment, Retrofit and Strengthening of Existing Reinforced Concrete Structures, Harmonization of KA. NE. IIE. with Eurocodes, Athens, 2017
 75. DIN 1045:1972-01, Reinforced Concrete Structures; Design and Construction; 1972.

76. Eder, M.A; El Ghazouli, A.Y.; Abdel-Fattah, T.; Vollum, R.L. Modelling and Experimental Assessment of Punching Shear in Flat Slabs with Shearheads. *Eng. Structures* 2010, 32 (12), 3911–3924.
77. Elwood, K. J.; Matamoros, A. B.; Wallace, J. W.; Lehman, D. E.; Heintz, J. A.; Mitchell, A. D.; Moore, M. A.; Valley, M. T.; Lowes, L. N.; Comartin, C. D.; Moehle, J. P. Update to ASCE/SEI 41 Concrete Provisions. *Earthquake Spectra* 2007, 23 (3), 493–523. <https://doi.org/10.1193/1.2757714>.
78. Elwood, K. J.; Moehle, J. P. Axial Capacity Model for Shear-Damaged Columns. *ACI Structural Journal* 2005, 10.
79. Elwood, K. J.; Moehle, J. P. Axial Capacity Model for Shear-Damaged Columns. *ACI Structural Journal* 2005, 10.
80. Elwood, K. Shaking Table Tests and Analytical Studies on the Gravity Load Collapse of Reinforced Concrete Frames. Ph. D. Dissertation, University of California, Berkeley, 2003.
81. EN 12390-6. Testing Hardened Concrete. Part 6: Tensile Splitting Strength of Test Specimens; Portuguese Institute for Quality, 2004; p 14.
82. EN 12615. Determination of Slant Shear Strength. In *Products and systems for the protection and repair of concrete structures. Test methods.* ; European Committee for Standardization, 1999.
83. Espeche, A. D.; León, J. Estimation of Bond Strength Envelopes for Old-to-New Concrete Interfaces Based on a Cylinder Splitting Test. *Construction and Building Materials* 2011, 25 (3), 1222–1235. <https://doi.org/10.1016/j.conbuildmat.2010.09.032>.
84. European Committee for Standardization. CYS EN 1504-3:2005: *Products and Systems for the Protection and Repair of Concrete Structures-Definitions, Requirements, Quality Control and Evaluation of Conformity-Part 3: Structural and Non-Structural Repair.* December 2005.
85. European Committee for Standardization. EN 1504-6:2006-*Products and Systems for the Protection and Repair of Concrete Structures - Definitions, Requirements, Quality Control and Evaluation of Conformity - Part 6: Anchoring of Reinforcing Steel Bar.* July 2006.
86. European Committee for Standardization. CYS EN 197-1:2011 - *Cement - Part 1: Composition, Specifications and Conformity Criteria for Common Cements;* 2011.

87. Evan C. B.; Frank J. V.; Michael P. C. Simplified Modified Compression Field Theory for Calculating Shear Strength of Reinforced Concrete Elements. *SJ* 2006, 103 (4). <https://doi.org/10.14359/16438>.
88. F. Raba Jr, S. L. S.; M. Mearing. Subbituminous Fly Ash Utilization in Concrete, in *Proceedings of Symposium on Fly Ash Incorporation in Hydrated Cement Systems*; Materials Research Society, 1981; pp 296–306.
89. Fardis, M. N. *Seismic Design, Assessment and Retrofitting of Concrete Buildings; Geotechnical, Geological, and Earthquake Engineering*; Springer Netherlands: Dordrecht, 2009; Vol. 8. <https://doi.org/10.1007/978-1-4020-9842-0>.
90. Fardis, M. N. *Seismic Design, Assessment and Retrofitting of Concrete Buildings; Geotechnical, Geological, and Earthquake Engineering*; Springer Netherlands: Dordrecht, 2009; Vol. 8. <https://doi.org/10.1007/978-1-4020-9842-0>.
91. FEMA 461. *Interim Testing Protocols for Determining the Seismic Performance Characteristics of Structural and Non-structural Components*. June 2007.
92. *Fib Model Code for Concrete Structures 2010*, International Federation for Structural Concrete (Fib), Federal Institute of Technology Lausanne-EPFL, 2013.
93. *Fibre Reinforced Concrete: Improvements and Innovations: RILEM-Fib International Symposium on FRC (BEFIB) in 2020*; Serna, P. , Llano-Torre, A. , Martí-Vargas, J. R. , Navarro-Gregori, J. , Eds. ; RILEM Bookseries; Springer International Publishing: Cham, 2021; Vol. 30. <https://doi.org/10.1007/978-3-030-58482-5>.
94. Fiebrich, M. H. *Influence of the Surface Roughness on the Adhesion between Concrete and Guniting Mortars Overlays*; Unterengstringen, Switzerland, 1994; pp 107–114.
95. Frank J. V; Michael P. Collins. The Modified Compression-Field Theory for Reinforced Concrete Elements Subjected to Shear. *ACI Structural Journal* 1986, 219–231.
96. Frosch, R. J. *Unified Design of Concrete Shear Strength*. 18.
97. Funari, M. F.; Spadea, S.; Fabbrocino, F.; Luciano, R. A. Moving Interface Finite Element Formulation to Predict Dynamic Edge Debonding in FRP-Strengthened Concrete Beams in Service Conditions. *Fibers* **2020**, *8*, 42.
98. Funari, M. F.; Verre, S. The Effectiveness of the DIC as a Measurement System in SRG Shear Strengthened Reinforced Concrete Beams. *Crystals* 2021, *11*, 265.

99. Garbacz, A.; Górka, M.; Courard, L. Effect of Concrete Surface Treatment on Adhesion in Repair Systems. *Magazine of Concrete Research* 2005, 57 (1), 49–60. <https://doi.org/10.1680/mac.2005.57.1.49>.
100. Genikomsou, A. Nonlinear Finite Element Analysis of Punching Shear of Reinforced Concrete Slab-Column Connections. Ph.D. Dissertation, University of Waterloo, 2015. <https://doi.org/10.12681/eadd/50321>.
101. Genikomsou, A. S.; Polak, M. A. Finite Element Analysis of Punching Shear of Concrete Slabs Using Damaged Plasticity Model in ABAQUS. *Engineering Structures* 2015, 98, 38–48. <https://doi.org/10.1016/j.engstruct.2015.04.016>.
102. Georgiou, A. Characterization of the Structural Performance of Strain-Hardening Fiber Cementitious Composites. Ph. D. Thesis, University of Cyprus, Nicosia, Cyprus, May 2017.
103. Georgiou, A.; Najmeh, E; Pantazopoulou, S. J., “Experimental Calibration of a Failure Criterion for Strain Hardening Cementitious Composites”. *Construction and Building Materials*, August 2021
104. Georgiou, A.; Pantazopoulou, S. J. Performance of Ductile FRCC under Cyclic Loads and Non-Linear FE Simulation. In *Proceedings of the FRC2018: Fibre Reinforced Concrete: from Design to Structural Applications Joint ACI-fib-RILEM International Workshop*, Desenzano, Italy, 27–30 June 2018; pp. 310–320.
105. Georgiou, A.; Pantazopoulou, S. Performance of SHFRCC-RC Concrete Members Under Cyclic Displacement Reversals. In *Earthquake Engineering Thessaloniki*; Thessaloniki, 2018; p 12.
106. Ghannoum, W. M. Experimental and Analytical Dynamic Collapse Study of a Reinforced Concrete Frame with Light Transverse Reinforcement. Ph. D. Dissertation, University of California, Berkeley, 2007.
107. Ghannoum, W. M; Matamoros, A. B. Nonlinear Modeling Parameters and Acceptance Criteria for Concrete Columns. In *SP-297: Seismic Assessment of Existing Reinforced Concrete Buildings*; American Concrete Institute, 2014. <https://doi.org/10.14359/51686898>.
108. Gomes A. M.; Appleton J. *Repair and Strengthening of Reinforced Concrete Elements under Cyclic Loading*. ; Paris, France, 1998.

109. Grammatikou, S.; Biskinis, D. B.; Fardis, M. N.;. Flexural Rotation Capacity Models Fitted to Test Results Using Different Statistical Approaches. International Federation for Structural Concre. <https://doi.org/10.1002/suco.201600238>.
110. Guan, H., Polak, M. A. Finite Element Studies of Reinforced Concrete Slab-Edge Column Connections with Opening. Canadian J. of Civil Engineering 34 (8), 952–965.
111. Guide to Materials Selection for Concrete Repair (ACI 546. 3R-14); American Concrete Institute, Ed.; ACI Committee 546; American Concrete Institute: Farmington Hills, Mich, 2014.
112. Hallgren M. Punching Shear Capacity of Reinforced High Strength Concrete Slabs. Ph.D. Dissertation, Bulletin No. 23, Department of Structural Engineering, Royal Institute of Technology, Stockholm, 1996.
113. Haroun, M. A.; Elsanadedy, H. M. Fiber-Reinforced Plastic Jackets for Ductility Enhancement of Reinforced Concrete Bridge Columns with Poor Lap-Splice Detailing. J. Bridge Eng. 2005, 10 (6), 749–757. [https://doi.org/10.1061/\(ASCE\)1084-0702\(2005\)10:6\(749\)](https://doi.org/10.1061/(ASCE)1084-0702(2005)10:6(749)).
114. Helal, Y.; Garcia, R.; Pilakoutas, K.; Guadagnini, M.; Hajirasouliha, I. Strengthening of Short Splices in RC Beams Using Post-Tensioned Metal Straps. Mater Struct 2016, 49 (1–2), 133–147. <https://doi.org/10.1617/s11527-014-0481-6>.
115. Hellenic Standards of Reinforced Concrete 2000. Hellenic Association of Seismic Design and Protection and Hellenic Association of Civil Engineers October 2000.
116. Hemmati, A., Kheyroddin, A.; Sharbatdar, M., Purk, Y.; Abolmali, A. Ductile Behavior of High-Performance Fiber Reinforced Cementitious Composite (HPFRCC) Frames, Construction and Building Materials 2016, 115, 681–689.
117. Henkhaus, K.; Pujol, S.; Ramirez, J. Axial Failure of Reinforced Concrete Columns Damaged by Shear Reversals. J. Struct. Eng. 2013, 139 (7), 1172–1180. [https://doi.org/10.1061/\(ASCE\)ST.1943-541X.0000673](https://doi.org/10.1061/(ASCE)ST.1943-541X.0000673).
118. Heyman J. Coulomb's Memoir on Statics. Cambridge University Press, London (1972).
119. Hindo K. R. In-Place Bond Testing and Surface Preparation of Concrete. Concr. Int. 1990, 12:46.

120. Hognestad, E. Study of Combined Bending and Axial Load in Reinforced Concrete Members; Technical Report of an Investigation; University of Illinois at Urbana Champaign Bulletin: Champaign, IL, USA, 1951.
121. Homrich, J. R.; Naaman, A. E. Stress-Strain Properties of SIFCON in Compression. Fibre Reinforced Concrete: Properties and Applications, American Concrete Institute 1987, SP-105, 283–304.
122. Hong, S. -G.; Lee, J. -H.; Choi, Y.; Gu, I. -Y. Seismic Strengthening of Concrete Columns by Ultrahigh-Performance Fiber-Reinforced Concrete Jacketing. *J. Struct. Eng.* 2021, 147 (10), 04021157. [https://doi.org/10.1061/\(ASCE\)ST.1943-541X.0003111](https://doi.org/10.1061/(ASCE)ST.1943-541X.0003111).
123. Huang S.; Guo X.; Zhang M. Study of Design Method and Similitude for Small-scale Reinforced Concrete Structural Models. *China Civil Eng. J* 45 (7), 32-8(in Chinese).
124. Hussein, H. H.; Walsh, K. K.; Sargant, S. M.; Steinberg, E. P. Interfacial Properties of Ultrahigh-Performance Concrete and High-Strength Concrete Bridge Connections. *J. Mater. Civ. Eng.* 2016, 28 (5), 04015208. [https://doi.org/10.1061/\(ASCE\)MT.1943-5533.0001456](https://doi.org/10.1061/(ASCE)MT.1943-5533.0001456).
125. Imai; Hiroshi; Yamamoto; Yoshie. A Study on Causes of Earthquake Damage of Izumi High School Due to Miyagi-Ken-Oki Earthquake in 1978. Transactions of the Japan Concrete Institute 1986.
126. Inel, M., A., M. A.; Pantazopoulou, S. J. Seismic Deformation Capacity Indices for Concrete Columns: Model Estimates and Experimental Results. *Magazine of Concrete Research.* <https://doi.org/10.1680/macr.2007.59.4.297>.
127. Ioannou, A. I.; Pantazopoulou, S. J.; Petrou, M. F.; Charmpis, D. C. Experimental Investigation of ECC Jackets for Repair of Pre-Damaged R. C. Members under Monotonic Loading. *Buildings* 2021, 11 (5), 180. <https://doi.org/10.3390/buildings11050180>.
128. Ioannou, A.; Pantazopoulou, S. J., G., S.; Illampas, R. Limit States Behaviour (or Failure) of Reinforced Concrete Columns; Hellenic Concrete Conference, 2018.
129. ISO 4287:1997 Geometrical Product Specifications (GPS) — Surface texture: Profile method — Terms, definitions and surface texture parameters
130. ISO BS. Geometrical Product Specifications (GPS) – Surface Texture: Profile Method – Terms, Definitions and Surface Texture Parameters. ; 1997.

131. James K. Wight; Mete A. Sozen. Shear Strength Decay in Reinforced Concrete Columns Subjected to Large Deflections Reversals. The National Science Foundation, University of Illinois, Urbana, Illinois August 1973.
132. James M. Wight; James G. Macgregor. Reinforced Concrete Mechanics and Design, 6th ed.; Pearson.
133. Jensen, B. C. Nogle Plasticitetsteoretiske Beregninger Af Beton Og Jernbeton,. PhD thesis, Technical University of Denmark, Copenhagen, Denmark, 1976.
134. Jinlong, P., Jie, G.; Junhun, C. Theoretical Modeling of Steel Reinforced ECC Column under Compressive Loading, *Science China Technological Sciences* 2015, 58, 889–898.
135. Júlio, E. N. B. S.; Branco, F. A. B.; Silva, V. D. Concrete-to-Concrete Bond Strength. Influence of the Roughness of the Substrate Surface. *Construction and Building Materials* 2004, 18 (9), 675–681. <https://doi.org/10.1016/j.conbuildmat.2004.04.023>.
136. Júlio, E.S.; Branco, F.; Silva, V. D. Structural Rehabilitation of Columns with Reinforced Concrete Jacketing: Column Rehabilitation with RC Jacketing. *Prog. Struct. Engng Mater.* 2003, 5 (1), 29–37. <https://doi.org/10.1002/pse.140>.
137. Kanda, T.; Li, V. C. Interface Property and Apparent Strength of High-Strength Hydrophilic Fiber in Cement Matrix. *Journal of Materials in Civil Engineering* 1998, 10 (1), 5–13. [https://doi.org/10.1061/\(ASCE\)0899-1561\(1998\)10:1\(5\)](https://doi.org/10.1061/(ASCE)0899-1561(1998)10:1(5)).
138. Kawashima, K. Damage of Bridges Due to the 2011 Great East Japan Earthquake. 20.
139. Kawashima, K.; Takahashi, Y.; Ge, H.; Wu, Z. ; Zhang, J. Reconnaissance Report on Damage of Bridges in 2008 Wenchuan, China, Earthquake. *Journal of Earthquake Engineering* 2009, 13 (7), 965–996. <https://doi.org/10.1080/13632460902859169>.
140. Keuser, M., M., G. Finite Element Models for Bond Problems. *Journal of Structural Engineering*, ASCE 113 (10), 2160–2173.
141. Kim, C. -G.; Park, H. -G.; Eom, T. -S. Cyclic Load Test and Shear Strength Degradation Model for Columns with Limited Ductility Tie Details. *J. Struct. Eng.* 2019, 145 (2), 04018249. [https://doi.org/10.1061/\(ASCE\)ST.1943-541X.0002254](https://doi.org/10.1061/(ASCE)ST.1943-541X.0002254).
142. Kim, C. G.; Park, H. G.; Eom, T. S. Cyclic Load Test and Shear Strength Degradation Model for Columns with Limited Ductility Tie Details. *J. Struct. Eng.*

- 2019, 145 (2), 04018249. [https://doi.org/10.1061/\(ASCE\)ST.1943-541X.0002254](https://doi.org/10.1061/(ASCE)ST.1943-541X.0002254).
143. Kriegh, J. D. Arizona Slant Shear Test: A Method to Determine Epoxy Bond Strength. *Journal of the American Concrete Institute* 1976, 73 (3), 372–373.
144. Kuo, W. W. Study on the Collapse Behavior of Nonductile Reinforced Concrete Frames Subjected to Earthquake Loading. Ph. D. Dissertation, Department of Construction Engineering, National Taiwan University of Science and Technology, Taipei, Taiwan, 2008.
145. Kwak, H. G.; Filippou, F.C. Finite Element of Reinforced Concrete Structures Under Monotonic Loading; UCB/SEMM-90/14; Structural Engineering, Mechanics and Materials Department of Civil Engineering University of California, Berkeley, 1990.
146. Labuz, J. F.; Zang, A. Mohr–Coulomb Failure Criterion. *Rock Mech Rock Eng* 2012, 45 (6), 975–979. <https://doi.org/10.1007/s00603-012-0281-7>.
147. Lankard, D. R.; Newell, J. K. Preparation of Highly Reinforced Steel Fibre Reinforced Concrete Composites; American Concrete Institute: Detroit, 1984; Vol. SP-81, p 277–306.
148. Lee, J.; Fenves, G. L. Plastic-Damage Model for Cyclic Loading of Concrete Structures. *Journal of Engineering Mechanics* 1998, 124 (8), 892–900. [https://doi.org/10.1061/\(ASCE\)0733-9399\(1998\)124:8\(892\)](https://doi.org/10.1061/(ASCE)0733-9399(1998)124:8(892)).
149. Lee, M. -G.; Wang, Y. -C.; Chiu, C. -T. A Preliminary Study of Reactive Powder Concrete as a New Repair Material. *Construction and Building Materials* 2007, 21 (1), 182–189. <https://doi.org/10.1016/j.conbuildmat.2005.06.024>.
150. Leung, C. K. Y.; Cao, Q. Development of Pseudo-Ductile Permanent Formwork for Durable Concrete Structures. *Mater Struct* 2010, 43 (7), 993–1007. <https://doi.org/10.1617/s11527-009-9561-4.1>
151. Li, M. Engineered Cementitious Composites for Bridge Decks. In *Advanced Composites in Bridge Construction and Repair*; Elsevier, 2014; pp 177–209. <https://doi.org/10.1533/9780857097019.2.177>.
152. Li, V. C. On Engineered Cementitious Composites (ECC). 2003, 1 (3), 16.
153. Li, V. C.; Wu, H. C. Conditions for Pseudo Strain Hardening in Fibre Reinforced Brittle Matrix Composites. *Journal of Applied Mechanics Review* 1992, 45 (8), 390–398.

154. Li, X.; Chen, K.; Hu, P.; He, W.; Xiao, L. ; Zhang, R. Effect of ECC Jackets for Enhancing the Lateral Cyclic Behavior of RC Bridge Columns. *Engineering Structures* 2020, 219, 110714. <https://doi.org/10.1016/j.engstruct.2020.110714>.
155. Li, Y.; Elwood, K. J. Assessment of ASCE/SEI 41 Concrete Column Provisions Using Shaking Table Tests. 23.
156. Li, Y. The Shaking Table Tests Column Database and Evaluation of Drift Capacity Models for Non-Ductile Columns. **2012**, 227.
157. Lin, C.S.; Scordelis, A.C. Nonlinear Analysis of RC Shells of General Form. *Journal of Structural Division, ASCE* 101 (ST3), 523–538.
158. Lubliner, J.; Oliver, J.; Oller, S.; Oñate, E. A Plastic-Damage Model for Concrete. *International Journal of Solids and Structures* 1989, 25 (3), 299–326. [https://doi.org/10.1016/0020-7683\(89\)90050-4](https://doi.org/10.1016/0020-7683(89)90050-4).
159. Lynn, A. C.; Moehle, J.; Mahin, S.; Holmes, W. Seismic Evaluation of Existing Reinforced Concrete Building Columns. *Earthquake Spectra* 1996, 12, 715–739. <https://doi.org/10.1193/1.1585907>.
160. Maalej, M.; Li, V. C. Introduction of Strain-Hardening Engineered Cementitious Composites in Design of Reinforced Concrete Flexural Members for Improved Durability. *ACI Struct. J* 1995, 92 (2), 167–176.
161. Mander, J. B.; Priestley, M. J. N.; Park, R. Theoretical Stress-Strain Model for Confined Concrete. *J. Struct. Eng.* 1988, 114 (8), 1804–1826. [https://doi.org/10.1061/\(ASCE\)0733-9445\(1988\)114:8\(1804\)](https://doi.org/10.1061/(ASCE)0733-9445(1988)114:8(1804)).
162. Martínez, J. Á. L. Characterization of the Tensile Behaviour of UHPFRC By Means of Four-Point Bending Tests. Ph. D. Thesis, Polytechnical School of Valencia, Valencia, Spain, March 2017.
163. Martín-Pérez, B.; Pantazopoulou, S. J. Mechanics of Concrete Participation in Cyclic Shear Resistance of RC. *J. Struct. Eng.* 1998, 126 (4), 633–641.
164. Martirosyan, A.; Xiao, Y. Flexural-Shear Behavior of High-Strength Concrete Short Columns. *Earthquake Spectra* 2001, 17 (4), 679–695. <https://doi.org/10.1193/1.1423656>.
165. Massicotte, B.; Boucher-Proulx, G. Seismic Retrofitting of Bridge Piers with UHPFRC Jackets. *Des. Build. UHPFRC* 2009, 531–540, doi:10.1002/9781118557839.ch35.
166. Matchulat, L.; Adolfo Matamoros. Mitigation of Collapse Risk in Vulnerable Concrete Buildings. Master of Science, University of Kansas 2008.

167. Mavros, M. Experimental and Numerical Investigation of the Seismic Performance of Reinforced Masonry Structures. Ph.D. Dissertation, University of California, San Diego, California, U.S.A., 2015.
168. Megalooikonomou, K. G.; Tastani, S. P.; Pantazopoulou, S. J. Effect of Yield Penetration on Column Plastic Hinge Length. Elsevier Ltd 2018, 156, 161–174. <https://doi.org/10.1016/j.engstruct.2017.11.003>.
169. Menétrey. Numerical Analysis of Punching Failure In Reinforced Concrete Structures. Master of Science, University of Colorado, Boulder.
170. Meyer, C; Okamura, H. Finite Element Analysis of Reinforced Concrete Structures. In Proceedings of the US-Japan Joint Seminar on Finite Element Analysis of Reinforced Concrete; Tokyo, Japan., 1985.
171. Michael M. Sprinkel, P. E.; Celik Ozyildirim, Ph. D. Evaluation of High-Performance Concrete Overlays Placed On Route 60 over Lynnhaven Inlet in Virginia; Technical; Virginia Transportation Research Council: Virginia United States, 2000.
172. Miguel A. Carbonell Munoz; Devin K. Harris, Ph. D.; A. M. ASCE; Theresa M. Ahlborn, Ph. D. ; P. E. , M. ASCE; David C. Froster. Bond Performance between Ultrahigh-Performance Concrete and Normal-Strength Concrete. J. Mater. Civ. Eng. 2014, 26 (8), 04014031-1: 04014031-9. [https://doi.org/10.1061/\(ASCE\)MT.1943-5533.0000890](https://doi.org/10.1061/(ASCE)MT.1943-5533.0000890).
173. Miguel, R. Ilgi Moble Building; Concrete Buildings Damaged in Earthquakes; Case Study; EERI, 2013.
174. Ministry of Transport of People’s Republic of China. Guidelines for Seismic Design of Highway Bridges (JTG/TB02-01-2008) [S]; Beijing, 2008.
175. Mircea, A. C.; Toader, T. P. Fracture Energy of Engineered Cementitious Composites. Proceedings 2020, 63, 8. <https://doi.org/10.3390/proceedings2020063008>
176. Moehle, J. P.; Eberhard, M. O. Bridge Engineering Handbook. 2000, 34.
177. Moersch E. Concrete-Steel Construction; McGraw-Hill, New York (English translation by E. P. Goordich), 1909.
178. Momayez; M. R. Ehsani; A. A. Ramezani pour; H. Rajaie. Comparison of Methods for Evaluating Bond Strength between Concrete Substrate and Repair Materials. Cement and Concrete Research 2004, 35, 748–757. <https://doi.org/10.1016/j.cemconres.2004.05.027>.

179. Mu B, Meyer C, Shimanovich S. Improving the interface bond between fiber mesh and cementitious matrix. *Cement Concrete Res* 2002;32(5):783–7.
180. Murphy, K. P. *Machine Learning: A Probabilistic Perspective*; Adaptive computation and machine learning series MIT Press: Cambridge, MA, 2012
181. Naaman, A. E. *A Statistical Theory of Strength for Fiber Reinforced Concrete*. Ph. D. Thesis, Massachusetts Institute of Technology, 1972.
182. Naaman, A. E. Advances in High Performance Fibre Reinforced Cement Based Composites. In *Proceedings of the International Symposium on Fibre Reinforced Concrete*; V. S. Parameswaran and T. S. Krishnamurti, Editors, Oxford IBH Publishing Ltd.: New Delhi, India, 1987; p 7. 87–7. 98.
183. Naaman, A. E. High Performance Fibre Reinforced Cement Composites. In *Proceedings of the IABSE Symposium on Concrete Structures for the Future*; Paris, France, 1987; p 371–376.
184. Naaman, A. E.; Argon, A.; Moavenzadeh, F. A Fracture Model for Fiber Reinforced Cementitious Materials. *Cement and Concrete Research* 1973, 3 (4), 397–411.
185. Naaman, A. E.; F. Moavenzadeh; F. J. McGarry. Probabilistic Analysis of Fiber Reinforced Concrete. *Journal of the Engineering Mechanics's Division, ASCE* 1974, 100 (EM2), 397–413.
186. Naaman, A. E.; Reinhardt, H. W. Characterization of High-Performance Fibre Reinforced Cement Composites. In *Proceedings of High-Performance Fibre Reinforced Cement Composites: HPFRCC 2, RILEM; E. & FN Spon: London, 1996; Vol. 31, pp 1–31.*
187. Naaman, A. E.; Reinhardt, H. W. High Performance Fibre Reinforced Cement Composites: HPFRCC 2, RILEM; E. & FN Spon: London, 1996; Vol. 31, p 505.
188. Nadai A. *Theory of flow and fracture of solids*. McGraw Hill, New York (1950)
189. Naderi, M. Analysis of the Slant Shear Test. *Journal of Adhesion Science and Technology* 2009, 23 (2), 229–245. <https://doi.org/10.1163/156856108X369589>.
190. Nagasaka, T. Effectiveness of Steel Fiber as Web Reinforcement in Reinforced Concrete Columns. *Transactions of the Japan Concrete Institute* 1982.
191. Naik, T. Personal Communication from Dr. T. Naik; University of Wisconsin: Milwaukee, WI, 1985.
192. Nayak, G.C.; Zienkiewicz, O.C. Elasto-Plastic Stress Analysis. *International Journal of Numerical Methods in Engineering* 5, 152–163.

193. Negele, A., Eligehausen., R.; Eligehausen, Ožbolt, J., Polak, M. A. Finite-Element Simulations on Punching Tests of Shear Retrofitted Slab-Column Connections. In Proc., IA-FraMCoS-6: International Association of Fracture Mechanics for Concrete and Concrete Structures; Catania, Italy, 2007; pp 911–918.
194. Ngo, D.; Scordelis, A.C. Finite Element Analysis of Reinforced Concrete Beams,. Journal of ACI 1967, 64 (3), 152–163.
195. Nilson, A.H. Internal Measurement of Bond Slip. Journal of ACI 1972, 69 (7), 439–441.
196. Ož bolt, J.; Li, Y.-J.; Kozar, I. Microplane Model for Concrete with Relaxed Kinematic Constraint. International Journal of Solids and Structures, in press. 2001..
197. Ohue, M.; Morimoto, H.; Fujii, S.; Morita, S. The Behavior of R. C. Short Columns Failing in Splitting Bond-Shear Under Dynamic Lateral Loading. Transactions of the Japan Concrete Institute 1985.
198. Ono, A.; Shirai, N.; Adachi, H.; Sakamaki, Y. Elasto-Plastic Behavior of Reinforced Concrete Column with Fluctuating Axial Force. 1989.
199. Opabola, E. A.; Elwood, K. J. Seismic Assessment of Reinforced Concrete Columns with Short Lap Splices. Earthquake Spectra 2021, 37 (3), 1726–1757. <https://doi.org/10.1177/8755293021994834>.
200. Oucif, C.; Ouzaa, K.; Mauludin, L. M. Cyclic and Monotonic Behavior of Strengthened and Unstrengthened Square Reinforced Concrete Columns. J. Appl. Comput. Mech. 2017, No. Online First. <https://doi.org/10.22055/jacm.2017.23514.1159>
201. Pantazopoulou, S. J. Role of Expansion on Mechanical Behavior of Concrete. Journal of Structural Engineering 1995, 121 (12), 1795–1805. [https://doi.org/10.1061/\(ASCE\)0733-9445\(1995\)121:12\(1795\)](https://doi.org/10.1061/(ASCE)0733-9445(1995)121:12(1795)).
202. Pantazopoulou, S. J.; Tastani, S. P.; Thermou, G. E.; Triantafillou, T.; Monti, G.; Bournas, D.; Guadagnini, M. Background to the European Seismic Design Provisions for Retrofitting RC Elements Using FRP Materials. Structural Concrete 2016, 17 (2), 194–219. <https://doi.org/10.1002/suco.201500102>.
203. Papavasileiou, G. S.; Charmpis, D. C.; Lagaros, N. D. Optimized Seismic Retrofit of Steel-Concrete Composite Buildings. *Eng. Struct.* **2020**, *213*, 110573.
204. Pardalopoulos, S. J.; Thermou, G. E.; Pantazopoulou S. J. Preliminary Seismic Assessment Method for Identifying R. C. Structural Failures. In Computational

Methods in Earthquake Engineering; Springer Dordrecht Heidelberg New York London, 2013; Vol. 2.

205. Pardalopoulos, S. J.; Thermou, G. E.; Pantazopoulou, S. J. Rapid Preliminary Seismic Assessment Methodology for Non-Conforming Reinforced Concrete Buildings. 2011, 17
206. Park, H. G.; Choi, K. K.; Kim, J. C. Shear Strength Model Based on Compression Zone Failure Mechanism, 2014.
207. Park, R.; Paulay, T. Reinforced Concrete Structures; J. Wiley & Sons: New York, 1975.
208. Park, R.; Priestley, M. N.; Gill, W. D. Ductility of Square-Confined Concrete Columns. J. Struct. Div. 1982,108, 929–950.
209. Parra-Montesinos, G. J.; Chompreda, P. Deformation Capacity and Shear Strength of Fiber-Reinforced Cement Composite Flexural Members Subjected to Displacement Reversals. J. Struct. Eng. 2007, 133 (3), 421–431. [https://doi.org/10.1061/\(ASCE\)0733-9445\(2007\)133:3\(421\)](https://doi.org/10.1061/(ASCE)0733-9445(2007)133:3(421)).
210. Parvin, A.; Wang, W. Behavior of FRP Jacketed Concrete Columns under Eccentric Loading. J. Compos. Constr. 2001, 5, 146–152.
211. Paultre, P.; Calais, É.; Proulx, J.; Prépetit, C. ; Ambroise, S. Damage to Engineered Structures during the 12 January 2010, Haiti (Léogâne) Earthquake. Can. J. Civ. Eng. 2013, 40 (8), 777–790. <https://doi.org/10.1139/cjce-2012-0247>.
212. Penelis, G. G.; Penelis, G. G. Concrete Buildings in Seismic Regions. 856.
213. Petr K.; David N. and Christopher A. Gwyddion user guide, Copyright © 2004–2007, 2009–2019
214. Polak, M. A. Shell Finite Element Analysis of RC Plates Supported on Columns for Punching Shear and Flexure. International J. for Comp.-Aided Eng. and Software 2005, 22 (4), 409–428.
215. Priestley, M. J. N.; Verma, R.; Xiao, Y. Seismic Shear Strength of Reinforced Concrete Columns. Journal of Structural Engineering 1994, 120 (8), 2310–2329. [https://doi.org/10.1061/\(ASCE\)0733-9445\(1994\)120:8\(2310\)](https://doi.org/10.1061/(ASCE)0733-9445(1994)120:8(2310)).
216. Pujol, S. Drift Capacity of Reinforced Concrete Columns Subjected to Displacement Reversals, Purdue University, 2002.
217. Ramadoss, P. and N Nagamani, K. Tensile Strength and Durability Characteristics of High-Performance Fibre Reinforced Concrete. Arabian Journal for Science and Engineering 2008, 33 (2B), 307–319.

218. Ramezaniapour, A. A. Cement Replacement Materials; Springer Geochemistry/Mineralogy; Springer Berlin Heidelberg: Berlin, Heidelberg, 2014. <https://doi.org/10.1007/978-3-642-36721-2>.
219. Randl, N.; Peyerl, M.; and Steiner, M., “Investigations on Adhesive Bond between High Performance Concrete Overlays and NSC Substrates,” Proceedings of fib Symposium 2016: Performance-Based Approaches for Concrete Structures, Cape Town, South Africa, 2016, 11 pp.
220. Raza, S.; Khan, M. K. I.; Menegon, S. J.; Tsang, H. -H. ; Wilson, J. L. Strengthening and Repair of Reinforced Concrete Columns by Jacketing: State-of-the-Art Review. Sustainability 2019, 11, 3208.
221. Reineck, K. H. Shear Design Integrated in The Design Concept of Strut-and-Tie Models for Structural Concrete; Universitas Pelita Harapan, Indonesia, 2007.
222. Richart F.E.; Brandtzaeg A.; Brown R. A Study of the Failure of Concrete under Combined Compressive Stresses. University of Illinois Engineering Experiment Station 1928.
223. Riyad S. Aboutaha, M. D. E.; James O. Jirsa, M. E. K. Rehabilitation of Shear Critical Concrete Columns by Use of Rectangular Steel Jackets. SJ 1999, 96 (1). <https://doi.org/10.14359/597>.
224. Riyad, A.; Fares, J.; Sara, S.; Mucip T. Final Report - Seismic Evaluation and Retrofit of Deteriorated Concrete Bridge Component; Syracuse University, 2013.
225. Rodriguez M; Park R. Repair and Strengthening of Reinforced Concrete Buildings for Seismic Resistance. Earthquake Spectra (EERI) 1991, 7 (3), 439–459.
226. Romualdi, J. P.; Mandel, J. A. Tensile Strength of Concrete Affected by Uniformly Distributed Closely Spaced Short Length of Wire Reinforcement. ACI Structural Journal 1964.
227. Rots, J.G.; Nauta, P.; Kusters, G.M.A.; Blaauwendraad, J. Smearred Crack Approach and Fracture Localization in Concrete. *HERON* 1985, 30 (1), 3–48.
228. S. J. Pantazopoulou; R. H. Mills. Microstructural Aspects of the Mechanical Response of Plain Concrete. Materials Journal, American Concrete Institute (ACI) 1995, Vol. 92 (6), 605–616.
229. Saad; Tom; Maswoswe; Justice; Derrell Manceaux. FHWA Seismic Retrofitting Seminar, 2010.
230. Santos, P. D. M. Assessment of the Shear Strength between Concrete Layers. PhD thesis, University of Coimbra-Department of Civil Engineering, 2009.

231. Scordelis, A.C.; Ngo, D.; Franklin, H.A. Finite Element Study of Reinforced Concrete Beams with Diagonal Tension Cracks. In Proceedings of Symposium on Shear in Reinforced Concrete; ACI Publication SP-42., 1974.
232. Scribner, C. F.; Wight, J. K. Strength Decay in R. C. Beams under Load Reversals. *J. Struct. Div* 1980, 106 (4), 861–876.
233. Sezen H.; Moehle, J. P.; Mosalam K. M. Seismic Behavior and Modeling of Reinforced Concrete Building Columns, University of California, 2002.
234. Sezen, H.; Moehle, J. P.; Mosalam, K. M. Seismic Behavior and Modeling of Reinforced Concrete Building Columns, University of California, 2002.
235. Shang, X.; Yu, J.; Li, L.; Lu, Z. Strengthening of RC Structures by Using Engineered Cementitious Composites: A Review. *Sustainability* 2019, 11 (12), 3384. <https://doi.org/10.3390/su11123384>.
236. Shang, X.; Yu, J.; Li, L.; Lu, Z. Strengthening of RC Structures by Using Engineered Cementitious Composites: A Review. *Sustainability* 2019, 11 (12), 3384. <https://doi.org/10.3390/su11123384>.
237. Shigeyuki, S.; Shirai, N.; Adachi, H.; Ono, A. Deformation of Reinforced Concrete Column with High or Fluctuating Axial Force. *Transactions of the Japan Concrete Institute* 1991.
238. Shin, Y. B. Dynamic Response of Ductile and Non-Ductile Reinforced Concrete Columns, University of California, Berkeley, 2007.
239. Sokoli, D.; Ghannoum, W. M. High-Strength Reinforcement in Columns under High Shear Stresses. *ACI Structural Journal* 2016, 113 (3). <https://doi.org/10.14359/51688203>.
240. Stoppenhagen DR; Jirsa JO; Wylie Jr. LA. Seismic Repair and Strengthening of a Severely Damaged Concrete Frame. *ACI Structural Journal* 1995, 92 (2), 177–187.
241. Su, R. S. Shake Table Tests on Reinforced Concrete Short Columns Failed in Shear. Master thesis, Department of Construction Engineering, National Taiwan University of Science and Technology, National Taiwan University of Science and Technology, 2007.
242. Syntzirma D. V.; Pantazopoulou S. J. Deformation Capacity of RC Members with Brittle Details Under Cyclic Loads. *ACI Special Publication* 2007, ACI-ASCE Committee 445 (Seismic Shear).

243. Syntzirma, D. V.; Pantazopoulou, S. J.; Aschheim, M. Load-History Effects on Deformation Capacity of Flexural Members Limited by Bar Buckling. *J. Struct. Eng.* 2010, 136 (1), 1–11. [https://doi.org/10.1061/\(ASCE\)ST.1943-541X.0000088](https://doi.org/10.1061/(ASCE)ST.1943-541X.0000088).
244. Szczerbiak, A. I. Declaration of Performance, 2015.
245. Taljaard, V. -L.; Gravett, D. Z.; Mourlas, C.; Markou, G.; Bakas, N.; Papadrakakis, M. Development of a New Fundamental Period Formula by Considering Soil-Structure Interaction with the Use of Machine Learning Algorithms; Athens, Greece, 2021; pp 3801–3809. <https://doi.org/10.7712/120121.8748.18534>.
246. Tasios P. T.; Dritsos S. E.; Kappos E. I.; Fardis M. N.; Chronopoulos M. Greek Standards for Assessment and Retrofit of Existing Structures. Athens February 2017.
247. Tastani, K. G. M.; S. J. Pantazopoulou. Reinforcement to Concrete Bond in Inelastic Regions of RC Frame Members. In *fib Bulletin “Advances on Bond in Concrete”*; The International Federation for Structural Concrete (fib); p 12.
248. Tastani, S. P.; Pantazopoulou, S. J. Direct Tension Pullout Bond Test: Experimental Results. *J. Struct. Eng.* 2010, 136 (6), 731–743. [https://doi.org/10.1061/\(ASCE\)ST.1943-541X.0000159](https://doi.org/10.1061/(ASCE)ST.1943-541X.0000159).
249. Tayeh, B. A.; Abu Bakar, B. H.; Megat Johari, M. A.; Voo, Y. L. Mechanical and Permeability Properties of the Interface between Normal Concrete Substrate and Ultra High-Performance Fiber Concrete Overlay. *Construction and Building Materials* 2012, 36, 538–548. <https://doi.org/10.1016/j.conbuildmat.2012.06.013>.
250. Tayeh, B. A.; Bakar, B. H. A.; Johari, M. A. M.; Ratnam, M. M. The Relationship between Substrate Roughness Parameters and Bond Strength of Ultra-High-Performance Fiber Concrete. *Journal of Adhesion Science and Technology* 2013, 27 (16), 1790–1810. <https://doi.org/10.1080/01694243.2012.761543>.
251. Taylor, R. L. FEAP - Finite Element Analysis Program, 2014.
252. Thaulow, S. Tensile Splitting Test and High Strength Concrete Test Cylinders. American Concrete Institute, *Journal of the American Concrete Institute* 1957, 53 (1), 699–706.
253. Thermou, G. E.; Elnashai, A. S. Seismic Retrofit Schemes for RC Structures and Local-Global Consequences. *Prog. Struct. Engng Mater.* 2006, 8 (1), 1–15.

254. Thermou, G. E.; Pantazopoulou, S. J. Fiber-Reinforced Polymer Retrofitting of Predamaged Substandard RC Prismatic Members. *J. Compos. Constr.* 2009, 13, 535–546.
255. Thermou, G. E.; Pantazopoulou, S. J. Metallic Fabric Jackets: An Innovative Method for Seismic Retrofitting of Substandard RC Prismatic Members. *Struct. Concr.* 2007, 8, 35–46.
256. Thermou, G. E.; Pantazopoulou, S. J.; Elnashai, A. S. Design Methodology for Seismic Upgrading of Substandard Reinforced Concrete Structures. *J. Earthq. Eng.* 2007, 11, 582–606.
257. Thermou, G. E.; Pantazopoulou, S. J.; M. ASCE; Elnashai, A. S.; F. ASCE. Analytical Modeling of Interface Behavior in Reinforced Concrete Jacketed Member; ASCE (American Society of Civil Engineers), Reston, VA., 2004.
258. Thermou, G., and Pantazopoulou, S. J. “Fiber – reinforced polymer retrofitting of substandard RC prismatic members”, *ASCE J. of Composites for Construction*, **13**(6):535-546, (Nov. (2009)).
259. Tjiptobroto, P.; Hansen, W. Model for Prediction of the Elastic Strain of Fibre Reinforced Composites Containing High Volume Fractions of Discontinuous Fibres. *ACI Materials Journal* 1983, 90 (2).
260. Tsonos, A. G. Effectiveness of CFRP-Jackets and RC-Jackets in Post-Earthquake and Pre-Earthquake Retrofitting of Beam–Column Subassemblages. *Engineering Structures* 2008, 30 (3), 777–793. <https://doi.org/10.1016/j.engstruct.2007.05.008>
261. Tureyen, A. K. and Robert, J. F. Concrete Shear Strength: Another Perspective. *ACI Structural Journal* 2003, 100 (5). <https://doi.org/10.14359/12802>.
262. Umehara, H.; Jirsa, J. O.; ASCE, M. Short Rectangular RC Columns Under Bidirectional Loadings. *Journal of Structural Engineering* 110(3), 605–618.
263. UNIDO. Building Construction Under Seismic Conditions in the Balkan Region. Post-Earthquake Damage Evaluation and Strength Assessment of Buildings under Seismic Conditions., Project REP/79/015. ; United Nations Industrial Developing Organization, UNDP/ UNIDO: Vienna, Austria, 1983; Vol. 4.
264. Vandoros, K. G.; Dritsos, S. E. Concrete jacket construction detail effectiveness when strengthening RC columns. *Constr. Build. Mater.* 2008, 22, 264–276.

265. Wang, W.; Liub, J.; Agostini, F., Davy., C. A.; Skoczylas, F.; Corvez, D. Durability of an Ultra High Performance Fibre Reinforced Concrete (UHPFRC) under Progressive Aging,. *Cement and Concrete Research*, 2014, 55, 1–13.
266. Webster, M. *The Assessment of Corrosion-Damaged Concrete Structures*. 318.
267. Wu C. L.; Su R. S; Hwang S. J.; Yang Y. S. Shake Table Tests on Reinforced Concrete Short Columns Failing in Shear; 2008.
268. Wu, C. L.; Loh, C. H.; Yang, Y. S. Shaking Table Tests on Gravity Load Collapse of Low-Ductility RC Frames under near-Fault Earthquake Excitation. *Advances in Experimental Structural Engineering* 2006, 725–732.
269. Wu, Y. -F.; ASCE, M.; Hu, B. Shear Strength Components in Reinforced Concrete Members. *J. Struct. Eng.* 2017, 16.
270. Xie, J.; Fu, Q.; Yan, J. -B. Compressive Behaviour of Stub Concrete Column Strengthened with Ultra-High-Performance Concrete Jacket. *Construction and Building Materials* 2019, 204, 643–658. <https://doi.org/10.1016/j.conbuildmat.2019.01.220>.
271. Xu, L.; Pan, J.; Chen, J. Mechanical Behavior of ECC and ECC/RC Composite Columns under Reversed Cyclic Loading. *J. Mater. Civ. Eng.* 2017, 29 (9), 04017097. [https://doi.org/10.1061/\(ASCE\)MT.1943-5533.0001950](https://doi.org/10.1061/(ASCE)MT.1943-5533.0001950).
272. Yang, Y.; Massicotte, B. ; Genikomsou, A. S. ; Pantazopoulou, S. J. ; Palermo, D. Comparative Investigation on Tensile Behaviour of UHPFRC. *Mater Struct* 2021, 54 (4), 147. <https://doi.org/10.1617/s11527-021-01747-1>.
273. Yavari, S.; Elwood, K. J.; Wu, C. L. 2009. Collapse of a Non-Ductile Concrete Frame: Evaluation of Analytical Models. *Earthquake Engineering & Structural Dynamics* No. 38, 225–241.
274. Youm H. S; Lim, W. Y.; Hong, S. G.; Joh, C. Interface Shear Strength between Ultra-High-Performance Concrete and Normal-Strength Concrete. *SJ* 2021, 118 (2). <https://doi.org/10.14359/51729350>.
275. Yuan, F.; Pan, J.; Dong, L.; Leung, C. K. Y. Mechanical Behaviors of Steel Reinforced ECC or ECC / Concrete Composite Beams under Reversed Cyclic Loading. *J. Mater. Civ. Eng.* 2014, 26 (8), 04014047. [https://doi.org/10.1061/\(ASCE\)MT.1943-5533.0000935](https://doi.org/10.1061/(ASCE)MT.1943-5533.0000935).
276. Yuan, R. L.; Cook, J. E. Study of a Class C Fly Ash Concrete. In *Proceedings of 1st International Conference on the Use of Fly Ash, Silica Fume, Slag, and Other*

Mineral Byproducts in Concrete; American Concrete Institute, Detroit, Special Publication: Montebello, PQ, 1983; Vol. SP-79, pp 307–319.

277. Zhang, Y.; Zhu, P.; Liao, Z.; Wang, L. Interfacial Bond Properties between Normal Strength Concrete Substrate and Ultra-High-Performance Concrete as a Repair Material. *Construction and Building Materials* 2020, 235, 117431. <https://doi.org/10.1016/j.conbuildmat.2019.117431>.
278. Zhao, X.; Wu, Y.-F.; Leung, A. Yt.; Lam, H. F. Plastic Hinge Length in Reinforced Concrete Flexural Members. *Procedia Engineering* 2011, 14, 1266–1274. <https://doi.org/10.1016/j.proeng.2011.07.159>.
279. Zhou, X.; Higashi; Yoichi, J.; Weishan, S.; Yasushi. Behavior of Reinforced Concrete Column Under High Axial Load. 1985.
280. Zhou, X.; Satoh, T.; Jiang, W.; Ono, A.; Shimizu, Y. Behavior of Reinforced Concrete Short Column Under High Axial Load. Transactions of the Japan Concrete Institute 1987.
281. Zhu, Z. F.; Wang, W. W. Experimental Study on Mechanical Behaviour of Circular Reinforced Concrete Columns Strengthened with FRP Textile and ECC. *J. Southeast Univ.* 2016, 46, 1082–1087.
282. Zilch, K.; Reinecke, R. Capacity of Shear Joints between High-Strength Precast Elements and Normal-Strength Cast-in-Place Decks; Orlando, USA, 2000.